VOL.
11
1959

THE PHYSICS AND CHEMISTRY OF SOLIDS

AN INTERNATIONAL JOURNAL

VOLUME 11 1959

Editor-in-Chief HARVEY BROOKS *Cambridge, Mass.*

Associate Editors H. B. G. CASIMIR *Eindhoven* · G. J. DIENES *Brookhaven* · JACQUES FRIEDEL *Paris* · E. M. LIFSHITZ *Moscow*

Editorial Advisory Board

U.S.A.: E. N. ADAMS, Pittsburgh · D. ALPERT, Illinois · L. APKER, Schenectady · J. BARDEEN, Illinois · D. S. BILLINGTON, Oak Ridge · R. G. BRECKENRIDGE, Cleveland · LEO BREWER, Berkeley, Calif. · E. BURSTEIN, Penn. J. A. BURTON, New Jersey · N. CABRERA, Virginia · C. C. DANIELSON, Iowa · I. ESTERMANN, Washington, D.C. J. C. FISHER, Schenectady · F. HERMAN, Princeton · CONYERS HERRING, New Jersey · A. R. VON HIPPEL, Cambridge, Mass. · J. H. HOLLOMON, Schenectady · W. V. HOUSTON, Houston · H. B. HUNTINGTON, Troy · H. M. JAMES, Purdue · JOHN G. KIRKWOOD, Yale · C. KITTEL, Berkeley, Calif. · W. KOHN, Pittsburgh · J. A. KRUMHANSL, Cleveland · A. W. LAWSON, Chicago · H. W. LEVERENZ, Princeton · O. T. MARZKE, Pittsburgh · B. T. MATTHIAS, New Jersey · L. R. MAXWELL, Silver Spring · JOSEPH E. MAYER, Chicago · E. W. MONTROLL, Maryland · DAVID PINES, Princeton · H. REISS, New Jersey · J. R. REITZ, Cleveland · A. ROSE, Princeton · O. C. SIMPSON, Argonne R. SMOLUCHOWSKI, Pittsburgh · F. H. SPEDDING, Iowa · D. TURNBULL, Schenectady · J. H. VAN VLECK, Harvard B. E. WARREN, Cambridge, Mass. · Eugene P. WIGNER, Princeton · B. H. ZIMM, Schenectady.

Canada: R. E. BURGESS, Vancouver · D. K. C. MACDONALD, Ottawa.

United Kingdom: A. CHARLESBY, Shrivenham, Berks · W. J. DUNNING and F. C. FRANK, Bristol · H. K. HENISCH, Reading · H. JONES, London · J. W. MITCHELL, Bristol · A. B. PIPPARD, Cambridge · M. H. L. PRYCE, Bristol R. A. SMITH, Malvern · K. W. H. STEVENS, Nottingham · F. C. TOMPKINS, London.

France: E. F. BERTAUT, Grenoble · A. GUINIER, PARIS · LOUIS NÉEL and LOUIS WEIL, Grenoble.

Germany: M. BORN, Bad Pyrmont · ULRICH DEHLINGER, Stuttgart · R. HILSCH and G. LEIBFRIED, Göttingen E. MOLLWO, Erlangen · H. PICK, Stuttgart · M. VON LAUE, Berlin · H. WELKER, Erlangen.

Italy: F. G. FUMI, Pavia.

Czechoslovakia: J. TAUC, Praha.

Japan: TOSHINOSUKE MUTO, Tokyo.

The Netherlands: A. MICHELS and G. W. RATHENAU, Amsterdam. *Sweden:* J. O. LINDE, Stockholm · PER-OLOV LÖWDIN, Uppsala.

Switzerland: G. BUSCH and P. SCHERRER, Zürich. *U.S.S.R.:* G. S. ZHDANOV, Moscow.

PERGAMON PRESS NEW YORK · LONDON · PARIS · LOS ANGELES

NOTES FOR CONTRIBUTORS

I. GENERAL

1. Submission of a paper to the *Journal of the Physics and Chemistry of Solids* will be taken to imply that it represents original research not previously published (except in the form of an abstract or preliminary report), that it is not being considered for publication elsewhere, and that if accepted, it will not be published elsewhere in the same form, in any language, without the consent of the editor-in-chief. It should deal with original research work in the field of the physics and chemistry of solids.

2. Papers should be submitted to the appropriate regional editor (all English-language papers to be sent to the U.S. editor).

3. Papers will be published as quickly as possible after acceptance, and, subject to space being available, should appear in the following issue, if this is due for publication not earlier than three months after the acceptance date. Short communications under the heading of "Letters to the Editor" will receive priority for publication, and will be published in the issue following receipt, if accepted not later than the beginning of the month preceding publication.

4. Fifty free reprints of each paper are supplied. Additional copies can be obtained at a reasonable cost if ordered when proofs are returned. A reprint order form will accompany first proofs.

II. SCRIPT REQUIREMENTS

1. Papers submitted should be concise and written in a readily understandable style. Scripts should be typed and double spaced and submitted in duplicate to facilitate refereeing.

It will be appreciated if authors clearly indicate any special characters used. An abstract, not exceeding 200 words, should be provided in the language of the paper. French and German papers should be submitted with English abstract and titles, but if this is not possible the abstract will be translated by the publishers. To conserve space, authors are requested to mark less important parts of the paper, such as details of experimental technique, methods, mathematical derivations, etc. for printing in small type. The technical description of methods should be given in detail only when such methods are new. Authors will receive proofs for correction when their papers are first set; page proofs will be sent only when the amount of alteration makes it advisable.

2. Illustrations should not be included in the typescript of the paper, and legends should be typed on a separate sheet. Line drawings which require redrawing should include all relevant details and clear instructions for the draughtsman. If figures are already well drawn it may be possible to reproduce them direct from the originals, or from good photo-prints if these can be provided. It is not possible to reproduce from prints with weak lines. Illustrations for reproduction should normally be about twice the final size required. The lettering should be sufficiently large and bold to permit this reduction. Photographs should only be included where they are essential.

3. Tables and figures should be so constructed as to be intelligible without reference to the text. Every table and column should be provided with an explanatory heading. Units of measure must always be clearly indicated. The same data should not be published in both tables and figures. The following standard symbols should be used on line drawings since they are easily available to the printers: ○, ●, +, ×, □, ■, △, ▲, ◇, ◆, ▽, ▼.

4. References are indicated in the text by superior numbers in parentheses, and the full reference should be given in a list at the end of the paper in the following form:

1. HILL R., *J. Iron St. Inst.* **158,** 177 (1948).
2. PEARSON C., *The Extrusion of Metals*. Chapman and Hall, London (1944).

Abbreviations of journal titles should follow those given for *Physics Abstracts*. It is particularly requested that authors' initials, and appropriate volume and page numbers, should be given in every case.

Footnotes, as distinct from literature references should be indicated by the following symbols—*, †, ‡, ‡‡, commencing anew on each page; they should *not* be included in the numbered reference system.

5. Due to the international character of the journal no rigid rules concerning notation and spelling will be observed, but each paper should be consistent within itself as to symbols and units.

VOL
11
195

VOL.
11
1959

VOL
11
195

CONTENTS

NUMBERS 1/2

I. S. JACOBS: Evidence for triangular moment arrangements in $MO \cdot Mn_2O_3$ 1

T. G. BERLINCOURT: Hall effect, resistivity and superconductivity of some metastable uranium-rich alloys . 12

P. ZWIETERING, H. L. T. KOKS and C. VAN HEERDEN: Quantitative aspects of the changes in the electrical conductivity of metals due to chemisorption 18

P. W. ANDERSON: Theory of dirty superconductors 26

M. D. BLUE: Hall coefficients of dilute copper alloys 31

J. DE LAUNAY, R. L. DOLECEK and R. T. WEBBER: Magnetoresistance of copper 37

R. F. BREBRICK: Minimum molar Gibbs free energy and small deviations from stoichiometry in crystalline binary compounds 43

A. GIANSOLDATI, J. O. LINDE and G. BORELIUS: Magnetic susceptibility and electrical resistivity of Au–Mn alloys 46

E. GILLAM: The penetration of positive ions of low energy into alloys and composition changes produced in them by sputtering 55

B. DONOVAN and N. H. MARCH: Screening of point singularities in metals, with particular reference to positron annihilation. 68

T. MORIYA: Piezomagnetism in CoF_2 73

F. ENGLERT: Comportement d'un petit système quantique dans un milieu faiblement dissipatif: quelques applications aux interactions coulombiennes. 78

J. C. ZAHNER and H. G. DRICKAMER: The effect of pressure on the absorption edge in heavy-metal halides . 92

J. S. SMART: Internal consistency of the Heisen–Dirac model for antiferromagnetism 97

P. G. DE GENNES, P. LAFORE et J. P. MILLOT: Amas accidentels dans les solutions solides désordonnées. . 105

H. L. SUCHAN and H. G. DRICKAMER: The effect of pressure on the absorption edge of certain molecular compounds 111

M. ASDENTE et J. FRIEDEL: Calcul de la résistivité des cavités sphériques dans le cuivre 115

M. H. COHEN, W. KÄNZIG and T. O. WOODRUFF: The hyperfine structure of the V_1-center 120

S. D. SMITH, T. S. MOSS and K. W. TAYLOR: The energy-dependence of electron mass in indium antimonide determined from measurements of the infrared Faraday effect 131

A. L. EDWARDS, T. E. SLYKHOUSE and H. G. DRICKAMER: The effect of pressure on zinc blende and wurtzite structures 140

J. F. HON and P. J. BRAY: Nuclear magnetic resonance studies of neutron-irradiated alkali halides. . . . 149

Letters to the Editor:

S. AMELINCKX, J. VENNIK and G. REMAUT: Electrical effects during cyclic stressing of sodium chloride . 170

H. KOELMANS, J. J. ENGELSMAN and P. S. ADMIRAAL: Low-temperature phase transitions in β-$Ca_3(PO_4)_2$ 172

C. N. R. RAO, A. TURNER and J. M. HONIG: Some observations concerning the effect of impurities on the anatase–rutile transition 173

T. MORIYA: Nuclear magnetic resonance frequency shift of ^{59}Co in CoF_2 175

Papers to be published in future issues

Erratum

NUMBERS 3/4

J. A. LEE, P. G. MARDON, J. H. PEARCE and R. O. A. HALL: Some physical properties of neptunium metal—II: A study of the allotropic transformations in neptunium 177

B. J. ALDER, J. R. VAISNYS and G. JURA: Penetration depth of surface effects in molecular crystals. . . 182

R. J. COLLINS and D. A. KLEINMAN: Infrared reflectivity of zinc oxide 190

M. GREEN and K. H. MAXWELL: Adsorption on clean germanium surfaces 195

D. HANEMAN: Photoelectric emission and work fractions of InSb, GaAs, Bi_2Te_3 and Ge 205

H. MEYER and T. A. SCOTT: Pure quadrupole resonance of N_2 in β quinol clathrates 215

J. S. KOUVEL and C. D. GAHAM, Jr.: Exchange anisotrophy in disordered Ni–Mn alloys 220

J. C. PHILLIPS: On the calculation of crystal field parameters 226

J. S. KASPER and J. S. KOUVEL: The antiferromagnetic structure of NiMn 231

F. A. TRUMBORE, E. M. PORBANSKY and A. A. TARTAGLIA: Solid solubilities of aluminium and gallium in germanium 239

D. F. GIBBONS: On the thermal expansion and Grüneisenfactor of vitreous silica 246

P. A. GIGUÈRE: On the anomalous thermodynamic properties of ice 249

D. J. OLIVER: Nuclear magnetic resonance in gallium antimonide 257

R. M. BOZORTH and S. GELLER: Interactions and distributions of magnetic ions in some garnet systems. . 263

VOL. 11 1959

B. S. Chandrasekhar: The Seebeck coefficient of bismuth single crystals 268
H. E. Weaver: Dielectric properties of single crystals of $SrTiO_3$ at low temperatures 274
J. A. Lee, J. P. Evans, R. O. A. Hall and E. King: Some physical properties of neptunium metal—III: The electrical resistivity and thermoelectric power of neptunium metal in the range 300–900°K . . . 278
A. Hoffmann, K. Reuschel and H. Rupprecht: Measurement of the Hall effect and conductivity of superpure silicon 284
C. T. Sah, H. Sello and D. A. Tremere: Diffusion of phosphorus in silicon oxide film 288
J. E. Zimmerman: Low-temperature lattice heat conduction in high-resistivity alloys 299
J. Villain: La structure des substances magnétiques 303
G. Offergeld and J. van Cakenberghe: Détermination de la composition à fusion congruente de semiconducteurs binaires par analyse thermique différentielle. Application à Bi_2Te_3, Sb_2Te_3, Bi_2Se_3 . . 310
G. T. Rado and J. R. Weertman: Spin wave resonance in a ferromagnetic metal 315
Letters to the Editor:
A. J. Frueh, Jr.: On the stability of non-stoichiometric compounds 334
J. I. Kaplan: Magnetic dipole induced normal mode in gadolinium iron garnets 335
M. A. Gintsburg: The theory of spin waves 336
A. M. Clogston, H. Suhl and L. R. Walker: Comments on the above letter by Dr. M. A. Gintsburg . 338
W. G. Spitzer, M. Gershenzon, C. J. Frosch and D. F. Gibbs: Optical absorption in *n*-type gallium phosphide 339
O. P. Manley: Conductivity and structure of Bi_2Te_3 341
K. Toman: The structure of ZnSb–CdSb alloys 342
F. Lukes: The temperature dependence of the refractive index of silicon 344
J. Tauc: Speculation on high voltage photoeffect in ZnS single crystals 345
H. Suhl, B. T. Matthias and E. Corenzwit: Some further results on ferromagnetism in relation to superconductivity 346
Papers to be published in future issues

VOL
11
195

AUTHOR INDEX TO VOLUME 11

Admiraal, P. S. 172
Alder, B. J. 182
Amelinckx, S. 170
Anderson, P. W. 26
Asdente, M. 115
Berlincourt, T. G. 12
Blue, M. D. 31
Borelius, G. 46
Bozorth, R. M. 263
Bray, P. J. 149
Brebrick, R. F. 43
Cakenberghe, J. van 370
Chandrasekhar, B. S. 268
Clogston, A. M. 338
Cohen, M. H. 120
Collins, R. J. 190
Corenzwit, E. 346
Dolecek, R. L. 37
Donovan, B. 68
Drickamer, H. G. 92, 111, 140
Edwards, A. L. 140
Engelsman, J. J. 172
Englert, F. 78
Evans, J. P. 278
Friedel, J. 115
Frosch, C. J. 339
Frueh, A. J., Jr. 334
Graham, C. D., Jr. 220
Geller, S. 263
Gennes, P. G. de 105
Gershenzon, M. 339
Giansoldati, A. 46
Gibbons, D. F. 246
Gibbs, D. F. 339
Giguère, P. A. 249
Gillam, E. 55
Gintsburg, M. A. 336
Green, M. 195
Heerden, C. van 18
Hall, R. O. A. 177, 278
Haneman, D. 205
Hoffmann, A. 284
Hon, J. F. 149
Honig, J. M. 173
Jacobs, I. S. 1
Jura, G. 182
Känzig, W. 120
Kaplan, J. I. 335
Kasper, J. S. 231
King, E. 278
Kleinman, D. A. 190
Koelmans, H. 172
Koks, H. L. T. 18
Kouvel, J. S. 220, 231
Lafore, P. 105
Launay, J. de 37
Lee, J. A. 177, 278
Linde, J. O. 46
Lukes, F. 344
Manley, O. P. 341
March, N. H. 68
Mardon, P. G. 177
Matthias, B. T. 346
Maxwell, K. 195
Meyer, H. 215
Millot, J. P. 105
Moriya, T. 73, 175
Moss, T. S. 131
Offergeld, G. 370
Oliver, D. J. 257
Pearce, J. H. 177
Phillips, J. C. 226
Porbansky, E. M. 239
Rao, C. N. R. 173
Rado, G. T. 315
Remaut, G. 170
Reuschel, K. 284
Rupprecht, H. 284
Sah, C. T. 288
Scott, T. A. 215
Sello, H. 288
Slykhouse, T. E. 140
Smart, J. S. 97
Smith, S. D. 131
Spitzer, W. G. 339
Suchan, H. L. 111
Suhl, H. 338, 346
Tartaglia, A. A. 239
Tauc, J. 345
Taylor, K. W. 131
Toman, K. 342
Tremere, D. A. 288
Trumbore, F. A. 239
Turner, A. 173
Vaisnys, J. R. 182
Vennik, J. 170
Villain, J. 303
Walker, L. R. 338
Weaver, H. E. 274
Webber, R. T. 37
Weertman, J. R. 315
Woodruff, T. O. 120
Zahner, J. C. 92
Zimmerman, J. E. 299
Zwietering, P. 18

VOL.
11
1959

VOL
11
195

J. Phys. Chem. Solids Pergamon Press 1959. Vol. 11. pp. 1–11. Printed in Great Britain.

EVIDENCE FOR TRIANGULAR MOMENT ARRANGEMENTS IN $MO \cdot Mn_2O_3$

I. S. JACOBS

General Electric Research Laboratory, Schenectady, New York

(*Received* 25 *February* 1959)

Abstract—Ferrimagnetic spinel-type compounds frequently have lower spontaneous magnetizations than predicted by the simple Néel model in which tetrahedral *A*-site moments are antiparallel to octahedral *B*-site moments. YAFET and KITTEL (*Phys. Rev.* **87**, 290 (1952)) suggested triangular moment arrangements, in which the moments on one kind of site subdivide into two groups making angles with each other. A linear increase in net magnetization with field at high field and low temperature is expected for the triangular arrangement, but not for the antiparallel ferrimagnetic one. Such an increase, or differential susceptibility at high fields, is observed on magnetization curves at 4·2°K in pulsed fields up to 140 kOe on compounds of the form $MO \cdot Mn_2O_3$ where M is Mn, Co, Zn or Mg, and mixtures thereof. It is absent in Fe_3O_4. These results support a triangular model and enable a direct measurement of the strength of the *B–B* interaction. The observed composition-dependence of the spontaneous moment and the high-field susceptibility are in approximate agreement with simple molecular field models. Assuming the absence of anisotropy fields exceeding 70 kOe, the spontaneous moment of Mn_3O_4 is found to be $1{\cdot}56 \pm 0{\cdot}04$ Bohr magnetons/molecule, with the *B*-site moments sub-divided into groups at angles. From a comparison with magnetic measurements at other temperatures, it is suggested that the net *A*-site moment is dominant.

1. INTRODUCTION

THE spontaneous magnetization at absolute zero of a number of ferrimagnetic compounds with spinel-type structure is significantly lower than predicted by the simple NÉEL[1] model with tetrahedral *A*-site moments antiparallel to octahedral *B*-site moments. An explanation may be the triangular arrangements suggested by YAFET and KITTEL[2]. Specifically they noted that when *A–A* or *B–B* antiparallel interactions are comparable to the *A–B* interaction, the moments on the *A* or *B* sites will divide into two parts, making an angle with each other, but with the resultant moment antiparallel to the moment on the other kind of site (*B* or *A*). Such a configuration is called a triangular arrangement. This idea has been applied qualitatively by GORTER[3] to several series of ferrimagnetic compounds. LOTGERING[4] applied the YAFET–KITTEL theory to "normal" spinels. Also, by examining the low-temperature magnetizations and the variation of magnetization with temperature, he found some evidence for triangular arrangements in the chromium spinels, $MnCr_2O_4$ and $FeCr_2O_4$. Recently, PRINCE[5] concluded that neutron-diffraction data on $CuCr_2O_4$ are consistent with a triangular arrangement. PICKART and NATHANS[6,7], however, also using neutron diffraction, found no evidence for ordered triangular arrangements in nickel and manganese ferrite-chromites whose magnetizations were abnormally low. They note that the neutron diffraction would be insensitive to such arrangements if they exist with only short-range rather than long-range order. In another study, using magnetic and X-ray diffraction measurements, on the series $MnCr_{2-t}Al_tO_4$, EDWARDS[8] has been able to account for the results within the YAFET–KITTEL–LOTGERING theory. The evidence for triangular moment arrangements has been occasionally indirect and frequently difficult to obtain. Thus, alternative suggestions have been and are still being offered to explain the low spontaneous magnetizations.[9]

A consequence of a triangular moment arrangement is that at fields higher than those required for ferrimagnetic domain alignment there should be a linear increase in the net magnetization with field.

This follows from simple consideration of the torques exerted on moments on that kind of site in which subdivision has occurred. By similar reasoning such a differential high-field susceptibility is absent in the simple antiparallel ferrimagnetic arrangement. (It may be noted that this manifestation of a triangular arrangement makes no requirement on the degree of order within the arrangement.) Measurements of magnetization curves at low temperature and in high fields, which are reported herein, show this differential susceptibility in several spinel-type compounds. This observation supports the YAFET–KITTEL suggestion and provides a direct measure of the *B–B* (or *A–A*) interaction.

2. EXPERIMENTAL

The compounds studied are powders of Mn_3O_4 and manganites with the formula $(M_xMn_{1-x})Mn_2O_4$, where M is Co, Zn or Mg. The values of x are roughly 0·5 and 1·0 for each M, and several other selected values. The Mn_3O_4 was prepared by J. S. PRENER of this laboratory from $MnSO_4$ with two firings in air at 1000°C. The other compounds were prepared by standard techniques from carbonates and oxides. They were calcined at 1000°C in air, ground, pressed into pellets, fired at 1150°C in air, and air-quenched. All were checked by X-ray diffraction and chemical analysis (except for one magnesium compound), determining the degree of phase formation and the resulting composition. Both nominal and analyzed compositions are given in Table 1. Spinel-type phase formation was complete, with one exception as noted therein.

The principal measurement made on each of these compounds and for comparison, on the antiparallel ferrimagnetic, Fe_3O_4, was the magnetization curve at 4·2°K. Pulsed fields up to 140 kOe were used, and the method of measurement has been described elsewhere.[10] Coercivity measurements were also made by the same technique, and by conventional ones. Fig. 1 shows results obtained on Mn_3O_4 and Fe_3O_4 powders. The high-field behavior shows a linear increase in magnetization for Mn_3O_4, as well as for all the other manganite compounds studied. This is absent for Fe_3O_4, within the sensitivity of the measuring technique.

In what follows, the observed differential high-field susceptibility is taken as evidence for a triangular arrangement, and the systems are analyzed from this point of view. It does not seem likely that this behavior is a conventional approach to saturation against a large magnetocrystalline anisotropy. The differential susceptibilities of Mn_3O_4 powder at 4·2°K and 20·4°K are nearly equal. The "approaches to saturation" plotted as $1/H^2$ for these temperatures are non-linear and nearly identical, while the coercivities change by an order of magnitude, from 16 kOe at 4·2°K to 1·7 kOe at 20·4°K. The change in coercivity suggests a significant change in magnetocrystalline anisotropy. If the change in moment was merely an approach to saturation, the change, for a given difference in fields, would be much less at 20·4°K than at 4·2°K.

It is important to emphasize, however, that the analysis assumes that the maximum anisotropy field does not exceed about half the maximum measuring field, or about 70 kOe. If the anisotropy field in certain crystallographic directions exceeds that value, then certain modifications are necessary. With the lower anisotropy field, the spontaneous magnetization of these powders is determined by extrapolation to $H = 0$ on the (M, H) curves, from the linear course at high fields. With the higher anisotropy fields, this procedure would be incorrect, and the apparent value should be corrected. If, for example, the anisotropy field within one crystal plane is less than 70 kOe, but a field over 140 kOe is required in a direction perpendicular to that plane, then the true spontaneous magnetization would be about $4/\pi$ times the apparent one. This correction factor would approach unity as the larger anisotropy field decreased toward about 70 kOe. An example of this behavior may be found in the comparison of single-crystal and powder measurements on metallic dysprosium.[11] The differential susceptibility at high fields provides a correct measure of the pertinent exchange interaction when the maximum anisotropy field is less than 70 kOe, for its value is determined from data above that field. For increasing anisotropy fields, the observed susceptibility may be higher at first, but then gradually decreases to a value lower than the correct one characterizing the exchange. In the limit of a very high-anisotropy field, the same factor $4/\pi$ should be invoked, in the symmetry case described above. In the absence of single-crystal studies, these corrections will be neglected, with the reservation that they be applied if subsequent work demonstrates the presence of very high-anisotropy fields. The qualitative features

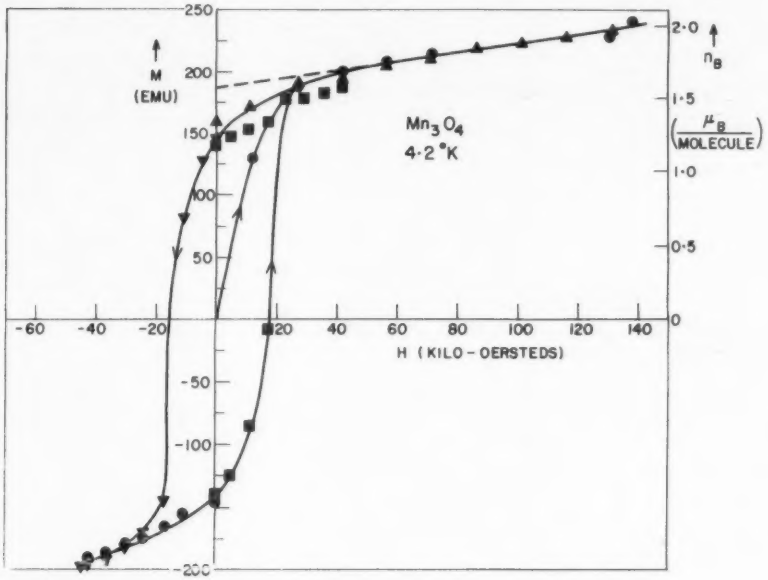

FIG. 1a

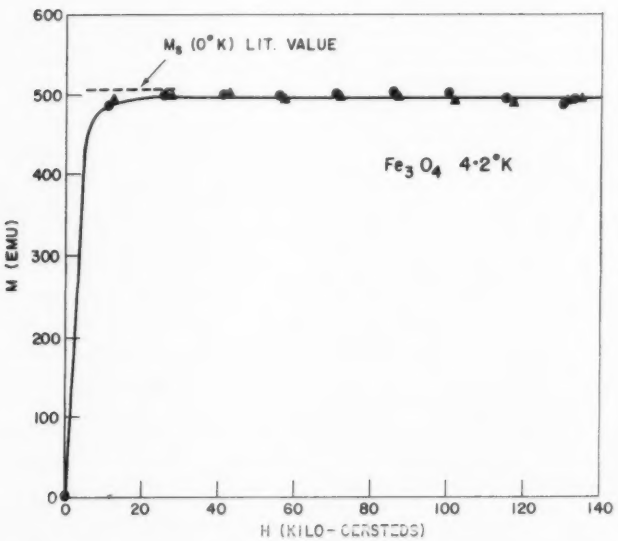

FIG 1b

FIG. 1. Magnetization per unit volume M versus field H for powder samples at 4·2°K. (a) Mn_3O_4; (b) Fe_3O_4.

of the present interpretation remain essentially intact in the presence of anisotropy fields much greater than 140 kOe.

The value of the spontaneous magnetization, M_0 in e.m.u./cm^3, and m_0 in Bohr magnetons (μ_B)/molecule, is presented in Table 1, for each compound. Also given are the intrinsic coercivity, H_{ci}, the volume susceptibility at high fields, κ, and the values corresponding thereto, except for M = Co. Since the tetragonal distortion of these compounds persists up to about 1300°K, the crystal fields acting on the cations are the same in the magnetically ordered and disordered states. Consequently, it is very unlikely that there is a reduced moment in the ferrimagnetic state arising from "spin quenching" in the crystal field.

Table 1. *Chemical analyses and magnetic parameters measured at* 4·2°K

Nominal composition	Analyzed composition*	M_0 (e.m.u./cm^3)	m_0 (μ_B/molecule)	H_{ci} (kOe)†	Vol. susc. ($10^4\kappa$, c.g.s.)	$n\beta$ (molar)
Mn_3O_4	$Mn_3O_{4.01}$	185±5	1·56±0·04	16±1	3·0±0·5	71±12
$Zn_{0.25}Mn_{2.75}O_4$	$Zn_{0.30}Mn_{2.70}O_{4.27}$	122±5	1·05±0·04	0·49	3·5±0·5	61±9
$Zn_{0.5}Mn_{2.5}O_4$	$Zn_{0.52}Mn_{2.48}O_{4.35}$	74±3	0·61±0·03	0·13	2·6±0·4	83±8
$Zn_{0.95}Mn_{2.05}O_4$	$Zn_{0.93}Mn_{2.07}O_{4.38}$	18±5	0·15±0·04	0	2·3±0·3	95±12
$Mg_{0.5}Mn_{2.5}O_4$	——	85±5	0·71±0·05	0·40	3·2±0·6	67±13
$Mg\ Mn_2O_4$	$Mg_{1.01}Mn_{1.99}O_{4.08}$	25±5	0·20±0·04	0	2·7±0·4	82±12
$Co_{0.5}Mn_{2.5}O_4$	$Co_{0.50}Mn_{2.50}O_{4.24}$	92±5	0·76±0·05	16±1	3·0±0·5	71±12
$Co_{0.75}Mn_{2.25}O_4$	$Co_{0.72}Mn_{2.28}O_{4.32}$	55±4	0·46±0·04	30±2	3·0±0·5	72±12
$Co_{0.95}Mn_{2.05}O_4$	$Co_{0.94}Mn_{2.06}O_{3.96}$‡	46±5	0·38±0·05	25±2	3·6±0·5	60±9

* Uncertainty in oxygen content is ±0·01 for Mn_3O_4 and ±0·06 for other compounds.

† Particle size of Mn_3O_4 powder is 1–5 μ. Other compounds screened to $d < 147\mu$ with many particles in 5–10 μ range.

‡ This sample contains an estimated 10 per cent content of second phase as (Co, Mn) O, determined by X-ray diffraction. The resulting composition of spinel-type phase is $Co_{0.92\pm0.02}Mn_{2.08\pm0.02}O_4$. Values of M_0 and κ are corrected for this dilution.

value of the interaction parameter $n\beta$, to be discussed below, which is the reciprocal of the molar differential susceptibility at high fields.

3. DISCUSSION

The compounds investigated are isomorphous with the mineral hausmannite, Mn_3O_4, which is a tetragonally distorted spinel ($c/a = 1{\cdot}16$). The question of cation valence assignment and distribution is approximately resolved. Various studies[12,13] and comparisons of properties have enabled assignment of M^{2+} to the tetrahedral sites, and most recent theoretical interpretations suggest [$Mn^{3+}Mn^{3+}$] as the octahedral site occupation.[14–17] In this view these compounds are "normal" spinels, having but one kind of ion in the octahedral sites.

Susceptibility measurements[18–20] in the paramagnetic state are in accord with the above cation assignment, and with the "spin-only" moment

Mn_3O_4 has a ferrimagnetic Néel temperature at about 43°K,[20,21] and the antiparallel assignment of moments would lead to a spontaneous moment m_0 of $|5-2(4)| = 3\mu_B$/molecule. The value obtained from Fig. 1 and Table 1 is $m_0 = 1{\cdot}56\pm \pm 0{\cdot}04\mu_B$ molecule. Values previously reported are 1·4[22] and 0·8.[20] The lower values are partly understandable inasmuch as the coercivity at 4·2°K is 16 kOe. To obtain a low moment with a triangular arrangement, it is clear that the *B*-site moments must divide, rather than those of the *A*-site. The various antiparallel and triangular ferrimagnetic arrangements are shown schematically in Fig. 2.

To satisfy the observed moment with a triangular arrangement, two choices are possible for the angle ψ_0 (see Fig. 2), depending on whether the net *A*-site moment, $|\boldsymbol{A}|$, is greater or less than the net *B*-site moment, $|\boldsymbol{B}|$. As presented here, the high-field measurements on a compound cannot resolve

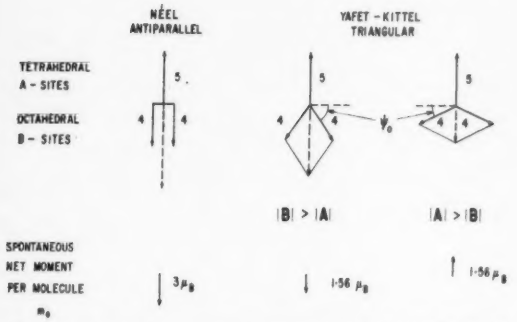

FIG. 2. Ferrimagnetic arrangements in $(Mn^{2+})[Mn_2^{3+}]O_4$ in zero external field. The triangular ferrimagnetic arrangements are drawn to yield the observed spontaneous moment, $m_0 = 1{\cdot}56 \pm 0{\cdot}04\mu_B$.

this ambiguity. In principle, however, much higher field measurements would enable a choice to be made, depending on whether a ferrimagnetic saturation occurred at $3\mu_B$/molecule (if spontaneous $|\boldsymbol{B}|$ exceeds $|\boldsymbol{A}|$), or no saturation occurred until the ferromagnetic one at $13\mu_B$/molecule (if $|\boldsymbol{A}|$ exceeds spontaneous $|\boldsymbol{B}|$). The fields required in these two cases are approximately $5{\cdot}5 \times 10^5$ Oe and $4{\cdot}5 \times 10^6$ Oe, respectively. The projected magnetization curves for Mn_3O_4 for the two cases $|\boldsymbol{A}| \gtrless |\boldsymbol{B}|$ are shown in Fig. 3. For the case of ferrimagnetic saturation at $3\mu_B$/molecule, there is a subsequent transition to ferromagnetic saturation at still higher fields. If the A–A interaction is zero or ferromagnetic, the transition occurs abruptly at a flip-over field of $4{\cdot}15 \times 10^6$ Oe, calculated from interaction constants evaluated below. Alternatively, if the A–A interaction is antiferromagnetic, the transition occurs gradually. It starts at a field somewhat higher than that required for ferrimagnetic saturation, proceeds with a different high-field susceptibility and reaches ferromagnetic saturation at a field exceeding the abrupt flip-over field. (See Appendix, Part 2.)

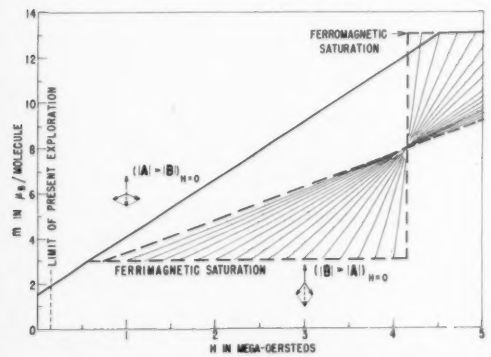

FIG. 3. Magnetization curves for Mn_3O_4, projected beyond the limit of present exploration. Predictions are given for the two triangular arrangements of Fig. 2.

4. ANALYSIS

In proceeding further, the notation and formulation of LOTGERING pertinent to 0°K will be used. The tetrahedral and octahedral site ions may be divided into subgroups A_1 and A_2, and B_1 and B_2, respectively. The Weiss constants relating these are 0, αn, $(1/2)\beta n$, βn and n for the interactions A_iA_i, $A_iA_{j\neq i}$, B_iB_i, $B_iB_{j\neq i}$ and A_iB_j, respectively. The constants are taken as positive for antiparallel interactions. The expressions for the net moment per mole on each kind of site are $\boldsymbol{A} = \boldsymbol{a}_1 + \boldsymbol{a}_2$ and $\boldsymbol{B} = \boldsymbol{b}_1 + \boldsymbol{b}_2$, with $|\boldsymbol{a}_i| = a = (1/2)\,N\mu_B g j_A$ and $|\boldsymbol{b}_i| = b = N\mu_B g j_B$, where N is Avogadro's number, μ_B the Bohr magneton, g the spectroscopic splitting factor (2 for the spin-only state), and j the quantum number (assumed to be spin-only). From a consideration of torques on a given B_i subgroup, arising from Weiss fields $-n\boldsymbol{a}_i$ and $-n\beta\boldsymbol{b}_{j\neq i}$ and an external field $\boldsymbol{H}$, in the direction of the spontaneous moment, it is readily shown (see Appendix, Part 1) that the moment per mole is given by

$$mN\mu_B = \pm 2a(1-1/\beta) + H/n\beta, \qquad (1)$$

where m is the moment/molecule in Bohr magnetons and the + sign infers $\beta > 1$, $|\boldsymbol{A}| > |\boldsymbol{B}|$. In zero field, the spontaneous moment/molecule is

$$m_0 = \pm g j_A (1-1/\beta), \qquad (2)$$

and the corresponding angle is given by

$$\sin\psi_0 = na/n\beta b. \qquad (3)$$

Thus the differential high-field susceptibility measures the B–B interaction, $n\beta$, and the spontaneous moment determines two possible values for β (or ψ_0).

Inasmuch as the high-field susceptibility depends only on the B sites, it should be insensitive to the kind of ion on A sites, if the structural parameters are similar. Measurements listed in Table 1 on the series of compounds for which the B-site

occupation is the same indicate a rough agreement with this premise. If, therefore, it is crudely assumed that $n\beta$ is a constant, the variation of m_0 may be examined with a view to understanding the variation of n, the A–B interaction parameter, with the kind of ion in the A site.

The expression for the moment/mole must first be rewritten to reflect the contributions from the different A-site ions. Let singly and doubly primed quantities refer to the values appropriate to complete occupation of A-sites by the first kind of ion (Mn^{2+}) or the second kind (Co^{2+}, Zn^{2+}, Mg^{2+}), respectively. Then the total A-site moment is given by

$$|A| = 2a = 2[a'(1-x)+a''x], \qquad (4)$$

where x is the fraction of A sites occupied by the second kind of ion. Invoking the simplest assumptions of randomness and additivity, the interaction field from A-site ions acting on B-site ions is given by

$$na = n'a'(1-x)+n''a''x. \qquad (5)$$

With $(n\beta)$ assumed constant, the variation of n with A-site ion, calls for new β-values, such that $(n\beta) = (n'\beta') = (n''\beta'')$. From the considerations leading to equation (1), the moment/mole is now given by

$$mN\mu_B = \pm 2[a'(1-x)(1-1/\beta')+ +a''x(1-1/\beta'')]+H/n\beta, \qquad (6)$$

where the $+$ sign infers that at $x = 0$, $\beta' > 1$ and $|\mathbf{A}| > |\mathbf{B}|$. To complete the analysis one inserts various values for a'', and relationships between n' and n'' (or β' and β'') and compares the resulting prediction with the observed values for m_0.

Non-magnetic A-site ion

This is the case for Zn^{2+} and Mg^{2+}, and is treated with $a'' = 0$. Then equation (6) reduces to

$$m_0 = \pm 2(a'/N\mu_B)(1-x)(1-1/\beta'). \qquad (7)$$

The variation of m_0 is thus expected to be a linear decrease, reaching zero at $x = 1$. This would be accompanied by a linear decrease in $\sin\psi_0$ (see equations (5) and (3)). The two possible values of β' which give the observed m_0 for Mn_3O_4 at $x = 0$, give identical behavior of m_0 as a function of x in equation (7). These two values are related by $1/\beta'_{A>B}+1/\beta'_{B>A} = 2$, and are $\beta'_{A>B} = 1{\cdot}45\pm 0{\cdot}02$ and $\beta'_{B>A} = 0{\cdot}76\pm 0{\cdot}01$. There is no basis here for a choice between $|A| > |B|$ or $|B| > |A|$.

The comparison of results with prediction is shown in Fig. 4 for both Mg and Zn substitution

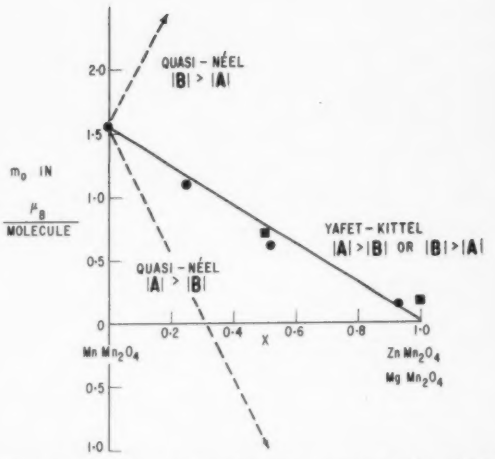

FIG. 4. Variation of spontaneous moment with A-site composition resulting from substitution of non-magnetic Zn^{2+} or Mg^{2+} ions. For "quasi-Néel" models, the B-site moment is held constant. ●—$(Zn_xMn_{1-x})Mn_2O_4$; ■—$(Mg_xMn_{1-x})Mn_2O_4$.

in the A site. There is good agreement with the relation derived for a triangular arrangement. If, instead, a quasi-Néel model were adopted in which the net B-site moment was unchanged, at least initially, when a non-magnetic A-site ion was introduced, then the value of m_0 would either rise steeply near $x = 0$, for $|B| > |A|$, or it would fall steeply for $|A| > |B|$. These linear relations, similar to data on M–Zn ferrite series,[3] are also shown in the figure. These models are clearly eliminated by the observed agreement in favor of the YAFET–KITTEL model in which the A–B interaction field is proportional to the net A-site moment.

Magnetic A-site ion

The Co^{2+} substitution series falls into this category, with $a'' \neq 0$. There is some ambiguity regarding the value of the Co^{2+} moment. One choice is the spin-only value of $gj_A = 3$. This is supported by the work of COSSEE[23], which shows that Co^{2+} in tetrahedral sites has an effective moment only slightly larger than the spin-only value. BONGERS,[19] however, found a Curie constant for $CoMn_2O_4$ rather larger than would be expected. Assuming a spin-only value for Mn^{3+}, a moment value for Co^{2+} may be derived from the Curie constant as $gj_A = 3{\cdot}7$, with j_A as the spin quantum

number and with a g-value larger than 2. While it may be dangerous to rely too heavily on the high-temperature susceptibility data, this represents an extreme second choice. At present a clear choice is not possible, so both values will be considered in the analysis.

A wide variety of relations between n' and n'' (or β' and β'') is possible, in the absence of specific theoretical considerations. Certain of these have been selected on an arbitrary basis, and the resulting expressions for m_0 from equation (6) plotted in Fig. 5 with the experimental data on this series from

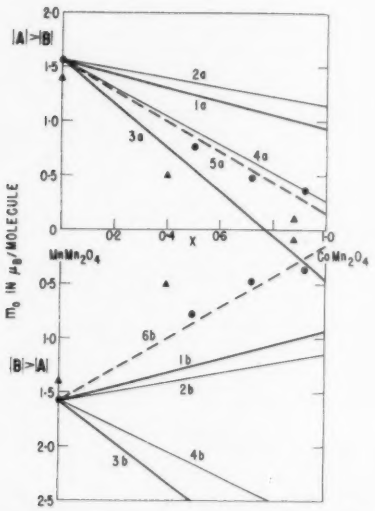

FIG. 5. Variation of spontaneous moment with A-site composition resulting from substitution of magnetic Co^{2+} ion, $(Co_xMn_{1-x})Mn_2O_4$. ●—present work; ▲—WICKHAM and CROFT.[22] Letters a, b distinguish equivalent starting points at Mn_3O_4. Simple models shown with heavy lines for $gj_A(Co^{2+}) = 3{\cdot}0$, with light line for $gj_A(Co^{2+}) = 3{\cdot}7$. Models 1 and 2 assume $n' = n''$. Models 3 and 4 assume $n'a' = n''a''$, or $|B| =$ constant. Dashed lines 5 and 6 are empirical linear fits to data, usable with either value of gj_A.

Table 1. The heavy solid lines refer to simple assumptions using $gj_A = 3$ for Co^{2+}, while the light solid lines refer to similar assumptions using $gj_A = 3{\cdot}7$ for Co^{2+}. The dashed lines are drawn empirically to fit the present data, and may be interpreted with either choice for gj_A. The letters a, b on the labels of these lines signify that the greater net site moment is $|A|$ or $|B|$, respectively, at the start of the line ($x = 0$, Mn_3O_4). Also shown

are data reported by WICKHAM and CROFT[22] for this range of composition. Their values are somewhat lower than those reported here. The apparent discrepancies are expected in view of the high coercivities and the lower measuring fields they used.

Perhaps the simplest assumption to make is $n'' = n'$ (or $\beta'' = \beta'$). It signifies that the A–B interaction field is proportional to the net A-site moment, as assumed for the series with Zn^{2+} and Mg^{2+}. It is plotted in Fig. 5 as 1a, 1b for gj_A $(Co^{2+}) = 3$ and 2a, 2b for gj_A $(Co^{2+}) = 3{\cdot}7$, with the letters a, b indicating the starting points. The β' values used are those given in the previous section. The functional dependence is independent of whether the dominant moment at Mn_3O_4 is $|A|$ or $|B|$. Comparison with the observed data rules out this assumption.

Another simple assumption is that the A–B interaction field does not change when Mn^{2+} is replaced by Co^{2+}. This is written as $n'a' = n''a''$ (or $\beta''a' = \beta'a''$). A consequence of this assumption is that the angle ψ_0, (equation (3)) and hence the net B-site moment, do not change with composition. In a special sense, this is a quasi-Néel model. The predicted behaviors of m_0 are plotted in Fig. 5 as 3a, 3b, and 4a, 4b, the former pair for $gj_A(Co^{2+}) = 3$ and the latter for $gj_A(Co^{2+}) = 3{\cdot}7$. The pair 3$b$ and 4b bear no relation to the observed data, while the pair 3a and 4a exhibit the same trend as the data and bracket them. In a preliminary report,[24] lacking the observation at $x = 0{\cdot}72$, the line 3a was prematurely chosen as giving reasonable agreement with experiment. The difference between lines 3a and 4a illustrates the sensitivity to the value of the Co^{2+} ion moment.

Before considering the dashed lines which are drawn empirically, it should be noted that the functional dependences of 3a and of 4a are not unique. Mirror-image lines of the type b may easily be constructed with the appropriate choices of n''. Such lines would lack only the constancy of the angle ψ_0 and the physical interpretation about the A–B interaction field assumed above.

The lines 5a and 6b are equivalent except for starting point, and are drawn as a *linear* fit to the observations. At $x = 1$, i.e. $CoMn_2O_4$, the extrapolated value of m_0 is $0{\cdot}15\mu_B$/molecule. The proximity of 5a to the lines 3a and 4a suggests that the A–B interaction field and B site angle change

but little, if 5*a* is the correct choice. Thus for 5*a* using gj_A (Co^{2+}) = 3, the description $\psi_0 = 25{\cdot}5°$, $\beta' = 1{\cdot}45$ at $x = 0$ changes to $\psi_0 = 20{\cdot}9°$, $\beta'' = 1{\cdot}05$ at $x = 1$. If the value of gj_A (Co^{2+}) is taken to be about 3·6, just smaller than the value of 3·7 derived above, then ψ_0 remains constant along 5*a*, and the corresponding value of β'' is 1·04. Should 5*a* prove to be a correct representation, it may be possible for neutron-diffraction experiments to distinguish between the two cases just considered. By contrast, the line 6*b* predicts more easily distinguished variation of *B*-site angle. For example, using gj_A (Co^{2+}) = 3, these values are $\psi_0 = 55{\cdot}4°$, $\beta' = 0{\cdot}76$ at $x = 0$ and they change to $\psi_0 = 23{\cdot}2°$, $\beta'' = 0{\cdot}95$ at $x = 1$. The results discussed so far do not enable a choice to be made between lines 5*a* and 6*b*, which are equally good representations of the observed spontaneous moment behavior.

Choice between alternatives

In each of the preceding sections, that for nonmagnetic or for magnetic *A*-site ion substitution, reasonable agreement with experiment was obtained in a way which left an ambiguity. In each case the choice was between $|A| > |B|$ or $|B| > |A|$ at $x = 0$, Mn_3O_4. While neutron-diffraction experiments in progress[25] should clarify the description in detail, it is the aim of this section to examine other magnetic data for a possible resolution of the ambiguity.

In the analysis employed here there are three interaction constants, n, α and β. The low-temperature, high-field measurements yield estimates of β and n, but not of α, which is a measure of the A_iA_j interaction. If α were known, estimates could be made of other magnetic parameters, namely T_a, the asymptotic Curie temperature derived from a linear extrapolation of the reciprocal susceptibility versus temperature curve at high temperatures, and T_f, the temperature at which spontaneous magnetization first appears on cooling from high temperature. A knowledge of α would also give information as to the variation of spontaneous moment with temperature and the positions and types of transitions between 0°K and the paramagnetic state. As discussed by YAFET and KITTEL and by LOTGERING, the triangular ferrimagnetic state (▷) does not, in general, give way to a paramagnetic state (**), and there are intervening states which are antiparallel ferrimagnetic (⇅) or paramagnetic in one subgroup and antiferromagnetic in the other (*↕). Since there are measurements on Mn_3O_4 of T_a[19] and of T_f[20,21] and of moment versus temperature,[21] it may be possible to reconcile the available information in such a way as to suggest a resolution of the ambiguity noted above.

The construction of an α–β diagram for Mn_3O_4, according to the formulation of LOTGERING,[4] is a useful guide. A portion thereof is shown in Fig. 6. It contains the following curves: (1) the curve $\alpha\beta = 1$, for $\alpha\beta < 1$ is

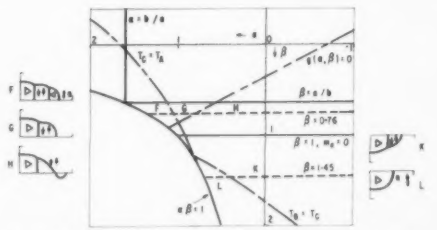

FIG. 6. α–β diagram for Mn_3O_4 according to YAFET and KITTEL, and LOTGERING. α = ratio of interactions A_iA_j/A_iB_j; β = ratio B_iB_j/A_iB_j. Dashed lines for β values yielding observed spontaneous moment. Moment–temperature curves shown for regions of interest *F*, ... *L*.

required for ferrimagnetism; (2) the lines $\beta = a/b$ and $\alpha = b/a$ (values of *a*, *b*, at 0°K), for $\beta > a/b$ is required for a triangular ferrimagnetic with angles between *B*-site ions at 0°K, and similarly for α and *A*-site ions; (3) the curve labelled $T_B = T_C$, where T_B is the ordering temperature for antiferromagnetism on the *B* sites and T_C is the Curie temperature for the appearance of spontaneous moment with an antiparallel ferrimagnetic; (4) the curve $T_A = T_C$, where T_A refers to *A*-site ion antiferromagnetism; (5) the line $\beta = 1$ separating the region which has $|A| > |B|$, $\beta > 1$ at 0°K, from that which has $|B| > |A|$, $\beta < 1$; (6) the line $g(\alpha, \beta) = 0$, which, together with the line $\beta = 1$, bounds the region in which there is a compensation point anomaly in the magnetization; and (7) the lines $\beta'_{A>B} = 1{\cdot}45$ and $\beta'_{B>A} = 0{\cdot}76$, which are the two alternate choices of β to account for the observed m_0. The two β' lines limit the sections to be examined. These are labelled *F*, *G*, *H* along $\beta'_{B>A} = 0{\cdot}76$ and *K*, *L* along $\beta'_{A>B} = 1{\cdot}45$. Region *F* is complex with three different ferrimagnetic configurations, between 0°K and T_f. The other regions are simpler, and the configurations are noted schematically on the diagram. The measurements of KOUVEL and TREAFTIS[21] show no evidence for a compensation point, so region *H* may be eliminated at the start. For the remaining regions, the diagram indicates which α values may be used to estimate particular types of T_f temperatures.

To collate the available information for Mn_3O_4 it is interesting to tabulate the various estimates of n, the A_iB_j interaction constant for the two choices $\beta'_{A>B} = 1{\cdot}45$ and $\beta'_{B>A} = 0{\cdot}76$. These are presented in Table 2. The first of these, n_1, is obtained from the differential high-field susceptibility of Mn_3O_4 listed in Table 1. The asymptotic Curie temperature extrapolations of BONGERS[19] provide other sources. As given by LOTGERING,

$$T_a = -(n/C_{at})(C_A{}^2\alpha/6 + C_B{}^2\beta + 4C_AC_B/3), \quad (8)$$

where C_A and C_B are the usual Curie constants per mole of A- or B-site ions with $C_{at} = (C_A + 2C_B)/3$. For $ZnMn_2O_4$ and $MgMn_2O_4$, C_A is zero and the value of T_a gives an independent estimate of $n\beta$, from which n_2 is computed. (This estimate neglects certain interactions within B-site subgroups.[4,8]) The T_a value for Mn_3O_4 may be used to estimate a lower limit for n, because the value of α has an upper bound at $1/\beta$. This is listed as n_3. In a related way the observed T_f may be used to calculate upper limits for n, listed as n_4, using the formulas appropriate to the particular region on the α–β diagram.[4] All the calculations for Table 2 use the spin-only values of C_A and C_B for Mn_3O_4.

*Table 2. Values of A_iB_j interaction constant, n, for Mn_3O_4 estimated from various sources.**

Case	β'	n_1	n_2	n_3	n_4
$\|A\| > \|B\|$	1·45	49±8	69±5	> 56	< 29
$\|B\| > \|A\|$	0·76	94±15	131±8	> 64	< 37

* n_1 from observed high-field susceptibility of Mn_3O_4
n_2 from asymptotic Curie temperature of $(Mg_xZn_{1-x})Mn_2O_4$
n_3 from asymptotic Curie temperature of Mn_3O_4
n_4 from ferrimagnetic Curie temperature of Mn_3O_4.

Considering the first three estimates of n for the two cases, those for $\beta' = 1{\cdot}45$ fall into a nearly overlapping group. Those for $\beta' = 0{\cdot}76$ seem to spread somewhat. It would improve if n_3 of this group were brought into the range between n_1 and n_2. However, this requires a value of α of $-2{\cdot}4$, placing it in the anomalous region H, which is ruled out. With regard to n_4, there is a disagreement of a factor of two from the other estimates in the former case, and by a greater factor in the latter case. This demonstrates a weakness in the ability of the simple theory to account for the observed behavior over a wide range of temperature. From another point of view, the disagreement may not be considered as too bad, and may then be taken to suggest a preference for the configuration with the value $\beta = 1{\cdot}45$ corresponding to a dominant moment on the A sites in Mn_3O_4. Stronger resolution of the ambiguity is desirable and may be provided by neutron-diffraction studies. The value of n_4 closest to the other estimates is obtained from region L of Fig. 6. With the suggested choice, the Mn–Co series of Fig. 5 is best represented by line 5*a* rather than line 6*b*.

5. CONCLUSION

The observation of a high-field differential susceptibility at low temperature in ferrimagnetic spinel-type compounds is shown to be a useful technique for detecting and measuring the triangular moment arrangements proposed by YAFET and KITTEL. As applied to a series of tetragonally distorted spinels ($MO \cdot Mn_2O_3$), with "normal" cation distribution, the measured high-field susceptibility is in approximate agreement with the prediction of the triangular array model. The behavior of the spontaneous moment as a function of the M-ion composition is amenable to description with simple molecular-field assumptions. Although certain fundamental ambiguities arise in the interpretation, it is possible to resolve them by reconciliation with magnetic measurements at other temperatures. It is concluded that Mn_3O_4 has a triangular moment arrangement at 4·2°K, in which the B-site moments are subdivided into two parts† making angles with each other. Assuming the absence of anisotropy fields exceeding 70 kOe, the net spontaneous moment of Mn_3O_4 is found to be $1{\cdot}56 \pm 0{\cdot}04 \mu_B$/molecule, and it is suggested that the A-site moment exceeds the net B-site moment.

Acknowledgements—The author wishes to thank C. P. BEAN, J. S. KASPER and R. E. CARTER for helpful discussions on the magnetic, crystallographic and chemical aspects of this study. Mrs. E. FONTANELLA and P. E. LAWRENCE rendered valuable assistance at all stages of sample preparation and measurement.

† If required by symmetry considerations, these two parts may be changed to four parts, without any alteration of the analysis.

APPENDIX

(1) The derivation of equation (1) proceeds from a consideration of the torques acting on the spin moment of the B_1 subgroup from the Weiss fields and the external field $\boldsymbol{H}$ pointing along the net moment direction. Using the definitions given just prior to equation (1), and with reference to the two triangular arrangements in Fig. 2, the Weiss field on a B_1 group moment is

$$\boldsymbol{h}_{B_1} = -n[\boldsymbol{a}_1+\boldsymbol{a}_2+(1/2)\beta\boldsymbol{b}_1+\beta\boldsymbol{b}_2].$$

The condition for equilibrium of the torques is given by

$$\boldsymbol{b}_1\times(\boldsymbol{h}_{B_1}+\boldsymbol{H}) = 0,$$

or

$$2nab\sin(\pi/2-\psi) = \pm Hb\sin(\pi/2\pm\psi)+n\beta b^2\sin 2\psi,$$

where the upper sign holds for $|\boldsymbol{A}| > |\boldsymbol{B}|$ and the lower for $|\boldsymbol{B}| > |\boldsymbol{A}|$. This reduces to

$$\sin\psi = (2na\pm H)/2n\beta b,$$

which shows the field-dependence of the angle, whose zero field value is given by equation (3). The net moment per mole is given by

$$mN\mu_B = |\boldsymbol{A}+\boldsymbol{B}| = \pm(2a-2b\sin\psi),$$

with the signs as designated above. Upon substitution for $\sin\psi$, equation (1) is obtained,

$$mN\mu_B = \pm 2a(1-1/\beta)+H/n\beta.$$

(2) The various "saturation" fields, H_s, and the ferrimagnetic-to-ferromagnetic transition fields of Fig. 3 are calculated from the expressions in Part (1) above. The ferromagnetic saturation occurs in the case where $|\boldsymbol{A}| > |\boldsymbol{B}|$ at $H = 0$. As in the preceding, the upper sign in the equations refers to this case. The ferrimagnetic saturation, to which the lower sign refers, occurs when $|\boldsymbol{B}| > |\boldsymbol{A}|$ at $H = 0$. The values of ψ at these saturation conditions are $\mp\pi/2$, or $\sin\psi = \mp 1$. Substituting into the expression for $\sin\psi$, one finds

$$H_s = 2n\beta b\pm 2na.$$

To avoid confusion between the different interaction parameters of the two cases, H_s should be rewritten in terms of the directly measured quantities $(n\beta)$ and m_0. Using equation (2) for m_0, H_s is given as

$$H_s = (n\beta)(2b\pm 2a-m_0N\mu_B)$$
$$= (n\beta)N\mu_B(2g_Bj_B\pm g_Aj_A-m_0).$$

For ferromagnetic or zero A_iA_j interaction the transition from ferrimagnetic to ferromagnetic states occurs abruptly at a flip-over field, H_f. This is obtained by equating the external field to the Weiss field acting on the A-site moments from the B-site moments in their saturated ferrimagnetic configuration. Thus

$$H_f = 2nb,$$

and, in terms of directly measured quantities,

$$H_f = (n\beta)N\mu_B(g_Bj_B/g_Aj_A)(2m_0+2g_Aj_A).$$

When the A_iA_j interaction is antiferromagnetic, considerations like those used in Part (1), above, show that the transition from ferrimagnetic to ferromagnetic saturation occurs gradually. It starts at a field $H = 2nb-2n\alpha a$ which is greater than that required for ferrimagnetic saturation of the original triangular ferrimagnetic. The magnetization increases by an analogous process to that occurring at the lower fields, with a differential susceptibility of $1/n\alpha$. Ferromagnetic saturation is finally attained at a field $H = 2nb+2n\alpha a$. Since α is not easily determined by direct measurements, these expressions have not been rewritten.

REFERENCES

1. Néel L., *Ann. Phys.* (*Paris*) **3**, 137 (1948).
2. Yafet Y. and Kittel C., *Phys. Rev.* **87**, 290 (1952).
3. Gorter E. W., *Philips Res. Rep.* **9**, 295, 321, 403 (1954).
4. Lotgering F. K., *Philips Res. Rep.* **11**, 190, 337 (1956).
5. Prince E., *Acta Cryst., Camb.* **10**, 554 (1957).
6. Pickart S. J., *Bull. Amer. Phys. Soc.* **3**, 42 (1958); see also *NAVORD Rep.* 6101, U.S. Naval Ordnance Laboratory, White Oak, Maryland.
7. Pickart S. J. and Nathans R., *Bull. Amer. Phys. Soc.* **3**, 231 (1958).
8. Edwards P. L., *Bull. Amer. Phys. Soc.* **3**, 43 (1958); see also *NAVORD Rep.* 6099, U.S. Naval Ordnance Laboratory, White Oak, Maryland.
9. Baltzer P. K. and Wojtowicz P. J., *J. Appl. Phys.* **30**, p. 27s (1959).
10. Jacobs I. S. and Lawrence P. E., *Rev. Sci. Instrum.* **29**, 713 (1958).
11. Behrendt D. R., Legvold S. and Spedding F. H., *Phys. Rev.* **109**, 1544 (1958).
12. Zn: Mason B., *Amer. Min.* **32**, 426 (1947); Romeijn F. C., *Philips Res. Rep.* **8**, 304 (1953).
13. Mg: Kasper J. S., unpublished work.
14. Goodenough J. B. and Loeb A. L., *Phys. Rev.* **98**, 391 (1955).
15. Dunitz J. D. and Orgel L. E., *J. Phys. Chem. Solids* **3**, 20, 318 (1957).
16. McClure D. S., *J. Phys. Chem. Solids* **3**, 311 (1957).
17. Goodenough J. B., *International Colloquium on Magnetism, Grenoble* (July 1958), Paper 28; *J. Phys. Radium*, to appear (1959).
18. Honda K. and Soné T., *Sci. Rep. Tohoku Imp. Univ.* **3**, 139 (1914).
19. Bongers P. F., Thesis, Leiden (1957), made available through the courtesy of Dr. G. H. Jonker.

20. Borovik–Romanov A. S. and Orlova M. P., *Zh. Eksper. Teor. Fiz.* **32,** 1255 (1957); translation *Sov. Phys. JETP* **5,** 1023 (1957).
21. Unpublished measurements on material used in this study, kindly made by J. S. Kouvel and H. N. Treaftis.
22. Wickham D. G. and Croft W. J., Lincoln Lab. Solid State Q.P.R., May, 1958, reported in ref. (17); *J. Phys. Chem. Solids* **7,** 351 (1958).
23. Cossee P., Thesis, Leiden (1956).
24. Jacobs I. S., *J. Appl. Phys.* **30,** p. 301*s* (1959).
25. Kasper J. S., *Bull. Amer. Phys. Soc.* **4,** 178 (1959).

VOL.
11
1959

J. Phys. Chem. Solids Pergamon Press 1959. Vol. 11. pp. 12–17. Printed in Great Britain.

HALL EFFECT, RESISTIVITY AND SUPERCONDUCTIVITY OF SOME METASTABLE URANIUM-RICH ALLOYS*

T. G. BERLINCOURT

Atomics International Division, North American Aviation, Inc., Canoga Park, California

(*Received* 30 *January* 1959)

Abstract—The Hall effect and electrical resistivity of metastable γ-phase (b.c.c.) binary alloys of uranium containing 11·6, 21·7 and 30·5 atomic percent molybdenum and 22·2 atomic percent niobium have been studied between $\sim$ 1°K and room temperature in magnetic fields up to 30 kG. The Hall coefficients of the latter three alloys were positive and only weakly temperature-dependent, while the Hall coefficient of the 11·6 atomic percent molybdenum alloy was strongly dependent upon both temperature and magnetic field. All samples exhibited superconductivity below $\sim$ 2°K and were characterized by weak negative temperature coefficients of resistivity between the transition temperatures and room temperature. Magnetic fields of $\sim$ 30 kG were required to restore the normal resistivity at 1·2°K. The bearing of the results of this investigation on an understanding of the electronic structure of the γ-phase is discussed.

1. INTRODUCTION

FROM 770°C to the melting point, uranium exists as a b.c.c. phase (γ-phase).[1] This phase can be retained at room temperature in uranium-rich binary alloys containing certain amounts of molybdenum and niobium provided that: (1) the sample is quenched from high temperatures or (2) the sample is irradiated in a nuclear reactor.[2–4] In the latter instance, the transformation to the metastable γ-phase is believed to take place via the Brinkman displacement spike mechanism.[3,5] The present investigation[6] was prompted by a report[3,4] of unusual behavior in the electrical resistivity versus temperature relation for the γ-phase alloys; viz. the existence of a small *negative* temperature coefficient of resistivity between liquid-helium temperature and room temperature. Such behavior is not confined to the metastable uranium alloys, for it has been observed above liquid-nitrogen temperature for b.c.c. phases in the titanium–niobium system by AMES and MCQUILLAN[7], in the titanium–vanadium system by BROTZEN *et al.*[8] and in the titanium–molybdenum system by YOSHIDA and TSUYA[9]. In the present instance it was believed that Hall-effect measurements on a series of alloys in which ρ (electrical resistivity) is nearly independent of T (temperature) should shed some light on the problem of the importance of electron scattering on the Hall coefficient R. As already noted,[10] the R versus T curves for uranium, titanium and copper are characterized by weak temperature-dependence in the residual- and linear-resistivity regions and strong temperature-dependence in the small-angle, electron-phonon scattering region. If such effects are indeed the consequence of changes in electron-scattering mechanisms, only weak temperature-dependence of R might be expected for the metastable γ-phase alloys, provided of course that temperature-induced changes of charge-carrier concentration are absent. The results to be described are in general accord with this view. In addition, the Hall data have interesting bearing on an understanding of the γ-phase and its unusual properties. Recently, CHANDRASEKHAR and HULM[11,12] (hereafter referred to as CH) and LOASBY[13] have proposed possible explanations for the unusual ρ versus T relation for the γ-phase alloys. These explanations hypothesize electronic structures which appear to be inconsistent with the Hall data obtained in this investigation.

* This research was supported by the U.S. Atomic Energy Commission.

The superconductivity detected in the present investigation was also independently discovered by CH and is of particular interest in light of the anomalous resistivity and metastability of the γ-phase.

2. SAMPLES AND EXPERIMENTAL METHODS

The raw materials for the alloys consisted of reactor grade uranium, Johnson-Matthey molybdenum, and Murex niobium. Samples were machined from argon-arc-melted buttons of the compositions listed in Table 1. They were then sealed into evacuated Vycor capsules, held at 930°C for periods up to 2 hr, and water-quenched without fracture of the capsule. The stabilization of the b.c.c. γ-phase structure was confirmed by X-ray examination, and the corresponding lattice parameters are listed in Table 1. Although BOSTROM and HALTEMAN[3] reported that water-quenching in the composition range 4–14 a/o (atomic percent) Mo may produce a diffusionless phase change to a base-centered orthorhombic α'-phase, no evidence was found for any appreciable quantity of this phase in the 11·6 a/o Mo sample.

The cryogenic, magnetic and electrical apparatus and procedures used in this investigation have been described elsewhere.[14,15]

3. EXPERIMENTAL RESULTS

(a) *Electrical resistivity and Hall effect*

The normal-state resistivity data are presented in Fig. 1 and, except for the case of the 11·6 a/o Mo alloy, are in good accord with the data of CH.[12]

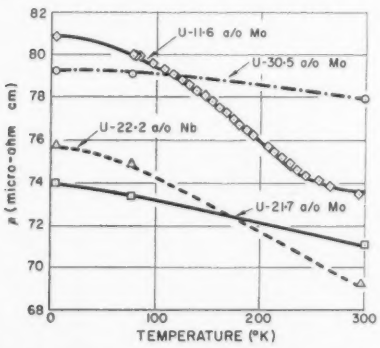

FIG. 1. Electrical resistivity versus temperature curves for metastable γ-phase U–Mo and U–Nb alloys.

In the present investigation all four samples exhibited negative temperature coefficients of resistivity, supporting the X-ray evidence for the γ-phase structure of the 11·6 a/o Mo alloy. On the other hand, CH reported a positive coefficient between 4·2 and 77°K and a negative coefficient between 77°K and room temperature for a sample of identical composition, which could indicate the presence of mixed phases.

The Hall coefficient data were less suggestive of similar structure for the 11·6 a/o Mo sample. Although three of the samples exhibited Hall voltages which were strictly linear in H (magnetic field strength) and only weakly temperature-dependent, the Hall coefficient for the 11·6 a/o Mo sample was strongly dependent upon both H and T. Nevertheless, in all instances, the Hall coefficients were positive, indicating dominance of hole conduction. The Hall coefficient data for the three "well-behaved" samples are compared with data[15]

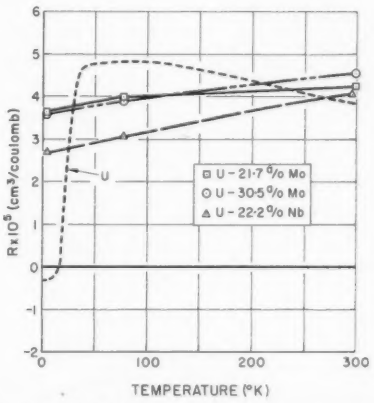

FIG. 2. Hall coefficient versus temperature curves for metastable γ-phase U–Mo and U–Nb alloys. Data[15] for pure α-uranium are included (dashed line) for comparison.

on pure α-uranium in Fig. 2. The close agreement with the α-uranium data at room temperature is somewhat surprising (and probably fortuitous) in view of the differences in crystal structure. The fact that the data for the 21·7 and 30·5 a/o Mo samples are nearly identical at all temperatures suggests that uranium and molybdenum contribute charge to the conduction process in much the same way. Thus the data appear to contradict LOASBY's conclusion[13] that contributions of four

and six electrons are made respectively by uranium and molybdenum. The lower Hall coefficient values for the niobium alloy imply that niobium contributes in a different way, which on naïve reasoning is not surprising, since uranium and molybdenum each have six electrons outside closed shells, whereas niobium has five.

The H- and T-dependences of the Hall coefficient of the 11·6 a/o Mo sample are shown in Fig. 3.

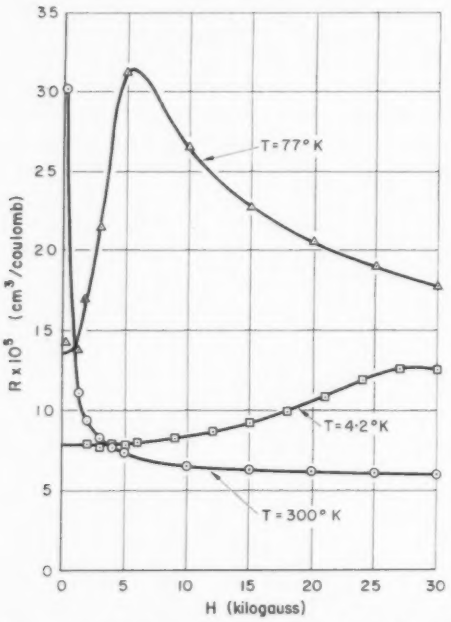

FIG. 3. Hall coefficient versus magnetic field curves at three temperatures for a metastable γ-phase uranium alloy containing 11·6 a/o Mo.

Because these results are so unusual for a metal in which the relaxation time is obviously very short, the sample was remounted and measured a second time at all three temperatures. The results were reproduced with a maximum difference of ~ 3 per cent at low fields and general agreement to 1 per cent. The observed behavior is suggestive of a very sensitive temperature-dependent electronic-structure condition which might characterize instability of the γ-phase and favor the transformation to the α'-phase.

An explanation of the similarity in the electrical-resistivity behavior for all alloys despite differing Hall-effect behavior involves various possibilities. As already emphasized,[15] the Hall effect appears to be much more sensitive to details of the electronic structure than is the resistivity. Because of the anomalously high resistivities of the γ-phase alloys at low temperatures, it appears that scattering processes are so dominant in determining the resistivity that the details of the electronic structure are of only secondary importance. It should be mentioned in this connection that for such a sensitive electronic condition as apparently exists in the 11·6 a/o Mo sample a sizeable magnetoresistance might be expected. However, none was observable for this alloy nor for the other alloys studied.

(b) *Superconductivity*

Because an excellent discussion of the superconductivity of the γ-phase alloys has already been given by CH,[12] the results of the present investigation will be described only briefly with emphasis on the additional aspects studied.

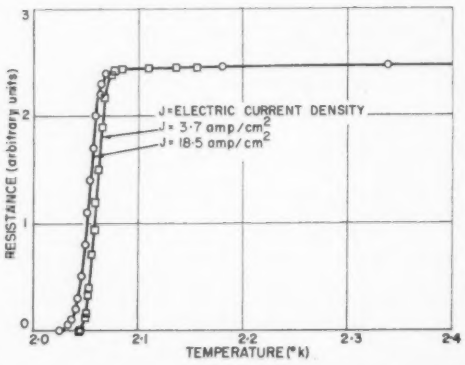

FIG. 4. Superconducting transitions for a metastable γ-phase uranium alloy containing 21·7 a/o Mo. This is typical of all four alloys studied.

All four alloys underwent superconducting transitions in the vicinity of 2°K. A typical resistive transition is illustrated for the 21·7 a/o Mo alloy in Fig. 4, and transition temperatures (T_c) for all four alloys are listed in Table 1. Because the transitions were dependent upon measuring current, and the measurements were carried out in the residual field (~ 200 G) of the electromagnet used for the Hall measurements, the transition temperature values listed in Table 1 are only approximate and correspond to the temperatures at

Table 1. Compositions, dimensions, lattice parameters and superconducting transition temperatures (resistive) of metastable γ-phase uranium alloy samples.

Sample	Dimensions (mm)	Lattice parameter (Å)	T_c (°K)
U–11·6 a/o Mo	32×8×0·289	3·44	1·85
U–21·7 a/o Mo	32×8×0·356	3·40	2·06
U–30·5 a/o Mo	32×8×0·264	3·39	1·97
U–22·2 a/o Nb	24×3·2×0·275	3·45	1·98

which the resistivities dropped to one-half their normal values for the smallest measuring current density (~4 A/cm²). Despite these uncertainties the temperatures listed in Table 1 are in fairly good accord with those obtained by CH, using the more reliable magnetic-moment-measurement technique. The transitions were unusually narrow (a few hundredths of a degree wide) for alloys despite the broadening effect of the residual field of the magnet. Narrow transitions are usually associated with very homogeneous, strain-free samples, while the metastable γ-phase alloys are undoubtedly highly strained.

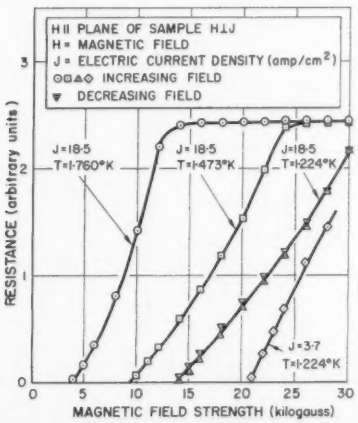

FIG. 5. Magnetic-field-induced superconducting transitions for a metastable γ-phase uranium alloy containing 21·7 a/o Mo. This is typical of the 30·5 a/o Mo and 22·2 a/o Nb samples as well.

Each alloy was restored to the normal state at several temperatures by the application of a magnetic field. The results for the 21·7 a/o Mo sample appear in Fig. 5 and are typical of the 30·5 a/o Mo and 22·2 a/o Nb samples as well. The character of the magnetic transitions for the 11·6 a/o Mo alloy was different, as illustrated in Fig. 6. In all instances, hysteresis effects were almost negligible,

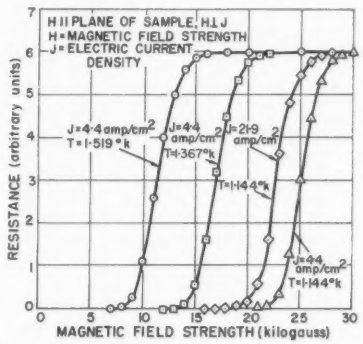

FIG. 6. Magnetic-field-induced superconducting transitions for a metastable γ-phase uranium alloy containing 11·6 a/o Mo.

the transitions were strongly dependent upon measuring current, and unusually high magnetic fields were required for the restoration of the normal resistance. The latter circumstance explains the good agreement between the values of T_c obtained by CH and the values obtained in the presence of a fairly sizeable residual field in the present investigation. The apparent large critical fields are in keeping with the commonly accepted belief that small filaments of material may remain superconducting at fields which destroy superconductivity in the main bulk of the sample.

4. DISCUSSION

Although the results obtained in this study fail

to provide a satisfactory explanation for the unusual electrical-resistivity behavior of the γ-phase alloys, the data do provide a basis for criticism of various proposed explanations. One such explanation is LOASBY's suggestion[13] that the electrical resistivity might be explained on the proposition of an electron-overlap condition in which more energy states become available for conduction electrons as the temperature and the population of a second zone are increased. Such a condition would most likely lead to a strong temperature-dependence of the Hall coefficient in contrast to the behavior of three of the alloys studied herein.

CH[12] have proposed a possible explanation based on the assumption of a broad, low density-of-states band and a narrow overlapping band characterized by a high density of states which varies rapidly with energy at the Fermi level. According to this explanation, the current is carried mainly by the broad-band electrons, the relaxation time for these electrons being inversely proportional to the density of states for the narrow band. H. JONES[16] has derived an expression for the temperature-dependence of resistivity for such a situation in terms of the slope and the curvature of the density-of-states curve for the narrow band at the Fermi level. As pointed out by CH, these parameters could have values in the γ-phase which would account for the observed resistivity behavior. However, such parameters would lead to a strongly temperature-dependent relaxation time for the broad-band electrons and a correspondingly strong temperature-dependence of the Hall coefficient, in contradiction with observation.

On the more constructive side, the present investigation has indicated that, despite recognized difficulties[15] in the interpretation of Hall data, the sensitivity of the Hall effect to details of the electronic structure is of considerable value in studies of the γ-phase alloys. It now appears that uranium and molybdenum contribute to the electronic structure in much the same manner in the γ-phase alloys, whereas niobium contributes in a slightly different way. Furthermore, the unusual resistivity behavior appears to be insensitive to details of the electronic structure, arising instead because of some gross characteristic common to the b.c.c. phases of all the systems U–Mo, U–Nb, U–Zr, Ti–Nb, Ti–Mo, and Ti–V. Because all of these alloys involve transition metals, it is natural to suspect a magnetic effect such as the spin-disorder electron-scattering effect recently reviewed by COLES[17]. Unfortunately, on the assumption of Mathiessen's rule (which might not be justified), it would not be possible to account for the negative temperature coefficient with a temperature-independent spin-disorder contribution. On the other hand, the importance of localized spin states in relation to resistivity, superconductivity and ferromagnetism has recently been clarified to such an extent[18–20] that it is reasonable to suspect that further developments in this direction might resolve the γ-phase problem.

Acknowledgements—The contributions of R. CHANG and J. D. MCCLELLAND in the preparation of samples are gratefully acknowledged. I am also indebted to D. B. BOWEN for suggesting these alloys as fruitful subjects for study.

Note added in proof: Recent measurements by R. R. HAKE, D. H. LESLIE and T. G. BERLINCOURT on b.c.c. alloys of the Ti–Mo system have revealed electron transport properties qualitatively very similar to those reported above for b.c.c. uranium alloys. One sample (18·3 atomic per cent Mo) exhibited zero resistance at 1·2°K in a magnetic field of 30 kG for a measuring current density of 34 A/cm^2.

REFERENCES

1. KATZ J. J. and RABINOWITZ E., *The Chemistry of Uranium* (National Nuclear Energy Series, Division VIII) Vol. 5, Part 1. McGraw-Hill, New York (1951).
2. KONOBEEVSKY S. T., PRAVDYUK N. F. and KUTAITSEV V. I., *Proceedings of the International Conference on the Peaceful Uses of Atomic Energy* Vol. 7, p. 433. United Nations, New York (1956).
3. BLEIBERG M. L., JONES L. J., and LUSTMAN B., *J. Appl. Phys.* **27,** 1270 (1956).
4. BOSTROM W. A. and HALTEMAN E. K., in *Advances in Nuclear Engineering*. Vol. 2, p. 184. Pergamon Press, London (1957).
5. BRINKHAM J. A., *J. Appl. Phys.* **25,** 961 (1954).
6. A brief account of a portion of this work appears in the *Proceedings of the Fifth International Conference on Low-Temperature Physics and Chemistry* pp. 492–6. University of Wisconsin Press (1958).
7. AMES S. L. and MCQUILLAN A. D., *Acta Met.* **2,** 831 (1954).
8. BROTZEN F. R., HARMON E. L., and TROIANO A. R., *Trans. Amer. Inst. Min. (Metall.) Engrs.* **203,** 413 (1955).
9. YOSHIDA S. and TSUYA Y., *J. Phys. Soc. Japan* **11,** 1206 (1956).

10. BERLINCOURT T. G., *Bull. Amer. Phys. Soc.* **2,** 136 (1957).
11. HULM J. K. and CHANDRASEKHAR B. S., *Proceedings of the Fifth International Conference on Low-Temperature Physics and Chemistry* pp. 280–2. University of Wisconsin Press (1958).
12. CHANDRASEKHAR B. S. and HULM J. K., *J. Phys. Chem. Solids* **7,** 259 (1958).
13. LOASBY R. G., *Proc. Phys. Soc.* **72,** 429 (1958).
14. BERLINCOURT T. G., *Phys. Rev.* **112,** 381 (1958).
15. BERLINCOURT T. G., *Phys. Rev.* (in the press).
16. JONES H., *Handbuch der Physik* Vol. 19, p. 227. Springer, Berlin (1956).
17. COLES B. R., *Advances in Phys.* **7,** 40 (1958).
18. MATTHIAS B. T., SUHL H. and CORENZWIT E., *Phys. Rev. Letters* **1,** 92 (1958).
19. ANDERSON G. S. and LEGVOLD S., *Phys. Rev. Letters* **1,** 322 (1958).
20. MATTHIAS B. T., SUHL H. and CORENZWIT E., *Phys. Rev. Letters* **1,** 499 (1958).

OL.
11
959

J. Phys. Chem. Solids Pergamon Press 1959. Vol. 11. pp. 18–25. Printed in Great Britain.

QUANTITATIVE ASPECTS OF THE CHANGES IN THE ELECTRICAL CONDUCTIVITY OF METALS DUE TO CHEMISORPTION

P. ZWIETERING, H. L. T. KOKS and C. VAN HEERDEN

Staatsmijnen in Limburg, Centraal Laboratorium, The Netherlands

(*Received* 25 *November* 1958; *revised* 26 *January* 1959)

Abstract—Measurements of the change in electrical conductivity of evaporated metal films caused by chemisorption on the surface are described. The quantitative results have made it possible to draw certain conclusions as to the effective valency of the metal surface atoms and the number of bonds formed for each adsorbed molecule. These conclusions are in agreement with the information obtained from the total number of adsorbed molecules per cm^2 of true surface area at full coverage. In agreement with the experimental results of other investigators, a change in bond type for hydrogen on iron and nickel at higher coverages is found.

1. INTRODUCTION

THE study of chemisorption phenomena on evaporated metal films of high purity has provided much valuable information on the fundamentals of chemisorption.

Besides accurate data about the strength of the chemisorptive bond as a function of relative coverage,[1,2] more information about the nature of this bond has been gained by studying the change in metallic properties of the adsorbent as a result of the chemisorption process. The direction and the strength of the dipole moment of the bond have been determined from measurements of the change in the thermoionic work function, or the photoemission, of the metal.[3–7] These data, combined with magnetic measurements on bulk catalysts, give strong evidence for the highly covalent character of the bond.[8] In addition to these methods, measurements of the changes in electrical conductivity of the metal film have also been applied to the study of chemisorption phenomena,[6,9,10] but quantitative data were still lacking.

The present paper reports quantitative results so far obtained with titanium, iron and nickel films, and such conclusions concerning the chemisorptive bond formed and the structure of this type of metal film as can be drawn from the results. Part of this work has already been published in preliminary form.[11]

2. EXPERIMENTAL

As the experimental set-up was only very briefly treated in our first paper, a more detailed description is given here.

The apparatus is shown schematically in Fig. 1. The main high-vacuum line is evacuated to 10^{-5}–10^{-6} mm Hg by a fast mercury-diffusion pump, backed by a rotary oil pump. To this vacuum line are connected two glass mercury-diffusion pumps, (P_1 and P_2), which can be baked out periodically. The whole apparatus is provided with mercury cut-offs instead of normal stopcocks. The essential part of the apparatus (in Fig. 1 surrounded by a dotted line) was heated at 300–400°C during the pumping period. Pumping was continued for one week (day and night), during which time the metal wire was heated electrically close to the sublimation temperature and periodically reduced with very pure hydrogen (drawn from the palladium thimble) to remove oxide impurities.

At the end of the pumping period the pressure was $2–5 \times 10^{-7}$ mm Hg (with the apparatus still hot). Cooling and inserting the second cold trap into a cooling bath (liquid nitrogen or solid

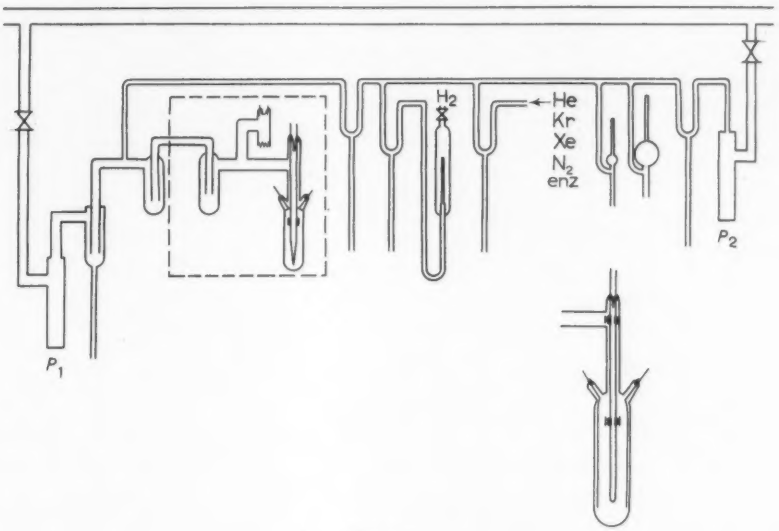

FIG. 1.

CO_2–acetone) gave a further decrease in pressure to $0{\cdot}5$–$1{\cdot}0 \times 10^{-7}$ mm Hg.

Then the metal wire* was evaporated on the wall of the vessel, which was cooled in liquid nitrogen (the geometrical surface area of the film-covered wall amounted to ~ 120 cm^2). The evaporation process was followed by measuring the resistance of the film between the two thin platinum wires fused opposite each other along the whole length of the vessel wall and connected to a Wheatstone bridge via two tungsten–glass seals (see insert Fig. 1).

Evaporation was stopped as soon as the film resistance reaches a value of a few ohms.

The conductivity (λ) of the films is metallic, and decreases when the film is warmed up to room temperature; immediately after this temperature has been reached, a slow irreversible increase sets in. This increase is due to sintering of the film and stops after a few hours. We always stabilized the films at room temperature over at least one night. After this time the conductivity is constant and changes with temperature in a reproducible way. The accuracy of the conductivity measurements is better than $0{\cdot}1$ per cent.

All volumes are calibrated with pure helium. Known amounts of adsorbate were introduced with the two McLeod manometers. The pressure in the adsorption vessel can be determined with the ionization manometer. This pressure is mostly less than 10^{-6} mm Hg, but for the higher equilibrium pressures (indicated numerically in the figures) thermal-flow corrections were applied, using the method of BENNETT and TOMPKINS[12].

The surface areas of the films were determined by the BET method, sometimes before, sometimes after the chemisorption measurements, using xenon as adsorbate at -183°C. For the surface area of a xenon atom, a value of $22{\cdot}3$ Å^2 was accepted.

3. RESULTS AND DISCUSSION

Figs. 2–6 give the experimental results for the chemisorption of various gases on titanium, iron, and nickel films. In all graphs the relative change in the electrical conductivity ($\Delta\lambda/\lambda_0$) is plotted against the number of adsorbed molecules per mg film weight. In each case the conductivity at first decreases linearly with the number of chemisorbed molecules. Later, a bend in the curve, or even an increase in conductivity, is sometimes noted.

* The spectroscopically pure iron and nickel wires (diameter $0{\cdot}5$ mm) were obtained from Johnson, Matthey and Co. Ltd., London. The titanium wire of the same purity (diameter $0{\cdot}3$ mm) was obtained from Hereaus, Hanau, Germany.

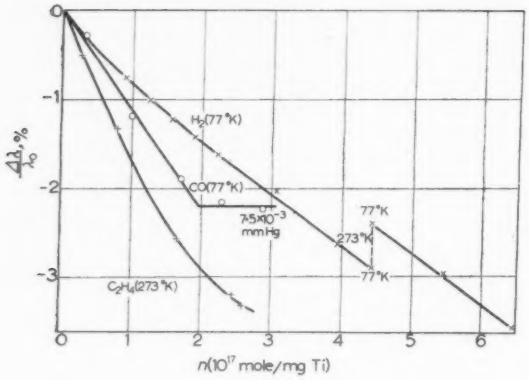

FIG. 2.

First let us consider the initial straight parts of the curves; from the slope of these the influence on the conductivity per chemisorbed molecule can be derived. As the conductivity is a bulk property of the metal, it is easy to make this derivation also

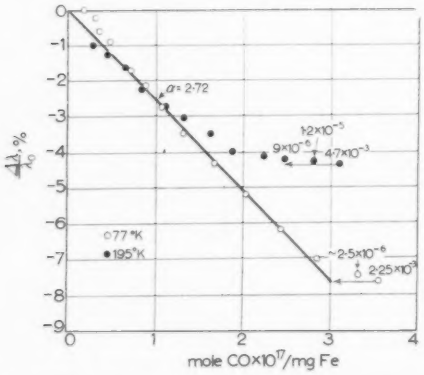

FIG. 3. Chemisorption of CO on evaporated iron film. ○ 77°K; ● 195°K.

relative to the total number of metal atoms present in the film. Thus we calculate the factor α given by

$$\alpha = -\frac{\Delta\lambda}{\lambda_0} \cdot N/n_a$$

in which N is the total number of metal atoms present in the film and n_a is the total number of adsorbed molecules. The values of α for the various cases investigated are given in Table 1.

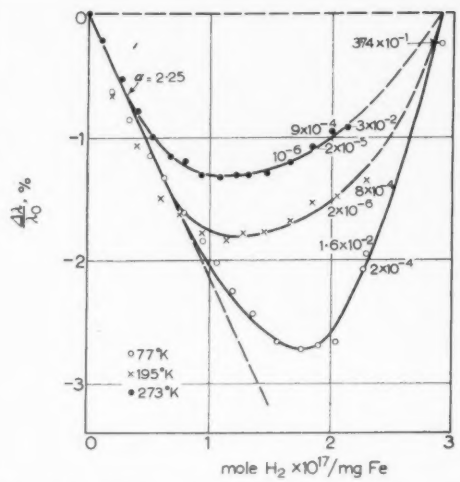

FIG. 4. Chemisorption of hydrogen on evaporated iron film. ○ 77°K; × 195°K; ● 273°K.

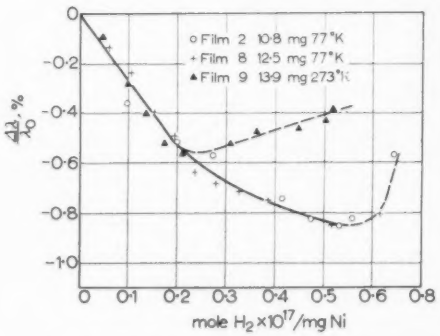

FIG. 5. Hydrogen on nickel at 77 and 273°K.

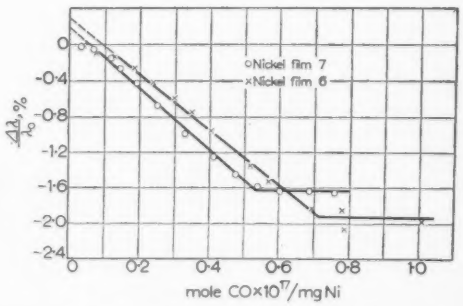

FIG. 6. CO at −196°C on nickel films.

Table 1. *Values of* α

Metal	Adsorbate	Temp. (°K)	α	Film weight (mg)
Ti	H_2	77	1·05	10·6
Ti	CO	77	1·35	10·1
Ti	C_2H_4	273	2·20	7·9
Fe	CO	77	av. 2·72	27·7
Fe	CO	195		24·3
Fe	H_2	77	av. 2·25	25·3
Fe	H_2	195		24·6
Fe	H_2	273		25·2
Ni	CO	77	3·57*	10·5 19·5
Ni	H_2	77 and 273	2·66	See Fig. 5

* Average of 3·80 and 3·35.

The values of α found experimentally are all of the order of unity. This very simple result means that by the formation of chemisorptive bonds the fractional decrease in the electrical conductivity roughly equals the fraction of the total number of metal atoms involved in the formation of these bonds.

Similar results for the *sorption* of hydrogen in various metals are already known from the literature.[13] SIEVERT showed that in a number of cases an increase in resistivity proportional to the amount of hydrogen taken up is found, and he calculated a proportionality factor K, which is directly comparable with the parameter α introduced here. The surprising result of the present investigation is, however, that, although the influence of a chemisorption is restricted to the surface of the metal, its effect is apparently equal to that of sorption in the bulk metal phase. In particular the results for hydrogen on titanium are of special interest in this connection. This metal is known to take up considerable amounts of hydrogen. From an estimate of the adsorptive capacity of the surface (see later), it is clear that even at liquid-nitrogen temperature this film takes up many more hydrogen molecules than could be chemisorbed on the surface. Nevertheless, the conductivity curve did not show any special indication of a transition from adsorption to sorption.

It cannot be demonstrated unambiguously if and where this transition occurs. So one could assume that the value of α found for hydrogen on titanium is the result of a mixed phenomenon over the whole range studied. The fact that this value is of the same order as that found for other gases on titanium and for hydrogen on other metals, where it is certain only chemisorption occurs, remains a strong indication that the effects of surface bonds and bonds formed in the bulk of the metal have an equal influence on the conductivity.

The experimental results for chemisorption would be trivial if the metallic film could be regarded as a homogeneous plate-like structure. The decrease in thickness of the conducting phase would then equal the fraction of the metal atoms involved in the chemisorption bond if the metal atoms occupied lost their metallic character. This picture must be rejected, however, in the light of what is known about the structure of these evaporated films. This knowledge may be summarized as follows:

(1) From all adsorption studies published, it appears that the real surface area is 10–50 times that of the geometrical surface area. The films have a porous structure, and the surface area per unit weight is independent of the film thickness.

(2) The electrical resistance of the pure film is much greater than that calculated from the known specific resistance of the metal and the dimensions of the film.

(3) Electron-diffraction diagrams show the normal pattern of the metal, but all reflections are greatly broadened. There are no indications that certain reflections show more marked broadening than others. Electron-microscopic photographs of replicas of the film show a granular structure. (Our own photographs are in complete agreement with those published by SACHTLER *et al.*[14])

All these facts strongly suggest that an evaporated film must be considered as a porous agglomerate of small metal crystals, which are sintered to such an extent that the contact resistance between the particles becomes negligible.

A value of $\alpha \sim 1$ for films of irregular dimension for which the resistance is concentrated in the region of small cross-section, can be understood only if the contribution of one given metal atom to the electrical conductivity extends over a distance

of a few hundred Å or more.* It seems reasonable to assume that this distance is of the order of the free-path length of the conduction electrons. However, the temperature coefficient of the resistance of the films, which is comparable with the temperature coefficient of the bulk metal, suggests that the free-path length is still smaller than the particle dimension.

It seems that the formation of the chemisorptive bond causes entrapment of valency electrons contributing normally to the conduction band. Obviously this does not mean that the electrons are *extracted* from the metal. The formation of a covalent bond, which may be polarized in either direction, traps one valency electron of the metal, thus always causing a proportional *decrease* in conductivity. In this connection it is interesting to note that ORIANI *et al.*[15], from measurements of the nuclear magnetic resonance of hydrogen in vanadium, tantalum and palladium, concluded that a covalent bond exists between the hydrogen and the metal atoms, contrary to the current view that the hydrogen is dissolved as protons in the metal.

4. QUANTITATIVE ASPECTS

Although the accuracy of the α values is not very high, an attempt may be made to derive more quantitative conclusions from the experimental values obtained.

We assume again that every metal atom contributes an equal amount to the conductivity, irrespective of whether it is situated on the surface or in the bulk. Chemisorption destroys this contribution. We designate by γ the number of chemical bonds per metal atom necessary to destroy this contribution completely. So γ may be put equal to the *effective valency* of a metal atom in the metal lattice (= number of valency electrons per metal atom). If we further define X as the number of chemical bonds formed per adsorbed molecule, it is clear that

$$\alpha = \frac{X}{\gamma}$$

Consequently, the value of α depends on two parameters, the first (γ) of which is determined by the characteristic properties of the metal phase, whereas the second (X) depends primarily on the chemisorbed molecule, though it is probably influenced also by the geometrical properties of the metal surface.

As to hydrogen, it is most likely, and in agreement with all experimental evidence, that the molecule, at least at lower coverages, dissociates in the chemisorption process so that two covalent bonds are formed per molecule, thus $X_{H_2} = 2$.

This leads us to the assumption that the γ values for titanium, iron and nickel are 1·9, 0·9 and 0·75, respectively. The values of X_{CO} and $X_{C_2H_4}$ for the different metals can now be calculated (see Table 2).

These results indicate that the bonding of a CO molecule involves the formation of more than two bonds for all the metals investigated, whereas for C_2H_4 at least four bonds are formed per molecule.

Table 2. Values of X

	Ti	Fe	Ni
H_2	2·0*	2·0*	2·0*
CO	2·56	2·45	2·65
C_2H_4	4·20	—	—

* Assumed values.

The latter conclusion is in good agreement with the experimental results of JENKINS and RIDEAL[16] for C_2H_4 on nickel. These authors showed that the ethylene molecule dissociates during chemisorption to form a acetylenic compound

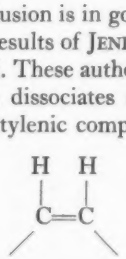

bonded to two metal atoms plus two hydrogen atoms each occupying one metal atom. The formation of about 2·5 bonds for one CO molecule is not so easy to understand. It might indicate that a few

* One might argue that as the resistance is concentrated in the "necks" between the particles, only the molecules chemisorbed in the "neck sites" will influence the conductivity. In that case, however, the value $\alpha = 1$ can only be understood if the improbable assumption is made that the ratio $\frac{\text{number of surface sites}}{\text{number of bulk atoms}}$ for the necks is equal to that for the total film.

CO molecules are bonded in a configuration in which also the O atom has formed a bond with the metal atom, as was supposed by TRAPNELL[17]. EISCHENS[18], however, did not find an indication of this type of bond from infrared-absorption studies of CO chemisorbed on nickel and platinum.

Another possibility is that a small contribution of bonds of the type

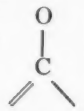

is the cause of the value $X = 2{\cdot}5$ found experimentally.

At higher coverages both the lines for C_2H_4 on titanium and for hydrogen on iron and nickel show a distinct change in bond type. Before discussing these effects, the difficulty of defining the surface coverage in absolute terms has to be dealt with, however. As was said above, the surface areas of the various films were estimated from the physical adsorption of xenon at −183°C. These measurements were made after completion of the chemisorption experiments. In agreement with the literature, a constant surface area per film weight was found for the different preparations, viz.

titanium	245 ± 15 cm²/mg
nickel	145 ± 25 cm²/mg
iron	400 ± 30 cm²/mg

In some cases the surface area was measured also before the chemisorption experiments—and incidentally the same phenomenon was observed as was noted by KLEMPERER and STONE[19]—namely an appreciable decrease in surface area during chemisorption, probably caused by sintering of the film owing to the evolution of the high heat of adsorption. We believe that this is also the cause of the scattering of the conductivity measurements (Fig. 6).

Titanium

In the case of titanium the main planes of the crystal lattice have the following surface densities:

$(10\bar{1}0)$ and $(01\bar{1}0)$	$0{\cdot}72 \times 10^{15}$ atoms/cm²
$(00\bar{1}1)$	$1{\cdot}35^{*} \times 10^{15}$ atoms/cm²
$(11\bar{2}0)$	$0{\cdot}84 \times 10^{15}$ atoms/cm²

* In our preliminary publication[11] we erroneously gave a number of $1{\cdot}15 \times 10^{15}$ atoms/cm² for this plane.

From a comparison of the number of adsorbed molecules with the surface area, it follows for both CO and C_2H_4 that the ultimate coverage is of the order of $0{\cdot}85 \times 10^{15}$ molecules/cm², so that the number of adsorbed molecules per site is of the order of one.

This means that at least the greater part of the CO molecules will be held on the surface as shown below:

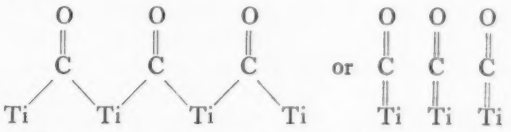

This is in agreement with there being two bonds available per titanium atom ($\gamma = 1{\cdot}9$), with a small contribution of multiple bonds as stressed above. The bend in the C_2H_4 curve demonstrates that the second part of the ethylene molecules adsorbed form many fewer bonds per molecule than the first part. Probably, these are bound on the sites already covered with hydrogen atoms forming

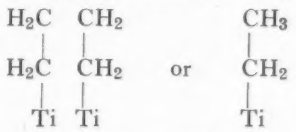

groups, as were observed on nickel by EISCHENS.[18]

Iron

For iron the variation in density of the different crystal planes is much higher, viz.

(111)	$0{\cdot}73 \times 10^{15}$ atoms/cm²
(100)	$1{\cdot}2 \times 10^{15}$ atoms/cm²
(110)	$1{\cdot}7 \times 10^{15}$ atoms/cm²

From a similar calculation to that described above, it appears that the number of chemisorbed CO molecules per cm² at −196°C agrees fairly closely with the site density of the (111) plane. Preferential orientation of the surface in this direction is highly improbable, however, as was shown by SACHTLER *et al.*[14] so that the agreement seems to be fortuitous. It appears therefore that CO on iron is bonded in configurations such as

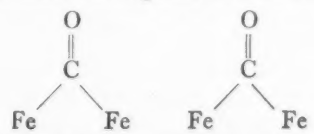

in agreement with the lower value of γ.

In the case of hydrogen a reversal of the conductivity effect is observed at higher coverages. This effect, which is also found on the nickel films, is in complete agreement with the analogous experiments by SACHTLER[10] and by SUHRMANN[6], while studies on the change in the thermoionic work function by chemisorption revealed the same effect.[7] Our results indicate that the curves incline to return symmetrically to a point $\Delta\lambda = 0$ when the amount of adsorbed hydrogen *molecules* equals the number of CO molecules on the same area. This apparently means that the hydrogen can be bonded in two distinct ways on iron or nickel. The first one clearly consists of covalently bonded hydrogen atoms. As soon as the coverage with H atoms has increased to such an extent that the heat of adsorption has decreased considerably, a second type of bonding becomes more favourable thermodynamically and starts gradually to replace the former one. This second type of bonding apparently does not involve conduction (i.e. valency) electrons. MIGNOLET[7], who treated this problem extensively, is of the opinion that chemisorbed H_2^+ ions are involved here. He demonstrates that mixing of the two bond types occurs earlier at the higher temperatures owing to entropy contributions; this has been confirmed by our experiments.

Nickel

With nickel films the same reversal effect is found, although not so clearly as with iron films. The main reason for this is likely to be that the surface area of the nickel films is much smaller, so that the measurements at higher surface coverages become more and more ambiguous. From the same comparison of the amounts adsorbed and the surface densities of the crystal planes, viz.

(100) $1{\cdot}61 \times 10^{15}$ atoms/cm^2
(110) $1{\cdot}14 \times 10^{15}$ atoms/cm^2
(111) $1{\cdot}87 \times 10^{15}$ atoms/cm^2

it will appear that the surface coverages both for CO and hydrogen are less than for the other metals. For CO a coverage of about 0·37 CO molecule/site is found. This is in agreement with the lower value of γ found for this metal.

The explanation of the reversal effect found for hydrogen on iron and nickel by the formation of H_2^+ ions on the surface involves the assumption that the complete ionic type of bonding in which an electron is transferred to the metal does not change the conductivity of the film. In this case no valency electron of the metal is involved, whereas the electron transferred from the molecule to the metal does not contribute to the conductivity, because of its immobilization by the positive counterion. So, contrary to the views often held,[6] we conclude that the formation of covalent bonds, polarized in either direction, or the formation of negative ions on the surface will always decrease the conductivity of the metal phase, whereas the conductivity will remain unchanged by the formation of positive ions.

In this connection it is interesting to note the experimental results of BONFIGLIOLI *et al.*[20] who measured the conductivity of evaporated gold and antimony films as a function of the charge on the metal, which was varied by applying strong electric fields at the surface. These investigators found a linear dependence of the conductivity in both directions. Obviously, in this case, transferred electrons, though confined to the surface, are free and are not trapped by positive counterions as in the case of chemisorption in the form of positive ions. It is a pity that, owing to lack of data, a figure comparable to our α, but calculated with the number of electrons transferred instead of the number of molecules adsorbed, cannot be obtained with fair accuracy, but a rough estimate points to a value of the order of $\alpha = 4$.*

Acknowledgements—The authors are highly indebted to Dr. R. WESTRIK and Mr. A. KIEL of this laboratory for their work on the electron diffraction and electrons microscopy on these films and for the many discussions concerning the structure of evaporated metal films in general.

REFERENCES

1. BEECK O., *Advances in Catalysis* Vol. 2, p. 151. Academic Press, New York (1950).
2. DE BOER J. H., *Advances in Catalysis* Vol. 8, p. 18. Academic Press, New York (1956).
3. DE BOER J. H., *Electron Emission and Adsorption Phenomena*. Cambridge University Press (1935).
4. BOSWORTH R. C. L., *J. Proc. Roy. Soc. N.S. Wales* **79**, 166 (1946) and earlier publications.
5. OATLEY C. W., *Proc. Phys. Soc.* **51**, 318 (1939).

* We thank Dr. W. M. H. SACHTLER (Kon. Shell Laboratories, Amsterdam) for bringing this paper by BONFIGLIOLI *et al.* to our attention.

6. SUHRMANN R., *Advances in Catalysis* Vol. 7, p. 303. Academic Press, New York (1955).
7. MIGNOLET J. C. P., *Rec. Trav. Chim.* **74,** 685 (1955).
8. BROEDER J. J., VAN REYEN L. L., SACHTLER W. M. H. and SCHUIT G. C. A., *Z. Elektrochem.* **60,** 838 (1956).
9. DE BOER J. H. and KRAAK H. H., *Rec. Trav. Chim.* **56,** 1103 (1937).
10. SACHTLER W. M. H., *J. Chem. Phys.* **25,** 751 (1956).
11. VAN HEERDEN C. and ZWIETERING P., *Proc. K. Ned. Akad. Wetensch.* **B60** 160 (1957).
12. BENNETT M. J. and TOMPKINS F. C., *Trans. Faraday Soc.* **53,** 185 (1957).
13. SMITH D. P., *Hydrogen in Metals.* University of Chicago Press (1948).
BRUNING H. and SIEVERT A., *Z. phys. Chem.* **A163,** 409 (1933).
SIEVERT A. and BRUNING H., *Z. phys. Chem.* **A174,** 365 (1935).
14. SACHTLER W. M. H., DORGELO G. and VAN DER KNAAP W., 4e *Réunion de Chimie Physique*, Paris (1954).
15. ORIANI R. A., MCCLIMENT E. and YOUNGBLOOD J. F., *J. Chem. Phys.* **27,** 330 (1957).
16. JENKINS G. I. and RIDEAL E., *J. Chem. Soc.* 2490 (1955).
17. TRAPNELL B. M. W., *Chemisorption* p. 182. Butterworths, London (1955).
18. EISCHENS R. P., FRANCIS S. A. and PILSKIN W. A., *J. Phys. Chem.* **60,** 194 (1956).
19. KLEMPERER D. F. and STONE F. S., *Proc. Roy. Soc.* **A243,** 375 (1957).
20. BONFIGLIOLI G., COEN E. and MALVANO R., *Phys. Rev.* **101,** 1281 (1956).

OL.
11
959

J. Phys. Chem. Solids Pergamon Press 1959. Vol. 11. pp. 26–30. Printed in Great Britain.

THEORY OF DIRTY SUPERCONDUCTORS

P. W. ANDERSON

Bell Telephone Laboratories, Murray Hill, New Jersey

(*Received* 3 *March* 1959)

Abstract—A B.C.S. type of theory (see BARDEEN, COOPER and SCHREIFFER, *Phys. Rev.* **108,** 1175 (1957)) is sketched for very dirty superconductors, where elastic scattering from physical and chemical impurities is large compared with the energy gap. This theory is based on pairing each one-electron state with its exact time reverse, a generalization of the k up, $-k$ down pairing of the B.C.S. theory which is independent of such scattering. Such a theory has many qualitative and a few quantitative points of agreement with experiment, in particular with specific-heat data, energy-gap measurements, and transition-temperature versus impurity curves. Other types of pairing which have been suggested are not compatible with the existence of dirty superconductors.

VOL
11
195

ONE of the most striking experimental facts about superconductivity is that it is often insensitive to enormous amounts of physical and chemical impurities. For one example, several substances in essentially an amorphous state have been shown to be superconductors, such as bismuth and beryllium films laid down at liquid-helium temperatures.[1] As another example, there are disordered alloy systems with 20–50 per cent of chemical scattering centers, but with transition temperatures comparable with those of pure elements.[2] These quantities of crystal imperfections are large enough to scatter the electrons at an extremely rapid rate. In fact, if we were to take the mean free time before scattering for the electron as a measure of the electrons' uncertainty in energy, that uncertainty in energy is large compared not only with the energy gap ϵ_0, but with the Debye energy $\hbar\omega_D$. Plane-wave states for the electrons definitely have this very large degree of energy uncertainty.

On the other hand, the experiments of SERIN *et al.*[3] have shown that, starting with a pure single crystal of a superconducting material, there is usually a rather sharp initial drop in the superconducting transition temperature as the first small percentage of chemical imperfection is added. They show that this initial drop is proportional to the extra resistivity caused by these imperfections, and therefore proportional to the amount of scattering. If the impurities which are introduced are magnetic ions rather than ordinary chemical impurities, MATTHIAS *et al*[4] have shown that this initial sharp drop continues, and superconductivity is very soon destroyed. On the other hand, for ordinary impurities the sharp drop stops rather soon and is replaced by a more gradual behavior, which seems to be determined primarily by the fact that the impurity adds or subtracts electrons from the band, changes the density of states, and in various ways gradually varies the parameters of the free electrons. Thus we may divide superconductivity into two regions: (1) the region of relatively pure superconductors where scattering has a rather sharp effect on superconducting transition temperatures; and (2) the region of very imperfect superconductors, where additional scattering has very little effect. It is the purpose of the present paper to give a theory of this region of the "dirty" superconductor.

The fundamental assumption we will make is that in this region the problem of the electron wave functions is best solved by first diagonalizing the scattering interaction between the electrons and the impurities, and then calculating the phonon interactions between electrons. Finally, one calculates from this the superconducting properties. That is, we find a new set of one-electron wave functions for the electrons, and then solve the problem of the interactions of the electrons in terms of these, rather than in terms of ordinary

plane-wave functions, such as are appropriate in the region of the pure superconductor. All of this, of course, assumes that the scattering is perfectly elastic, as it is from any form of chemical or physical imperfection. (At the low temperatures where superconductivity is important, inelastic phonon scattering does not play an important role.) So what we do is simply to assume that somebody has solved for us the extremely difficult problem of the wave functions of the electrons in the presence of the scatterers, and write down the resulting wave function $\psi_{n\sigma}$:

$$\psi_{n\sigma} = \sum_{\boldsymbol{k}} (n|\boldsymbol{k})\phi_{\boldsymbol{k}\sigma}, \tag{1}$$

where $\phi_{\boldsymbol{k}\sigma}$ are the Bloch waves and $(n|\boldsymbol{k})$ the unitary transformation solving the scattering problem. (We give ψ_n a spin index σ; this may not be valid in heavy elements because of spin-orbit coupling, but the theory is still valid there.)

The basic observation which we make is that if $\psi_{n\sigma}$ is such an exact one-electron wave function in the presence of scatterers, and if the scatterers are nonmagnetic, the time-reversed wave function, $(\psi_{n\sigma})^*$, is also an exact wave function of the one-electron Hamiltonian. What is more, $(\psi_{n\sigma})^*$ has the same energy as $\psi_{n\sigma}$ itself. We shall call this energy E_n. The time-reversed wave function $(\psi_{n\sigma})^*$ is:

$$(\psi_{n\sigma})^* = \sum_{\boldsymbol{k}} (n|\boldsymbol{k})^*\phi_{-\boldsymbol{k}-\sigma}. \tag{2}$$

Now, having the correct one-electron wave functions, we proceed to derive the phonon interaction between these electrons. It is not at all correct simply to transform the B.C.S. interaction[5] directly into the interaction between these new wave functions $\psi_{n\sigma}$; the reason for this is that $\psi_{n\sigma}$ contains plane wave functions which have quite different energies, and in particular, in the presence of strong scattering contains wave functions from outside of the region where the B.C.S. electron interaction is attractive. Therefore, this method would lead us to the conclusion that the interaction between electrons is altered rather seriously. Actually, it is correct instead to write down the interaction between these new scattered-electron wave functions and the phonons, and then to do the second-order perturbation theory which gives us the interaction between the electrons caused by the phonons. When the calculation is done this way, the energy denominators in the second-order perturbation theory contain the energies not of the initial plane-wave states, $E_{\boldsymbol{k}}$, but rather the energies E_n of the scattered one-electron states. Whether or not the interaction is attractive depends primarily on what these energy denominators are. Therefore, we find that the attractiveness or not of the interaction is now a function not of $E_{\boldsymbol{k}}$, the energy of the plane-wave states, but of E_n, the energy of the scattered-electron states. Without going into excessive detail, we simply write down the part of the interaction which corresponds to the B.C.S. truncated Hamiltonian:[5]

$$\mathcal{H}_{\text{red.}} = -\sum_{n,n'} V_{nn'} c_n^* c_{-n}^* c_{-n'} c_{n'},$$

$$V_{nn'} = \sum_{\boldsymbol{k},\boldsymbol{k}'} \frac{|(n|\boldsymbol{k})|^2 |(n'|\boldsymbol{k}')|^2 |M_{\boldsymbol{k}-\boldsymbol{k}'}|^2 \hbar\omega_{\boldsymbol{k}-\boldsymbol{k}'}}{(\hbar\omega_{\boldsymbol{k}-\boldsymbol{k}'})^2 - (E_n - E_{n'})^2}. \tag{3}$$

Here c_n^* and c_{-n}^* are creation and destruction operators for electrons in state $\psi_{n\sigma}$ and $(\psi_{n\sigma})^*$, $M_{\boldsymbol{k}-\boldsymbol{k}'}$ and $\hbar\omega_{\boldsymbol{k}-\boldsymbol{k}'}$ have the usual meaning, and $(n|\boldsymbol{k})$ is defined in equation (11).

This interaction is summed over all the plane wave functions which are contained in the scattered function n, with a coefficient which is given by the square of the amount of the state contained in the state n. Normalization requires the following equation:

$$\sum_{\boldsymbol{k}} |(n|\boldsymbol{k})|^2 = 1. \tag{4}$$

Because of equation (4), if the parameters entering in the interaction were constants, as was assumed by B.C.S., the interaction would be exactly the same for the scattered state as it was for the plane-wave state. As it is, the interaction is not a constant, but at best only roughly so, and expression (3) picks out of the total interaction only the constant part. That is, the interaction (3) is strictly the average interaction over all the states going to make up the scattered state n. Since the states which make up this scattered state are, at least under conditions of strong scattering, taken more or less randomly from all the regions of the Fermi surface, we conclude that the interaction will be (aside

from a smooth energy dependence) a constant, averaged over the entire Fermi surface.

The rest of the interaction, the part which was removed in the truncated Hamiltonian of B.C.S., is changed in a very radical way. In the pure substance the rest of the interaction can be thought of as an interaction between pairs which do not have exactly zero total momentum but rather some finite momentum. However, under conditions of strong scattering this part of the interaction does not take this form at all; each individual matrix element is smaller by a number of the order of the total number of electrons. This is because the momentum selection rule no longer holds, so that there is no reason why any individual matrix element should vanish. This increases the total number of matrix elements and must therefore decrease their magnitude. Thus, in the scattered state the B.C.S. part of the interaction, or rather the transformed B.C.S. part, plays a much more obviously unique role than it does in the pure superconductor.

One final comment about this interaction: obviously if the scattering is strong enough the procedure which we have followed, of first diagonalizing the one-electron Hamiltonian including scattering, and then introducing the electron–phonon interaction and the interaction between the electrons which results from it, is correct. When we ask the question: at what degree of scattering is this no longer the correct procedure? the first guess would be that one should find some average amount of electron–phonon interaction and when the scattering becomes less than that the procedure is no longer correct. However, it is fairly easy to convince oneself that this is not the correct way, but that the diagonalization of the one-electron part of the Hamiltonian is correct at very much smaller amounts of scattering. As a matter of fact, the procedure we have followed seems to be correct until the actual interaction *between* the electrons caused by the electron–phonon interaction begins to come in to play. That is, it is correct until $\hbar/\tau$ becomes comparable with the energy gap, which is a reasonable measure of the electron–electron interaction. This is, in fact, the experimental criterion for the transition from the region of strong scattering, as here defined, to the region of weak scattering.[3]

Now we shall draw some physical conclusions from these ideas. First we should observe that it is possible to solve the B.C.S. integral equation and derive a theory of superconductivity just as well as in the new situation with the new averaged interaction and the scattered wave functions ψ_n as it was in the old situation with the old interaction and the plane-wave functions ψ_k. A general result, which is fairly easy to prove, is that the energy gap, and therefore the transition temperature, will always be slightly smaller for the scattered states than they would be in the pure case, essentially because the average taken in the scattered case is not as favorable as one gets in the pure case. This explains why it is that in the pure superconductor region the transition temperature drops so radically, and yet stops dropping after one gets into the region of strong scattering; and at the same time it explains why this drop is relatively small, because one does not expect the difference between the two energy gaps to be very large. Thus, we see that these ideas explain fairly satisfactorily the general features of SERIN's results. It is also clear that when the time-reversal transformation cannot be made, that is, when the energy of the state ψ_n is not the same as the energy of ψ_{-n}, all this cannot be done, and the transition temperature will continue to drop as the degree of magnetic scattering increases.

An interesting question is what size of particles and at what degree of scattering will superconductivity actually cease. The first point is that, as long as the particle size remains fairly large, no quantity of scattering which leaves the substance a metal would seem to be capable of actually destroying superconductivity, because the average which is taken over the Fermi surface does not depend in any important way on the actual amount of scattering. On the other hand, on reducing the particle size, we will begin to get to the point at which the scattered wave functions ψ_n have energies E_n which are separated by discrete energy gaps. That is, their energies must extend over something like the total Fermi energy, which is about 10 eV; and if there were only about a thousand electrons, that would mean that the energy differences between the states would be of the order of 0·01 eV. With such energy differences among the E_n, superconductivity would no longer be possible; in fact, it is fairly easily seen that the energy differences must be less than the energy gap. That means that

particles with fewer than about 10^4–10^5 electrons will begin to be affected. So far no experiments are reported on particles of this order of magnitude of size, although the particles used in REIF's nuclear-resonance experiments are beginning to approach this point.[6]

Another conclusion is that the B.C.S. theory in its original form, assuming a constant interaction, will be more nearly correct in the dirty superconductor region that it will be for pure superconductors; that is, in the impure superconductors the interaction is relatively a constant, and therefore the energy gap itself will be a constant and the thermal and other results of B.C.S. should be nearly exact. On the other hand, in pure single crystals of superconductors, one can very quickly show that the energy gap will be a strong function of the momentum vector on the Fermi surface, because most superconductors have fairly complicated Fermi surfaces, and it would be a miracle if the interactions were sufficiently constant to maintain a constant energy gap. There are two types of experiments which bear on this point. One type of experiment is the electronic specific heat and, in fact, various recent experiments[7] show deviations from the exponential specific-heat curve of the B.C.S. theory in the direction which would be expected if the energy gap were a function of position on the Fermi surface. Experiments on less perfect single crystals have shown less such deviations, as is to be expected. On the other hand, most of the direct experiments, in particular the experiments of TINKHAM and his co-workers[8] on the optical measurement of the energy gap and the experiments of HEBEL and SLICHTER[9] measuring the density of states by the relaxation time in nuclear resonance, are necessarily undertaken in the dirty superconductor region. In the case of TINKHAM's experiments, the measurement is necessarily made near a surface, while the other measurement is made on small particles. Therefore, neither of these types of experiments would have been expected to show any considerable anisotropy of the energy gap. The former do not; the structure observed in the latter experiments[10] is probably a collective excitation.[11] The question of the experimental investigation of the anisotropy is a fascinating one which remains open so far as I know. Our conclusion is that the recent experiments on the detailed investigation of the specific-heat curve must be considered as being more of a confirmation of the B.C.S. theory than vice versa, because they show that the expected anisotropy of the energy gap is actually there.

In conclusion I should like to make a number of acknowledgements and apologies. In the first place various notions about time reversal and superconductivity have appeared independently in a number of places. Most particularly, ABRAHAMS and WEISS at Rutgers have made similar calculations, and BARDEEN and MATTIS[12] have used a related wave function. In the second place, the idea of the anisotropy of the energy gap occurred independently to COOPER and to PIPPARD and HEINE[13]. Thus, the purpose of the present paper is merely to summarize in a physically consistent way all of these ideas, and to show that there is good agreement qualitatively with experiments. I should also acknowledge interesting discussions with C. HERRING and H. SUHL.

A final comment is that the nucleus is itself a dirty superconductor in the sense that the nucleus is a very fine particle with only a very small number of Fermi particles in it. Thus, it is not surprising to find that the theory of nuclei contains a "pairing" concept for $+m_1 - m$ pairs[14] which shows very great similarity to the discussion in this paper.

It is hard to see how any explanation other than time-reversal invariance will explain all these facts; in particular, the suggestions of inexact pairings or pairings of parallel-spin electrons advanced relative to the explanation of Knight shift results[15] certainly fail of agreement with the facts about dirty superconductors. It seems to the author that these considerations represent the strongest arguments that the theory of superconductivity must have some relation to zero-momentum, opposite-spin pairs.

REFERENCES

1. LAZAREV B. G., SUDOVTSEV A. I. and SMIRNOV A. P., *Zh. Eksper. Teor. Fiz.* **33,** 1059 (1958); (translation) *Sov. Phys. (J.E.T.P.)* **6,** 816 (1958).
2. MATTHIAS B. T., WOOD E. A., CORENZWIT E. and BALA V. B., *J. Phys. Chem. Solids* **1,** 188 (1956).
3. LYNTON E. A., SERIN B. and ZUCKER M., *J. Phys. Chem. Solids* **3,** 165 (1957).
4. MATTHIAS B. T., SUHL H. and CORENZWIT E., *Phys. Rev. Letters* **1,** 92 (1958).
5. BARDEEN J., COOPER L. N. and SCHREIFFER J. R., *Phys. Rev.* **108,** 1175 (1957).

6. REIF F., *Phys. Rev.* **106,** 208 (1957).
7. PHILLIPS N. E., *Phys. Rev. Letters* **1,** 363 (1958). BOORSE H. A., *Phys. Rev. Letters* **2,** 391 (1959).
8. RICHARDS P. L. and TINKHAM M., *Phys. Rev. Letters* **1,** 318 (1958).
9. HEBEL L. C. and SLICHTER C. P., *Phys. Rev.* **107,** 901 (1957).
10. TINKHAM M., RICHARDS P. L. and GINSBURG D., private communication.
11. ANDERSON P. W., *Phys. Rev.* **112,** 1900 (1958).
12. BARDEEN J. and MATTIS D. C., *Phys. Rev.* **111,** 412 (1958).
13. PIPPARD A. B. and HEINE V., *Conference on Properties of Metals at Low Temperature,* Geneva, N.Y. (1958).
14. BOHR A. and MOTTELSON B. R., private communication; M. G. MAYER, *Phys. Rev.* **78,** 22 (1950).
15. HEINE V. and PIPPARD A. B., *Phil. Mag.* **3,** 1046 (1958).

VOL.
11
195

J. Phys. Chem. Solids Pergamon Press 1959. Vol. 11. pp. 31–36. Printed in Great Britain.

HALL COEFFICIENTS OF DILUTE COPPER ALLOYS

M. D. BLUE

Honeywell Research Center, Hopkins, Minnesota

(*Received* 15 *December* 1958; *revised* 16 *February* 1959)

Abstract—The Hall coefficients of dilute alloys of Mn, Fe, Co, Ni, Zn, Sn, Si and Ge in copper have been measured as a function of composition at room temperature and 77°K with fields up to 10 kG. Two sets of Cu–Mn alloys have been prepared from purified manganese. In one set, special efforts were made to reduce the impurity oxygen content of the manganese. The dependence of the Hall coefficient on composition is different for the two sets, although both have a minimum near 4 per cent manganese. For all these dilute substitutional alloys, the Hall coefficients are independent of magnetic field.

OL.
11
959

1. INTRODUCTION

In our study of the electrical properties of copper alloys, we have decided to examine systematically the Hall coefficients of some of these alloys at various temperatures and compositions. While much work has been done on the Hall coefficients of alloys containing transition metals, very little work has been done recently on alloy systems of the non-ferromagnetic metals. The purpose of the present paper is to report the data gathered in this investigation and other pertinent data from the literature with a view to defining the problem involved in their explanation. All measurements are for substitutional single-phase binary alloys.

2. SPECIMEN PREPARATION AND MEASUREMENT

The copper used in these alloys was obtained from the American Smelting and Refining Company and was reported spectrographically pure. The Hall coefficient for pure copper was obtained from specimens cut from Johnson, Matthey and Co. spectrographically standardized copper sheet. The manganese, iron, cobalt and tin were also obtained from Johnson, Matthey and Co. Zinc was obtained from the American Smelting and Refining Company. These solute metals had a purity greater than 99·9 per cent. Nickel was obtained from Vacuum Metals Corp. and had a purity greater than 99·8 per cent.

One group of alloys was made using oxygen-free manganese prepared in the laboratory from Johnson, Matthey and Co. electropure manganese. Oxygen was removed by heating the purified metal under a nitrogen atmosphere and gradually admitting hydrogen as the metal approached its melting temperature. These alloys will be referred to as Cu–Mn(2). The alloys of copper and untreated Johnson, Matthey electropure manganese will be referred to as Cu–Mn(1).

The alloys were melted in vacuum or under a helium atmosphere, and left in the molten state at 1200–1250°C from 30–60 min. The molten alloys were agitated by hand several times during this period to assist in attaining homogeneity. Alumina or quartz crucibles were used.

The resulting alloy ingots were rolled, etched, and annealed above 800°C in vacuum for several hours. The annealing process was repeated after a final rolling to a thickness less than 0·02 mm. The thickness was convenient for measurements with an Ames dial thickness gauge reading directly to 10^{-4} in.

Samples approximately 65×10 mm were cut from the annealed alloy sheet, and contained long projecting Hall probes. Misalignment voltages were eliminated by lightly filing the probes. The probes were joined to annealed copper wires above the sample. Placing these junctions adjacent to one another minimized random noise and any contribution from the Ettingshausen effect.

A 12-in. Varian electromagnet (calibrated with a Rawson rotating-coil fluxmeter) was used to provide fields up to 10 kG. A primary sample current

of about 8 A was supplied by storage batteries, and measured with a mirror-backed ammeter. The Hall voltage was measured with a Rubicon thermo-free two-channel potentiometer and a high-sensitivity galvanometer.

The electrical measurements yielding the Hall coefficient divided by the thickness were reproducible to within 1 per cent. The thickness was also reproducible to better than 1 per cent. Thus the Hall coefficients of the specimens are believed reproducible to better than 2 per cent. Deviations greater than this were sometimes found for specimens obtained from various portions of the same alloy, as in some of our Cu–Mn(1) alloys, for example. The source of these variations is believed to be sample inhomogeneities.

Table 1. *Hall coefficients of dilute copper alloys*

Alloy	Sample number	Atomic per cent solute	At 300°K $-R(\text{cm}^3/\text{C})$	At 77°K $-R(\text{cm}^3/\text{C})$
Cu	10A	0·0	5·07	5·51
	10B	0·0	5·08	5·58
Cu–Mn (1)	11A	0·86	5·41	6·15
	11B	0·86	5·37	5·95
	12A	1·71	5·63	6·46
	12B	1·71	5·71	6·66
	13A	2·23	5·97	7·10
	13B	2·23	5·98	—
	14A	4·29	6·09	7·22
	14B	4·29	6·01	—
	15A	5·46	5·77	6·82
	15B	5·46	5·75	6·75
	16A	6·38	5·77	6·71
	16B	6·38	5·88	—
	17A	7·25	5·90	6·75
	17B	7·25	5·90	6·59
	18A	8·46	5·89	6·65
	18B	8·46	5·87	—
Cu–Mn (2)	21A	0·73	5·28	6·09
	21B	0·73	5·30	6·08
	22A	3·02	5·45	6·58
	22B	3·02	5·57	6·53
	23A	4·69	5·52	6·56
	23B	4·69	5·52	6·57
	24A	8·89	5·37	5·38
	24B	8·89	5·38	5·30
Cu–Ni	31A	0·82	5·12	5·70
	31B	0·82	5·06	5·73
	32A	1·07	5·10	5·63
	32B	1·07	5·06	5·68
	33A	1·60	5·34	6·08
	33B	1·60	5·32	6·15
	34A	2·53	5·37	6·29
	34B	2·53	5·31	6·13
	35A	5·62	6·30	7·32
	35B	5·62	5·95	6·89
	36A	7·96	7·05	7·88
	36B	7·96	7·08	8·08

Table 1—continued

Alloy	Sample number	Atomic per cent solute	At 300°K $-R$(cm³/C)	At 77°K $-R$(cm³/C)
Cu–Zn	41A	0·84	5·03	5·51
	41B	0·84	5·05	5·26
	42A	3·25	4·88	5·65
	42B	3·25	4·88	5·49
	43A	5·55	4·73	6·10
	43B	5·55	4·69	6·23
Cu–Ge	51A	0·89	5·64	5·78
	51B	0·89	5·71	—
	52A	3·43	5·67	5·45
	52B	3·43	5·62	—
	53A	6·03	5·17	5·22
	53B	6·03	5·21	—
Cu–Si	61A	2·46	5·17	5·15
	61B	2·46	5·03	4·95
	62A	8·46	4·40	4·37
	62B	8·46	4·38	—
Cu–Sn	71A	2·40	5·06	4·92
	71B	2·40	5·06	4·88
	72A	5·05	4·81	4·67
	72B	5·05	4·88	4·72
Cu–Co	81A	0·09	4·91	4·98
	81B	0·09	5·15	5·23
Cu–Fe	91A	0·11	5·10	5·59
	91B	0·11	5·03	5·63
Cu–Cd (2)	—	9·56	3·65	—
	—	32·6	4·67	—
Cu–Sb (3)	—	32·4	2·17	—

Specimens for Hall measurements were cut from opposite ends of the rolled alloy sheet. If the Hall coefficients of the specimens differed by more than 2 per cent, a measurement was made on a sample cut from a center portion of the alloy sheet. With rare exceptions, this additional sample had a Hall coefficient lying between the values found for the end specimens. The majority of the data presented here represent the extreme values for each alloy. Alloys of copper and the ferromagnetic elements had the least uniform characteristics. A few alloys which obviously were non-uniform in their Hall coefficients and the temperature variation of their Hall coefficients were discarded.

3. RESULTS

The compositions of the alloys and the Hall coefficients are given in Table 1. In addition to the Hall-coefficient measurements, the resistivities of the Cu–Ni and Cu–Mn samples were measured. Although the sample geometry was not ideal for this type of measurement, the results were useful as an additional check on the solute content of the alloys.

The impurity resistivity per atomic per cent for the Cu–Ni alloys agreed within 5 per cent with the value found by LINDE.[1] The resistivity of the Cu–Mn alloys made with oxygen-free manganese were found to be within 5 per cent of the value

found for other Cu–Mn alloys made in this laboratory, but were about 6 per cent above LINDE's value at low manganese concentrations. No consistent resistivity difference between Cu–Mn(1) and Cu–Mn(2) alloys was found. However, the Cu–Mn(1) alloys had greater scatter in Hall coefficient and resistivity data as a function of composition than the Cu–Mn(2) alloys.

The measurements of sample resistivity were considered sufficient indication that no gross deviations in composition occurred during their preparation.

In Fig. 1 the Hall constants as a function of composition at 300°K are presented for the alloys. Also

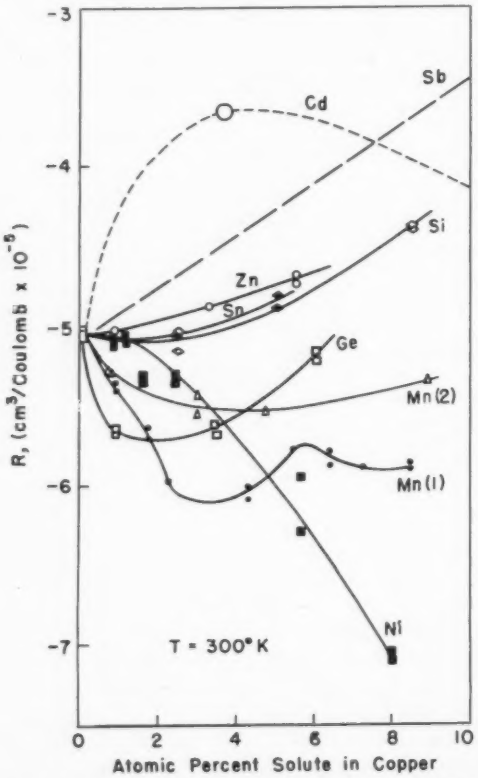

FIG. 1. Hall coefficients of copper alloys at 300°K as a function of solute concentration. Included are the data of RICHARDS and EVANS (1) for Cu–Cd and STEPHENS and EVANS (2) for Cu–Sb alloys.

included are the data of RICHARDS and EVANS[2] for Cu–Cd, and STEPHENS and EVANS[3] for Cu–Sb. The data for the Cu–Sn alloys agrees well with the results of ANDREWARTHA and EVANS[4] and FRANK[5] in the copper-rich region. The results for Cu–Ni agree well with those of FLANAGAN and AVERBACH[6] and SCHINDLER and PUGH[7].

The data at 77°K are presented on Fig. 2. A similar temperature variation of the Hall coefficient

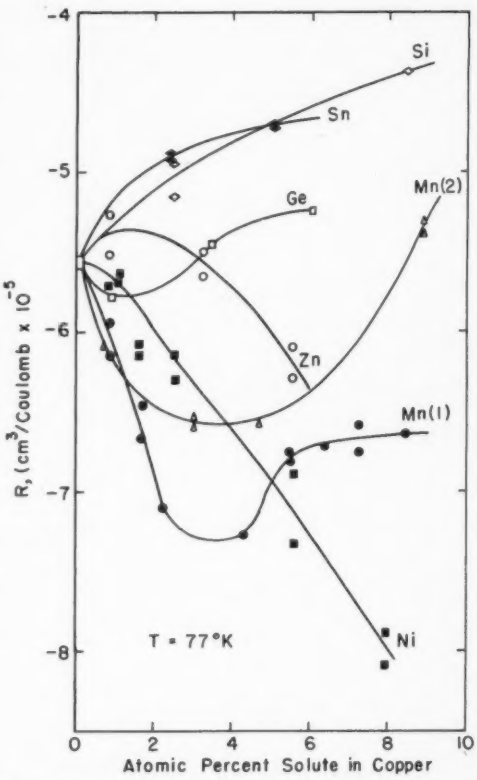

FIG. 2. Hall coefficients of copper alloys at 77°K as a function of solute concentration.

for copper has already been reported by FUKUROI and IKEDA[8].* Our measurements of the temperature-dependence of the Hall coefficient of copper indicate a monotonic decrease toward more negative values with a decrease in temperature from 300°K to about 4°K, in contrast to a minimum at about 200°K indicated by FRANK[9].

* The same temperature variation of the Hall coefficient of pure copper is also reported in a recent paper by BERLINCOURT[10]. However, the low-temperature size effects observed by BERLINCOURT would not be observable at 77°K and above.

The Cu–Co and Cu–Fe data are omitted in these figures. The limited solubility of the cobalt and iron in copper at room temperature restricts the possible range of single-phase alloys of these metals.

The dependence of Hall coefficient on concentration has a minimum near 4 per cent manganese for both Cu–Mn(1) and Cu–Mn(2) alloys. Measurements of the temperature-dependence of the Hall constant of the Cu–Mn(1) alloys show a gradual decrease with a decrease in temperature, as indicated by a comparison of Figs. 1 and 2. Preliminary measurements indicate that for Cu–Mn(1) alloys the Hall coefficient continues to decrease as the temperature decreases to the temperature of liquid helium.

OL.
11
959

4. DISCUSSION

The room-temperature value of the Hall coefficient for pure copper indicates an effective 1·45 electrons per atom. This value decreases monotonically to 1·30 electrons per atom at 77°K. These anomalously high values probably result from nonspherical energy surfaces.

Several band models for copper have been proposed by various writers. In particular, a model proposed by OLSON and RODRIGUEZ[11] to fit magnetoresistance data gives values of 1·22 and 1·09 electrons per atom respectively at 300 and 77°K, using the experimentally obtained Hall coefficients at these temperatures. A value of 1 electron per atom is to be expected from free-electron theory. The difference could be reduced by refinement of the model (the magnetoresistance data were also not fitted to within experimental error), but it is evident that energy surfaces of this type will explain the observed deviations from free-electron theory.

The cause of the temperature variation of the Hall coefficient of pure copper is obscure. The temperature-dependence of the Fermi level and lattice parameter will not explain the observed change of about 10 per cent in the Hall coefficient between 77 and 300°K.

The simple valence picture predicts the qualitative behavior of the Hall coefficient as a function of solute concentration with fair accuracy. Thus, elements such as zinc and cadmium, lying to the right of copper in the Periodic Table, would be expected to contribute electrons to the conduction band, causing the Hall coefficient to become less negative. Elements such as nickel, lying to the left of copper, would be expected to remove electrons from the conduction band, causing the Hall coefficient to become more negative.

This simple approach does not explain such details as the initial decrease on the Hall coefficient of the Cu–Ge alloys, or the decrease at 77°K of the Hall coefficient of Cu–Zn alloys at the larger zinc concentrations.

As discussed by FRIEDEL[12], the slope of the Fermi level versus solute concentration for copper alloys should approach zero for small concentrations of solutes near to copper in the Periodic Table. This is the result of the complete screening of the impurity potential at small distances by localized electrons from the conduction band. At small impurity concentrations, the electron density—and hence the Fermi energy and the Hall coefficient—are all the same as in the pure metal. As shown in Fig. 1, at room temperature the slope of the curve of Hall coefficient against solute concentration is almost zero for many solute elements at small concentrations. As Fig. 2 indicates, such an effect is not apparent at 77°K. Even at room temperature, however, the predicted variation in Fermi level with concentration is too small to explain the observed variation of Hall coefficient for higher solute concentrations.

The effect of oxygen on the Hall coefficient of Cu–Mn alloys was surprising. As mentioned previously, no definite effect of oxygen on the room-temperature resistivity of these alloys could be observed. It would be of interest to search for possible effects due to oxygen on the resistivity and other properties of Cu–Mn alloys at very low temperature.

Acknowledgement—The assistance of members of the Solid State Section of the Research Center in the preparation and measurement of the alloys is greatly appreciated.

REFERENCES

1. LINDE J. O., *Ann. Phys.* (*Leipzig*) **15**, 219 (1932).
2. RICHARDS W. and EVANS E. J., *Phil. Mag.* **13**, 201 (1932).
3. STEPHENS E. and EVANS E. J., *Phil. Mag.* **7**, 161 (1929).

4. ANDREWARTHA G. G. and EVANS E. J., *Phil. Mag.* **31,** 265 (1941).
5. FRANK V., *K. Danske Vidensk. Selsk., Mat.-Fys. Medd.* **30,** No. 4 (1955).
6. FLANAGAN W. F. and AVERBACH B. L., *Phys. Rev.* **101,** 1441 (1956).
7. SCHINDLER A. I. and PUGH E. M., *Phys. Rev.* **89,** 295 (1953).
8. FUKUROI T. and IKEDA T., *Sci. Rep. Res. Inst. Tohoku Univ.* A8, No. 3 (1956).
9. FRANK V., *Appl. Sci. Res.* B6, 379 (1957).
10. BERLINCOURT T. G., *Phys. Rev.* **112,** 381 (1958).
11. OLSON R. and RODRIGUEZ S., *Phys. Rev.* **108,** 1212 (1957).
12. FRIEDEL J., *Advances in Phys.* **3,** 446 (1954).

VOL
11
195

J. Phys. Chem. Solids Pergamon Press 1959. Vol. 11. pp. 37–42. Printed in Great Britain.

MAGNETORESISTANCE OF COPPER

J. de LAUNAY, R. L. DOLECEK and R. T. WEBBER

U.S. Naval Research Laboratory, Washington, D.C.

(*Received* 29 *December* 1958; *revised* 5 *March* 1959)

Abstract—The magnetoresistance of copper has been measured at 297, 78 and 4·2°K. In a transverse field of 100 kG at room temperature, the resistance increased about ¼ per cent and, within experimental error, was a quadratic function of the applied magnetic field. At the lower temperatures the field-dependence of the transverse magnetoresistance is considerably less than quadratic and approaches linearity at high fields. Considerable temperature-dependence for Kohler's rule was found. Saturation of the longitudinal magnetoresistance at high fields was observed at 4·2°K. The change in longitudinal resistance for saturation is of the order of the initial resistance in zero field and was found to be independent of temperature for the range 2·0–4·2°K and of measuring current for the range 0·1–2·0 A. The ratio of the transverse to the longitudinal magnetoresistance of a specimen was found to be a linear function of the applied field. These new features of magnetoresistive behavior can serve to stimulate the development of an adequate theory of longitudinal and transverse magnetoresistance.

1. INTRODUCTION

An estimate of the magnetoresistance of copper at room temperature was made by Kapitza[1], who also obtained measurements of the transverse effect at liquid-nitrogen temperature, using pulsed fields. Measurements in these intervals for fixed applied fields were not available for comparison. These measurements have now been made and the data are presented in this report.

Recent measurements at liquid-helium temperatures[2–5] give qualitative confirmation of Kohler's rule; however, the form of the field-dependence of the magnetoresistance at large applied fields and for large temperature changes was not well established, and the dissimilarities between the longitudinal and transverse magnetoresistances remained undetermined. In the present study the temperature-dependence of Kohler's rule has been demonstrated at liquid-nitrogen temperature, and the field-dependence of both magnetoresistances have been measured to high fields (100 kG). The transverse and longitudinal magnetoresistances were found to have completely different forms of field-dependence. Saturation of the longitudinal magnetoresistance of a specimen was observed, while the transverse magnetoresistance continued as a linear function of the applied field. A linear dependence on applied field of the ratio of transverse to longitudinal magnetoresistance was discovered.

2. EXPERIMENTAL STUDY

Measurements were made of the high-field transverse and longitudinal magnetoresistances of high-purity copper at room temperature, liquid-nitrogen temperature, and liquid-helium temperature.* The specimens used were 1-in. lengths of approximately 0·2-mm diameter polycrystalline copper wire annealed in high vacuum just prior to measurement. Ratios of resistance at 0°C to resistance at liquid-helium temperature of the order of 700 were obtained on annealing. For these specimens we estimate a value of $2{\cdot}4 \times 10^{-3}$ cm for the electron mean free path at 4·2°K, which is a factor of ten smaller than the diameter of the specimen used, and a factor of 30 larger than the radius of the electron orbit in the applied field of 100 kG.

Data on specimen characteristics are given in Table 1. Resistance measurements were made by

* The copper was prepared by the American Smelting and Refining Company and had a claimed purity of 99·999 per cent. This material was drawn into wires and furnished to us through the courtesy of Dr. H. Sherman of the Los Alamos Scientific Laboratory.

Table 1. *Characteristics of specimens*

Specimen	Diameter (mm)	$S = \left[\frac{R_{273°K}}{R_T}\right]_{H=0}$	Lead attachment	Vacuum annealing
1a	0·241	606 at 4·2°K	Soldered	4 hr at 400°C
1b	0·241	0·895 at 297°K 7·68 at 78°K 581 at 4·2°K	Soldered	4 hr at 400°C
2	0·394	738 at 4·2°K 738 at 2·7°K	Soldered	4 hr at 400°C

standard potentiometric techniques. The reproducibility between runs was about 1 per cent. The transverse and longitudinal results will be presented separately, since it has been found that at low temperatures the two magnetoresistances, though related, have completely different forms of field-dependence.

3. EXPERIMENTAL RESULTS AND DISCUSSION

In a transverse field of 100 kG at room temperature, the resistance increased about $\frac{1}{4}$ per cent, as shown in Fig. 1, where the change in resistance

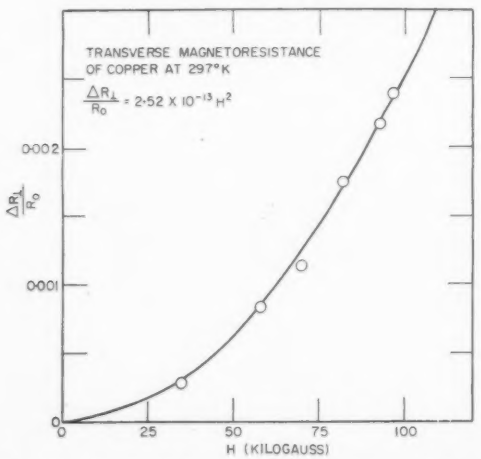

FIG. 1. Magnetoresistance, in a transverse field, of copper specimen lb at room temperature (297°K).

(ΔR) divided by the zero field resistance (R_0) is plotted as ordinate and the applied transverse magnetic field as abscissa. Within experimental error the magnetoresistance observed is a quadratic function of the applied magnetic field. The curve in Fig. 1 is a plot of the function

$$\frac{\Delta R}{R_0} = 2{\cdot}52 \times 10^{-13} H^2. \qquad (1)$$

The close correlation of the data to a quadratic dependence is evident.

KAPITZA[1] estimated that the room-temperature increase of resistance was probably not larger than 1 or 2 per cent at 300 kG. Extrapolation of the quadratic function to 300 kG gives a 2·3 per cent increase of resistance, in good agreement with KAPITZA's estimate.

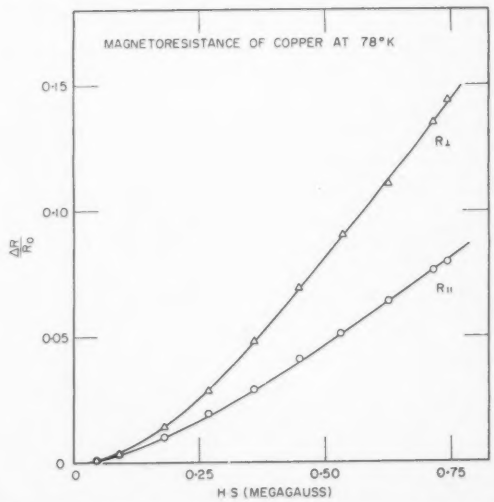

FIG. 2. Magnetoresistance, in transverse and longitudinal fields, of copper specimen lb ($S = 7{\cdot}68$) at 78°K. The abscissa is the product of H, the magnetic field applied, and S, the zero field resistance ratio. Data curves for transverse and longitudinal magnetoresistance are labelled $R_\perp$ and $R_\parallel$ respectively.

The magnetoresistance of copper at 78°K was found to be considerably larger than at room temperature. The longitudinal and transverse magnetoresistances of specimen 1b at liquid-nitrogen temperature are given in Fig. 2. The detailed field-dependence of the resistance proved to be considerably less than quadratic (equation (1)); nor could a satisfactory fit be made to the data by using the arbitrary equation $\Delta R/R_0 = aH^n$ (where n is an adjustable parameter). A satisfactory fit to the data was found possible by using the arbitrary formula

$$\frac{\Delta R}{R_0} = \frac{aH^2}{1+bH} \qquad (2)$$

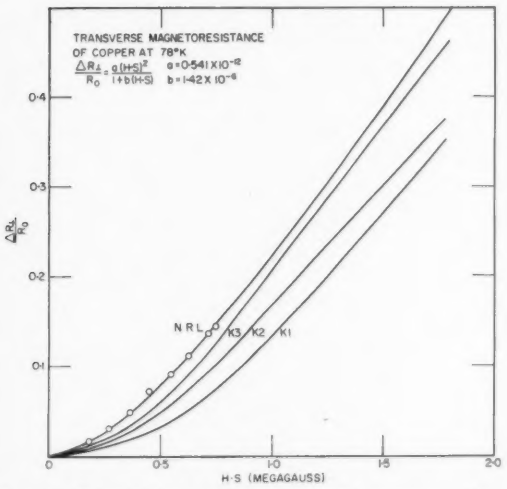

FIG. 3. Comparison of transverse-field magnetoresistance at 78°K with the results of KAPITZA (K curve): $K1$ (Hartmann and Braun-hard); $K2$ (Hilger-semi-annealed); $K3$ (Hartmann and Braun-annealed). The curve through the NRL data was drawn by utilizing equation (2) with the constants given in the upper left-hand corner.

which has a linear field-dependence at high fields. The data can also be fitted with an expression of the form

$$\frac{\Delta R}{R_0} = \frac{aH^n}{1+bH^n} \qquad (3)$$

For liquid-nitrogen temperature, equation (3) gives a good fit to the data, using $n \sim 1{\cdot}9$ for the transverse magnetoresistance and $n \sim 1{\cdot}7$ for the longitudinal. However, these expressions when extrapolated to values of $H \sim 200$ kG show marked deviations from KAPITZA's data, which do not indicate any saturation of the magnetoresistance of copper at 78°K for applied field up to $H \sim 300$ kG. The transverse magnetoresistance observed at 78°K is given in Fig. 3, together with a plot of the arbitrary formula (equation (2)) extrapolated for comparison with the results (K curves) of KAPITZA. To permit comparison of samples of varying purity, values of $H \times S$ are plotted as abscissae, where H is the applied field and S is the ratio of the resistance of the specimen at 0°C to the zero field resistance of the specimen at the temperature of observation. The measured magnetoresistance has the same general field-dependence as that observed by KAPITZA. However, the measurements at this temperature do not extend to as large values of $H \times S$ as those reached by KAPITZA, and therefore the so-called linear dependence at high fields is confirmed only by extrapolation and not by measurement.

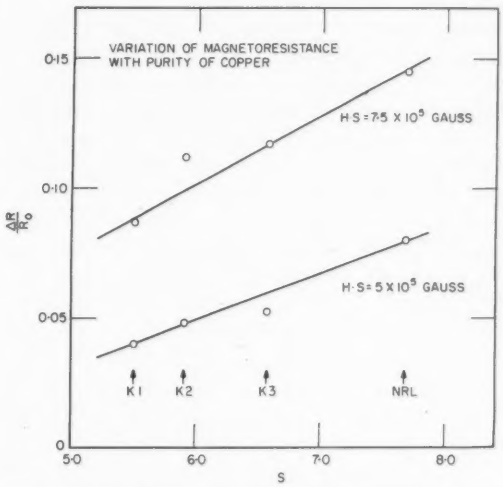

FIG. 4. Dependence of magnetoresistance on purity as measured by the resistance ratio S for four samples; NRL specimen 1b and the three specimens of KAPITZA[1] $K1$, $K2$, and $K3$. The two curves are for different values of applied field: $H \times S = 7{\cdot}5 \times 10^5$ G and $H \times S = 5 \times 10^5$ G. Kohler's rule would require the slopes of the constant $H \times S$ curves to be zero. This pronounced dependence of $\Delta R/R_0$ on S is not observed in the copper data for 4·2°K.

For liquid-nitrogen temperature, the data of Fig. 3 suggest that $\Delta R/R_0$ at fixed $H \times S$ may be a smooth function of the purity parameter (S). This is illustrated in Fig. 4. If the net increase in purity (S) of the specimens were to arise from the algebraic sum of a decrease in point defects and an increase in dislocations, then differences in density of dislocations in the specimens might account for the deviations, as the magnitudes of $H \times S$ used in the measurements were not large compared to the critical reduced field of 512 kOe/$\mu\Omega$ cm estimated by VAN BUEREN[6]. Actually, the differences in specimen purity presumably arise from differences in the degree of annealing, and this supports such a hypothesis. Disagreement arises for the case of specimens $K3$ and NRL 1b, which were both annealed at temperatures above 400°C where a relative increase in dislocations with annealing is difficult to understand, and one is inclined to suspect that some other scattering process is causing the deviation. Transverse magnetoresistance data at 4·2°K do not exhibit this relationship. Although the magnitudes of $H \times S$ used for the comparisons at 4·2°K are much larger than the critical reduced field estimate, interpretation is complicated by the observation that while the transverse magnetoresistance data all coalesce to a single function of $H \times S$, the longitudinal magnetoresistance data for the same samples do not. Further study of this is in progress.

A test of the temperature-independence of Kohler's rule is possible through comparison of the overlap in data obtained at different temperatures of observation. Fig. 5 presents such a plot of the transverse and longitudinal magnetoresistances of sample 1b at the three temperatures 297, 78, and 4·2°K. There is a distinct departure from Kohler's rule in the overlap regions of both the longitudinal and transverse magnetoresistances by as much as 30 per cent. This is consistent with the observation by BOROVICK[3] at liquid-hydrogen temperatures. The data presented in Fig. 5 are all for a single specimen of constant purity and thus demonstrate the temperature-dependence without the disturbing influence of change in specimen purity.

As suggested by the data in Fig. 5, saturation of the longitudinal magnetoresistance has been observed at liquid-helium temperatures. Because the longitudinal magnetoresistance at saturation is considerably smaller than the transverse effect, the specimen must be carefully aligned with the field to prevent the appearance of spurious observations. Accurate correction for misalignment by use of the Voigt–Thomson formula[7] is not possible in this case, for experimentally measured values are found to deviate by as much as 30 per cent

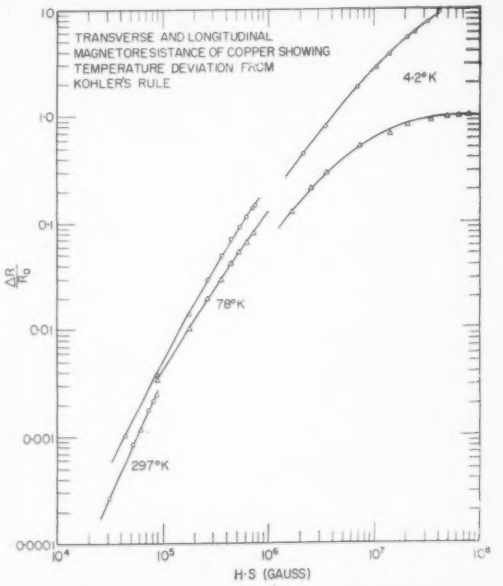

FIG. 5. Logarithmic Kohler plot of the magnetoresistance of copper specimen 1b. Circle data points (upper curve) are for transverse magnetoresistance and triangular data points (lower curve) are for longitudinal magnetoresistance.

from values calculated by the formula, the larger deviations occurring near longitudinal alignment. Microscopic anisotropy could render the Voigt–Thomson formula inapplicable for the polycrystalline specimens used. That the specimens behaved as polycrystalline specimens was determined by rotation of the field about the axis of the specimen for which the transverse magnetoresistance observed remained constant to within 1 per cent. The data show accurate two-fold symmetry with perhaps eight small ($\sim$ 2 per cent) undulations in the magnetoresistance, but no large asymmetry effects such as were observed by MACDONALD[8] on alkali-metal specimens.

Measurements of the longitudinal magnetoresistance of copper at 4·2°K are given in Fig. 6,

together with a plot of equation (3), using $n = 1{\cdot}3$, $a = 9{\cdot}62 \times 10^{-10}$ and $b = 9{\cdot}01 \times 10^{-10}$. The saturation curve was found to be temperature-independent for the range 2·0–4·2°K and independent of measuring current for the range 0·1–2·0 A. The data presented are for two samples differing in resistance ratio by 27 per cent. Correcting the data

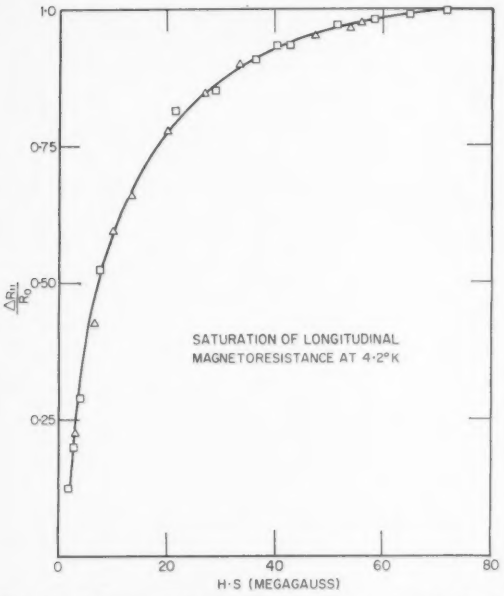

FIG. 6. Magnetoresistance of copper in longitudinal magnetic fields at 4·2°K. Square data points are for specimen 1b ($S = 581$); triangular data points are for specimen 2 ($S = 738$). The solid curve is calculated from equation (3) with $n = 1{\cdot}3$.

of OLSEN and RINDERER[4] for sample misalignment, one obtains a longitudinal-magnetoresistance curve suggestive of Fig. 6 with saturation near $\Delta R/R_0 \sim 1$. However, subsequent measurements on other specimens[10] have given longitudinal saturation values more nearly $\Delta R/R_0 \sim 2$, even though the transverse magnetoresistance of these specimens obeyed Kohler's rule very closely. The source of this variation in saturation magnetoresistance is now under study.

The magnetoresistance of copper specimen 1a at 4·2°K in a transverse magnetic field is given in Fig. 7. In contrast to the longitudinal case (Fig. 6), where the magnetoresistance has reached effective saturation at $H \times S$ values above 40 MG, the transverse magnetoresistance is increasing linearly in the $H \times S$ range from 40 to 60 MG, reaching a value of $\Delta R/R_0 = 13{\cdot}07$ at 101 kG, the highest field used. Thus the field-dependence of the transverse magnetoresistance at 4·2°K cannot be represented by saturating-type expressions. Given also in Fig. 7 are sample datum points of other workers to show the equivalence of observations made by different observers employing differing techniques

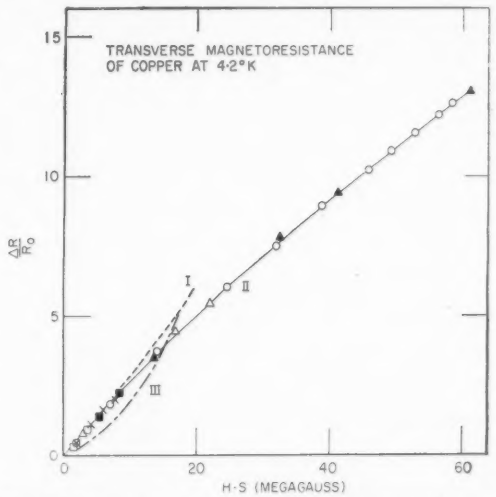

FIG. 7. Comparison of the transverse magnetoresistance of copper observed at 4·2°K. Curve I is the observation of CHAMBERS[5], curve III the observation of OLSEN and RINDERER[4], and curve II an average of other data. Data are plotted as: ⊙ ($S = 606$), Sample 1a, present work; × ($S = 127$) LOGAN[9]; Δ ($S = 367$) and ▲ ($S = 980$) DOLECEK[10]; □ ($S = 156$) and ■ ($S = 413$) BOROVICK[3].

of measurement and samples of a wide range in resistance ratio S (100 to 1000). The only significant deviations are for the data of OLSEN and RINDERER[4], which probably result from the difficult technique associated with the use of pulsed fields, and the data of CHAMBERS[5], for which differences in sample geometry may be responsible.

It is of interest that the ratio of transverse to longitudinal magnetoresistance is approximately a linear function of the applied field. This is shown in Fig. 8, where the ratio of transverse to longitudinal magnetoresistance is plotted as a function of applied field for the entire range up to near-saturation. The curve is a plot of the functional

relationship given in the upper corner of the figure. This linear relationship has been found to hold for all specimens; however, here again the actual values of the constants in the equation are found to be temperature-sensitive and depend on specimen purity in a manner not completely accounted

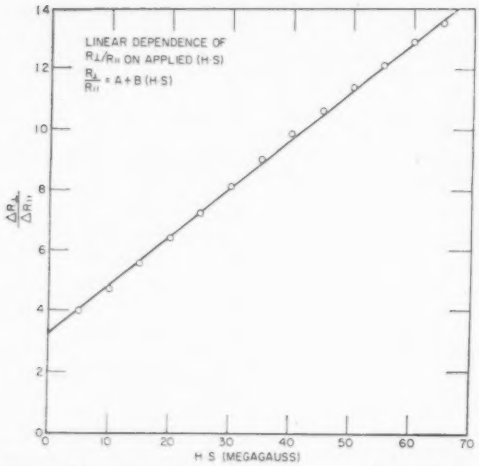

FIG. 8. Magnetoresistance of copper specimen 1b, showing linear dependence of the ratio of transverse to longitudinal magnetoresistance on applied magnetic field.

for by the use of the resistance ratio S, and the data may indicate a decrease in the slope at large applied fields.

The observed saturation of the longitudinal magnetoresistance should provide an excellent basis for further development of the theory of magnetoresistance. Recently, ZIMAN[11] has indicated how saturation of the longitudinal magnetoresistance may be explained. A successful model should provide for the relatively large longitudinal and transverse magnetoresistances at low fields, with saturation of the longitudinal in the observable range of $H \times S < 100$ MG, and give the ratio of transverse to longitudinal magnetoresistance as a linear function of $H \times S$. From such a model information on the mean free path, relaxation times, and scattering processes could become available.

4. SUMMARY

At room temperature a quadratic dependence of the magnetoresistance on applied field was observed. At liquid-nitrogen temperature a satisfactory fit to the data was found possible by using an arbitrary function which permitted a transition from a quadratic to a linear dependence at high fields. At liquid-helium temperature, in contrast to a linear field-dependence observed for the transverse magnetoresistance, saturation of the longitudinal magnetoresistance was found to occur at a value of the order of the zero field resistance. A temperature-dependence of Kohler's rule for magnetoresistance has been demonstrated, and some isothermal deviation between samples was noted at 78°K. Kohler's rule was found to be applicable to the transverse magnetoresistance of copper at 4·2°K, but not to the longitudinal magnetoresistance, particularly near saturation.

REFERENCES

1. KAPITZA P., *Proc. Roy. Soc.* A**123,** 292 (1929).
2. YNTEMA G. B., *Phys. Rev.* **91,** 1388 (1953).
3. BOROVICK E. S., *Zh. Eksper. Teor. Fiz.* **27,** 355 (1954).
4. OLSEN J. L. and RINDERER L., *Nature, Lond.* **173,** 682 (1954).
5. CHAMBERS R. G., *Proc. Roy. Soc.* A**238,** 344 (1957).
6. VAN BUEREN H. G., *Philips Res. Rep.* **12,** 190 (1957).
7. JAN J.-P., *Solid State Physics* (Ed. F. SEITZ and D. TURNBULL) Vol. 5, p. 15. Academic Press, New York (1957).
8. MACDONALD D. K. C., *Phil. Mag.* **2,** 97 (1957).
9. LOGAN J. K., U.S. Naval Research Laboratory, unpublished data for two temperatures, 1·7 and 4·2°K.
10. DOLECEK R. L., U.S. Naval Research Laboratory, unpublished data for specimens annealed; (Δ) for 4 hr at 800°C and (▲) for 4 hr at 700°C, with 8 hr cooling time.
11. ZIMAN J. M., *Phil. Mag.* **3,** 1117 (1958).

J. Phys. Chem. Solids Pergamon Press 1959. Vol. 11. pp. 43–45. Printed in Great Britain.

MINIMUM MOLAR GIBBS FREE ENERGY AND SMALL DEVIATIONS FROM STOICHIOMETRY IN CRYSTALLINE BINARY COMPOUNDS

R. F. BREBRICK

U.S. Naval Ordnance Laboratory, White Oak, Maryland

(*Received* 4 *February* 1959)

OL.
11
959

Abstract—It is shown that the minimum molar Gibbs free energy for a binary compound showing small deviations from the stoichiometric composition can be calculated from the standard free energy of formation. The significance of the minimum-free-energy curve on a pressure-temperature projection of the phase diagram is discussed. In particular, its displacement from the intrinsic curve may serve to establish another relation among the energy parameters defining the crystal model.

1. INTRODUCTION

IMPROVEMENTS have been made recently in the theory relating the concentrations of defects in crystals,[1–3] and the significance of these improvements has been established by experimental studies.[2,4] In regard to binary compound crystals one type of question answered by the theory is the following: given the field of existence for the crystal on a log (partial pressure of one vapor species) versus $1/T$ plot, what is the internal structure of this field? The internal structure might be exhibited by lines of constant net electronic-carrier concentration, $n-p$, the line of zero concentration being the intrinsic line. Here the significance of another type of line, that of minimum molar Gibbs free energy, is discussed. A binary compound, whose stoichiometric composition is MX, is considered.

2. THE CURVE OF MINIMUM MOLAR GIBBS FREE ENERGY

Provided that the deviation from the stoichiometric composition is small compared to the total concentration of lattice sites, the change in the chemical potential of one crystal component arising from a change in the crystal composition is accompanied by a nearly equal and opposite change in the chemical potential of the other component. The molar Gibbs free energy of the crystal is then independent of crystal composition to a good approximation.[5] If, at the composition limits of the crystal's stability, the concentration of the predominant point defect is 1 per cent of the concentration of lattice sites, then the free energy varies with composition by this percentage or less. Strictly speaking, however, the free energy of the crystal depends on its composition. It has been appreciated for some time, on the basis of a simple thermodynamic argument, that the molar Gibbs free energy of a binary phase is a minimum when the chemical potentials of the two components are equal. Thus a binary crystal, MX, showing small deviations from stoichiometry, has a minimum molar free energy when the chemical potentials of the two components are equal to one another and, to a good approximation, to one-half the molar free energy of the crystal.

At any temperature it is convenient to measure all chemical potentials relative to those of the ideal monatomic gases M and X at 1 atm pressure. The arbitrary choice of this standard state does not affect the value of the crystal composition possessing the minimum molar free energy at a given temperature. At this composition the chemical potential of the X component, μ_x, is related to the molar free energy of the crystal, F, by the equation:

$$\mu_x-\mu_x^0 = (F-\mu_m^0-\mu_x^0)/2 = \Delta F^0{}_{m,x}/2 \quad (1)$$

Here μ_x^0 and μ_m^0 are chemical potentials of the

ideal monatomic gases X and M respectively at 1 atm pressure. They are the arbitrary zeros of chemical potential. The quantity $\Delta F^0_{m,x}$ is the standard free energy of formation of the crystal. Since it will be convenient to use another standard state later, we have symbolically indicated the standard state as a subscript on this quantity. If the vapor phase in equilibrium with the crystal is ideal, equation (1) may be rewritten as follows:

$$RT \ln p_x = \Delta F^0_{m,x}/2 \tag{2}$$

The corresponding equation for the pressure of the diatomic gaseous species, X_2, in equilibrium with the crystal of minimum free energy is given by:

$$RT \ln p_{x_2} = \Delta F^0_{m,x_2} - (\tfrac{1}{2}\mu_{x_2}{}^0 - \mu_x{}^0) \tag{3}$$

where the standard state for the free energy of formation, $\Delta F^0_{m,x_2}$, is now the ideal gases, M and X_2, each at 1 atm pressure. The quantity in parenthesis is the free energy of transformation of the ideal gas X to the ideal gas X_2 at 1 atm pressure. Such quantities are tabulated for many elements.[6]

3. SIGNIFICANCE OF THE MINIMUM FREE ENERGY

The standard free energy of formation has been measured over various temperature ranges for many crystalline compounds. Its significance for the theory of defects in crystals has been limited to obtaining the equilibrium constant for the mass-action law relating the partial pressures of certain gaseous species in the equilibrium crystal–vapor system, i.e.

$$\left.\begin{aligned} p_m p_x &= \exp(\Delta F^0_{m,x}/RT) \\ p_m p_{x_2}{}^{\frac{1}{2}} &= \exp(\Delta F^0_{m,x_2}/RT) \end{aligned}\right\} \tag{4}$$

Equations (2) and (3) for the minimum molar Gibbs free-energy curve have a wider significance, however. First of all from a practical point of view, although the curve of minimum free energy need not necessarily fall in the solidus field at all, it can serve as a guide when necessary as to roughly what partial pressures might be used to reach equilibrium with the crystal. Secondly, in one treatment of the complex problem of melting, the crystal composition of minimum free energy has been assumed to have the highest melting point, i.e. to be the composition at the invariant melting point.[7] The intersection of the minimum free-energy curve with the three-phase line serves as an experimental check on this assumption for a particular case. Finally, if the minimum-free-energy line and the intrinsic line are known, their relative displacement may be used to establish relations between certain energy parameters defining the crystal model.

As an example of the last point, consider a binary ionic crystal in which vacancies in the cation and anion sublattices are the predominant point defects.[5] The chemical potentials of the metallic component, μ_m, and the non-metallic component, μ_x, are given respectively by:

$$\left.\begin{aligned} \mu_m &= RT \ln S/V_C + E_f - \zeta_{hC} + U - RT \ln K_C \\ \mu_x &= RT \ln S/V_A - E_f - \zeta_{hA} + U - RT \ln K_A \end{aligned}\right\} \tag{5}$$

where here the chemical potentials are measured relative to the ideal monatomic gases, M and X, each at 1 atm pressure; the Fermi level, E_f, is measured relative to that for the stoichiometric crystal; ζ_{hC} and ζ_{hA} are the energies required to create a cation and an anion vacancy respectively; K_C and K_A are the contributions of the cations and anions respectively to the vibrational modes of the crystal; U is one-half the crystal lattice energy per cation–anion pair relative to the above standard state; S is the total concentration of sites in each sublattice; and V_C and V_A are respectively the concentrations of ionized cation and anion vacancies. In the intrinsic crystal the concentrations of ionized cation and anion vacancies are equal to each other and to the square root of the Schottky constant. Assume that the electronic energy-band structure is such that in the intrinsic crystal only a negligible fraction of the vacancies of each kind are un-ionized, i.e. the crystal is simultaneously intrinsic and stoichiometric. The ratio of the partial pressure of gaseous X atoms in equilibrium with the crystal of minimum free energy, p_x (min. F), to that in equilibrium with the intrinsic crystal, p_x (int.), is then given by:

$$\begin{aligned} 2 \ln[p_x(\text{min. } F)/p_x(\text{int.})] &= \\ \ln[p_{x_2}(\text{min. } F)/p_{x_2}(\text{int.})] &= \\ -(\zeta_{hC} - \zeta_{hA} + RT \ln K_C/K_A)/RT & \end{aligned} \tag{6}$$

In conclusion a numerical example is given for PbS. In Table 1 are listed: the standard free energy of formation of PbS from the ideal monatomic lead

VOL. 11 1959

Table 1.

T(°K)	$-\Delta F^\circ_{Pb,\,S_2}\times 10^{-3}$ (cal/mole PbS)	$(\mu_S-\frac{1}{2}\mu_{S_2})\times 10^{-3}$ (cal/mole S)	$\log p_{S_2}$(min. F) (p in atm)	$\log p_{S_2}$(int.) (p in atm)
800	48·67	30·81	−4·9	−4·3
900	44·25	29·39	−3·6	−3·4
1000	39·57	27·97	−2·5	−2·5
1100	34·97	26·54	−1·7	−1·8
1200	29·75	25·10	−0·85	−1·2
1300	25·27	23·67	−0·27	−0·75

vapor and the ideal diatomic sulfur vapor, each at 1 atm pressure;[8] the standard free energy of formation of gaseous diatomic sulfur from the monatomic species, both at 1 atm pressure and ideal;[6] the log of the partial pressure in atmospheres of gaseous diatomic sulfur in equilibrium with the crystal of minimum free energy as calculated by equation (3); and the log of the partial pressure of gaseous diatomic sulfur in equilibrium with the intrinsic or stoichiometric crystal as determined experimentally.[4] Above 800°K the intrinsic and minimum free energy curves are quite close but with slightly different slopes. Thus if the vacancy model is correct, one finds with the aid of equation (6) that nine kcal/mol more are required to create a lead vacancy than a sulfur vacancy. Moreover, the composition of PbS at the invariant melting point has been found[4] to correspond to about 6×10^{18} excess lead atoms/cm^3, and is therefore not that at which the crystal has a minimum free energy. This is evidence in addition to the shape of the three-phase line that the isothermal free-energy/composition curves for liquid and solid are not both symmetrical about the composition PbS.

Note added in proof: The difference in the energies required to create an ionized anion vacancy and an ionized cation vacancy, $\zeta_{hA}-\zeta_{hC}$, can be obtained in terms of more familiar energy parameters by reference to the grand partition function (Eq. 3 of Reference 5). It is equal to (a) the difference in the energies required to remove an anion and a cation from inside the crystal to infinity plus (b) the sum of the ionization energies of the anion and the metal atom plus (c) twice the intrinsic Fermi level measured relative to an electron at rest at infinity. The term (c) is negative and might dominate even in the case where term (a) is positive.

REFERENCES

1. Reiss H., *J. Chem. Phys.* **21,** 1209 (1953).
2. Kroger F. A., Vink H. J. and van den Boomgaard J., *Z. Phys. Chem.* (*Leipzig*) **203,** 1 (1954).
3. Kroger F. A. and Vink H. J., *Solid State Physics* (Ed. F. Seitz and D. Turnbull) Vol. 3, pp. 310–438. Academic Press, New York (1956).
   Kroger F. A. and Vink H. J., *J. Phys. Chem. Solids* **5,** 208 (1958).
4. Bloem J. and Kroger F. A., *Z. phys. Chem.* (*Frankfurt*) **7,** 1 (1956).
5. Brebrick R. F., *J. Phys. Chem. Solids* **4,** 190 (1958).
6. Stull D. R. and Sinke G. C., *Thermodynamic Properties of the Elements*. American Chemical Society, Washington, D.C. (1956).
7. Hodgkinson R. J., *J. Electronics* **1,** 612 (1956).
8. Bloem J., Kroger F. A. and Vink H. J., *Report of the Conference on Defects in Crystalline Solids* (Bristol 1954) p. 273. Physical Society, London (1955).
   Bloem J., *Philips Res. Rep.* **11,** 273 (1956).

J. Phys. Chem. Solids Pergamon Press 1959. Vol. 11. pp. 46–54. Printed in Great Britain.

MAGNETIC SUSCEPTIBILITY AND ELECTRICAL RESISTIVITY OF Au–Mn ALLOYS

A. GIANSOLDATI, J. O. LINDE and G. BORELIUS

Physics Department, Kungl, Tekniska Högskolan, Stockholm, Sweden

(*Received* 30 *December* 1958; *revised* 20 *March* 1959)

Abstract—From magnetic measurements made on Au–Mn alloys in both the states, ordered and disordered, the magnetic moment μ of the manganese atoms and the Weiss temperature Θ of the alloys have been determined. In the temperature range used (90–1020°K), the electrical resistivity of the alloys has also been determined. The Θ values of the alloys are found to vary regularly with composition, being positive at low and negative at high manganese concentrations. Resistivity/concention curves have been obtained in three different states of the alloys, the atomic as well as the magnetic order being considered. The magnetic and the electrical measurements show a marked dependence of the magnetic transformation points on the degree of atomic order of a given alloy, the Curie and the Néel points being displaced toward lower temperatures with decreasing atomic ordering of the alloy.

VOL. 11 195

1. INTRODUCTION

THE alloy system gold–manganese is characterized by a fairly large number of ordered crystal phases. Magnetically, the alloys are of great interest, some of the phases showing transformations to the ferromagnetic and others to the antiferromagnetic state in the lower temperature range.

As a continuation of earlier investigations in this laboratory on the magnetic[1,3a] and resistance[4,5] properties of the alloys, we give in the present paper the results of measurements on alloys containing 10–75 atomic per cent manganese.

2. METHODS OF MEASUREMENTS

The arrangement used for measuring the paramagnetic susceptibility allows measurements to be made on wires, rods or powders in the range from room temperature up to about 800°C.[1] The directly measured atomic (mole) susceptibility values χ' were corrected for the superimposed diamagnetism as follows. Denoting the atomic fraction of manganese of a given alloy by α, we have (disregarding the diamagnetism of the manganese atoms) for the atomic paramagnetic susceptibility χ of the alloy

$$\chi = \chi' - (1-\alpha)\chi_d \qquad (1)$$

where χ_d is the diamagnetic atomic susceptibility of gold (for which the value $\chi_d = -29\times10^{-6}$ was used). The effective, atomic magnetic moment μ of the manganese atoms in the alloy has been evaluated by means of the Curie–Weiss formula

$$\chi = \frac{C}{T-\theta} \quad \text{or} \quad \frac{1}{\chi} = \frac{T}{C} - \frac{\theta}{C} \qquad (2)$$

and

$$\mu = \sqrt{\left(\frac{3kC}{N\alpha}\right)} \qquad (3)$$

where k is Boltzmann's constant and N Avogadro's number. The quantities C and θ for a given specimen are obtained from the slope and the intercept on the T-axis of the straight line in a $1/\chi$ versus T diagram.

The resistivity measurements were carried out with a potential bridge. When measuring the temperature-dependence of the resistance, silver wires were attached to the samples as potential leads.

3. RESULTS

(a) *The primary gold-rich solid solutions*

To supplement the earlier measurements in this range by GUSTAFSSON[1] and KRONQVIST and GIANSOLDATI[2], we have measured an alloy with 10·0 atomic per cent manganese. As shown in

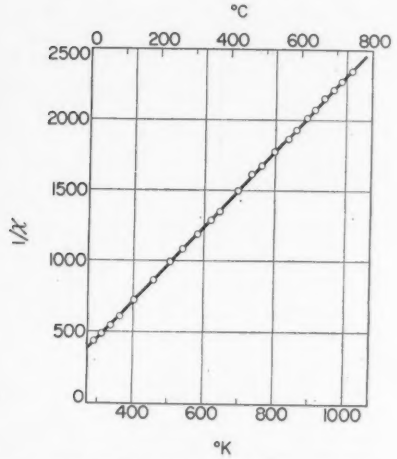

FIG. 1. $1/\chi$ against temperature for an alloy containing 10 atomic per cent manganese.

Fig. 1, the χ values obey the Curie–Weiss law over the whole range of temperatures covered by the measurements. From the graph one obtains

$$C = 0{\cdot}381;\ C/\alpha = 3{\cdot}81;\ \mu/\mu_B = 5{\cdot}6;\ \theta = 118$$

μ_B being the Bohr magneton.

(b) *The range of the* Au_4Mn *phase*

Alloys of this composition range could, when quenched from temperatures above the transition point, be rolled and drawn to wires. In Figs. 2–3 the $1/\chi$ versus T curves are given for two alloys in this concentration range. (An alloy with 20·5 per cent manganese has also been investigated.) The transition of the alloys occurring slightly above 400°C has all the features of an order–disorder transformation. Thus the high-temperature

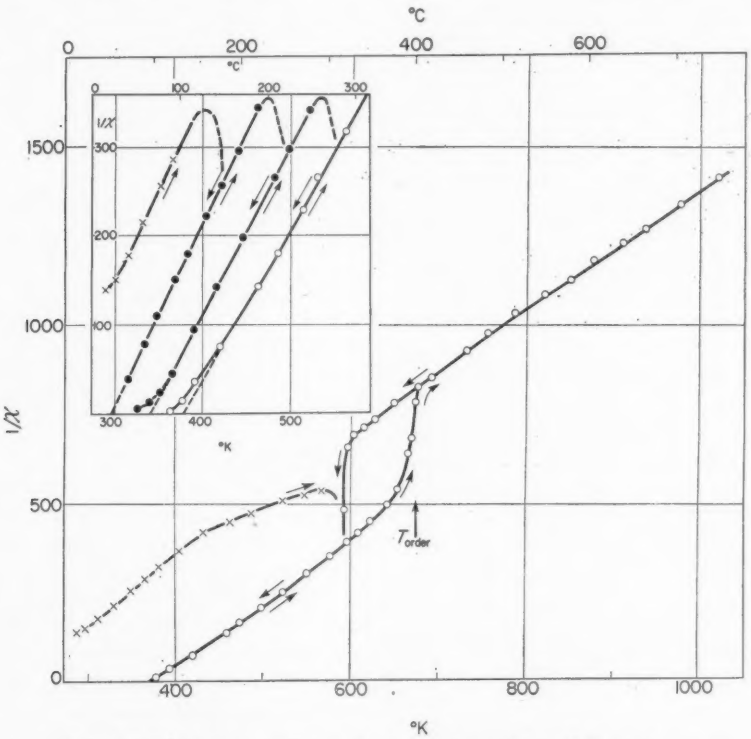

FIG. 2. $1/\chi$ against temperature for an alloy containing 18·5 atomic per cent Mn. (Inset diagram for the low-temperature region shows the displacement of the Curie point T_c with change in the degree of order).

× Quenched from 550°C
● Intermediate rate of temperature change
○ Slow rate of temperature change

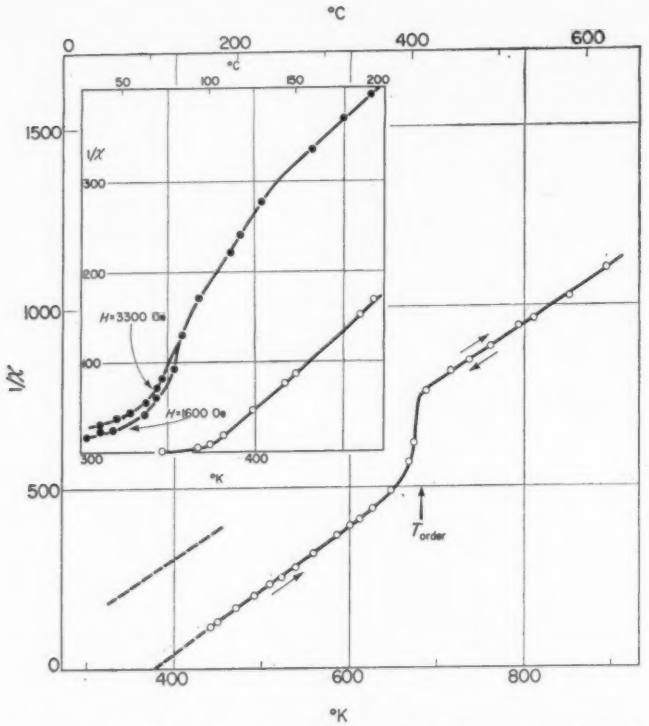

FIG. 3. $1/\chi$ against temperature for an alloy containing 23·0 atomic per cent manganese.

– – – Quenched from 550°C
● Intermediate cooling rate from high-temperature region
○ Slow rate of temperature change

state of the alloys can be retained at room temperature by quenching. The crystal structure of the ordered phase is of the Ni_4Mo[6] type. From the linear part of the $1/\chi$ versus T curves above the transition point, T_{order}, the following magnetic data have been obtained for the two alloys:

$$\alpha = 0{\cdot}185; \quad T_{order} = 402°C; \quad C = 0{\cdot}656;$$
$$\mu/\mu_B = 4{\cdot}9; \quad \theta = 186$$
$$\alpha = 0{\cdot}23; \quad T_{order} = 408°C; \quad C = 0{\cdot}625;$$
$$\mu/\mu_B = 4{\cdot}8; \quad \theta = 203.$$

The influence of the order–disorder transformation on the magnetic quantities will be discussed in Section 6. The more perfectly ordered states show, as was first found by KUSSMANN and RAUB[7], a ferromagnetic Curie point T_c at about 363°K (90°C). This point is displaced, as the present measurements show (Figs. 2–5), in the direction of lower temperatures with decreasing atomic ordering of a given alloy.

The two transitions of the alloys (magnetic and order–disorder), and the displacement of T_c with change of degree of order appear still more distinctly in the resistivity temperature/diagrams given in Figs. 4 and 5. In the paramagnetic range the change of resistivity with temperature is rather small for the disordered as well as for the ordered state (at temperatures far enough below the transition point). Below the ferromagnetic Curie point the resistances of the ordered alloys show a temperature-dependence similar to that of a pure metal. Thus the temperature coefficient of resistance of the alloys in the fully ordered state differs very little from that of pure gold.

VOL
11
195

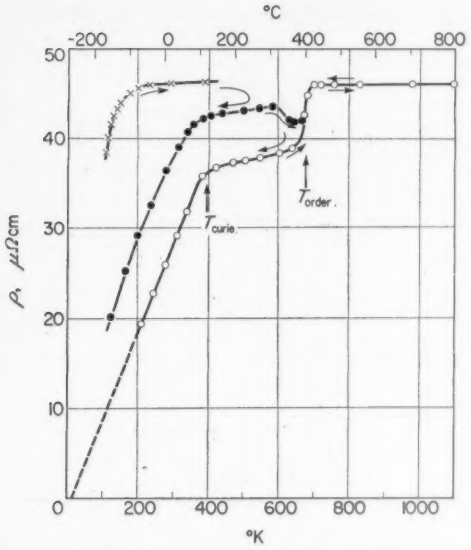

FIG. 4. Electrical resistivity against temperature for an alloy containing 18·5 atomic per cent manganese.

× Quenched from 550°C
○ Cooled slowly
● Intermediate state of order

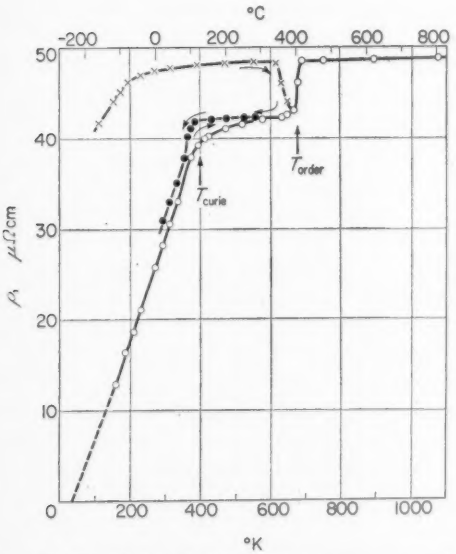

FIG. 5. Electrical resistivity against temperature for an alloy containing 20·5 atomic per cent manganese.

× Quenched from 550°C
○ Cooled slowly
● Intermediate rate of temperature change

(c) *The* Au_2Mn *phase*

According to the phase diagram suggested by RAUB *et al.*[8] the ordered phase Au_2Mn has a rather narrow range of homogeneity and exists only below about 730°C. MEYER and TAGLANG[9] have shown that Au_2Mn has an antiferromagnetic transformation at about 90°C, and transforms into a ferromagnetic state in a strong magnetic field (pseudo-ferromagnetism).

The specimen of this composition used in our investigations was too brittle, even after quenching

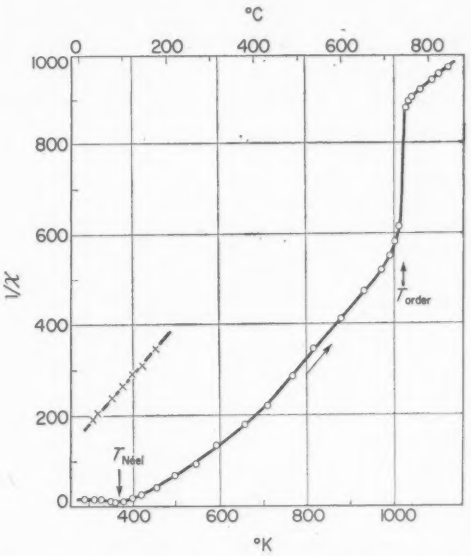

FIG. 6. $1/\chi$ against temperature for the alloy Au_2Mn.

× Quenched from 840°C
○ Slow rate of change of temperature

from high temperature, to be rolled or drawn to wire. It was obtained in the form of a rod by casting. To homogenize it, the rod was annealed for many hours at about 700°C.

Figure 6 shows the $1/\chi$ versus T diagrams for the specimen. The antiferromagnetic transformation occurs apparently at about 100°C. The transformation at about 740°C seems to be of the order–disorder type. The magnetic data obtained for the alloy above 740°C are:

$$C = 1{\cdot}25; \quad C/\alpha = 3{\cdot}7; \quad \mu/\mu_B = 5{\cdot}5; \quad \theta = -96.$$

Because of the continuous change of the degree of ordering that occurs below the transformation

point, it is in our opinion questionable whether an evaluation of the atomic moment μ from the slope of the curve in this temperature range is permissible for Au_2Mn. For the disordered metastable state of the sample at low temperatures (20–180°C), obtained by quenching from above the transition point, the following data have been obtained:

$$C = 0{\cdot}943;\quad C/\alpha = 2{\cdot}83;\quad \mu/\mu_B = 4{\cdot}5;\quad \theta = 126.$$

The order–disorder transformation and the magnetic transformation are also well marked in the resistivity/temperature diagram (Fig. 7).

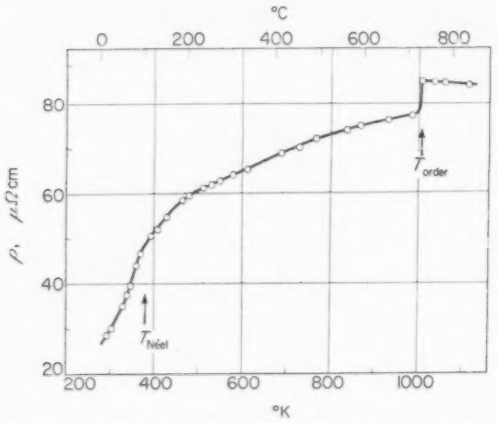

FIG. 7. Electrical resistivity against temperature for the alloy Au_2Mn.

(d) *The composition range of* $AuMn_3$

In this range we have made measurements on three alloys with 73·5, 75·0 and 76·5 atomic per cent manganese. The 73·5 per cent alloy was obtained in a ductile state after quenching and could be rolled into rod. After rolling it was homogenized by annealing at 1000°C. The two other samples were also prepared in the form of rods by casting. We have reason to believe that the 73·5 per cent alloy had reached a more homogenous state than the other two (not described here).

The results of the magnetic measurements on the 73·5 per cent alloy are shown in Fig. 8. The alloy has a transition point at about 660°C. For the state of the alloy that is stable above the transition point (which state also can be retained at room temperature by quenching), the magnetic susceptibility follows the Curie–Weiss law. The magnetic data obtained from the graph are:

$$C = 3{\cdot}08;\quad C/\alpha = 4{\cdot}19;\quad \mu/\mu_B = 5{\cdot}8;$$
$$\theta = -1840.$$

Below the transition point the magnetic susceptibility increases slightly with time on prolonged annealing. This may be caused by a slight continuous structural change below the discontinuous

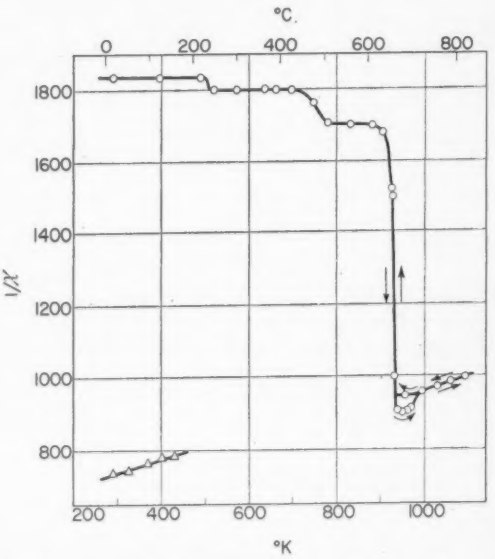

FIG. 8. $1/\chi$ against temperature for an alloy containing 73·5 atomic per cent manganese.

△ Quenched from 850°C
○ Slow rate of temperature change

one at 660°C, or it may indicate a new structural transformation in the lower temperature range. The ordered alloy shows in the lower temperature ranges a paramagnetic susceptibility which is practically independent of temperature.

Figure 9 gives the results of electrical-resistivity measurements on the 73·5 per cent alloy. In the range above the transition point at 660°C, the resistivity is approximately independent of temperature. This is also the case for the quenched metastable sample at low temperatures. Below the magnetic transition point the temperature–dependence of the resistivity indicates a continuous antiferromagnetic ordering process of the type found earlier for the Au_3Mn and the AuMn

phases.[3,5] It may also be mentioned that cold-worked samples of the alloy show a fairly large change in resistivity when annealed in the temperature range 100–200°C (about 15 per cent decrease of resistivity in the case of highly cold-worked samples, indicating a cold-work effect on the resistivity of this magnitude).

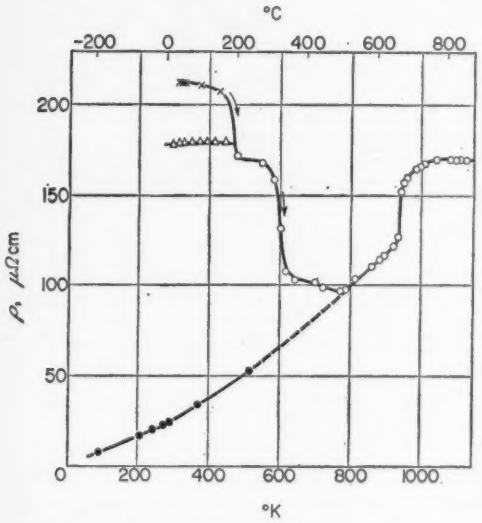

FIG. 9. Electrical resistivity against temperature of an alloy containing 73·5 atomic per cent manganese.
× Cold-worked
△ Quenched from 850°C
● Cooled slowly
○ Slow rate of temperature change

X-ray investigations on the system gold–manganese which are going on in this laboratory have shown the existence of conflicting structures in the composition range of $AuMn_3$. These phenomena have to be left for further investigation.

4. THE PHASE DIAGRAM

The various forms of the phase diagram of the gold–manganese system proposed in the literature are in some cases inconsistent. Thus BUMM and DEHLINGER[10] give a continuous series of solid solutions in the concentration range 0–93 atomic per cent manganese at temperatures just below the solidus line, while the investigations by RAUB *et al.*[8] ("ZWIKKER's diagram") have given a diagram characterized a.o. by one solubility gap at about 33 atomic per cent manganese and another at 75 per cent. Further, the range of concentration of the γ-manganese structure is much larger in ZWIKKER's diagram than in that of BUMM and DEHLINGER.

The contributions to the phase diagram made by the present investigation and earlier investigations in this Institute[3,5] are mainly restricted to the structural and magnetic transitions occurring in the lower temperature range. In that range our results agree for the most part with those of earlier authors.[7–9]

For the high-temperature range and manganese concentrations around 75 atomic per cent, the results of our investigations support the diagram of BUMM and DEHLINGER rather than that of ZWIKKER[8]. Thus we have been able to obtain a single-phase alloy with 73·5 atomic per cent at 1000°C, which would not be possible according to the phase diagram of RAUB *et al.*, but quite possible with that of BUMM and DEHLINGER.

The 50 atomic per cent–alloy is at the upper limit of the present measurements still in an ordered state, as can be concluded from the results of the resistivity measurements[5] (see Section 5). The phase diagram of ZWIKKER[8] is consistent with the assumption that the ordered state for this alloy is stable right up to the melting point.

5. THE RESISTIVITY PROPERTIES

The resistivity/temperature characteristics of the alloys found in this and earlier investigations at this Institute[3,5] enable us to make a survey of the electrical properties of the system. Qualitatively the regularities may be valid also for some other alloy systems showing order–disorder transformations as well as magnetic transformations in the lower temperature range.

We have to consider three different temperature ranges, each characterized by the state of order occurring for the atomic arrangements or/and the paramagnetic moments of the magnetic atoms at a given temperature:

(1) The range above the structural transition point (order–disorder transformation) where the homogeneous alloys have disordered arrangement of the gold and manganese atoms at the lattice points and disordered magnetic spins of the Mn atoms (*state of atomic and magnetic disorder*).

(2) The range below the structural transformation point but above the magnetic transformation point (*state of atomic order and magnetic disorder*).

(3) The range below the temperature of the onset of spontaneous magnetization (*state of atomic and ferro- or antiferromagnetic order*), both these sorts of order increasing with decreasing temperature.

In the gold–manganese system all three states occur for the Au_4Mn, Au_3Mn and Au_2Mn phases in the sequence of temperature ranges outlined above. For AuMn the state (1) is (if it exists) not reached in the temperature range of our measurements. In the case of $AuMn_3$, the second state is not observed. The order–disorder transformation for that alloy is accompanied by a change of the crystal lattice type (from face-centred cubic to body-centred cubic).[11] It can be assumed that the b.c.c. lattice favours the onset of magnetic as well as of structural order at the transformation point.

In the temperature range of both atomic and magnetic order, the change of resistivity with the temperature ($d\rho/dt$) is high for alloys with the stoichiometric composition of a given structure. In the range of atomic order and magnetic disorder, $d\rho/dt$ is small and varies with the degree of order, the order being in its turn a function of the temperature. In the range of atomic and magnetic disorder, $d\rho/dt$ follows the general laws for the resistivity of primary solid solutions recently discussed by one of the authors.[12]

The absolute values of the resistivity of the alloys in the different stages discussed above may conveniently be compared by means of the residual resistivities valid at 0°K. For the stages (1) and (2), the residual resistivity values are obtained approximately by linear extrapolation of the high-temperature parts of the ρ/T curves to $T = 0$°K. In the lowest temperature range the ρ/T curves are, for the case of ideally ordered alloys, quite in agreement with the assumption that the resistance is zero at 0°K. The residual resistivities obtained in this way are given in Fig. 10. It is obvious from this, that the 50 per cent alloy is still structurally ordered in the temperature range above the magnetic transformation point. From the results of Fig. 10 it is also apparent that state (2) is absent in the 73·5 per cent alloy, this being in accordance with the conclusion drawn from the magnetic measurements. It is interesting to note that the resistivity curve for the structurally disordered alloys is a straight line over the whole concentration range investigated (0–73·5 atomic per cent manganese).

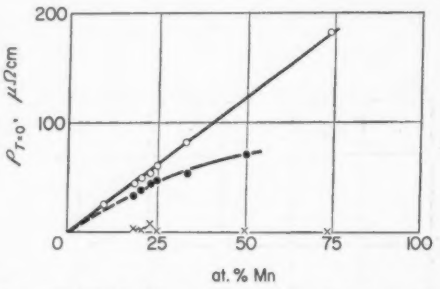

FIG. 10. Resistivity values extrapolated to $T = 0$°K versus concentration of manganese for gold–manganese alloys in different states of order. (The values for the alloys with 25·0 and 50·0 atomic per cent manganese are from Reference 5.)

○ Atomic and magnetic disorder
● Atomic order, magnetic disorder
× Atomic and magnetic order

From the results of Figs. 4–5 can be assumed that the magnetic ordering does not appear to the full extent in states of imperfect atomic order (obtained by quenching of the samples from different higher temperatures). Another interesting fact is that the magnetic transition point is displaced towards lower temperatures with increasing structural disorder of a given alloy (Figs. 2–5).

6. THE MAGNETIC PROPERTIES

(a) *The magnetic moment of the manganese atoms*

In Table 1 we give the values of the magnetic moment of the manganese atoms in the alloys. We would point out that the values obtained for the temperature range below the structural transformation point are uncertain owing to the following circumstances. In this range an appreciable influence of temperature on the degree of structural order is, as is well known, to be expected. As the value of $1/\chi$ is found to increase with decreasing order, a continuous change in the degree of order will make the computed μ-values too low. The possibility of a real change in the atomic magnetic moment with order seems, however, in our opinion not to be definitely excluded.

Table 1. *Magnetic data for the* Au–Mn *alloys*

Alloy (At. % Mn)	μ/μ_B	Θ	Temperature range (°C)	State of the alloy
10·0	5·6	118	20–800	Disordered
18·5	5·1	186	400–800	Disordered
	5·2	373	100–200	Ordered
20·5	4·7	212	400–800	Disordered
	4·7	388	200–400	Ordered
23·0	4·7	203	400–600	Disordered
	4·4	378	200–300	Ordered
25·0	4·7	208	600–800	Disordered
	5·4	140	20–300	Ordered
33·3	5·5	−96	750–850	Disordered
50·0	5·7	−280	300–800	Ordered
73·5	5·8	−1840	700–850	Disordered

For the states below the magnetic transformation points, we have no measurements of μ. Values found from data given in the literature[7,9] are

$$Au_4Mn \qquad \mu = 4{\cdot}5\mu_B,$$

$$Au_2Mn \qquad \mu = 3{\cdot}5\mu_B.$$

These values are obtained from measurements of the saturation magnetization and are, as is well known, not directly comparable with the effective μ values deduced from paramagnetic measurements.

(b) *Values of the Weiss temperature* Θ

Table 1 contains the Weiss Θ values for the alloys. In Fig. 11 these values are also given graphically as a function of the manganese concentration c of the alloys. From the figure it is seen that Θ varies regularly with c, changing over from positive to negative values at about 30 atomic per cent manganese. From the diagram it can also be seen that the transformation to atomic order of the alloy brings about a change of Θ in the direction of higher absolute values. Also for very low concentrations of manganese ($c \lesssim 2$ atomic per cent) Θ changes over to negative values, as is seen from data in the insert diagram of Fig. 11. The values are in this case derived from measurements reported by GUSTAFSSON.[1]

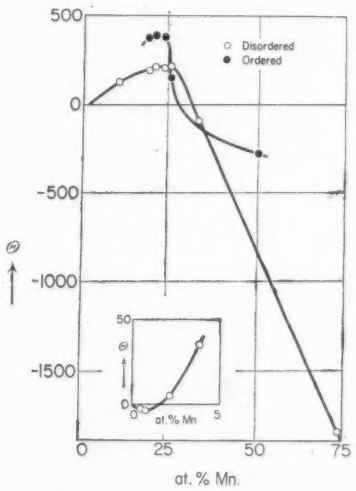

FIG. 11. Values of the Weiss temperature Θ against the concentration of manganese. (Inset diagram for low-concentration range gives data evaluated from Reference 1.)

○ Disordered
● Ordered

The μ values given in the table show that this quantity is lower by about 1 Bohr magneton for alloys in the concentration range 18–23 atomic per cent manganese than for other alloys of the system. Assuming that the same electron configuration is valid for the manganese atoms in the alloys as in the gaseous state of pure manganese, the theoretical paramagnetic μ value should be given by the expression

$$\mu = \mu_B = \sqrt{[4S(S+1)]}. \qquad (4)$$

Thus $\mu_{\text{theor}} = 5{\cdot}92\ \mu_B$ for $S = 5/2$.

The values obtained in this investigation deviate in the direction of lower values from μ_{theor}, but the deviation is in some cases rather small.

Acknowledgement—This investigation has been supported economically by the Swedish Natural Science Research Council.

REFERENCES

1. GUSTAFSSON G., *Ann. Phys. Lpz.* **25,** 545 (1936).
2. KRONQVIST E. and GIANSOLDATI A., *Ark. Fys.* **7,** 343 (1953).
3. GIANSOLDATI A., *J. Phys. Radium* **16,** 342 (1955).
3a. GIANSOLDATI A., LINDE J. O. and BORELIUS G., *J. Phys. Chem. Solids* **9,** 183 (1959).
4. LINDE J. O., *Ann. Phys. Lpz.* **10,** 52 (1931); **15,** 219 (1931).
5. GIANSOLDATI A. and LINDE J. O., *J. Phys. Radium* **16,** 341 (1955).
6. HARKER D., *J. Chem. Phys.* **12,** 315 (1944). WANTANABE D., *Acta Cryst., Camb.* **10,** 483 (1957).
7. KUSSMANN A. and RAUB E., *Z. Metallk.* **47,** 9 (1956).
8. RAUB E., ZWIKKER U. and BAUR H., *Z. Metallk.* **44,** 312 (1953).
9. MEYER A. and TAGLANG P., *C.R. Acad. Sci., Paris* **239,** 961, 1611 (1954); *J. Phys. Radium* **17,** 457 (1956).
10. BUMM H. and DEHLINGER K., *Metallwirtsch.* **13,** 23 (1934).
11. HUMBLE STEN G. To be published.
12. LINDE J. O., *Physica, s'Grav.* **24,** 109 (1958).

J. Phys. Chem. Solids Pergamon Press 1959. Vol. 11. pp. 55–67. Printed in Great Britain.

THE PENETRATION OF POSITIVE IONS OF LOW ENERGY INTO ALLOYS AND COMPOSITION CHANGES PRODUCED IN THEM BY SPUTTERING

E. GILLAM

Division of Tribophysics, Commonwealth Scientific and Industrial Research Organization, University of Melbourne, Australia

(*Received* 9 *February* 1959)

OL.
11
959

Abstract—Thin sheets of the alloy Cu_3Au were prepared so that electron-diffraction patterns could be obtained from them by transmission. After bombardment of the alloy with argon ions of various energies up to 5000 eV, the diffraction patterns consisted of distinct doublets, indicating the formation of a layer with a composition different from that of the original alloy. Initially, the sputtering produced a thin layer of alloy, uniform in composition and more gold-rich than Cu_3Au; subsequent sputtering under identical conditions eroded three times as much copper as gold from the surface. Helium and xenon ions were also used to show that the composition and thickness of the layer both depend on the size of the ion and its energy. Some other alloys developed altered layers. It was shown that with silver–palladium alloys the composition of the altered layer also depends on the composition of the original alloy. The thickness of the altered layer is taken to be a measure of the penetration of the ions. A discussion of current theories of radiation damage shows that they do not account fully for the observations.

1. INTRODUCTION

THE removal of atoms from the surface of a metal by bombarding it with positive ions ("sputtering" it) with energies of up to a few thousand electron-volts, has been studied mostly with targets consisting of pure metals, and alloys have seldom been used. There have been several reviews of the subject recently,[1–4] but it is still not well understood, partly because there is some disagreement about the minimum amount of energy an ion needs to remove a metal atom (for a given metal–ion combination), a quantity usually referred to as the "threshold energy" for sputtering.[2,3,5–8]

The possibility that the ions penetrate some distance into the surface layers was used by KEYWELL[9] in developing a radiation-damage theory of sputtering, but any physical changes they may cause are difficult to exploit experimentally if the ion energies are low. Consequently, there have been no published measurements of the penetration into metals of ions with energies up to 4000 eV, although several ways have been found of estimating the penetration of higher-energy ions (above 30 keV)[10–13] for comparison with the theory of BOHR[14] or with the application of neutron-cooling theory[15] to particle penetration into solid matter.

The present paper describes a new effect found in the electron-diffraction patterns (taken by transmission) of certain alloys after ion bombardment, which has proved to be a sensitive indicator of the occurrence of sputtering, and which can be used to estimate the depth of penetration of even very low-energy ions.

Previous work on the sputtering of alloys has been reported by ASADA and QUASEBARTH[16], who found that for alloys of copper with very small amounts of gold, the gold was removed by ion bombardment faster than the copper, leaving the original alloy more copper-rich. FISHER and WEBER[17], however, have stated that alloys such as 70:30 brass and stainless steel sputter in krypton in such a way that the material removed from the target has the same composition as the original alloy. HANAU[18] has confirmed this for some aluminium alloys.

Electron diffraction has been used by LADAGE[19] and CASTAING[20] to study alloys after ion bombardment. LADAGE used reflection electron diffraction after bombarding β-brass surfaces with 2000-eV ions, but could detect no unusual surface layers. CASTAING's experiments were similar to those described here, but he did not find any unusual effect because his alloy was of aluminium with 4 per cent copper, and this alloy is not suitable for showing the effect described in this paper.

In this investigation thin sheets of the alloy Cu_3Au were further thinned down by an electropolishing technique, so that electron-diffraction patterns could be obtained from them by transmission. When its diffraction pattern had been recorded, a specimen was made the cathode in a gas discharge at a low pressure, and each side of it in turn bombarded with positive ions. It was then re-examined by transmission electron diffraction. Helium, argon and xenon ions were used to bombard Cu_3Au. Other alloys were also investigated.

2. SPECIMEN PREPARATION AND EXPERIMENTAL PROCEDURE

(a) *Alloy preparation*, Cu_3Au

A slug of the alloy was prepared by placing 38·32 g of commercially refined gold and 36·96 g of copper into a clean silica tube of diameter 0·5 in., and melting them together by heating in an induction furnace coil, with the silica tube continuously evacuated by a rotary pump. The tube temperature was taken up to 1100°C and held there for 5 min before slowly cooling to room temperature. Examination by X-rays showed that the alloy was homogeneous, but it was too tough to swage down to a size suitable for cold-rolling to a thin strip. All specimens were therefore made from pieces cut from this slug, which were melted again *in vacuo* in a silica tube of 0·1 in. internal diameter. The resulting round specimens were cold-rolled to strips a few thousandths of an inch thick.

In the cold-rolled state this alloy is disordered. As some specimens of the ordered alloy were required, pieces of the cold-rolled strip were heated for 64 hr at 360°C *in vacuo*, and cooled to room temperature at an average rate of 1·5°C/min.

(b) *Electropolishing technique for* Cu_3Au

HEIDENREICH[21] first prepared specimens from bulk metals thinned down sufficiently to transmit electrons and give diffraction patterns. An improvement on his method is to electropolish both sides of a thin piece of metal foil simultaneously, using pointed electrodes placed opposite to each other on either side of the foil.[22] This eventually forms a hole in the foil, around which the metal edges are so thin that electron-diffraction patterns can be obtained by transmission.

For Cu_3Au, the only electrolyte found suitable was that of BAKISH and ROBERTSON[23], and with this a good polish could be obtained, though the darkening of the solution, together with the vigorous bubbling that occurred during polishing, made continuous operation to the formation of a hole difficult, and the rapid detection of the hole impossible.

An alternative method was therefore devised to produce the holes, the electropolishing being performed on both sides of the specimen simultaneously by spraying the electrolyte on to it through platinum nozzles which acted as cathodes. A polythene pump of the type described by SYKES *et al.*[24] was used to produce the flow of electrolyte in a way shown schematically in Fig. 1.

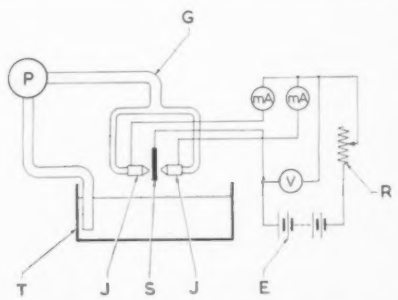

FIG. 1. Schematic diagram for electropolishing to a hole by a continuous-flow method.

E Accumulator
G Polythene tube
J Platinum nozzles
P Polythene pump
R Rheostat
S Specimen
T Polythene trough

Into the exit hole of the pump a polythene **T**-piece was forced, the arms of the **T** leading round to each side of the specimen, which was fixed directly above the pump with its plane vertical. The specimen strip, of dimensions $1 \times \frac{1}{4}$ in., was

covered on both sides by a quick-setting acrylic compound of the type used for dental repairs, except for two circular patches of diameter $\frac{1}{8}$ in. directly opposite each other near the lower end, and a small part at the upper end for electrical connection. Platinum nozzles of exit diameter also $\frac{1}{8}$ in. were fixed into the ends of the arms of the **T**-piece, and were held pointing towards and just above the exposed circular patches of the specimen. This enabled a beam of light to be focussed on one of the circular patches on one side of the specimen. By adjusting the flow of electrolyte and the nozzle-to-specimen distance, the current density could be controlled until polishing was achieved on each side of the specimen. The electrolyte flowed off the specimen back into the pump for recirculation. The appearance of a hole in the specimen was observed by looking at it from the opposite side to the one on which the light beam was focussed. The apparatus was used in a fume-cupboard, as hydrogen cyanide gas was given off by the polishing reaction. When a hole appeared in the polished metal, the specimen was moved away from the nozzles and washed with distilled water. The protecting acrylate was pulled off and any small particles of it remaining were dissolved in acetone.

(c) *Other alloys*

For reasons which will become apparent, the alloy Cu_3Au was the most suitable one to use, but several other alloys were investigated, namely, cupro-nickel (with 20 per cent nickel by weight), AgAu, Ag_3Mg, α-brass, and alloys of silver and palladium with a range of compositions. They were prepared commercially and cold-rolled to make strip suitable for the experiment. They were electropolished to form holes, in the apparatus used for Cu_3Au, and the electrolytes the materials used for the cathode nozzles and the other polishing conditions are given in Table 1.

(d) *Sputtering apparatus*

The first experiments with Cu_3Au, and those with all other alloys except the silver–palladium ones, were carried out with a simple discharge chamber of glass in which the specimen (cathode) and a tungsten plate (anode) were separated by a few inches. Argon was leaked into the evacuated chamber through an Edwards valve and pumped away by a mercury-diffusion pump after passing through liquid-air traps. A discharge passing a current of 0·5 mA could be maintained at voltages between 300 and 5000 V by varying the pressure in the chamber between 80 μ Hg (for 300 V) and 12 μ Hg (for 5000 V).

In order, however, to sputter at very low voltages, and at pressures of only 1 or 2μ whatever the voltage, the chamber was modified by the introduction of an axial magnetic field, a heated tungsten filament, and an electrode arrangement identical to that described by OGILVIE[25]. In such a discharge, most of the ions strike the cathode with an energy almost equal to Ve, where V is the applied voltage and e the electronic charge (BACKUS[26]). For the experiments in which sputtering was followed by evaporation of copper on to the specimen, a second (coiled) tungsten filament was added, which could be heated independently of the one used for low-voltage sputtering.

(e) *Experimental procedure*

When a hole had been formed in a specimen by polishing, electron-diffraction patterns were recorded, using 50-kV electrons from areas round the hole thin enough to transmit electrons. Each side of the specimen in turn was then sputtered under chosen conditions of discharge voltage, recorded ion current,* gas pressure and sputtering time. In most cases both sides had the same treatment, but in some, to show up new effects, the two sides were sputtered at different voltages. After each sputtering treatment electron-diffraction patterns were again recorded.

On inserting a specimen into the discharge chamber, the chamber was evacuated to a pressure of 10^{-6} mm Hg and tested to ensure that it was free from air leaks. The inert gas was then leaked in and a steady pressure attained. The discharge was then established and maintained stable by controlling the intensity of the magnetic field and filament heating current. For a few minutes the pressure usually rose as the apparatus degassed, but ultimately the pressure dropped to its original value, and all reported sputtering times were

*The current recorded by a meter in series with the specimen consists of a positive-ion current and a secondary-electron current emitted from the specimen.

Table 1. *Electropolishing conditions for thinning various alloys for electron-diffraction examination*

Alloy	Electrolyte	Cathode	Voltage	Current density (A/cm^2)
Cupro-nickel	Conc. orthophosphoric acid	Copper	2·5–3·0	0·25
Brass (25% zinc by weight)	Conc. orthophosphoric acid	Copper	1·3–1·6	0·10
AgAu	Solution of: 60 g potassium cyanide 30 g potassium ferrocyanide 10 g silver cyanide in 1 l. water	Platinum	5·5	2–4
Ag_3Mg	32·4 g silver cyanide 19·5 g potassium cyanide 41·5 g potassium carbonate 20 ml conc. orthophosphoric acid in 1 l. water	Platinum	0·9–1·3	0·05
Silver–palladium alloys:				
(1) 20% Pd	30 g potassium cyanide 35 g silver cyanide 38 g potassium carbonate 1 l. distilled water	Platinum	0·5	0·07
(2) 40% Pd		Platinum	5·0	0·07
(3) 70% Pd	25 g potassium cyanide 500 ml water 50 ml conc. ammonium hydroxide	Platinum	5·0–6·0	1·0
(4) 95% Pd		Platinum	5·0–6·0	2·0

measured from this moment. The time of sputtering was different for different voltages, varying from 2 or 3 hr at very low voltages to 15–30 min at 5000 V. The ion current was higher for low voltages and vice versa, so that the power dissipation in the specimen was always low enough to prevent it from reaching a temperature higher than 80°C.

In some experiments, copper was evaporated on to the specimen to provide a calibrating layer. After the diffraction pattern of the sputtered specimen had been obtained, the specimen was returned to the chamber, and a weighed strip of abraded and cleaned copper foil was placed on the coiled tungsten filament which had previously been degassed by flashing. The specimen was then re-sputtered for a few minutes under exactly the same conditions as previously, after which the sputtering was stopped, the apparatus evacuated to 10^{-6} mm Hg, and a current passed through the coiled tungsten filament until the copper formed itself into a molten bead and then evaporated. A further electron-diffraction pattern was then obtained from the specimen.

3. RESULTS AND INTERPRETATION

(a) *The formation of a layer of altered composition*

(i) *Cold-rolled* Cu_3Au. Patterns obtained from cold-rolled Cu_3Au before ion bombardment were similar to those described by HIRSCH *et al.*[27] for beaten and etched gold foil, consisting of spotty arcs connected by diffuse smears (Fig. 2). The arcs were parts of Debye–Scherrer rings corresponding to the face-centred cubic lattice of Cu_3Au. For some specimens extra rings indicated the presence of impurities remaining from the electropolishing procedure. Figure 3 is typical of the patterns obtained from the same specimen after bombardment with argon ions, showing the disappearance of impurities and the formation of distinct doublets in the alloy pattern. For each original spotty arc, there appeared a sister arc displaced towards the centre of the pattern. These doublets were very similar to those obtained by

OL.
11
959

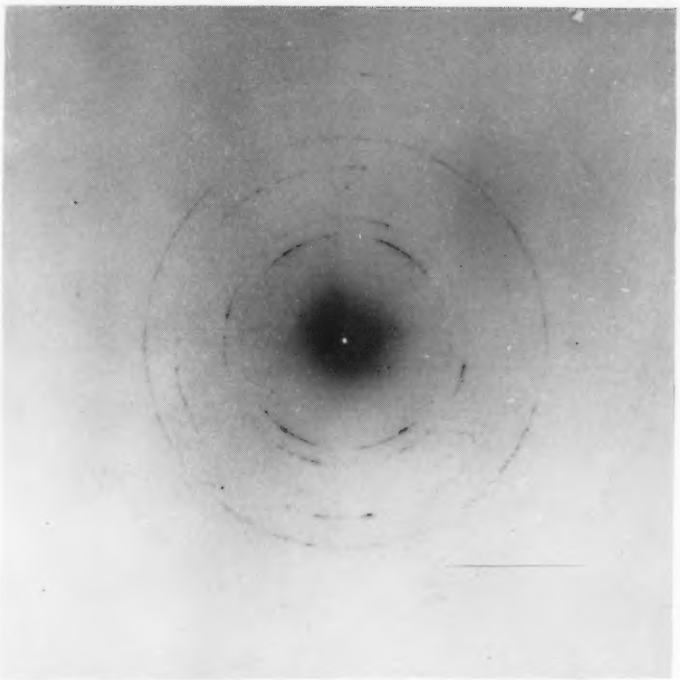

FIG. 2. Cold-rolled Cu_3Au. Transmission pattern by electron diffraction.

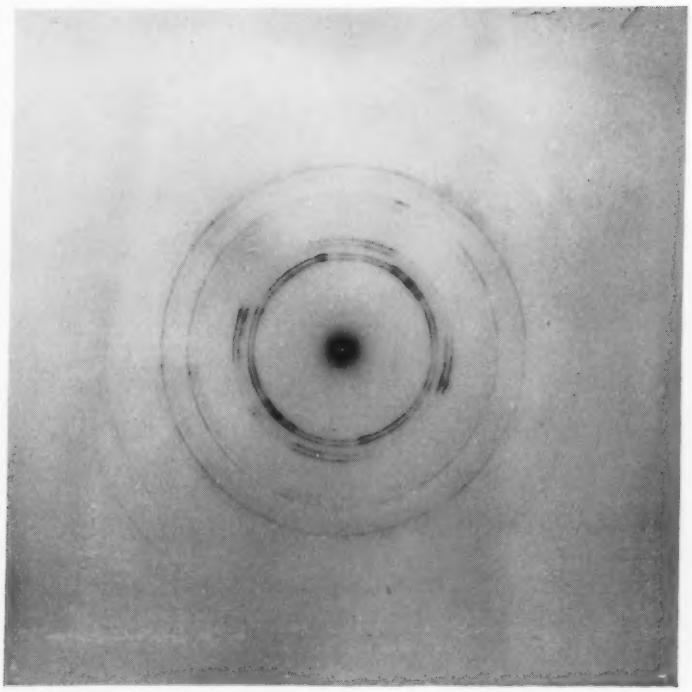

FIG. 3. Cold-rolled Cu_3Au. Transmission pattern after bombarding both sides with argon ions (voltage 500 V, positive-ion current 0·25 mA, pressure 5×10^{-3} mm Hg, time 30 min.)

[*facing page* 58

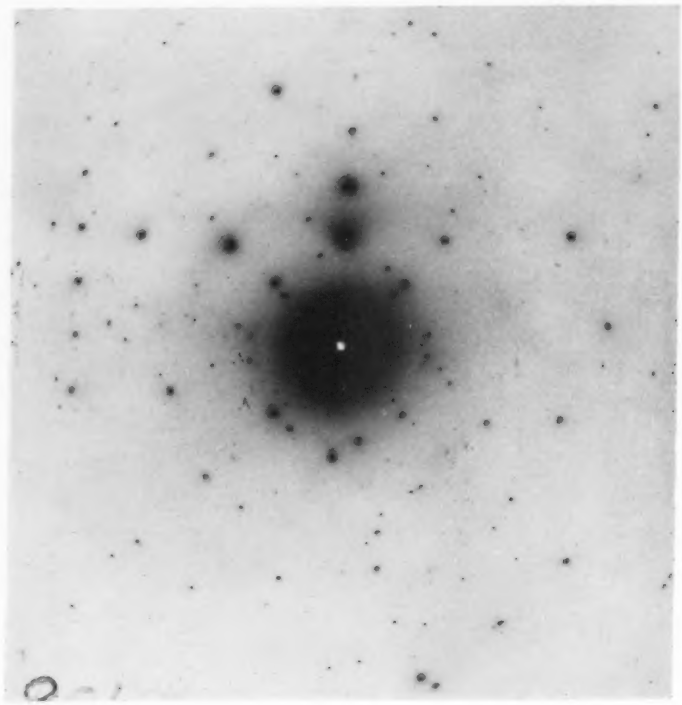

FIG. 4. Ordered Cu_3Au. Transmission pattern by electron diffraction.

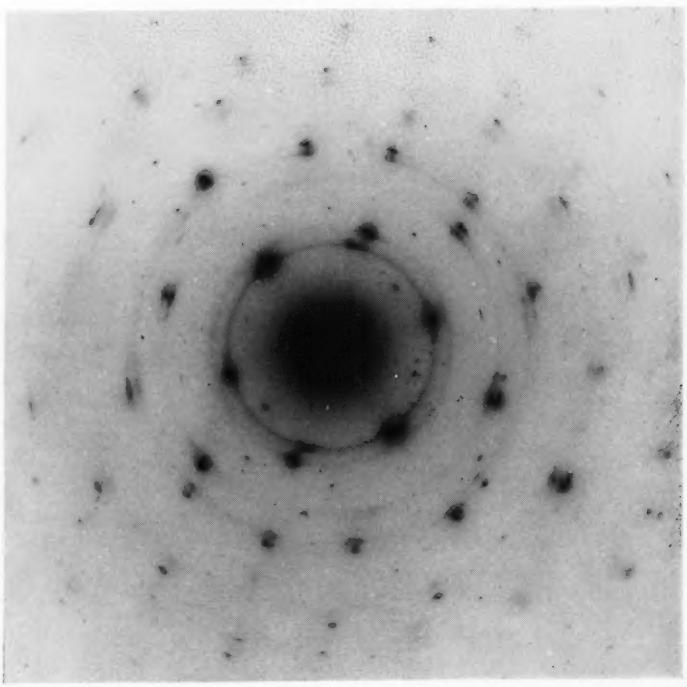

FIG. 5. Ordered Cu_3Au bombarded both sides with argon ions (voltage 2500 V, positive-ion current 1 mA, pressure $1{\cdot}4 \times 10^{-2}$ mm Hg, time 30 min).

VOL
11
195

VOL.
11
1959

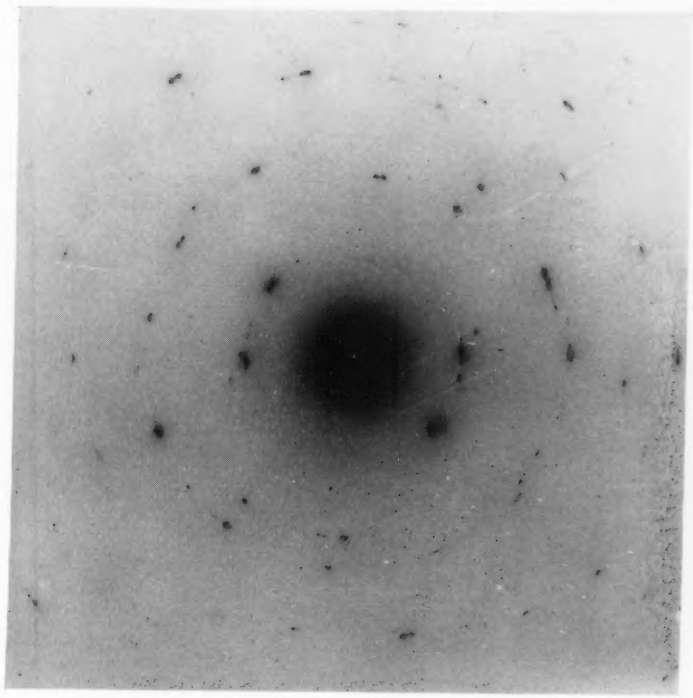

FIG. 7. Pure copper (annealed). Transmission pattern.

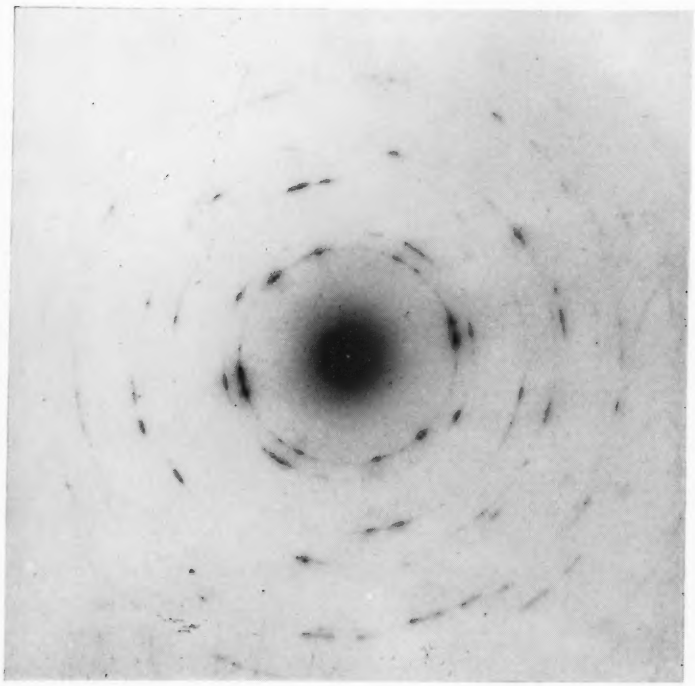

FIG. 8. Pure copper (as Fig. 7) bombarded with argon ions. Transmission pattern.

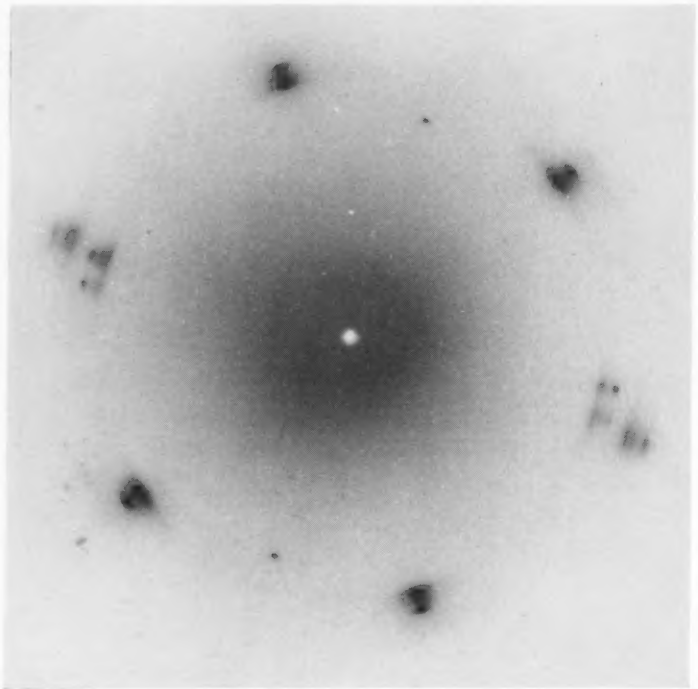

FIG. 10. Ordered Cu_3Au (sputtered). 500 V one side; 5000 V other side. Transmission pattern enlarged to show details.

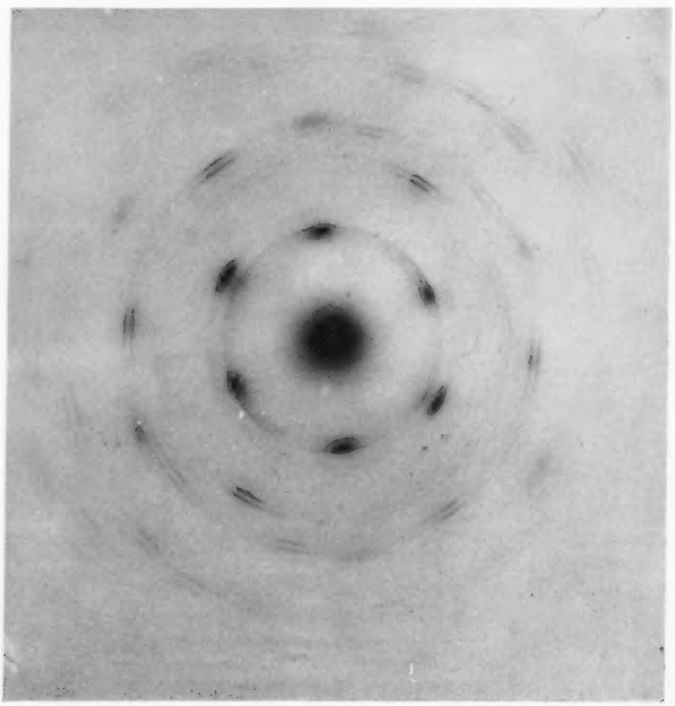

FIG. 11. Cold-rolled Cu_3Au. 80-V argon-ion bombardment plus copper evaporated on.

FINCH and SUN[28] after they had electrodeposited layers of copper on single-crystal films of platinum, but in the case of the alloy, metal on the specimen could not be deposited by the back-diffusion of sputtered material because of the low gas pressure used and consequent high mean free path in the gas. To confirm this, two pieces of metal, both electropolished to holes, one of copper and one of silver, were placed side by side and bombarded under the same conditions as with the alloy. No copper was detected on the silver, nor any silver on the copper.

(ii) *Ordered* Cu_3Au. The diffraction pattern of a specimen of the ordered alloy is shown in Fig. 4. The pattern of sharp spots resulted from several large crystals of different orientations round the edge of the hole, and super-lattice spots such as (100), (110), etc., were abundant. After ion bombardment, the area round the same hole gave the pattern of Fig. 5. Each spot resulting from a fundamental reflection became a doublet, but this was not so for the superlattice spots, which remained as single spots. Thus, some of the original ordered Cu_3Au was still present in the thin region, being presumably unaffected by the ion bombardment. In addition, epitaxially related to the Cu_3Au, was another alloy in which no ordering was present, owing either to its different composition or to another disordering effect by ion bombardment.

These patterns showed clearly that the effect of ion bombardment on the alloy Cu_3Au was the formation of a layer of alloy of different composition having a larger lattice parameter than the original alloy, and therefore enriched in gold. The layer was of an essentially uniform composition, since the reflections from it were not smeared into the Cu_3Au reflections, but were quite separate and distinct. This layer could be partly removed by dipping the bombarded specimen into the polishing solution for a few seconds, after which electron-diffraction patterns showed that the intensity of the inner of the doublet arcs had decreased considerably relative to that of the outer arcs. This fact, together with the epitaxial nature of the doublet, indicated that the specimen had the structure illustrated in Fig. 6. An indication that the effect was a general surface effect, and not one occurring locally at the edge of the hole, was given by the observation that if the specimen was protected from the impinging ions except for a circular patch (by an aluminium mask), the circular patch appeared yellow after bombardment at low voltages, compared with the reddish-gold colour of the protected alloy.

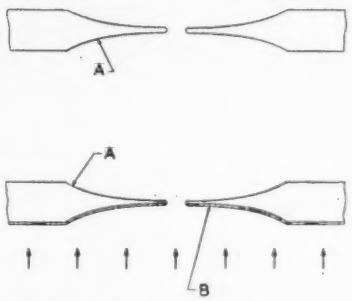

FIG. 6. Composition change by ion bombardment.
A Original alloy
B Altered layer of different composition
↑ Direction of bombarding argon ions.

The doublet is not caused by argon ions embedding themselves in a surface layer and producing an apparent composition change. For this would occur with a pure metal, and a specimen of copper (Fig. 7, before bombardment) does not show doublets after ion bombardment (Fig. 8).

(b) *Properties of the altered layer*

The patterns of both the cold-rolled and the ordered alloys give further information about the nature of the layer. An estimate can be made of its thickness by comparing the intensity of a Cu_3Au reflection with its sister reflection from the altered layer. Control experiments with evaporated films of Cu_3Au showed that comparable diffraction patterns could be obtained with 50-kV electrons from a thickness of this alloy of about 300 Å. Figure 3 shows that the reflections from the layer and substrate are about equal in intensity, so that very approximately—as both sides of the specimen were bombarded—the layer on each side was 75 Å thick. A closer approximation could be made by condensing a layer of suitable metal of known thickness on the specimen, a method adopted for studying the effects of using different inert gases.

There is evidence in the patterns that the layer suffered some damage. In the case of the annealed

specimen (Fig. 5), whereas the spots of the Cu_3Au substrate remained sharp after bombardment, the sister spots of the surface layer were broader, more diffuse, and showing arcing round the Debye–Scherrer ring. Thus, although the orientation of the layer is essentially the same as that of the substrate, some disorientation has occurred. It is to be noted that disorientation also occurred on the pure copper specimen (Fig. 8), where it is comparable to that produced by cold-work.[25]

When a specimen was repeatedly bombarded under the same experimental conditions, and electron-diffraction patterns were taken between bombardments, it was found that the doublets showed the same separation and relative intensity. The hole in the specimen became gradually larger and the weight decreased. The bombardment therefore removed metal, the initial stage being illustrated in Fig. 9 (a); the ratio of the removal of copper to that of gold was more than 3:1, and a layer was established which was richer in gold than Cu_3Au. Once this layer had been formed, however, the sequence shown in Fig. 9(b) was operative, the removal of a layer from the surface of

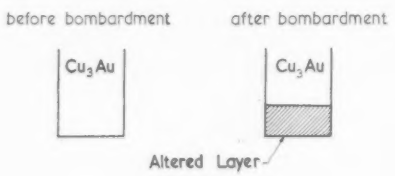

FIG 9(a)

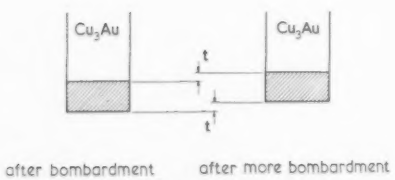

FIG. 9(b)

FIG. 9. Removal of alloy by ion bombardment.
(a) Initial stage of formation of the altered layer.
(b) Subsequent removal of material maintaining the altered layer.

thickness t being accompanied by a composition change in a layer of the same thickness within the specimen. This resulted in a net loss of material from the metal which was of the same composition as the original alloy. This last result agrees with the findings of FISHER and WEBER[17] and of HANAU[18].

(c) *The effects of energy and size of ions*

Figure 10 shows convincingly that the composition of the altered layer is dependent on the discharge voltage and hence on the ion energy. After this specimen had been bombarded on one side only in a 5000-V discharge, a doublet pattern was found; on then bombarding the other side in a 500-V discharge, the triplet pattern of Fig. 10 was obtained.

A series of experiments was carried out to investigate how the composition and the thickness of the altered layer varied with both the discharge voltage and with the size of the bombarding ion. Three inert gases were used—helium, argon and xenon—and for each of these, three voltages: 80, 400 and 4000 V. After each bombardment the doublet pattern was recorded, and then a layer of copper of thickness about 100 Å was condensed on to the specimen. This resulted in a triplet diffraction pattern in which the separation of the inner doublet is identical with that of the previous doublet, and the outermost reflection comes from the copper (Fig. 11). The relative intensities of corresponding reflections from the altered layer and the copper layer were judged by comparing them with a calibrating plate on which a diffraction pattern had been recorded with a range of exposure times. From these relative intensities the thickness of the altered layer was estimated, after the necessary corrections had been made for the difference in scattering factors of copper and gold atoms for 50-keV electrons.[29] The composition of the altered layer was derived from its lattice parameter. The results are given in Table 2.

Copper was used rather than gold for the calibrating layer, as the altered layer caused by ion bombardment was invariably gold-rich, and the two reflections would have been too close if gold had been used. Diffraction patterns were always taken within a few minutes after a copper evaporation, as evaporated copper oxidizes in air, though not enough to give trouble in less than 24 hr.[29]

The same Cu_3Au specimen was used for this series of experiments. This meant that on going to a different voltage or a different gas, the altered

VOL. 11 195

Table 2. Composition and thickness of the altered layer on Cu_3Au *for various ions and voltages*

Bombarding ion	Discharge voltage (V)	Positive ion current (mA)	Time of bombardment of each side (min)	Estimated thickness of altered layer (Å)	Composition of altered layer (atomic-per cent gold)
Helium	80	0·4	90 90	80	93±2
	400	0·1	60 30	30	43±2
	4000	0·05	30 30	40	40±2
Argon	21	0·6	30 30	—	82±2
	80	0·4	90 45	30	55±2
	400	0·2	50 30	30	48±2
	4000	0·03	30 15	40	43±2
Xenon	16	0·6	240 240	—	60±2
	80	0·4	60 30	30	45±2
	400	0·1	20 15	30	39±2
	4000	0·02	30 15	40	34±2

layers of the previous sputter and the evaporated copper layer had to be removed before representative data for the new bombarding conditions could be established. It was found that the 100-A copper layer had been removed after approximately 30 minutes' bombardment at 80 V and a recorded positive current of helium ions of 0·4 mA. The total time of bombardment was chosen in this case to be $1\frac{1}{2}$ hr on each side of the specimen. The rate of removal of material increased with the discharge voltage, so that shorter bombarding times were used at higher voltages, as shown in Table 2. The ion current was selected for a given voltage so that the power dissipated in the specimen was in all cases not more than 0·2 W.

The gas pressure in all cases was 1 μ Hg.

A few bombardments were carried out at lower voltages, but were not followed by the evaporation of the copper calibrating layer. In argon, an altered layer was obtained with a discharge voltage of 21 V, and in xenon at 16 V, the composition of the altered layer being given for each case in Table 2.

(d) *Experiments with other alloys*

For the study of composition changes by ion bombardment, using the effect described in this paper, a binary alloy should have the following properties:

(i) A solid solution should be formed at all compositions.

(ii) The lattice parameters of the two (pure)

metals should be as different as possible, and their alloys should show a continuously increasing change of lattice constant as the proportion of one metal is increased from 0 to 100 per cent.

It is clear from the variations of lattice constant with composition in such alloys (see, for instance, Ref. 30) that the copper–gold system is the best to use, and it has the additional advantage of showing the order–disorder phenomenon, so that the original material (ordered) and the layer of altered composition (disordered) can be unequivocally identified in the same diffraction pattern. Alloys of copper and nickel, and those of silver and palladium, should show the effect, whereas the silver–gold alloys, having only a slight variation of lattice parameter with composition, should not give resolvable doublets in electron-diffraction patterns taken under the conditions of these experiments.

Other cold-rolled alloys used in this study were cupro-nickel, AgAu, α-brass, Ag_3Mg and silver–palladium alloys of various compositions.

(i) *Cupro-nickel.* A specimen of cupro-nickel with 20 per cent nickel by weight was bombarded in helium discharges at 500 and 3250 V after being electropolished to a hole, as previously described. Doublets were similar to those obtained with Cu_3Au.

(ii) *AgAu, α-brass, Ag_3Mg.* The discharge voltages used for these three alloys were:

(1) AgAu: 1250, 1500 and 2500 V. (Argon pressure 13–17 μ Hg).

(2) α-brass: 1500 and 3000 V. (Argon pressure 10–19 μ Hg).

(3) Ag_3Mg: 500 and 5000 V. (Argon pressure 10–30 μ Hg).

Although these alloys were used several times, and cleaning and removal of material occurred, no extra reflections were found in their patterns. For AgAu none was expected, according to the discussion given above. For Ag_3Mg a suitable change in composition could result in the formation of a new phase, and the possibility existed that new reflections corresponding to a body-centred cubic phase would be found together with the face-centred cubic pattern of Ag_3Mg. They were not, however, discovered, the composition of the altered layer presumably being too close to the original composition.

(iii) *Silver–palladium alloys.* Diffraction patterns were obtained from each of four electropolished alloys containing 20, 40, 70 and 95 atomic per cent palladium, respectively. These patterns consisted of spotty arcs with radii corresponding to the four compositions. They were bombarded with argon ions in low-pressure discharges (1 μ Hg) at applied voltages of 80 and 40. No doublets could be resolved in the patterns of the alloys containing 20 and 40 per cent palladium, but they were found for those containing 70 and 95 per cent. The other experimental conditions and the compositions of the altered layers are given in Table 3. A discharge at 300 V was also used for the 40 per cent palladium specimen, but no resolvable doublet pattern was found.

It has been noted above that CASTAING[20] used an aluminium–4 per cent copper alloy prepared for examination by electron diffraction in transmission. He bombarded the alloy with ions in a 3000-V discharge, but did not observe any doublet patterns, but as there is only 4 per cent of copper initially, the changes in composition, and therefore in lattice parameter, of the surface layer are likely to be too small to produce resolvable doublets.

VOL. 11 1959

DISCUSSION

From the experiments described above, the following conclusions can be drawn:

(1) When a binary alloy is bombarded with positive ions of an inert gas, initially more of one of the metals is removed than of the other, and a thin layer of alloy of a new and uniform composition is formed on the surface.

(2) When this layer has been established, subsequent bombardment under the same conditions gradually erodes the alloy, but the surface layer is always present, with the same composition and thickness.

(3) The orientation of the layer is essentially the same as that of its substrate, though some damage in the form of disorientation is present.

(4) For an alloy of fixed initial composition, the composition and thickness of the altered layer depend on the energy of the ions and on their size (Table 2).

(5) For given bombarding conditions, the composition of the altered layer depends on the composition of the bombarded alloy (Table 3).

(6) Both copper and gold can be removed from the alloy Cu_3Au by bombardment with argon ions in a 20-V discharge, and with xenon ions in a 16-V

Table 3. Composition changes in silver–palladium alloys after bombardment with argon ions

Composition of alloy before bombardment (atomic-per cent palladium)	Discharge voltage (V)	Positive ion current (mA)	Time of bombardment of each side (hr)	Composition of altered layer (atomic-per cent palladium)
20	80	0·5	1	No resolvable doublet
40	80	0·5	1	No resolvable doublet
70	80	0·5	1	46±4
95	80	0·5	1	13±4
20	40	0·6	2	No resolvable doublet
40	40	0·6	2	No resolvable doublet
70	40	0·6	2	46±4
95	40	0·6	2	17±4

discharge. The relation of these results to threshhold energies for sputtering will be discussed elsewhere.

For Cu_3Au, both in the initial stage and during subsequent sputtering, more copper is removed than gold. This is the reverse of the result of ASADA and QUASEBARTH[16], who used mercury and water ions at a pressure of 0·2 mm Hg, though redeposition of material may have occurred at such a pressure.

The formation of the altered layer can be explained by reference to Fig. 12, which shows schematically how the number of sputtered atoms per incident positive ion may be expected to vary with the discharge voltage[1,3,6] for the bombardment of pure metals. The vertical ordinate can be regarded as the probability that an atom will be removed when an incident ion makes an impact with the surface. Its value depends on the sputtering conditions and on the material of the target. It is reasonable to suppose that for the individual components in an alloy, curves of a similar form can be drawn.

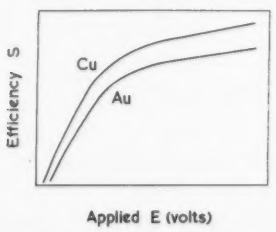

FIG. 12. General form of relationship between sputtering efficiency and sputtering voltage for pure metals.

Considering the alloy Cu_3Au, if the probability of removal for copper were equal to that for gold, three times more copper would be removed than gold, and the alloy would be sputtered without the formation of the altered layer. If it is supposed, however, that the probability curve for gold in Cu_3Au falls below that of copper, as shown in Fig. 12, the ratio of copper atoms removed to gold atoms removed is more than 3:1, and an alloy more gold-rich than Cu_3Au is formed. Furthermore, if the ratio of the probabilities increases with decreasing voltage, the composition of the altered layer will be richer in gold the lower the voltage, and this is found to be so (Table 2).

Once the altered layer has been formed, it is always present during subsequent ion bombardments under the same conditions, and the material removed from the alloy has the composition Cu_3Au (Fig. 9(a)). It might be supposed that the composition of the altered layer adjusts itself, so that the probabilities of removal of copper and gold from the surface are now equal, resulting in its steady erosion. The remaining atoms to make up the composition Cu_3Au of the total sputtered material would then have to come from the original alloy just behind the inner boundary of the altered layer and escape from the surface. This process, however, implies that for the same bombarding conditions the composition of the altered layer would always be the same whatever the composition of the original alloy. The results obtained with the alloys of silver and palladium contradict this idea.

Another possibility is that the composition of the altered layer is adjusted so that the probabilities of removal from it of copper and gold are such that three atoms of copper are removed for one of gold. This would tend to make the altered layer even more gold-rich at the surface, and some kind of rapid transport of atoms from the region behind the inner boundary of the altered layer is again required to restore its composition; but in this case they do not need sufficient energy to escape from the surface. This process, however, does not imply that the composition of the altered layer will be the same for all original compositions of the alloy: an alloy which was initially Cu_2Au, for example, will form an altered layer whose composition is such that two atoms of copper are removed for one of gold. For the same bombarding conditions, the composition of the altered layer will be different from that in the case of Cu_3Au.

It is clear that in order to retain the altered layer in successive bombardments, some atoms in the Cu_3Au alloy just behind the boundary of the altered layer must receive sufficient energy to be removed from their positions in the crystal whenever material is sputtered from the surface. The energy required to displace an atom permanently from a stable site in a well-bound solid is usually taken to be 25 eV,[32] though DUGDALE[31] has suggested a value < 12 eV for copper atoms in Cu_3Au.

(a) *Temperature spikes*

SEITZ and KOEHLER[32] describe a theory of "temperature spikes" in discussing radiation damage in solids. According to this, a spherical volume with a radius,

$$r = (10Q/4\pi N)^{\frac{1}{4}}, \qquad (1)$$

centred on the point of collision, can attain a temperature above the melting point (assumed to be 1000°K) for a time of the order of 10^{-11} sec, where Q (in eV) is the energy received by a displaced atom in a collision, and N is the number of atoms per unit volume. It is considered that 10^{-11} sec is quite sufficient time for processes to occur such as the direct interchange of neighbouring atoms, or the formation of vacancy–interstitial pairs. This "mixing" process has been evoked to explain why the ordered alloy Cu_3Au is disordered by neutron bombardment more rapidly than would be expected simply from the number of atoms displaced. KINCHIN and PEASE[33] have criticized the temperature-spike theory on the grounds that the macroscopic concept of temperature should not be applied to the small volumes involved.

However, one could take this radius, r, as an approximate measure of the depth to which the formation of vacancies and interstitials, and the interchange of atoms, can occur when an atom at the surface of the metal receives energy from an impinging ion. Values of r have been calculated for copper from equation (1) (the values for gold are little different) on the assumption that the total energy of the ion is liberated in one temperature spike. In Table 4 these values are compared with the estimated thickness of the altered layer in Cu_3Au. It is seen that the orders of magnitude are comparable, though there are notable discrepancies at low voltages.

(b) *Ion penetration*

Instead of having a long-range effect through the medium of temperature spikes, the ions may penetrate into the crystal by repeated collisions with the metal atoms and themselves dislodge atoms near the boundary of the altered layer. The fundamental theory of the penetration of atomic particles through matter is that of BOHR[14], and his expression for the range of fast particles in

Table 4. Radii of temperature spikes, and theoretical penetration of ions in metals compared with the estimated thickness of the altered layer

Ion	Bombarding voltage (V)	Radius of temperature spike r (Å)	Theoretical penetration (Å) (neutron-cooling theory)		Thickness of altered layer (Å)
			in Cu	in Au	
Helium	80	9·0	6·3	8·0	80
	400	15·4	32	40	30
	4000	33·5	320	400	40
Argon	80	9·0	< 1	< 1	30
	400	15·4	1·4	1·5	30
	4000	33·5	14	15	40
Xenon	80	9·0	Theory	< 1	30
	400	15·4	not	< 1	30
	4000	33·5	valid	3·3	40

The penetration depth, d (Å), was calculated from formulae derived from those of NIELSON:[10]

$$d = \frac{100}{\rho} 0{\cdot}7 E_1 \{\xi(1-\overline{\cos\phi})\}^{-\frac{1}{2}} \frac{(Z_1^{\frac{2}{3}}+Z_2^{\frac{2}{3}})^{\frac{1}{2}}}{Z_1 Z_2} \frac{A_2^2}{(A_1+A_2)}$$

where

$$\xi = 1+\frac{(A_2-A_1)^2}{2A_1A_2} \ln\left(\frac{A_2-A_1}{A_1+A_2}\right)$$

and

$$\overline{\cos\phi} = \frac{2A_1}{3A_2}.$$

Z_1, Z_2 and A_1, A_2 are the atomic numbers and mass numbers of the incoming and target particles, respectively, E_1 is the kinetic energy of an incoming particle (KeV) and ρ the density of the target.

solids has been used by NIELSEN[10] and HINES[11], who found good agreement with their experimental results. In the present experiments, however, although the energies of the ions used were sufficiently low for their collisions with the atoms of the solid to be regarded as collisions between hard spheres, other criteria laid down by BOHR were not fulfilled, and his equation for the range does not apply.

The neutron-cooling theory of ion penetration in solids[10,12] can be used when the mass number of the ion is less than that of the atoms in the target, and this is the case in the present experiments (with the exception of xenon bombarding copper). Theoretical penetration depths according to this theory are included in Table 4. Again, the thickness of the altered layer is much larger than theoretical prediction at low ion energies.

This theory of ion penetration, however, neglects the periodic nature of the crystal and the possibility that ions can move much more easily in certain directions within the crystal. Interstitial atoms in face-centred cubic crystals are considered to be mobile,[34,35] and any movement of this nature must involve a forcing aside of the crystal atoms, which return elastically to their positions when the disturbance has passed. A penetrating ion might be regarded as a fast-moving interstitial atom, in which case deeper penetrations would be expected than those given by the simple collision theory. Such an ion could reach the Cu_3Au substrate just behind the altered layer with sufficient energy to

displace an atom or atoms. If this happens the thickness of the altered layer can be taken as an approximate measure of the depth to which the ions penetrate.

Ion bombardment is one of the methods by which radiation damage can be induced in solids, and, though the energies used in this work are considerably lower than those usual in studies of radiation damage,[35] it is to be expected that vacancies and interstitial atoms will be created as a result of collisions between ions and atoms and between displaced atoms and other metal atoms. Some mutual annihilation of vacancies and interstitials could occur, but it seems likely that an excess of interstitials is formed.[25] Although it has been suggested that in Cu_3Au only the copper atoms can persist as interstitials[32] (the energy required to form a gold interstitial is much higher than that for copper), the excess interstitial atoms probably consist of copper and gold atoms and atoms of the bombarding material. However, both vacancies and interstitials are mobile at temperatures well below room temperature and are thought to anneal out by being absorbed on surfaces or grain boundaries, or at dislocations.

One could imagine that during the initial formation of the altered layer on Cu_3Au the impinging ions remove much more copper than gold at the surface, and form vacancies and interstitials along their paths within the alloy. Many vacancies may migrate into clusters and the lattice collapse to form dislocation rings. Most of the interstitials will be copper atoms, and most of these may migrate to the surface, as they possess high mobility. By doing this they will tend to restore the composition at the surface (which has become more gold-rich), but this will merely result in a continuation of the state of affairs in which much more copper is sputtered off than gold. Ultimately (as the ions have only a limited penetration into the metal) an equilibrium situation will be reached where the interstitial and vacancy migration just compensates for the further loss of copper from the alloy layer already deficient in copper.

The thickness of the altered layer does not vary as much as might be expected with sputtering voltage between 80 and 4000 V. The layer for the 80-V helium discharge is particularly thick, but very little material is sputtered off in the latter case (the composition is nearly pure gold, and for helium 80 V must lie close to the threshold for gold). No explanation of this fact can at present be given.

Acknowledgements—I am indebted to my colleagues, particularly Dr. G. J. OGILVIE and Dr. J. V. SANDERS, for advice and discussion, and to Mr. A. A. THOMSON for his able assistance with experiments. The silver–palladium alloys were kindly supplied by Dr. P. KLEMENS, C.S.I.R.O., Division of Physics, Sydney.

REFERENCES

1. MASSEY H. S. W. and BURHOP E. H. S., *Electronic and Ionic Impact Phenomena* pp. 578–594. Oxford University Press (1952).
2. GUNTHERSCHULZE A., *Vacuum* **3,** 360 (1953).
3. WEHNER G. K., *Advances in Electronics and Electron Physics* Vol. 7, pp. 239–298. Academic Press, New York (1955).
4. FRANCIS G., *Handbuch der Physik* Vol. 22, pp. 154–161. Springer, Berlin (1956).
5. COMPTON K. T. and LANGMUIR I., *Rev. Mod. Phys.* **2,** 123 (1930).
6. STRACHAN J. F. and HARRIS N. L., *Proc. Phys. Soc.* B**69,** 1148 (1956).
7. BRADLEY R. C., *Phys. Rev.* **93,** 719 (1954).
8. MORGULIS N. D. and TISHCHENKO V. D., *Izv. Akad. Nauk. SSSR, Ser. Fiz.* **20,** 1190 (1956).
9. KEYWELL F., *Phys. Rev.* **97,** 1611 (1955).
10. NIELSEN K. O., *Electromagnetically Enriched Isotopes and Mass Spectrometry* pp. 68–81. Butterworths London (1956).
11. HINES R. L., *J. Appl. Phys.* **28,** 587 (1957).
12. GIANOLA U. F., *J. Appl. Phys.* **28,** 868 (1957).
13. BARNES R. S., REDDING G. B. and COTTRELL A. H., *Phil. Mag.* **3,** 97 (1958).
14. BOHR N., *Kgl. Danske Vidensk. Selsk., Mat.-fys. Medd.* **18,** No. 8 (1948).
15. GLASSTONE S. and EDLUND M. C., *The Elements of Nuclear Reactor Theory*. D. van Nostrand, New York (1952).
16. ASADA T. and QUASEBARTH K., *Z. Phys. Chem.* A**143,** 435 (1929).
17. FISHER T. F. and WEBER C. E., *J. Appl. Phys.* **23,** 181 (1952).
18. HANAU R., *Phys. Rev.* **76,** 153 (1949).
19. LADAGE A., *Z. Phys.* **144,** 354 (1956).
20. CASTAING R., *Rev. Métall.* **52,** 669 (1955).
21. HEIDENREICH R. D., *J. Appl. Phys.* **20,** 993 (1949).
22. BOLLMANN W., *Phys. Rev.* **103,** 1588 (1956).
23. BAKISH R. and ROBERTSON W. D., *J. Metals* **7,** 424 (1955).
24. SYKES E. C., HADDRELL V. J., HAINES H. R. and MOTT B. W., *J. Inst. Met.* **83,** 166 (1954–55).
25. OGILVIE G. J., *J. Phys. Chem. Solids* **10,** 222 (1959).
26. BACKUS J., *Gaseous Electrical Discharges in Magnetic Fields* p. 353. McGraw-Hill, New York (1949).
27. HIRSCH P. B., KELLY A. and MENTER J. W., *Proc. Phys. Soc.* B**68,** 1132 (1955).

28. FINCH G. I. and SUN C. H., *Trans. Faraday Soc.* **32,** 852 (1936).
29. PINSKER Z. G., *Electron Diffraction* p. 162. Butterworths, London (1953).
30. BARRETT C. S., *Structure of Metals* p. 221, Fig. 7. McGraw-Hill, New York (1952).
31. DUGDALE R. A., *Report of Conference on Defects in Crystalline Solids* p. 246. Physical Society, London (1955).
32. SEITZ F. and KOEHLER J. S., *Solid State Physics* (Ed. F. SEITZ and D. TURNBULL), Vol. 2 pp. 305–448. Academic Press, New York (1956).
33. KINCHIN G. H. and PEASE R. S., *Rep. Progr. Phys.* **18,** 1 (1955).
34. COTTRELL A. H., *Met. Rev.* **1,** 479 (1956).
35. DIENES G. J. and VINEYARD G. H., *Radiation Effects in Solids.* Interscience Publishers, New York (1957).

OL.
11
959

J. Phys. Chem. Solids Pergamon Press 1959. Vol. 11. pp. 68–72. Printed in Great Britain.

SCREENING OF POINT SINGULARITIES IN METALS, WITH PARTICULAR REFERENCE TO POSITRON ANNIHILATION

B. DONOVAN

Department of Physics, Bedford College, London

and

N. H. MARCH

Department of Physics, The University, Sheffield

(*Received* 25 *February* 1959)

VOL.
11
195

Abstract—The treatment of point singularities in metals initiated by MOTT yields an infinitely large electronic density at a positive point charge, owing to the failure of the Thomas–Fermi approximation in this region. In the physically interesting problems involving positron annihilation, the positron lifetime depends on the electron density at the positron, and to obtain a useful result it is necessary to improve the statistical treatment. The present work discusses the modifications resulting from the introduction of von Weizsäcker's correction. In the high-density limit, an analytical development can be given that reveals the essential changes thus brought about. For real metallic densities, however, a laborious numerical calculation is necessary; we have carried this through for a unit positive charge embedded in an electron gas of density equal to that of the valence electrons in copper. The electron density at the point charge is eight or nine times the average electron density, indicating a positron lifetime of $(1{\cdot}8 \pm 0{\cdot}2) \times 10^{-10}$ sec. Comparison is made with the previous treatment of positron lifetimes by DANIEL and FRIEDEL. Brief reference is also made to the general subject of impurities and imperfections in the light of the present findings.

1. INTRODUCTION

A GOOD deal of interest has been aroused recently by the use of positron annihilation as a tool for probing the electronic structure of solids. However, it is becoming increasingly clear that any accurate interpretation of the experimental results from such annihilation is going to require a rather careful quantitative study of the effect of the positron on the metal, and also of the positron wave function. Previous work has shown that the positron wave function in a metal such as copper differs very appreciably from a plane wave; although the calculations which have been made independently by DANIEL[1] and the present writers[2] have actually treated the positron as though it moved in a uniform distribution of electrons, we do not expect that the inclusion of a potential representing the clustering of electrons preferentially in the neighbourhood of the point charge would greatly affect the nature of the positron wave function, even though it is now known that the calculation of positron lifetimes requires a somewhat careful estimate of this density. FERRELL[3], in his review of the theory of positron annihilation, to which the reader is referred for further details, remarks that the usual simple treatment of point charges in a free electron gas proposed by MOTT[4] and extended and improved by later workers (for details see especially the reviews by FRIEDEL[5] and MARCH[6]) fails in this region, since the potential is too strongly varying for the Thomas–Fermi approximation to be reliable. It has been suggested (Dr. J. FRIEDEL, private communication; ALFRED and MARCH[7]) that the inclusion of von Weizsäcker's correction ought to lead to a significant improvement on the original Thomas–Fermi results, and Dr. FRIEDEL has informed us that he has carried out some

computations of the von Weizsäcker correction which may be particularly important, for example, in the calculation of the interaction energy between two vacancies. Our interest here, however, is mainly in the electron density, and we shall discuss the general effect of the von Weizsäcker correction from this point of view in the present paper. Some analytical progress can be made in the high-density limit, and this is reported in Section 2. Then, in Section 3, the results of a numerical computation for a singly charged centre embedded in a free electron gas are reported, the density being taken as that appropriate for the conduction electrons in copper. The results of our computations are then discussed from the standpoint of positron lifetimes in Section 4, and an earlier calculation by DANIEL and FRIEDEL[8] is referred to. Finally, the relevance of our results to the general problems connected with the treatment of impurities and imperfections in metals is briefly discussed, and a comparison is made with some unpublished work by QUINN and FERRELL[9] reported in a brief abstract.

2. EFFECT OF THE VON WEIZSÄCKER CORRECTION—HIGH-DENSITY LIMIT

Suppose the density of electrons in the unperturbed gas is n_0; when the perturbation due to a charge Z (using atomic units throughout) at the origin is introduced, let the new density be $n(r)$ and the perturbing potential be $V(r)$, r being the distance from the origin. If E_m is the Fermi energy, then we have

$$n_0 = \frac{2^{\frac{3}{2}}}{3\pi^2} E_m^{\frac{3}{2}} \tag{1}$$

and if we introduce r_s as the radius of the sphere containing one electron in the unperturbed metal, then we have further that

$$n_0 = \frac{3}{4\pi r_s^3}. \tag{2}$$

The equation of von Weizsäcker may then be written (see, for example, MARCH[6]):

$$\frac{3^{\frac{5}{3}}\pi^{\frac{4}{3}}}{.2} n^{\frac{5}{3}} + \frac{1}{8}\left[\frac{(\nabla n)^2}{n^2} - \frac{2\nabla^2 n}{n}\right] - V = E_m \tag{3}$$

and the perturbing potential V is related to the change in density $n-n_0$ by the Poisson equation:

$$\nabla^2 V = 4\pi(n-n_0). \tag{4}$$

If we neglect the terms in equation (3) which involve derivatives of n, then we obtain the usual treatment, and exact numerical solutions are now available from the independent investigations of FUJIWARA[10] and ALFRED and MARCH[11]. These solutions will later prove useful in solving the above equations numerically, but for the moment we will consider only the high-density limit $r_s \to 0$, in which case we can obtain a useful analytical development. Introducing a suitable dimensionless variable ρ defined by

$$\rho = r/r_s, \tag{5}$$

we may develop the potential and density in terms of an expansion parameter $r_s^{\frac{1}{2}}$.

Explicitly we write

$$\frac{n-n_0}{n_0} = r_s\alpha_2 + 0(r_s^{\frac{3}{2}}) \tag{6}$$

and

$$V = \frac{1}{r_s}\left[\frac{Z}{\rho} + 0(r_s)\right] \tag{7}$$

where α_2 is a function of ρ only. It is easily verified that α_2 satisfies the differential equation

$$\frac{3^{\frac{5}{3}}\pi^{\frac{4}{3}}}{4^{\frac{5}{3}}}\alpha_2 - \frac{1}{4}\nabla^2\alpha_2 = \frac{Z}{\rho}. \tag{8}$$

The general solution of equation (8) is easily written down as

$$\alpha_2 = \frac{A\exp(-c\rho)}{\rho} + \frac{B\exp(c\rho)}{\rho} + \frac{4^{\frac{5}{3}}}{3^{\frac{5}{3}}\pi^{\frac{4}{3}}} \cdot \frac{Z}{\rho}; \quad c = (12\pi^2)^{\frac{1}{2}}. \tag{9}$$

In the framework of the present approach it is then clear that we must take as the particular solution

$$\alpha_2 = \frac{4^{\frac{5}{3}}}{3^{\frac{5}{3}}\pi^{\frac{4}{3}}} \frac{Z}{\rho}[1 - \exp(-c\rho)]. \tag{10}$$

It might perhaps be objected that this is not an allowable form for α_2, because of the apparent fall-off as ρ^{-1} for large ρ. However, this is purely a

consequence of our expansion procedure, and an argument presented in the Appendix shows that equation (10) can be derived by suitably expanding a density which does indeed normalize correctly. We find that, to this order in r_s, we have the result that as ρ tends to zero

$$\frac{n-n_0}{n_0} \to 2{\cdot}3^{1/2}\left[\frac{4}{9\pi}\right]^{\frac{1}{2}} Zr_s = 1{\cdot}81Zr_s. \qquad (11)$$

This then is the increase in density predicted in the limit $r_s \to 0$ by the von Weizsäcker method. It is of interest to note that if we employ a linearization approximation (see Appendix) in equation (3), rather than a direct expansion in $r_s^{\frac{1}{2}}$, then the same result follows and the next term may also be estimated. It is found that for $Z = 1$ we may write

$$\frac{n-n_0}{n_0} = 1{\cdot}81r_s - 1{\cdot}28r_s^{\frac{1}{2}}. \qquad (12)$$

However, it can soon be verified by the insertion of numerical values in the linearization solutions that the approximations break down before we reach realistic metallic densities (for example, for copper, $r_s = 2{\cdot}66$ atomic units), and it is then necessary to solve the full von Weizsäcker equation. We turn now to discuss how this has been carried out.

3. CASE OF REAL METALLIC DENSITIES

We have found no general analytical method which gives reliable results for real densities, and therefore we have devised a procedure for solving equations (3) and (4) numerically. However, for small r, exact series expansions can be developed, and these prove very useful in the numerical solution of the problem. In principle the potential V can be eliminated between equations (3) and (4), and from the resulting equation for the density it may be shown that

$$n(r) = n(0)[1+b_1r+b_2r^2+b_3r^3+b_4r^4+\ \ldots] \qquad (13)$$

where

$$b_1 = -2Z$$

b_2 is a disposable constant of integration

$$9b_3 = 18Z^3 - 15Zb_2 - 4A\alpha^{\frac{1}{2}}Z$$

$$30b_4 = -18Z^4 - 5Z^2b_2 + 20A\alpha^{\frac{1}{2}}Z^2 + 4A\alpha^{\frac{1}{2}}b_2 + 12b_2^2 - 4\pi(\alpha - n_0).$$

Here, for convenience we have written $\alpha = n(0)$, and

$$A = \frac{3^{\frac{1}{2}}\pi^{\frac{1}{2}}}{2}.$$

Similarly the series for V may be written

$$V = \frac{Z}{r}\left[1+\frac{K_1}{Z}r+\frac{2\pi}{3Z}(\alpha-n_0)r^3+ +\frac{2\pi\alpha}{Z}\left\{\frac{b_1r^4}{6}+\frac{b_2r^5}{10}+\frac{b_3r^6}{15}+\frac{b_4r^7}{21}+\ \ldots\right\}\right] \qquad (14)$$

with

$$K_1 = A\alpha^{\frac{1}{2}} + \tfrac{5}{2}Z^2 - \tfrac{3}{2}b_2 - E_m.$$

Using these starting series, numerical integration outwards can be commenced, and for $Z = 1$ and $r_s = 2{\cdot}66$ we have, by a method of successive approximations, converged on a self-consistent solution satisfying the conditions

$$n \to n_0 \text{ as } r \to \infty$$

$$\int_0^\infty (n-n_0)4\pi r^2\, dr = 1.$$

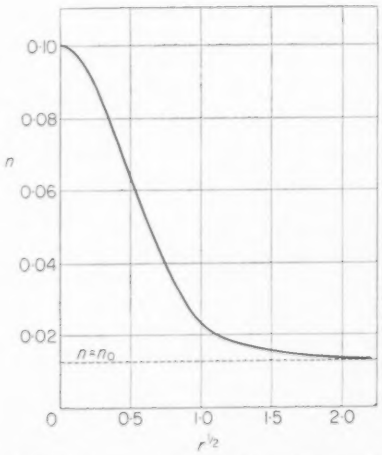

FIG. 1. Density round unit positive charge embedded in free electron gas of density corresponding to $r_s = 2{\cdot}66$.

It seems unnecessary to go into detail concerning the somewhat involved numerical techniques employed, except to say that we discontinued the calculation as soon as our main object of estimating the density $n(0)$ at the origin was achieved to

adequate accuracy. We are able with fair certainty to quote a value $n(0) = 0{\cdot}11 \pm 0{\cdot}01$, and we thought it of interest to plot in Fig. 1 a density which must be quite near to the correct curve in order to show the general features of the von Weizsäcker predictions (actually $n(0) = 0{\cdot}100$ and $b_2 = 2{\cdot}62$ for this solution). The corresponding self-consistent potential seems to be virtually indistinguishable from the Thomas–Fermi values[11] for $r > \sim 2{\cdot}5$, although for smaller values of r the potential is less heavily screened, as is consistent with the finite density at the origin given by the von Weizsäcker treatment.

4. POSITRON LIFETIME IN COPPER METAL

We now apply our result giving the increase in density at the point singularity to the calculation of the lifetime of a positron in copper. The rate of annihilation is proportional to the electron density $n(0)$ at the positron, and we can write for the lifetime τ (see, for example, FERRELL[3])

$$\tau = \frac{n_0}{n(0)} \cdot \frac{r_s^3}{1{\cdot}2} \cdot 10^{-10} \text{ sec.} \qquad (15)$$

Assuming our model can reasonably represent the clustering of the electrons round a positron in a metal, we may insert for copper $r_s = 2{\cdot}66$ atomic units and $n(0)/n_0 = 8{\cdot}7 \pm 0{\cdot}8$. We then find

$$\tau = (1{\cdot}8 \pm 0{\cdot}2) \times 10^{-10} \text{ sec.}$$

The experimental result is subject to considerable uncertainty, a value of $(1{\cdot}2 \pm 0{\cdot}5) \times 10^{-10}$ sec being given by BELL and GRAHAM[12], whereas GERHOLM[13] gives $(2{\cdot}7 \pm 0{\cdot}3) \times 10^{-10}$ sec. Our result seems therefore in reasonable agreement with experiment. It should be noted that it is appreciably larger than the value obtained by DANIEL and FRIEDEL[8] ($0{\cdot}7 \times 10^{-10}$ sec).

5. GENERAL COMMENTS ON THE IMPURITY PROBLEM

We think that the von Weizsäcker correction should give a good improvement over the previous self-consistent treatments based on the unmodified Thomas–Fermi approximation. This will be particularly the case in regions where the potential is varying rapidly, and, for negatively charged point singularities, in classically forbidden regions, into which it permits the wave functions to extend.

Even so, it is a somewhat difficult matter to assess the overall accuracy of the von Weizsäcker scheme, although it has been recently shown to have a firm theoretical basis as a variational method (MARCH and YOUNG[14]). The one significant comparison which it seems possible to make at the present time is with a result quoted only in a short abstract by QUINN and FERRELL[9]. These writers state that by a Hartree field calculation they find a result of the form of equation (12), but quantitatively given by

$$\frac{n - n_0}{n_0} = 2{\cdot}96 r_s - 1{\cdot}28 r_s^{\frac{3}{2}} + \ldots \qquad (16)$$

It will be noted that while the coefficients of $r_s^{\frac{3}{2}}$ are numerically equal, there is a significant difference in the leading term. If, as seems likely, equation (16) is more accurate than equation (12), then it seems that the von Weizsäcker method might be somewhat underestimating the density at the point singularity. However, it should be remembered that at a value of $r_s \sim 2{\cdot}7$, equations (12) and (16) are not useful.

6. CONCLUSION

We have shown how the perturbations induced in a free electron gas by a point singularity may be usefully studied by means of the von Weizsäcker method. While, however, general results have been obtained for very high densities, for real metallic densities laborious numerical calculation is necessary and has been carried out for a single positive charge in a gas of density equal to that in copper metal. Finally, application has been made to the lifetime of a positron in copper, a value of $1{\cdot}8 \times 10^{-10}$ sec being obtained, in reasonable agreement with experiment.

Acknowledgement—One of us (N.H.M.) wishes to acknowledge that this work has been sponsored in part by the Office, Chief of Research and Development, U.S. Department of Army, through its European Office.

REFERENCES

1. DANIEL E., *J. Phys. Radium* **18**, 691 (1957).
2. DONOVAN B. and MARCH N. H., *Phys. Rev.* **110**, 582 (1958).

3. FERRELL R. A., *Rev. Mod. Phys.* **28,** 308 (1956).
4. MOTT N. F., *Proc. Cambridge Phil. Soc.* **32,** 281 (1936).
5. FRIEDEL J., *Advances in Phys.* **3,** 44 (1954).
6. MARCH N. H., *Advances in Phys.* **6,** 1 (1957).
7. ALFRED L. C. R. and MARCH N. H., *Phil. Mag.* **2,** 985 (1957).
8. DANIEL E. and FRIEDEL J., *J. Phys. Chem. Solids* **4,** 111 (1958).
9. QUINN J. J. and FERRELL R. A., *Bull. Amer. Phys. Soc.* **3,** 53 (1958).
10. FUJIWARA H., *J. Phys. Soc. Japan* **10,** 339 (1955).
11. ALFRED L. C. R. and MARCH N. H., *Phil. Mag.* **46,** 759 (1955).
12. BELL R. E. and GRAHAM R. L., *Phys. Rev.* **90,** 644 (1953).
13. GERHOLM T. R., *Ark. Fys.* **10,** 523 (1956).
14. MARCH N. H. and YOUNG W. H., *Proc. Phys. Soc.* **72,** 182 (1958).

APPENDIX

We show here how the results embodied in equations (11) and (12) may be derived by a linearization procedure resembling that employed earlier by MOTT,[4] who neglected the von Weizsäcker correction. Since, as discussed earlier, for high densities $n-n_0/n_0$ is $0(r_s)$, an order-of-magnitude argument shows that in the limit $r_s \to 0$ the term in $(\nabla n)^2$ in equation (3) may be omitted.

Thus we can consider the equations

$$\frac{3^{\frac{2}{3}}\pi^{\frac{4}{3}}}{2} n^{\frac{2}{3}} - \frac{1}{4} \cdot \frac{\nabla^2 n}{n} - V = E_m \qquad \text{(A.1)}$$

and

$$\nabla^2 V = 4\pi(n-n_0) = 4\pi\delta.$$

We now replace $n-n_0$ by the linearized form $\frac{2}{3}n_0^{-\frac{1}{3}}\delta$, and we must then solve

$$V = \frac{\pi^{\frac{4}{3}}\delta}{3^{\frac{1}{3}}n_0^{\frac{1}{3}}} - \frac{1}{4}\frac{\nabla^2\delta}{n_0} \qquad \text{(A.2)}$$

and

$$\nabla^2 V = 4\pi\delta. \qquad \text{(A.3)}$$

It should be emphasized that in contrast to the original treatment of MOTT, in which n is infinite at the point charge, n is finite in our case and in the limit $r_s \to 0$, δ is indeed a correction to n_0 everywhere.

Investigation now reveals that equations (A.2) and (A.3) may be solved in a straightforward manner. Thus, it is easily verified that we may write for δ:

$$\delta = A\left[\frac{\exp(-\alpha_+ r)}{r} - \frac{\exp(-\alpha_- r)}{r}\right] \qquad \text{(A.4)}$$

and correspondingly for V

$$V = \left(\frac{\pi^{\frac{4}{3}}}{3^{\frac{1}{3}}n_0^{\frac{1}{3}}} - \frac{\alpha_+^2}{4n_0}\right)A\frac{\exp(-\alpha_+ r)}{r} - \left(\frac{\pi^{\frac{4}{3}}}{3^{\frac{1}{3}}n_0^{\frac{1}{3}}} - \frac{\alpha_-^2}{4n_0}\right)A\frac{\exp(-\alpha_- r)}{r} \qquad \text{(A.5)}$$

where

$$\alpha_\pm^2 = \frac{2\pi^{\frac{4}{3}}}{3^{\frac{1}{3}}} n_0^{\frac{2}{3}}\left[1 \pm \left(1 - \frac{4\cdot 3^{\frac{2}{3}}}{\pi^{\frac{8}{3}}n_0^{\frac{4}{3}}}\right)^{\frac{1}{2}}\right]. \qquad \text{(A.6)}$$

In order that V shall tend to Z/r as r tends to zero, we must take

$$A = \frac{4n_0 Z}{(\alpha_-^2 - \alpha_+^2)}. \qquad \text{(A.7)}$$

It is easily verified that δ given by equations (A.4) and (A.7) normalizes correctly, and that on expansion in terms of $r_s^{\frac{1}{2}}$, equation (10) is reproduced. Equation (11) then follows immediately, and the estimate of the next term given in equation (12) has been made using equations (A.4), (A.6) and (A.7). We should emphasize that while equation (11) is an exact consequence of the von Weizsäcker method in the high-density limit, the term of $0(r_s^{\frac{3}{2}})$ in equation (12) is subject to approximation.

Finally, we may note from equation (A.6) that as soon as $4\cdot 3^{2/3}/\pi^{\frac{4}{3}}n_0^{\frac{1}{3}} (= 1{\cdot}99 r_s)$ becomes comparable with unity, the above treatment cannot be valid. Since $r_s = 2{\cdot}66$ for copper, the necessity for the entirely numerical investigation reported in Section 3 for realistic metallic densities is immediately confirmed.

VOL 11 195

J. Phys. Chem. Solids Pergamon Press 1959. Vol. 11. pp. 73–77. Printed in Great Britain.

PIEZOMAGNETISM IN CoF_2

T. MORIYA*

Bell Telephone Laboratories, Murray Hill, New Jersey

(*Received* 11 *February* 1959; *revised* 13 *March* 1959)

Abstract—It is pointed out that in antiferromagnetic iron-group difluorides, MnF_2, FeF_2 and CoF_2, a linear compression in the *ab*-plane can produce magnetization along the *c*-axis. The magnitude of this piezomagnetic moment is evaluated theoretically for CoF_2, in which the largest effect is expected. The estimated order of magnitude of the magnetization is a few tenths cgs under a pressure of 100 kg/cm² along the [110] direction.

OL.
11
959

1. INTRODUCTION

THE possible existence of piezomagnetism in some antiferromagnetic crystals has recently been pointed out by DZIALOSHINSKI[1] from considerations of crystal symmetry. He mentioned as examples α—Fe_2O_3 and MnF_2, FeF_2 and CoF_2. In these fluorides, he states, shear strains σ_{xz}, σ_{yz} will be accompanied by magnetization along the y, x directions respectively, though he does not give their orders of magnitude.

The purpose of the present note is to point out that in MnF_2, FeF_2 and CoF_2 even a linear compression in the *ab*-plane, say along the [110] direction, can produce magnetization along the *c*-axis, and to estimate its order of magnitude in the case of CoF_2, in which the piezomagnetic moment is expected to be especially large.

The crystal structures of iron-group difluorides are of the rutile type.[2] There are two kinds of cation sites, the corner and the body-center sites, in these crystals, as shown in Fig. 1. The crystalline fields around these two kinds of site differ only in that their principal axes, x and y, are interchanged. In their antiferromagnetic states, the ions on one kind of site form one sublattice, say of up spins, and those on the other kind of site form another sublattice of down spins. The sublattice magnetizations are along the $\pm$ *c*-directions.

When the linear compression in the *ab*-plane is applied, the crystalline fields around the two kinds of site are no longer the same, even if we allow for a rotation around the *c*-axis by 90°. The magnetic moments of the two kinds of spin in the exchange field should in general differ owing to the different anisotropic fine-structure couplings and the different *g*-factors. Therefore, net magnetization will arise just as in ferrimagnets, provided that the lifetime for the interchange of the + and − sublattices is sufficiently long, as is actually the case.

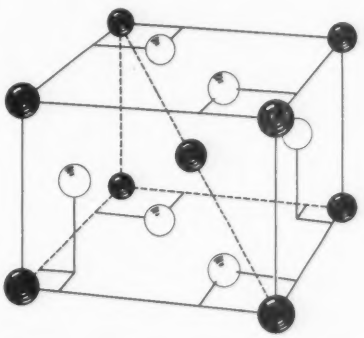

FIG. 1. The rutile-type crystal structure of CoF_2. Solid circles are cations, open circles anions.

This effect will be most significant in CoF_2, less so in FeF_2, and least in MnF_2. In MnF_2 magnetic anisotropy is much smaller than in the other fluorides, and it arises mainly from dipole–dipole interaction between spins; the crystalline electrical field contributes only 10 per cent to the anisotropy.[3] Piezomagnetism will thus be smallest in

* On leave of absence from Tokyo Metropolitan University.

this substance. In FeF_2 the electric splitting of spin levels is comparable with the exchange interaction, and in CoF_2 the former is even larger than the latter. In this situation, the sublattice magnetization depends to a considerable extent on the electric splitting. In fact, theoretically the sublattice spin value in CoF_2 is 1·19 at 0°K,[4] which is considerably smaller than 3/2. On the other hand the sublattice spin value in FeF_2 is estimated to be 1·99, very near to 2, at 0°K.[5] This fact seems to suggest that piezomagnetism of the type we are considering here is much larger in CoF_2 than in FeF_2.

2. PIEZOMAGNETISM IN ANTIFERROMAGNETIC CoF_2

A theoretical study of the magnetic anisotropy of CoF_2 has been made by NAKAMURA and TAKETA[4]. The experimental results[6] seem to be well explained, at least semiquantitatively, by their theory.* Here we shall adopt their model, i.e. we shall assume that we can safely take a spin Hamiltonian that implies that the lowest excited orbital state lies well above the ground orbital state, which itself is not degenerate. Adopting the molecular-field approximation, we have the following Hamiltonian for the spins on the two sublattices:

$$H^{(i)} = -D_i S_{iz}^2 - E_i(S_{ix}^2 - S_{iy}^2) + \boldsymbol{S}_i \cdot \boldsymbol{h}_i, \quad (1)$$

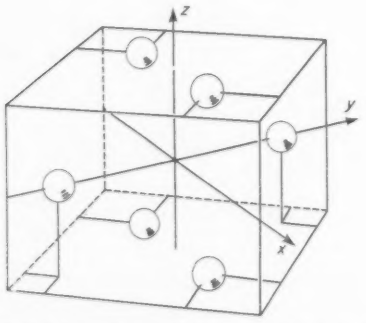

FIG. 2. Definition of co-ordinate axes for $i = 1$ sites. For $i = 2$, the x- and y-axes are interchanged.

* Paramagnetic resonance of Co^{2+} in ZnF_2 has been observed by TINKHAM[7] and by STOUT[8]. They have given the g-values and the hyperfine coupling constants within the lowest Kramers doublet ($S' = 1/2$ manifold). NAKAMURA and TAKETA's theory seems to be consistent with these measured values.[9]

where $i = 1,2$ represents ions on the + and − sublattices, respectively, and

$$\left.\begin{aligned} \boldsymbol{h}_1 &= 2Jz\langle \boldsymbol{S}_2 \rangle \\ \boldsymbol{h}_2 &= 2Jz\langle \boldsymbol{S}_1 \rangle, \end{aligned}\right\} \quad (2)$$

J being the exchange integral, z the number of nearest magnetic neighbors. The definition of the co-ordinate axes are shown in Fig. 2 for $i = 1$. The eigenvalues of equation (1) are easily obtained as follows:

$$\left.\begin{aligned} E_1^{(i)} &= -\tfrac{5}{4}D_i + \tfrac{1}{2}h_i - \{(D_i - h_i)^2 + 3E_i^2\}^{\frac{1}{2}} \\ E_2^{(i)} &= -\tfrac{5}{4}D_i - \tfrac{1}{2}h_i + \{(D_i + h_i)^2 + 3E_i^2\}^{\frac{1}{2}} \\ E_3^{(i)} &= -\tfrac{5}{4}D_i + \tfrac{1}{2}h_i + \{(D_i - h_i)^2 + 3E_i^2\}^{\frac{1}{2}} \\ E_4^{(i)} &= -\tfrac{5}{4}D_i - \tfrac{1}{2}h_i - \{(D_i + h_i)^2 + 3E_i^2\}^{\frac{1}{2}}. \end{aligned}\right\} \quad (3)$$

We know that $D_1 > 0$, $D_2 > 0$ and we assume without loss of generality $h_1 < 0$, $h_2 > 0$, $E_1 > 0$, $E_2 < 0$. Then we see from inspection of equation (3) that the lowest state energies of ions 1 and 2 are respectively

$$\left.\begin{aligned} E_1^{(1)} &= -\tfrac{5}{4}D_1 + \tfrac{1}{2}h_1 - \{(D_1 - h_1)^2 + 3E_1^2\}^{\frac{1}{2}} \\ E_4^{(2)} &= -\tfrac{5}{4}D_2 - \tfrac{1}{2}h_2 - \{(D_2 + h_2)^2 + 3E_2^2\}^{\frac{1}{2}}. \end{aligned}\right\} \quad (4)$$

The sublattice magnetizations at 0°K are obtained as follows:

$$\left.\begin{aligned} \frac{M_z^{(1)}}{g\mu_B} &= \frac{\partial E_1^{(1)}}{\partial h_1} = \tfrac{1}{2} + \frac{(D_1 - h_1)}{\{(D_1 - h_1)^2 + 3E_1^2\}^{\frac{1}{2}}} \\ \frac{M_z^{(2)}}{g\mu_B} &= \frac{\partial E_4^{(2)}}{\partial h_2} = -\tfrac{1}{2} - \frac{(D_2 + h_2)}{\{(D_2 + h_2)^2 + 3E_2^2\}^{\frac{1}{2}}} \end{aligned}\right\} \quad (5)$$

In the normal state under no compression, where

$$D_1 = D_2, \qquad E_1 = -E_2 = E, \quad (6)$$

we get

$$\begin{aligned} \frac{M_{z0}^{(1)}}{g\mu_B} &= -\frac{M_{z0}^{(2)}}{g\mu_B} = S_0 \\ &= \tfrac{1}{2} + \frac{D + 2Jz S_0}{\{(D + 2Jz S_0)^2 + 3E^2\}^{\frac{1}{2}}}. \end{aligned} \quad (7)$$

Under a compression, the relations (6) no longer hold; we write instead

$$\langle S_z^{(1)} \rangle = S_0 + \delta S_1, \qquad \langle S_z^{(2)} \rangle = -S_0 + \delta S_2, \quad (8)$$

$$\left.\begin{aligned} D_1 &= D+\delta D_1, \qquad D_2 = D+\delta D_2, \\ E_1 &= E+\delta E_1, \qquad E_2 = -E+\delta E_2. \end{aligned}\right\} \quad (9)$$

δS_i, δD_i, δE_i are regarded as linear functions of strain or stress. Inserting equations (8) and (9) into (5), we get

$$\delta S_1+\delta S_2 = \frac{3E^2D\left(\frac{\delta D_1-\delta D_2}{D}\right)-3E^2(D+2JzS_0)\left(\frac{\delta E_1+\delta E_2}{E}\right)}{\{(D+2JzS_0)^2+3E^2\}^{\frac{1}{2}}+6E^2Jz}. \quad (10)$$

There is another contribution to the piezomagnetic moment, i.e. the change of g-factors due to compression. Writing

$$\left.\begin{aligned} g_{1z} &= g_z+\delta g_1, \\ g_{2z} &= g_z+\delta g_2, \end{aligned}\right\} \quad (11)$$

we have as a net magnetic moment per pair of spins

$$(\delta g_1-\delta g_2)\mu_B S_0. \quad (12)$$

Summing up the contributions (10) and (12) and using the following numerical values of parameters estimated by NAKAMURA and TAKETA:

$$D_k' = 17{\cdot}9k, \qquad E = 36{\cdot}2k, \qquad 2Jz = 34{\cdot}8k,$$
$$S_0 = 1{\cdot}19, \quad (13)$$

we get

$$\delta M_1+\delta M_2 = g_z\mu_B\left\{-0{\cdot}3\frac{\delta E_1+\delta E_2}{E}+\right.$$
$$\left.+0{\cdot}09\frac{\delta D_1-\delta D_2}{D}+1{\cdot}19\frac{\delta g_1-\delta g_2}{g_z}\right\} \quad (14)$$

at 0°K. We can easily show that the influence of the change of J, the exchange interaction, due to compression is not important; it vanishes in the first-order effect.

We have now only to estimate δE, δD and δg as a function of strain or stress. However, to do this is not an easy task at present because of the absence of any clear understanding of the origin of the crystalline electrical field in this crystal. We can consider the contributions to the crystalline electrical field from distant charge, overlapping charge and partial covalent bonds. Though these iron-group difluorides may be regarded as more ionic than oxides or hydrated salts, where the covalent-bond contribution seems to be predominant, the numerical calculation of the crystalline electrical field based on the point-charge model did not give a result which could explain the magnetic anisotropy of this salt.[10]

We are here compelled to content ourselves with the following simple reasoning. Equation (14) consists of three terms, of which the first one seems to be the largest, since the orthorhombic character of the crystalline electrical field is essential in this problem. The second and the third terms might roughly be of the same order of magnitude, as we see from the following considerations. According to the crystalline-field theory, D, E and g are written as follows:

$$D = \frac{\lambda^2}{2}(2\Lambda_z-\Lambda_x-\Lambda_y),$$

$$E = \frac{\lambda^2}{2}(\Lambda_x-\Lambda_y),$$

$$g_z = 2(1-\lambda\Lambda_z),$$

$$\Lambda_x = \sum_i \frac{(g|L_x|i)(i|L_x|g)}{E_i-E_g}, \text{ etc.},$$

where λ is the spin-orbit coupling constant, and g and i represent the ground and the excited orbital states, respectively. If we tentatively assume that $\delta\Lambda_x \cong -\delta\Lambda_y$, we get

$$\frac{\delta g_z}{g_z} \cong \frac{-\lambda\Lambda_z}{1-\lambda\Lambda_z}\cdot\frac{\delta D}{D} = \frac{g_z-2}{g_z}\cdot\frac{\delta D}{D}. \quad (15)$$

The numerical value for CoF_2 is $(g_z-2)/g_z \cong 0{\cdot}2$.

In order to get some idea on the order of magnitude, we shall take only the first term of equation

(14) and further assume

$$\frac{\delta E_i}{E_i} = \frac{\delta A_i}{A_i}, \tag{16}$$

where A_i is defined by the following expression for the crystalline field potential around the ion of the ith kind:

$$V_i(r) = A_i(x^2-y^2)+B_i(3z^2-r^2)+ \\ +(\text{fourth-order terms}).$$

If we take account of the contributions to A_i from the six fluorine ions nearest to the Co^{2+} ion and regard them as point charges, we can easily calculate $\delta A_i/A_i$ as a function of strain or stress. We shall show the result when a linear stress is applied along the [110] direction, the x-axis in Fig. 2. Assuming uniform deformation in the crystal, we get

$$\frac{\delta A_i}{A_i} = (-15s_{2i}-0{\cdot}3s_{1i}+13s_{3i})T, \tag{17}$$

where s_{ij}'s are elastic compliance factors. Further assuming, though not necessarily correctly from the microscopic point of view,

$$s_{22} = s_{11}, \qquad s_{12} = s_{21}, \qquad s_{31} = s_{32}, \tag{18}$$

we get

$$\frac{\delta A_1+\delta A_2}{A} = 15(s_{11}-s_{12})T, \tag{19}$$

where the relation $A_1 = -A_2 = A$ was used.* We estimate therefore, taking $s_{11} \sim 10^{-6}$ cm^2/kg,

$$\delta M_1+\delta M_2 \cong -5g_z\mu_B(s_{11}-s_{12})T \\ \cong -5\times 10^{-6}g_z\mu_B T(\text{in kg/cm}^2). \tag{20}$$

Under a compression of 100 kg/cm^2, we get a magnetic moment of $0{\cdot}6\times 10^{-3}$ Bohr magnetons per ions, which corresponds to a magnetization of $M = 0{\cdot}2$ cgs.

Finally, we should mention that the actual magnitude may be larger than the above-estimated value, because the actual crystalline field potential, to which overlapping charges and partial covalent bonds may make contributions, may show stronger dependence on the interionic distance than that calculated on the point-charge assumption.

3. DISCUSSION

We have shown in this note that in antiferromagnetic MnF_2, FeF_2 and CoF_2 even a linear compression in the *ab*-plane produces a magnetic moment along the *c*-direction. This effect is considered to be especially significant in CoF_2. An order estimation for CoF_2 shows that the piezomagnetic moment of this type is considerable.

This effect will be observed by direct measurements of the piezomagnetic moment if the crystal has only one domain or a small number of domains. Fluorine and/or cobalt nuclear resonance[11] will provide a sensitive method for detecting the possible unbalance of the sublattice magnetizations. This method will not be affected by the existence of domains. Optical Faraday rotation[12] and the method of observing domains by using superconducting (niobium) powder[13]† may make it possible to see antiferromagnetic domain patterns, or to see whether domains really exist or not in antiferromagnetic CoF_2. In conclusion, we would stress that the piezomagnetic moment will be reversed in sign when the antiferromagnetic sublattice magnetizations are reversed in sign. This suggests the possibility of measuring the relaxation time for the interchange of the sublattice magnetizations in an antiferromagnet.

Acknowledgements—The writer wishes to thank Dr. P. W. ANDERSON for reading the manuscript and for kind advice. He has also benefited from conversations with Drs. R. M. BOZORTH, A. M. CLOGSTON, J. F. DILLON, V. JACCARINO and A. L. SCHAWLOW.

REFERENCES

1. DZIALOSHINSKI I. E., *Zh. Eksper. Teor. Fiz.* **33,** 807 (1957); (translation) *Sov. Phys. JETP* **6,** 621 (1958).
2. NAGAMIYA T., YOSIDA K. and KUBO R., *Advances in Phys.* **4,** 1 (1955).
3. KEFFER F., *Phys. Rev.* **88,** 608 (1952).

* $(\delta B_1-\delta B_2)/B$ was calculated in the same way, and the value is $-6(s_{11}-s_{12})T$. We see, therefore, from equation (14) that the second term is one order of magnitude smaller than the first term and of the same sign.

† By applying an external magnetic field of adequate magnitude, we can make the magnetic field on the surface of one kind of domains larger than H_c, while that on the surface of another kind of domains smaller than H_c.

4. NAKAMURA T. and TAKETA H., *Progr. Theor. Phys.* **13,** 129 (1955).
5. HOMMA A., *Busseiron-kenkyu* **4,** 358 (1958).
6. STOUT J. W. and MATARRESE L. M., *Rev. Mod. Phys.* **25,** 338 (1953).
7. TINKHAM M., *Proc. Roy. Soc.* A**236,** 535 (1956).
8. STOUT J. W., private communication.
9. TOSHIMA S. and NAKAMURA T., to be published.
10. MORIYA T., MOTIZUKI K., KANAMORI J. and NAGAMIYA T., *J. Phys. Soc. Japan* **11,** 211 (1956).
11. JACCARINO V., *Phys. Rev.* **107,** 1196 (1957).
12. DILLON J. F., *J. Appl. Phys.* **29,** 539 (1958).
13. SCHAWLOW A. L., MATTHIAS B. T., LEWIS H. W. and DEVELIN G. E., *Phys. Rev.* **95,** 1344 (1954).

OL.
11
959

J. Phys. Chem. Solids Pergamon Press 1959. Vol. 11. pp. 78–91. Printed in Great Britain.

COMPORTEMENT D'UN PETIT SYSTÈME QUANTIQUE DANS UN MILIEU FAIBLEMENT DISSIPATIF: QUELQUES APPLICATIONS AUX INTERACTIONS COULOMBIENNES

F. ENGLERT

Université libre de Bruxelles, Bruxelles

(*Received* 7 *February* 1959)

VOL
11
195

Résumé—L'étude du comportement d'un petit système quantique dans un milieu faiblement dissipatif est développée à l'aide d'un formalisme hamiltonien; l'effet du milieu considéré apparaît dans cet hamiltonien à l'aide d'opérateurs "renormalisés" qui sont obtenus à partir des opérateurs primitifs par l'action d'un tenseur d'admittance dynamique dépendant de la température, différant de celui de KUBO (*J. Phys, Soc. Japan* **12,** 570 (1957)) par le remplacement d'un commutateur par un produit. Ce tenseur, qui satisfait à des relations de causalité, de symétrie et à des relations thermodynamiques, se réduit, lorsque les systèmes sont composés de particules interagissant par un potentiel binaire, essentiellement à la transformée de Fourier unilatérale de la fonction de corrélation de paire de VAN HOVE (*Physica* **24,** 409 (1958)); ce résultat permet de généraliser l'hamiltonien des porteurs minoritaires de PINES et NOZIÈRES (*Phys. Rev.* **109,** 762 (1958)). La théorie générale est appliquée à l'étude des interactions coulombiennes, et certains résultats nouveaux sont obtenus dans le cas des particules chargées traversant un gaz d'électrons et dans celui des excitons dans les solides.

Abstract—A Hamiltonian formalism is developed to study the behavior of a small quantized system in a weakly dissipative medium; the effect of the medium appears in this Hamiltonian through "renormalized" operators which are obtained from the primitive ones with the help of a temperature-dependent dynamical admittance tensor, differing from KUBO's admittance (*J. Phys. Soc. Japan* **12,** 570 (1957)) by the replacement of a commutator by a product. This tensor, which exhibits causality, symmetry and thermodynamical relations, is shown, when the systems consist of particles interacting through a binary potential, to be essentially the one-sided Fourier transform of VAN HOVE's correlation function (*Physica* **24,** 409 (1958)); using this result, it is possible to generalize the PINES–NOZIÈRES (*Phys. Rev.* **109,** 762 (1958)) minority-carriers technique. The general theory is applied to Coulomb interactions, and some new results concerning charged particles moving in an electron gas and excitons in solids are derived.

1. INTRODUCTION

DANS de nombreux problèmes de physique, on est amené à étudier le comportement d'un petit système, c'est-à-dire d'un système comportant peu de degrés de liberté dans un milieu en comportant en principe une infinité; on peut alors essayer de caractériser l'effet du milieu considéré sur ce système à l'aide de quelques grandeurs physiques : constante diélectrique, perméabilité magnétique, fonctions de corrélation, etc., et qui peuvent souvent être obtenues, du moins partiellement, expérimentalement.

Cette étude est liée à celle de la réponse du grand système, c'est-à-dire du milieu considéré, à une sollicitation extérieure; ce problème a été traité notemment par CALLEN[1,2], et plus récemment par KUBO[3], d'une manière générale dans l'approximation linéaire dans laquelle il se ramène à la détermination d'un tenseur d'admittance qui, comme l'a montré KUBO, est la transformée de Fourier unilatérale d'un commutateur. Nous verrons qu'une admittance dynamique, différant de l'admittance de KUBO par le remplacement du commutateur par un produit, permet d'introduire l'effet du grand système, supposé faiblement dissipatif, dans un hamiltonien effectif décrivant le petit système; ces résultats généralisent ceux exposés dans une note précédente.[4]

La dérivation de cet hamiltonien effectif fait l'objet de la deuxième partie de ce travail; on l'obtient, après avoir effectué une transformation unitaire correspondant au second ordre de la théorie des perturbations, en prenant une moyenne statistique de l'hamiltonien transformé sur les états du grand système; le tenseur d'admittance dynamique qui s'introduit dans cet hamiltonien effectif se sépare naturellement en un tenseur équivalent à celui de KUBO et en une correction dynamique. Nous effectuons ensuite le lien avec la théorie de WANGSNESS et BLOCH[5-9] qui décrit l'évolution du petit système dans le formalisme de la matrice densité de von Neumann.

Dans la troisième partie, les propriétés du tenseur d'admittance dynamique sont étudiées avec plus de détails : relations de symétrie, de causalité, et relations thermodynamiques; ces dernières lient la correction dynamique aux admittances de KUBO et donnent un aspect nouveau des relations de fluctuation–dissipation. Finalement la séparation du tenseur d'admittance dynamique en tenseur hermitien et antihermitien est illustrée du point de vue physique par leur lien respectif avec les problèmes de self-énergie et de dissipation.

Le formalisme général est appliqué dans la quatrième partie aux systèmes de particules interagissant par un potentiel binaire; dans ce cas, les résultats précédents se simplifient par l'utilisation d'une représentation de l'interaction diagonalisant le tenseur d'admittance dynamique; celui-ci apparaît alors simplement comme la transformée de Fourier unilatérale de la fonction de corrélation de paire de VAN HOVE[10,11]. Après avoir défini les fonctions diélectriques, nous comparerons nos résultats à ceux de FANO[12] et à ceux de PINES et NOZIÈRES[13,14] et nous discuterons les modifications que notre théorie apporte à l'hamiltonien effectif des porteurs minoritaires de ces derniers.[13] Nous donnerons ensuite quelques propriétés générales des fonctions diélectriques qui se déduisent aisément des relations établies dans la troisième partie.

La dernière partie est consacrée à quelques applications aux interactions coulombiennes; les résultats classiques de LINDHARD[15] concernant la self-énergie complexe et la perte d'énergie d'une particule chargée traversant un gas d'électrons sont étendus, compte tenu du caractère dynamique de la particule et de la température du gaz. Les fonctions diélectriques dans les solides parfaits, qui peuvent être calculées rigoureusement dans l'hypothèse de la "random phase approximation" de PINES et NOZIÈRES[13], sont ensuite utilisées pour déterminer l'effet polarisant des électrons de valence sur les états excitons dans les cristaux polarisables où l'interaction électron–trou apparaît sous la forme d'un potentiel effectif généralisant très simplement le potentiel coulombien.

2. HAMILTONIEN EFFECTIF

Considérons un système décrit par un hamiltonien H tel que

$$H = H_0 + H_{\text{int}} \tag{2.1}$$

où H_{int} est suffisemment faible pour qu'on puisse se limiter au second ordre en H_{int} dans un calcul de perturbation.

Effectuons la transformation unitaire

$$\tilde{H} = e^{-F} H e^{F} \tag{2.2}$$

où l'opérateur antihermitien F est donné par

$$F = \sum_m \frac{1}{E_m - H_0 - i\epsilon} H_{\text{int}} |m\rangle\langle m|. \tag{2.3}$$

Dans cette expression, E_m et $|m\rangle$ sont respectivement valeur propre et vecteur propre normé à l'unité de H_0; ϵ est un nombre réel quelconque que nous choisirons positif. La somme est étendue à l'ensemble complet de vecteurs propres orthonormés de H_0 dont le spectre est supposé discret; tout spectre continu pouvant être considéré comme la limite d'un spectre discret lorsque les dimensions spatiales du système croissent indéfiniment, l'expression (2.3) peut être conservée dans le cas général.

Au second ordre en H_{int}, l'équation (2.2) donne pour l'hamiltonien $\tilde{H}$

$$\tilde{H} = H + [H, F] - \tfrac{1}{2}[F, [H_0, F]]. \tag{2.4}$$

On a, si $|q\rangle$ et $|p\rangle$ sont deux vecteurs propres de H_0

$$\langle q|[H_0, F]|p\rangle = \left\{ -1 - \frac{i\epsilon}{E_p - E_q - i\epsilon} \right\} \langle q|H_{\text{int}}|p\rangle \tag{2.5}$$

d'où

$$[H_0, F] = -H_{\text{int}} - i\epsilon F \tag{2.6}$$

et par conséquent, en portant (2.6) dans (2.4)

$$\tilde{H} = H_0 - i\epsilon F + \mathscr{R} H_{\text{int}} F \tag{2.7}$$

où le signe $\mathscr{R}$ indique que seule la partie hermitienne de l'opérateur considéré doit être conservée.

Les éléments de matrice de $-i\epsilon F$ entre états propres de H_0 sont les mêmes, dans la limite $\epsilon \to 0$, que ceux de H_{int} entre les états de même énergie de H_0 et sont nuls dans les autres cas; ϵ est donc un paramètre qui mesure la quantité d'éléments non diagonaux de H_{int} conservée après la transformation (2.2); nous traduirons ce fait en posant

$$-i\epsilon F = H_{\text{int}}{}^{(\epsilon)} \tag{2.8}$$

et l'équation (2.7) peut s'écrire

$$H = H_0 + H_{\text{int}}{}^{(\epsilon)} + \\ + \mathscr{R} \sum_m H_{\text{int}} \frac{1}{E_m - H_0 - i\epsilon} H_{\text{int}} |m\rangle\langle m|. \tag{2.9}$$

Si ϵ tend vers 0, l'hamiltonien (2.9) décrit le système considéré au second ordre en H_{int} à l'aide des états propres de H_0; toutefois nous supposerons dans l'exposé de la théorie générale que ϵ est petit mais fini afin d'éviter toute ambiguïté; le passage à la limite dans les résultats finaux ne présentera en général pas de difficultés, le système considéré étant de dimensions spatiales infinies.

Considérons maintenant le cas où H est l'hamiltonien de deux systèmes dont l'interaction est donnée par H_{int}; nous poserons

$$H_0 = H^\sigma + H^s \tag{2.10}$$

où H^σ et H^s décrivent les deux systèmes en l'absence d'interaction. Le système $s+\sigma$ est placé dans un thermostat à la température T et nous supposerons que σ est suffisemment petit pour ne pas modifier l'équilibre de température du système s qui lui peut être pris aussi grand que l'on veut; si d'autre part la durée de vie τ des états propres de H^σ, qui au second ordre en H_{int} est due aux transitions réelles provoquées par $H_{\text{int}}{}^{(\epsilon)}$ (avec $\epsilon\tau \gg \hbar$), est appréciable, on peut décrire le système σ compte tenu de l'effet de polarisation du grand système s, par l'hamiltonien effectif obtenu en prenant une moyenne statistique de $\tilde{H}$ sur les états de s.

Introduisons l'opérateur densité $p^s(T)$ relatif au système s à la température T; on a

$$p^s(T) = \sum_{m^s} |m^s\rangle p_{m^s}(T) \langle m^s| \tag{2.11}$$

où $|m^s\rangle$ est un vecteur propre de H^s et $p_{m^s}(T)$ le poids statistique affectant l'état $|m^s\rangle$ à la température T; on peut aussi écrire

$$p^s(T) = c \exp(-H^s/kT) \tag{2.12}$$

où c est une constante normalisant la trace de $p^s(T)$, prise sur les états du système s, à l'unité. L'hamiltonien effectif peut alors s'écrire

$$H_{\text{eff}} = H^\sigma + \text{Tr} p^s(T)\{\tilde{H} - H_0\} \tag{2.13}$$

la trace étant prise sur les états du système s.

Posons

$$H_{\text{int}} = \sum_p V_p U_p{}^+ = \sum_p V_p{}^+ U_p \tag{2.14}$$

où les opérateurs V_p et U_p (et leurs adjoints) ne dépendent respectivement que des variables des systèmes s et σ; un développement du type (2.14) est toujours possible, par exemple en choisissant les U_p de telle manière qu'ils forment un système d'opérateurs orthonormés complet relativement au système σ. Désignons par E_{m^s} et E_{m^σ} les valeurs propres de H^s et H^σ correspondants aux vecteurs propres $|m^s\rangle$ et $|m^\sigma\rangle$; on a

$$\text{Tr} p^s(T) H_{\text{int}}{}^{(\epsilon)} \\ = \sum_p \langle V_p{}^+ \rangle_T \sum_{m\sigma} \frac{-i\epsilon}{E_{m^\sigma} - H^\sigma - i\epsilon} U_p |m^\sigma\rangle\langle m^\sigma| \tag{2.15}$$

$\langle V_p{}^+ \rangle_T$ étant la moyenne de $V_p{}^+$ à la température T. Définissant par analogie avec (2.8)

$$U_p{}^{(\epsilon)} = \sum_{m^\sigma} \frac{-i\epsilon}{E_{m^\sigma} - H^\sigma - i\epsilon} U_p |m^\sigma\rangle\langle m^\sigma| \tag{2.16}$$

on peut écrire (2.15) sous la forme

$$\text{Tr} p^s(T) H_{\text{int}}{}^{(\epsilon)} = \sum_p \langle V_p{}^+ \rangle_T U_p{}^{(\epsilon)}. \tag{2.17}$$

On trouve aisément pour les termes du second ordre,

$$\text{Tr} p^s(T) \mathscr{R} \sum_m H_{\text{int}} \frac{1}{E_m - H_0 - i\epsilon} H_{\text{int}} |m\rangle\langle m| \\ = \mathscr{R} \sum_q U_q{}^+ \dot{U}_q = \mathscr{R} \sum_q \dot{U}_q{}' U_q{}^+ \tag{2.18}$$

où

$$\langle n^\sigma|\hat{U}_q|m^\sigma\rangle = \sum_p \pi_{qp}(\omega_{m^\sigma n^\sigma};\, T)\langle n^\sigma|U_p|m^\sigma\rangle \tag{2.19}$$

$$\langle n^\sigma|\hat{U}_q{}'|m^\sigma\rangle = \sum_p \pi_{qp}{}'(-\omega_{m^\sigma n^\sigma};\, T)\langle n^\sigma|U_p|m^\sigma\rangle \tag{2.20}$$

en définissant

$$\hbar\omega_{m^\sigma n^\sigma} = E_{m^\sigma} - E_{n^\sigma};\quad \hbar\omega_{m^s n^s} = E_{m^s} - E_{n^s} \tag{2.21}$$

et

$$\pi_{qp}(\omega;\, T) = \frac{1}{\hbar}\sum_{m^s} p_{m^s}(T)\sum_{n^s}\frac{\langle m^s|V_q|n^s\rangle\langle n^s|V_p{}^+|m^s\rangle}{\omega-\omega_{n^s m^s}-i\epsilon} \tag{2.22}$$

$$\pi_{qp}{}'(\omega;\, T) = \frac{1}{\hbar}\sum_{m^s} p_{m^s}(T)\sum_{n^s}\frac{\langle m^s|V_p{}^+|n^s\rangle\langle n^s|V_q|m^s\rangle}{\omega-\omega_{n^s m^s}+i\epsilon} \tag{2.23}$$

De (2.13), (2.17), (2.18), on obtient

$$H_{\text{eff}} = H^\sigma + \sum_p \langle V_p{}^+\rangle_T U_p{}^{(e)} + \mathscr{R}\sum_q U_q{}^+\hat{U}_q. \tag{2.24}$$

Pour l'interprétation physique du tenseur (2.22), il est commode de poser

$$U_q{}^1 = \tfrac{1}{2}\{\hat{U}_q + \hat{U}'_q\} \tag{2.25}$$

$$U_q{}^2 = \tfrac{1}{2}\{\hat{U}_q - \hat{U}'_q\} \tag{2.26}$$

On voit immédiatement que $U_q{}^1$ et $U_q{}^2$ peuvent être définis par l'équation (2.29) où l'on remplace $\pi_{qp}(\omega;\, T)$ respectivement par

$$P_{qp}{}^1(\omega;\, T) = \tfrac{1}{2}\{\pi_{qp}(\omega;\, T) + \pi_{qp}{}'(-\omega;\, T)\} \tag{2.27}$$

$$P_{qp}{}^2(\omega;\, T) = \tfrac{1}{2}\{\pi_{qp}(\omega;\, T) - \pi_{qp}{}'(-\omega;\, T)\}. \tag{2.28}$$

Introduisant les opérateurs (2.25) et (2.26) dans (2.24), on obtient la forme suivante de l'hamiltonien effectif

$$H_{\text{eff}} = H^\sigma + \sum_p \langle V_p{}^+\rangle_T U_p{}^{(e)} + \tfrac{1}{2}\mathscr{R}\sum_q \{[U_q{}^+,\, U_q{}^1]_+ + [U_q{}^+,\, U_q{}^2]\} \tag{2.29}$$

où $[\ ]_+$ désigne un anticommutateur.

Dans les termes du second ordre de (2.24) et (2.29), le système s s'introduit uniquement par l'intermédiaire des tenseurs $\pi_{qp}(\omega;\, T)$, ou $P_{qp}{}^1(\omega;\, T)$ et $P_{qp}{}^2(\omega;\, T)$ qui font passer des éléments de matrice de U_p aux éléments de matrice "renormalisés" par les transitions virtuelles du grand système s. Nous appelerons ces tenseurs, suivant une terminologie courante dans l'étude des phénomènes linéaires, des *tenseurs d'admittance*; toutefois, l'hamiltonien (2.29) où intervient un commutateur montre que le tenseur $P_{qp}{}^2(\omega;\, T)$ n'interviendrait pas si l'opérateur U_p était remplacé par la fonction $U_p(t)$ qui correspondrait à la variable dynamique U_p dans le cas où le système σ pourrait être remplacé par un ensemble de forces extérieures agissant sur s; le tenseur $P_{qp}{}^2(\omega;\, T)$ apparaît ainsi comme une correction dynamique au tenseur d'admittance $P_{qp}{}^1(\omega;\, T)$ que nous identifierons d'ailleurs plus loin (à un facteur $-\frac{1}{2}$ près) à celui introduit par KUBO[3] qui caractérise, dans l'approximation linéaire, la réponse d'un opérateur du système s à une sollicitation extérieure. Pour résumer cette discussion, nous appelerons plus particulièrement $\pi_{qp}(\omega;\, T)$ le *tenseur d'admittance dynamique* du système s à la température T, $P_{qp}{}^1(\omega;\, T)$ le *tenseur d'admittance classique* et $P_{qp}{}^2(\omega;\, T)$ la *correction dynamique*.

Nous conclurons ce paragraphe en comparant H_{eff} à l'opérateur d'évolution qui apparaît dans la théorie de WANGSNESS et BLOCH. La théorie de WANGSNESS et BLOCH[5], développée par BLOCH[6,7], REDFIELD[8] et FANO[9], décrit l'évolution de la matrice densité d'un petit système en présence d'un grand système. Dans le cas qui nous concerne (H^σ indépendant du temps), l'équation donnant cette évolution peut s'écrire (équation (2.56) de BLOCH[7])

$$i\hbar\frac{\partial\sigma}{\partial t} = [\hat{H},\, \sigma] + \Gamma(\sigma) \tag{2.30}$$

où

$$\hat{H} = \hbar E + \hbar\Delta + \hbar\Gamma \tag{2.31}$$

en adoptant les notations de BLOCH.

L'opérateur $\hat{H}$ diffère de H_{eff} par

(1°) la présence de termes non diagonaux au premier ordre dans $\hbar\Delta$ qui sont éliminés par notre transformation unitaire,

(2°) l'absence du terme causal $i\epsilon$,

(3°) une approximation que BLOCH et REDFIELD ont effectué pour rendre $\hbar\Gamma$ hermitien.

Toutefois, si cette dernière approximation n'est pas faite, si on néglige les termes non diagonaux de $\hbar\Delta$ (d'ailleurs sans grande influence sur l'évolution de σ comme l'a montré BLOCH), on peut écrire (2.30) sous la forme

$$i\hbar\frac{\partial\sigma}{\partial t} = [H_{\text{eff}}, \sigma]+\Gamma'(\sigma) \tag{2.32}$$

où H_{eff} apparaît explicitement et où $\Gamma'(\sigma)$ diffère de $\Gamma(\sigma)$ non seulement parce que l'approximation du (3°) n'a pas été faite, mais aussi par suite du passage dans $\hat{H}$ de la partie hermitienne d'un terme contenant le facteur causal $i\epsilon$. Nous voyons donc que notre H_{eff} est implicitement contenu dans la théorie de WANGSNESS et BLOCH sous sa forme récente[7,8] mais que son explicitation n'apparaît pas clairement sous forme d'un hamiltonien approximatif.

3. PROPRIÉTÉS DES TENSEURS D'ADMITTANCE

Définissons par $f(\omega) = T^{\omega}f(t)$ la transformée de Fourier de $f(t)$; on a

$$f(t) = \frac{1}{2\pi}\int \exp(i\omega t)f(\omega)\,d\omega \tag{3.1}$$

$$f(\omega) = \int \exp(-i\omega t)f(t)\,dt = T^{\omega}f(t). \tag{3.2}$$

Cherchons la transformée de Fourier inverse du tenseur d'admittance dynamique,

$$\pi_{qp}(t;\,T) = \frac{1}{2\pi}\int \exp(i\omega t)\pi_{qp}(\omega;\,T)\,d\omega \tag{3.3}$$

$$= \frac{1}{\hbar}\frac{1}{2\pi}\sum_{m^s} p_{m^s}(T)\sum_{n^s}\langle m^s|V_q|n^s\rangle\times$$

$$\times\langle n^s|V_p{}^{+}|m^s\rangle\int\frac{\exp(i\omega t)}{\omega-\omega_{n^sm^s}-i\epsilon}\,d\omega.$$

Après intégration dans le plan complexe ω, on obtient

$$\pi_{qp}(t;\,T) = i/\hbar\langle V_q(0)V_p{}^{+}(t)\rangle_T u_\epsilon(t) \tag{3.4}$$

où $u_\epsilon(t)$ vaut $\exp(-\epsilon t)$ pour $t>0$ et 0 pour $t<0$; $V_p{}^{+}(t)$ est l'opérateur $V_p{}^{+}$ à l'instant t dans la représentation d'Heisenberg du système s non perturbé (représentation d'interaction), c'est-à-dire

$$V_p{}^{+}(t) = \exp[+(i/\hbar)H^st/\hbar]V_p{}^{+}\exp[-(i/\hbar)H^st/\hbar]. \tag{3.5}$$

Par un calcul analogue, on obtient

$${}'\pi_{qp}(t;\,T) = -i/\hbar\langle V_p{}^{+}(t)V_q(0)\rangle_T u_\epsilon(t) \tag{3.6}$$

où ${}'\pi_{qp}(t;\,T)$ est cette fois la transformée de Fourier inverse de $\pi_{qp}{}'(-\omega;\,T)$.

De (3.4), (3.6), (2.27), (2.28), on déduit

$$\pi_{qp}(\omega;\,T) = T^{\omega}(i/\hbar)u_\epsilon(t)\langle V_q(0)V_p{}^{+}(t)\rangle_T \tag{3.7}$$

$$P_{qp}{}^{1}(\omega;\,T) = T^{\omega}(i/2\hbar)u_\epsilon(t)\langle[V_q(0)V_p(t)]\rangle_T \tag{3.8}$$

$$P_{qp}{}^{2}(\omega;\,T) = T^{\omega}(i/2\hbar)u_\epsilon(t)\langle[V_q(0)V_p(t)]^{+}\rangle_T. \tag{3.9}$$

La relation (3.8) montre que le tenseur d'admittance classique est à un facteur $-\frac{1}{2}$ près égal à celui de KUBO qui décrit la réponse $\Delta V_p{}^{+}(t)$ à une sollicitation extérieure proportionnelle à V_q. D'autre part la correction dynamique apparaît comme une fonction de corrélation du type fréquemment envisagé en mécanique statistique. On sait que les théorèmes de fluctuation–dissipation étudiés notemment dans les références (1), (2) et (3) relient des admittances à des fonctions de corrélations; ces théorèmes apparaissent ici liés à l'existence d'un tenseur du type (3.7) qui caractérise entièrement, à l'ordre envisagé, l'effet du système s sur un petit système σ et nous allons d'ailleurs retrouver des théorèmes analogues en étudiant maintenant les propriétés des tenseurs d'admittance.

(a) *Relations de causalité*

Désignons par $\pi_{qp}{}^{S}(\omega;\,T)$ et $\pi_{qp}{}^{A}(\omega;\,T)$ les parties hermitienne et antihermitienne du tenseur $\pi_{qp}(\omega;\,T)$, c'est-à-dire

$$\pi_{qp}{}^{S}(\omega;\,T) = \tfrac{1}{2}\{\pi_{qp}(\omega;\,T)+\pi_{pq}{}^{*}(\omega;\,T)\} \tag{3.10}$$

$$\pi_{qp}{}^{A}(\omega;\,T) = \tfrac{1}{2}\{\pi_{qp}(\omega;\,T)-\pi_{pq}{}^{*}(\omega;\,T)\} \tag{3.11}$$

et définissons de manière analogue les tenseurs $P_{qp}{}^{1S}$, $P_{qp}{}^{1A}$, $P_{qp}{}^{2S}$, $P_{qp}{}^{2A}$.

Considérons la fonction de la variable complexe $\pi_{qp}{}^{c}(\omega;\,T)$ définie par le prolongement de la fonction $\pi_{qp}(\omega;\,T)$ définie en (2.22) dans tout le plan.

Cette fonction est analytique partout sauf sur l'axe réel où elle présente des singularités qui dans la limite où le spectre de H^s est continu deviennent des lignes de discontinuité; à l'infini, cette fonction décroît en module comme $1/|\omega|$.

Intégrant la fonction $\pi_{qp}{}^c(\omega'; T)/\omega-\omega'$ le long des contours C_1 et C_2 (Fig. 1) on obtient d'après le théorème de Cauchy

$$\pi_{qp}{}^c(\omega+i\epsilon; T) = -\frac{1}{i\pi}\int_{-\infty}^{+\infty}\frac{\pi_{qp}{}^c(\omega'+i\epsilon; T)}{\omega-\omega'}\,d\omega' \tag{3.12}$$

$$\pi_{qp}{}^c(\omega-i\epsilon; T) = \frac{1}{i\pi}\int_{-\infty}^{+\infty}\frac{\pi_{qp}{}^c(\omega'-i\epsilon; T)}{\omega-\omega'}\,d\omega'. \tag{3.13}$$

Dans ces relations, ω et ω' sont réels et le signe $\int$

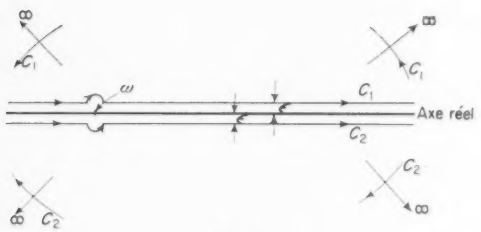

FIG. 1.

signifie que seule la valeur principale de l'intégrale doit être considérée.

Tenant compte de

$$\pi_{qp}(\omega; T) = \pi_{qp}{}^c(\omega-i\epsilon; T) \tag{3.14}$$

$$\pi_{pq}{}^*(\omega; T) = \pi_{qp}{}^c(\omega+i\epsilon; T) \tag{3.15}$$

et de (3.10), (3.11) on obtient en ajoutant et en soustrayant membre à membre (3.12) et (3.13)

$$\pi_{qp}{}^S(\omega; T) = \frac{1}{i\pi}\int_{-\infty}^{+\infty}\frac{\pi_{qp}{}^A(\omega; T)}{\omega-\omega'}\,d\omega' \tag{3.16}$$

$$\pi_{qp}{}^A(\omega; T) = \frac{1}{i\pi}\int_{-\infty}^{+\infty}\frac{\pi_{qp}{}^S(\omega; T)}{\omega-\omega'}\,d\omega'. \tag{3.17}$$

On vérifie immédiatement que ces relations sont valables séparément pour les tenseurs $P_{qp}{}^1(\omega; T)$ et $P_{qp}{}^2(\omega; T)$; elles sont du type des relations de Kramers–Kronig et contiennent les équations (7.3) et (7.4) de KUBO.[3]

(b) *Relations thermodynamiques*

De (3.11), (2.22) et (2.23) on déduit aisément

$$\pi_{qp}{}^A(\omega; T) = \frac{i}{\hbar}\sum_{m^s} p_{m^s}(T)\sum_{n^s}\langle m^s|V_q|n^s\rangle\times$$

$$\times\langle n^s|V_p{}^+|m^s\rangle\frac{\epsilon}{(\omega-\omega_{n^sm^s})^2+\epsilon^2} \tag{3.18}$$

$$\pi'_{qp}{}^A(-\omega; T) = -\pi_{qp}{}^A(\omega; T)\exp(-\hbar\omega/kT) \tag{3.19}$$

Pour établir cette dernière relation on a tenu compte de

$$p_{m^s}(T) = p_{n^s}(T)\exp(-\hbar\omega_{n^sm^s}/kT) \tag{3.20}$$

$$\exp(-\hbar\omega_{n^sm^s}/kT)\frac{\epsilon}{(\omega-\omega_{n^sm^s})^2+\epsilon^2}$$

$$= \exp(-\hbar\omega/kT)\frac{\epsilon}{(\omega-\omega_{n^sm^s})^2+\epsilon^2} \tag{3.21}$$

cette dernière égalité n'étant rigoureuse que dans la limite $\epsilon\to 0$†, De (3.18), (3.19), on déduit immédiatement en considérant (2.27) et (2.28)

$$P_{qp}^{1A}(\omega; T) = \pi_{qp}^{A}(\omega; T)\frac{1-\exp(-\hbar\omega/kT)}{2} \tag{3.22}$$

$$P_{qp}^{2A}(\omega; T) = \pi_{qp}^{A}(\omega; T)\frac{1+\exp(-\hbar\omega/kT)}{2} \tag{3.23}$$

$$P_{qp}^{1A}(\omega; T) = P_{qp}^{2A}(\omega; T)\,\mathrm{Th}(\hbar\omega/2kT). \tag{3.24}$$

Ces relations entre parties antihermitiennes des tenseurs d'admittance peuvent s'écrire en fonction des parties hermitiennes à l'aide des relations (3.16) et (3.17) si le passage à la limite $\epsilon\to 0$ se fait sans ambiguïté. Considérant en particulier la relation (3.24), on retrouve ainsi les théorèmes de fluctuation–dissipation sous une forme nouvelle.

† Les relations thermodynamiques ne sont donc rigoureuses qu'après passage à la limite $\epsilon\to 0$.

Les relations (3.22), (3.23), (3.24) sont particulièrement simples si $T = 0$; on a alors

(a) $\omega > 0$

$$P^{1A}_{qp}(\omega; 0) = P^{2A}_{qp}(\omega; 0) = \tfrac{1}{2}\pi_{qp}{}^{A}(\omega; 0) \tag{3.25}$$

(b) $\omega < 0$

$$P^{1A}_{qp}(\omega; 0) = -P^{2A}_{qp}(\omega; 0) \quad ; \quad \pi_{qp}{}^{A}(\omega; 0) = 0. \tag{3.26}$$

(c) *Relations de symétrie*

Comparant (2.22) et (2.23), on obtient

$$\pi_{-q-p}{}^{*}(\omega; T) = \pi_{qp}{}'(\omega; T) \tag{3.27}$$

où les tenseurs d'indice $-q$, $-p$, sont définis par le remplacement dans les tenseurs d'indice q et p des opérateurs V_q et $V_p{}^{+}$ par leurs adjoints. Tenant compte de (3.27), les relations (2.27) et (2.28) impliquent

$$P^{1*}_{-q-p}(-\omega; T) = P^{1}_{qp}(\omega; T) \tag{3.28}$$

$$P^{2*}_{-q-p}(-\omega; T) = -P^{2}_{qp}(\omega; T). \tag{3.29}$$

Nous terminerons ce paragraphe en établissant quelques relations qui préciseront le sens physique des parties hermitiennes et antihermitiennes du tenseur d'admittance.

Evaluons d'abord la self-énergie ΔE_{m^σ} correspondant à un état propre $|m^\sigma\rangle$ de H^σ; nous ne tiendrons pas compte du terme $\sum_p \langle V_p{}^{+}\rangle_T U_p{}^{(\epsilon)}$ dans (2.24); ce terme est d'ailleurs rigoureusement nul dans de nombreux cas (voir ci-après) par suite des propriétés d'invariance du système s. On a alors d'après (2.27)

$$\Delta E_{m^\sigma} = \sum_q \langle m^\sigma | \mathscr{R} U_q{}^{+} U_q | m^\sigma \rangle \tag{3.30}$$

ou, après un calcul élémentaire,

$$\Delta E_{m^\sigma} = \sum_{pq}\sum_{n^\sigma} \pi_{qp}{}^{S}(\omega_{m^\sigma n^\sigma}; T)\times$$
$$\times \langle m^\sigma | U_q{}^{+} | n^\sigma \rangle \langle n^\sigma | U_p | m^\sigma \rangle \tag{3.31}$$

D'autre part, la probabilité de transition par unité de temps de l'état $|m^\sigma\rangle$ à l'état $|n^\sigma\rangle$ vaut dans l'approximation de Born, si l'état initial du système s est déterminé par l'équilibre de température

$$P^{n^\sigma}_{m^\sigma} = \frac{2\pi}{\hbar^2}\sum_{pq}\sum_{m^s} p_{m^s}(T)\sum_{n^s}\langle m^s | V_q | n^s\rangle \times$$
$$\times \langle n^s | V_p{}^{+} | m^s\rangle \langle m^\sigma | U_q{}^{+} | n^\sigma\rangle \langle n^\sigma | U_p | m^\sigma\rangle \times$$
$$\times \delta(\omega_{m^\sigma n^\sigma} - \omega_{n^s m^s}) \tag{3.32}$$

ce qui s'écrit, en comparant avec (3.18) dans la limite $\epsilon \to 0$,

$$iP^{n^\sigma}_{m^\sigma} = \frac{2}{\hbar}\sum_{pq}\pi_{qp}{}^{A}(\omega_{m^\sigma n^\sigma}; T)\times$$
$$\times \langle m^\sigma | U_q{}^{+} | n^\sigma\rangle \langle n^\sigma | U_p | m^\sigma\rangle. \tag{3.33}$$

Définissant la largeur d'un état par

$$\hbar P_{m^\sigma} = \Gamma_{m^\sigma} \tag{3.34}$$

où P_{m^σ} est la probabilité totale de transition par unité de temps de $|m^\sigma\rangle$ dans un état quelconque on a

$$i\frac{\Gamma_{m^\sigma}}{2} = \sum_{pq}\sum_{n^\sigma}\pi_{qp}{}^{A}(\omega_{m^\sigma n^\sigma}; T)\times$$
$$\times \langle m^\sigma | U_q{}^{+} | n^\sigma\rangle \langle n^\sigma | U_p | m^\sigma\rangle. \tag{3.35}$$

Nous pouvons définir une self-énergie complexe (cf. LINDHARD[15]), par

$$\epsilon_{m^\sigma} = \Delta E_{m^\sigma} + i(\Gamma_{m^\sigma}/2) \tag{3.36}$$

ce qui donne

$$\epsilon_{m^\sigma} = \sum_{pq}\sum_{n^\sigma}\pi_{qp}(\omega_{m^\sigma n^\sigma}; T)\times$$
$$\times \langle m^\sigma | U_q{}^{+} | n^\sigma\rangle \langle n^\sigma | U_p | m^\sigma\rangle. \tag{3.37}$$

De (3.32) on peut également déduire l'énergie cédée par unité de temps dW_{m^σ}/dt par le système σ au système s lorsque le système σ se trouve initialement dans l'état $|m^\sigma\rangle$

$$i\frac{dW_{m^\sigma}}{dt} = \sum_{pq}\sum_{n^\sigma} 2\omega_{m^\sigma n^\sigma}\pi_{qp}{}^{A}(\omega_{m^\sigma n^\sigma}; T)\times$$
$$\times \langle m^\sigma | U_q{}^{+} | n^\sigma\rangle \langle n^\sigma | U_p | m^\sigma\rangle. \tag{3.38}$$

Ces exemples montrent clairement que $\pi_{qp}{}^{A}(\omega; T)$ caractérise l'effet dissipatif et

$\pi_{qp}{}^{S}(\omega; T)$ l'effet polarisant du système s; le lient causal entre ces effets est exprimé par les relations (3.16) et (3.17); remarquons que les résultats établis ici tiennent compte du caractère dynamique du système σ et de la température du système s.

4. SYSTÈMES DE PARTICULES INTERAGISSANT PAR UN POTENTIEL BINAIRE

(a) *Hamiltonien effectif et tenseurs d'admittance*

Les résultats précédents sont particulièrement simples lorsque les systèmes s et σ sont composés de particules interagissant par un potentiel binaire; soit $v(r)$ le potentiel d'interaction entre deux particules de s et $V(r)$ le potentiel d'interaction entre une particule de s et une particule de σ.

Plaçons le système $\sigma+s$ dans une boite de volume V soumise aux conditions aux limites périodiques*; soit $v(q)$, $V(q)$, $\rho_{\vec{q}}{}^{s}$, $\rho_{\vec{q}}{}^{\sigma}$, les transformées de Fourier de $v(r)$, $V(r)$, $\rho^{s}(\vec{r})$, $\rho^{\sigma}(\vec{r})$ où

$$\rho^{s}(\vec{r}) = \sum_{i} \delta(\vec{r}-\vec{r}_{i}{}^{s}) \tag{4.1}$$

$\vec{r}_{i}{}^{s}$ étant la coordonée vectorielle d'une particule du système s.

L'hamiltonien H^{s} s'écrit

$$H^{s} = H_{0}{}^{s}+\sum_{\vec{q}} \frac{v(q)}{2V}(\rho_{\vec{q}}{}^{s}\rho_{-\vec{q}}{}^{s}-N) \tag{4.2}$$

où $H_{0}{}^{s}$ contient l'énergie cinétique des N particules du système s et éventuellement leur énergie potentielle dans un champ extérieur. D'autre part

$$H_{\mathrm{int}} = \sum_{\vec{q}} \frac{V(q)}{V} \rho_{\vec{q}}{}^{s}\rho_{-\vec{q}}{}^{\sigma}. \tag{4.3}$$

Pour appliquer la théorie générale développée en 2 et 3, il suffit d'effectuer la correspondance

$$U_{\vec{q}}{}^{+} \to [V(q)/V]\rho_{\vec{q}}{}^{\sigma}; \quad V_{\vec{q}}{}^{+} \to \rho_{\vec{q}}{}^{s}. \tag{4.4}$$

Si le système s est invariant par rapport aux translations, on vérifie que les éléments non diagonaux des tenseurs d'admittance sont nuls; les éléments diagonaux s'écrivent

$$\pi_{\vec{q}}(\omega; T) = \frac{1}{\hbar}\sum_{m^{s}} p_{m^{s}}(T) \sum_{n^{s}} \frac{|\langle n^{s}|\rho_{\vec{q}}{}^{s}|m^{s}\rangle|^{2}}{\omega-\omega_{n^{s}m^{s}}-i\epsilon} \tag{4.5}$$

$$P_{\vec{q}}{}^{1}(\omega; T) = \frac{1}{2\hbar}\sum_{m^{s}} p_{m^{s}}(T)\times$$

$$\times \sum_{n^{s}} \left\{ \frac{|\langle n^{s}|\rho_{\vec{q}}{}^{s}|m^{s}\rangle|^{2}}{\omega-\omega_{n^{s}m^{s}}-i\epsilon} + \frac{|\langle n^{s}|\rho_{-\vec{q}}{}^{s}|m^{s}\rangle|^{2}}{-\omega-\omega_{n^{s}m^{s}}+i\epsilon} \right\} \tag{4.6}$$

$$P_{\vec{q}}{}^{2}(\omega; T) = \frac{1}{2\hbar}\sum_{m^{s}} p_{m^{s}}(T)\times$$

$$\times \sum_{n^{s}} \left\{ \frac{|\langle n^{s}|\rho_{\vec{q}}{}^{s}|m^{s}\rangle|^{2}}{\omega-\omega_{n^{s}m^{s}}-i\epsilon} - \frac{|\langle n^{s}|\rho_{-\vec{q}}{}^{s}|m^{s}\rangle|^{2}}{-\omega-\omega_{n^{s}m^{s}}+i\epsilon} \right\}. \tag{4.7}$$

Les relations (3.7), (3.8), (3.9) peuvent s'écrire

$$\pi_{\vec{q}}(\omega; T) = \mathrm{T}^{\omega}(i/\hbar)\langle \rho_{-\vec{q}}{}^{s}(0)\rho_{\vec{q}}{}^{s}(t)\rangle_{T} u_{\epsilon}(t) \tag{4.8}$$

$$P_{\vec{q}}{}^{1}(\omega; T) = T^{\omega}(i/2\hbar)\langle [\rho_{-\vec{q}}{}^{s}(0)\rho_{\vec{q}}{}^{s}(t)]\rangle_{T} u_{\epsilon}(t) \tag{4.9}$$

$$P_{\vec{q}}{}^{2}(\omega; T) = T^{\omega}(i/2\hbar)\langle [\rho_{-\vec{q}}{}^{s}(0)\rho_{\vec{q}}{}^{s}(t)]_{+}\rangle_{T} u_{\epsilon}(t). \tag{4.10}$$

Ces résultats peuvent être mis sous une forme différente si on remarque que $\langle \rho_{-\vec{q}}{}^{s}(0)\rho_{\vec{q}}{}^{s}(t)\rangle_{T}$ est la transformée de Fourier de la fonction $NG(\vec{r}, t; T)$ où $G(\vec{r}, t; T)$ est la fonction de corrélation de paire de Van Hove[10] à la température T qui s'écrit

$$G(\vec{r}, t; T) = \frac{1}{N}\left\langle \int \rho^{s}(\vec{r}'-\vec{r}, 0)\rho^{s}(\vec{r}', t)\, d\vec{r}' \right\rangle_{T} \tag{4.11}$$

où les opérateurs $\rho^{s}(\vec{r}, t)$ sont définis par (4.1) si on considère $\vec{r}_{i}{}^{s}$ comme dépendant du temps. Les égalités (4.8), (4.9), (4.10) deviennent

$$\pi_{\vec{q}}(\omega; T) = T^{\vec{q},\omega}(i/\hbar)u_{\epsilon}(t)NG(\vec{r}, t; T) \tag{4.12}$$

$$P_{\vec{q}}{}^{1}(\omega; T) = T^{\vec{q},\omega}(i/\hbar)u_{\epsilon}(t)\ \mathrm{Im}\ NG(\vec{r}, t; T) \tag{4.13}$$

$$P_{\vec{q}}{}^{2}(\omega; T) = T^{\vec{q},\omega}(i/\hbar)u_{\epsilon}(t)\ \mathrm{Re}\ NG(\vec{r}, t; T) \tag{4.14}$$

où $T^{\vec{q},\omega}$ indique la transformée de Fourier de la fonction considérée, dans l'espace et dans le temps; les parties réelles et imaginaire pure de la fonction de corrélation sont caractérisées par les signes Im et Re.

L'hamiltonien effectif (2.24) prend la forme

* La limite $\epsilon \to 0$ doit être prise après passage à la limite $V \to \infty$.

simple

$$H_{\text{eff}} = H^{\sigma} + \mathscr{R} \sum_{\bar{q}} \frac{V^2(q)}{V^2} \rho_{\bar{q}}{}^{\sigma} \rho_{-\bar{q}}{}'^{\sigma} \quad (4.15)$$

avec

$$\langle n^{\sigma} | \rho_{-\bar{q}}{}'^{\sigma} | m^{\sigma} \rangle = \pi_{\bar{q}}(\omega_{m^{\sigma} n^{\sigma}}; T) \langle n^{\sigma} | \rho_{-\bar{q}}{}^{\sigma} | m^{\sigma} \rangle \quad (4.16)$$

ou sous la forme (2.29)

$$H_{\text{eff}} = H^{\sigma} + \tfrac{1}{2} \sum_{\bar{q}} \frac{V^2(q)}{V^2} \{ [\rho_{\bar{q}}{}^{\sigma}, \rho_{-\bar{q}}{}^{1\sigma}]_{+} + [\rho_{\bar{q}}{}^{\sigma}, \rho_{-\bar{q}}{}^{2\sigma}] \} \quad (4.17)$$

où $\rho_{-\bar{q}}{}^{1\sigma}$ et $\rho_{-\bar{q}}{}^{2\sigma}$ sont définis par (4.16) où l'on remplace $\pi_{\bar{q}}(\omega; T)$ respectivement par $P_{\bar{q}}{}^{1}(\omega; T)$ et $P_{\bar{q}}{}^{2}(\omega; T)$. Dans (4.17), le signe $\mathscr{R}$ est inutile, le terme entre accolades étant hermitien.

(b) *Fonctions diélectriques*

L'hamiltonien effectif (4.15) ou (4.17) généralise l'hamiltonien des porteurs minoritaires de PINES et NOZIÈRES[13,14]. La nature de cette généralisation apparaîtra clairement si nous considérons un système s composé des particules de même nature que celles du système σ en négligeant toutefois les interactions d'échange entre s et σ. On a alors $v(r) = V(r)$ et les hamiltoniens (4.15) ou (4.17) peuvent s'écrire

$$H_{\text{eff}} = H_0 + \mathscr{R} \sum_{\bar{q}} \frac{v(q)}{2V} (\rho_{\bar{q}} \rho_{-\bar{q},c} - n) \quad (4.18)$$

ou

$$H_{\text{eff}} = H_0 + \mathscr{R} \sum_{\bar{q}} \frac{v(q)}{2V} (\rho_{\bar{q}} \rho_{-\bar{q},a} - n) + \sum_{\bar{q}} \frac{v(q)}{4V} [\rho_{\bar{q}} \rho_{-\bar{q},b}]. \quad (4.19)$$

Dans ces hamiltoniens, l'indice σ a été sous-entendu, et n est le nombre de "porteurs minoritaires" considérés. On a

$$\rho_{-\bar{q},c} = \rho_{-\bar{q}} + \frac{2v(q)}{V} \rho_{-\bar{q}}{}' \quad (4.20)$$

$$\rho_{-\bar{q},a} = \rho_{-\bar{q}} + \frac{2v(q)}{V} \rho_{-\bar{q}}{}^{1} \quad (4.21)$$

$$\rho_{-\bar{q},b} = \frac{2v(q)}{V} \rho_{-\bar{q}}{}^{2}. \quad (4.22)$$

On peut alors calculer les éléments de matrice des opérateurs $\rho_{-\bar{q}, c}$, $\rho_{-\bar{q}, a}$, $\rho_{-\bar{q}, b}$, par des formules analogues à (4.16) en remplaçant successivement $\pi_{\bar{q}}(\omega; T)$ par

$$\Delta_{\bar{q}}(\omega; T) = 1 + \frac{2v(q)}{V} \pi_{\bar{q}}(\omega; T) \quad (4.23)$$

$$D_{\bar{q}}{}^{1}(\omega; T) = 1 + \frac{2v(q)}{V} P_{\bar{q}}{}^{1}(\omega; T) \quad (4.24)$$

$$D_{\bar{q}}{}^{2}(\omega; T) = \frac{2v(q)}{V} P_{\bar{q}}{}^{2}(\omega; T). \quad (4.25)$$

Ces fonctions peuvent s'écrire sous la forme

$$\Delta_{\bar{q}}(\omega; T) = T^{\bar{q},\omega} \left\{ \delta(\bar{r})\delta(t) + \frac{2i}{\hbar} \frac{N}{V} u_{\epsilon}(t) \times \times \int v(\bar{r} - \bar{r}') G(\bar{r}', t; T)\, d\bar{r}' \right\} \quad (4.26)$$

$$D_{\bar{q}}{}^{1}(\omega; T) = T^{\bar{q},\omega} \left\{ \delta(\bar{r})\delta(t) + \frac{2i}{\hbar} \frac{N}{V} u_{\epsilon}(t) \times \times \int v(\bar{r} - \bar{r}') \operatorname{Im} G(\bar{r}', t; T)\, d\bar{r}' \right\} \quad (4.27)$$

$$D_{\bar{q}}{}^{2}(\omega; T) = T^{\bar{q},\omega} \left\{ \frac{2i}{\hbar} \frac{N}{V} u_{\epsilon}(t) \int v(\bar{r} - \bar{r}') \operatorname{Re} G(\bar{r}', t; T)\, d\bar{r}' \right\}. \quad (4.28)$$

L'hamiltonien (4.18) a la même forme que celui de PINES et NOZIÈRES[13] mais est valable indépendemment de l'hypothèse du "random phase approximation" utilisée par ces auteurs. De plus, dans cette hypothèses, même à $T = 0$, l'hamiltonien (4.18) est différent; la fonction $\Delta_{\bar{q}}(\omega; T)$ contient en effet, outre le terme $1/\epsilon_{\bar{q}}(\omega)$ de PINES et NOZIÈRES, un terme dynamique $D_q{}^{2}(\omega; T)$ que nous avons déjà signalé auparavant,[4] et un terme imaginaire lié à l'absorption.

La fonction $D^{1}{}_{\bar{q}}(\omega; T)$ est identique à l'inverse de la constante diélectrique définie par PINES et NOZIÈRES[14] à $T = 0$ comme le montre l'équation (4.24) et (4.6); l'équation (4.27) l'identifie immédiatement à celle, équivalente, de FANO[12].

D'une manière générale, nous appelerons les fonctions (4.26), (4.27) et (4.28), des *fonctions dielectriques.*

Pour terminer ce paragraphe, donnons les relations générales auxquelles satisfont les fonctions diélectriques et qui sont des conséquences immédiates des relations générales établies en 3.

(i) *Relations de causalité*

Les égalités (2.16) et (3.17) donnent

$$\mathrm{Im}\Delta_{\bar{q}}(\omega;\,T)=\frac{1}{i\pi}\int_{-\infty}^{+\infty}\frac{d\omega'}{\omega-\omega'}\,\mathrm{Re}\{\Delta_{\bar{q}}(\omega';\,T)-1\} \tag{4.29}$$

$$\mathrm{Re}\{\Delta_{\bar{q}}(\omega;\,T)-1\}=\frac{1}{i\pi}\int_{-\infty}^{+\infty}\frac{d\omega'}{\omega-\omega'}\,\mathrm{Im}\Delta_{\bar{q}}(\omega',\,T) \tag{4.30}$$

et des relations analogues pour $D_{\bar{q}}^{1}(\omega;\,T)$ et $D_{\bar{q}}^{2}(\omega;\,T)$.

(ii) *Relations thermodynamiques*

$$\mathrm{Im}\,D_{\bar{q}}^{1}(\omega;\,T)=\mathrm{Im}\Delta_{\bar{q}}(\omega;\,T)\frac{1-\exp(-\hbar\omega/kT)}{2} \tag{4.31}$$

$$\mathrm{Im}\,D_{\bar{q}}^{2}(\omega;\,T)=\mathrm{Im}\Delta_{\bar{q}}(\omega;\,T)\frac{1+\exp(-\hbar\omega/kT)}{2} \tag{4.32}$$

$$\mathrm{Im}\,D_{\bar{q}}^{1}(\omega;\,T)=\mathrm{Im}\,D_{\bar{q}}^{2}(\omega;\,T)\,\mathrm{Th}\frac{\hbar\omega}{2kT} \tag{4.33}$$

Au zéro absolu, ces relations deviennent

(a) $\omega>0$

$$\mathrm{Im}\,D_{\bar{q}}^{1}(\omega;\,0)=\mathrm{Im}\,D_{\bar{q}}^{2}(\omega;\,0)=\tfrac{1}{2}\,\mathrm{Im}\Delta_{\bar{q}}(\omega;\,0) \tag{4.34}$$

(b) $\omega<0$

$$\mathrm{Im}\,D_{\bar{q}}^{1}(\omega;\,0)=-\mathrm{Im}\,D_{\bar{q}}^{2}(\omega;\,0)\;;\;\mathrm{Im}\Delta_{\bar{q}}(\omega;\,0)=0 \tag{4.35}$$

(iii) *Relations de symétrie*

$$D_{-\bar{q}}^{1*}(-\omega;\,T)=D_{\bar{q}}^{1}(\omega;\,T) \tag{4.36}$$

$$D_{-\bar{q}}^{2*}(-\omega;\,T)=-D_{\bar{q}}^{2}(\omega;\,T) \tag{4.37}$$

5. QUELQUES APPLICATIONS AUX INTERACTIONS COULOMBIENNES

(a) *Particule chargée traversant un gaz d'électrons*

Nous allons traiter les problèmes de self-énergie et de dissipation liés au passage d'une particule chargée dans un gaz d'électrons et nous comparerons nos résultats à ceux obtenus dans la limite classique par LINDHARD[15].

Utilisant les notations définies en 4,

$$v(q)=\frac{4\pi e^2}{q^2}\quad;\quad V(q)=\frac{4\pi ze^2}{q^2} \tag{5.1}$$

ze étant la charge de la particule incidente.

La formule générale (3.37) devient ici, si $\bar{k}$ désigne le vecteur d'onde de la particule incidente et si on introduit la fonction diélectrique $\Delta_{\bar{q}}(\omega;\,T)$ qui ne dépend maintenant que de la grandeur du vecteur $\bar{q}$,

$$\epsilon_k=\frac{z^2e^2}{4\pi^2}\int\frac{1}{q^2}\{\Delta_q(\omega_{\bar{k},\bar{k}-\bar{q}};\,T)-1\}\,d\bar{q} \tag{5.2}$$

dans la limite du spectre continu. Dans cette formule, $\omega_{\bar{k},\bar{k}-\bar{q}}=\bar{v}_{\bar{k}}\cdot\bar{q}-\omega_q$ où $\omega_q=\hbar q^2/2m$ et $\bar{v}_{\bar{k}}=\hbar\bar{k}/m$ est la vitesse de la particule incidente; l'élément de volume $d\bar{q}$ peut se mettre sous la forme

$$d\bar{q}=dS\,d\omega\frac{1}{|\mathrm{grad}_{\bar{q}}\omega|}=\frac{2\pi q}{v_k}\,dq\,d\omega \tag{5.3}$$

dS étant l'élément d'aire de la surface $\omega(\bar{q})=\omega=$ constante. Le domaine d'intégration de (5.2) est représenté à la Fig. 2; les courbes $\omega_{\max}(q)$ et $\omega_{\min}(q)$ sont des paraboles d'équation

$$\omega_{\max}(q)=v_kq-\omega_q\quad;\quad\omega_{\min}(q)=-v_kq-\omega_q \tag{5.4}$$

et la courbe $\omega_{\max}$ passe par un maximum pour $\omega=\omega_k$; on voit que si ω_k tend vers l'infini, le domaine tend vers le domaine limité par les deux droites $\omega=v_kq$, $\omega=-v_kq$, symétriques par rapport à l'axe Oq. En intégrant par rapport à ω en premier lieu, on obtient

$$\epsilon_k=\frac{z^2e^2}{2\pi v_k}\int_0^{\infty}\frac{1}{q}\,dq\int_{-v_kq-\omega_q}^{v_kq-\omega_q}\{\Delta_q(\omega;\,T)-1\}\,d\omega \tag{5.5}$$

Il résulte des relations (4.36) et (4.37) que si la particule incidente a une énergie suffisante pour que le domaine d'intégration de la Fig. 2 puisse être remplacé par le domaine symétrique mentionné plus haut, on peut remplacer Re $\Delta_q(\omega;\,T)$ dans (5.5) par Re $D_q^1(\omega;\,T)$ et Im $\Delta_q(\omega;\,T)$ par

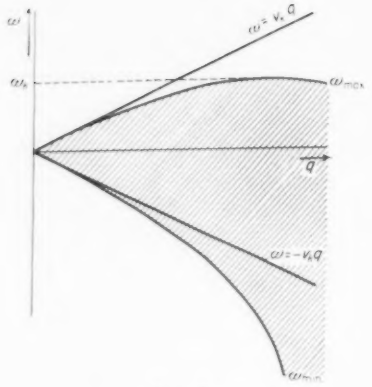

FIG. 2.

Im $D_q^2(\omega; T)$. L'expression résultante a toutefois le désavantage de ne pas faire apparaître clairement le lien causal entre la self-énergie et la largeur de l'état considéré qui s'exprime dans les relations (4.29) et (4.30); elle permet cependant de définir une expression correspondant à (5.5) dans le cas classique à l'aide de la fonction diélectrique classique si la contribution à l'intégrale des fréquences ω telles que $\omega < kT/\hbar$ est négligeable (ce qui est toujours le cas si $T = 0$). Dans ce cas en effet, la relation (4.33) permet de remplacer dans cette intégrale Im $D_q^2(\omega; T)$ par Im $D_q^1(\omega; T)$ sgn(ω), où sgn(ω) est la signature de ω qui vaut 1 pour $\omega > 0$ et -1 pour $\omega < 0$; définissant alors

$$D_{\bar{q},c}^1(\omega; T) = \mathrm{Re}\, D_{\bar{q}}^1(\omega; T) + \mathrm{Im}\, D_{\bar{q}}^1(\omega; T)\,\mathrm{sgn}(\omega) \tag{5.6}$$

l'expression (5.5) s'écrit dans ce cas, à l'aide de (5.6), sous une forme identique à la formule classique (4.26) de LINDHARD[15].*

De l'équation (3.38) on déduit par un calcul identique au précédent l'énergie perdue par unité de temps par la particule incidente

$$i\frac{dW_k}{dt} = \frac{z^2e^2}{\pi v_k}\int_0^\infty \frac{1}{q}\,dq \int_{-v_kq-\omega_q}^{v_kq-\omega_q} \mathrm{Im}\Delta_q(\omega; T)\,d\omega \tag{5.7}$$

et on peut discuter ce résultat de la même manière que l'équation (5.5); cette fois, si l'énergie de la particule incidente est grande, on peut directement remplacer Im $\Delta_q(\omega; T)$ par Im $D_q^1(\omega; T)$ à toute température.

(b) *Fonctions diélectriques dans les solides parfaits à $T = 0$*

L'évaluation de la fonction $D_{\bar{q}}^1(\omega; 0)$ dans les solides parfaits est très simple dans l'hypothèse R.P.A. ("random phase approximation") de PINES et NOZIÈRES[14]; l'équation (29) de ces auteurs nous permet d'écrire, tenant compte de l'identité, signalée en 4, entre $D_{\bar{q}}^1(\omega; 0)$ et leur fonction $1/\epsilon_{\bar{q}}(\omega)$,

$$D_{\bar{q}}^1(\omega; 0) = \frac{1}{F_{\bar{q}}(\omega)} \tag{5.8}$$

et

$$F_{\bar{q}}(\omega) = 1 - \sum_s \frac{4\pi e^2}{Vq^2\hbar}|\sigma_{\bar{q},s}|^2 \times \times \left\{\frac{1}{\omega - \omega_{\bar{q},s} - i\epsilon} + \frac{1}{-\omega - \omega_{\bar{q},s} + i\epsilon}\right\} \tag{5.9}$$

où la somme est étendue à tous les états non perturbés par les interactions coulombiennes, symbolisés par l'indice s, qui diffèrent de l'état de base par l'excitation d'un seul électron; les $\sigma_{\bar{q},s}$ sont les éléments de matrice de l'opérateur $\rho_{\bar{q}}$ entre l'état s et l'état de base, et $\hbar\omega_{\bar{q},s}$ la différence d'énergie non perturbée entre l'état s et l'état de base.

Tenant compte de (4.35), (4.34), (4.30), on peut écrire, la limite $\epsilon' \to 0$ devant être prise après intégration,

$$\Delta_{\bar{q}}(\omega; 0) = 1 + \frac{2}{i\pi}\int_0^\infty \frac{d\omega'}{\omega - \omega' - i\epsilon'}\,\mathrm{Im}\,\frac{1}{F_{\bar{q}}(\omega')} \tag{5.10}$$

et la fonction Im $1/F_{\bar{q}}(\omega')$ est définie pour une valeur aussi petite que l'on veut de ϵ, mais non nulle. Considérons la fonction de variable complexe $1/F_{\bar{q}}^c(\omega)$ obtenue par prolongement de la fonction (5.8) dans le plan complexe ω; cette fonction est analytique partout sauf sur l'axe réel où elle admet des lignes de discontinuité correspondant au spectre de bande des états à un électron excité et éventuellement des poles s'il y a dans

* *Note ajoutée à la correction.* Par l'utilisation de propagateurs, R. A. FERRELL et J. J. QUINN, *Phys. Rev.* **112**, 812 (1958), obtiennent un résultat qui à $T = 0$ est équivalent à (5,2) (quoique formellement différent) si la particule incidente est discernable du gaz d'électrons.

l'approximation considérée, des oscillations stables de plasma; à l'infini, elle tend vers 1. L'intégrale dans (5.10) peut alors être évaluée dans le plan complexe le long du contour C dessiné en trait plein sur la Fig. 3 et

$$\Delta_{\bar{q}}(\omega;0) = 1+\frac{i}{\pi}\int_C \frac{d\omega'}{\omega-\omega'-i\epsilon'}\frac{1}{F_{\bar{q}}^{c}(\omega')} \tag{5.11}$$

Prolongeons le contour C par le contour en traits

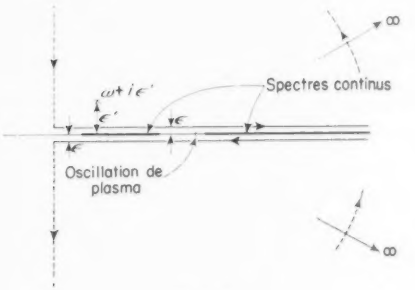

FIG. 3.

pointillés; le calcul de (5.11) se réduit alors au calcul du résidu au pole $\omega' = \omega+i\epsilon'$, à celui de la contribution à l'infini qui vaut -1 et le long de l'axe imaginaire. On a

$$\Delta_{\bar{q}}(\omega;0) = [2/F_{\bar{q}}(\omega)]u(\omega)+A_{\bar{q}}(\omega) \tag{5.12}$$

où $u(\omega)$ vaut 1 pour $\omega > 0$ et 0 pour $\omega < 0$; $A_{\bar{q}}(\omega)$ est réel et vaut

$$A_{\bar{q}}(\omega) = -\frac{2}{\pi}\int_0^\infty \frac{1}{F_{\bar{q}}^{c}(i\zeta)}\frac{\omega}{\omega^2+\zeta^2}d\zeta. \tag{5.13}$$

Remarquons que l'on peut calculer, à l'approximation envisagée, les fonctions diélectriques directement à partir des formules de définition (4.23) et (4.5); en effet dans la R.P.A., les éléments de matrice intervenant dans ces formules peuvent être calculées exactement en généralisant aux solides parfaits les méthodes employées par SAWADA[16] et BROUT[17] dans les gaz d'électrons libres. Cette méthode, que nous ne développerons pas ici, donne également les résultats (5.8) et (5.12) mais a l'avantage de montrer clairement comment les difficultés qui pourraient apparaître par suite de la présence d'états liés dans la limite $V \to \infty$ (oscillations de plasma) disparaissent en fait si on évalue correctement les fonctions d'onde du spectre continu, le résultat étant formellement indépendant des oscillations de plasma; ceci, loin d'être paradoxal, est simplement dû au fait que les propriétés de ces états, dont l'existence est impliquée par des conditions d'unitarité, sont implicitement contenues dans le spectre continu. Notons enfin que les fonctions diélectriques n'ont de sens que si $\bar{q}$ est petit devant les vecteurs de translation primitive du réseau réciproque car ce n'est que dans ce cas que l'on peut considérer que le solide est invariant par rapport aux translations; cette condition est d'ailleurs en général nécessaire pour que la R.P.A. soit approximativement valable.

(c) *Etats excitons dans les cristaux polarisables*

Dans les isolants et les semiconducteurs, les termes négligés dans la R.P.A. sont reponsables d'effets qualitatifs importants par suite de l'existance d'une bande interdite et donnent naissance à des états liés du type exciton. Nous nous limiterons ici au cas des critaux très polarisables où l'exciton peut être traité dans le modèle continu de WANNIER[18] et nous déterminerons l'effet polarisant des électrons de valence en négligeant les interactions d'échange de la paire électron–trou avec ceux-ci; cette approximation est valable pour les états excitons triplets.[19]

L'hamiltonien de la paire électron–trou, compte tenu de l'effet polarisant des électrons de valence, est donné par (4.18) où $v(q) = -4\pi e^2/q^2$, $n = 2$ et H_0 est l'hamiltonien de la paire électron–trou en l'absence d'interactions coulombiennes; l'utilisations de (4.18) implique l'invariance de translation du système polarisant, ce qui est une bonne approximation dans les cristaux polarisables où seules les composantes de $\rho_{\bar{q}}$ telles que $\bar{q} \ll \overline{K}$, $\overline{K}$ étant une translation du réseau réciproque, jouent un rôle important dans le terme d'interaction; l'électron et le trou sont en effet en moyenne séparés par de nombreuses distances interatomiques. Si $kT \ll E_i$ où E_i est la largeur de la bande interdite, la fonction $\Delta_{\bar{q}}(\omega; T)$ qui intervient dans $\rho_{\bar{q},\,c}$ peut être prise à $T = 0$ et est donnée dans la R.P.A. par (5.12). Comme les interactions importantes dues au terme coulombien dans (4.18) proviennent de vecteurs $\bar{q}$ petits, nous supposerons qu'elles ne provoquent de transitions qu'entre

états dont la différence d'énergie est faible devant E_i; on peut alors remplacer $\Delta_{\bar{q}}(\omega; 0)$ par $\Delta_{\bar{q}}(0; 0) = D_{\bar{q}}^{-1}(0; 0)$ que nous écrirons plus simplement $D_{\bar{q}} = 1/F_{\bar{q}}$ où la fonction $F_{\bar{q}}$ peut être définie par l'équation (5.9) pour $\omega = 0$; remarquons d'ailleurs que si cette approximation n'était pas valable nous obtiendrions un terme imaginaire dans $\Delta_{\bar{q}}(\omega; 0)$, ce qui donnerait un élargissement des états excitons et éventuellement leur disparition.

L'hamiltonien (4.18) s'écrit alors en seconde quantification

$$H = H_0 - \sum_{\bar{q}} \frac{2\pi e^2}{V q^2} \frac{1}{F_{\bar{q}}} (r_{\bar{q}}^+ r_{\bar{q}} - 2F_{\bar{q}}) \tag{5.14}$$

avec

$$H_0 = \sum_{\bar{k}, m_c} E_{\bar{k}, m_c} a_{\bar{k}, m_c}^+ a_{\bar{k}, m_c} + \sum_{\bar{k}, m_v} E_{\bar{k}, m_v} b_{\bar{k}, m_v}^+ b_{\bar{k}, m_v}. \tag{5.15}$$

Dans (5.15), $a_{\bar{k}, m_c}^+$ est l'opérateur de création de l'électron de vecteur d'onde $\bar{k}$ dans la $m_c^{\text{ième}}$ bande de conduction du cristal non perturbé par les interactions coulombiennes et $b_{\bar{k}, m_v}^+$ l'opérateur de création du trou de vecteur d'onde $\bar{k}$ (ou l'opérateur de destruction de l'électron de vecteur d'onde $-\bar{k}$) de la $m_v^{\text{ième}}$ bande de valence; $E_{\bar{k}, m_c}$ est l'énergie de l'électron créé par $a_{\bar{k}, m_c}^+$ et $E_{\bar{k}, m_v}$ celle du trou créé par $b_{\bar{k}, m_v}^+$ (c'est-à-dire l'énergie de l'électron détruit, changée de signe). L'opérateur $r_{\bar{q}}^+$ dans (4.14) est l'opérateur $\rho_{\bar{q}}$ en seconde quantification et provoque des transitions à l'intérieur des bandes de conduction et de valence; les éléments de matrice de $\rho_{\bar{q}}$ définissant $r_{\bar{q}}^+$ sont pris entre états propres de H_0 dans l'espace de configuration, la fonction d'onde du trou étant la fonction complexe conjugée de celle de l'électron manquant.

Considérons le cas où le cristal présente une bande de conduction et une bande de valence qui peuvent être décrites dans l'approximation des masses effectives que nous supposerons isotropes; soient m_c et m_v les masses effectives dans ces bandes et posons

$$\mu = \frac{m_c m_v}{m_c + m_v}. \tag{5.16}$$

Si $|\psi_0\rangle$ est le vecteur propre de H_0 correspondant à l'état dans lequel aucun électron du cristal n'est excité, on peut représenter par $d^+(k)|\psi_0\rangle$ un état de H_0 dans lequel un électron de vecteur d'onde k est passé de la bande de valence dans la bande de conduction en conservant le même vecteur d'onde; on a alors

$$d^+(\bar{k}) = a_{\bar{k}}^+ b_{\bar{k}}^+ \tag{5.17}$$

si l'on omet les indices m_c et m_v. L'hamiltonien (5.14) permet d'écrire

$$H\, d^+(\bar{k})|\psi_0\rangle = \left(E_i + \frac{\hbar^2 k^2}{2\mu}\right) d^+(\bar{k})|\psi_0\rangle - \tag{5.18}$$

$$- \sum_{\bar{q}} \frac{2\pi e^2}{Vq^2} \frac{1}{F_{\bar{q}}} (r_{\bar{q}}^+ r_{\bar{q}} - 2F_{\bar{q}})\, d^+(\bar{k})|\psi_0\rangle$$

avec

$$r_{\bar{q}}^+ = \sum_{\bar{k}} \{a_{\bar{k}+\bar{q}}^+ a_{\bar{k}} + b_{\bar{k}+\bar{q}}^+ b_{\bar{k}}\} \tag{5.19}$$

où nous avons assimilé à l'unité les éléments de matrice de $\rho_{\bar{q}}$, ce qui est valable si $\bar{q} \ll \bar{K}$. De (5.19) et (5.17) on déduit

$$r_{\bar{q}}^+ r_{\bar{q}}\, d^+(\bar{k})|\psi_0\rangle = \{2\, d^+(\bar{k}) + d^+(\bar{k}-\bar{q}) + d^+(\bar{k}-\bar{q})\}|\psi_0\rangle \tag{5.20}$$

et par conséquent, si on porte ce résultat dans (5.18) en omettant le terme constant E_i et en tenant compte de

$$d^+(\bar{k}+\bar{q}) = \exp(\bar{q}.\mathrm{grad}_{\bar{k}})\, d^+(\bar{k}) \tag{5.21}$$

on obtient un hamiltonien $H(\bar{k})$ valable pour les paires électron–trou de vecteur d'onde total nul,

$$H(\bar{k}) = \frac{\hbar^2 k^2}{2\mu} - \sum_{\bar{q}} \frac{4\pi e^2}{Vq^2} \frac{1}{F_{\bar{q}}} \exp(\bar{q}.\mathrm{grad}_{\bar{k}}) - \tag{5.22}$$

$$- \sum_{\bar{q}} \frac{4\pi e^2}{Vq^2} \left(\frac{1}{F_{\bar{q}}} - 1\right)$$

Le dernier terme de (5.22) est une constante que nous pouvons omettre; elle est de la nature d'une self-énergie et peut être comparée à (5.2). Dans une représentation où la variable $\bar{\beta}$ conjuguée de $\hbar\bar{k}$ est diagonale, (5.22) s'écrit alors

$$H(\bar{\beta}) = -\frac{\hbar^2}{2\mu} \Delta_{\bar{\beta}} - \sum_{\bar{q}} \frac{4\pi e^2}{Vq^2} \frac{1}{F_{\bar{q}}} \exp(-i\bar{q}.\bar{\beta}). \tag{5.23}$$

VOL.
11
1959

Cet hamiltonien décrit le mouvement autour de leur centre de masse de deux particules interagissant par un potentiel $V(\bar{\beta})$ tel que

$$V(\bar{\beta}) = -\sum_{\bar{q}} \frac{4\pi e^2}{Vq^2} \frac{1}{F_{\bar{q}}} \exp(-i\bar{q}.\bar{\beta} \quad (5.24)$$

c'est-à-dire du potentiel coulombien e^2/β dont les composantes de Fourier sont divisées par $F_{\bar{q}}$; pour β grand ce potentiel tend vers $e^2/\epsilon\beta$ où $\epsilon = F_0$ si $F_{\bar{q}}$ est isotrope pour $\bar{q} \to 0$, ϵ étant la constante diélectrique statique des électrons de valence; pour β petit, il tend vers e^2/β ($F_{\bar{q}}$ tend vers 1 si q tend vers l'infini). Ceci correspond à une représentation très physique du phénomène* et nous conduit à concevoir les spectres d'excitons dans les cristaux polarisables comme des spectres hydrogénoïdes perturbés, la perturbation consistant essentiellement en une levée de la dégénérescence n—1 telle que les états de grand moment angulaire soient moins liés et telle que les états les plus liés (dont l'orbite est donc plus petite) le soient relativement plus que ceux du modèle hydrogénoïde. Toutes ces conclusions sont bien en accord avec les résultats expérimentaux de GROSS[20] et d'autres.[21]

Remerciements—Je tiens à remercier vivement Monsieur le Professeur GÉHÉNIAU qui m'a beaucoup aidé et encouragé dans la conduite de ce travail. Je remercie Messieurs les Professeurs AIGRAIN, MONTROLL, PINES et le Docteur PHILIPPOT pour d'intéressantes discussions.

*Remarquons toutefois que le potentiel (5.24) n'est pas nécessairement valable si $\bar{q} \gtrsim \overline{K}$.

BIBLIOGRAPHIE

1. CALLEN H. B. et WELTON T. A., *Phys. Rev.* **83,** 34 (1951).
2. CALLEN H. B., BARASH M. L. et JACKSON J. L., *Phys. Rev.* **88,** 1382 (1952).
3. KUBO R., *J. Phys. Soc. Japan* **12,** 570 (1957).
4. ENGLERT F., *Nuovo Cimento* **10,** 560 (1958).
5. WANGSNESS R. K. et BLOCH F., *Phys. Rev.* **89,** 728 (1953)
6. BLOCH F., *Phys. Rev.* **102,** 104 (1956).
7. BLOCH F., *Phys. Rev.* **105,** 1206 (1957).
8. REDFIELD A. G., *I.B.M. J. Res. and Dev.* **1,** 1 (1957).
9. FANO U., *Rev. Mod. Phys.* **29,** 74 (1957).
10. VAN HOVE L., *Phys. Rev.* **95,** 249 (1954).
11. VAN HOVE L., *Physica, s'Grav.* **24,** 409 (1958).
12. FANO U., *Phys. Rev.* **103,** 1202 (1956).
13. NOZIÈRES P. et PINES D., *Phys. Rev.* **109,** 762 (1958).
14. NOZIÈRES P. et PINES D., *Nuovo Cimento* **9,** 470 (1958).
15. LINDHARD J., *K. Danske Vidensk. Selsk., Mat. Fys. Medd.* **28,** No. 8 (1954).
16. SAWADA K., *Phys. Rev.* **106,** 372 (1957).
17. BROUT R., *Phys. Rev.* **108,** 515 (1957).
18. WANNIER G. H., *Phys. Rev.* **52,** 191 (1937).
19. TAKEUTI Y., *Progr. Theor. Phys.* **18,** 421 (1957).
20. GROSS E. F., *Nuovo Cimento,* Suppl. au Vol. **3,** 672 (1956).
21. NIKITINE S., *J. Chim. Physique* **55,** 620 (1958).

J. Phys. Chem. Solids Pergamon Press 1959. Vol. 11. pp. 92–96. Printed in Great Britain.

THE EFFECT OF PRESSURE ON THE ABSORPTION EDGE IN HEAVY-METAL HALIDES*

J. C. ZAHNER and H. G. DRICKAMER

Department of Chemistry and Chemical Engineering, University of Illinois, Urbana, Illinois

(*Received* 5 *February* 1959; *revised* 5 *March* 1959)

Abstract—The effect of pressure has been measured on the absorption edge of ten heavy-metal halides. In general, a large decrease in the gap is obtained with increasing pressure. The differences between the data on thallous halides and previous data on AgCl and AgBr are explained tentatively in terms of differences in band structure postulated by SEITZ and MARTIENSSEN. Compounds which crystallize in the same lattice show closely similar shifts with pressure (or density) regardless of the halide involved. HgI_2 returns to the high-temperature form above 13,000 atm at room temperature, as has been previously noted by BRIDGMAN.

VOL
11
195

THE effect of pressure has been measured on the absorption edges of ten heavy-metal halides. The sources of the chemicals used, the values of ν_0 (the point from which the edge was measured at zero pressure), and the pressure ranges are summarized in Table 1. The high-pressure optical techniques have been described elsewhere.[1–3] The results are discussed under four headings below.

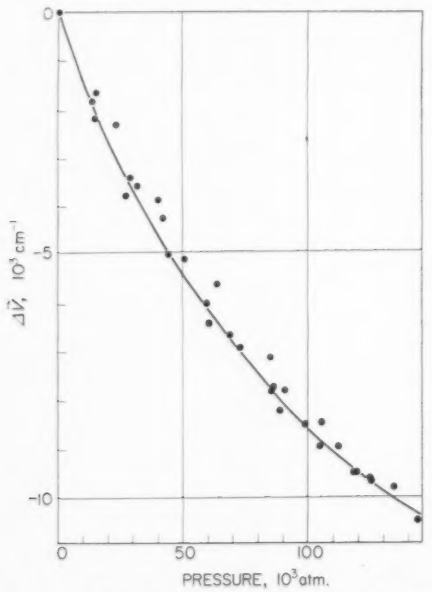

FIG. 1. TlCl: shift of absorption edge with pressure.

Thallium halides

TlCl and TlBr crystallize in the cubic CsCl structure at 1 atm. TlI has a rather complex symmetry but transforms to the CsCl structure at 5000 atm. The shifts with pressure are shown in Figs. 1–3. The gap decreases rapidly for all three halides. In

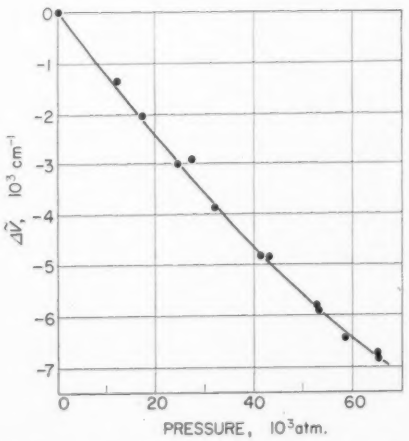

FIG. 2. TlBr: shift of absorption edge with pressure.

* This work was supported in part by U.S. Atomic Energy Commission Contract AT(11–1)–67, Chemical Engineering Project 5.

Table 1. *Sources of chemicals and values of* ν_0, α *and pressure ranges*

Compound	Source and quality	ν_0 (cm^{-1})	α (cm^{-1})	Pressure range (10^3 atm)
TlCl	Fisher Scientific Co. (reagent)	27,300	150	140
TlBr	A. D. Mackay (C.p.)	23,950	170	65
TlI	Fisher Scientific (purified)	21,840	200	125
$PbCl_2$	Fisher Scientific (reagent)	32,300	200	160
$PbBr_2$	Fisher Scientific (purified)	26,400	130	155
PbI_2	City Chemical Corp., N.Y. (C.p.)	19,010	200	30
$HgCl_2$	Matheson, Coleman, and Bell (reagent)	36,440	200	170
$HgBr_2$	Matheson, Coleman, and Bell (reagent)	29,350	220	210
HgI_2 (powder)	Matheson, Coleman, and Bell (C.p.)	18,450	340	45
HgI_2 (crystal)	R. H. Bube, RCA	17,900	180	
$BiBr_3$	Fisher Scientific (C.p.)	21,500	110	75

particular, at 120,000 atm the gap for TlI has decreased by 80 per cent. Crude conductivity measurements* indicate an increase of conductivity by a factor of 10^7 from 5000 to 150,000 atm for this compound.

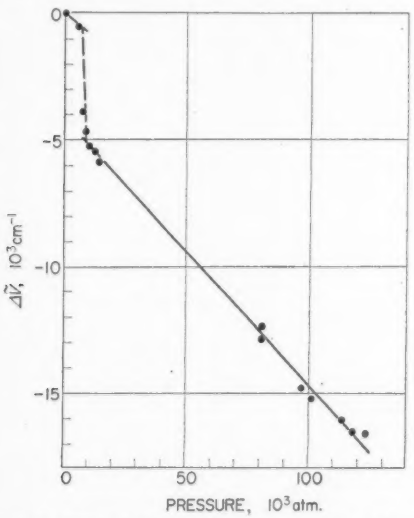

FIG. 3. TlI: shift of absorption edge with pressure.

Fig. 4 plots the shift of the edge versus relative volume, using BRIDGMAN'S[4] density data. The shifts are remarkably similar, particularly for the chloride and bromide, which probably indicates that the conduction-band wave functions can be constructed largely from Tl^+ ion wave functions.

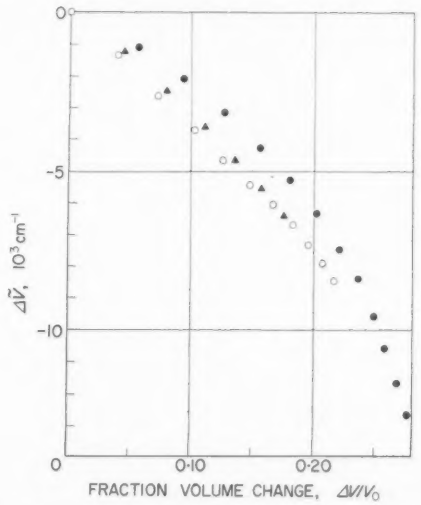

FIG. 4. Shifts of the TlX's (CsCl structures). ○ TlCl, ▲ TlBr, ● TlI.

These large shifts in the edge are to be contrasted with the very small shifts (about 4–5 per cent of the TlX shifts) shown by AgCl and AgBr in both the

* The measurements were made in a high-temperature high-pressure optical apparatus to be described elsewhere. From the shape of the curve on a log conductivity versus pressure graph, it was assumed that the contact resistance did not change appreciably above 5000 atm.

NaCl and CsCl structures.[3] We believe a plausible explanation can be offered for this difference. SEITZ[5] has postulated a band structure as shown in Fig. 5a for AgCl, where the tail corresponds to the indirect band-to-band transition. There is

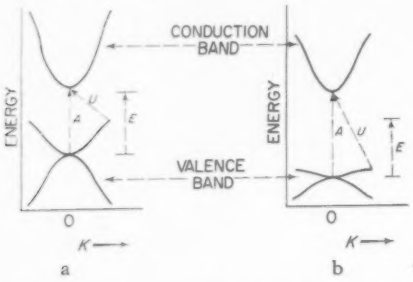

FIG. 5. Schematic types of bands: (a) AgCl type; (b) TlCl type.

A Direct transitions
U Indirect transitions
E Exciton transitions

evidence from mobility measurements[6] that AgCl has a large deformation potential, corresponding to a rapid shift of the bottom of the conduction band with lattice dilation. The small change in the gap with pressure would then indicate that the "wings" of the valence band also deform rapidly with pressure. A considerable change in the shape of the edge (of the silver halides) with combined temperature and pressure[7] also is consistent with this hypothesis.* On the other hand, there are indications[8] that the gap as measured in the tail of the thallous halides is a direct transition to the exciton state (or the conduction band) (see Fig. 5b).

In these latter compounds then the shift of the absorption edge with pressure is probably directly related to the deformation of the bottom of the conduction band, and is large. The similarities in the density-gap plot (Fig. 4) discussed above are also consistent with this hypothesis.

One would further postulate that the anomalous behavior of AgI can be explained by the above consideration. AgI, in contrast to AgCl and AgBr, showed a very large shift with pressure in the NaCl phase, and a blue shift at the 115,000-atm transition, presumably to the CsCl structure. The shift in the CsCl structure was very similar to the shifts for AgCl and AgBr in that phase. The shift of the AgI edge with density is of the same order as the shifts for the thallous halides, so that quite possibly one is measuring the direct transition in this phase of AgI. Above the transition, one would speculate that the indirect transition is being measured as in AgCl and AgBr.

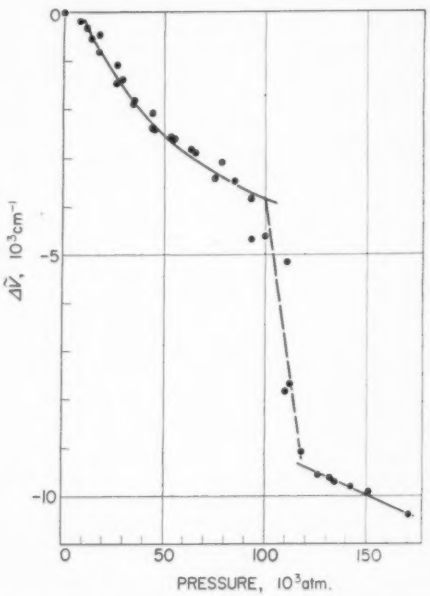

FIG. 6. $HgCl_2$: shift of absorption edge with pressure.

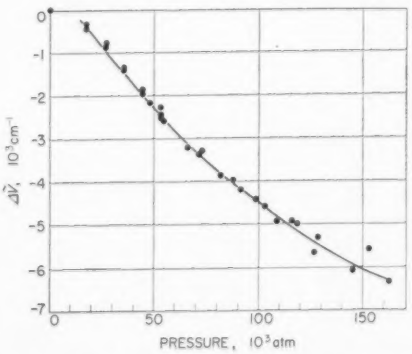

FIG. 7. $PbCl_2$: shift of absorption edge with pressure.

* An apparatus has been developed which permits optical measurements up to 200,000 atm and 400°C. Preliminary results have been obtained on the silver halides over this range.

VOL 11 195

Compounds of V_h^{16} symmetry

$HgCl_2$, $PbCl_2$ and $PbBr_2$ all crystallize in a lattice having V_h^{16} symmetry. The shifts with pressure are shown in Figs. 6–8. These crystals are difficult to fuse with pressure, so that the shifts below

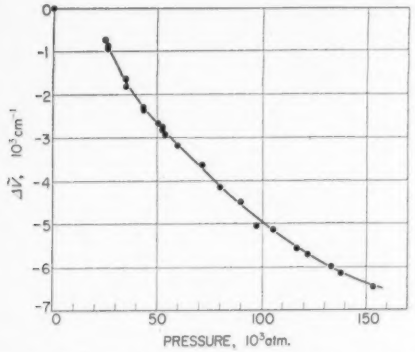

FIG. 8. $PbBr_2$: shift of absorption edge with pressure.

25,000 atm have little significance. $HgCl_2$ has a phase transition at 90,000 atm accompanied by a very large shift of the edge. No trace was found of a transition at 20,000 atm discovered by BRIDGMAN[9], probably because of the difficulty in fusing the material. Fig. 9 shows the shifts for all three

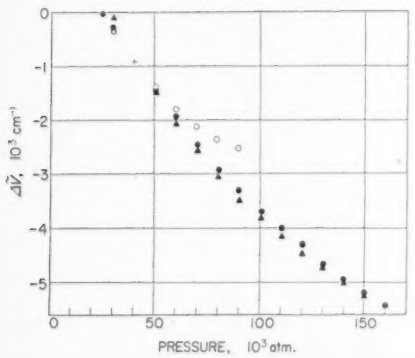

FIG. 9. Shifts of the V_h^{16} structures. ● $PbCl_2$, ▲ $PbBr_2$, ○ $HgCl_2$.

compounds with pressure plotted from 25,000 atm as zero. The shifts are remarkably similar, particularly for $PbCl_2$ and $PbBr_2$. Probably the compressibilities do not vary much between these two compounds, so that one can postulate that one is measuring the deformation of the conduction band which can be constructed from Pb^{++} wave functions.

HgI_2

The behavior of HgI_2 is rather different from that of the other halides. Data were obtained for this compound both on the powder and on a single crystal furnished by R. H. BUBE. The results corresponded exactly, as seen in Fig. 10. At room

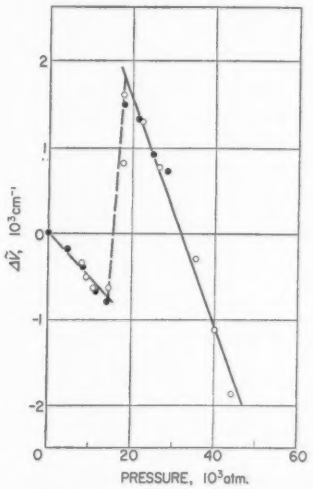

FIG. 10. HgI_2: shift of absorption edge with pressure. ● Crystal, ○ Pellet.

temperature and 1 atm it crystallizes in the D_{4h}^{15} lattice. At about 13,000 atm at room temperature a phase transition occurs. BRIDGMAN[10] has shown that the high-pressure, room-temperature phase is the same phase (C_{2v}^{12}) as that obtained above

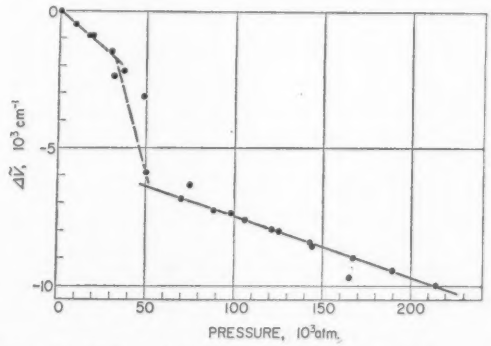

FIG. 11. $HgBr_2$: shift of absorption edge with pressure.

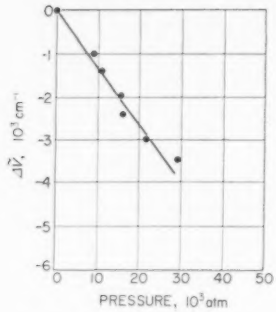

FIG. 12. PbI_2: shift of absorption edge with pressure.

127°C at 1 atm. Indeed, one obtains a large blue shift in the edge, as would be expected for a transformation from "red" to "yellow" HgI_2. BUBE[11]

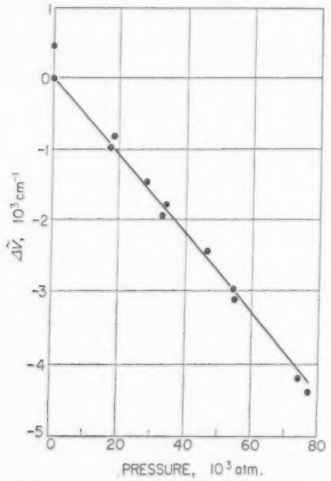

FIG. 13. $BiBr_3$: shift of absorption edge with pressure.

measured the temperature coefficient of the edge in both places. It is interesting to note that the relative shifts per °C of the two phases are almost exactly the same as the relative shifts per atmosphere.

Miscellaneous systems

Data were also obtained for PbI_2, $HgBr_2$ and $BiBr_3$ (Figs. 11–13). In all cases the edge shifted red with pressure. A phase transition was noted in $HgBr_2$ at about the same pressure as that reported by BRIDGMAN[9].

Acknowledgements—The authors wish to thank F. SEITZ and F. D. BROWN for most helpful discussions. They would also like to thank R. H. BUBE, of the RCA Laboratories, for the single crystal of HgI_2.

REFERENCES

1. FITCH R. A., SLYKHOUSE T. E. and DRICKAMER H. G., *J. Opt. Soc. Amer.* **47,** 1015 (1957).
2. SLYKHOUSE T. E. and DRICKAMER H. G., *J. Phys. Chem. Solids* **7,** 207 (1958).
3. SLYKHOUSE T. E. and DRICKAMER H. G., *J. Phys. Chem. Solids* **7,** 210 (1958).
4. BRIDGMAN P. W., *Proc. Amer. Acad. Arts Sci.* **76,** 1 (1945).
5. SEITZ F., *Rev. Mod. Phys.* **23,** 328 (1951).
6. BROWN F. C., *Paper K-1, Amer. Phys. Soc. Meeting,* Chicago (Nov., 1958).
7. BALCHAN A. S. Private Communication.
8. MARTIENSSEN W., *J. Phys. Chem. Solids* **8,** 294 (1959).
9. BRIDGMAN P. W., *Proc. Amer. Acad. Arts Sci.* **72,** 45 (1937).
10. BRIDGMAN P. W., *Proc. Amer. Acad. Arts Sci.* **51,** 55 (1915).
11. BUBE R. H., *Phys. Rev.* **106,** 703 (1957).

VOL
11
195

J. Phys. Chem. Solids Pergamon Press 1959. Vol. 11. pp. 97–104. Printed in Great Britain.

INTERNAL CONSISTENCY OF THE HEISENBERG–DIRAC MODEL FOR ANTIFERROMAGNETISM*

J. S. SMART†

Chemistry Department, Brookhaven National Laboratory, Upton, L.I., N.Y.

(*Received* 29 *January* 1959)

Abstract—An attempt is made to investigate the internal consistency of the Heisenberg–Dirac model for antiferromagnets with nearest-neighbor interactions only. The Bethe–Peierls–Weiss approximation and the results of BROWN and LUTTINGER are used to obtain relations between the Néel temperature and the exchange integral, J, and between the susceptibility at the Néel temperature and J. By combining these relations with experimental values of T_N and $\chi(T_N)$ for a given compound, two distinct values of J can be deduced. These values should agree if the theory is internally consistent. Comparisons have been made with experimental data on six antiferromagnetic compounds which seem to satisfy the nearest-neighbors-only restriction. The agreement is about as good as could be expected, considering the estimated experimental error.

Approximate values of $|J|/k$ deduced for the compounds MnF_2, FeF_2, $LaFeO_3$, $LaCrO_3$, $KFeF_3$ and $KCoF_3$ are 1·8, 3·0, 27, 28, 6·0 and 12°K, respectively.

1. INTRODUCTION

THE Heisenberg–Dirac model[1] of co-operative magnetic phenomena has as its basis the assumption that the interaction between a pair of magnetic atoms i and j is

$$V_{ij} = -2J_{ij}\mathbf{S}_i \cdot \mathbf{S}_j \qquad (1)$$

where J_{ij} is an exchange interaction between the ith and jth atoms and $\mathbf{S}_i$ and $\mathbf{S}_j$ are the spin operators. Thus the Hamiltonian operator for a system of N atoms is

$$\mathscr{H} = -2\sum_{i<j}^{N}\sum_{j=1}^{N} J_{ij}\mathbf{S}_i \cdot \mathbf{S}_j \qquad (2)$$

If the system is a crystal which contains only one type of magnetic atom, it is possible to take advantage of the inherent symmetry and rewrite the Hamiltonian in the form

$$\mathscr{H} = -2\sum_{k=1}^{N'} J_k \sum_{k\text{th neighbors}} \mathbf{S}_i \cdot \mathbf{S}_j \qquad (3)$$

The sum over k is over sets of neighbors, from the nearest to the most distant (N'), while the second sum is over all pairs of kth nearest neighbors. J_k is the exchange interaction between kth nearest neighbors. As the magnitude of the exchange interaction generally diminishes rapidly with distance, only a limited number of values of k need be considered. In practice there are many cases where only one term is sufficient and very few where more than two are necessary.

Although it has not been possible to obtain exact solutions for this model, various approximations which have been tried have yielded results in good qualitative agreement with experiment. For example, the simplest approximation of all, the molecular-field method, gives a description of ferro-, antiferro- and ferrimagnetism which is generally good at all temperatures, although wrong in some details. Improved agreement can be obtained by using other approximations, which are more precise but are valid only in a limited temperature range. Thus, high-temperature

* Research performed under the auspices of the U.S. Atomic Energy Commission. A preliminary account of this work was given at the Washington Meeting of the American Physical Society, May 1958.

† Present address: Office of Naval Research, Department of the Navy, Washington 25, D.C.

approximations such as the OGUCHI[2], BETHE–PEIERLS–WEISS[3] and constant-coupling[4] methods take account of short-range-order effects which are neglected in the molecular-field treatment. Perhaps the biggest defect of the Heisenberg–Dirac model is its apparent failure to predict an ordered ground state in antiferromagnetism at absolute zero;[5] the relation of this point to the results of this paper will be taken up in the discussion.

Despite the apparent successes of the Heisenberg–Dirac model, a number of objections have been raised against it;* the objectors have suggested that the agreement with experiment is only superficial, merely reflecting the fact that any model which introduces an apparent spin interaction to account for the effects of the Pauli Principle will have some measure of success. There exists in the literature considerable controversy over the validity of the model, and the matter is by no means settled at the present time. In principle, a pragmatic test could be made for any specific system by calculating the relevant exchange integrals, evaluating the partition function, and combining these results to derive such properties as the Curie temperature, spontaneous magnetization, susceptibility, etc. In practice, neither of the two results required can at present be obtained with any overall degree of accuracy. The calculation of exchange integrals is still in a primitive state, and for some systems it is not even clear which integrals are the important ones. The second step, the evaluation of the partition function (or its equivalent operation, the diagonalization of $\mathscr{H}$) is on somewhat better footing; although, as previously stated, no exact solution has been obtained, the various approximations do lead to detailed and specific predictions which can be correlated and compared with experiment.

Thus, the situation now existing is that arguments based on first principles have failed to obtain any measure of agreement about the validity of the Heisenberg–Dirac model, while a straightforward test of the type described in the previous paragraph is impossible because of mathematical difficulties. However, to set our sights on a much more modest goal, it should in principle be possible at least to check the *internal consistency* of the model. As an example, consider an antiferromagnetic system with nearest-neighbor interactions only. Given an adequate theory, the value of the exchange integral J could be obtained from experiment in any one of a number of ways; examples of measurements which would provide a value of J are: (*a*) Néel temperature, (*b*) susceptibility at the Néel temperature, (*c*) inelastic neutron scattering,[7] (*d*) specific heat[8] and (*e*) excitation of spin-wave resonances.[9] If the theory is self-consistent, the values of J obtained from the different measurements should be the same within experimental error. The desirability of such comparisons is obvious, but very little has been done along these lines in the past. Probably the principal reason is that the more rigorous theoretical treatments have generally been limited to spin $\frac{1}{2}$ and to nearest-neighbor interactions only, while practically all of the experimental data are on more complex systems.

Of the methods mentioned in the previous paragraphs whereby J may be evaluated, appreciable experimental data exist only on the Néel temperature, the susceptibility and the specific heat. HOFMANN *et al.*[8] have previously used the specific-heat data on ferromagnetic and antiferromagnetic systems to make estimates of exchange interactions. In the present paper, we shall see what results can be obtained by using the Néel temperature and susceptibility data. For the necessary theoretical relations, either the Bethe–Peierls–Weiss or the constant-coupling approximation to the Heisenberg–Dirac model might be used; these two methods are generally regarded as the best approximations for the high-temperature range ($T \geqslant T_N$) and they give essentially identical results, both for the Néel points and the susceptibilities. We have chosen to use the B–P–W method, mainly because BROWN and LUTTINGER[10] have already extended this method to obtain the partition function and the Néel temperature for arbitrary spin. Thus only the susceptibility is needed, and their first result makes its calculation a straightforward, though tedious, matter. However, like BROWN and LUTTINGER, we have retained the nearest-neighbors-only restriction, as formulation of the B–P–W method for both arbitrary spin and more than one set of interactions leads to equations of staggering complexity. BROWN and LUTTINGER have also derived a classical approximation of the

* See SLATER[6] for a detailed exposition of the objections to the Heisenberg–Dirac model.

VOL 11 195

B–P–W method in which the spin operators are regarded as classical vectors of length $[S(S+1)]^{\frac{1}{2}}$. It will be instructive to use the results of this method, and of the molecular-field method as well, to determine values of J and to make comparisons with the values determined from the B–P–W method itself. The relevant equations are given in the next section.

2. EQUATIONS FOR THE NÉEL TEMPERATURE AND SUSCEPTIBILITY AT THE NÉEL TEMPERATURE

(a) *Molecular-field theory*

The molecular-field theory gives the following well-known results:

$$\frac{|J|}{k}=\frac{3T_N}{2nS_0(S_0+1)} \tag{4a}$$

$$\frac{|J|}{k}=\frac{3C_M}{4nS_0(S_0+1)\chi_M(T_N)} \tag{4b}$$

In these equations, T_N is the Néel temperature, C_M the molar Curie constant, χ_M the molar susceptibility, n the number of nearest neighbors for each atom and S_0 the spin of each atom in units of $\hbar$.

(b) *Classical Bethe–Peierls–Weiss theory*

The relation between J and T_N is

$$\frac{|J|}{k}=\frac{T_N\mathscr{L}^{-1}\left(\frac{1}{n-1}\right)}{2S_0(S_0+1)} \tag{5a}$$

where $\mathscr{L}^{-1}$ is the inverse Langevin function. BROWN and LUTTINGER do not give an expression for the susceptibility, but by the usual methods we find

$$\frac{|J|}{k}=\frac{(n-2)C_M\mathscr{L}^{-1}\left(\frac{1}{n-1}\right)}{4(n-1)S_0(S_0+1)\chi_M(T_N)} \tag{5b}$$

(c) *Bethe–Peierls–Weiss theory*

BROWN and LUTTINGER give the partition function for a B–P–W cluster of a center atom and its n nearest neighbors in the form

$$Z(j,\,h_0,\,h_1)=Z_{00}(j)+Z_{20}(j)h_0^2+ +Z_{11}(j)h_0h_1+Z_{02}(j)h_1^2 \tag{6}$$

Here

$j = J/kT$ (note that $j<0$ for antiferromagnetism)
$h_0 = g\beta H_0/J$
$h_1 = g\beta H_1/J$
H_0 = applied magnetic field
H_1 = effective field acting on shell of nearest neighbors
β = Bohr magneton

The functions $Z_{k\ell}(j)$ are perhaps best defined by first defining the sums

$$\mathscr{S}_nf(j)=\sum_{S_1}\omega(S_1)\sum_{S}\exp(j\sigma_0)(2S+1)f(j) \tag{7a}$$

$$\mathscr{S}_n'f(j)=\sum_{S}\delta_S{}^0\omega(S_0)f(j) \tag{7b}$$

The sum over S is from $|S_1-S_0|$ to S_1+S_0, and the sum over S_1 is from 0 to nS_0, except for the term $S_1=S_0$, $S=0$, which is taken care of by the $\mathscr{S}_N'$ term. Also

$\omega(S_1)$ = number of ways of forming spin S_1 from n spins S_0.

$\sigma_0 = S(S+1)+S_1(S_1+1)-S_0(S_0+1)$
$\sigma_1 = S(S+1)-S_1(S_1+1)+S_0(S_0+1)$
$\delta_S{}^0$ = Kronecker delta

Then

$$Z_{00}(j)=\mathscr{S}_n(1)+\mathscr{S}_n'(1) \tag{8a}$$

$$24Z_{20}(j)=\mathscr{S}_n\{[S(S+1)]^{-1}(\sigma_0{}^2j^2+\sigma_0\sigma_1[S(S+1)]^{-1}j)\}-4\mathscr{S}_n'(j) \tag{8b}$$

$$12Z_{11}(j)=\mathscr{S}_n\{[S(S+1)]^{-1}(\sigma_0\sigma_1j^2-\sigma_0\sigma_1[S(S+1)]^{-1}j)\}+4\mathscr{S}_n'(j) \tag{8c}$$

$$24Z_{02}(j)=\mathscr{S}_n\{[S(S+1)]^{-1}(\sigma_1{}^2j^2+\sigma_0\sigma_1[S(S+1)]^{-1}j)\}-4\mathscr{S}_n'(j) \tag{8d}$$

The Bethe–Peierls–Weiss theory does not provide an explicit relation between J and T_N analogous to equations (4a) and (5a), but $j_N = J/kT_N$ is determined from the relation

$$nZ_{11}(j_N)+2Z_{02}(j_N) = 0 \qquad (9a)$$

Values for j_N for different values of n and S_0 are tabulated in reference (11). Again, by extending BROWN and LUTTINGER's results, we find for the relation between J and $\chi_M(T_N)$

$$\frac{J}{k} = \frac{4Z_{02}(j_N)Z_{20}(j_N)-Z_{11}^2(j_N)}{j_N Z_{00}(j_N)\{2Z_{02}(j_N)-nZ_{11}(j_N)\}}\times \times\frac{3C_M}{S_0(S_0+1)\chi_M(j_N)} \qquad (9b)$$

3. COMPARISONS WITH EXPERIMENT

The gist of the previous section is that each theory gives relations of the form

$$\frac{|J|}{k} = \phi(n, S_0)T_N \qquad (10a)$$

and

$$\frac{|J|}{k} = \Gamma(n, S_0)\frac{C_M}{\chi_M(T_N)} \qquad (10b)$$

Values of ϕ and Γ for $n = 6$ and 8 and for $S_0 = 1/2, 1, 3/2, 2$ and $5/2$ are given in Table 1. Because of the labor involved, values of Γ were computed only for $S_0 = 1/2, 3/2, 5/2$, the values for $S_0 = 1, 2$ being obtained by interpolation. This procedure may introduce a small error, if, as seems likely, there is a small integral-half integral alternation in Γ; however, calculations indicate that the error introduced in this way is less than 1 per cent and thus considerably smaller than the average experimental error in the available data.

In selecting experimental data for use in the consistency check, we must be careful to choose only compounds which satisfy the nearest-neighbor-interactions-only restriction. Moreover, as the B–P–W method is limited to cases in which nearest neighbors of a given atom are not themselves nearest neighbors, we must also include this restriction. The list of such compounds for which adequate data on T_N and $\chi_M(T_N)$ exist is extremely limited. There is, of course, no hard and fast rule for deciding how many sets of interactions are important in a particular crystal, and at best the decision rests on indirect evidence. Some indications can usually be obtained from the crystal structure and magnetic structure; perhaps the most quantitative information comes from the ratio θ/T_N, where θ is the constant in the high-temperature approximation to the susceptibility,

$$\chi(T) = C/(T+\theta)$$

Table 1. Values of ϕ and Γ as given by the molecular-field (MF), the classical Bethe–Peierls–Weiss (BPWc), and the Bethe–Peierls–Weiss (BPW) theories. The top number of each pair is ϕ and the bottom number is Γ.

S_0	$n = 6$			$n = 8$		
	MF	BPWc	BPW	MF	BPWc	BPW
1/2	0·3333 0·1667	0·410 0·164	0·499 0·1445	0·2500 0·1250	0·289 0·124	0·316 0·115
1	0·1250 0·0625	0·154 0·0615	0·162 0·0587	0·09375 0·04687	0·1085 0·0465	0·1107 0·0451
3/2	0·06667 0·03333	0·08203 0·0328	0·08396 0·0321	0·05000 0·02500	0·05787 0·0248	0·05869 0·0245
2	0·04167 0·02083	0·05128 0·0205	0·05200 0·0202	0·03125 0·01563	0·03617 0·0155	0·03648 0·0153
5/2	0·02857 0·01429	0·03515 0·01406	0·03549 0·0139	0·02143 0·01071	−0·02480 0·0107	0·02495 0·0106

Table 2. Values of θ/T_N for some antiferromagnetic compounds

Compounds	θ/T_c		Temperature range
	Exp.	BPW theory (*nn* only)	
MnF_2	1·18*	1·16	4–5 T_N
FeF_2	1·48†	1·17	2–3 T_N
$LaFeO_3$	—	1·24	
$LaCrO_3$	1·78‡	1·26	2–3 T_N
$KFeF_3$	1·52§	1·25	3–4 T_N
$KCoF_3$	1·36§	1·26	3–4 T_N

* Reference (17).
† H. BIZETTE and B. TSAI, *C.R. Acad. Sci., Paris* **212,** 119 (1941).
‡ Reference (20).
§ N. ELLIOTT. Private communication.

For example, for the simplest case of two sublattices, the ratio should lie in the range 1·1–1·5 if only one type of interaction is present (the exact value depending on n and S_0). However, as LI[11] has pointed out, if θ is deduced from measurements at temperatures not too high compared with T_c, then values larger than the theoretical one must be expected.

Six compounds—MnF_2, FeF_2, $LaFeO_3$, $LaCrO_3$ $KFeF_3$ and $KCoF_3$—have been chosen for the comparison. MnF_2 and FeF_2 both have the rutile structure, in which the magnetic lattice is body-centered tetragonal. Strictly speaking, each magnetic atom has two nearest neighbors, one in each direction along the c-axis. However, it seems likely that the important interactions are super-exchange interactions between a "central" atom and its eight corner neighbors, and the neutron-diffraction results[12] support this view. The other four compounds all have pseudo-perovskite structures,[13,14] in which the magnetic lattice is approximately simple cubic. Each magnetic atom has six nearest neighbors and is separated from each of them by an intervening anion. The neutron-diffraction data[15,16] are consistent with the idea that the principal magnetic interaction in these compounds is a superexchange interaction between nearest neighbors. Table 2 gives the available information on the θ/T_c values. The last column shows the range of temperatures in which the susceptibility measurements from which θ was determined were made.

The experimental data which are needed, in conjunction with equations (10a) and (10b), to determine J are given in Table 3. In view of the results of BIZETTE and TSAI[19] on the effect of particle reorientation on the magnetic susceptibility of antiferromagnetic compounds, it would be preferable to use only data on single crystals. Unfortunately, such data have been obtained only for MnF_2; however, for this compound there are two different sets of data, due to FONER[17] and to BIZETTE and TSAI.[19] We have quoted only FONER's data in the table, but the two sets are in good agreement and give essentially the same results for J. The results on the other four compounds have been taken on polycrystalline samples. The accuracy of these results is difficult to assess, but it is probably around ± 10 per cent, as compared to an estimate[17] of ± 2 per cent for the MnF_2 data. The $LaFeO_3$ values are perhaps the least reliable, inasmuch as there is some evidence[20] of a first-order phase transition in this material near the Néel temperature.

The last column of Table 3 gives the values of C_M which were used in the calculation. In principle, it would be better to use experimental values of C_M, as this helps to take into account certain effects, such as the orbital contribution to the susceptibility, which cannot be estimated accurately by theoretical methods. However, if the data are not taken at very high temperatures, the measured values may be considerably in error. We have compromised by using the theoretical spin-only

Table 3. Data on antiferromagnetic compounds

Compounds	n	S_0	T_N(°K)	$\chi_M(T_N)$ (cgsu/mol)	C_M
MnF_2	8	5/2	68*	0·0251*	4·38
FeF_2	8	2	79†	0·0196†	3·88†
$LaFeO_3$	6	5/2	740‡	0·00211‡	4·38
$LaCrO_3$	6	3/2	320‡	0·00196‡	1·88
$KFeF_3$	6	2	115§	0·0113‖	3·38‖
$KCoF_3$	6	3/2	135§	0·00835‖	3·54‖

* Reference (17).
† H. BIZETTE and B. TSAI, *C.R. Acad. Sci., Paris* **212,** 119 (1941).
‡ Reference (20).
§ Reference (14).
‖ N. ELLIOTT. Private communication.

values where they seem to be applicable (for MnF_2, $LaFeO_3$, $LaCrO_3$) and the experimental values in the other three cases.

As the evaluation of $|J|/k$ by the three different theories shows much the same pattern for each of the six compounds, it will be sufficient for comparison of the theories to show the detailed results for a single system only. Table 4 gives such results

Table 4. Values of $|J|/k$ for FeF_2

	$\|J\|/k$ from	
	T_N	$\chi(T_N)$
MF	2·47	3·12
BPWc	2·86	3·10
BPW	2·88	3·06

for FeF_2. First of all, we notice that the discrepancy between the corresponding values of $|J|/k$ decreases as we go from the molecular-field theory to the B–P–W theory; this gives some confidence that the more rigorous theory does give quantitatively better results. Also, the molecular-field theory gives too high a value for $|J|$ by the T_N method and too low a value by the $\chi(T_N)$ method; from equations (10a) and (10b), one can see that this behavior is a direct consequence of the fact that the molecular-field theory overestimates both the Néel temperature and the susceptibility at the Néel temperature.

Table 5 gives the $|J|/k$ values determined for all five compounds by the B–P–W equations. The last column, marked W, lists $|J|/k$ values proposed by HOFMAN *et al.*[8] from their analysis of the specific heats of antiferromagnetic compounds.

Table 5. Values of $|J|/k$ determined by B–P–W theory

Compound	Values of $\|J\|/k$ from		
	T_N	$\chi(T_N)$	W
MnF_2	1·70	1·87	1·73*
FeF_2	2·88	3·03	3·01*
$LaFeO_3$	26·3	28·9	—
$LaCrO_3$	26·9	30·8	—
$KFeF_3$	5·98	6·04	—
$KCoF_3$	11·3	13·6	—

* Reference 8.

4. DISCUSSION

The agreement between the values of J obtained by different methods on the same compound is seen to be reasonably good. The discrepancy that does exist may be attributed to one of four causes: (*a*) a defect in the Heisenberg–Dirac model itself, (*b*) a defect in the B–P–W approximation, (*c*) the existence of more than one kind of interaction in the compounds studied, and (*d*) experimental error. We have no way of separating these various contributions, but it is worth noting that the

average discrepancy is little, if any, larger than would be expected from the estimated experimental error alone. Obviously, no general conclusions can be drawn from an analysis of data on only six compounds, but the results are sufficiently encouraging to suggest that further investigations of this type be made. It would be desirable to extend the comparisons by studying more compounds and by making several different kinds of observations on the same compound.

We would like to remark again that the results recorded in Table 5 bear only on the self-consistency of the Heisenberg–Dirac model and not on its general validity. What the results do suggest is that for each of the six compounds there exists a number, J, which, when inserted in the appropriate B–P–W– equations, will give a reasonably quantitative (say, ± 10 per cent) description of the high-temperature properties of these systems. It is, of course, in keeping with the spirit of the Heisenberg–Dirac model to interpret the J's as exchange integrals, and those who are interested in the calculation of such integrals may find useful information in a comparison of the magnitudes of the values of J in Table 5. For example, it appears that in the iso-structural perovskite-type compounds, the superexchange through oxygen is appreciably larger than that through fluorine. This result is consistent with general ideas about the relation between superexchange and electronegativity of the intervening anion.[18,21] Moreover, it is tempting to attribute the difference in J value between FeF_2 and $KFeF_3$, where the two compounds have the same anion and the same magnetic cation, to the smaller Fe^{++}–F^-–Fe^{++} bond angle in FeF_2. These remarks, however, must be regarded only as speculations.

In connection with the general validity of the Heisenberg–Dirac model of antiferromagnetism, MARSHALL[5] has studied the ground state predicted by this model for spin $\frac{1}{2}$ and for simple lattices with nearest-neighbor interactions only. His results indicate that the ground state is disordered in all the cases investigated, and thus antiferromagnetism does not occur. This result, however, is not as incompatible with ours as might seem at first glance. For instance, the Heisenberg–Dirac model may still produce antiferromagnetism for $S_0 > \frac{1}{2}$. Also, the ground-state investigations refer to the low-temperature properties of the system, while our comparisons have been concerned with the high-temperature properties; there is no reason in principle why the model should not give correct predictions in one temperature range and not in the other. As an example of a way in which this might happen, MARSHALL has noted that there are probably some ordered states which have energies almost as low as the ground state, and thus the introduction of some other small terms, notably anisotropy, into the Hamiltonian might be sufficient to produce an ordered ground state without affecting the high-temperature properties very much. The calculations of TAKETA and NAKAMURA[22] lend some support to this argument.

Acknowledgements—I am indebted to L. CORLISS, N. ELLIOTT, J. HASTINGS and S. FONER for permitting me to quote some of their unpublished experimental results; to W. MARSHALL for some comments on the discussion; and to Miss D. L. DUFFY for her invaluable assistance with the computations.

REFERENCES

1. See, for instance, VAN VLECK J. H., *The Theory of Electric and Magnetic Susceptibilities* p. 316. Oxford University Press (1932).
2. OGUCHI T., *Progr. Theor. Phys.* **13,** 148 (1955).
3. WEISS P. R., *Phys. Rev.* **74,** 1493 (1948).
4. YVON J., *Cah. Phys.* Nos. 31–32 (1948).
   NAKAMURA T., *Busseiron-Kenkyu* No. 63, 12 (1953).
   KASTELEIJN P. W. and VAN KRANENDONK J. *Physica s'Grav.* **22,** 317, 367 (1956).
   KIKUCHI R., *Ann. Phys., New York* **4,** 1 (1958).
5. MARSHALL W., *Proc. Roy. Soc.* A**232,** 48 (1955).
6. SLATER J. C., *Rev. Mod. Phys.* **25,** 199 (1956).
7. BROCKHOUSE B. N., *Phys. Rev.* **106,** 859 (1957).
   IYENGAR P. K. and BROCKHOUSE B. N., *Bull. Amer. Phys. Soc.* **3,** 195 (1958).
8. HOFMANN J. A., PASKIN A., TAUER K. J. and WEISS R. J., *J. Phys. Chem. Solids* **1,** 45 (1956).
9. KITTEL C., *Phys. Rev.* **110,** 1295 (1958).
10. BROWN H. A. and LUTTINGER J. M., *Phys. Rev.* **100,** 685 (1955).
11. LI Y.-Y., *Phys. Rev.* **84,** 721 (1951).
12. ERICKSON R. A. and SHULL C. G., *Phys. Rev.* **83,** 208 (1951).
13. YAKEL H. L., *Acta Cryst., Camb.* **8,** 394 (1955) ($LaFeO_3$ and $LaCrO_3$).
14. MARTIN R. L., NYHOLM R. S., and STEPHENSON N. C., *Chem. and Ind. (Rev.)* 83 (1956) ($KFeF_3$ and $KCoF_3$).
15. KOEHLER W. C. and WOLLAN E. O., *J. Phys. Chem. Solids* **2,** 100 (1957) ($LaFeO_3$ and $LaCrO_3$).

16. CORLISS L. M. and HASTINGS J. H., private communication ($KFeF_3$ and $KCoF_3$).
17. FONER S., private communication.
18. BIZETTE H., *Ann. Phys., Paris* **1,** 233 (1946).
19. BIZETTE H. and TSAI B., *C.R. Acad. Sci., Paris* **238,** 1575 (1954).
20. JONKER G. H., *Physica* **22,** 707 (1956). Results in fair agreement with JONKER's are given by WATANABE H., *Sci. Rep. Res. Inst. Tohoku Univ.* **A8,** 14 (1956), and BENOIT R., *C.R. Acad. Sci., Paris* **240,** 2389 (1955).
21. ANDERSON P. W., *Phys. Rev.* **79,** 350 (1950).
22. TAKETA H. and NAKAMURA T., *J. Phys. Soc. Japan* **11,** 919 (1956).

VOL.
11
195

J. Phys. Chem. Solids Pergamon Press 1959. Vol. 11. pp. 105–110. Printed in Great Britain.

AMAS ACCIDENTELS DANS LES SOLUTIONS SOLIDES DÉSORDONNÉES

P. G. de GENNES,* P. LAFORE et J. P. MILLOT

Centre d'études nucléaires de Saclay, Gif s. Yvette (S. et O.)

(*Received* 2 *February* 1959)

Résumé—On envisage une solution solide où des atomes "actifs" A sont substitués, au hasard, aux noeuds d'une matrice inactive B. On étudie un phénomène de propagation qui fait seulement intervenir les atomes A. Ce cas se rencontre notamment pour les bandes d'impuretés des semi-conducteurs, et pour les ondes de spin d'un alliage à un constituant ferromagnétique.

Il existe une concentration critique en atomes B, en dessous de laquelle, par un effet purement géométrique, ces atomes ne forment que des édifices moléculaires, ou "amas", de dimensions finies (paires, triplets, etc.). Dans ce domaine, le spectre des niveaux d'énergie est discret. Au contraire, pour toutes les concentrations supérieures à la valeur critique, il existe des amas infinis, donnant un spectre continu et une conductivité statique finie.

Abstract—The paper deals with some propagation phenomena in binary solid solutions AB, the wave being carried by A atoms only. Such a situation is encountered in impurity bands for semi-conductors, and also for spin waves in alloys with one ferromagnetic component. It is found that below a critical percentage of A atoms (depending on the range of the couplings) the A atoms always belong to finite "clusters" (different clusters being unlinked by the wave equation). The eigenvalues spectrum of the wave equation is then discrete. Above the critical percentage, one finds both finite and non-finite clusters; the eigenvalue spectrum has a continuous component, and a finite static conductivity may occur.

1. INTRODUCTION

SOIT une solution solide AB, où des atomes "actifs" A sont substitués, au hasard, aux noeuds (i) du réseau périodique de la matrice B. Deux exemples nous serviront à préciser ce que nous entendons par atomes "actifs".

1*er Exemple* : les atomes A sont porteurs de spins S, et couplés ferromagnétiquement entre eux par une énergie d'échange. La matière B est, elle, magnétiquement inactive. La question de savoir dans quelles conditions un tel alliage admet un point de Curie bien défini a été soulevée par FRIEDEL[1]. On peut y apporter une réponse au moins partielle, en étudiant, aux basses températures, la stabilité de l'ordre ferromagnétique à l'égard des premières excitations de spin. Il faut donc déterminer les niveaux d'onde de spin de l'alliage désordonné. Ce sont les valeurs propres E de l'équation de propagation

$$Ea_i = 2\Sigma'_j a_j J_{ij} \qquad (1)$$

où a_i représente l'ampliude de la déviation du i^e spin, et où la somme Σ'_j est limitée aux sites qui sont également occupés par des atomes A.

2*e Exemple* : les atomes A forment une "bande d'impuretés" dans un semi-conducteur. A chaque atome A, situé au site (i), est associé une orbitale $\phi_i(R)$, et on cherche, dans l'approximation des liaisons fortes, des fonctions d'onde à un électron de la forme

$$\phi(R) = \sum_i a_i \phi_i(R) \qquad (2)$$

Si les ϕ_i relatives à des sites différents sont orthogonales, on a encore pour les a_i une équation du type (1).

Dans la suite, nous nous limiterons au cas où seuls les premiers voisins sont couplés entre eux. Cette simplification correspond mal aux situations

* Presently with the Department of Physics, University of California, Berkeley, California.

physiques usuelles, mais elle sera utile pour mettre en relief les résultats essentiels (ceux-ci ne sont pas modifiés qualitativement tant que la portée des couplages reste finie). Par un choix convenable de l'échelle des énergies, (1) peut alors être écrite :

$$Ea_i = \Sigma_j'' a_j \tag{3}$$

où la somme Σ_j'' est limitée aux premiers voisins de l'atome A, occupés par des atomes A. C'est à cette forme réduite que nous nous intéresserons dans la suite.

Lorsque tous les noeuds du réseau sont occupés par des atomes A, les solutions de (3) sont des ondes planes $a_i = \exp(i\mathbf{k} \cdot R_i)$ (où R_i est la coordonnée du ie site) et les niveaux correspondants sont

$$E(k) = \Sigma_j^{(1)} \exp\{i\mathbf{k}(R_j - R_i)\} \tag{4}$$

Dans (4), la somme $\Sigma^{(1)}$ est étendue à tous les premiers voisins d'un site quelconque (i). Le fait essentiel est que ces niveaux forment un spectre *continu*. Introduisons maintenant des atomes B. Si leur concentration est faible, ils produisent une simple déformation du spectre continu.

Au contraire, aux faibles concentrations en atomes A, ceux-ci sont pour la plupart isolés. Il leur est associé un seul niveau $E = 0$ fortement dégénéré. Quelques atomes A forment des paires et donnent deux niveaux $E = \pm 1$. Quelques uns encore forment des triplets et donnent trois niveaux, etc. La série ainsi engendrée converge rapidement dans ce domaine (voir Section 3) et le spectre global est *discret*.

Que se passe-t-il dans le domaine intermédiaire? Chaque atome A appartient à un "amas" de n atomes A. L'équation de propagation ne couple que les atomes d'un même amas. Le rang n de l'amas peut être fini ou infini. Les amas infinis jouent un rôle à part : ils contribuent seuls au spectre continu et aux phénomènes de transport sur des distances macroscopiques. Il est donc essentiel de déterminer le pourcentage d'atomes A engagés dans des amas infinis. Nous exposons ici deux méthodes d'approximation qui permettent de calculer ce pourcentage. L'application et l'extension de ces calculs en vue de l'étude du spectre de valeurs propres, ou de la conductivité, sera faite dans une publication séparée (à paraître dans le *Journal de Physique*).

2. ÉTUDE GÉOMETRIQUE DES AMAS

Faisons choix d'un site origine O (quelconque) et soit $P_n(x)$ la probabilité pour que O soit occupé par un atome A qui appartienne à un amas de rang n. Nous poserons par convention

$$P_0(x) = y \tag{5}$$

$$= 1 - x \tag{6}$$

Les probabilités $P_n(x)$ pour n fini se calculent de la façon suivante : pour chaque forme possible d'amas contenant O, on détermine : (a) le rang n de l'amas; (b) le nombre m d'atomes B qui sont voisins d'au moins un atome A de l'amas. Ces m sites constituent l'adhérence de l'amas. Soit A_{nm} le nombre total d'amas qu'il est possible de réaliser, contenant O, de rang n et d'adhérence formée de m atomes B. On a

$$P_n(x) = \sum_m A_{nm} x^n y^m \tag{7}$$

Les facteurs y spécifient que tous les points de l'adhérence sont bien des atomes B. Nous donnons dans le Tableau 1 les valeurs des $P_n(x)$ relatives

Tableau 1. *Valeurs de* $P_n(x)$

(1) Réseau cubique simple

$$P_1 = xy^6$$
$$P_2 = 6x^2y^{10}$$
$$P_3 = 36x^3y^{13} + 9x^3y^{14}$$
$$P_4 = x^4(32y^{15} + 204y^{16} + 96y^{17} + 12y^{18})$$
$$P_5 = x^5(60y^{17} + 495y^{18} + 1140y^{19} + 780y^{20} + 180y^{21} + 15y^{22})$$

(2) Réseau cubique centré

$$P_1 = xy^8$$
$$P_2 = 8x^2y^{14}$$
$$P_3 = x^3(12y^{20} + 36y^{19} + 36y^{17})$$

(3) Réseau cubique à faces centrées

$$P_1 = xy^{12}$$
$$P_2 = 12x^2y^{18}$$
$$P_3 = x^3(24y^{23} + 126y^{24})$$

à quelques types de réseaux, et pour les premiers ordres n.*

* Similar tables (for $n \leqslant 3$) have been previously given by R. E. BEHRINGER, *J. Chem. Phys.* **29**, 537 (1958).

La probabilité pour que O appartienne à un amas infini d'atomes A est obtenue par différence :

$$P_\infty(x) = S(x) = 1 - \sum_0^\infty P_n(x) \qquad (8)$$

En limitant dans (8) la somme à ses premiers termes, on obtient une valeur approchée par excès de $S(x)$. L'aspect des courbes ainsi obtenue (Fig. 1) suggère l'existence de deux domaines de concentration dans lesquelles le comportement de $S(x)$ diffère.

Aux faibles concentrations, $S(x)$ est *identiquement nulle*. En effet,

(a) $S(x)$ et ses dérivées convergent uniformément sur un segment fini (Ox_c). Pour un réseau cubique simple par exemple, l'adhérence m est inférieure à $4n+2$ (cette valeur étant obtenue par un amas en forme de chaine linéaire) :

$$P_n(x) > (\sum_m A_{nm}) x^n y^{4n+2}$$

La série $\sum_n P_n$ converge puisque sa somme est bornée par I; et la valeur maxima de xy^4 est $4^4/5^5$.

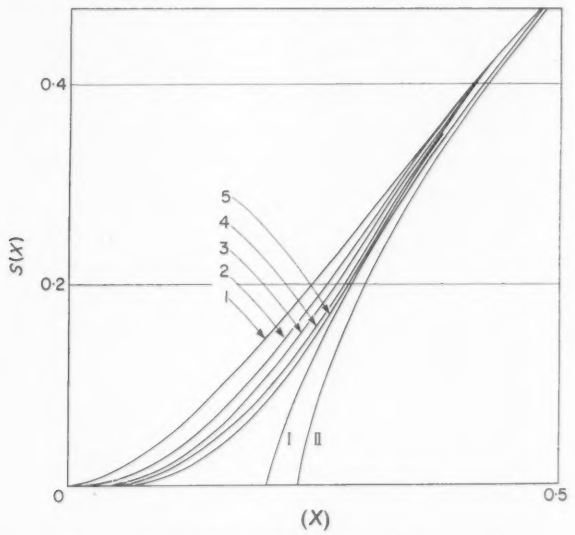

FIG. 1*. Probability $S(x)$ that a given lattice site 0 belongs to an infinite cluster. (The lattice is simple cubic.) Curves (1), (2), ... (n) are overestimates of $S(x)$. (Curve (n) gives the probability that 0 belongs to a cluster containing $n+1$ atoms or more.) Curves I and II are deduced, respectively, from the first and second approximations described in text.

Aux fortes concentrations (pratiquement pour $x \lesssim 0{\cdot}5$), $S(x)$ est très voisin de x d'après la Fig. 1. Presque tous les atomes A sont engagés dans un même amas infini et la série (8) converge rapidement. Toutefois, nous ne sommes pas parvenus à démontrer la convergence uniforme de (8) dans ce domaine.

Donc $(\sum_m A_{nm})$ est majoré par le terme de rang n d'une série géométrique de raison $5^5/4^4$, ce qui suffit à montrer la propriété.

(b) Les dérivées $(d^n/dx^n S)_{x=0}$ sont toutes nulles : pour la dérivée d'ordre n, seuls interviennent les amas de rang $q \leqslant n$. Substituons donc au cristal infini un cristal fini de f_n atomes, assez grand pour contenir tous les amas de rang $q \leqslant n$ et leurs adhérences. Soient P_q' les probabilités qui se substituent aux P_q dans ces conditions

*Although the paper is written in French the captions are given in English to make the major results accessible in both languages.

$$\sum_0^f P_q' = 1$$

$$P_q' = P_q \text{ pour } q \leqslant n$$

donc

$$\left(\frac{d^n}{dx^n}S\right)_{x=0} = \left[\frac{d^n}{dx^n}\sum_0^n P_q(x)\right]_{x=0}$$

$$= \left[\frac{d^n}{dx^n}\sum_0^n P_q'(x)\right]_{x=0}$$

$$= \left[\frac{d^n}{dx^n}\sum_0^f P_q'(x)\right]_{x=0} = 0 \qquad (9)$$

Donc sur un segment Ox_c, $S(x)$ est égale à $S(o)$, donc est nulle : *il n'y a pas d'amas infinis dans ce domaine de concentration.*

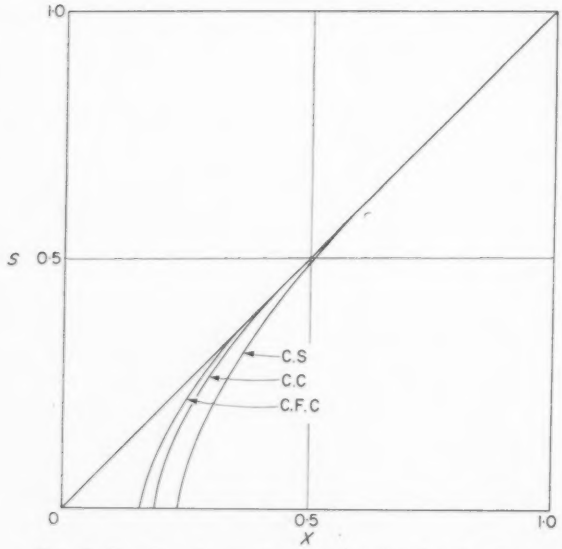

FIG. 2. Results of second approximation for the three cubic lattices.

Nous allons maintenant substituer à (8) un développement approché qui lui est identique pour les premiers termes, que nous pouvons sommer, et qui fait apparaître directement un "point critique" x_c. La méthode consiste à dénombrer les premiers amas construits à partir de O, puis à itérer la construction de ces amas pour en obtenir de plus grands. L'itération est approchée, car elle n'exclut pas certains recouvrements entre les parties successives de l'amas ou de l'adhérence. Nous en exposerons le principe sur le réseau cubique simple, et nous citerons simplement les résultats pour d'autres réseaux. Posons

$$F(x) = \sum_0^\infty P_n(x) = 1 - S(x) \qquad (10)$$

$$= y + x[G(xy)]^6$$

$$(y = 1-x) \qquad (11)$$

Dans (11), nous avons séparé le cas où O est un atome B, et la fonction $G(xy)$ doit engendrer des amas à partir d'un premier voisin P_1 de O, sachant que O est un atome A.

On écrit donc dans la première approximation

$$G = y + xG^5 \qquad (12)$$

(L'exposant 5, au lieu de 6, tient compte du fait que O est déjà un atome A). Dans la deuxième approximation, on remplace (12) par un système

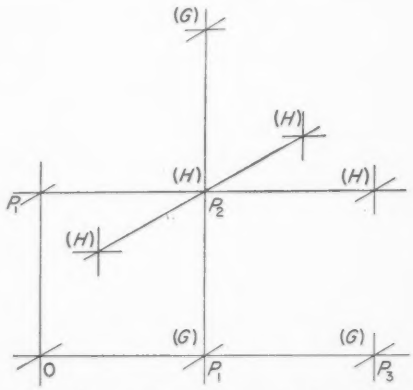

FIG. 3. Iteration of clusters in a simple cubic lattice.

d'équations, destiné à construire au mieux les amas de 3 atomes A. Ici, ces amas sont de deux types, selon que les trois points sont alignés ou forment un angle droit. Pour engendrer les amas à partir de P_2 (Fig. 3) sachant que O et P_1 sont des atomes A, nous introduirons une nouvelle fonction $H(xy)$.

Par contre, nous engendrons ceux qui sont issus de P_3; nous utilisons encore G (en effet, la présence d'un atome A en O ne limite la construction des amas à partir de P_3 que pour des rangs élevés). On pose donc

$$G = y + xGH^4 \qquad (13)$$

Il faut maintenant une équation pour H. Lorsque O, P_1, P_2 sont des atomes A, il reste seulement 4 sites voisins de P_2 à explorer (P_1' a été exploré en même temps que P_1 grâce au facteur G^6 dans (11)). Pour ces 4 sites, on néglige, comme pour P_3, le fait que O est occupé, ce qui donne

$$H = y + xGH^3 \qquad (14)$$

(11) et (12) ou bien (11), (13) et (14) déterminent F en fonction de x et $y = 1-x$ dans la 1ère et dans la 2e approximation respectivement. (Les systèmes correspondants pour différents réseaux sont regroupés dans le Tableau 2).

Tableau 2

	1e approximation	2e approximation
Cubique simple	$G = y+xG^5$	$G = y+xH^4G$ $H = y+xH^3G$
Cubique à faces centrées	$G = y+xG^7$	$G = y+xG^5H^2$ $H = y+xG^3H$
Cubique centré	$G = y+xG^7$	$G = y+xGH_1^3H_2^2$ $H_1 = y+xGH_1^2H_2$ $H_2 = y+xGH_1^3H_2^2$

Si l'on voulait réaliser des approximations d'ordre supérieur, il ne faudrait pas seulement modifier le système qui donne G, mais aussi l'équation (11). Que peut-on déduire en pratique des systèmes du Tableau 2? On vérifie d'abord, en développant la solution en série de x et y considérés comme variables indépendantes, que les premiers termes du développement (10) sont correctement reproduits et que les termes suivants sont peu différents numériquement de la valeur exacte.

D'autre part, quelque soit le réseau (tridimensionnel) et l'ordre d'approximation (1 ou 2) lorsque l'on fait $y = 1-x$, chaque système admet pour $F(x)$ deux solutions réelles sur l'intervalle (01), dont l'une est $F = 1$, et dont l'autre est telle que $F(1) = 0$. Les deux déterminations se coupent pour une valeur x_c de l'intervalle 01. Partant de $x = 0$, on doit d'abord suivre la première, puis à partir de x, la seconde détermination. Les résultats sont représentés sur les Figures 1 et 2. On suit clairement, grâce à cette approximation, l'apparition des amas infinis. Les points critiques x_c estimés de cette façon sont donnés dans le Tableau 3.

Tableau 3

	1ère approximation	2ième approximation
Cubique simple	0·200	0·224
Centré	0·143	0·192
Face centrée	0·091	0·162

Il est interessant de comparer ces valeurs à celles de SATO *et al.*[2] obtenues par une methode très differente.

Mentionnons ici les propriétés particulières de la chaîne linéaire. Pour tout $x \neq 1$, il n'y a que des amas finis d'atomes A. $S(x)$ est nul pour $x < 1$ et discontinu pour $x = 1$. Ceci est dû au fait qu'un nombre même faible d'atomes B répartis sur la chaîne suffit à la couper en segments finis.

3. CONCLUSIONS

Par un effet purement géométrique, les atomes A ne forment aux basses concentrations que des édifices purement "moléculaires", ou amas. Aux concentrations plus élevées, ils forment en outre des édifices "macromoléculaires" ou amas de rang infini. Ces derniers apparaissent brusquement à une concentration bien déterminée, x_c; la valeur numérique de x_c dépend uniquement de la structure du réseau.

Nous n'avons calculé ici cette concentration critique que pour des couplages entre premiers voisins. On retrouverait toutefois le même phénomène dans tous les cas tridimensionnels pourvu que la portée des couplages entre atomes actifs soit finie (x_c étant évidemment d'autant plus faible que cette portée est grande).

Ces résultats sont à rapprocher des théorèmes généraux de BROADBENT et HAMMERSLEY[3], relatifs à une situation voisine où les liaisons entre atomes (et non la position de ces atomes) sont aléatoires. La transposition de ces théorèmes à la situation qui nous intéresse ne nous fournit malheureusement qu'une borne inférieure pour la concentration critique.

Nous n'avons pas abordé ici les problèmes de densité de niveaux, ni les phénomènes de transport dans la bande formée par les atomes A. Ces questions sont étudiées plus en détail dans l'article déjà mentionné du *Journal de Physique*. Qualitativement, les conclusions rejoignent celles d'ANDERSON[4], qui sont relatives à une situation beaucoup plus générale. L'intérêt du modèle simple que nous avons adopté est d'expliquer, dans un cadre moins abstrait, l'origine et les effets des "amas accidentels". Nous en résumons ici les principales applications physiques :

(1) Lorsque les atomes A sont des porteurs de moments magnétiques couplés ferromagnétiquement, le spectre des ondes de spin se déforme au fur et à mesure que l'on ajoute des atomes B, puis disparaît pour $x = x_c$. Pour $x < x_c$, le système se compose comme une collection d'amas finis d'atomes A et sa fonction de partition est donc une fonction régulière de la température : il n'y a pas de point de Curie bien défini dans ce domaine.

(2) Lorsque les atomes A forment une bande d'impuretés dans un semi-conducteur comme Ge ou Si, il est tentant de relier x_c, à la concentration critique qui apparaît aux basses températures pour la conductivité et pour le temps de relaxation spin réseau. L'interprétation de cette dernière propriété repose sur le fait que des électrons itinérants subissent plus fortement l'action perturbatrice du réseau que des électrons liés à des atomes A isolés.

Toutefois, nous ne pensons pas que ce problème puisse être résolu sans tenir compte des corrélations de Coulomb entre porteurs.

Remerciements—Nous voudrions enfin remercier les Professeurs J. FRIEDEL et A. HERPIN pour plusieurs discussions sur ces questions, et le Dr. P. W. ANDERSON qui a eu l'amabilité de nous transmettre son manuscrit avant publication. Nous remercions d'autre part, Madame PILLARD et M. GRANDIDIER, qui ont effectué les calculs numériques.

BIBLIOGRAPHIE

1. FRIEDEL J., Communication orale au colloque de Magnétisme de Strasbourg (1957).
2. SATO H., ARROTT A. et KIKUCHI R., *J. Phys. Chem. Solids* **10**, 19 (1959).
3. BROADBENT S. R. et HAMMERSLEY J. M., *Proc. Cambridge Phil. Soc.* **53**, 629 (1957).
4. ANDERSON P. W., *Phys. Rev.* **109**, 1492 (1957).

VOL
11
195

J. Phys. Chem. Solids Pergamon Press 1959. Vol. 11. pp. 111–114. Printed in Great Britain.

THE EFFECT OF PRESSURE ON THE ABSORPTION EDGE OF CERTAIN MOLECULAR COMPOUNDS*

H. L. SUCHAN and H. G. DRICKAMER

Department of Chemistry and Chemical Engineering, University of Illinois, Urbana, Illinois

(*Received* 2 *March* 1959; *revised* 26 *March* 1959)

Abstract—The effect of pressure has been measured on the optical absorption edges of certain molecular crystals, including Hg_2Cl_2, Hg_2Br_2, Hg_2I_2, CI_4, SnI_4, CBr_4, $SnBr_4$ and CI_3H. In general, the gap decreases with pressure at a rate which tends to accelerate with increasing pressure. The rate of shift of the edge depends strongly on the halogen involved, in contrast to ionic crystals where the shift of the edge depends largely on the structure and the cation. An extrapolation of the data indicates that by 300,000 atm most molecular iodides would have zero optical gap.

VOL. 11 1959

THE effect of pressure has been measured on the absorption edges of a series of halogenated molecular crystals, including Hg_2Cl_2, Hg_2Br_2, Hg_2I_2, CBr_4, CI_4, $SnBr_4$, SnI_4 and CI_3H. Table 1 lists the sources of the crystals, the wavelength at atmospheric pressure from which the edge was measured and the approximate absorption coefficient at which the shift was measured. All samples were studied in the form of fused powders. The high-pressure optical techniques have been described elsewhere.[1–3] The shifts with pressure are shown in Figs. 1–5. The mercurous halides all crystallize in the tetragonal D_{4h}^{17} structure, CI_4 and SnI_4 have the cubic T_h^6 structure, CBr_4 and $SnBr_4$ have the monoclinic C_{2h} point group, while CI_3H crystallizes in the hexagonal C_{6h}^6 lattice.

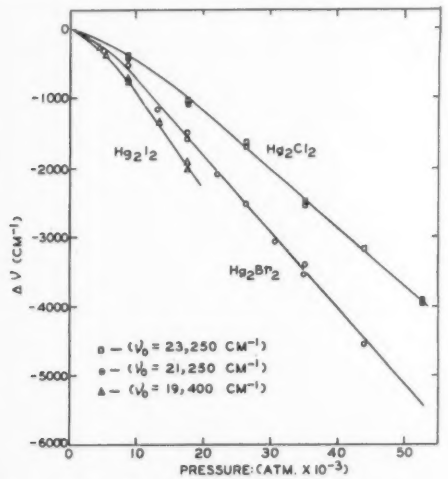

FIG. 1. Shift of the absorption edges of the mercurous halides with pressure.

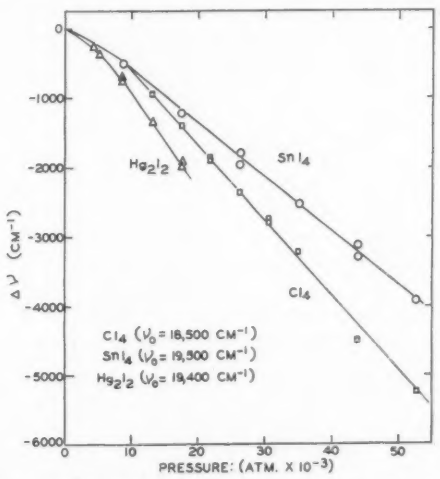

FIG. 2. Shift of the absorption edges of several molecular iodides with pressure.

*This work was supported in part by U.S. Atomic Energy Commission Contract AT(11–1)–67, Chemical Engineering Project 5.

The samples were fused into pellets in a press under 20,000 atm. The pellets were inserted into

Table 1. *Sources and properties of compounds studied*

Compound	Source and estimated purity	ν_0 at 1 atm (cm^{-1})	$\alpha(cm^{-1})$
Hg_2Cl_2	J. T. Baker Chemical Reagent grade	23,250	115
Hg_2Br_2	City Chemical Corp. CP grade	21,250	160
Hg_2I_2	Fisher Scientific Co. N.F.	19,400	410
CBr_4	Eastman Kodak Reagent	30,250	65
CI_4	*	18,500	180
CI_3H	Merck and Co N.F.	23,000	280
$SnBr_4$	British Drug Houses Ltd. Reagent	28,600	100
SnI_4	Fisher Scientific Co. Purified reagent	19,500	170

* Prepared by the method of LISTER M. W. and SUTTON L. E., *Trans. Faraday Soc.* **37**, 393 (1951).

the bomb between salt crystals and fused in, using 30,000 atm pressure. On several occasions a given sample was run up to 50,000 atm two or more times, and the shift of the edge with pressure was identical in each run. Previous studies[3,7] comparing soft materials as powders and single crystals gave identical results. The shifts were measured relatively high on the edge at $\alpha \cong 100$–$300\ cm^{-1}$, because in this region the shifts were independent of absorption coefficient. Out farther on the tail ($\alpha \cong 10$–30), the shifts depended somewhat on α.

All substances showed a red shift with pressure, which, in general, was linear or accelerated with increasing pressure (see Figs. 1–4). Compressibility data are available only for CI_3H,[4] but BRIDGMAN[4,5] has measured the compressibility of many molecular crystals. [In Fig. 5 the shift of the edge for CI_3H is plotted versus pressure (solid curve) and versus relative density (dotted curve).] In every case the compressibility decreased rapidly with increasing pressure (usually by a factor of 4–6 in 50,000 atm). It is clear, then, that all these crystals would show a decrease of optical energy gap with compression which would increase

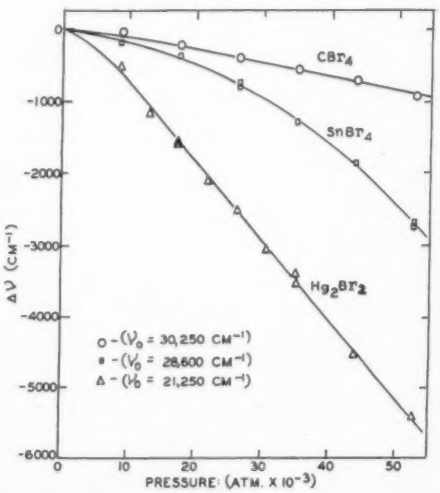

FIG. 3. Shift of the absorption edges of several molecular bromides with pressure.

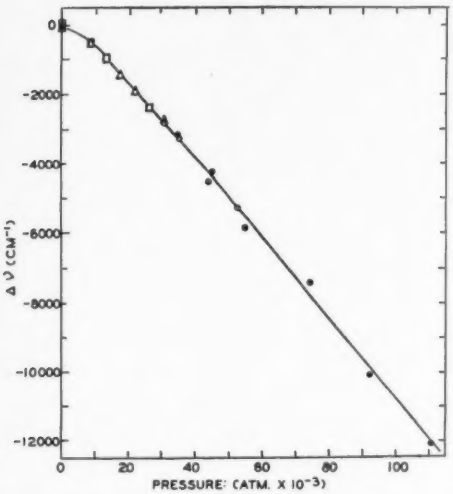

FIG. 4. Shift of the absorption edge of CI_4 with pressure ($\nu_0 = 18{,}500$ cm^{-1}).

rapidly with increasing compression. Such a shift has been noted for sulfur.[6]

There appear to be no quantitative theoretical studies of crystals of this type, but certain regularities can be noted, particularly in comparison with previous studies on ionic halides.[3,7] In ionic halides having the same lattice symmetry and cation, the shift with pressure was substantially independent of the anion, probably indicating that the bottom of the conduction band consisted of metal-ion wave functions only. For the molecular crystals (e.g. Fig. 1), the shifts depend rather definitely on which halogen is involved. The very close similarity in the compressibilities of the halogenated molecular crystals measured by BRIDGMAN almost surely eliminates the possibility that the spread in shifts with pressure is primarily a result of varying compressibility. It seem reasonable that both the ground state (top of the valence band) and excited state (bottom of the conduction band or exciton state) involve halogen-ion wave functions.

Both the atmospheric edge and the shift with pressure are much more similar among the iodides than among the bromides. This would seem to imply that, in the iodides, both the top of the valence band and the bottom of the conduction band are strongly dominated by the iodine wave functions while in the bromides the carbon, tin and mercurous wave functions must contribute to a somewhat greater extent.

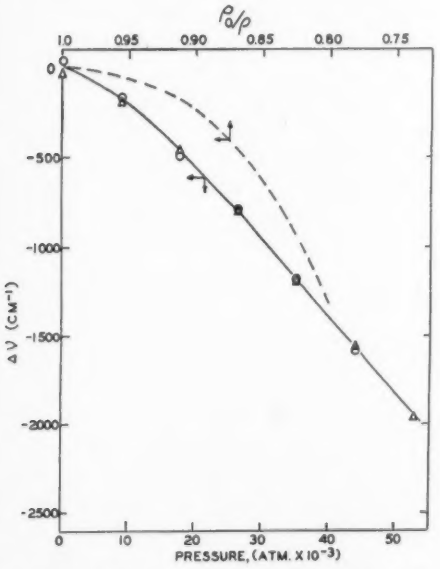

FIG. 5. Shift of the absorption edge of CHI_3 with pressure and the density ($\nu_0 = 23{,}000$ cm^{-1}).

Table 2. Estimated pressure to reduce the optical energy gap to zero at 25°C

Compound	ν_0 at 1 atm (cm^{-1})	Pressure P_m (atm)
CBr_4	30,250	1,670,000
$SnBr_2$	28,600	366,000
Hg_2C1_2	23,250	284,000
CHI_3	23,000	283,000
Hg_2Br_2	21,250	195,000
SnI_4	19,500	258,000
Hg_2I_2	19,400	144,000
CI_4	18,500	167,000

Table 2 shows the pressure at which the optical absorption edge apparently extrapolates to zero. For some compounds (e.g. CI_4) the extrapolation is quite accurate; for others, particularly CBr_4, the extrapolation is so large as to have little or no quantitative meaning. It seems clear that the gap will have disappeared for all the iodides below 300,000 atm.

Acknowledgements—The authors wish to acknowledge the suggestions and advice of F. SEITZ. H. L. SUCHAN would like to express appreciation for a fellowship from the standard Oil Company (Ohio).

REFERENCES

1. FITCH R. A., SLYKHOUSE T. E. and DRICKAMER H. G., *J. Opt. Soc. Amer.* **47,** 1015 (1957).
2. SLYKHOUSE T. E. and DRICKAMER H. G., *J. Phys. Chem. Solids* **7,** 207 (1958).
3. SLYKHOUSE T. E. and DRICKAMER H. G., *J. Phys. Chem. Solids* **7,** 210 (1958).
4. BRIDGMAN P. W., *Proc. Amer. Acad. Arts Sci.* **76,** 55 (1948).
5. BRIDGMAN P. W., *Proc. Amer. Akad. Arts Sci.* **72,** 229 (1938); **74,** 21 (1940); **76,** 55 (1948).
6. SLYKHOUSE T. E. and DRICKAMER H. G., *J. Phys. Chem. Solids* **7,** 275 (1958).
7. ZAHNER J. C. and DRICKAMER H. G., *J. Phys. Chem. Solids* **11**, 92 (1959).

VOL
11
195

J. Phys. Chem. Solids Pergamon Press 1959. Vol. 11. pp. 115–119. Printed in Great Britain.

CALCUL DE LA RÉSISTIVITÉ DES CAVITÉS SPHÉRIQUES DANS LE CUIVRE

M. ASDENTE* et J. FRIEDEL

Faculté des Sciences, Université de Paris, Paris 6e

(*Received* 10 *March* 1959)

Résumé—Nous avons calculé la résistivité introduite dans le cuivre par des cavités sphériques de différentes tailles.

Les cavités ont été représentées par des potentiels carrés, dont la hauteur a été fixée afin de calculer exactement l'effet d'écran provoqué par les électrons de conduction. Le problème de diffusion a été résolu exactement par la méthode des ondes partielles. La résistivité supplémentaire par lacune présente un faible maximum pour des cavités contenant deux lacunes; elle décroit lentement pour des cavités plus grandes; elle n'est diminuée que de moitié pour des cavités contenant 100 lacunes; la section efficace de diffusion est encore nettement inférieure, dans ce cas, à la section classique d'une sphère dure de même rayon.

Abstract—The authors have calculated the resistivity introduced in copper by spherical cavities of different sizes. These voids are represented by square potentials whose height is calculated in order to determine exactly the influence of the screening conduction electrons. The diffusion problem has been completely solved by the partial wave method.

The supplementary resistivity increment due to one vacancy exhibits a small maximum for voids composed of two vacancies, and slowly decreases for the larger cavities. This resistivity increment is only decreased by one-half of its initial value for voids containing 100 vacancies. The effective diffusion cross-section is still much smaller, in this case, than the classical cross-section of a hard sphere of the same radius.

1. INTRODUCTION

Nous considérons la diffusion des électrons de conduction d'un métal par des cavités sphériques de différentes tailles, et nous allons ainsi déterminer la résistivité introduite par lacune en fonction du nombre des lacunes dans ces cavités.

On peut penser que, pour des cavités de très grands rayons a, cette quantité décroît comme $1/a$. Nous voulons savoir si une telle loi est encore valable pour des rayons a qui ne sont pas très grands vis-à-vis des dimensions atomiques, et en particulier si la résistivité par lacune ne commence pas par croître avec a pour de petits rayons. Un effet de ce type avait été suggéré par MOTT[1] pour expliquer la résistivité des alliages à amas de GUINIER[2].

2. GÉNÉRALITÉ SUR LA MÉTHODE

Nous avons calculé la diffusion des électrons dans l'approximation de choc élastique, avec une surface de Fermi sphérique. Si l'on suppose le potentiel à symétrie sphérique, on a alors pour le temps de vie τ des électrons :

$$\frac{1}{\tau} = Nv \int (1-\cos\delta) I(\delta)\, d\omega \qquad (1)$$

où N est le nombre de centres de diffusion par unité de volume, v la vitesse des électrons diffusés, $I(\delta)$ la section efficace de diffusion à l'angle δ et $d\omega$ l'élément d'angle solide.

La résistivité $\Delta\rho$ provoquée par une concentration c des centres de diffusion est alors donnée par l'expression :

$$\Delta\rho = c\frac{mv}{pe^2} 2\pi \int (1-\cos\delta) I(\delta) \sin\delta\, d\omega$$

où p est le nombre d'électrons de valence par atome,

*Laboratori CISE, Milano, Italia.

v la vitesse des électrons au niveau de Fermi, m et e respectivement leur masse et leur charge.

Nous avons considéré des cavités sphériques représentées par un potentiel carré dont nous avons déterminé le rayon a_n en imposant que le volume correspondent soit égal au volume des n lacunes dans la cavité, et la hauteur V_n en imposant que la charge déplacée soit égale à la charge Q_n soustraite par la cavité.

On peut résoudre alors exactement le problème en développant la fonction d'onde de l'électron au niveau de Fermi en ondes sphériques dont la partie radiale doit vérifier l'équation :

$$\frac{d^2G_l}{dr^2}+\left(k'^2-\frac{l(l+1)}{2}\right)G_l=0 \qquad (3)$$

où $k'^2=k^2-k_0^2=\dfrac{m^2v^2}{\hbar^2}-\dfrac{2mV}{\hbar^2}$

et $V=V_n$ pour $r\leqslant a_n$

$V=0$ pour $r>a_n$.

La solution de l'équation (3) donne à grande distance des fonctions non perturbées mais caractérisées par des déphasages η_l qui dépendent de k', c'est-à-dire de V_n (formule (4)[3]) :

$$\operatorname{tg}\eta_l=(-1)^l\frac{ka_nJ_{l+\frac{1}{2}}(k'a_n)J_{l-\frac{1}{2}}(ka_n)-k'a_nJ_{l+\frac{1}{2}}(ka_n)J_{l-\frac{1}{2}}(k'a_n)}{ka_nJ_{l+\frac{1}{2}}(k'a_n)J_{-l+\frac{1}{2}}(ka_n)+k'a_nJ_{-l-\frac{1}{2}}(ka_n)J_{l-\frac{1}{2}}(k'a_n)} \qquad (4)$$

On peut remarquer que les déphasages η_l dépendent du métal considéré seulement à travers la quantité ka_n qui est la même pour tous les métaux de même valence.

On peut ainsi exprimer d'une façon très générale $\Delta\rho$ (5) et la condition d'écran (6) par les déphasages[4] :

$$\frac{\Delta\rho}{c}=\frac{2h}{e^2p}\frac{1}{k}\sum_l l\sin^2(\eta_l-\eta_{l-1}) \qquad (5)$$

$$\frac{2}{\pi}\sum_l(2l+1)\eta_l=Q_n \qquad (6)$$

3. MÉTHODE DE CALCUL

Pour avoir une idée sur la valeur qu'il fallait choisir pour V_n, nous avons d'abord calculé les déphasages η_l correspondants à différentes valeurs de n avec $k'=0$, c'est-à-dire avec un potentiel de même hauteur que l'énergie des électrons. Dans ce cas, les déphasages sont donnés par la formule (7) plus maniable que (4) :

$$\operatorname{tg}\eta_l=(-1)^l\frac{\dfrac{ka}{2l+1}J_{l-\frac{1}{2}}(ka)-J_{l+\frac{1}{2}}(ka)}{\dfrac{ka}{2l+1}J_{-l+\frac{1}{2}}(ka)+J_{-l-\frac{1}{2}}(ka)}. \qquad (7)$$

L'introduction des déphasages ainsi calculés dans la formule (5) nous a permis de déterminer que, jusqu'aux valeurs de n que nous avons considérées ($1\leqslant n\leqslant 100$), il fallait choisir un potentiel plus petit que l'énergie des électrons pour avoir une valeur exacte d'écran.

Nous avons obtenu des informations plus précises sur le potentiel en analysant la variation de Q_n avec $(k'a_n)^2$

$$\left[\frac{\partial}{\partial(k'a_n)^2}\frac{2}{\pi}\sum_l(2l+1)\eta_l\right]_{k'a_n=0}=\frac{2}{\pi}\left\{\frac{1}{3}\frac{ka_n}{1+(ka_n)^2}+\sum_{l\geqslant 1}\frac{1}{2l+3}\frac{ka_n}{2l+1}\frac{\operatorname{tg}\eta_l}{1+\operatorname{tg}^2\eta_l}\times\right.$$

$$\left.\times\frac{J_{l-\frac{1}{2}}(ka_n)J_{-l-\frac{1}{2}}(ka_n)+J_{l+\frac{1}{2}}(ka_n)J_{-l+\frac{1}{2}}(ka_n)}{\left[\dfrac{ka_n}{2l+1}J_{l-\frac{1}{2}}(ka_n)-J_{l+\frac{1}{2}}(ka_n)\right]\left[\dfrac{ka_n}{2l+1}J_{-l+\frac{1}{2}}(ka_n)+J_{-l-\frac{1}{2}}(ka_n)\right]}\right\} \qquad (8)$$

Cela nous a permis de déterminer la variation qu'il fallait apporter à $k'a_n$, pour obtenir à peu

près les bonnes valeurs du potentiel. A ce point le calcul a été confié à une machine à calcul qui nous a donné, pour chaque n, les valeurs du potentiel et des déphasages qui vérifiaient la formule (6) jusqu'à la 5e décimale.

4. RÉSULTATS

Les valeurs numériques des déphasages et du potentiel ont été calculées pour un métal monovalent et les $\Delta\rho$ correspondants pour le cuivre; on obtiendrait des allures tout à fait analogues pour les autres métaux monovalents.

Les bonnes valeurs du potentiel sont représentées dans la Fig. 1 en fonction du nombre n

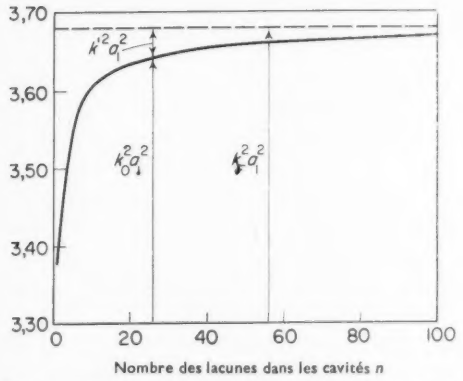

FIG. 1. Variation de $k_0^2a_1^2$ et $k'^2a_1^2 = (k_F^2 - k_0^2)a_1^2$ avec le nombre n de lacunes par cavité. $\frac{1}{2}k_0^2$ est la hauteur du potentiel, $\frac{1}{2}k_F^2$ l'énergie de Fermi et a_1 le rayon d'une lacune.

des lacunes dans la cavité. La droite donne l'énergie cinétique des électrons et la valeur du potentiel choisi pour le calcul de première approximation ($k'a_n = 0$).

Les résultats pour $\Delta\rho/cn$ sont reportés dans la Fig. 2, courbe 1, où nous avons représenté la résistivité par lacune en fonction du nombre des lacunes dans la cavité.

Pour donner une idée sur la façon dont $\Delta\rho/cn$ varie avec la hauteur du potentiel, nous avons reporté encore sur la Fig. 2 les résistivités obtenues d'une façon tout à fait analogue, par des potentiels de *mêmes dimensions géométriques* mais de hauteur différente et toujours indépendante de n.

Ils sont respectivement égaux à l'énergie des électrons de Fermi ($k'a_n = 0$) pour la courbe 2, à l'énergie d'extraction des électrons (DEXTER[5]) pour la courbe 3, et infinis pour la courbe 4.

Les différentes courbes, sauf la 2 qui correspond à un potentiel à peu près de la bonne valeur,

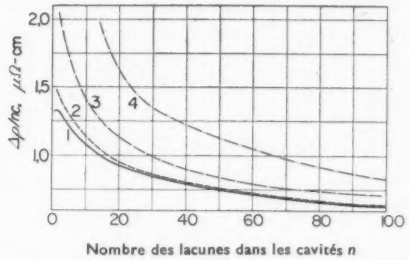

FIG. 2. Résistivité par lacune ($\Delta\rho/nc$) en fonction du nombre n de lacunes par cavité. 1—potentiel $\frac{1}{2}k_0^2$ de la Fig. 1; 2—$k_0 = k_F$; 3—potentiel de DEXTER[5]; 4—k_0 infini. $a_n = a_1\sqrt[3]{(n)}$ pour les quatre courbes.

sont assez éloignées de la courbe 1. Evidemment, dans ces trois cas, la condition d'écran n'a pas été satisfaite. Pour faire une comparaison entre les résultats relatifs à des potentiels de forme différente, mais vérifiant la relation (6), nous avons effectué le calcul de $\Delta\rho/nc$ pour des potentiels ayant une hauteur égale à celle de deux des potentiels précédents ($k'a_n = 0$, $V_n = \infty$) mais en ajustant le rayon a_n de la sphère de façon que la relation d'écran (6) soit satisfaite.

Les résultats sont représentés sur la Fig. 3 (courbes 2′ et 4′), où nous avons aussi reporté la

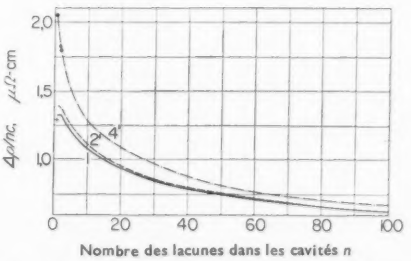

FIG. 3. Résistivité par lacune ($\Delta\rho/nc$) en fonction du nombre n de lacunes par cavité. 1—comme Fig. 2; 2′ et 4′ comme 2 et 4 (Fig. 2) en ajustant le rayon a_n pour satisfaire la relation (6). Sur 4′, $(\Delta\rho/nc) = 0{,}25$ $\mu\Omega$-cm pour $n = 2500$. Pour $n = 1$, le point donne la valeur de JONGENBURGER[6]; la croix donne la valeur d'ABELÈS[7]; pour $n = 2$, le point et le losange donnent les valeurs de SEEGER[8] pour des potentiels respectivement sphérique et ellipsoïdal.

courbe 1 de la Fig. 1. Les trois modèles présentent un accord assez bon, surtout pour les grandes valeurs de n. Ceci montre que, dans des calculs de ce genre, le point critique est la relation (6) plutôt que la forme du potentiel choisi. Les courbes montrent que la résistivité par lacune décroît assez lentement : pour $n = 100$, elle est encore presque moitié de sa valeur pour les lacunes isolées.

En ce qui concerne les petites cavités, même les valeurs calculées en tenant compte de la relation (6) diffèrent sensiblement entre elles. Le rapprochement avec des calculs analogues exécutés pour la *monolacune* avec des potentiels plus soignés,[9] fait penser qu'il est plus correct d'ajuster la hauteur du potentiel en laissant inaltérées les dimensions géométriques de la lacune : c'est cette méthode qui a été utilisée ici pour la courbe 1.*

En passant de la monolacune à la *bilacune*, la condition d'écran entraine une forte augmentation du potentiel qui se répercute par une très légère augmentation du $\Delta\rho/nc$, plutôt que par une diminution. Naturellement, l'approximation sphérique n'est pas directement applicable pour la bi- et trilacune; à ce propos, nous avons reporté toujours sur la Fig. 3, les données de SEEGER[8] relatives à la bilacune, données obtenues en considérant un potentiel infini et en ajustant les dimensions géométriques de la cavité de façon à satisfaire la relation (6).

Une comparaison entre les deux approximations géométriques différentes de SEEGER, l'une à cavité sphérique et l'autre à cavité ellipsoïdale, montre que, dans ce dernier cas, le $\Delta\rho/nc$ est supérieur de ~ 2 pour cent; cela peut faire penser que, si l'on tenait plus correctement compte dans nos approximations de la forme géométrique, le léger maximum observé pour la bilacune pourrait être encore augmenté, bien qu'assez peu. Seul un calcul plus rigoureux pourrait naturellement donner une réponse sûre.

Nous avons comparé la quantité $\sigma_n = 2\pi \int (1 - \cos\delta) I(\delta) \sin\delta \, d\delta$, que l'on peut considérer comme la section efficace pour ces problèmes de conductibilité électronique, avec la section classique πa_n^2 d'une sphère dure de rayon a_n. Le résultat est représenté sur Fig. 4.

On peut remarquer que l'approximation de sphère dures classiques ne reproduit pas l'allure

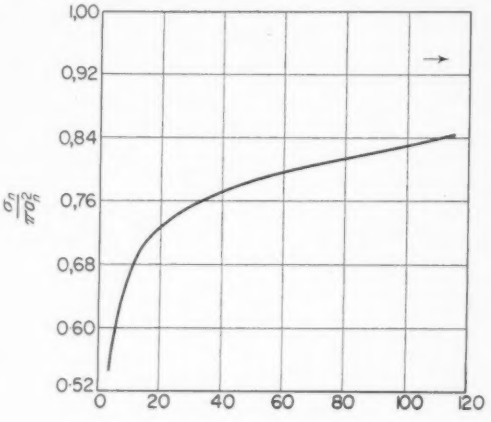

FIG. 4. Rapport de la section efficace σ_n d'une cavité à la section efficace classique πa_n^2 d'une sphère dure de même rayon a_n. Valeurs déduites de la courbe 1 (Fig. 2 et 3), et portées en fonction du nombre n de lacunes par cavité. Le flèche donne la valeur du rapport déduite de la courbe 4′ (Fig. 3) pour $n = 2500$.

du phénomène dans le domaine étudié par nous, mais que on peut s'attendre à un meilleur accord pour de plus *grandes cavités* (on a vérifié par exemple que le rapport considéré Fig. 4 est voisin de 1 pour $n = 2500$).

On pourrait penser considérer la section efficace A quantique pour un potentiel infini et pour de plus grandes cavités en utilisant la formule asymtotique pour les déphasages

$$\eta_l = -ka + l(\pi/2) \text{ pour } l \leqslant ka \text{ et } \eta_l = 0 \text{ pour } l > ka \tag{9}$$

d'une façon analogue à ce que l'on a fait pour la section de diffusion totale.[10] En fait, il ne semble pas que cette hypothèse soit très justifiée : l'allure asymptotique est valable seulement pour $l \ll ka$, et il y a un assez grand intervalle dans lequel la formule (9) n'est pas applicable. Et pour $l \sim ka$, elle entraine même des déphasages de signe contraire. D'autre part, dans nos formules, soit pour le calcul, de $\Delta\rho$, soit pour l'application de la condition d'écran, il y a toujours un facteur l qui

*La Fig. 3 montre que, pour la monolacune, nous trouvons pour k_0 et $\Delta\rho$ des valeurs un peu différentes d'ABELÈS[7], qui a utilisé les mêmes approximations. Ces différences sont uniquement dûes à une meilleure précision des calculs faits à la machine pour la détermination du potentiel et des déphasages.

renforce la contribution des déphasages à grand l. Ainsi la charge déplaçée calculée avec l'approximation (9) n'a même pas le bon signe. On s'est donc contenté d'une comparaison avec la formule classique.

Remerciements—M.lle ASDENTE tient à remercier le Professeur GERMAGNOLI pour son constant encouragement.

BIBLIOGRAPHIE

1. MOTT N. F., *J. Inst. Met.* **60,** 267 (1937).
3. GEISLER A. H., *Phase Transformations in Solids.* Wiley, New York (1951).
FINK K. L., KENSINGTON N. et VAN HORN K. R., *Trans. Amer. Inst. Min. (Metall.) Engrs.* **99,** 132 (1932).
3. MOTT N. F. et MASSEY H. S. W., *The Theory of Atomic Collisions* p. 38. Clarendon Press, Oxford (1949).
4. FRIEDEL J., *Phil. Mag.* **43,** 153 (1952).
5. DEXTER D. L., *Phys. Rev.* **103,** 107 (1956).
6. JONGENBURGER P., *Appl. Sci. Res.* B**3,** 237 (1953).
7. ABELÈS M. F., *C.R. Acad. Sci., Paris* **237,** 796 (1953).
8. SEEGER A., *J. Phys. Chem. Solids* **6,** 324 (1958).
9. BLATT F. J., *Solid State Physics* (Ed. F. SEITZ and D. TURNBULL), Vol. 4, p. 321. Academic Press, New York (1957).
10. MOTT N. F. et MASSEY H. S. W. *The Theory of Atomic Collisions* p. 39. Clarendon Press, Oxford (1949).

OL.
11
959

J. Phys. Chem. Solids Pergamon Press 1959. Vol. 11. pp. 120–130. Printed in Great Britain.

THE HYPERFINE STRUCTURE OF THE V_t-CENTER

M. H. COHEN*, W. KÄNZIG and T. O. WOODRUFF

General Electric Research Laboratory, Schenectady, New York

(*Received* 27 *March* 1959)

Abstract—The structure of a new electron-deficient color center (V-center) in LiF has been determined from its paramagnetic-resonance hyperfine spectrum. The electron deficiency is localized on three fluoride ions which form an obtuse isosceles triangle lying in a (001) plane with the height along a [110] direction. The orbital of the unpaired electron is primarily determined by the crystalline field and is of the π-type, in contrast to previously discussed V-centers. There is evidence that the electron deficiency is associated with an aggregate of three vacancies, so that the charge is compensated.

1. INTRODUCTION

AMONG the alkali halides, the fluorides are particularly suitable for a determination of the structure of electron-deficient color centers, V-centers, by means of electron spin resonance. The existence of a single naturally occurring fluorine isotope, ^{19}F, which has nuclear spin 1/2 and a large nuclear magnetic moment, gives rise to relatively simple resolved hyperfine spectra which have a chance to be interpretable, even for rather complex centers. In this paper we shall describe the structure determination of an electron-deficiency center in LiF by means of a study of its hyperfine spectrum.† The structure of this new V-center differs significantly from that of other V-type centers.[2–4] It is not primarily determined by a molecular σ bond between halide ions. Instead, the orbital involves π bonds, which indicates that the crystalline field plays a very important part, in contrast to the case of other V-centers. The electron deficiency is localized on three fluoride ions, which form an isosceles triangle. We therefore call the new center throughout this paper a V_t-center. It is not yet known which optical absorption bands are associated with it.

It is very probable that the V_t-center exists also in other alkali halides. However, its hyperfine spectrum in chlorides, bromides or iodides would be extremely complicated and difficult to identify.

2. GENERATION AND DETECTION OF THE V_t-CENTER

The V_t-center is present in LiF crystals (obtained from the Harshaw Chemical Company) after X-irradiation at liquid-nitrogen temperature, together with several other types of paramagnetic centers.[2–4] The paramagnetic-resonance spectrum of the V_t-center is most readily observed in absorption at 20°K. At this temperature a convenient power level can be chosen ($H_1 \sim 0{\cdot}1$ G), so that the resonances of most other paramagnetic centers are saturated. The shape of the resonance lines is essentially gaussian at 20°K and below. The static line width is ~ 12 G at 20°K. The absorption signal saturates more easily than the dispersion signal, indicating that the lines are inhomogeneously broadened.[5] Above 40°K the lines have distinct Lorentzian tails, and near 50°K the spectrum becomes smeared out. Upon recooling, it reappears unaltered, indicating that the smearing out is due not to some annealing or recombination process, but merely to a shortening of the relaxation time.

Irreversible changes take place, however, when the LiF crystal (X-rayed at 78°K) is warmed up to 130°K. At this temperature important annealing processes occur. The V-centers described in earlier work[3] disappear. Thermoluminescence, release

*Permanent address: Institute for the Study of Metals, University of Chicago, Chicago, Illinois.

†The results of a preliminary analysis have been previously reported.[1]

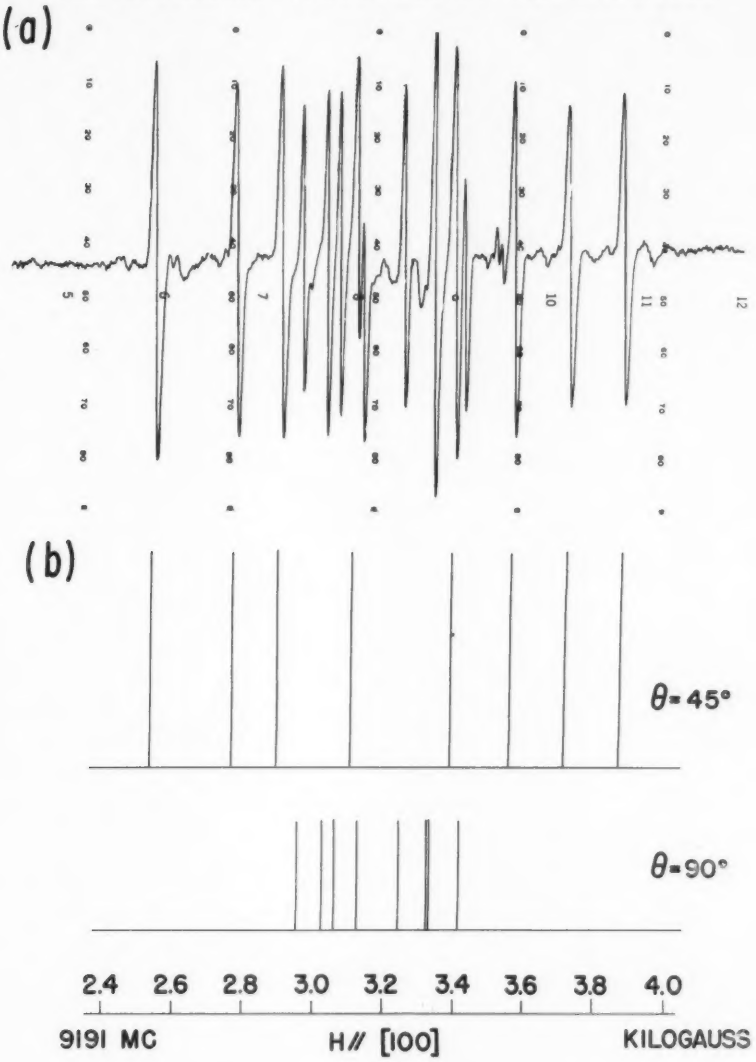

FIG. 1.

(a) Paramagnetic-resonance spectrum of the V_t-center for $H_0 \| [100]$. Derivative of absorption recorded at liquid-hydrogen temperature. Frequency 9·191 kMc. (a few weak lines due to other types of centers could not be completely suppressed).

(b) Decomposition of the experimental spectrum into two basic spectra.

of charge, changes of the optical absorption spectrum and an anomalous volume change have been observed.[6,7] The concentration of V_t-centers increases by a factor of two to three through these annealing processes. This may indicate that it is an uncharged center. The V_t-center disappears irreversibly at a temperature between 150 and 205°K. Possibly the thermoluminescence and the charge release observed near 190°K[6,7] are connected with this annealing process.

3. DESCRIPTION AND QUALITATIVE INTERPRETATION OF THE HYPERFINE SPECTRUM

The paramagnetic-resonance absorption spectra

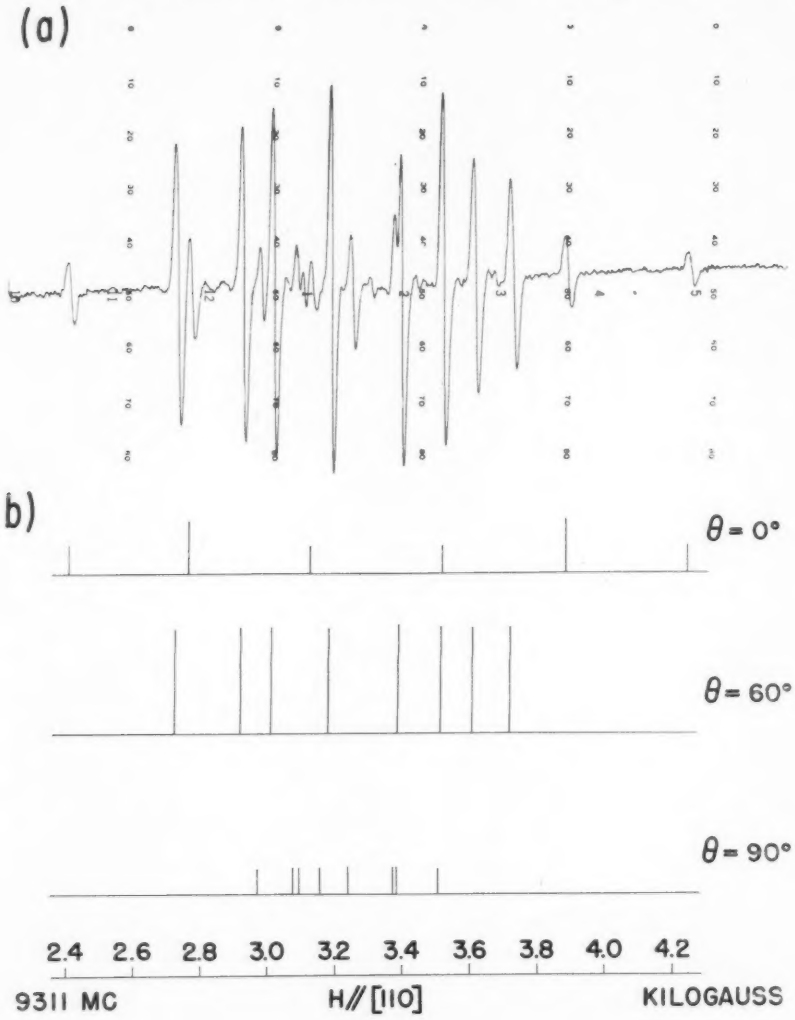

FIG. 2.

(a) Paramagnetic resonance spectrum of the V_t-center for $H_0 \| [110]$. Derivative of absorption recorded at liquid-hydrogen temperature. Frequency 9·311 kMc.
(b) Decomposition of the experimental spectrum into three basic spectra.

of the V_t-center taken at liquid-nitrogen temperature with the d.c. magnetic field H_0 parallel to the crystal axes [100], [110] and [111] are reproduced in Figs. 1–3. If the field H_0 is rotated by a few degrees about the axes [001] or [011], the lines split in a way similar to that described in detail for the V-center.[3] The lines in a given spectrum split in a different way and thus can be classified according to their splitting patterns, i.e. the spectra can be decomposed into "basic spectra". In Figs. 1–3 these basic patterns are represented schematically by the line drawings underneath the recorder traces.

For $H_0 \| [100]$ (Fig. 1), one finds two basic spectra, each consisting of eight lines of almost equal intensity. The intensity ratio of the two

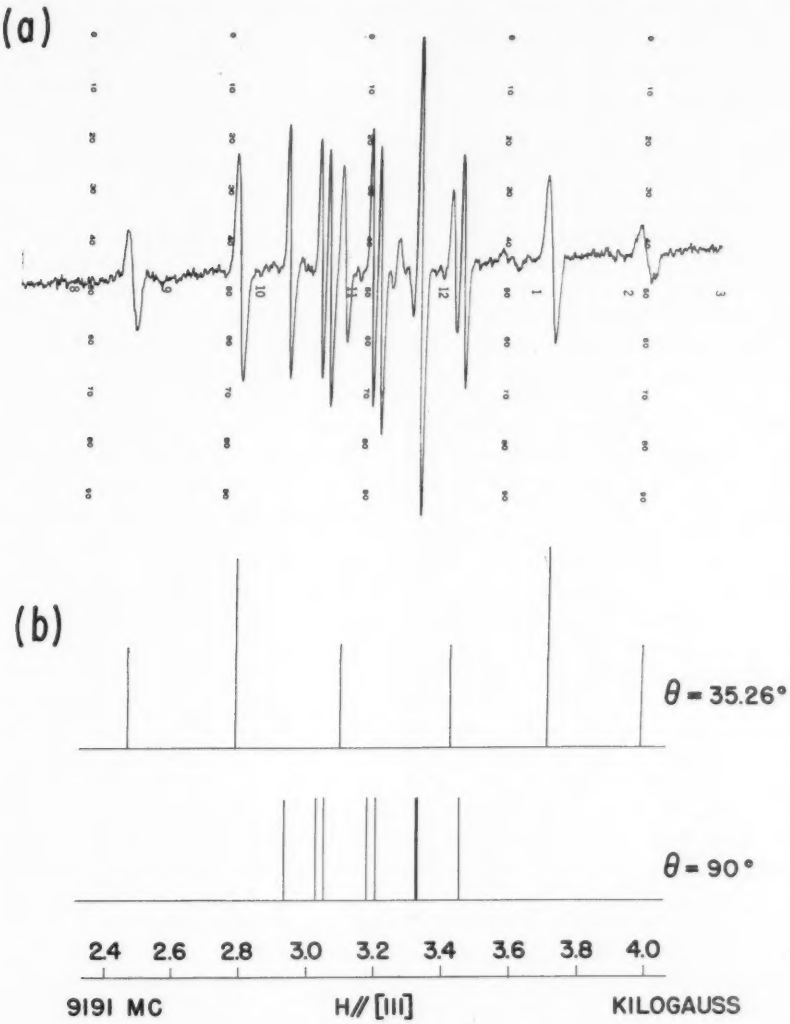

FIG. 3.

(a) Paramagnetic resonance spectrum of the V_t-center for H_0||[111]. Derivative of absorption recorded at liquid-hydrogen temperature. Frequency 9·191 kMc.

(b) Decomposition of the experimental spectrum into two basic spectra.

spectra is about 4:2. For H_0||[110] (Fig. 2), *three* basic spectra are observed, with an intensity ratio of about 1:4:1. Two of these consist of eight lines of about equal intensity, whereas in one basic spectrum two lines are degenerate, so that a six-line pattern with the intensity sequence 1:2:1:1:2:1 results. For H_0||[111] (Fig. 3), the spectrum decomposes into two basic spectra of roughly equal intensities. One of these is an eight-line pattern with equally intense lines; the other one is a six-line pattern with the intensity sequence 1:2:1:1:2:1.

The numbers of basic spectra, as well as the ratios of their integrated intensities, are the same

as for the V-center.[2,3] Thus we can conclude that the V_t-center has orthorhombic overall symmetry with axes parallel to $[\bar{1}10]$, [110] and [001].[2,3] All equivalent sets of axes are equally populated.

The average g-shift is positive; a more quantitative determination is very difficult and was not carried out. The total spread of the paramagnetic-resonance spectrum of the V_t-center for any orientation of the crystal in the d.c. magnetic field is very close to the spread of the V-center spectrum[3] for the same orientation. These two facts indicate that the spectrum is the hyperfine spectrum of an electron deficiency (hole) on fluorine ions, as in the case of the V-center. A comparison of the orientation-dependence of the total spread with that of the V-center spectrum suggests that the axis of maximum total hyperfine interaction is parallel to a [110]-type axis of the crystal. In Figs. 1–3 the basic spectra are characterized by the angle θ between the d.c. magnetic field and this axis of the center.

The basic patterns of eight ($=2^3$) equally intense lines show that hyperfine interaction occurs with three fluorine nuclei. The six-line patterns with the intensity sequence 1:2:1:1:2:1, on the other hand, suggest that two of the nuclei are equivalent with respect to special orientations of the d.c. magnetic field. Hence the symmetry of the center is the symmetry of an isosceles triangle. From the orientations in which the six-line patterns occur, we can infer without ambiguity that the plane of the triangle is a (001) plane. Therefore, the following principal axes can be chosen for the entire center:

Height (or base) of the triangle	$\xi_0 = [\bar{1}10]$.
Base (or height) of the triangle	$\eta_0 = [110]$.
Normal of the plane of the triangle	$\zeta_0 = [001]$.

The ξ_0-axis can be defined as the axis of maximum hyperfine spread. At this stage of the analysis it cannot be decided whether it is parallel to the height or to the base of the triangle.

At this point it is useful to consider the tensors $\boldsymbol{T}^{(i)}$ which describe the hyperfine interaction with the three fluorine nuclei $i = 1, 2, 3$. The nuclei 1 and 3 are located on the base of the isosceles triangle and nucleus 2 is on the apex. The principal axes of the hyperfine tensors are designated by ξ_t, η_t, ζ_t. The symmetry of the entire center requires then:

(1) The principal axes of $\boldsymbol{T}^{(2)}$ are parallel to the principal axes of the entire center.
(2) The principal axes of $\boldsymbol{T}^{(1)}$ and $\boldsymbol{T}^{(3)}$ are rotated by an angle $+\delta$ or $-\delta$, respectively, about ζ_2 with respect to the axes ξ_2, η_2, ζ_2 (see Fig. 4).

The axes ξ_i are chosen to be the axes of maximum hyperfine interaction with the nucleus i.

The geometrical argument which led to the conclusion that two nuclei are equivalent requires now some qualification. Consider, e.g., the case where $\boldsymbol{H}_0$ is along a [110]-type axis of the crystal. Purely geometrically, the nuclei on the base of the triangle (numbers 1 and 3) are equivalent with respect to $\boldsymbol{H}_0$, no matter whether $\boldsymbol{H}_0$ is along the base or along the height. Therefore, one would naively expect that in Fig. 2 the basic spectrum labelled $\theta = 90°$ should be a six-line pattern just as in the case of the spectrum labelled $\theta = 0°$. Similar geometrical considerations would suggest that the 90°-spectra in Fig. 1 and 3 should be six-line spectra, in contrast to the observation. However, it was shown in the work on the V-center[3] that for holes on fluoride ions degeneracies of this kind are lifted when the angle θ between the field $\boldsymbol{H}_0$ and the axis of maximum hyperfine interaction is close to a right angle (within about 20°). One can, therefore, conclude that the axes of maximum hyperfine interaction with nuclei 1 and 3 (axes ξ_1 and ξ_3) deviate by an angle of less than 20° from the axis ξ_2. Fig. 4 illustrates schematically the possible configurations of the axes of hyperfine interaction with the three nuclei.

4. DETERMINATION OF THE TENSORS OF HYPERFINE INTERACTION

As in earlier work,[1] we now analyze the hyperfine splitting in terms of a spin Hamiltonian of the form

$$\mathscr{H} = g_0\beta_0\left\{\frac{g}{g_0}S_zH_z + \boldsymbol{S}\cdot\sum_i \boldsymbol{T}^{(i)}\cdot\boldsymbol{I}^{(i)}\right\} \qquad (1)$$

where g_0 is the spectroscopic splitting factor of the free electron and g that of the V_t-center for the particular orientation in the d.c. magnetic field H_z. Here β_0 is the Bohr magneton, and $\boldsymbol{S}$ is the spin operator of the electron and $\boldsymbol{I}^{(i)}$ that of the nucleus i.

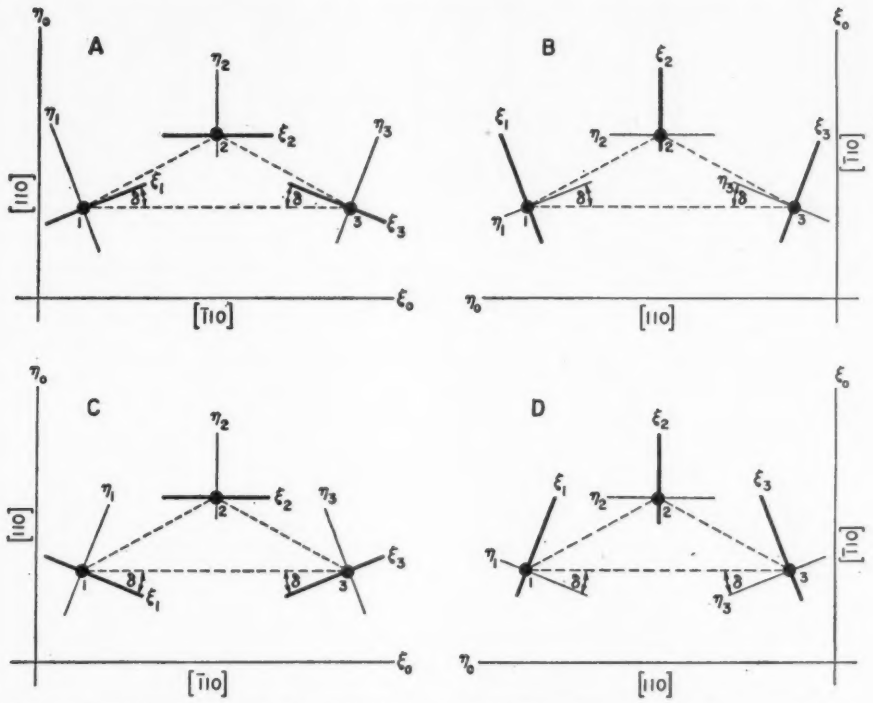

FIG. 4. Possible orientations of the principal axes of the hyperfine tensors that are compatible with the qualitative features of the hyperfine spectra. The axes ξ_i (thick lines) are the axes of maximum hyperfine interaction.

We shall now show that a first-order approximation yields a sufficiently accurate description of the hyperfine spectrum. In this approximation the hyperfine splitting can be represented as the sum of the contributions a_1, a_2 and a_3 from the three nuclei $i = 1, 2, 3$. We characterize the lines in the basic spectra by the nuclear quantum numbers m_i. The labelling given in Fig. 5 turns out to be the correct one. The basic patterns contain four independent line separations: d_1, d_2, d_3 and d_4. Second-order terms are automatically eliminated by measuring these separations as shown in Fig. 5. The three contributions a_i should be consistent with the following four equations:

$$\left.\begin{aligned} d_1 &= a_1+a_2+a_3 \\ d_2 &= -a_1+a_2+a_3 \\ d_3 &= a_1+a_2-a_3 \\ d_4 &= -a_1+a_2-a_3 \end{aligned}\right\} \qquad (2)$$

where one puts $a_1 = a_3$, $d_2 = d_3$ for the six-line pattern. It is found that these linear relations hold within a few per cent for all basic pattern in Figs. 1–3 (except, of course, for the 90° pattern). Table 1 summarizes the a_i values derived from the measured line separations d_j.

Table 1. *Contribution of the three nuclei to the hyperfine splitting for various basic spectra*

Direction of H_0	Angle between H_0 and ξ_0	a_1 (G)	a_2 (G)	a_3 (G)
[100]	0°	362	1122	362
[111]	35·26°	299	924	299
[100]	45°	192	808	334
[110]	60°	151	601	244

In the first-order approximation, the hyperfine splitting in gauss is given by the eigenvalues of the

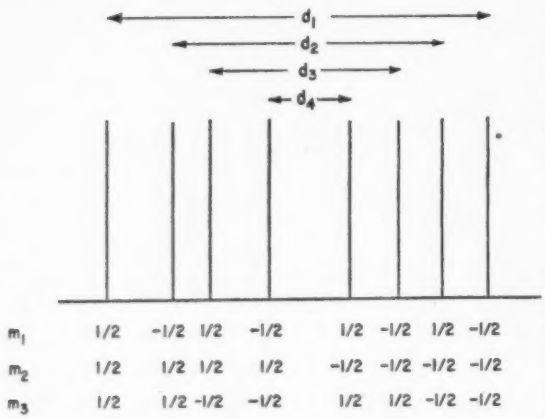

FIG. 5. Assignment of nuclear magnetic quantum numbers to the hyperfine lines of the basic spectra.

projection on the axis of the d.c. magnetic field of

$$\sum_i \boldsymbol{T}^{(i)} \cdot \boldsymbol{I}^{(i)}.$$

Therefore, the hyperfine tensors $\boldsymbol{T}^{(i)}$ can be determined directly from the quantities a_i in Table 1.

The possible orientations of the principal axes ξ_i, ζ_i and η_i that are consistent with the observed symmetry are sketched in Fig. 4. The tensor $\boldsymbol{T}^{(2)}$ is readily calculated, since it is diagonal in the system $\xi_2 = [\bar{1}10]$, $\eta_2 = [110]$ and $\zeta_2 = [001]$. Thus we have:

$$a_2(\theta) \approx g_0/g\sqrt{(\alpha^2[T_{\xi\xi}{}^{(2)}]^2+\beta^2[T_{\eta\eta}{}^{(2)}]^2+\gamma^2[T_{\zeta\zeta}{}^{(2)}]^2)}.$$

Here $g_0/g \approx 1$, and α, β and γ are the direction cosines of the d.c. magnetic field in the ξ_2, η_2, ζ_2 system. The four experimental values for $a_2(\theta)$ listed in Table 1 are consistent with such a tensorial relationship.

Table 2. Components of the diagonalized hyperfine tensors.

Nucleus i	$\lvert T_{\xi\xi}\rvert$ (G)	$\lvert T_{\eta\eta}\rvert$ (G)	$\lvert T_{\zeta\zeta}\rvert$ (G)
$i = 2$	1122	212	268
$i = 1$ and 3	378	142	80

The determination of the tensors $\boldsymbol{T}^{(1)}$ and $\boldsymbol{T}^{(3)}$ requires a little more algebra, since the angle of tilt δ (see Fig. 4) is an additional unknown quantity. Note that $\boldsymbol{T}^{(1)}$ and $\boldsymbol{T}^{(3)}$ differ only in the sign of δ. The experimental values of $a_1(\theta)$ and $a_3(\theta)$ are consistent with a tilt $\delta = 17°$. The resulting principal components of the three (diagonalized) tensors are listed in Table 2.

5. ELECTRONIC STRUCTURE OF THE V_I-CENTER

The interpretation and analysis of the hyperfine spectrum (hfs) given in Sections 3 and 4 establish that the spectrum arises from a hole localized on three F^- ions. The hole interacts with the nuclei both directly via its own dipole–dipole and contact interactions and indirectly through exchange polarization of the core.[8–10]* This hyperfine interaction is completely characterized by the hyperfine tensors $\boldsymbol{T}^{(i)}$ introduced in equation (1). It is convenient to decompose each hyperfine tensor $\boldsymbol{T}^{(i)}$ into a traceless part $\boldsymbol{P}^{(i)}$ and an invariant part $\boldsymbol{S}^{(i)}$:

$$\left.\begin{aligned} &\boldsymbol{P} = \boldsymbol{T}-\boldsymbol{S}, \\ &\boldsymbol{S} = S\boldsymbol{U}, \text{ where } \boldsymbol{U} = \text{unit tensor} \\ &S = \tfrac{1}{3}\,\mathrm{tr}\,(\boldsymbol{T}). \end{aligned}\right\} \quad (3)$$

In the vicinity of each of the three nuclei, the wave function of the hole resembles an atomic $2p$-function possibly hybridized with an atomic s-function. The p-part of the wave function contributes only to $\boldsymbol{P}$ and the s-part only to $\boldsymbol{S}$ through the direct interaction; for that reason we call $\boldsymbol{P}$ the p-part and $\boldsymbol{S}$ the s-part of $\boldsymbol{T}$. The nature of the indirect contribution can be understood as follows. Core electrons of spin opposite to the hole have an exchange interaction with it, whereas those of the same spin do not. As a result, the orbital wave functions of two core electrons of opposite spin differ somewhat. In particular, the values at the nucleus of the $1s$ and of the $2s$ wave functions are no longer the same for both spin directions. Thus, through exchange polarization of the core, a p-electron or hole can given rise to a non-vanishing s-part, even in the absence of hybridization.†

*The possibility of core polarization was neglected in Ref. (1), and was brought to our attention independently by Professor C. LONGUET-HIGGINS, Dr. J. A. POPLE, Dr. E. W. HART and Dr. G. D. WATKINS.

†There is also a modification of $\boldsymbol{P}$ but it is of no significance for the present considerations.

Separation of the tensors $\boldsymbol{T}^{(i)}$ into their respective s- and p-parts provides a basis for the qualitative determination of the electronic structure of the V_k-center. The principles employed in the analysis are derived from the following properties possessed by $\boldsymbol{T}$ in the atomic case and in the tight-binding limit: (i) For a p_ξ function, the principal components of $\boldsymbol{P}$ satisfy the relations

$$P_{\xi\xi} = -2P_{\eta\eta} = -2P_{\zeta\zeta} \qquad (4)$$

i.e. the maximum component of $\boldsymbol{P}$, $P_{\xi\xi}$, is along the lobe of the p-function. (ii) The part of S arising from hybridization of the p-function with an s-function has the same sign as $P_{\xi\xi}$. (iii) The part of S arising from core polarization has a sign opposite to that of $P_{\xi\xi}$. The basis for statement (iii) is an approximate numerical calculation made for an electron in the $2p$-shell of Na^+.[10] A physical analysis of the core-polarization effect then shows that the same sign should hold for a hole in the $2p$-shell of F^-.

The wave function of the hole in the V_k-center can be represented as a linear combination of atomic orbitals (LCAO). The actual hyperfine tensors $\boldsymbol{T}^{(i)}$ of the V_k-center then differ from what would be expected in the tight-binding limit primarily because of the overlap of the atomic orbitals centered on adjacent nuclei within the center. The narrowness of the individual lines of the spectrum indicates that overlap with atoms outside the center can be neglected. The effect of overlap within the center is to replace the equalities in (4) by a set of inequalities which can readily be inferred from the qualitative features of a given LCAO wave function. Statements (i), (ii) and (iii) are essentially unaffected by overlap, provided the overlap is not too great.

Only the magnitudes of the principal components of the $\boldsymbol{T}^{(i)}$ are determined from experiment. We have accordingly decomposed the $\boldsymbol{T}^{(i)}$ into s- and p-parts for all possible choices of the signs of $T_{\eta\eta}$ and $T_{\zeta\zeta}$ relative to that of $T_{\xi\xi}$, which is assumed positive for convenience. Examination of the results, given in Table 3, shows that the maximum component of $\boldsymbol{P}$ is $P_{\xi\xi}$ for each nucleus, whatever the choice of sign. We can immediately conclude from (i) that the lobes of the atomic p-functions in the LCAO wave function nearly coincide in direction with the principal axes ξ_i. The LCAO wave functions satisfying this requirement are depicted in Fig. 6 for each of the possible sets of axes shown in Fig. 4.

Table 3. Decomposition of the hyperfine tensors

Nucleus (i)	Sign	S	$P_{\xi\xi}$	$P_{\eta\eta}$	$P_{\zeta\zeta}$
2	++	534	588	−322	−266
	+−	355	767	−143	−623
	−+	393	729	−605	−125
	−−	**214**	**908**	**−426**	**−482**
1 and 3	++	**200**	**178**	**−58**	**−120**
	+−	147	231	−5	−227
	−+	105	273	−247	−25
	−−	52	326	−194	−132

The signs given in the second column refer to $T_{\eta\eta}$ and $T_{\zeta\zeta}$ in that order; the sign of $T_{\xi\xi}$ is assumed positive. The decomposition is carried out according to equation (3). The bold-face entries are those which satisfy equation (5) and hence are consistent with the proposed electronic structure.

For possibilities A and C of Fig. 6, the presence of a p-function along ξ on the central atom forces the wave function to be odd with respect to reflection in the $\eta_0\zeta_0$ plane passing through the central nucleus. Therefore, no hybridization with an s-function can occur on this nucleus, and $S^{(2)}$ must arise entirely from core polarization, so that it can only be negative, according to (iii). But Table 3 shows that $S^{(2)}$ is positive whatever the choice of sign, which rules out possibilities A and C.

Since the interaction of the unpaired electron with nuclei other than $i = 1$, 2 and 3 is small, we can consider the V_k-center to be a triatomic "molecule-ion". From the above analysis of the hyperfine splitting we can infer that it is almost linear. If this molecule-ion were in free space, the hole would very probably be in a $p\sigma$ state. However, we have just ruled out the possibilities of $p\sigma$ type, A and C in Fig. 6, leaving only possibilities of $p\pi$ type, B and D. The molecular binding is therefore probably weak compared to the interaction with the crystal field, indicating (*a*) that the interatomic separations are larger than those in ordinary molecules and (*b*) that there is a strong crystal field. From (*a*), it seems likely that all three atoms are near sites occupied in a perfect crystal. From (*b*), it seems likely that the molecule-ion is closely associated with a charged lattice defect. Since the annealing behavior suggests that the

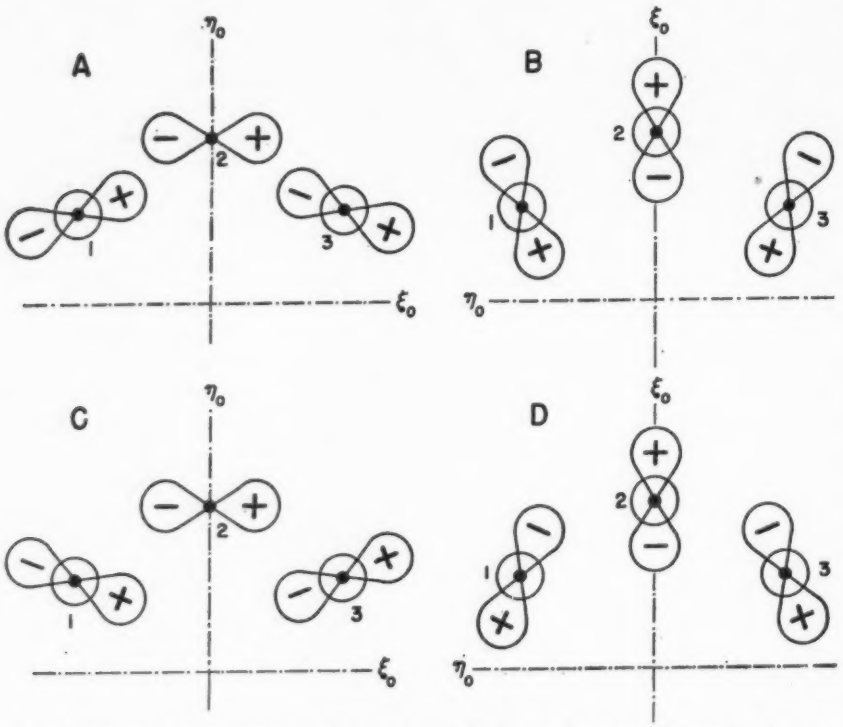

FIG. 6. Schematic representation of the various LCAO wave functions discussed in the text. The p-parts are represented by figure eights and the s-parts by circles. The relative signs of the p-parts have been assigned to give the highest energy for the level in which the electron is missing. Note the following symmetry requirements:

(a) In possibilities A and C, no s-function is allowed on the center nucleus 2, and the signs of the s-functions on the outside nuclei 1 and 3 must be opposite.

(b) In possibilities B and D, s-function on the center nucleus 2 is possible, and the signs of the s-functions on the nuclei 1 and 3 are the same.

The relative signs of the s- and p-function are specified later.

V_t-center as a whole is neutral, the lattice defect probably has a single negative charge. The simplest such defects are a positive-ion vacancy, negative-ion interstitial, and two positive-ion vacancies bound to a negative-ion vacancy in a common nearest-neighbor position. It is difficult to imagine a center containing either a positive-ion or a negative-ion interstitial which has the observed symmetry and orientation, as well as approximate collinearity of the three atoms. Further, the interstitial center would not be consistent either with (*a*) or with (*b*). We therefore propose the atomic structure depicted in Fig. 7 for the V_t-center.

This model for the V_t-center corresponds in a general way to SEITZ's[11] model for the center that gives rise to the optical V_4-band in KCl and KBr.[11] Unfortunately, none of the optical absorption bands in X-rayed LiF has been established to be the analogue of the V_4-band in KCl and KBr, nor have we attempted to correlate our magnetic resonance spectrum with an optical absorption band in LiF. The identity $V_t = V_4$ will be very difficult to prove, particularly because the hyperfine spectrum of the V_t-center is probably so complicated in KCl and KBr that it would be impossible to recognize and analyze it.

The crystal fields produced by the three vacancies displace the three fluorine atoms towards

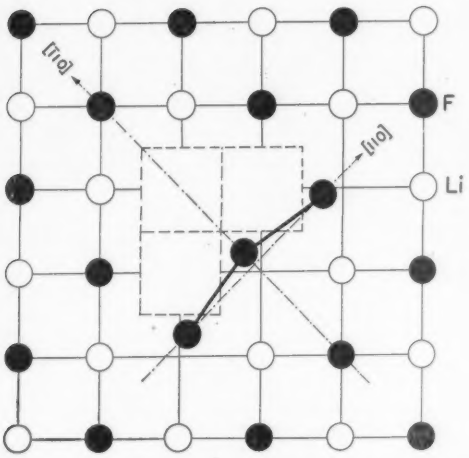

FIG. 7. Proposed association of the triatomic "molecule-ion" with a vacancy complex.

the vacancy complex in the manner indicated in Fig. 7 because of the net positive charge on each atom. In addition to its displacement, each atom is polarized so as to increase the probability of finding the hole near the vacancy complex. This polarization is the source of the high degree of s–p hybridization indicated by the large values of $S^{(i)}$ in Table 3. The polarization argument rules out possibility B, leaving only D (see Fig. 6), and requires that the relative signs of the s- and p-orbitals on a single atom be as shown in Fig. 8. Finally, the requirement of maximum energy for the electron-deficient energy level leads to the relative signs of the orbitals on different atoms shown in Fig. 8, which completes the qualitative determination of the electronic structure of the V_t-center.

We must now establish that the proposed electronic structure is consistent with the observed hfs. We use principles (i)–(iii) to do so, noting that the relative weakness of the interatomic bonding lends an *a posteriori* justification to the approximations made in the analysis. The overlaps suggested by Fig. 8 reduce the amplitude of the wave function in the regions between atoms 1 and 2 and between atoms 2 and 3, the effect being maximal in the $\xi_0\eta_0$ plane. The inequalities corresponding to equation (4) are therefore

$$2|P_{\zeta\zeta}^{(i)}| \gtrsim |P_{\xi\xi}^{(i)}| \gtrsim 2|P_{\eta\eta}^{(i)}| \qquad (5)$$

Further, $P_{\zeta\zeta}$ and $P_{\eta\eta}$ should both be negative, but this occurs for all choices of sign. There is indeed one choice of signs for each nucleus which is

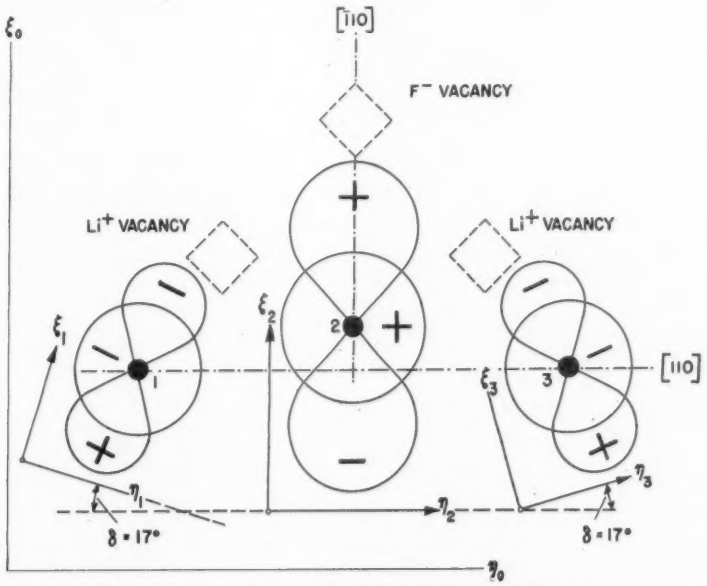

FIG. 8. Relative signs and orientation of the wavefunctions suggested by crystalline-field and energy-level considerations.

consistent with equation (5), namely the choice corresponding to the bold-face entries in Table 3.

We note that the pattern of overlap in Fig. 8 suggests an angle of tilt for the p-functions on nuclei 1 and 3 somewhat larger than δ. We also note that the large, positive values of S for all three nuclei suggest a relatively small value for the core-polarization contribution to S.

To summarize, by comparative consideration of hyperfine tensors, annealing behavior, molecular energy levels, symmetry properties and crystal fields, we have determined both the structure of the V_k-center and the signs of the hyperfine tensor components. It is noteworthy that this analysis proved possible and that it unexpectedly led us to a wave-function of $p\pi$ type.

Acknowledgement—The authors thank Dr. V. HEINE, Professor C. LONGUET-HIGGINS, Dr. J. A. POPLE, Dr. E. W. HART and Dr. G. D. WATKINS for illuminating discussions on the problem of core polarization.

REFERENCES

1. COHEN M. H., KÄNZIG W. and WOODRUFF T. O., *Phys. Rev.* **108,** 1096 (1957).
2. CASTNER T. G. and KÄNZIG W., *J. Phys. Chem. Solids* **3,** 178 (1957).
3. WOODRUFF T. O. and KÄNZIG W., *J. Phys. Chem. Solids* **5,** 268 (1958).
4. KÄNZIG W. and WOODRUFF T. O., *J. Phys. Chem. Solids* **9,** 70 (1959).
5. PORTIS A. M., *Phys. Rev.* **91,** 1071 (1953).
6. GHORMLEY J. A. and LEVY H. A., *J. Phys. Chem.* **56,** 548 (1952).
7. WIEGAND D. A. and SMOLUCHOWSKI R., *Phys. Rev.* **110,** 991 (1958).
8. PRATT G. W., *Phys. Rev.* **102,** 1303 (1956).
9. HEINE V., *Phys. Rev.* **107,** 1002 (1957).
10. COHEN M. H., GOODINGS D. A. and HEINE V., *Proc. Phys. Soc.* **73,** 811 (1959).
11. SEITZ F., *Rev. Mod. Phys.* **26,** 7 (1954).

VOL
11
195

J. Phys. Chem. Solids Pergamon Press 1959. Vol. 11. pp. 131–139. Printed in Great Britain.

THE ENERGY-DEPENDENCE OF ELECTRON MASS IN INDIUM ANTIMONIDE DETERMINED FROM MEASUREMENTS OF THE INFRARED FARADAY EFFECT

S. D. SMITH,* T. S. MOSS and K. W. TAYLOR†

Royal Aircraft Establishment, Farnborough, Hants.

(*Received* 9 *February* 1959; *revised* 1 *April* 1959)

VOL. 11 959

Abstract—Measurements of Faraday rotation due to free electrons have been used to deduce values of dE/dk as a function of k_P for the conduction band of InSb. An E/k curve is obtained by numerical integration to a height of 0·15 eV from the bottom of the band. The results show excellent agreement with the band shape calculated by KANE by the $k \cdot p$ perturbation. A value of m_0^*, the mass at $k = 0$, is found from the slope of dE/dk at $k = 0$, the average value obtained being 0·0143 m_0.

The rotation due to free electrons is found to have an opposite sense to that associated with inter-band transitions.

1. INTRODUCTION

THE Faraday effect, i.e. the rotation of the plane of polarization of a beam of radiation under the influence of a magnetic field along the direction of propagation, is given by:

$$\theta = \tfrac{1}{2}(\omega l/c)(n_+ - n_-) \qquad (1)$$

where ω is the circular frequency, l the thickness of the specimen, and n_+ and n_- are the refractive indices for the right and left circularly polarized components of the plane-polarized beam.

At wavelengths beyond the absorption edge of a semiconductor, this differential magnetic dispersion has two origins: (*a*) free carriers in either valence or conduction bands, when the effect measures the differential dispersion to be associated with cyclotron-resonance absorption, and (*b*) bound carriers, in which the dispersion is associated with the absorption found in band-to-band magneto-optical effects. The rotation due to (*b*) has been found for many materials since 1877 and recently for some semiconductors by VON KIMMEL[1]. The rotation is characterized by a dependence on wavelength as $1/\lambda^2$.

MITCHELL[2] suggested that the free-carrier effect, which by contrast increases as λ^2, could be used to determine the effective mass of free carriers. In the present paper measurements of this effect are described, and the method is used to explore the conduction band shape in indium antimonide. The measurement of dispersion, implicit in the Faraday rotation, is, unlike absorption, independent of collision time τ and depends only upon the structure of the energy band and the number of carriers (see also SPITZER and FAN[3]). Thus, by comparison with a cyclotron-resonance (CR) experiment, the requirements are far less stringent, and measurements may be performed under a wide variety of conditions of temperature, number of carriers wavelength and magnetic field.

The Faraday effect is of particular interest in the study of the conduction band of InSb, where the CR measurements (DRESSELHAUS *et al.*[4], KEYES *et al.*[5]) show that the band is markedly non-parabolic, although the energy surfaces are spherical.

Indium antimonide is also convenient because the rotation depends on $1/m^{*2}$ and is therefore large. Small magnetic fields only are required, and the conditions may be chosen so that the quantum effects associated with large Landau splitting in high fields and at very low temperatures may be

*Present address: Imperial College Field Station, Silwood Farm, Ascot, Berks.

†Present address: Royal Marsden Hospital, London, S.W.7.

avoided, with resultant simplification of the theoretical treatment.

It should be noted that the infrared free-carrier Faraday effect, in which $\omega \gg \omega_c$ and $\tau\omega \gg 1$, gives quite different information from the microwave effect observed by RAU and CASPARI[6] (where $\omega < \omega_c$), which essentially measures the mobility of the carriers.

The experimental values of m^* obtained as a function of k_F, the wave vector at the Fermi surface, are compared with theoretical predictions from KANE's band theory.[7]

Preliminary measurements on InSb were described by us at the Brussels Solid State Congress and the Rochester Semiconductor Conference.

2. THEORY OF FREE CARRIER ROTATION

(a) *Simplified theory*

We shall first discuss the rotation in a simple classical form and then show how it can be generalized to the conditions of our experiment by quoting results from the treatment of STEPHEN and LIDIARD[8]. From the classical equation of motion of an electron of mass, m^*, in a field B parallel to the direction of the radiation, the complex refractive indices $(n_\pm - ik_\pm)$ for right and left circularly polarized radiation are given by:

$$(n_\pm - ik_\pm)^2 = \epsilon + \frac{Ne^2/m^*\omega\epsilon_0}{-\omega \pm \omega_c \pm i/\tau} \qquad (2)$$

where $\omega_c = eB/m^*$ is the cyclotron resonance frequency.

Now

$$2n_\pm k_\pm = \mp \frac{Ne^2}{m^*\omega\epsilon_0} \cdot \frac{1/\tau}{(-\omega \pm \omega_c)^2 + 1/\tau^2} \qquad (3)$$

gives CR absorption for n_+k_+, which depends upon $1/\tau$ and hence the relaxation mechanism. Observation of the resonance itself requires further that $\omega\tau \gg 1$. By contrast the magnetic dispersion is given by:

$$n_\pm^2 - k_\pm^2 = -\frac{Ne^2}{m\omega\epsilon_0} \frac{(\omega \pm \omega_c)}{(-\omega \pm \omega_c)^2 + 1/\tau^2} \qquad (4)$$

Observation of Faraday rotation well away from resonance in small magnetic fields implies $\omega^2 \gg \omega_c^2$, $\omega^2 \gg (1/\tau)^2$ at wavelengths $\sim 20\mu$ and $k^2 \ll n^2$. Hence from equations (4) and (1) we obtain:

$$\frac{n\theta}{l} = \frac{BNe^3}{2c\epsilon_0 m^{*2}\omega^2} \qquad (5)$$

which is seen to be independent of τ. The rotation may also be expressed in terms of free-carrier dispersion:

$$\frac{\theta}{l} = \frac{\omega_c\lambda}{2c} \cdot \frac{dn}{d\lambda} = \frac{eB}{m} \cdot \frac{\lambda}{2c} \cdot \frac{dn}{d\lambda} \qquad (6)$$

In comparison with the observation of the cyclotron resonance frequency ω_0, measurement of θ away from resonance implies observing the integrated effect of all sources of magnetic dispersion. However, lattice vibrations of atoms (*Reststrahlen* bands) do not contribute (owing to the dependence on $1/m^{*2}$), and in the case of InSb the holes in the valence bands, having a much larger effective mass, also give a negligible effect in intrinsic or n-type material. Thus, if the interband effect is made negligible by using wavelengths sufficiently far from the absorption edge, the rotation is dominated by cyclotron-resonance dispersion of conduction electrons.

(b) *General result*

STEPHEN and LIDIARD[8], in a general treatment, relate the Faraday rotation, θ, to the imaginary part of the conductivity in the magnetic field. This conductivity term may be expressed in tensor notation (ABELES and MEIBOOM[9]) for arbitrary energy surfaces.

(c) *Quantum limits and the non-quadratic dependence of E on k*

The conductivity may be obtained from the Boltzmann transport equation, so that it is relevant to examine the quantum limits to discover under what conditions this treatment holds. With low magnetic fields, the conduction band can be filled to a much higher energy than the distance between adjacent Landau levels, so that the average energy of the electrons $\gg h\omega_c$ (Fig. 1). Also λ must be $\gg \sqrt{(h\tau/2m)}$, which is well satisfied for wavelengths $> 10\mu$, so that the wave-packet approach inherent in the Boltzmann treatment is justified.

For the particular case of degenerate filling and spherical energy surfaces, STEPHEN and LIDIARD[8]

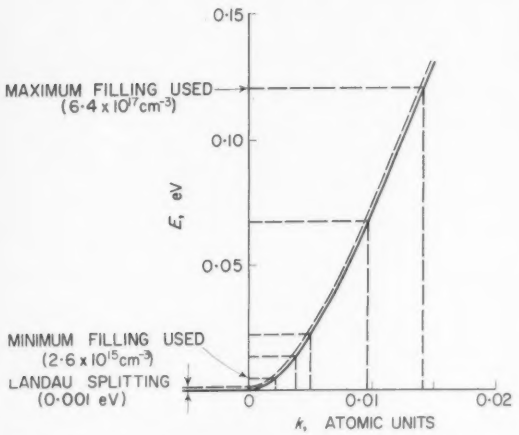

FIG. 1. Schematic representation of Landau splitting and positions of Fermi levels involved in the experiments.

find from the Boltzmann treatment that:

$$\frac{\theta}{l} = \frac{BNe^3}{2nc\epsilon_0\omega^2}\left(\frac{1}{\hbar^2 k}\cdot\frac{dE}{dk}\right)_F^2 \qquad (7)$$

where the subscript F means that k and dE/dk are taken at the Fermi surface. This result is independent of the form of the E versus k curve. The rotation θ is thus still given by equation (5), in which:

$$\frac{1}{m^*} = \frac{1}{\hbar^2 k_F}\left(\frac{dE}{dk}\right)_F \qquad (8)$$

Thus, by varying k_F, i.e. by varying

$$N = \frac{2}{(2\pi)^3}\frac{4\pi k_F^3}{3} \qquad (9)$$

the shape of the E versus k curve can be explored. (A similar result for the case of free-carrier dispersion of degenerate materials in the absence of a magnetic field has been obtained by SPITZER and FAN[3]). In the case of spherical surfaces and when $E \propto k^2$, this result reduces to the more usual effective mass concept, namely

$$\frac{1}{m^*} = \frac{1}{\hbar^2}\cdot\frac{d^2E}{dk^2}$$

With a parabolic band, this latter result is obtained independently of the statistics. The possibilities are summarized in Table 1.

The number of carriers N is determined by Hall-effect measurements, and in the degenerate case this is given simply by:

$$R = \frac{1}{Ne}$$

and is again independent of the form of $E(k)$ for spherical surfaces.

(d) *Interband Faraday effect and the sense of rotation*

Under the conditions laid down in (*c*), this rotation will be of the form $\omega^2 AB/(\omega^2-\omega_g^2)^2$, where ω_g is the frequency corresponding to the energy gap. It may be deduced from a paper by BURSTEIN *et al.*† that the sense of the rotation is clockwise looking along the radiation for a semiconductor with simple bands, but may depend upon the detailed nature of the valence band in more complex situations. The free-carrier effect has a rotation which is anti-clockwise looking along the radiation for electrons, and the opposite for holes. It will be seen that in nearly all cases the interband effect is

† To be published in *Phys. Rev*, see *Phys. Rev. Letters* **2**, 15 (1959).

Table 1. *Interpretation of m* for spherical energy surfaces*

Band shape	Degenerate statistics	Non-degenerate statistics
$E \propto k^2$	$\frac{1}{m^*} = \frac{1}{\hbar^2}\cdot\frac{d^2E}{dk^2}$	$\frac{1}{m^*} = \frac{1}{\hbar^2}\cdot\frac{d^2E}{dk^2}$
E not $\propto k^2$	$\frac{1}{m^*} = \frac{1}{\hbar^2 k_F}\left(\frac{dE}{dk}\right)_F$	Can be computed if E–k relationship is known

negligible, but, if necessary, corrections may be applied to estimate the total free-carrier effect.

3. EXPERIMENTAL

(a) *Summary of experimental conditions*

Dividing the Faraday rotation θ by the free-carrier absorption coefficient K, we obtain:

$$\frac{\theta}{lK} = \mu B \qquad (10)$$

where μ is the mobility. This determines the energy that can be transmitted through a specimen for a given rotation θ and so affects the sensitivity of the measurement.

The experimental conditions used were:

(i) The wavelength region 15–20μ was chosen to minimize absorption-edge effects, to give sufficient variation to test λ^2-dependence and yet still retain sufficient energy for accurate measurements. As described later, a suitable polarizer for this region had to be made.

(ii) It was necessary to use temperatures low enough to ensure that the samples were degenerate, so that k_F was well defined. This also had the virtue of increasing μ, and so increasing the sensitivity. This requirement was readily met by cooling with liquid nitrogen.

(iii) The magnetic field was varied between 500 and 5000 G to check linearity. Thereafter most measurements were made at 2000 G, at which field $\hbar\omega_c \doteqdot 0{\cdot}002$ eV.

(iv) The number of carriers varied between 3×10^{14} and $6{\cdot}4\times10^{17}$ cm^{-3} in the specimens examined. The upper limit could be extended if suitable material were available, whereas for the lowest concentrations rotations were comparable with residual interband effects. At the lowest filling $E_F - E_c$ was several times $\hbar\omega_c$.

(b) *The apparatus*

The polarizer and analyser were both constructed from piles of 12 sheets of polyethylene (8μ thick) set at the Brewster angle. The use of polyethylene instead of selenium, which has previously been used for infrared polarizers, has a number of advantageous features. The construction of the polarizer is extremely simple and a polarization of over 90 per cent is achieved. The polyethylene however, scatters significantly in the visible region, so that the image of the source is quite diffuse when viewed through the polarizer. An examination of the infrared image was made by focussing the source (a Nernst filament) on the entrance slit of a spectrometer and noting the change in signal as the source was moved progressively perpendicular to the optical axis of the system through a distance of a few millimetres. At 16μ (i.e. 30 times visible wavelengths), it was found that the image was not distorted appreciably. Absorption bands exist in polyethylene up to 14μ, but beyond this it shows excellent transparency. However, the polarizer can be used at selected wavelengths down to 6μ, and Faraday rotations were measured over the whole range 6–20μ.

Radiation from the source passed normally through the specimens and was at an angle of 50° to the magnetic induction B, the rotation being proportional to the resolved component of the field along the direction of the radiation. After passing through the polarizer, the beam was focussed on to an area of specimen 2×5 mm and thence through the analyser on to the entrance slit of a Leiss double monochromator in which either KBr or NaCl prisms were used. As the optics of the spectrometer cause significant polarization, the "analyser" was arranged to polarize in the same plane as the spectrometer and the "polarizer" made rotatable.

Observations were made by driving the polarizer through 180° from the "parallel" position through the "crossed" position and recording the detector (thermocouple) output. A symmetrical minimum was recorded. A contactor marked every 5° on the chart, and the position of the minimum was found from a number of symmetrical points (away from the minimum) where the signal was changing rapidly with angle. The magnetic field was then reversed, so reversing the rotation. The scan was repeated and the angular distance between the two minima found. Accuracy of $\pm1°$ was usually obtained.

Measurements at 77°K were made with the specimen clamped between copper plates in contact with liquid nitrogen in a cell with KRS 5 windows.

(c) *Hall-effect measurements to determine N*

Specimens $10\times1\times1$ mm with ground surfaces were cut from material adjacent to that on which

VOL 11 195

the Faraday rotation was measured. Subsequently, the actual specimens for which the rotation was measured were used. Dimensions were uniform to ~ 1 per cent and the length-to-width ratio was $> 5{:}1$ to avoid end effects. Spring-loaded platinum point contacts were used for both current and Hall probes, as soldered contacts gave unreliable results on the purer specimens owing to the introduction of impurities. The small diffusion length (a few microns) in InSb ensures that injection effects are negligible. Results obtained were independent of the dimensions and probe pressure, the spread in the Hall coefficient being < 5 per cent.

A number of considerations lead to the use of the relation:

$$R = \frac{1}{Ne} \qquad (11)$$

to evaluate the electron density: (i) the product of carrier density and mobility for holes was in all cases < 2 per cent of that of the electrons; (ii) STEPHEN and LIDIARD[8] have shown that equation (11) applies for degenerate filling in the case of spherical surfaces independent of the form of $E(k)$; (iii) R was constant for fields > 800 G and the measuring field was > 1000 G; R was slightly greater below 800 G, a result also found by FREDERIKSE and HOSLER[10] so that the use of the high-field approximation is well supported; (iv) several workers[11–14] have shown that energy-independent scattering applies at least up to room temperature.

Determinations of carrier densities are estimated to be accurate within ± 5 per cent.

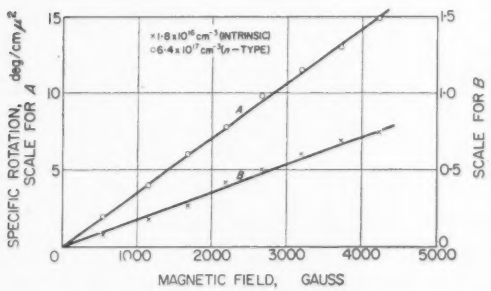

FIG. 2. Magnetic-field dependence of Faraday effect in InSb.

4. RESULTS

(a) *Dependence of Faraday rotation on magnetic field*

The linear dependence on magnetic field predicted by equation (5) was tested for fields between 500 and 5000 G. The results for two specimens with 2×10^{16} and $6{\cdot}4\times10^{17}$ conduction electrons are shown in Fig. 2. Good linearity is found in both cases, the greater scatter in the case of the intrinsic specimen being due to the sharp temperature-dependence of the number of carriers under these conditions.

(b) *Wavelength-dependence*

The primary measurements of the wavelength-dependence of Faraday rotation at 77°K for specimens with N between 3×10^{14} and $6{\cdot}4\times10^{17}$ cm^{-3} are shown in Figs. 3 and 4. The free-carrier effect increasing as λ^2 is arbitrarily plotted positive, and the results show that the interband effect has the opposite sense. To determine the free-carrier

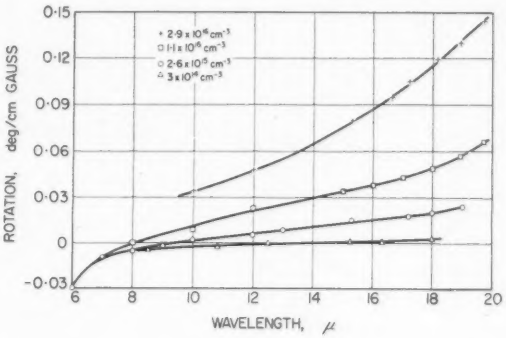

FIG. 3

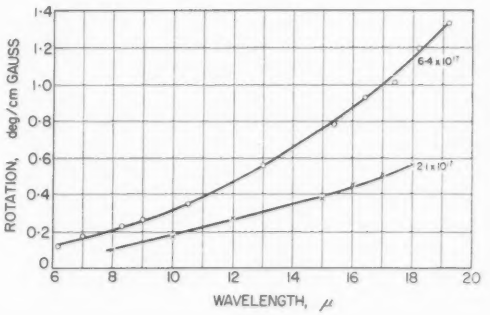

FIG. 4

FIGS. 3 and 4. Faraday rotation in InSb.

effect, and hence the effective mass of electrons in the conduction band, it is necessary in some cases to subtract this residual interband effect. The results for the 3×10^{14} cm^{-3} specimen show that this residual is negligible in all other specimens beyond 15μ, as the band-to-band effect does not depend significantly on carrier concentration. Near the absorption edge, however, the gap shift with filling will influence the interband effect.

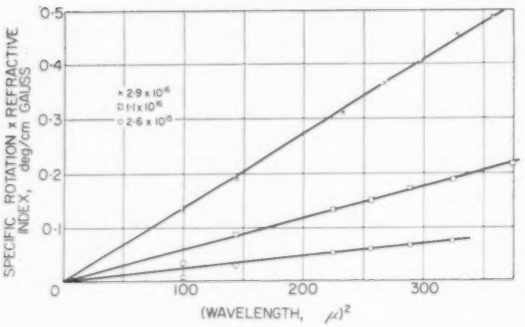

FIG. 5. Wavelength-dependence of Faraday effect in InSb.

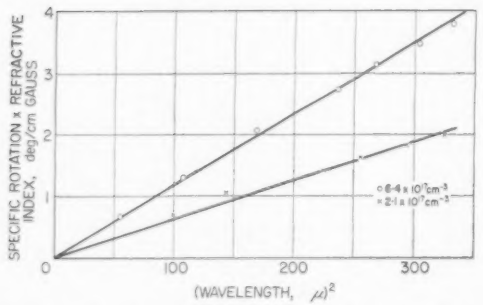

FIG. 6. Wavelength-dependence of Faraday effect in n-type InSb.

The frequency-dependence of the rotation is exhibited in Figs. 5 and 6, in which $n\theta$ is plotted against λ^2. Good straight lines are obtained between 10 and 20μ for the three highest electron densities. For the cases of $N=1{\cdot}1\times10^{16}$ and $N=2{\cdot}6\times10^{15}$, the points at $\lambda^2=100$ have dropped below the lines as a result of the residual interband rotation, which is more nearly comparable with the free-carrier effect up to longer wavelengths in these purer specimens than in the impure ones. Good linearity is still obtained however between 15 and 20μ. It should also be noted that the value of refractive index, $n(\lambda)$, depends upon the number of free carriers. Moss *et al.*[15] have shown that at $N=2{\cdot}0\times10^{16}$, the largest contribution to the dispersion comes from the *Reststrahlen* band. Thus, for electron concentrations up to 3×10^{16}, the dispersion, which amounts to $2\frac{1}{2}$ per cent in n from 12–20μ, is essentially independent of carrier concentration, so that the measured dispersion[15] for $N=2{\cdot}0\times10^{16}$ was used to compute $n\theta$ for all the cases in Fig. 5. For higher concentrations, the free-carrier effect dominates the dispersion and for $N=6{\cdot}4\times10^{17}$ amounts to ~25 per cent in n between 12 and 20μ. Values of n for the $6{\cdot}4\times10^{17}$ cm^{-3} specimen were taken from SPITZER and FAN[3] and verified by a determination of relative dispersion by interference fringes on the actual specimen. Values of n for the case of $N=2{\cdot}0\times10^{17}$ could be calculated satisfactorily by adding the appropriate free-carrier effect to our measured dispersion for $N=2{\cdot}0\times\times10^{16}$.

By determining effective mass from the slope of $n\theta$ versus λ^2, it was therefore possible to avoid spurious interband rotation and to correct satisfactorily for any free-carrier dispersion, so that neither of these effects caused significant errors in the values of m^*. The values of m^* for the various specimens which should be accurate to ±5 per cent, are quoted in Table 2. Values of k_F calculated from equation (9) are also given.

Table 2

N (cm^{-3})	Refractive index × specific rotation at 18μ	m^*/m_0	k_F (atomic units)
$6{\cdot}4\times10^{17}$	3850	0·029	0·014
$2{\cdot}0\times10^{17}$	2040	0·022	0·0096
$2{\cdot}9\times10^{16}$	450	0·0178	0·0050
$1{\cdot}1\times10^{16}$	193	0·0165	0·0037
$2{\cdot}6\times10^{15}$	71	0·0131	0·0023
$\sim3\times10^{14}$	~8	~0·013	

The value obtained for 3×10^{14} is inaccurate, as the rotation was very small, but is consistent with a mass of 0·013.

5. DISCUSSION

From the values of m^*/m_0 in Table 2 we may obtain values of $dE/dk = k_F/m^*$ (in atomic units where $\hbar = m_0 = 1$) as a function of k_F, and these are plotted in Fig. 7. This presentation allows us to extrapolate to $k = 0$, where, on theoretical grounds,[7] we expect $dE/dk = 0$ and further $1/m^* = d^2E/dk^2$ at $k = 0$.

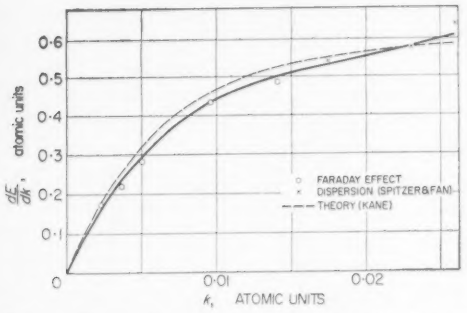

FIG. 7. Slope of conduction band in InSb (in atomic units).

From Fig. 7 values of dE/dk are obtained at equal intervals Δk of k. Hence values of ΔE are obtained which can be integrated numerically to give $E(k)$. The results are shown in Fig. 8.

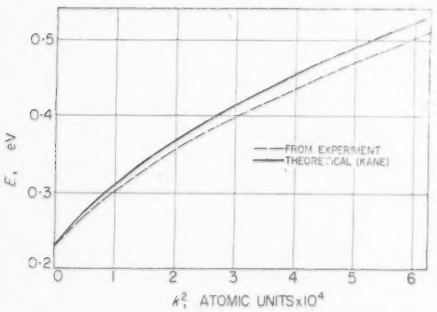

FIG. 8. Conduction band in InSb.

In order to make a direct comparison between KANE's calculations[7] and the experimental results of Fig. 7, we require theoretical values of dE/dk as a function of k. From the $k \cdot p$ perturbation approach, KANE[7] finds that the conduction band is given by

$$E'(E'-E_G)(E'+\Delta)-k^2P^2(E'+2\Delta/3) = 0 \qquad (12)$$

where

$$E' = E-\hbar^2k^2/2m_0 \qquad (13)$$

E_G is the energy gap at 0°K (0·23 eV), Δ is a measure of the spin-orbit splitting and is estimated as 0·9 eV, and P^2 is the matrix element, which is given by:

$$\frac{2P^2}{3}\left(\frac{2}{E_G}+\frac{1}{E_G+\Delta}\right) = \hbar^2/m_0{}^*-\hbar^2/m_0 \qquad (14)$$

where $m_0{}^*$ is the effective mass at $k = 0$. KANE takes $P^2 = 0{\cdot}44$ atomic units.

Equation (12) includes the valence and conduction band interactions only. KANE makes a more refined calculation to include perturbations due to higher bands, the greatest effect being to reduce E by about 4 per cent at the highest k value (0·015 atomic units) of our experimental points. The term $\hbar^2k^2/2m_0$ is negligible compared with E over this same range.

From equation (12):

$$\frac{dE'}{dk} = 650k\frac{(E'+0{\cdot}6)^2}{2E'^3+2{\cdot}47E'^2+0{\cdot}805E'-0{\cdot}124}$$

eV per atomic unit

where k is found from equation (12).

The theoretical values of dE/dk, shown dashed in Fig. 7, are in good agreement with the experimental points. KANE's theoretical band shape is therefore strongly supported by our experimental results, as are also his band-structure constants. The value of E_G(0·23 eV) is that appropriate to 0°K. At 77°K, the temperature used for the Faraday measurements, the energy gap is 0·225 eV, but this difference is too small to have any significance. The results indicate that the band shape is not sensitive to small changes in E_G and also that it is unchanged by the filling of the conduction band inherent in the measurements at large k_F.

The comparison has been extended to include the results of SPITZER and FAN[3], who deduce an effective mass from measurements of free-carrier dispersion. Their measurements were made on heavily doped degenerate material, where free-carrier dispersion is dominant (i.e. $N > 2\times10^{17}$), and the interpretation of m^* is identical with that in the Faraday method. Their results (shown in Fig. 7) join smoothly with the Faraday measurements near $k = 0{\cdot}015$ atomic units and extend the comparison to $k = 0{\cdot}025$ atomic units, or 0·3 eV above

the bottom of the conduction band. At this point the number of carriers is 4×10^{18} and the agreement with theory is somewhat worse.

To illustrate the non-parabolic nature of the conduction band, the experimental values of $E(k)$ obtained by integrating Fig. 7 are plotted against k^2 in Fig. 8. Good agreement is again obtained with KANE's theory.

As the conduction band must become parabolic as $k\to0$, the slope of dE/dk at $k=0$ in Fig. 7, gives a method of finding m_0^*, the effective mass at $k=0$. However, it is not possible to draw the tangent to the curve of Fig. 7 with great accuracy, and it is preferable to compute values of m_0^* from equations (12) and (14). It may be shown that (in atomic units),

$$\frac{1}{m_0^*}=\frac{A}{m^*}\left[\frac{k^2}{m^*E_G}+\sqrt{1+\left(\frac{k^2}{m^*E_G}\right)^2}\right]-1 \quad (15)$$

where the parameter $A=1$ for small energies and $A=0{\cdot}97$ for energies $\sim0{\cdot}1$ eV above the bottom of the conduction band. This expression is accurate to $<\pm1$ per cent for the experimental points measured and is also very insensitive to the value used for Δ, the spin-orbit splitting. For example, changing Δ from 0·5 to 1·4 eV changes m_0^* by <1 per cent.

The results are given in Table 3.

Table 3. Computed effective mass at $k=0$

k	m^*/m_0	m_0^*/m_0
0·014	0·029	0·0146
0·0096	0·022	0·0140
0·0050	0·0178	0·0153
0·0037	0·0165	0·0152
0·0023	0·0131	0·0127

The average for the zero-k mass is thus:

$$m_0^*=0{\cdot}0143m_0(\pm0{\cdot}0005m_0).$$

The main sources of error responsible for the scatter in the results are measurements of Ne and possible differences in N in the Hall and Faraday effect experiments. The measurement of the resolved field due to difficulty in determination of the angle between the magnetic field and the direction of the radiation in the material may give a small additional error.

In order to compare the results with other experimental determinations of effective mass, it is necessary to decide which part of the E–k curve is involved in such measurements. For example, the microwave cyclotron-resonance experiments of DRESSELHAUS *et al.*[4] used a very small magnetic field and a small number of optically excited carriers. A value of $m^*=0{\cdot}013\ m_0$, consistent with a low value of k, was obtained.

Infra-red CR measurements at high magnetic fields involve transitions over a significant range of energies in the conduction band, and the theoretical treatment of WALLIS[16] has established the form of the CR absorption as a function of frequency for a non-parabolic conduction band. WALLIS was unable to make a detailed comparison with the measurements of KEYES *et al.*,[5] since these give the absorption coefficient as a function of magnetic field at a fixed frequency. Under these conditions, both the concentration of conduction electrons and the fourth-order constant μ are functions of field. This constant is given by:

$$\mu=m_0^{*2}\hbar\omega_c|\mathscr{E}_c^{xxxx}| \quad (16)$$

where ω_c is the resonant frequency implied by a mass m_0^* and from KANE's theory

$$\mathscr{E}_c^{xxxx}=-\left[\frac{m_0}{m_0^*}-1\right]^2\Big/4E_Gm_0^2 \quad (17)$$

WALLIS has estimated μ from the linear dependence of apparent effective mass, m_l^*, on magnetic field, which was observed by KEYES *et al.*[5] From the slope of the experimental data ($8\mu m_0^*/H$) and taking $m_l^*=0{\cdot}013m_0$ and $H=80{,}000$ G, he finds $\mu=0{\cdot}06$. WALLIS also estimates μ theoretically from equations (16) and (17) by taking $m_0^*=0{\cdot}013m_0$ and $E_G=0{\cdot}18$ eV, whence at 80,000 G $\mu=0{\cdot}096$, which is only in order-of-magnitude agreement with the experimental value.

The good agreement with KANE's theory found in the present work suggests that the *theoretical* estimate should be reliable, and substituting our value of $0{\cdot}0143m_0$ for m_0^*, we obtain $\mu=0{\cdot}088$ for $E_G=0{\cdot}18$ eV at 80,000 G, or otherwise from equation (17):

$$\mathscr{E}_c^{xxxx}=-\frac{124}{E_G}\quad\text{(in atomic units).}$$

In the work of BOYLE and BRAILSFORD[17], at a wavelength of 80μ, the transitions would be from $\sim 0{\cdot}008$ to $\sim 0{\cdot}023$ eV above the bottom of the (zero field) conduction band. As this energy spread is small, the effective mass found must be representative of the value only a little above $k = 0$. The result obtained, $m^* = 0{\cdot}0146\, m_0$, is thus in accord with the present work.

In the magneto-absorption experiments of ZWERDLING *et al.*[18], the transitions involved are from the valence band to the conduction band. As the hole masses are relatively high, the main effect is due to conduction electrons, the lowest energy transitions being to the first Landau level at $\frac{1}{2}\hbar\omega_c$ above the bottom of the band. These workers used fields of 20,000–40,000 G, corresponding to energies 0·01–0·02 eV above the bottom of the conduction band, and obtained a mass of $m^* = 0{\cdot}014\, m_0$. As the method of analysis used assumed m^* to be independent of energy, and as the valence band may have a significant effect in this experiment, the agreement with the present work is probably as good as can be expected.

We may conclude that the Faraday effect gives a very satisfactory method for determination of conduction-band shape and a method to determine m_0^*, i.e. the mass at the bottom of the band. The accuracy of determination of individual masses is somewhat less than that with CR or magneto-absorption, but the experiment is more flexible and the interpretation more certain.

Acknowledgements—Thanks are due to Dr. D. G. AVERY, Royal Radar Establishment, Malvern, for assisting in the supply of InSb; to Dr. A. B. LIDIARD and Dr. M. J. STEPHEN for helpful discussions; and to Miss D. WEBBER and Mr. I. D. BIRCH for assistance with the experiments.

This paper is British Crown Copyright and is published by permission of the Controller, H.B.M. Stationery Office.

REFERENCES

1. VON KIMMEL H., *Z. Naturforsch.* **12a,** 1016 (1956).
2. MITCHELL E. W. J., *Proc. Phys. Soc.* B**68,** 973 (1955).
3. SPITZER W. G. and FAN H. Y., *Phys. Rev.* **106,** 882 (1957).
4. DRESSELHAUS G., KIP A. F., KITTEL C. and WAGONER G., *Phys. Rev.* **98,** 556 (1955).
5. KEYES R. J., ZWERDLING S., FONER S., KOLN H. H. and LAX B., *Phys. Rev.* **104,** 1804 (1956).
6. RAU R. R. and CASPARI M., *Phys. Rev.* **100,** 632 (1955).
7. KANE E. O., *J. Phys. Chem. Solids* **1,** 249 (1957).
8. STEPHEN M. J. and LIDIARD A. B., *J. Phys. Chem. Solids* **9,** 43 (1959).
9. ABELES B. and MEIBOOM S., *Phys. Rev.* **95,** 31 (1954).
10. FREDERIKSE A. P. R. and HOSLER W. R., *Phys. Rev.* **108,** 1136 (1957).
11. EHRENREICH H., *J. Phys. Chem. Solids* **2,** 131 (1957).
12. HOWARTH D. J., JONES R. H. and PUTLEY E. H., *Proc. Phys. Soc.* B**70,** 124 (1957).
13. HILSUM C. and BARRIE R., *Proc. Phys. Soc.* **71,** 676 (1958).
14. KURNICK S. W. and ZITTER R. N., *J. Appl. Phys.* **27,** 278 (1956).
15. MOSS T. S., SMITH S. D. and HAWKINS T. D. H., *Proc. Phys. Soc.* **70,** 776 (1957).
16. WALLIS R. F., *J. Phys. Chem. Solids* **4,** 101 (1957).
17. BOYLE W. S. and BRAILSFORD A. D., *Phys. Rev.* **107,** 903 (1957).
18. ZWERDLING S., LAX B. and ROTH L. M., *Phys. Rev.* **108,** 1402 (1957).

J. Phys. Chem. Solids Pergamon Press 1959. Vol. 11. pp. 140–148. Printed in Great Britain.

THE EFFECT OF PRESSURE ON ZINC BLENDE AND WURTZITE STRUCTURES*

A. L. EDWARDS, T. E. SLYKHOUSE and H. G. DRICKAMER

Department of Chemistry and Chemical Engineering, University of Illinois, Urbana, Illinois

(*Received* 6 *January* 1959; *revised* 13 *February* 1959; *further revised* 1 *April* 1959)

Abstract—The effect of pressure has been measured on the absorption edges of GaP, GaAs, GaSb, ZnS, ZnSe, ZnTe, ZnO and CdS. A tentative interpretation can be given consistent with previous work on silicon and germanium. Regularities in the shifts in horizontal and diagonal sequences are discussed.

An absorption peak which appears (irreversibly) on the low-energy side of the edge of the higher-molecular-weight compounds, and grows with pressure, indicates either the formation of a disordered phase or some chemical decomposition. For GaAs and GaSb both events may be present, but for ZnTe the former course seems definitely the more probable.

VOL.
11
195

THE effect of pressure has been measured on the absorption edges of GaP, GaAs, GaSb, ZnS, ZnSe, ZnTe, ZnO and CdS. The first six of these have the zinc blende structure, while the last two have the wurtzite structure at 1 atm, but transform to zinc blende under pressure.

The apparatus and procedure has been previously described,[1–3] and results have been discussed for germanium and silicon[3] which will be compared with the present results.

1. GROUP IIIB–VB COMPOUNDS

(*a*) *Gallium phosphide*

Single crystals of GaP were obtained from Dr. A. A. GIARDINI, of the U.S. Army Signal Research and Development Laboratory. The samples used for the pressure runs were very slightly doped with titanium, which was not expected to have any effect on the pressure shift of the absorption edge. Figure 1 presents the data obtained from 1 to 50,000 atm. For the highest absorption coefficient, $\alpha = 100\ \text{cm}^{-1}$, there is an initial blue shift with pressure. Above 22,000 atm, the shift is red for all values of α below $100\ \text{cm}^{-1}$, with a slope of $-1{\cdot}7(10^{-6})$ eV/atm.

(*b*) *Gallium arsenide*

Single crystals of GaAs were obtained from Dr. J. H. WHELAN, of the Bell Telephone Laboratories.

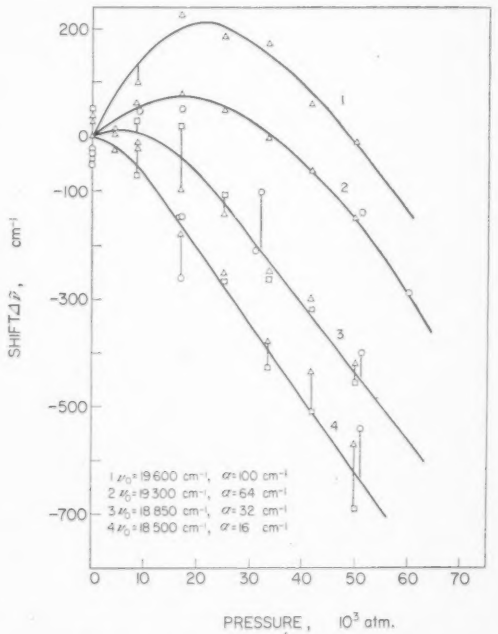

FIG. 1. Shift of gallium phosphide absorption edge with pressure.

*This work was supported in part by U.S. Atomic Energy Commission Contract AT(11-1)-67, Chemical Engineering Project 5.

They were *n*-type with a specific resistivity of 0·08Ω-cm. The results are shown in Fig. 2. The initial energy gap is about 1·4 eV at $\alpha = 30$ cm^{-1}. The absorption edge shifts blue with

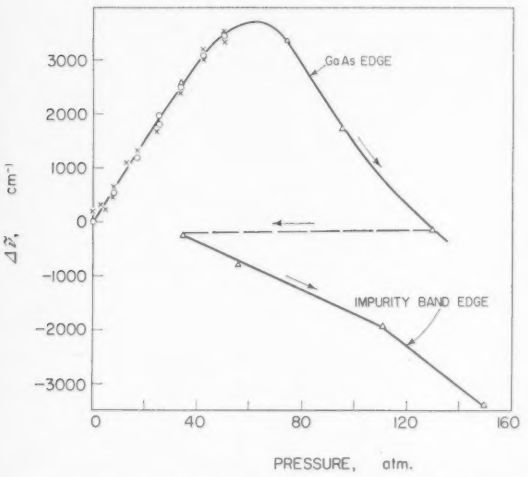

FIG. 2. Shift of gallium arsenide absorption edge with pressure ($\nu_0 = 11{,}850$ cm^{-1}, $\alpha = 50$ cm^{-1}).

pressure, the initial slope being 9·4 (10^{-6}) eV/atm, rising to a maximum shift of 0·465 eV at 60,000 atm. The red shift above 60,000 atm has a slope of roughly —8·7 (10^{-6}) eV/atm, and may be due

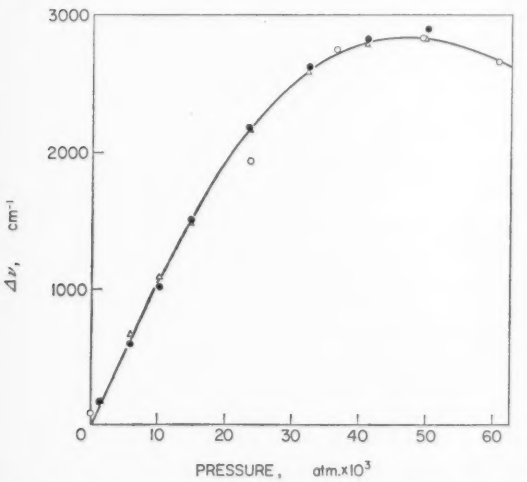

FIG. 3. Shift of gallium antimonide absorption edge with pressure ($\nu_0 = 5620$ cm^{-1}, $\alpha \simeq 20$ cm^{-1}).

in part to the indirect (100) transition, and in part be due to the irreversible effects discussed below.

(c) *Gallium antimonide*

The GaSb was obtained from Dr. J. H. WHELAN, of the Bell Telephone Laboratories. It was of unknown but high purity. The results are shown in Fig. 3. The initial transition has an energy gap of 0·7 eV at $\alpha = 20$ cm^{-1}, compared to 1·5 eV for GaAs and 2·4 eV for GaP. The initial blue shift of GaSb has a slope of 12·3 (10^{-6}) eV/atm. indicating a more rapid rise of the conduction-band minimum than in GaAs. The maximum apparent shift of 0·35 eV occurs at about 50,000 atm, after which the red shift, probably corresponding to the indirect (100) transition, begins.

2. GROUP IIB–VIB COMPOUNDS

(a) *Zinc blende type*

(i) *Zinc sulfide.* Pure zinc sulfide single crystals in the zinc blende structure were obtained from L. W. STROCK, of Sylvania Electric Products Inc. The initial optical energy gap was found to be 3·5 eV, and is considered to be the transition at $\boldsymbol{k} = 0$, as is indicated by a band-structure calculation being carried out by SHAKIN and BIRMAN[4]. The shift with pressure, shown in Fig. 4,

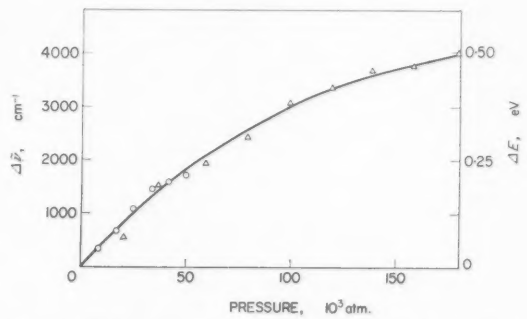

FIG. 4. Shift of zinc sulfide absorption edge with pressure ($\alpha = 60$ cm^{-1} measured from $\nu_0 = 28{,}600$ cm^{-1}).

consists of a monotonic blue shift, appearing to approach a maximum of about 0·50 eV at the highest pressure obtained, 180,000 atm. The initial slope of 5·7 (10^{-6}) eV/atm compares with 9(10^{-6}) eV/atm obtained by PIPER *et al.*[5] for hexagonal ZnS (wurtzite) up to 1700 atm. One

would expect comparable results for the wurtzite form, as the band structure is probably very similar to that of the zinc blende.

Figure 7 shows the absorption-edge shift plotted against relative volume compression, obtained from the data of BRIDGMAN[6]. The rate of change of energy gap with bond length, assuming isotropic compression, is 6·2 eV/Å, at 1 atm.

(ii) *Zinc selenide.* Pure single crystals of ZnSe were obtained from Dr. R. H. BUBE, of RCA Laboratories. The shift of the absorption edge was measured at 65 cm^{-1}, for which the initial energy gap was 2·58 eV. The results, shown in Fig. 5, are quite similar to the results for ZnS.

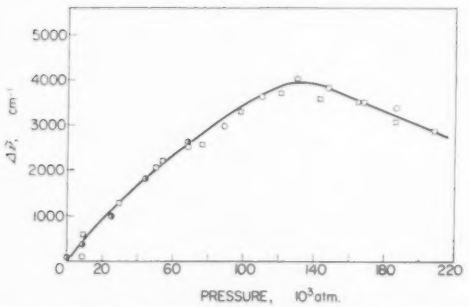

FIG. 5. Shift of zinc selenide absorption edge with pressure ($\nu_0 = 20{,}800$ cm^{-1}, $\alpha = 65$ cm^{-1}).

The initial shift is blue, with a slope of 6·0(10^{-6}) eV/atm at 1 atm. The maximum shift is 0·49 eV at 130,000 atm, followed by a red shift with a slope of about —2·0(10^{-6}) eV/atm.

From BRIDGMAN's compressibility data, the shift has been plotted against relative compression in Fig. 7, which shows a slope of 3·3 eV/Å up to 15,000 atm ($\Delta V/V_0 = 0{\cdot}032$), a slope of 4·6 eV/Å up to 130,000 atm ($V/V_0 = 0{\cdot}130$), and a slope of —4·0 eV/Å above 130,000 atm.

(iii) *Zinc telluride.* The source of the zinc telluride single crystals used here was Dr. R. N. HALL, of the General Electric Company. The particular samples used were made from a stoichiometric mixture of zinc and tellurium, which contained a few parts per million of copper, resulting in a resistivity of about 1Ω-cm. The shift of the absorption edge with pressure is shown in Fig. 6. The initial sharp red shift of the edge is thought to be due to surface effects during the fusing of the salt around the sample, so the shift was measured from an extrapolated zero point of 18,300 cm^{-1} or 2·27 eV. The shift from 4000 to 45,000 atm is blue, with a slope of 6·0(10^{-6}) eV/atm. The portion of the curve from 5000 to 40,000 atm is completely reversible, and is possibly due to the direct transition at $\boldsymbol{k} = 0$.

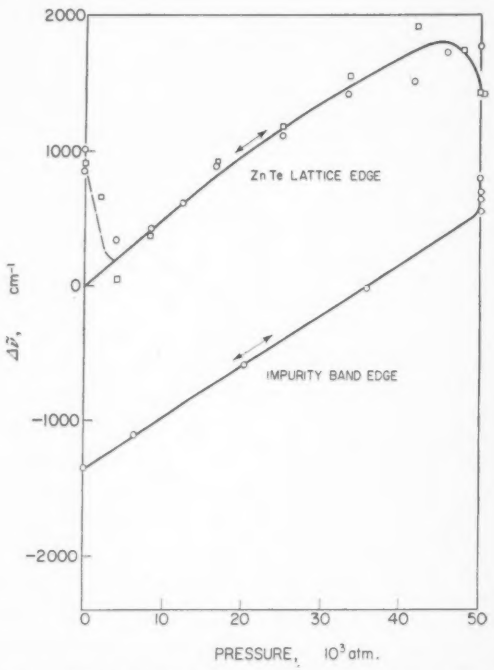

FIG. 6. Shift of zinc telluride absorption edge with pressure ($\nu_0 = 18{,}300$ cm^{-1}, $\alpha = 64$ cm^{-1}).

Above 45,000 atm, a time-dependent irreversible red shift takes place, reaching an equilibrium value about 0·18 eV below the original energy gap. In several runs, equilibrium was reached in about 20 min. On reduction of pressure, the shift parallels the original shift, with a slope of 4·7 (10^{-6}) eV/atm, the energy gap reaching a final value of 2·10 eV at 1 atm. This last shift is reversible over the range 1–50,000 atm and is interpreted tentatively below.

From the plot of shift against compression (Fig. 7), the shift of energy gap with bond length is found to be 3·18 eV/Å up to the beginning of the phase change at 7·5 per cent volume compression.

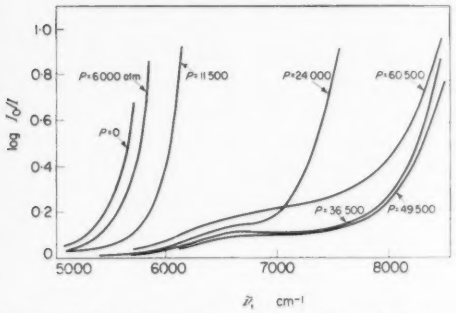

FIG. 7. Shift of absorption edges of zinc sulfide selenide, and telluride with compression ($\alpha = 65$ cm^{-1}).

(b) *Wurtzite type*

The compounds ZnO and CdS are closely related to the other compounds included in this work, not only in structure, but also in many important physical and electronic properties. A transformation under pressure to the zinc blende structure from their original wurtzite form was expected, and did in fact occur in both cases.

(i) *Zinc oxide.* Single crystals of zinc oxide were obtained from Dr. A. R. HUTSON, of the Bell Telephone Laboratories. These crystals were in the form of needles about 0·25 in. long and some 0·004–0·010 in. in dia., making them most suitable for the 250,000-atm bomb. The shift of the absorption edge observed with pressure is shown in Fig. 8. A blue shift with pressure first occurs, at an increasing rate with higher pressure. The slope changes from $0{\cdot}6(10^{-6})$ eV/atm at 1 atm to $1{\cdot}9(10^{-6})$ eV/atm at 100,000 atm. At a pressure of about 100,000 atm, the light transmitted by the sample began to cut off, and reached a minimum at pressures ranging from 130,000 to 150,000 atm in different runs. The sample then cleared up somewhat, and the shift shown by the upper curve in Fig. 9 was measured. The red shift at the transition amounts to about —0·10 eV, and the initial slope of the upper curve is $1{\cdot}9(10^{-6})$ eV/atm at 130,000 atm.

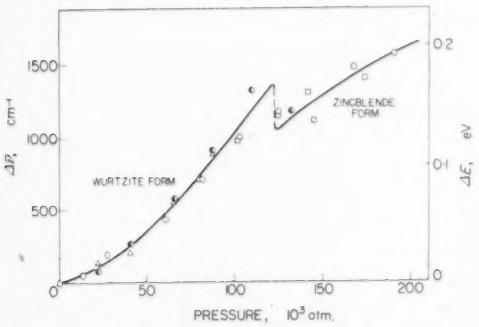

FIG. 8. Shift of zinc oxide absorption edge with pressure ($\alpha = 60$ cm^{-1} measured from $\nu_0 = 25{,}300$ cm^{-1}).

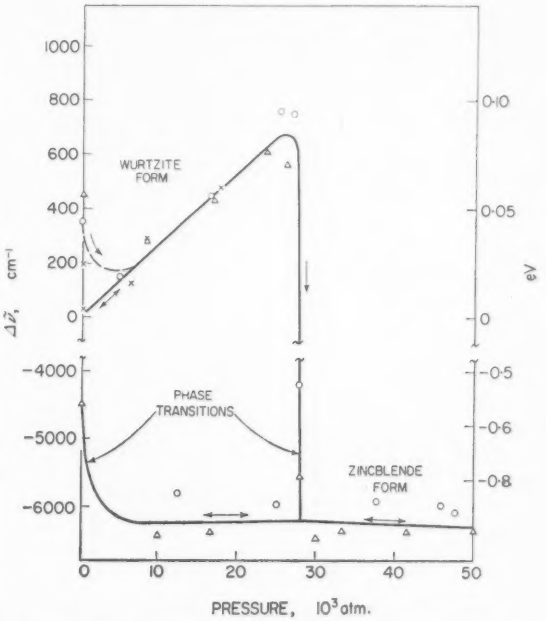

FIG. 9. Shift of cadmium sulfide absorption edge with pressure ($\nu_0 = 20{,}110$ cm^{-1}, $\alpha = 64$ cm^{-1}).

(ii) *Cadmium sulfide.* This material was obtained in the form of large crystals and polycrystalline masses in the wurtzite structure from Dr. E. C. STEWART, of the Harshaw Chemical Company. The shift of the absorption edge with pressure is shown in Fig. 9. The initial red shift up to 5000 atm is thought to be due to a partial phase change to the zinc blende form induced by shear during the fusing of the salt pellet around the sample. The shift was therefore measured from an extrapolated zero value of 2·50 eV, which is not the true energy gap at atmospheric pressure. Once the pressure exceeded 5000 atm, a reduction in pressure did give a shift down to the extrapolated zero, and the shift was reversible from 0 to 25,000 atm. The initial slope of the shift is $3{\cdot}3(10^{-6})$

eV/atm, and remains fairly constant up to 27,500 atm, at which point a large red shift of about 0·8 eV occurs, presumably due to the transition to the zinc blende structure. This transition resulted in a loss of most of the light available, and in only two runs could the edge be measured beyond the transition. There was no measurable tendency for the new absorption edge to shift with pressure, either increasing or decreasing, until the pressure was reduced below 10,000 atm. The sample then cleared up gradually and the absorption edge slope of the shift with pressure. The following discussion is intended to emphasize the effect of asymmetry in the crystal potential for compounds in isoelectronic sequences, for which the total number of electrons are equal, and for which the bond lengths are almost equal.

The interpretations are based on the (perhaps rash) assumption that the red shifts are due to a transition to a minimum in the (100) direction in the conduction band, as has been reasonably well established for germanium.[9]

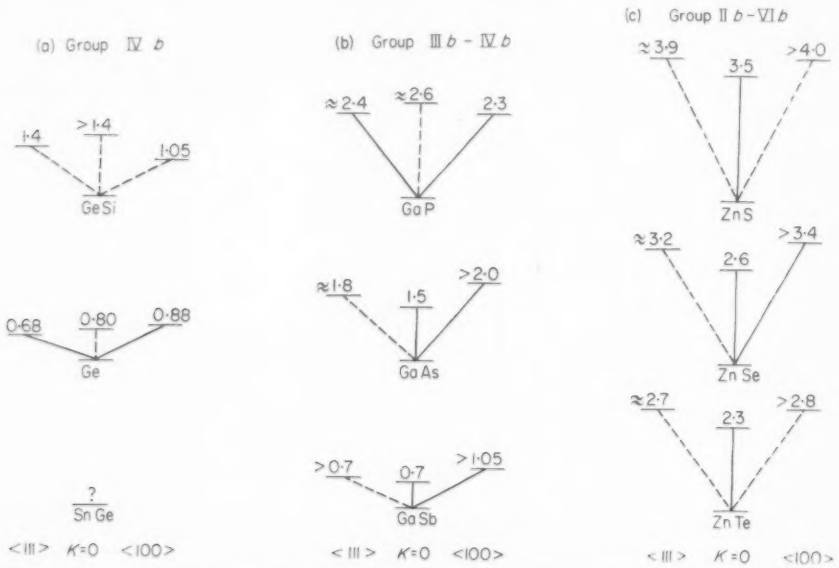

FIG. 10. Estimated conduction-band levels of semiconductors (above valence-band maximum 300°K).

shifted blue again, reaching a final value of 0·56 eV less than the original zero point. No further change was observed after the sample had remained in the bomb for several days at atmospheric pressure.

3. COMPOUNDS IN VARIOUS SEQUENCES

A speculative outline of the results of the previous sections is presented in Fig. 10, which illustrates the energy gaps that are known or can be estimated for the direct and indirect transitions at atmospheric pressure. Table 1 summarizes the effect of pressure in these transitions, with the pressure range in which each occurs and the

(a) SiGe, GaP *and* ZnS

The bond length in this sequence varies from 2·36 to 2·39 Å, and the total number of electrons is 23 per atom. The system silicon–germanium has been investigated by JOHNSON and CHRISTIAN[7] who found a sharp break in the plot of energy gap versus composition at about 15 mole per cent silicon, indicating a difference in the band structure of these two elements. Pressure measurements by PAUL and WARSCHAUER[8] in the range 1–8000 atm on germanium–silicon alloys were consistent with HERMAN'S[9] picture of the band structure, and the behavior of the band minima of these two elements under pressure, i.e.

Table 1. *Effect of pressure on band structure of semiconductors*

Compound	ΔE_g(eV)* (1 atm)	P(10^3 atm)	Speculated transition direction†	$d\Delta E_g/dP$‡ (10^{-6}eV/atm)	$d\Delta E_g/dr$§ (eV/Å)	Max. blue shift (eV)
Si	1·08	0–140	(100)[10,11]	−2·0	−1·12	
Ge	0·70	0–50 50–129	(111)[11] (100)[3]	+8·0 −1·2	3·8 −0·6	0·15
GaP	2·34	0–20 20–50	(111) or (000) (100)	1·8 −1·7		0·02
GaAs	1·47	0–60 60–130	(000) or (111)[12,13] (100)	+9·4 −8·7		0·47
GaSb	0·70	0–50 50	(000) or (111) (100)	+12·3 ?		0·35
ZnS	3·54	0–180	(000) or (111)[4]	+5·7	6·2	0·50
ZnSe	2·57	0–130 130–210	(000) or (111) (100)	+6·0 −2·0	4·6	0·50
ZnTe	2·26	0–45	(000) or (111)	+6·0	3·2	0·22
ZnO	3·14 (wtz) (Znbl)	0–130 130–220	(111) or (000) (111) or (000)	0·6–1·9 1·9		0·15 0·20
CdS	2·50 (wtz) 1·7 (Znbl)	0–27·5 27·5–50 50–10	(000) or (111) ? ?	+3·3 ≈0 ≈0		0·08 ≈0 ≈0

*Zero point from which shift was measured.

†More probable direction is given first in uncertain cases. Where no reference is given, the estimate is based on the direction and magnitude of the pressure shift found in this paper.

‡Slope of shift at 1 atm, or average slope after a reversal of shift direction. These are, in general, estimated for $\alpha = 20$–65 cm^{-1}, since in only a few cases are values available for $\alpha = 0$. E.g., at $\alpha = 0$ for germanium the slope is $5{\cdot}0 \times 10^{-6}$ eV/atm.[10]

§Based on bond length.

the rise of the (111) minimum in the conduction band and the lowering of the (100) minimum, relative to the maximum of the valence band. The 50:50 germanium–silicon alloy has an energy gap of 1·05 eV, due to the transition to the (100) minimum, and the (111) minimum is about 0·35 eV higher, or 1·4 eV above the valence band, according to the data of JOHNSON and CHRISTIAN[7].

The effect of increasing asymmetry in this sequence seems to be a general rise in the conduction band relative to the valence band, the rate of rise being greatest for the minimum in the (100) direction. In ZnS, the (apparent) (100) minimum is at least 0·5 eV above the lowest conduction band level, thus explaining the fact that ZnS has an initial blue shift while GaP shifts red. Following this trend, one would expect the next member of this sequence, CuCl, to have a large blue shift with pressure before the red shift which should eventually follow.

(b) Ge, GaAs *and* ZnSe

In this sequence, the bond length is between 2·43 and 2·45 Å, with a total of 32 electrons per atom. The conduction-band minimum rises relative to the valence band, with the (100)

minimum rising the most rapidly, as the asymmetry of the compound increases. There is evidence in this sequence that the (111) minimum rises faster than the minimum at $\boldsymbol{k} = 0$, since the (111) minimum is lower in germanium and the $\boldsymbol{k} = 0$ transition is considered to be lower in energy for GaAs.[12,13] If this is generally true, then the transition in ZnSe should be direct, and the blue-shifting transitions of GaP and ZnS in the last sequence might also be direct at atmospheric pressure. Considering the Kronig one-dimensional model from the viewpoint of SERAPHIN[14] and of WELKER and WEISS[15], the planes perpendicular to the (111) direction may be represented by potential troughs having different depths, as there are alternate planes containing like atoms. It is found that the energy gap for this model increases with an increase in the difference between the two potential troughs, other parameters being constant. In the real crystal then, an electron state with a propagation vector $\boldsymbol{k}$ in the (111) direction should have a greater energy gap between its ground state and its excited state, as the potential difference of the two planes increases. This corresponds to a rise of the Λ_1 state in the conduction band above the similar state in the valence band, which are both in the (111) direction. An electron propagating in the (100) direction encounters alternate layers containing like atoms also, so that the energy gap in the (100) direction should also increase with increasing asymmetry or electronegativity of the bonds. In the immediate vicinity of $\boldsymbol{k} = 0$, one would expect smaller effects, as the charge distribution in space of the atomic *s*-functions from which the $^1\Gamma_2$ state is made up is not directional, and the atomic *p*-functions making up the $^3\Gamma_{22}$ state in the valence band are directed only toward like atoms, and are thus less affected by a charge difference between unlike atoms.

The next member of the sequence, CuBr, has a greater energy gap than ZnSe, and if the tendency described above continues, the transition at atmospheric pressure should be direct, and should shift blue with pressure before eventually shifting red with the (100) transition.

(c) GeSn, GaSb *and* ZnTe

The first member of this series is not known to exist. However, an extrapolation by HERMAN[9] indicates that its conduction and valence band would overlap by about 0·5 eV, in which case it would be a metal and be of little interest here. The remaining members exhibit the same dependence on degree of asymmetry as the two preceding sequences. The bond lengths vary from 2·63 to 2·65 Å and there are 41 electrons per atom. The initial transition is probably direct in both compounds, with slopes of 12·3 for GaSb and 6·0 for ZnTe, in 10^{-6} eV/atm. The apparent maximum shift obtained for GaSb indicates that the least possible distance of the (100) minimum above the $\boldsymbol{k} = 0$ minimum at atmospheric pressure is 0·35 eV. The next compound of the sequence is CuI, which has a higher energy gap than ZnTe, and, like CuCl and CuBr, probably has a direct transition at 1 atm, and a large blue shift of the energy gap with pressure, shifting red again at some pressure above 100,000 atm, or at about 10–12 per cent volume compression. It must be borne in mind, of course, that these three 1B–VIIB compounds may not be stable in the zinc blende form at high pressures, and could transform to the NaCl or CsCl structure.

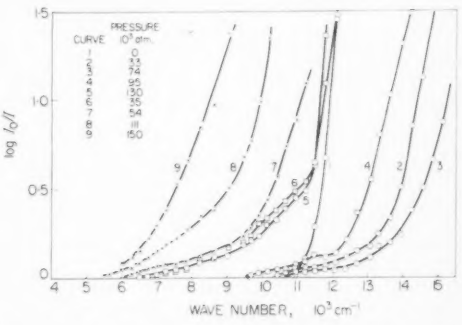

FIG. 11. Log I_0/I versus wave number for gallium arsenide.

4. COMPOUNDS WITH DISORDERING TRANSFORMATIONS

The three compounds of highest molecular weight included in this work were GaAs, GaSb and ZnTe, and these three exhibited similar effects under pressure. Figs. 11–13 show the shape of the absorption curves at different pressures for typical runs with these compounds. In each case, an absorption band appears in the long-wavelength tail of the absorption band at a sufficiently high

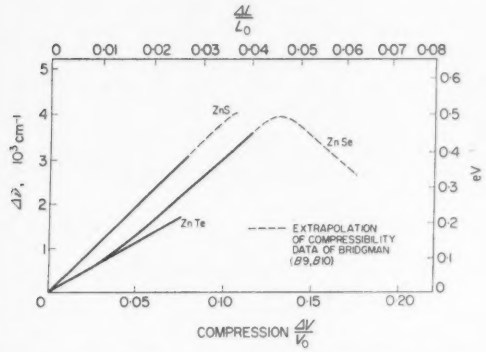

FIG. 12. Log I_0/I versus wave number for gallium antimonide.

pressure, which may in part account for the rapid shift in GaAs at high pressure. The minimum pressure at which the band first occurs depends slightly on the size and preparation of the sample and on the method of loading the sample in the bomb. In general, a higher transition pressure was obtained the smaller and more perfect the sample, and the greater the difference between the height of the sample and the height of the salt pellet between the pistons. Thus, the mechanism of the process is most likely accelerated by imperfections and shear in the sample. GONSER and OKKERSE[16] have obtained a phase change of GaSb at temperatures below the melting point

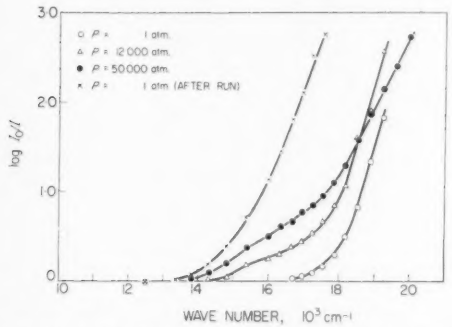

FIG. 13. Log I_0/I versus wave number for zinc telluride.

Table 2. Effect of pressure on the disorder transition of semiconductors

Compound	$P(10^3$ atm) for $T_t = 27°C$*	$P(10^3$ atm) at which band appeared†
ZnS	184±119	Not<180
ZnSe	153±100	Small at 90
ZnTe	121± 79	12–45
GaP	218±119	Not < 50
GaAs	188±100	90–120
GaSb	130±70	60

*Calculated using $\Delta E = 9\pm3$ kcal/mole for ZnS, ZnSe, and ZnTe, $\Delta E = 12\pm2$ kcal/mole for GaP, GaAs, and GaSb, and using $\Delta V = 6$–14 per cent of V_m in all cases.

†Very small peaks were present at lower pressures in the case of ZnTe, GaAs, and GaSb, probably due to impurities included during crystal growth. Microscopic dark specks were originally present in ZnTe, which could act as nucleating centers for phase change.

Table 3. Effect of pressure on the decomposition of semiconductors

Compound	ΔE_{dec}* (kcal/mole)	P for 70·7% decomp. (10^3 atm)	P for 0·71% decomp. (10^3 atm)†	$P_{absorb.}$ Peak obs. (10^3 atm)
Zns	48±5	1150±512	968±568	Not<180
ZnSe	34±3	641±313	482±378	Small at 90
ZnTe	29±3	445±217	342±259	12–45‡
GaP	16±2	350±181	204±242	Not<50
GaAs	11±1	209±102	80±154	90–120
GaSb	10±	152±75	49±117	60

*Ref. (17, 18); GaP and GaAs values assumed proportional to ZnS and ZnSe values, resp. $\Delta V = 614$ per cent of V_m.

†Where lower limit is negative, equilibrium decomposition would exceed 0·71 per cent at zero pressure.

‡Peaks did not increase greatly in size until a pressure of 45,000 atm. was reached.

by neutron irradiation, and report that the new form is a glassy solid with the liquid structure and has a volume about 8 per cent less than the normal form. The energy accompanying this process is within several per cent of the heat of fusion.

The absorption at the front of the edge could be due to the formation of this disordered state by pressure or to chemical decomposition. Table 2 shows the calculated range of pressures for melting at room temperature, using reasonable ranges of values for ΔH and ΔV. Table 3 shows similar results for 70·7 and 0·71 per cent decomposition. GaAs, GaSb and ZnTe all approach the melting pressure in the range where the band appears. Decomposition could also occur in significant amounts in GaAs and GaSb, but this is less likely for ZnTe.

It might be possible to prepare semiconductors or phosphors with controlled and uniform impurity levels by a combined application of pressure and temperature.

Acknowledgements—The authors wish to acknowledge the helpful suggestions and advice of J. BARDEEN, F. SEITZ and H. BROOKS and to thank J. H. WHELAN, A. R. HUTSON, R. H. BUBE, A. A. GIARDINI, L. W. STROCK, and E. C. STEWART, who furnished single crystals. A. L. EDWARDS would like to thank the DuPont Company for fellowship support.

REFERENCES

1. FITCH R. A., SLYKHOUSE T. E. and DRICKAMER H. G., *J. Opt. Soc. Amer.* **47,** 1015 (1957).
2. SLYKHOUSE T. E. and DRICKAMER H. G., *J. Phys. Chem Solids* **7,** 207 (1958).
3. SLYKHOUSE T. E. and DRICKAMER H. G., *J. Phys. Chem. Solids* **7,** 210 (1958).
4. SHAKIN C. and BIRMAN J., *Phys. Rev.* **109,** 810, 818 (1958).
5. PIPER W. W., MARPLE D. T. F. and JOHNSON P. D., *Phys. Rev.* **110,** 223 (1958).
6. BRIDGMAN P. W., *Proc. Amer. Acad. Arts Sci.* **74,** 425 (1942); **76,** 1 (1945).
7. JOHNSON E. R. and CHRISTIAN S. M., *Phys. Rev.* **95,** 560 (1954).
8. PAUL W. and WARSCHAUER D. M., *J. Phys. Chem. Solids* **6,** 6 (1958).
9. HERMAN F., *J. Electronics* **1,** 103 (1955).
10. PAUL W. and WARSCHAUER D. M., *J. Phys. Chem. Solids* **5,** 89, 102 (1958).
11. PAUL W. and PEARSON G. L., *Phys. Rev.* **98,** 1755 (1955).
12. CALLAWAY J., *J. Electronics* **2,** 330 (1957).
13. GRAY P. V. and EHRENREICH H., *Bull. Amer. Phys. Soc.* **3,** 255 (1958).
14. SERAPHIN B., *Z. Naturforsch.* **9a,** 450 (1954).
15. WELKER H. and WEISS H., *Solid State Physics* (Ed. F. SEITZ and D. TURNBULL) Vol. 3, p. 1. Academic Press, New York (1956).
16. GONSER V. and OKKERSE B., *J. Phys. Chem. Solids* **7,** 55 (1958).
17. KIR'IASHKINA E. I., POPOV F. M., BILENKO D. I. and KIR'IASHKIN V. I., *Sov. Phys.* **2,** 69 (1955).
18. SCHOTTKY W. F. and BEVER M. B., *Acta Met.* **6,** 320 (1958).

J. Phys. Chem. Solids Pergamon Press 1959. Vol. 11. pp. 149–169. Printed in Great Britain.

NUCLEAR MAGNETIC RESONANCE STUDIES OF NEUTRON-IRRADIATED ALKALI HALIDES*†

J. F. HON‡ and P. J. BRAY

Department of Physics, Brown University, Providence, Rhode Island

(*Received* 18 *September* 1958; *revised* 6 *April* 1959)

Abstract—Nuclear magnetic resonance techniques have been used to investigate radiation damage in some alkali halides. The resonances of ^{7}Li, ^{23}Na, ^{81}Br and ^{127}I were studied to determine the concentration and arrangement of defects in neutron-irradiated single crystals of NaI, LiI, KI and KBr. A method of analysis was developed, based on changes of line shape due to defect-induced quadrupolar effects. The experimental results are in fairly good agreement with theoretical predictions based, principally, on the methods of SEITZ and KOEHLER and of BRINKMAN. Information has been obtained on the strength of screening in coulomb potentials for atom–atom collisions and on the deformation of ion cores by charges external to the ions. Evidence for orientation of dislocations in preferred directions has been noted in crystals of NaI and KI.

1. INTRODUCTION

THE work reported here is part of a program of application of nuclear magnetic resonance (NMR) techniques to the study of defects in solids. The principles of NMR are available in several review articles,[1,2] as is a discussion of defects in crystalline solids.[3] An excellent review of the effect of defects on NMR has been presented by BLOEMBERGEN[4].

The effect of dislocations on NMR in ionic crystals was first investigated by WATKINS[5] and WATKINS and POUND[6]. COHEN and REIF[7,8] have investigated the effects of vacancies, interstitials, and foreign atoms on NMR. The present paper is concerned with the defects generated in alkali halide crystals by reactor irradiation.

Defects influence the intensity, shape and spin-lattice relaxation time of the NMR. In Section 2, this influence is traced to its origin in defect-induced changes in magnetic dipole–dipole couplings and electrical quadrupole interactions, and quantitative relations are established between the observed changes of the NMR and the density and distribution of the defects. The present picture of defect formation by irradiation is also discussed. After a discussion of the experimental apparatus and an outline of procedure, the experimental determinations of defect concentration and distribution in the irradiated crystals are given in Section 5 and compared with values obtained from theory. A summary of conclusions and evaluation of the NMR technique as applied to radiation-damage studies are given in Section 6.

2. THEORY

According to SEITZ[3], imperfections in crystals can be classified as: (1) dislocations, (2) vacant lattice sites and interstitial atoms, (3) free electrons and holes, (4) foreign atoms in either substitutional or interstitial positions, (5) lattice phonons and (6) excitons. For the present work, only the first three types need be considered. These imperfections can change the shape and intensity of the NMR by altering the magnetic and electric field conditions at the nuclei, and can change the spin-lattice relaxation time T_1 by adding to the coupling between the nuclei and the lattice. This latter change may, for example, arise from an electron or hole trapped in the lattice. The paramagnetic

*Research supported by the U.S. Atomic Energy Commission under Contract AT(30–1)–1880.

†Submitted by J. F. HON in partial fulfillment of the requirements for the degree of Doctor of Philosophy at Brown University.

‡Present address: Atomics International, Canoga Park, California.

property of the resultant center tends to reduce T_1. If T_1 is sufficiently reduced, the NMR line will be broadened. Experimental evidence indicates that this effect is not observable in the crystals investigated, presumably because T_1 was already quite short in the unirradiated crystals due to quadrupolar interactions, and the effect will not be discussed further.

In the following sections, the possible imperfection-induced changes in magnetic field or electric field gradient at a resonating nucleus are discussed.

(a) *Dipolar effects*

A resonating nucleus in a solid will be subject to both the externally applied magnetic field, $\boldsymbol{H}_0$, and an internal magnetic field from its environment. If the solid is non-ferromagnetic and contains no uncoupled electrons, the internal magnetic fields are due to the nuclear magnetic moments themselves (diamagnetic and second-order paramagnetic shielding from bound electrons is neglected in this treatment). The influence of the magnetic dipole moments on line shape is best given by the second-moment calculation of VAN VLECK[9]. The second moment is defined as

$$\langle \Delta\nu^2 \rangle_{\text{ave}} = \int_0^\infty (\nu - \nu_0)^2 g(\nu)\, d\nu \qquad (1)$$

where ν_0 is the resonant frequency and $g(\nu)$, the shape function of the resonance line, is defined so that

$$\int_0^\infty g(\nu)\, d\nu = 1. \qquad (2)$$

The relationship between the second moment and the line width is particularly simple for a Gaussian line shape. In that case the separation in frequency, $\Delta\nu_{p-p}$, between the two peaks of the experimentally observed first derivative of the absorption curve is given by:[10]

$$\Delta\nu_{p-p} = 2(\langle \Delta\nu^2 \rangle_{\text{ave}})^{\frac{1}{2}}. \qquad (3)$$

To determine the effect of defects on the dipolar line width in alkali halides, it is instructive to consider a somewhat simpler solid, namely, a solid with only one nuclear species where the spins lie on a simple cubic lattice. For the case of spin systems having cubic symmetry, the second moment has the form:[9]

$$\langle \Delta\nu^2 \rangle_{\text{ave}} = \tfrac{3}{8}\gamma^4 h^{-2}[a + b(\lambda_1^4 + \lambda_2^4 + \lambda_3^4)] \qquad (4)$$

where γ is the nuclear gyromagnetic ratio, h is Planck's constant, and λ_1, λ_2 and λ_3 are the direction cosines of $\boldsymbol{H}_0$ with respect to the cubic axes. The constants a and b are given by:

$$a = \sum_k r_k^{-6}[7 - 9(\mu_k^4 + \nu_k^4 + \xi_k^4)] \qquad (5)$$

and

$$b = \sum_k r_k^{-6}[-9 + 15(\mu_k^4 + \nu_k^4 + \xi_k^4)] \qquad (6)$$

where μ_k, ν_k and ξ_k are the direction cosines with respect to the cubic axes of the displacement vector, $\boldsymbol{r}_k$, from the resonating nucleus to the kth neighboring nucleus. Equations (3)–(6) show that the effect of the spin–spin interaction in the solid is to give a resonance line whose width is dependent on the strength of the interaction.

Consider now point defects and their effect on the second moment. A vacancy would correspond to removing a term and an interstitial to adding a term in equation (4). Because of the r^{-6} dependence, an interstitial is more effective in changing the sum (equation (4)) than a vacancy since an interstitial is closer to its nearest neighbors than a vacancy (relaxation of the lattice is ignored here). Since the purpose of this section is to show that these effects are small, the larger effect of an interstitial will be considered. The interstitial positon in a simple cubic lattice is in the center of the cube, so that r_i for the nearest nuclei is $\sqrt{(\frac{3}{2})}\, a_0$ and $\mu^4 = \nu^4 = \xi^4 = 1/9$. The changes in a and b for these eight nearest nuclei are then:

$$\delta a = \frac{9{\cdot}48}{a_0^6} \qquad (7)$$

and

$$\delta b = -\frac{9{\cdot}48}{a_0^6}. \qquad (8)$$

For the twenty-four next-nearest nuclei $r_i = \sqrt{(11/2)}\, a_0$, $\mu_i^4 = 1/121$, $\nu_i^4 = 1/121$, and $\xi_i^4 = 81/121$, so that:

$$\delta a = 0{\cdot}0399/a_0^6 \qquad (9)$$

and

$$\delta b = 0{\cdot}0620/a_0^6. \qquad (10)$$

The changes in a and b for the eight nearest nuclei cause a change of approximately 50 per cent in the second moment. However, the changes in a and b for the next-nearest nuclei are almost negligible. A rough extension of this procedure shows that a 10 per cent change in the second moment, which is about the minimum change experimentally observable, would require a defect density of more than one defect per one hundred atoms. Such a high degree of damage is not achieved in the present experiments.

The effect of strains, introduced by point defects or dislocations, on the dipolar second moment must also be considered. The variation of the sums a and b due to strain can be approximated by:

$$\delta a = -\sum_k \frac{6}{r_k{}^7}\Delta r_k\{7-9(\mu_k{}^4+\nu_k{}^4+\xi_k{}^4)\} \tag{11}$$

and

$$\delta b = -\sum_k \frac{6}{r_k{}^7}\Delta r_k\{-9+15(\mu_k{}^4+\nu_k{}^4+\xi_k{}^4)\}, \tag{12}$$

ignoring changes in μ_k, ν_k and ξ_k, where Δr_k is the strain. Because of the r^{-7} dependence, these effects have an even shorter range than those considered in the preceding paragraphs and can be ignored.

The alkali halides, with the exception of cesium halides, have a face-centered cubic lattice. Disregarding species, the nuclei lie on a simple cubic lattice. From VAN VLECK's general result for cubic systems, equation (4), the second moment in NaCl-type structures would be the sum of two terms having the same form as the simple cubic case,

$$\langle\Delta\nu^2\rangle_{\text{ave}} = A[a_1+b_1(\lambda_1{}^4+\lambda_2{}^4+\lambda_3{}^4)]+ \\ +B[a_2+b_2(\lambda_1{}^4+\lambda_2{}^4+\lambda_3{}^4)] \tag{13}$$

where the first term is the sum over like species and the second term is the sum over unlike species. The net result is

$$\langle\Delta\nu^2\rangle_{\text{ave}} = C[a_3+b_3(\lambda_1{}^4+\lambda_2{}^4+\lambda_3{}^4)]. \tag{14}$$

Since this has the same form as that for the simple cubic case, equation (4), the arguments presented above are valid. In alkali halides, then, dipolar effects can be ignored as a source of radiation-induced changes in the NMR if the defect density is less than 10^{-2} defects per atom.

(b) *Quadrupolar effects*

Quite often there are, in addition to the internal magnetic fields, internal electric fields in a solid. If the resonating nucleus possesses an electrical quadrupole moment, it will interact with the gradient of the electrical field at the nuclear site. This quadrupolar interaction can alter the spacing of the magnetic energy levels, which are equally spaced in the absence of such a perturbation, and split the NMR line.

POUND[11] has derived the properties of this quadrupolar interaction for the case in which it is small with respect to the magnetic interaction of the nucleus and the static field $\boldsymbol{H}_0$. Additional computations have been made by BERSOHN[12], VOLKOFF[13] and COHEN and REIF[14]. The interaction energy depends on the scalar quadrupole moment Q, the electric field-gradient tensor $\nabla\boldsymbol{E}$ and the orientation of $\boldsymbol{H}_0$ with respect to the principal axis system of the electrical field-gradient tensor. The components of $\nabla\boldsymbol{E}$ in its principal axis system, in which it is diagonal, are often written as ϕ_{xx}, ϕ_{yy} and ϕ_{zz} where

$$|\phi_{zz}| \geqslant |\phi_{yy}| \geqslant |\phi_{xx}|. \tag{15}$$

With the help of Laplace's equation,

$$\phi_{xx}+\phi_{yy}+\phi_{zz} = 0, \tag{16}$$

these three components can be specified by two parameters, η (the asymmetry parameter) and q, where

$$eq \equiv \phi_{zz} \tag{17}$$

and

$$\eta \equiv \left|\frac{\phi_{xx}-\phi_{yy}}{\phi_{zz}}\right|. \tag{18}$$

When the electrical field-gradient tensor exhibits rotational symmetry about the z-axis, $\phi_{xx} = \phi_{yy}$ and $\eta = 0$. In this case the quadrupolar energy depends on Q, q, and the angle θ between the z-axis and the external magnetic field $\boldsymbol{H}_0$. First-order perturbation theory gives the new transition frequencies as[4]

$$\nu_{m\to m-1} = \nu_0+(2m-1)(3\cos^2\theta-1)\frac{3e^2qQ}{8I(2I-1)h} \tag{19}$$

where ν_0 is the single NMR frequency in the absence of quadrupolar effects and I is the nuclear spin. Since the change in energy levels depends on m, the magnetic quantum number, the quadrupole interaction removes the degeneracy in the magnetic transition frequencies. When I is a half-integer, the transition between the $m = \frac{1}{2}$ and $m = -\frac{1}{2}$ levels is unchanged (see equation (19)). However, in this case second-order perturbation theory gives:

$$\nu_{m=\frac{1}{2}\rightarrow m=-\frac{1}{2}} = \nu_0 + \\ + \frac{9}{64} \cdot \frac{2I+3}{4I^2(2I-1)} \left(\frac{e^2qQ}{h}\right)^2 \frac{1}{\nu_0} (1-9\cos^2\theta) \times \\ \times (1-\cos^2\theta) \qquad (20)$$

which, because of the ν_0^{-1} dependence, is field-dependent ($\nu_0 = \gamma Ho/2\pi$). Fig. 1 shows how the

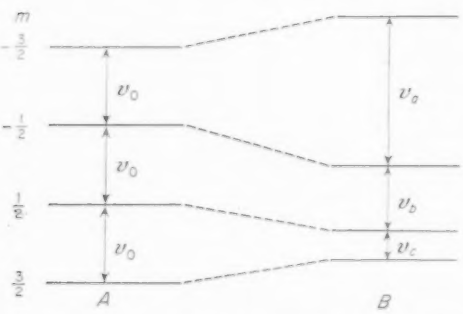

FIG. 1. Energy levels and transition frequencies: (a) magnetic interaction only; (b) magnetic and quadrupolar interaction. $\nu_b = \nu_0$ if the quadrupolar interaction is sufficiently small in comparison to the magnetic interaction.

quadrupolar interaction alters the spacing of the magnetic energy levels, and the transition frequency, for the case of $I = 3/2$ and a particular value of the angle θ.

The electrical field-gradient generated at a resonating nucleus by surrounding ions depends upon the deformation of the ion core surrounding the nucleus. This deformation arises from polarization by the external charges and from mechanical squeezing or constraint of the ion core by neighboring atoms.

The electrical polarization effect can be described in terms of an antishielding parameter[15] γ_∞. The electric field-gradient at the nucleus is $(1-\gamma_\infty)$ times the electric field-gradient that would exist at the nucleus if there were no ion core. The values of γ_∞ have been calculated for a number of free ions by FOLEY *et al.*[15], STERNHEIMER and FOLEY[16], DAS and BERSOHN[17], and WIKNER and DAS[18]. The values are presented in Table 1 as collected from several papers. It is clear that for all but the very lightest ions the multiplication of the electric field-gradient arising from ion core polarization must be taken into account.

The effect of the ion core on the electric field-gradient when the ion is in a solid is still an open question. Both effects, polarization and mechanical squeezing or constraint, can be taken into account by replacing the coupling constant e^2qQ/h in our equations by $\lambda e^2qQ/h$, where λ includes both the factor $1-\gamma_\infty$ from polarization and also the mechanical effect. Experiments by WATKINS[5] involving the bromine NMR lines in KBr initially indicated that λ for Br is about 10. This represents a reduction by about a factor of 10 from the free-ion value given in Table 1. An analysis of the ^{23}Na line in $NaNO_2$ by HON and BRAY[19] suggests that λ is about unity for Na in $NaNO_2$. This represents a reduction by a factor of 5 from the free-ion value. Both of these results are in agreement with the simple physical picture that atoms surrounding an ion in a lattice should hinder the deformation of the core by electric fields and hence reduce the antishielding effect. However, BERSOHN's[20] analysis of the ^{23}Na line in $NaNO_3$ and $NaClO_3$ yields a value of λ in both compounds nearly equal to the computed $1-\gamma_\infty$ for Na^+. Further, experiments by REIF[8] on AgBr suggest that λ for Br in AgBr is much larger than the original value for Br in KBr given by WATKINS. WATKINS has now re-interpreted his experiment (see p. 414 of reference (14)). His new values of λ are 100 for Br in KBr and 300 for ^{127}I in KI. It is clear that some uncertainty exists as to the true values of λ. However, experiments[21] involving ultrasonically-induced spin transitions give further evidence that λ for ^{23}Na in NaCl is between 1 and 5, while $\lambda(^{127}\text{I})/\lambda(^{23}\text{Na}) \sim 11$ in NaI. The values of λ employed in analysis of the present experiments are given under Procedure.

The quadrupolar interaction in ionic crystals can be computed in the following manner. Consider each ion to be a point charge at the ion site. The potential due to such a charge is e/r, which,

when differentiated twice, gives the electric field-gradient tensor $\nabla \boldsymbol{E}$. In a co-ordinate system such that the charge (ion) is on the z-axis, $\nabla \boldsymbol{E}$, at the origin, is given by:

$$\left.\begin{aligned} \phi_{zz} &= \frac{2e}{z^3} = eq \\ \phi_{yy} &= \frac{-e}{z^3} = -\tfrac{1}{2}eq \\ \phi_{xx} &= \frac{-e}{z^3} = -\tfrac{1}{2}eq \end{aligned}\right\} \quad (21)$$

with all other components zero. Since $\phi_{yy} = \phi_{xx}$, η vanishes (equation (18)) and the electric field-gradient tensor for a single point charge has rotational symmetry. The quadrupolar interaction of a nucleus at the origin with this field-gradient gives the satellite splitting (equation (19)), to first order, as

$$\delta\nu = A\frac{e}{r^3}(3\cos^2\theta - 1) \quad (22)$$

where θ is the angle between $\boldsymbol{H}_0$ and the axis of symmetry and A is given by

$$A = \frac{2m-1}{4I(2I-1)} \cdot \frac{3e\lambda Q}{h}. \quad (23)$$

The total splitting due to the entire lattice is then

$$\delta\nu = A\sum_i \frac{ei}{r_i^3}(3\cos^2\theta_i - 1). \quad (24)$$

At a distance from a point charge, the electric field and its gradient are reduced by the dielectric properties of the crystal. A multiplicative factor $\beta\epsilon$, given by

$$\beta\epsilon = \frac{2\epsilon+3}{5\epsilon} \quad (25)$$

where ϵ is the static dielectric constant, should be introduced.[14] This factor is about $\frac{1}{2}$ for alkali halides. Since the factor is close to unity and because the quadrupolar interaction is of short range (r^{-3} dependence), we will neglect the effect of the dielectric properties.

In perfect cubic crystals the crystallographic axes are principal axes of the field-gradient tensor. The x–x, y–y and z–z components of the tensor are equal from cubic symmetry and, hence (equation (16)), each must be zero. In a perfect crystal, then $\delta\nu$ of equation (24) vanishes, and all NMR transitions of a given nuclear species occur at the same frequency, ν_0. If the crystal is not perfect, however, those nuclei in the vicinity of an imperfection no longer have an environment of cubic symmetry. The resulting quadrupolar interaction can be evaluated from equation (24).

The effect of dislocations will be considered first. For cubic ionic crystals, the quadrupolar splitting of the NMR line is due to changes in the sum in equation (24) ascribable to the stresses produced by the dislocation. The splitting is given by

$$\delta\nu = A\sum_i e_i\left(\Delta r_i\frac{\partial}{\partial r_i} + \Delta\cos\theta_i\frac{\partial}{\partial\cos\theta_i}\right)\frac{1}{r_i^3}(3\cos^2\theta_i - 1) \quad (26)$$

since $\delta\nu = 0$ in the unstressed crystal. WATKINS[5] calculated $\delta\nu$ due to an edge dislocation, approximately, by considering only the displacements of the nearest neighbors of a resonating nucleus. His result, when $\boldsymbol{H}_0$ is in a [1, 0, 0]-type direction, is

$$\delta\nu = -A\frac{36e}{a_0^3}\frac{\sigma xy}{G}\mu_1\mu_2 \quad (27)$$

for an edge dislocation formed by putting an extra half-plane of atoms along the y' axis and ending at the z' axis (the primes denote the co-ordinate system of the dislocation). In this equation a_0 is the nearest-neighbor distance, μ_1 and μ_2 are the direction cosines of $\boldsymbol{H}_0$ with respect to the x' and y' axes of the coördinate system of the dislocation, σxy is the shear stress, and G the shear modulus. In an entirely analogous fashion, the splitting due to the stresses of a screw dislocation has been calculated[22,23] as:

$$\delta\nu = -D\sin 2\theta\sin\phi \quad (28)$$

when $\boldsymbol{H}_0$ is along a [1, 0, 0]-type direction and the axis of the screw dislocation is in the z' direction. θ is the angle between $\boldsymbol{H}_0$ and the z' axis ($\cos\theta = \mu_3$) and ϕ is the angle between the projection of $\boldsymbol{H}_0$ in the $x'y'$ plane and the normal to the z' axis from the resonant nucleus. This expression for $\delta\nu$ shows explicitly that $\delta\nu$ is independent of a rotation

of the $x'y'z'$ co-ordinate system about the z' axis, a result expected from the cylindrical symmetry of the screw dislocation. In equation (28), the quantity D is given by

$$D = \frac{36Aeb}{a_0{}^3 4\pi r} \tag{29}$$

where b is the periodicity of atoms along the z' axis and r is the length of the normal from the z' axis to the resonating nucleus.

Equations (27) and (28) display the approximate dependence of the splitting, $\delta\nu$, on the orientation of an edge or screw dislocation, respectively, with respect to $\boldsymbol{H}_0$, when $\boldsymbol{H}_0$ is in a [1, 0, 0]-type direction. WATKINS[5] assumed the dislocations to be oriented at random and averaged over the distribution to account for the loss of intensity of the ^{127}I NMR line in KI crystals and the ^{79}Br and ^{81}Br lines in KBr crystals. However, it is clear from a study of equations (27) and (28) that $\delta\nu$ can vanish if there is preferential orientation of the dislocations in certain directions. A discussion of this possibility, and the discovery of such a condition in some NaI and KI single crystals, has been presented elsewhere.[23] The condition is of particular value for the radiation-damage studies reported here, since, if $\delta\nu = 0$ in the absence of radiation damage, the satellite transitions ($m \rightarrow m = 1$, $m \neq \frac{1}{2}$) are present in the single, unsplit observed resonance and radiation-induced defects can affect the resonance by first-order quadrupolar effects (equation (19)). If, on the other hand, the satellite transitions are already split out at all orientations of $\boldsymbol{H}_0$, they are generally unobservable and the defects can influence the remaining central $m = \frac{1}{2} \rightarrow$ $\rightarrow m = -\frac{1}{2}$ transition only through second-order (equation (20)) and higher-order perturbations which are less effective.

The next defect to be discussed is the point defect, either a vacancy or an interstitial ion. For the first part of this discussion, the crystal is assumed to be perfect except for point defects. The frequency splitting, due to the quadrupole interaction, of the NMR line of a nucleus in the region of a point defect is given by equation (22), where $\boldsymbol{r}$ is the distance from the defect to the nucleus and θ is the angle between $\boldsymbol{r}$ and $\boldsymbol{H}_0$. The effect of a large number of such defects on the NMR line will be considered in a phenomenological manner first suggested by BLOEMBERGEN.[4] Fig. 2 depicts a representative NMR signal (the first derivative of the absorption curve). Experimentally, the signal is no longer observed when $|\delta\nu| > \delta\nu_m$, for then the signal becomes lost in the noise. The parameter

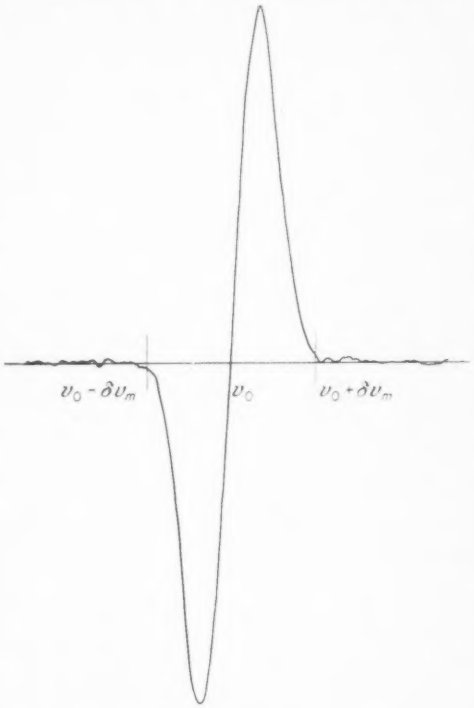

FIG. 2. Representative nuclear magnetic resonance signal, showing noise level and extent in frequency of observable response.

$\delta\nu_m$ is determined experimentally. In order to simplify the computation, it is assumed that each nucleus in the perfect crystal gives its contribution to the resonance line at ν_0. Actually, because of the dipole broadening and possible quadrupole broadening arising from dislocations and strains in the unirradiated crystal, the shape function $g(\nu - \nu_0)$ is not a delta function, and the line has a finite width. The effect of finite line width on the following calculations has been investigated[22] with the conclusion that the finite width of the line adds only to the detail of the argument and not to the gross effects.

If a nucleus in a crystal containing point defects has a quadrupolar interaction such that the splitting of the NMR line for this nucleus is greater

than $\delta\nu_m$, its contribution to the line is no longer observed. This experimental observation is in accordance with the model that the frequency spectrum of splittings in the crystal is a broad distribution, all of which falls below the noise level. For first-order splitting (splitting of the transitions other than the central $m = \frac{1}{2} \rightarrow m = -\frac{1}{2}$ transition) this condition, $\delta\nu > \delta\nu_m$, is:

$$\frac{2m-1}{4I(2I-1)} \frac{3e^2\lambda Q}{hr^3} |(3\cos^2\theta - 1)| > \delta\nu_m \quad (30)$$

or

$$r^3 < \frac{2m-1}{4I(2I-1)} \frac{3e^2\lambda Q}{h\delta\nu_m} |(3\cos^2\theta - 1)|. \quad (31)$$

When made into an equality, equation (31) defines a volume, $Ve^{(1)}$, such that all the nuclei within this volume surrounding a point defect have their NMR signal split out to the extent that the satellite transitions no longer contribute to the observed NMR line.

A large number of defects will affect a large portion of the volume of the crystal, and the intensity of the observed line will be diminished. The intensity change can be computed in the following way. If V is the volume of the sample, the line intensity, I_0, of the perfect crystal will be

$$I_0 = bV \quad (32)$$

where b is a proportionality factor. If V_t is the total volume of the crystal wherein the contributions of the nuclei are removed from the line, the intensity of the line in the imperfect crystal is:

$$I = b(V - V_t). \quad (33)$$

The quantity ΔI, defined as

$$\Delta I = \frac{I_0 - I}{I_0}, \quad (34)$$

is given by

$$\Delta I = \frac{V_t}{V}. \quad (35)$$

If there are N defects, an approximate estimate of ΔI can be found by taking V_t to be

$$V_t = NVe, \quad (36)$$

from which

$$\Delta I = NVe/V = \rho Ve \quad (37)$$

where ρ is the density of defects. In first order, however, the central line ($m = \frac{1}{2} \rightarrow m = -\frac{1}{2}$ transition) is unchanged when the spin is half-integral. The volume affected in first order is a function of m, $Ve^{(1)}(m)$. This quantity can be obtained by integration, using r as the function of θ given in equation (31), and is [22]

$$Ve^{(1)}(m) = 2{\cdot}42 \frac{2m-1}{I(2I-1)} \frac{e^2\lambda Q}{h\delta\nu_m}. \quad (38)$$

The change in intensity for each transition other than the $m = \frac{1}{2} \rightarrow m = -\frac{1}{2}$ transition is then

$$\Delta I^{(1)}(m) = g(m) Ve^{(1)}(m) \quad (39)$$

where $g(m)$ is the fraction of the total intensity of the perfect crystal line contributed by the $m \rightarrow \rightarrow m \rightarrow 1$ transition. In practice, the total change of intensity of the line from first-order effects is taken as

$$\Delta I^{(1)} = g\rho Ve^{(1)} \quad (40)$$

where $Ve^{(1)}$ is the average of $Ve^{(1)}(m)$ over the appropriate m values and g is the fraction of intensity contributed to the perfect crystal line by all transitions other than $m = \frac{1}{2} \rightarrow m = -\frac{1}{2}$.

The frequency splitting of the central line, to second order, is

$$\delta\nu = \frac{9}{64} \cdot \frac{2I+3}{4I^2(2I-1)} \times \times \frac{1}{\nu_0} \left(\frac{2e^2\lambda Q}{hr^3} \right)^2 (1 - 9\cos^2\theta)(1 - \cos^2\theta). \quad (41)$$

The equation defining the volume affected per defect for the central line is

$$r^3 = \frac{2e^2\lambda Q}{h} \left[\frac{9}{64} \cdot \frac{2I+3}{4I^2(2I-1)} \cdot \frac{1}{\nu_0\delta\nu_m} + + |(1 - 9\cos^2\theta)|(1 - \cos^2\theta) \right]^{\frac{1}{3}}. \quad (42)$$

A numerical integration, employing this $r(\theta)$ function, yields:[22]

$$Ve^{(2)} = 1{\cdot}48 \left[\frac{2I+3}{I^2(2I-1)} \cdot \frac{1}{\nu_0\delta\nu_m} \right]^{\frac{1}{3}} \frac{e^2\lambda Q}{h}. \quad (43)$$

Because of the factor $\nu_0^{-\frac{1}{3}}$, this volume is field-dependent. The change in intensity of the central

line ascribable to second-order effects is:

$$\Delta I^{(2)} = \rho V e^{(2)}. \tag{44}$$

If the defect density, ρ, is large and the defects are scattered at random in the crystal, equations (40) and (44) will overestimate the effect of the defects on ΔI, since there will be some overlapping of the volumes, Ve, affected by each defect. The values of ΔI (equations (40) and (44)) corrected for this overlap of randomly distributed defects are

$$\Delta I^{(1)} = g[1 - \exp(-\rho V e^{(1)})] \tag{45}$$

and

$$\Delta I^{(2)} = [1 - \exp(-\rho V e^{(2)})] \tag{46}$$

which reduce to the values of equation (40) and (44) for small values of ρ. The calculation of the corrected values is indicated in Appendix A.

If the defects are clustered in such a way that the average distance between nearest-neighbor defects in a cluster is less than the radius of the volume, Ve, affected per defect, their effect on the NMR line will be even less than if scattered randomly. That is, there will be more overlapping of affected volumes than is accounted for by the random-distribution model. The corrected values of ΔI in this case are

$$\Delta I^{(1)} = g[1 - \exp(-\rho_c V e^{(1)'})] \tag{47}$$

and

$$\Delta I^{(2)} = [1 - \exp(-\rho_c V e^{(2)'})] \tag{48}$$

where ρ_c is the density of clusters (number of clusters per unit volume) and

$$\left.\begin{aligned} Ve^{(1)'} &= [n^{\frac{1}{3}}d + Ve^{(1)\frac{1}{3}}]^3 \\ Ve^{(2)'} &= [n^{\frac{1}{3}}d + Ve^{(2)\frac{1}{3}}]^3. \end{aligned}\right\} \tag{49}$$

n is the number of defects in a cluster and d is the average separation between adjoining defects in a cluster. The calculation of the corrected values (equations (47)–(49)) is indicated in Appendix B.

When the clusters are caused by neutron irradiation, ρ_c is given by the number of neutron–atom collisions per unit volume,

$$\rho_c = \frac{\sigma_e \phi_t}{{a_0}^3} \tag{50}$$

where σ_e is the elastic scattering cross-section, ϕ_t is the appropriate total neutron flux and a_0 is the nearest-neighbor distance between atoms in the crystal.

The angular properties of the effect of point defects on the NMR line have yet to be determined. Fig. 3 indicates the geometry of the situation. The axis of rotation of the crystal is chosen as the z axis, so $\boldsymbol{H}_0$ is always in the x–y plane. $\boldsymbol{r}_k$ is the displacement vector from a defect to the kth atom. If the $(\lambda_i)_k$ are the direction cosines of $\boldsymbol{r}_k$ with respect to the x, y and z axes,

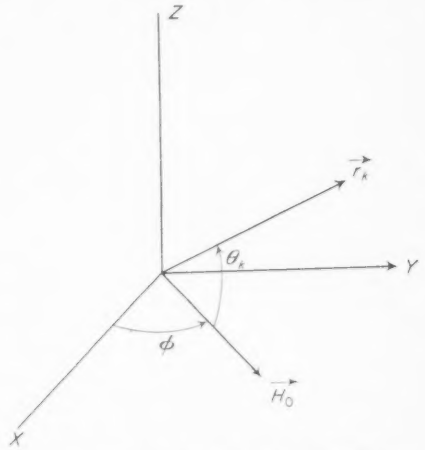

FIG. 3. Geometry for splitting of NMR line.

$$\operatorname{Cos}\theta_k = (\lambda_1)_k \cos\phi + (\lambda_2)_k \sin\phi \tag{51}$$

and the frequency shift of the satellite transitions of the kth nucleus is (equation (22)), after some manipulation,

$$\delta\nu_k = \frac{Ae}{{r_k}^3}\{3[1-(\lambda_3)_k]^2 \sin^2(\phi+\delta_k) - 1\}. \tag{52}$$

δ_k is given by

$$\delta_k = \tan^{-1}(\lambda_1)_k/(\lambda_2)_k. \tag{53}$$

Because of the phase factor, δ_k, the angles at which extrema of equation (52) occur vary over the entire range of ϕ when all the nuclei affected by the defect are considered. Hence, the effect of a point defect on the NMR is independent of the orientation of $\boldsymbol{H}_0$ with the crystallographic axes when the defect affects a large number of nuclei.

There is one other matter to consider. Both an interstitial and a vacancy produce strain in the crystal. Assuming that a point defect produces very nearly the same strain as a spherical inclusion

in an elastic medium, the strain would have the form[24]

$$\Delta r = \frac{a}{R^3} \tag{54}$$

where R is the distance from the defect to the nucleus in question. Substitution of this value in equation (26) gives a frequency shift of the form

$$\delta\nu = -3\frac{Aa}{R^3}\sum_i \frac{e_i}{r_i^4}(3\cos^2\theta_i - 1). \tag{55}$$

A multiplicative factor should be placed on the right side of equation (55) to include the effects of antishielding and mechanical distortion of the ion cores. However, the strain effects are generally smaller than the effects produced by the electrical charge of the defect[8,14] and both effects depend in the same manner (r^{-3} or R^{-3}) on an appropriate distance. Hence, the strain effects may effectively be incorporated into the parameter λ.

(c) *Radiation damage*

In this section, attention will be focused on that part of radiation damage theory[25–28] concerned with neutron irradiation. The principal interest is in the results of elastic neutron–atom collisions, although, in the case of lithium halides the inelastic collisions

$$_3Li^6 + _0n^1 \rightarrow _2He^4 + _1H^3 + 4{\cdot}8 \text{ MeV} \tag{56}$$

are quite important.

In the present experiments, the samples were irradiated in a nuclear reactor to take advantage of the high neutron flux and consequent heavy radiation damage. As a result, the energy of the incident neutrons ranged from thermal energy (1/40 eV) up to the energy of fission neutrons (2 MeV). Except for the lithium halides, the incident neutrons of interest are of high energy and the effect of the flux can be approximated by considering only that 10 per cent of the beam with an average energy of 1 MeV. Such neutrons are non-relativistic and behave like classical billiard balls during the neutron-atom collision.[27] The energy, E', transferred to a lattice atom of mass M in such a collision by a neutron of mass 1 a.m.u. (atomic mass units) and energy E_0 is

$$E' = E'_m \sin^2(\theta/2) \tag{57}$$

where

$$E'_m = \frac{4M}{(M+1)^2}\cdot E_0 \tag{58}$$

is the maximum energy which can be transferred and θ is the scattering angle in the center-of-mass system.[27] The average energy transferred for isotropic scattering is

$$\overline{E'}_m = E'_m/2. \tag{59}$$

It is assumed that the energy, E', transferred from the neutron to the atom must be greater than the energy, E_d (commonly 25 eV), of binding of the atom to its normal site in order for a displacement to take place.

Since the primary displaced atom may have an energy many times E_d, it may displace additional atoms through atom–atom collisions. It may also lose energy by increasing lattice vibrations or, since it is ionized, by exciting electrons to higher energy states. The total number of displacements following an initial primary displacement has been the subject of theoretical study by Seitz[29], Snyder and Neufeld[30–32], Harrison and Seitz[33], and Seitz and Koehler[27]. These calculations are based on the assumptions that the collisions are all of the binary, hard sphere type; that the atoms in the solid all have the same mass and may be treated as being randomly distributed; and that each lattice atom is bound to its normal lattice site in a square-well potential of depth E_d. These assumptions result in an integral equation, first derived and solved by Snyder and Neufeld, for the number of displacements, $g(X_1)$, produced by a primary displacement with energy $E = X_1E_d$. Seitz and Koehler give the solution, obtained by numerical integration, as:

$$g(X_1) = 0{\cdot}56(1+X_1) \qquad X_1 \geqslant 4. \tag{60}$$

The average value, $\bar{\nu}$, of $g(X_1)$ is obtained by averaging $g(X_1)$ over the energy distribution of primary displacements. For fast neutron irradiation the distribution function is $\sin^2\theta/2$ (equation (57)), which for isotropic scattering gives the result

$$\bar{\nu} = 0{\cdot}56 + 0{\cdot}28\frac{E'_m}{E_d}. \tag{61}$$

It is interesting to note that if no energy were lost to lattice vibrations $\bar{\nu}$ should be $\overline{E'}_m/E_d$ or 0·50

E'_m/E_d. Equation (61) indicates that about half of the energy is lost in lattice vibrations.

It is pointed out by SEITZ and KOEHLER[27] that the hard-sphere collision model is valid for collisions involving atoms with atomic mass as low as 10 a.m.u. Collisions involving atoms of mass less than 10 a.m.u. are not necessarily isotropic in the energy range of the knocked-on atoms produced by 1-MeV neutrons. However, SEITZ and KOEHLER show[27] that even in this case equation (61) gives a good approximation to the average number of displacements per primary event.

SAMPSON *et al.*[34] have developed a procedure allowing use of a continuous, rather than a square-well, potential binding an atom to its normal site. The procedure changes some of the details of the computation but leaves the general results intact.

The assumption that the atoms are randomly situated removes any directional effects which would be important if the mean free path, L_d, between displacement collisions is small, but much less important if this mean free path is large. Computations of L_d will be discussed below.

The problem of the energy lost to electronic excitation by knocked-on atoms has been treated by SEITZ and KOEHLER[27] with the following conclusions. In terms of an energy parameter,

$$\epsilon = \frac{M_e}{M} E \tag{62}$$

where M is the mass of the atom interacting with an electron, E is the energy of the atom, and M_e is the electron mass, the atom has an appreciable probability of exciting only those electrons for which the transition energies are less than or equal to ϵ. Electrons more tightly bound are unaffected. Further, those electrons of the atom bound with energies greater than ϵ will not be swept off by crystalline fields.

From equations (58) and (62) it is possible to find the maximum energy parameter, ϵ_m, for primary displacements caused by 1-MeV neutrons. Using an M_e of 1/2000 a.m.u., the value is

$$\epsilon_m = 2\times 10^3/(M+1)^2 \text{ eV}. \tag{63}$$

In insulators, the minimum transition energy is the energy, Eg, of the gap between the filled valence band and the empty conduction band. Eg is usually about 10 eV. As long as ϵ_m is less than 10 eV, there will be no appreciable electronic excitation. Using this, the condition on M is

$$(M+1)^2 > 200 \tag{64}$$

or, roughly, as long as M is larger than 13 a.m.u. there will be only a negligible amount of energy lost to electronic excitation. This condition is satisfied except in the case of lithium halides. A particularly important exception is the case of the light and very energetic products of the reaction given in equation (56). In that case, the following approximation is made. Until the reaction products are reduced in energy so that $\epsilon < Eg$, all energy lost will result in electronic excitation with no displacements. As soon as ϵ becomes less than Eg, energy is no longer lost in electronic excitation, but only through production of displacements and into lattice vibrations.

This discussion of radiation damage so far yields no information as to the spatial distribution of the displacements in the crystal lattice. The damage consists of patches of disrupted crystal associated with each neutron–atom collision which transfers an energy greater than E_d to the atom. Since the mean free path for elastic neutron–atom collisions is long (of the order of 1 cm), the affected regions will all arise from different neutrons and the patches will be randomly distributed. Within each region, however, the nature of the damage and the size of the region will depend on the mean free path, L_d, between atom–atom collisions. If L_d is much greater than the nearest-neighbor separation, a_0, of atoms in the crystal, the defects will be Frenkel pairs of vacancies (empty sites of displaced atoms) and interstitials (displaced atoms). On the other hand, if $L_d < a_0$, the concept of Frenkel pairs is no longer meaningful, because the vacancies and interstitials would recombine immediately. However, if $L_d < a_0$ a large amount of energy is dissipated in a limited region about the neutron–atom collision point, heating the lattice to temperatures above its melting point. After resolidification, the lattice in this region may be considerably disrupted compared to the normal crystal. This is the basis of BRINKMAN's "displacement spike".

The problem of determining this mean free path has been attacked by BRINKMAN[35a] whose procedure is equivalent to assuming the potential of

VOL 11 195

interaction between colliding atoms to have the form[35b]

$$V(r) = \frac{Z^2}{2r_0} \frac{\exp(-r/r_0)}{1-\exp(-r/2r_0)} \qquad (65)$$

where Z is the atomic number of the colliding atoms. For a collision between like atoms, r_0 would be given by

$$r_0 = \xi a_h / z^{1/3} \qquad (66)$$

where a_h is the radius of the first Bohr orbit in hydrogen. The resulting solution[35] for L_d is a strong function of the screening parameter ξ. As BROOKS[36] points out, a typical L_d for 1-MeV neutrons, using $\xi = 1$, is several lattice spacings. The Frenkel-pair picture would be appropriate in this case. BRINKMAN, however, prefers a value for ξ of 2·09, as derived by OZEROFF[37]. This reduces L_d to the order of one lattice spacing and the displacement spike picture would be appropriate.

Equations (47)–(49), and their accompanying discussion, show that the interpretation of the effects of irradiation on the NMR signal depends strongly on the mean free path between atom–atom collisions. Values of the defect separation, d, deduced from the present experiments appear later in this paper.

The fraction of atoms displaced in the crystal is given by

$$f_d = \bar{\nu}\sigma_c\phi_t \qquad (67)$$

where $\bar{\nu}$ is given by equation (61), σ_c is the elastic scattering cross-section for 1-MeV neutrons, and θ_t is the integrated fast neutron flux (taken as 1-MeV neutrons composing 10 per cent of the total flux).

3. EXPERIMENTAL APPARATUS

In the course of this work, two magnets were used: a permanent magnet* with cylindrical pole faces 6 in. in dia., a gap-width of 1½ in., and a nominal field of 5250 G; an electromagnet† with 6-in. dia. pole faces, capable of producing a field of 9000 G for a gap of 1½ in.

The radio-frequency spectrometer was originally purchased from Nuclear Magnetics Corporation, but was thoroughly modified and improved before the present experiments were carried out. Descriptions of the construction and operation of such spectrometers, employing a POUND–KNIGHT–WATKINS regenerative oscillator, are given in references (5) and (38). Details of the modification of the present instrument are given elsewhere,[22] but two points are of general interest.

The performance of the radio-frequency oscillator-amplifier unit depends quite strongly on the characteristics of the first r.f. amplifier tube (6AK5). The same is true for the oscillator tube (6BZ7), though to a somewhat lesser extent. In order that the unit operate at its best, a 6AK5 with high gain (large gm) should presumably be used. However, a selection, based on actual in-spectrometer performance, among 50 tubes all with about the same high-gm value may yield two or three of such exceptional characteristics that the signal-to-noise ratio of the final recorded NMR signal is improved by a factor of 3–5. These exceptional tubes may revert to normal behavior in a few hours or may last for months. The behavior is unexplained. 403B tubes made by Ericsson of Sweden appear to be best, but RCA 5654 and G.E. 6AK5 tubes have also been used.

Fluorescent lights of the "instant start" type were found to give appreciable r.f. interference. The older slow-starting type give interference only when a bulb is old. It was found necessary to shield the resonance probe in the magnet completely and to ground the shield to the chassis of the radio-frequency unit.

The magnetic field is sinusoidally modulated (through use of Helmholtz coils attached to the resonance probe‡) with a modulation amplitude much smaller than the line width. Hence, after passing through a narrow-band amplifier[5] and phase-sensitive detector,[5] the signal is presented on the recorder as the first derivative of the absorption curve.

4. PROCEDURE

(a) *Irradiation*

All of the samples investigated were irradiated in the nuclear reactor at the Brookhaven National Laboratory. The crystals used were Harshaw§ material with the exception of KBr crystals, which were obtained from the Optovac Company.‖ The crystals were grown from very pure materials and become even more pure in the growth process.[39]

The samples were wrapped in aluminum foil, previous to irradiation, to give protection against damage in handling and against moisture. Some of the materials, particularly LiI and NaI, are quite deliquescent.

Initial experiments on the ^{81}Br NMR line in KBr indicated that the reactor-produced damage

*Indiana Steel Products Company, Valparaiso, Ind.

†Model V-4007 electromagnet and model V-2200 regulated magnet power supply, Varian Associates, Palo Alto, California.

‡Design and constructional details of these probes are given elsewhere.[22]

§The Harshaw Chemical Company. 1945 East 97th Street, Cleveland 6, Ohio.

‖Optovac Company, North Brookfield, Mass.

responsible for observable changes in the NMR lines anneals, though slowly, at room temperature. The air-cooled sites in the reactor are far above room temperature and the water-cooled facility is at about 30°C. To reduce the ambient temperature during irradiation, CO_2 from a cylinder of compressed CO_2 was allowed to leak over the samples. This procedure kept the ambient temperatures at 0°C or lower, unless lithium halides were included among the specimens. Internal heating from the reaction of equation (56) drove the temperature up in the latter case.

The samples generally become radioactive through the nuclear absorption of neutrons. With the exception of activity from ^{36}Cl in NaCl, the halflife of this induced activity is of the order of a day or less, and the samples are soon safe for handling.

Unfortunately, the facility at Brookhaven for irradiation at liquid-nitrogen temperature was not in operation during these experiments.

(b) *Investigation*

After irradiation, the samples are kept at dry-ice temperature until they are to be investigated. When a sample is needed, it is placed in a desiccator and allowed to come to room temperature, at which all the present investigations are made. The sample is then mounted on a goniometer, for rotation in the magnetic field, and inserted in the resonance probe. The irradiated crystal and an unirradiated crystal are run interchangeably, as a function of the orientation of $\boldsymbol{H}_0$ with respect to the crystalline axes, without changing any spectrometer setting. Since the volume of the resonance probe containing the sample is quite small, a negligible absorption of moisture by the sample occurs during a run.

Most of the crystals are in the form of cylinders $\frac{1}{2}$ in. long and $\frac{7}{16}$ in. in dia. and can be oriented on the basis of their cleavage characteristics. Since the irradiated and control samples are not identical in weight, they are weighed with an analytic balance and the intensities of the NMR lines are adjusted accordingly.

A calibration signal[5] is used so that resonances obtained at different r.f. levels can be compared. Saturation studies of irradiated and unirradiated specimens indicated no observable change in T_1, the spin-lattice relaxation time.

(c) *Analysis*

The values of the quadrupole moment, Q, used in the computations were taken from a table of nuclear data compiled by Varian Associates. This table is reproduced in reference (2).

In almost every case, no change in line shape was noted between irradiated and unirradiated specimens. That is, $g_2(\nu-\nu_0) = pg_1(\nu-\nu_0)$, where p is simply a number and g_2 and g_1 are the shape functions of the lines in the irradiated and unirradiated crystals, respectively. Hence, the ratio of intensities is taken to be the ratio of the experimental maximum derivatives when the lines to be compared are recorded under identical conditions.

In calculating the number of defects to be expected from irradiation, the crystal is assumed to be a monatomic solid. The number of defects depends on the maximum energy transferred from the incident neutron to the target atom. Since more energy is transferred to a light atom than a heavy atom the solid behaves, on the average, more as though it consisted of the lighter atoms. A monatomic mass equal to the geometric mean of the constituent atoms is used, as an approximation, because this mean is closer to the mass of the lighter atom. The elastic scattering cross section is taken as the arithmetic mean of the cross section for each constituent atom since it is just a geometrical concept.

In ionic crystals, the number of defects per atom which can affect the NMR line is twice the fraction of atoms displaced, since both the displaced atom (interstitial) and its empty lattice site (vacancy) can affect the line.

BINDER and STURM[40] have found that in LiF the average number of displacements per nuclear reaction (equation (56)) is $1{\cdot}4\times10^3$, which agrees rather well with the estimate of $1{\cdot}9\times10^3$ given by SEITZ and KOEHLER[27]. The geometric mean of the masses of lithium and iodine is about twice the geometric mean of the masses of lithium and fluorine. Since $\bar{\nu}$ (equation (61)) is approximately inversely proportional to the first power of the atomic mass (equations (58) and (61)), an estimate of $1{\cdot}0\times10^3$ displacements per reaction (equation (56)) is used in predicting the fraction of displaced atoms in LiI.

The values of the parameter λ (see Section 2(b)) used in analyzing the data were chosen by reducing the free ion results, $1-\gamma_\infty$, by an amount

VOL 11 195

suggested by the rather meager experimental data available. For lithium, the factor $1-\gamma_\infty$ is practically unity (Table 1), so λ is chosen to be unity. This choice should be sufficiently accurate in view of the experimental accuracy of the present experiments. The factor $1-\gamma_\infty$ for sodium is 5·5 (Table 1). Because there is data indicating λ may be about the same as $1-\gamma_\infty$[20,21] and other data indicating λ may be about unity,[19,21] a value of 3 is chosen. Values of $\lambda = 30$ for Br and $\lambda = 60$ for I were chosen at the time of performing and analyzing the present experiments. The choice of $\lambda = 30$ for Br was based on the experiments of REIF[8] which suggest a λ larger than that originally deduced by WATKINS.[5] The re-interpretation[14] by WATKINS, yielding values of 100 for Br in KBr and 300 for I in KI, is not in good agreement with the value of 40 for Br in KBr and the lower bound of 50 for I in KI suggested by OTSUKA on the basis of his recent[41] NMR studies of dislocations in KBr and KI. Consequently, we have retained our original choice of λ values. A discussion of these λ values, based on the present investigations, will be given later in this paper.

Table 1. Calculated values of the antishielding parameter, γ_∞, for certain free ions

Ion	γ_∞	Reference
Li^+	+ 0·26	a
Na^+	− 4·1	b
	− 4·5	a
K^+	− 12·8	c
Rb^+	− 49·3	c
	− 70·7	b
Cs^+	−110·4	c
	−143·5	b
Cl^-	− 49·3	c
	− 56·6	b
Br^-	− 99·0	c
I^-	−178·8	c

(a) DAS T. P. and BERSOHN R., *Phys. Rev.* **102**, 733 (1956).
(b) STERNHEIMER R. M. and FOLEY H. M., *Phys. Rev.* **102**, 731 (1956).
(c) WIKNER E. G. and DAS, T. P., *Phys. Rev.* **109**, 360 (1958).

5. EXPERIMENTAL RESULTS

(a) NaI

Figure 4 displays the recordings at $\nu_0 = 7{\cdot}20$

FIG. 4. NMR line of ^{127}I in a single crystal of NaI as the crystal is rotated about a [1, 0, 0]-type direction (approximately) normal to H_0. When $\phi = 79°$ and 166°, H_0 is nearly in a [1, 0, 0]-type direction.

Mc/s of the ^{127}I line in an unirradiated crystal as a function of the orientation of H_0 with respect to the crystalline axes. The rotation is nominally about a [1, 0, 0]-type axis, but misorientation by as much as 3° may exist. The origin of the angle ϕ is arbitrary, but the intensity anomalies, discussed elsewhere,[23] do occur when H_0 is in closest approach to [1, 0, 0]-type directions. They are most clearly seen in the plot (Fig. 5) of the product of the maximum derivative, Dm, and the square of the separation in frequency, $\Delta\nu_{p-p}$, between the two peaks of the derivative curve. This product should be constant as a function of angle if only dipolar effects are present.[42] It is clear that first order quadrupolar effects from radiation-induced defects are important when H_0 is at or near [1, 0, 0] orientations, while only second-order quadrupolar effects are important for other orientations of H_0.

Plots of Dm versus ϕ for ^{127}I in unirradiated and irradiated crystals of NaI are given in Figs. 6 and 7, respectively. The irradiated crystal received a total integrated fast neutron flux of $4{\cdot}1\times10^{17}$ nvt. (This, and subsequent figures for fast neutron dosages, rest on an assumption that the reactor fast flux can be approximated by 1-MeV neutrons composing 10 per cent of the total flux. More accurate flux measurements will be made in future experiments). Cooling during irradiation was attempted, but, owing to heating from lithium halides in the same container, the temperature rose on several occasions above room temperature.

Comparison of Figs. 6 and 7 shows that the irradiation decreases the line intensity only in the sharp peaks associated with the intensity anomaly (the broad sinusoidal variations of Dm in both plots arise from dipolar effects). Hence, the defect density is large enough to give first-order quadrupolar effects, but not large enough to affect the central line in second order.

The results of analysis are given in Table 2. Here ρ_r is the defect density deduced from the measured ΔI by using the random-distribution model (equation (45)). ρ is the expected density calculated with the methods of SEITZ and KOEHLER[27]: $\rho = 2f_d$, where f_d is the fraction of atoms displaced (equation (67)). d is the average separation between nearest-neighbor defects in a cluster deduced (equations (47)–(50)) from ΔI by assuming the cluster model and that the number of

Table 2. Tabulation of theoretical and experimental results

Crystal	Nucleus	ΔI	ρ_r (a)	ρ (b)	d (c)	r_e (d)
NaI	^{127}I (1st order)	0·290	$3{\cdot}3\times10^{-3}$	$2{\cdot}9\times10^{-5}$	10	51
	^{127}I (2nd order)	<0·05	$3{\cdot}3\times10^{-3}$	$<1{\cdot}6\times10^{-4}$	<6	14
	^{23}Na (1st order)	<0·05	$3{\cdot}3\times10^{-3}$	$<7{\cdot}8\times10^{-4}$	<8	9·6
LiI	^{127}I (2nd order)	0·516	$2{\cdot}9\times10^{-1}$	$2{\cdot}8\times10^{-3}$		12
	^{7}Li (1st order)	0·082	$2{\cdot}9\times10^{-1}$	$5{\cdot}4\times10^{-3}$		5·6
KI	^{127}I (2nd order); 1st set	0·067	$2{\cdot}3\times10^{-3}$	$2{\cdot}2\times10^{-4}$	9	15
	^{127}I (2nd order); 2nd set	0·104	$1{\cdot}1\times10^{-3}$	$3{\cdot}4\times10^{-4}$	14	
KBr	^{81}Br (2nd order) 2 months' delay	0·27	$3{\cdot}6\times10^{-3}$	$2{\cdot}5\times10^{-3}$	13	10
	^{81}Br (2nd order) 3 months' delay	0·15	$3{\cdot}6\times10^{-3}$	$1{\cdot}3\times10^{-3}$		

(a) Expected defect density in defects/atom.

(b) Defects/atom deduced from experiment.

(c) Average nearest-neighbor separation (in Å) of defects in a cluster.

(d) Effective radius (in Å) of volume affected by defect.

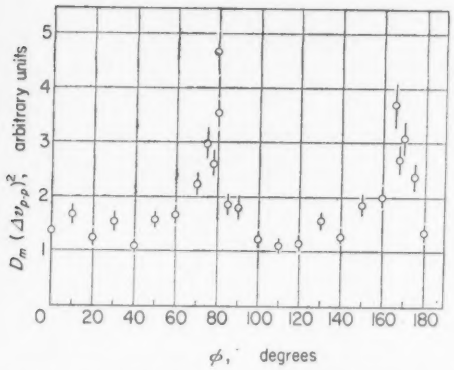

FIG. 5. Product of *Dm* and $(\Delta\nu_{p-p})^2$ versus angle of rotation (ϕ) for ^{127}I line in NaI.

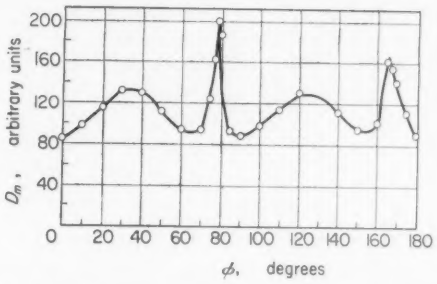

FIG. 6. Maximum derivative (*Dm*) versus angle of rotation (ϕ) for ^{127}I line in unirradiated NaI.

defects, n, per cluster is the theoretical $2\bar{\nu}$. Values of $\delta\nu_m$, a_0 and σ used in the analysis are given in Table 3.

Table 3. *Values of* a_0, σ *and* $\delta\nu_m$

Crystal	a_0 (a)	σ (b)	$\delta\nu_m$ (d)	
NaI	3·23	5	^{23}Na	4·5
			^{127}I	2
LiI	3·0	(945[c])	^{7}Li	7·5
			^{127}I	5
KI	3·53	4·5	^{127}I	1·25
KBr	3·29	3·5	^{81}Br	2

(a) Nearest-neighbor distance between atoms (Å). F. SEITZ, *Modern Theory of Solids*. McGraw-Hill Book Co., New York (1940).

(b) Elastic scattering cross-section in barns for 1-MeV neutrons. D. J. HUGHES and R. B. SCHWARTZ, *Neutron Cross-Sections*. Brookhaven National Laboratory (1957). Value given is average for constituents of crystal.

(c) Capture cross-section in barns for thermal neutrons. See reference in footnote (b). This value of σ must be weighted according to the atomic per cent of ^{6}Li in the crystal in computing f_d.

(d) Experimental maximum frequency shift from ν_0, in Kc/s, beyond which a contribution to the NMR line is unobservable.

Thermal annealing during irradiation may partially explain why the experimentally determined defect density, ρ_r, in irradiated NaI is about 100 times smaller than the expected density, ρ. The other possibility is that the random-distribution model is not applicable in this case. The effective radius of a defect when first-order effects on the ^{127}I line are considered is about 51 Å (deduced from $Ve^{(1)}$). Using the cluster model, d is only 10 Å on the assumption that $n = 2\nu$. The overlap of affected regions within a cluster is very great on this basis. Of course, if annealing has occurred, d will be larger.

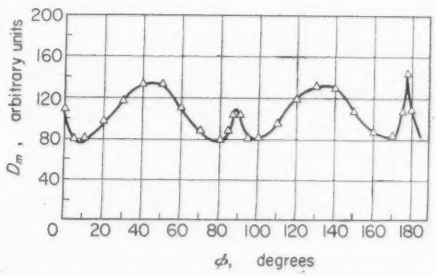

FIG. 7. Maximum derivative (*Dm*) versus angle of rotation (ϕ) for ^{127}I line in neutron-irradiated NaI.

The ^{23}Na resonance in NaI shows no intensity anomaly (Fig. 8). This lack of quadrupolar effects from dislocations is expected since λQ for ^{127}I is about 150 times larger than λQ for ^{23}Na. The satellite transitions contribute to the observed resonance at all orientations of H_0 with respect to the crystal axes. ΔI for the ^{23}Na line is zero within experimental error for the irradiation received. If it is assumed that ΔI can be as large as 0·05 and still be unobservable due to experimental error, $\rho_r < 7{\cdot}8 \times 10^{-4}$ defects/atom. The effective radius of $Ve^{(1)}$ for first-order effects on the ^{23}Na line is 9·6 Å. Since this radius $r_e^{(1)}$, is comparable to d (obtained from the relatively accurate measurement of first-order effects on the ^{127}I line) while

$d \geqslant 2r_e$ is necessary for the validity of the random distribution model, the value $\rho_r < 7{\cdot}8\times10^{-4}$ defects/atom is only an order-of-magnitude estimate. A smaller upper limit on ρ_r is given by considering second-order effects on the ^{127}I line. Comparing the lines in the irradiated and unirradiated crystals at angles where there is no first-order contribution to the ^{127}I line, the change in intensity is zero. Assuming again $\Delta I < 0{\cdot}05$, the random-distribution model gives $\rho_r < 1{\cdot}6\times10^{-4}$ defects/atom. The effective radius of a defect when second-order effects on the ^{127}I resonance are considered is 14 Å (deduced from $Ve^{(2)}$). Again, the defect density given by ρ_r is not reliable. Upper bounds on d, obtained by applying the cluster-model equations to the ^{23}Na (first-order effects) and ^{127}I (second-order effects) measurements are included in Table 2 for completeness, though their accuracy is very questionable.

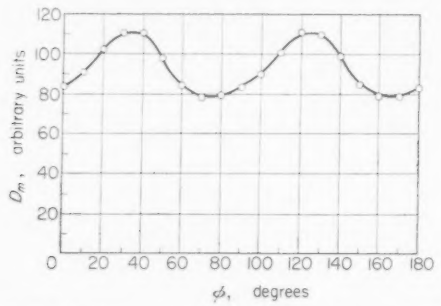

FIG. 8. Maximum derivative (Dm) versus angle of rotation (ϕ) for ^{23}Na line in NaI.

(b) LiI

There is no intensity anomaly in the ^{127}I line in the unirradiated crystal, which indicates that the dislocations are randomly oriented. The satellite transitions are presumably split out so as to be unobservable. The observed line is then the central $m = \frac{1}{2} \rightarrow m = -\frac{1}{2}$ transition and only second-order effects can give intensity changes. The irradiation history is the same as that of the NaI.

Fig. 9 shows Dm versus ϕ for the ^{127}I line in both the unirradiated and the irradiated crystals at a field of 8450 G. The intensity change is $\Delta I = 0{\cdot}516$, which gives $\rho_r = 2{\cdot}8\times10^{-3}$ defects/atom.

If the intensity change is due to second-order effects, it should be larger at lower fields because of the ν_0^{-1} dependence of $Ve^{(2)}$ (equation (43)). The NMR lines in the unirradiated and irradiated crystals were compared at a field of 4100 G. This gave $\Delta I = 0{\cdot}67$. Because of the lower signal-to-noise ratio at the lower field, this result is rather inaccurate. However, the ratio $\Delta I_{4100}/\Delta I_{8450} = 1{\cdot}3$ compares favorably with the ratio $[(\nu_0)\,8450/(\nu_0)\,4100]^{\frac{1}{3}} = 1{\cdot}43$, which corroborates the assumption that only second-order effects are important.

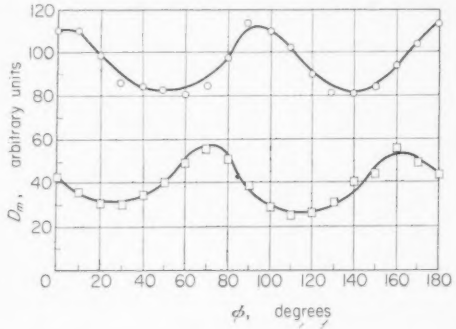

FIG. 9. Maximum derivative (Dm) versus angle of rotation (ϕ) for ^{127}I line in unirradiated LiI (○) and neutron-irradiated LiI (⊡).

The use of $\bar{\nu} = 1{\cdot}0\times10^3$ in this case yields an expected defect density of $\rho = 2{\cdot}9\times10^{-1}$ defects/atom. This value is undoubtedly unrealistic because of radiation annealing,[43] and it is also probable that significant thermal annealing occurred. This criticism of the experiment is emphasized by application of the cluster model. Use of $n = 2\bar{\nu} = 2{\cdot}0\times10^3$ in equation (49) for d yields a value smaller than the nearest-neighbor distance (3·00 Å) between atoms.

Because λQ is so much smaller for ^{7}Li than for ^{127}I, the satellite transitions are not split out in the unirradiated crystal and all transitions contribute to the observed line. Fig. 10 shows Dm versus ϕ for the ^{7}Li line in both the unirradiated and irradiated crystals. The intensity change is $\Delta I = 0{\cdot}082$, which gives $\rho_r = 5{\cdot}4\times10^{-3}$ defects/atom. Again, application of the cluster model, using $n = 2\bar{\nu} = 2{\cdot}0\times10^3$ in equation (49), yields a value of d which is meaningless (approximately half of the nearest-neighbor distance between atoms in the crystal). It is concluded that extensive radiation annealing (and some thermal annealing) occurred in this material. The investigation of radiation

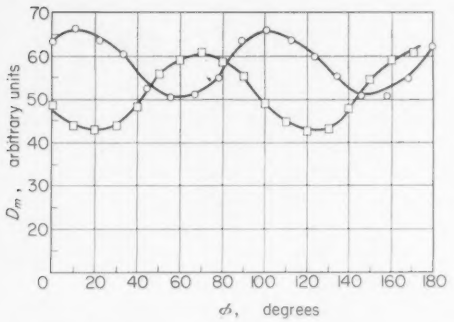

FIG. 10. Maximum derivative (*Dm*) versus angle of rotation (ϕ) for ^{7}Li line in unirradiated LiI (○) and neutron-irradiated LiI (⊡).

damage in LiI must be repeated with shorter irradiation periods.

(c) KI

The ^{127}I line in the unirradiated crystal shows an anomaly which is similar to the intensity anomaly of the ^{127}I line in NaI. However, the splittings do not all go to zero when $\boldsymbol{H}_0$ is in a [1, 0, 0]-type direction, but are distributed over a frequency range several times the width of the central line. This can be seen in Fig. 11 in the broad shoulders which appear at certain orientations as the crystal is rotated about a [1, 0, 0]-type axis. A discussion of this phenomenon has been given elsewhere.[23]

The first set of KI samples investigated have the same history of irradiation as the NaI and LiI crystals discussed above. Consequently, part of the damage was annealed. Enough damage remained, however, to remove any trace of the satellite transitions (constituting the shoulders of the line) when $\boldsymbol{H}_0$ is in a [1, 0, 0]-type direction. Fig. 12 shows *Dm* versus ϕ for both the irradiated and unirradiated crystals. No quantitative results were obtained from the first-order affects. However, there is some decrease in intensity of the line at $\phi = 45°$, which must be due to second-order effects. The decrease in intensity, $\Delta I = 0{\cdot}067$, yields $\rho_r = 2{\cdot}2 \times 10^{-4}$ defects/atom, as compared to the expected value $\rho = 2{\cdot}3 \times 10^{-3}$ defects/atom. The average radius of the volume affected per defect is 15 Å (deduced from $Ve^{(2)}$), so that the average separation between adjacent defects should be roughly 30 Å or greater if the model of

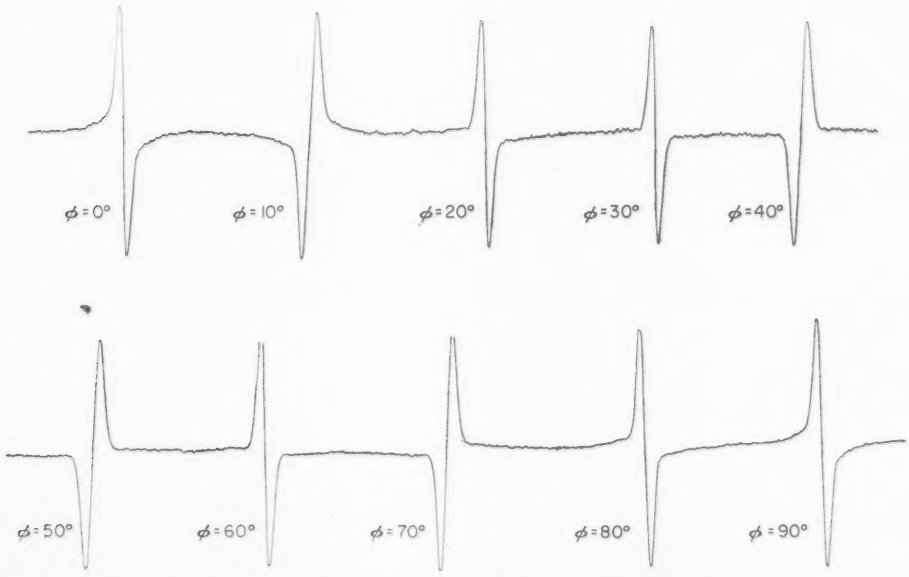

FIG. 11. NMR line of ^{127}I in a single crystal of KI as the crystal is rotated about a [1, 0, 0]-type direction normal to H_0. When $\phi = 0°$ and 90°, H_0 is in a [1, 0, 0]-type direction.

randomly distributed defects is to be valid. The cluster model gives $d = 9$ Å. Hence, the defects are apparently arranged in clusters with a large overlap of affected regions within a cluster.

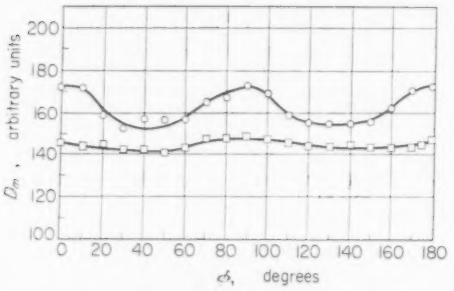

FIG. 12. Maximum derivative (Dm) versus angle of rotation (ϕ) for ^{127}I line in unirradiated KI (○) and neutron-irradiated KI (⊡).

Another set of samples were maintained at 0°C or lower during an irradiation with an integrated fast flux of $2{\cdot}0\times10^{17}$ nvt. Very little annealing should have occurred in this case. The line intensity change of $\Delta I = 0{\cdot}104$ yields $\rho_r = 3{\cdot}4\times\times10^{-4}$ defects/atom, while the expected concentration is $\rho = 1{\cdot}1\times10^{-3}$ defects/atom. However, the cluster model yields $d = 14$ Å, again indicating that the defects occur in clusters. Comparison of the neutron dosages, ϕ, and ΔI values in the two cases ($\phi = 4{\cdot}1\times10^{17}$ nvt, $\Delta I = 0{\cdot}067$; $\phi = 2{\cdot}0\times\times10^{17}$ nvt, $\Delta I = 0{\cdot}104$) confirms the occurrence of significant thermal annealing in the first crystal. Consequently, the value $d = 14$ Å computed for the second crystal is accepted as the more accurate value.

(d) KBr

A crystal of KBr was used in the first experiment of the series reported here. The unirradiated crystal showed no intensity anomalies. The dislocations are assumed to be oriented at random, and the observed line is essentially only the central transition. The sample was irradiated* in a water-cooled hole in the Brookhaven reactor, with an integrated fast neutron flux of $6{\cdot}6\times10^{-17}$ nvt. After irradiation the sample was kept at room temperature.

*The authors are indebted to Dr. VANCE SAILOR, of the Brookhaven National Laboratory, for this irradiation.

The sample was not investigated until two months after removal from the reactor (because of a breakdown of the NMR equipment), at which time the observed intensity change was $\Delta I = 0{\cdot}27$. From this, it can be deduced that $\rho_r = 2{\cdot}5\times10^{-3}$ defects/atom. Three months after removal from the reactor, $\Delta I = 0{\cdot}15$ and $\rho_r = 1{\cdot}3\times10^{-3}$ defects/atom. The predicted defect density, without annealing, was $\rho = 3{\cdot}6\times10^{-3}$ defects/atom. The computed d value (13 Å) is only slightly larger than the value $r_e^{(2)} = 10$ Å for the effective radius of the volume $Ve^{(2)}$. Hence, the cluster model is apparently required.

6. DISCUSSION

The clustering of the defects produced by a primary displaced atom is substantiated by these experiments. If the defects were uniformly distributed (random model) throughout the crystal, there would be line broadening of the type observed by REIF.[8,14] However, no change of line shape occurred on irradiation. Further evidence arises from application of the cluster model. All computed values of d (Table 2) are such that $d \lesssim r_e$, whereas $d \geqslant 2r_e$ should be found if the random model is applicable.

Table 2 lists the average nearest-neighbor distance between defects in a cluster. Since, with the exclusion of lithium halides, the number of displacement collisions is half the number of defects, the average distance between displacement collisions is $2^{\frac{1}{3}}\,d$ or $1{\cdot}26\,d$. The data for NaI, KI and KBr indicate that the mean free path between displacement collisions is approximately 4 or 5 times the nearest-neighbor separation, a_0, for irradiation effects due to fast neutrons. The mean free path between displacement collisions depends on the parameter ξ (equation (66)) which measures the strength of the screening in the screened coulomb potentials of the colliding atoms. The above results indicate that the value of unity, which gives the mean free path between displacement collisions as several lattice spacings, is better than the value of 2·09, which gives about one lattice spacing.

The ρ_r values (Table 2) depend inversely on the first power of λ. If the random model were applicable, comparison of experimental ρ_r and computed ρ values would be a sensitive means of checking assumed values of λ. Unfortunately, the

apparent clustering of defects thwarts any assessment of the assumed λ values. The computed values of d depend only on $\lambda^{\frac{1}{3}}$ in a subordinate term (equations (38), (43) and (49)).

A large density of color centers is produced in all of the crystals during irradiation. It has already been remarked that these centers do not noticeably affect the spin-lattice relaxation time T_1. However, the large spin–spin interactions between these centers and neighboring nuclei could conceivably be responsible for the observed decreases of NMR line intensities in the irradiated crystals. The data indicate that this is not the case. A representative Hamiltonian for the interaction is

$$H = a\bar{I}\cdot\bar{S} \tag{68}$$

where $\boldsymbol{I}$ is the nuclear spin and $\boldsymbol{S}$ is the electron spin (consideration of the F-center model is probably sufficient for the present discussion). The constant a is given by

$$a = -\frac{16}{3}\pi\frac{\mu_B\mu|\psi|^2}{I} \tag{69}$$

where μ_B is the magnetic moment of the electron forming the color center, μ is the magnetic moment of the nucleus, and ψ is the wave function of the electron at the nucleus. If this interaction were causing the intensity decreases in NaI, the effect would be larger for the ^{23}Na line than for the ^{127}I line (μ/I and probably $|\psi|^2$ are larger in the former case). No effect was observed on the ^{23}Na line, while the ^{127}I resonance was strongly decreased in intensity. The LiI results provide an even stronger argument, since μ/I of ^{7}Li is even larger than that of ^{23}Na and yet the ^{127}I line is again affected more than the ^{7}Li resonance.

Additional experiments involving reactor irradiation and NMR investigation of NaI at lower temperatures and perhaps additional irradiation must be carried out to secure measurable effects in both the ^{23}Na and ^{127}I NMR lines. This will allow an internal check of the data through comparison of the two resonances when both are influenced by first-order quadrupolar effects. The rubidium and cesium halides become too radioactive to permit sufficient reactor irradiation. However, they are under study in a program involving charged-particle irradiation. A compound such as RbBr is of particular interest, since all the constituent nuclei are of approximately the same mass and all have large λQ values.

The present experiments, whose results have appeared in brief form elsewhere,[44–46] establish the usefulness of NMR techniques in quantitative studies of radiation damage in solids. The method of analysis, while not as comprehensive as the treatment of COHEN and REIF[14] which became available after these experiments were completed, appears adequate to obtain valuable information.

Acknowledgements—We are indebted to Dr. ARNOLD SILVER, now at the Scientific Laboratory of the Ford Motor Company, and P. A. CASABELLA, of Brown University, for discussion and suggestions in the course of this work. P. J. RING and J. G. O'KEEFE, of Brown University, have also contributed. We wish to thank PAUL COLSMANN, JACK FLOYD, and their associates in the Isotopes and Special Materials Section of the Brookhaven Laboratory for their suggestions and efforts in carrying out the irradiations.

APPENDIX A

The correct ΔI for large defect densities can be calculated in the following manner. The problem is analogous to that of computing how much volume is removed from a volume V after n scoops, each of volume Ve, are taken out at random. Let $V(n)$ be the total volume removed after n scoops. $V(n)$ is related to $V(n-1)$ by

$$V(n) = V(n-1)+Ve\left[1-\frac{V(n-1)}{V}\right] \tag{A.1}$$

where the second term on the right is the average amount scooped out on the nth scoop when n is a fairly large number. Rearrangement yields

$$\frac{V(n)}{Ve} = 1+r\frac{V(n-1)}{Ve} \tag{A.2}$$

where $r = 1-(Ve/V)$ and is always less than unity. The solution of this difference equation of first order is

$$V(n) = Ve\left[\frac{1-r^n}{1-r}\right]. \tag{A.3}$$

If V is taken as unit volume, n becomes the density of defects, ρ. The total volume removed per unit volume is

$$V_t(\rho) = 1-(1-Ve)^{\rho}. \tag{A.4}$$

Rearranging and taking the logarithm of both sides gives

$$\ln[1-V_t(\rho)] = \rho\ln(1-Ve). \tag{A.5}$$

Since $Ve \ll 1$,

$$V_t(\rho) = 1 - \exp(-\rho Ve). \qquad \text{(A.6)}$$

Equations (45) and (46) follow from (35).

It should be noted that an analysis of radiation damage in terms of the change, ΔI, in the NMR signal can also be made from the approach and equations previously given by BLOEMBERGEN[4] and BLOEMBERGEN and ROWLAND[47]. This approach considers the number of lattice sites surrounding a nucleus which, if occupied by a defect, will cause the loss of the resonance contribution from that nucleus. Neither of the two methods is exact for all cases in its present state of development. A refined treatment, incorporating both approaches, will be presented in a subsequent paper concerned with investigations under more accurately measured conditions of neutron flux, crystal temperature during irradiation, post-irradiation annealing, etc. Equations (45)–(49) of this paper are sufficient for the present analysis and agree within experimental error with the alternative[4,47] analysis.

APPENDIX B

The change in intensity of the NMR line in the case of clustered defects can be computed approximately in the following manner. Assume that each cluster is a sphere of radius R. Let r_e be the effective radius of the volume, Ve, affected by each defect in a cluster. The volume, Ve', affected by each cluster is taken as

$$Ve' = \frac{4\pi}{3}(R+r_e)^3 \qquad \text{(B.1)}$$

where it is assumed that there are no nuclei unaffected within the cluster and the actual (unknown) shape of the cluster is approximated by a sphere. R is obtained from the fact that the number of defects, n, in a cluster is

$$n = \frac{4\pi}{3}(R/d)^3 \qquad \text{(B.2)}$$

where d is the average separation between adjoining defects in the cluster. r_e is given by

$$Ve = \frac{4\pi}{3} r_e^3. \qquad \text{(B.3)}$$

The volume affected by a cluster is then

$$Ve' = (n^{\frac{1}{3}}d + Ve^{\frac{1}{3}})^3. \qquad \text{(B.4)}$$

Equations (47)–(49) result when the clusters are randomly distributed in the crystal.

REFERENCES

1. PAKE G. E., *Amer. J. Phys.* **18,** 438, 473 (1950).
2. PAKE G. E., *Solid State Physics* (Ed. F. SEITZ and D. TURNBULL) Vol. 2 p. 1. Academic Press, New York (1956).
3. SEITZ F., *Imperfections in Nearly Perfect Crystals* (Ed. W. SHOCKLEY *et al.*) p. 3. Wiley, New York (1952).
4. BLOEMBERGEN N., *Defects in Crystalline Solids* (Report of the 1954 Bristol Conference), p. 1. Physical Society, London (1955).
5. WATKINS G. D., Ph. D. Thesis, Harvard University (1952).
6. WATKINS G. D. and POUND R. V., *Phys. Rev.* **89,** 658 (1953).
7. COHEN M. H. and REIF F. *Defects in Crystalline Solids* (Report of the 1954 Bristol Conference). Physical Society, London (1955).
8. REIF F., *Phys. Rev.* **100,** 1597 (1955).
9. VAN VLECK J. H., *Phys. Rev.* **74,** 1168 (1948).
10. SHULMAN R. G., WYLUDA B. J. and ANDERSON P. W., *Phys. Rev.* **107,** 953 (1957).
11. POUND R. V., *Phys. Rev.* **79,** 685 (1950).
12. BERSOHN R., *J. Chem. Phys.* **20,** 1505 (1952).
13. VOLKOFF G. M., *Canad. J. Phys.* **31,** 820 (1953).
14. COHEN M. H. and REIF F., *Solid State Physics* (Ed. F. SEITZ and D. TURNBULL), Vol. 5. Academic Press, New York (1957).
15. FOLEY H. M., STERNHEIMER R. M. and TYCKO D., *Phys. Rev.* **93,** 734 (1954).
16. STERNHEIMER R. M. and FOLEY H. M., *Phys. Rev.* **102,** 731 (1956).
17. DAS T. P. and BERSOHN R., *Phys. Rev.* **102,** 733 (1956).
18. WIKNER E. G. and DAS T. P., *Phys. Rev.* **109,** 360 (1958).
19. HON J. F. and BRAY P. J., *Bull. Amer. Phys. Soc.* **2,** 225 (1957).
20. BERSOHN R., *Bull. Amer. Phys. Soc.* **1,** 215 (1956).
21. PROCTOR W. G. and ROBINSON W. A., *Phys. Rev.* **104,** 1344 (1956).
    JENNINGS D. A., TANTTILA W. H. and KRAUS O., *Phys. Rev.* **109,** 1059 (1958).
    TAYLOR E. F., Ph. D. Thesis, Harvard (1958).
22. HON J. F., Ph.D. Thesis, Brown University (1958).
23. HON J. F. and BRAY P. J., *J. Appl. Phys.* **30,** 1425 (1959).
24. TIMOSHENKO S., *Theory of Elasticity*. McGraw-Hill, New York (1934).
25. SLATER J. C., *J. Appl. Phys.* **22,** 237 (1951).
26. SEITZ F., *Phys. Today* **5,** No. 6 (1952).
27. SEITZ F. and KOEHLER J. S., *Solid State Physics* (Ed. F. SEITZ and D. TURNBULL) Vol. 2, p. 305. Academic Press, New York (1956).
28. DIENES G. J. and VINEYARD G. H., *Radiation Effects in Solids.* Interscience Publishers, New York (1957).
29. SEITZ F., *Disc. Faraday Soc.* **5,** 271 (1949).
30. SNYDER W. S. and NEUFELD J., *Bull. Amer. Phys. Soc.* **29,** 23 (1949).
31. NEUFELD J. and SNYDER W. S., *Phys. Rev.* **99,** 1326 (1955).
32. SNYDER W. S. and NEUFELD J., *Bull. Amer. Phys. Soc.* **1,** 32 (1956).

33. HARRISON W. and SEITZ F., *Phys. Rev.* **98,** 1530 (1955).
34. SAMPSON J. B., HURWITZ H. and CLANCY E. F., *Phys. Rev.* **99,** 1657 (1955).
35a. BRINKMAN J. A., *J. Appl. Phys.* **25,** 961 (1954).
35b. BRINKMAN J. A. Private communication.
36. BROOKS H., *Annual Review of Nuclear Science* Vol. 6. Annual Reviews, Palo Alto, California (1956).
37. OZEROFF J. D., *Knolls Atomic Power Laboratory*, General Electric Company, *Report* 205 (1949).
38. POUND R. V. and KNIGHT W. D., *Rev. Sci. Instrum.* **21,** 219 (1950).
39. BUCKLEY H. E., *Crystal Growth*. Wiley, New York (1951).
40. BINDER D. and STURM W. J., *Phys. Rev.* **107,** 106 (1957).
41. OTSUKA E., *J. Phys. Soc. Japan* **13,** 1155 (1958).
42. PURCELL E. M., BLOEMBERGEN N. and POUND R. V., *Phys. Rev.* **70,** 988 (1946).
43. COOPER H. G., KOEHLER J. S. and MARX J. W., *Phys. Rev.* **94,** 496 (1954).
44. HON J. F. and BRAY P. J., *Bull. Amer. Phys. Soc.* **2,** 267 (1957).
45. HON J. F. and BRAY P. J., *Bull. Amer. Phys. Soc.* **2,** 344 (1957).
46. BRAY P. J. and HON J. F., *Bull. Amer. Phys. Soc.* **3,** 22 (1958).
47. BLOEMERGEN N. and ROWLAND T. J., *Acta Met.* **1,** 731 (1953).

OL.
11
959

Electrical effects during cyclic stressing of sodium chloride

(*Received* 8 *April* 1959)

In order to explain the temperature-dependence of the mechanical strength of ionic crystals of the sodium chloride type, Eshelby *et al.*[1] have extended to dislocations Lehovec's[2] idea of a surface space-charge layer, resulting from a difference in the formation energy of the two kinds of vacancies. According to these authors, a dislocation should carry a positive line charge, resulting from the presence of an excess of positively charged jogs;[3] moreover it should be surrounded by a cylindrical Debye–Hückel cloud of vacancies of opposite sign, so that overall electrical neutrality is maintained. This assumption was also proposed as a possible explanation for the electrical effects observed by Fischback and Nowick[4] and Caffyn and Goodfellow[5] on the plastic deformation of NaCl.

To test this assumption in a more direct way, the following experiment was performed. A bent sodium chloride crystal was clamped in a jig, as shown in Fig. 1. The two ends to which the forces were applied were carefully shielded and grounded so that eventually friction-induced charges would be carried away. A gold electrode was evaporated on to the central part, and connected by means of a gold wire to the input of an electrometer tube and then to an oscilloscope. The crystal was brought into vibration in the frequency range 10–100 c/s by means of loud-speaker coil system, which was placed far enough away and carefully shielded to avoid any transmission to the crystal other than purely mechanical. The amplitude of vibration was kept so small that no appreciable plastic deformation could take place, the only possible effect thus being a forced vibration of the dislocations around their equilibrium position.

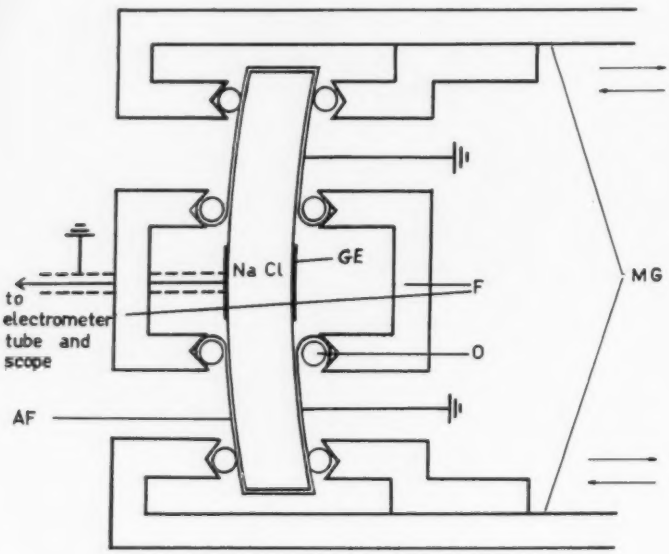

Fig. 1. Grip system for vibrating crystal.

GE = gold electrode
AF = aluminium foil
O = rubber **O**-rings
F = fixed steel grips
MG = movable grips

The method of deformation favours pure bending, with a maximum moment in the central part.

VOL.
11
1959

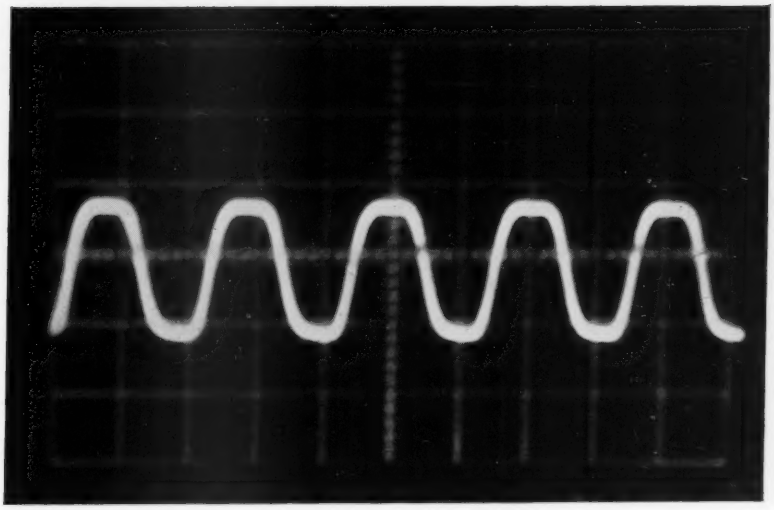

FIG. 3. Oscilloscope trace of response of sodium chloride crystal to vibration. One division corresponds to 1 mV.

[*Facing page* 171

VOL
11
195

The dislocations of the majority sign, induced by bending, are expected to move inward from both sides of the neutral plane if the instantaneous deformation is such as to increase the curvature (Fig. 2a); the reverse is true for deformation in the opposite sense (Fig. 2b). This situation is visualized in Fig. 2.

It is clear that the crystal now contains a system of vibrating dipoles which induce charges on the electrode applied to the surface. Opposite faces of the crystal should acquire the same charge in the same phase of vibration and a charge of the opposite sign in the opposite phase. For a sinusoidal input signal, the signal shown in Fig. 3 was observed on the oscilloscope. It is thought that this is the effect sought, since other possible minor effects were carefully eliminated. A piezoelectric effect is very improbable, since its existence would be in conflict with the crystal symmetry of NaCl. The possibility that bending may cause deviations from symmetry giving rise to piezoelectric effects can however not completely be excluded. A phase difference was found between the signal applied to the loud-speaker coil and the output signal of the crystal. Although part of this phase difference is certainly due to inertia of the mechanical transmission, especially at the higher frequencies, it is also what one would expect from the theoretical picture. The measurement of the phase difference between applied shear stress and the output signal is clearly of considerable interest in the study of the interaction of vacancies and moving dislocations. The method described here is therefore a promising tool for this type of study.

Acknowledgement—This work is part of a research scheme supported by the Institut pour l'Encouragement de la Recherche Scientifique dans l'Industrie et l'Agriculture (C.E.S.). We wish to thank Prof. Dr. W. DEKEYSER for his continuous interest.

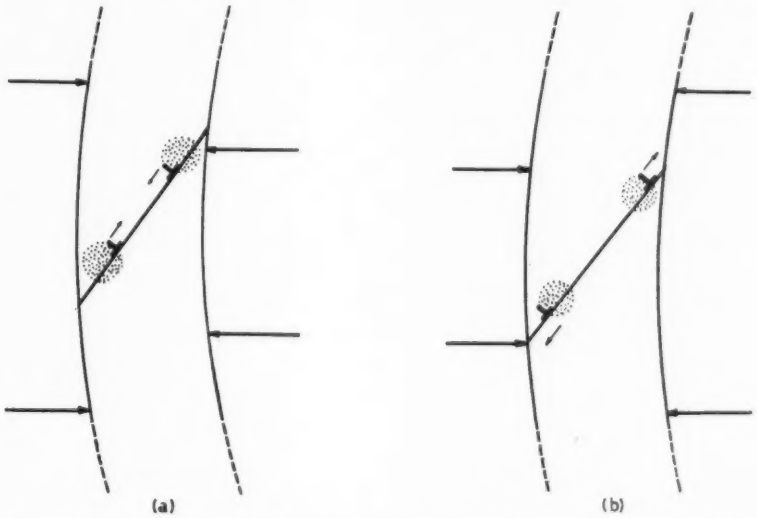

FIG. 2. Schematic picture of dislocation movement with respect to vacancy cloud.

Laboratorium voor Kristalkunde,
Rozier 6,
Gent, Belgium.

S. AMELINCKX
J. VENNIK
G. REMAUT

References

1. ESHELBY J. D., NEWEY C. W. A., PRATT P. L. and LIDIARD A. B., *Phil. Mag.* **3,** 76 (1958).
2. LEHOVEC K., *J. Chem. Phys.* **21,** 1123 (1953).
3. SEITZ F., *Rev. Mod. Phys.* **23,** 328 (1951).
4. FISCHBACH D. B. and NOWICK A. S., *Phys. Rev.* **98,** 1543 (1955); *J. Phys. Chem. Solids* **5,** 302 (1958).
5. CAFFYN J. E. and GOODFELLOW T. L., *Nature, Lond.* **178,** 878 (1955).

Low-temperature phase transitions in β-$Ca_3(PO_4)_2$ and related compounds.

(*Received* 2 *April* 1959)

On measuring the temperature-dependence of the luminescence of β-$Ca_3(PO_4)_2$ activated with divalent tin[1] an anomalous behaviour of the luminescence intensity was found. When samples of the phosphor were cooled down quickly from room temperature, they showed a bright luminescence at −190°C (excitation: $\lambda = 2537$ Å), whereas on cooling slowly almost no luminescence was observed at low temperatures. On reheating these samples, the luminescent intensity versus temperature curve showed two anomalous jumps in the regions around −40 and +35°C (Fig. 1,

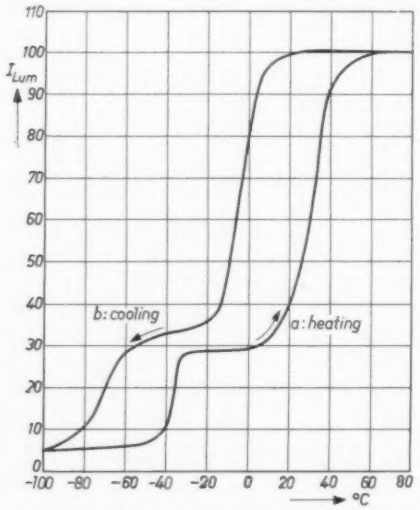

Fig. 1. Anomalous temperature-dependence of the luminescence in β-$Ca_3(PO_4)_2$–Sn; heating and cooling rate ~3°/min.

curve a). In the reverse direction (cooling), the jumps occurred at lower temperatures (Fig. 1, curve b). This behaviour strongly suggests the occurrence of two low-temperature phase transitions in β-$Ca_3(PO_4)_2$–Sn, which is a rather striking phenomenon to take place in a compound at approximately 1700°C below its melting-point. The effect described might cause complications in cases where β-$Ca_3(PO_4)_2$ phosphors (or the related phosphors to be described further on) are used in fluorescent lamps which occasionally are operated at low temperatures, for instance in street lighting.

The presence of two phase transitions in β-$Ca_3(PO_4)_2$ could be confirmed by calorimetric measurements. The C_p versus T curve showed two peaks in the same temperature regions. Because the peaks were also present in samples which did not contain tin, the transitions cannot be connected with the presence of the tin. The sum of the heat effects connected with the transitions was found to be about 1700 cal/mole, the sum of the transition entropies being approximately 9·2 cal/°C-mole. In order to get measurable effects, we had to take rather large samples of β-$Ca_3(PO_4)_2$, resulting in retardation effects in the calorimetric measurements. For this reason, and also because the transitions are sluggish (cf. Fig. 1), the peaks in the specific heat versus temperature curve often were not very well resolved. We therefore could not safely divide the values of the total heat and entropy effects given above into contributions of the separate transitions.

We also investigated a number of Sr-orthophosphates modified with small amounts of smaller cations such as Mg, Zn, Ca, Cd and Al. These modified orthophosphates, which also give bright phosphors on activation with divalent tin, probably have the same structure as β-$Ca_3(PO_4)_2$[2]. In fact these phosphors also showed the same transitions as β-$Ca_3(PO_4)_2$, even in about the same temperature regions as is shown in Fig. 2. The total energy and entropy effects agree to within 10 per cent with those found for the transitions in β-$Ca_3(PO_4)_2$.

β-$Ca_3(PO_4)_2$ is found in nature as the mineral Whitlockite. It shows a high-temperature transition at 1180°C to α-$Ca_3(PO_4)_2$. The β-$Ca_3(PO_4)_2$ is very suitable as a host lattice in phosphor making. Up to now efficient phosphors have been prepared with Tl, Ce (Mn), Sn (Mn), and Cu (Mn) as activating impurities. The structure of β-$Ca_3(PO_4)_2$ has been investigated by Mackay[3,4], who found that the rhombohedral unit cell contains 7 molecules of $Ca_3(PO_4)_2$. This is in conflict with the space-group R_{3c}, which requires an even number of molecules per unit cell. On the basis of his X-ray work, Mackay came to the conclusion that in β-$Ca_3(PO_4)_2$ there is some statistical distribution of the type in which N atoms occupy M equivalent

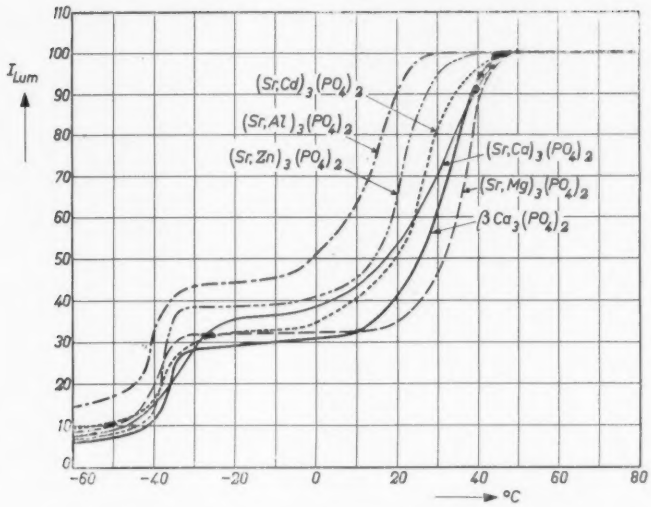

FIG. 2. Anomalous temperature-dependence of the luminescence in tin-activated (modified) Sr-orthophosphates; heating rate ~3°/min.

positions, where $M>N$. In this way the conflicting evidence of the space-group and the contents of unit cell can be reconciled. The low-temperature transitions in β-$Ca_3(PO_4)_2$ and related substances may be connected with ordering effects in this random distribution, but much more work will be needed to substantiate this speculation.

Acknowledgements—The authors are indebted to Prof. Dr. J. VOLGER for his advice and for providing facilities for the calorimetric measurements.

H. KOELMANS
J. J. ENGELSMAN
P. S. ADMIRAAL

Philips Research Laboratories,
N.V. Philips' Gloeilampenfabrieken,
Eindhoven, Netherlands.

References

1. BUTLER K. H., *J. Electrochem. Soc.* **100,** 250 (1953).
2. KOELMANS H. and COX A. P. M., *J. Electrochem. Soc.* **104,** 442 (1957).
3. MACKAY A. G., Ph. D. Thesis, London University (1952).
4. MACKAY A. G., *Acta Cryst., Camb.* **6,** 744 (1953).

Some observations concerning the effect of impurities on the anatase–rutile transition

(*Received* 27 *March* 1959)

THE rutile transition of spectroscopically pure anatase has been recently investigated in the temperature range 610–735°C.[1] The kinetics of this transformation was found to be second order, with an activation energy of ~100 kcal/mole. It seemed of interest to study the effect of controlled quantities of impurities on this transition.

The peroxidized titania solution was prepared from titanium metal as described earlier.[1] To aliquots of this solution were added one of the following ionic impurities: Sb^{5+}, Al^{3+}, Zn^{2+}; $PO_4^{\equiv}$, $So_4^{=}$ and Cl^{-}. The amounts were adjusted so as to yield a 5 atomic per cent concentration of a given impurity in the final samples. (The anionic impurities were added as aqueous solutions of the free acids. The cationic impurities were prepared as oxides from soluble metal salts, using NH_4OH; after filtration, the oxide was redissolved in conc. NH_4OH). Titania gel and TiO_2 were then obtained in the usual manner.[1]

The data, based on intensity measurements of X-ray diffraction lines,[2] are summarized in Table 1; the antimony-doped samples could not be

Table 1. Conversion of anatase to rutile in the absence and presence of impurities (per cent rutile as a function of time and temperature)

	708°C					737°C					870°C				
	1 hr	2 hr	3 hr	4 hr	8 hr	1 hr	2 hr	3 hr	4 hr	8 hr	1 hr	2 hr	3 hr	4 hr	6 hr
TiO_2 (pure)	95	100	100	100	100	97	100	100	100	100	100	100	100	100	100
Zn^{2+}	76	94	95	96	100	90	100	100	100	100	100	100	100	100	100
Cl^-	49	74	83	—	92	78	79	—	86	100	100	100	100	100	100
Al^{3+}	0	0	0	0	4	0	0	0	0	7	72	91	100	100	100
$SO_4^=$	0	0	0	0	0	0	0	0	0	9	29	—	64	72	93
PO_4	0	0	0	0	0	0	0	0	0	0	0	0	0	6	8

investigated because of the excessive volatilization of the impurity above 700°C. Inspection of the data shows the following: (1) all the impurities investigated had an adverse effect on the transition, i.e. they stabilized the anatase structure. (2) The degree of stabilization is in the order $Zn^{2+}<Al^{3+}$ for cations and $Cl^-<So_4^=<PO_4^{\equiv}$ for anions. (3) Within the rather large experimental uncertainties, the rates of conversion follow the second-order law encountered in the pure samples.

The increasing retardation effect of the anions can be readily correlated with the increasing bulk of the anions and the augmented stability of the corresponding titanium salts. For the transition from anatase ($a_0 = 3{\cdot}77$ Å, $c_0 = 9{\cdot}51$ Å; $\rho = 3{\cdot}899$ g/cm³ to rutile ($a_0 = 4{\cdot}58$ Å, $c_0 = 2{\cdot}96$ Å; $\rho = 4{\cdot}250$ g/cm³) is accompanied by a marked contraction of the tetragonal unit cell; it is quite reasonable that bulky foreign groups should inhibit the transition. The retardation effect of the cations cannot be attributed to a size effect, since the metal-to-oxygen distances in ZnO, γ-Al_2O_3 and TiO_2 are comparable. However, in view of the large degree of ionic character of the host lattice, it is of interest that the retardation effect of the foreign ions increases with their charge. A complete interpretation cannot be provided until the manner in which the foreign ions are accommodated in the TiO_2 lattice has been clarified. In particular, the fact that the doped and pure anatase exhibit the same lattice parameters must be explained.

The above findings are in essential agreement with other information available in the literature, though it must be recognized that the method of sample preparation used here differs significantly from that employed elsewhere. Hydrolysis of $TiCl_4$ yields rutile at temperatures in the range 400–600°C,[3–5] but in the presence of $SO_4^=$ or in the hydrolysis of $Ti(SO_4)_2$, the transition temperature rises to the range 800–1050°C.[5–8] The $PO_4^{\equiv}$ ion has been observed to have a marked retardation effect.[3] HÜTTIG and KOSTERHON[9] observed that the transition temperature is shifted to somewhat higher values when TiO_2, prepared from the chloride or sulfate by hydrolysis, is exposed to HCl vapor.

Department of Chemistry,
Purdue University,
Lafayette, Indiana,
U.S.A.

C. N. R. RAO*
A. TURNER
J. M. HONIG

References

1. CZANDERNA A. W., RAO C. N. R. and HONIG J. M., *Trans. Faraday Soc.* **54,** 1069 (1958).
2. SPURR R. A. and MYERS H., *Analyt. Chem.* **29,** 760 (1957).
3. BARKSDALE J., *Titanium, its Occurrence, Chemistry and Technology*. Ronald Press, New York (1949).
4. KUBO T. and SHINRIKI K., *J. Chem. Soc. Japan, Industr. Chem. Sect.* **56,** 149 (1953).
5. SCHOSSBERGER F., *Z. Krist.* **104,** 358 (1942).
6. PAMFILOV A. V. and IVANCHEVA E. G., *Zh. Obshch. Khim.* **7,** 2774 (1937); **10,** 736 (1940).

*Present addresses: Department of Chemistry and Radiation Laboratory, University of California, Berkeley, California (CNRR); School of Chemical Technology, North Dakota Agricultural College, Fargo, North Dakota (AT); M.I.T. Lincoln Laboratory, Lexington 73, Massachusetts (JMH).

7. PARRAVANO N. and CAGLIOTI V., *Gazz. Chim. Ital.* **64,** 429 (1934); *Congr. Internat. Quím. Pura y Aplicada (Madrid)* **3,** 304 (1936).
8. BIRKS L. S. and FRIEDMAN H., *Rev. Sci. Instrum.* **18,** 576 (1947).
9. HÜTTIG G. F. and KOSTERHON K., *Kolloid. Z.* **89,** 202 (1939).

Nuclear magnetic resonance frequency shift of ^{59}Co in CoF_2

(*Received* 8 *April* 1959)

NUCLEAR magnetic resonance of ^{59}Co nuclei in antiferromagnetic CoF_2 has recently been observed by JACCARINO[1]. The high resonance frequencies are attributed to the strong magnetic hyperfine field at the nucleus produced by the antiferromagnetically aligned electron spin on it. He also found that the apparent gyromagnetic ratio is larger than that in a diamagnetic crystal by about 20 per cent. Half of this field-proportional shift is attributed to the magnetic hyperfine field produced by that portion of the Co^{2+} spin which is induced by the external magnetic field; the antiferromagnetic parallel susceptibility does not vanish even at 0°K.[2]

We shall here point out that the other half of the field-proportional shift comes from the magnetic interaction between the nuclear spin and the orbital magnetic moment of the Co^{2+} ion induced by the external magnetic field. This type of shift is usually called a chemical shift,* though the magnitude is usually much smaller.

The magnetic field at a cobalt nucleus produced by the electronic orbital moment is written as:

$$\boldsymbol{H}' = -2\mu_B \left\langle \sum_k \frac{\boldsymbol{l}_k}{r_k^3} \right\rangle, \tag{1}$$

where $\langle\ \rangle$ denotes a statistical average over the electronic states; $\boldsymbol{l}_k$ and $\boldsymbol{r}_k$ denote the orbital angular momentum divided by $\hbar$ and the position vector of the kth electron assuming the nucleus to be at the origin, respectively. When the ground orbital state is not degenerate, equation (1) vanishes unless an external field is applied. The external magnetic field, $\boldsymbol{H}_0$, polarizes the ground orbital state to give a nonvanishing expectation value of equation (1). With the use of a perturbation method, assuming that all the excited orbital states lie well above the ground state, we get:

$$\boldsymbol{H}' = 4\mu_B^2 \left\langle \frac{1}{r^3} \right\rangle \left(1 + \frac{3\eta e^2 Q}{8I(2I-1)\gamma_N \hbar \mu_B} \right) \boldsymbol{\Lambda} \cdot \boldsymbol{H}_0, \tag{2}$$

$$\boldsymbol{\Lambda} = \sum_n \frac{(g|\boldsymbol{L}|n)(n|\boldsymbol{L}|g)}{E_n - E_g}, \tag{3}$$

where $\boldsymbol{\Lambda}$ is a tensor; g and n represent the ground and the excited orbital states under no external magnetic field, respectively; $\boldsymbol{L}$ represents the orbital angular momentum of the cobalt ion. The second term in the bracket in equation (2) is the contribution from the quadrupole interaction which is not of primary importance. $\boldsymbol{\Lambda}$ is related to the temperature-independent susceptibility by

$$2\mu_B^2 \boldsymbol{\Lambda} = \boldsymbol{\chi}_\infty. \tag{4}$$

The total field-proportional shift is then given by

$$\left.\begin{aligned} \Delta \boldsymbol{H} &= \boldsymbol{\sigma} \cdot \boldsymbol{H}_0, \\ \boldsymbol{\sigma} &= \boldsymbol{\sigma}_S + \boldsymbol{\sigma}_L, \\ \boldsymbol{\sigma}_S &= \frac{1}{N\gamma_N \hbar \mu_B} \boldsymbol{A} \boldsymbol{g}^{-1} (\boldsymbol{\chi} - \boldsymbol{\chi}_\infty), \\ \boldsymbol{\sigma}_L &= 2\left\langle \frac{1}{r^3} \right\rangle \frac{1}{N} \boldsymbol{\chi}_\infty, \end{aligned}\right\} \tag{5}$$

where the bold symbols are tensors; $\boldsymbol{A}$ the hyperfine coupling tensor, $\boldsymbol{g}$ the g-tensor. The principal values of $\boldsymbol{A}$ can be determined by using the paramagnetic-resonance data for Co^{2+} in ZnF_2 given by TINKHAM[5] and by STOUT[6]. According to STOUT, we have†

*The first theoretical study of chemical shift was made by RAMSEY[3]. A particular case of ^{59}Co in diamagnetic salts has been studied both experimentally and theoretically.[4] The magnitude of the chemical shift of Co^{3+} in diamagnetic salts is a few per cent, which is one order of magnitude smaller than in CoF_2. Our relation (5) between σ_L and χ_∞ holds in this case, too. The writer is indebted to Dr. R. G. SHULMAN for calling his attention to these studies on diamagnetic cobalt salts.

†We assume that the hyperfine coupling tensor of Co^{2+} in CoF_2 is equal to that of Co^{2+} in ZnF_2. The negative sign of A_y is reasonable from a theoretical point of view.

$$\left.\begin{aligned} A_x/g_x = A'_x/g'_x &= \quad 1{\cdot}65\times10^{-3}\ \text{cm}^{-1}, \\ A_y/g_y = A'_y/g'_y &= -3{\cdot}61\times10^{-3}\ \text{cm}^{-1}, \\ A_z/g_z = A'_z/g'_z &= \quad 1{\cdot}78\times10^{-3}\ \text{cm}^{-1}, \end{aligned}\right\} \quad (6)$$

where A', g' are the effective values of A and g within the lowest Kramers doublet ($S' = \frac{1}{2}$ manifold), respectively; the x, y and z axes are along the [110], [1$\bar{1}$0] and [001] directions, respectively. The value of $\langle(1/r^3)\rangle$ may be taken to be practically the same as that in hydrated salts, for which the empirically determined value is $\langle(1/r^3)\rangle_{Co^{2+}} = 5{\cdot}2$ atomic unit.[7] Thus we get:

$$\left.\begin{aligned} \sigma_x &= 8{\cdot}8(\chi_x - \chi_{x\infty}) + 117\chi_{x\infty}, \\ \sigma_y &= -19{\cdot}2(\chi_y - \chi_{y\infty}) + 117\chi_{y\infty}, \\ \sigma_z &= 9{\cdot}5(\chi_z - \chi_{z\infty}) + 117\chi_{z\infty}. \end{aligned}\right\} \quad (7)$$

The values of χ have been measured, while those of χ_∞ have been determined by NAKAMURA and TAKETA[8] from the analysis of the magnetic-susceptibility data. By using these values, we get:

$$\sigma_{Lx} = 12\times10^{-2}, \qquad \sigma_{Ly} = 1{\cdot}3\times10^{-2},$$
$$\sigma_{Lz} = 9{\cdot}4\times10^{-2}. \quad (8)$$

At 0°K, $\chi_{\|} - \chi_{\|\infty} \simeq 10^{-2}$ and therefore the total shift along the z-direction amounts to nearly 20 per cent, which explains the observed value. We see from equations (7) and (8) that the contributions from the two sublattices to the perpendicular susceptibility can be measured separately by a nuclear-resonance experiment with the external field along the a- or b-axis. This type of large shift in the resonance frequency is expected also in the nuclear resonances of the other transition elements such as Cu^{2+}, Mn^{3+} and V^{2+}.

Acknowledgement—The writer wishes to thank Dr. V. JACCARINO and Dr. P. W. ANDERSON for helpful discussions.

Bell Telephone Laboratories,
Murray Hill, N.J.
T. MORIYA*

References

1. JACCARINO V., *Phys. Rev. Letters* **2,** 163 (1959).
2. STOUT J. W. and MATARRESE L. M., *Rev. Mod. Phys.* **25,** 338 (1953).
3. RAMSEY N. F., *Phys. Rev.* **77,** 567; **78,** 699 (1950); **83,** 540 (1951).
4. PROCTOR W. C. and YU F. C., *Phys. Rev.* **81,** 20 (1951).
   GRIFFITH J. S. and ORGEL L. E., *Trans. Faraday Soc.* **53,** 601 (1957).
   FREEMAN R., MURRAY G. R. and RICHARDS R. E. *Proc. Roy. Soc.* A**242,** 455 (1957).
5. TINKHAM M., *Proc. Roy. Soc.* A**236,** 535 (1956).
6. STOUT J. W., private communication.
7. ABRAGAM J., HOROWITZ A. and PRYCE M. H. L., *Proc. Roy. Soc.* A**230,** 169 (1955).
8. NAKAMURA T. and TAKETA H., *Progr. Theor. Phys., Osaka* **13,** 129 (1955).

*On leave of absence from Tokyo Metropolitan University, Tokyo, Japan.

VOL
11
195

OL.
11
959

ERRATUM

E. N. ADAMS and T. D. HOLSTEIN, Quantum theory of transverse galvano-magnetic phenomena, *J. Phys. Chem. Solids* **10,** 254–276 (1959).

The sentence on p. 257, following equation 3.10, first column, should have read as follows:

We may then obtain the value of the density matrix at very large times as the limit approached by the Laplace transform $P(s)$ as the Laplace parameter approaches zero through positive real values.

VOL.
11
195

J. Phys. Chem. Solids Pergamon Press 1959. Vol. 11. pp. 177–181. Printed in Great Britain.

SOME PHYSICAL PROPERTIES OF NEPTUNIUM METAL II

A STUDY OF THE ALLOTROPIC TRANSFORMATIONS IN NEPTUNIUM

J. A. LEE, P. G. MARDON, J. H. PEARCE, and R. O. A. HALL

Metallurgy Division, Atomic Energy Research Establishment, Harwell, Berks.

(*Received* 10 *March* 1959)

Abstract—The phase transformations in neptunium metal have been studied by thermal analysis, dilatometry, and resistivity measurements. The values obtained were: $\alpha \rightarrow \beta 280 \pm 5°C$, $\beta \rightarrow \gamma 577 \pm 3°C$, and $\gamma \rightarrow$ liquid $637 \pm 2°C$.

Results of the X-ray examination of the crystal structures of the three phases are compared with those of ZACHARIASEN (*Acta Cryst.* **5**, 660, 664 (1952)).

1. INTRODUCTION

THE earliest reported work on the metallurgy of neptunium[1,2] was on a milligramme scale. The X-ray work of ZACHARIASEN showed the existence of three allotropic modifications, and values were given for the transformation temperatures. The only other data obtained were the melting point and the macroscopic room-temperature density.

The present authors set out to confirm these results by well-established thermal-analysis and dilatometric techniques on samples weighing up to 10 g. Values for the transformation temperatures were also obtained from electrical-resistance measurements and are quoted in the present paper. (A full description of the resistivity work will be given in the final paper in this series; specific-heat measurements have been reported in the first paper of the series.[3])

X-ray studies were undertaken at temperatures up to 600°C with a Unicam high-temperature camera, and at room temperature with a Guinier focussing-type camera.

2. EXPERIMENTAL METHODS

(a) *Specimen purity*

A spectrographic analysis of the material[8] has given as the major impurities 0·34 per cent calcium and 0·22 per cent uranium.

(b) *Thermal analysis*

A differential-thermocouple method was used, as developed for work on plutonium and its alloys.[4] The apparatus was modified by mounting the specimen and the tantalum standard side by side instead of one above the other. By using amplification factors of the order of 100 X, it was possible to obtain sizeable "kicks" at the transition temperatures with a sample weighing only 1 g.

(c) *Dilatometry*

For this measurement a simple silica-tube vacuum dilatometer, which has been described elsewhere,[4] was used. The specimen was a cylinder $\frac{1}{2}$ in. long by $\frac{1}{4}$ in. diameter, prepared by arc melting the original neptunium bead and then machining the ends square.

The density of this rod was determined by the conventional displacement method.

(d) *X-ray examination*

The room-temperature photographs were taken in a Guinier focussing-type camera specially designed for the handling of α-active specimens;[5] the high-temperature photographs were taken in a standard Unicam high-temperature camera which had been modified to reduce the probability of the silica capillary being shattered.[4]

To reduce the oxygen contamination of the specimen to a minimum, the filings for the high-temperature work were prepared and sealed in the capillary under *vacuo*. Nevertheless, at temperatures over 500°C, NpO, probably formed

Table 1. *Transition temperatures for neptunium metal* (°C)

Phase change	Heating values*			Cooling values*		Values obtained in U.S.A.
	Thermal analysis	Dilatometry	Resistivity	Dilatometry	Resistivity	
$\alpha \rightarrow \beta$	286±5	273±5	285±5	263±5		278[1]
$\beta \rightarrow \gamma$	578±3	577±10	574±5	577±10	574±5	*c*550–570[1]
$\gamma \rightarrow$liq.	637±2	640±5				640±1[2]

*Heating and cooling rates approximately 2°C min.

by interaction between the neptunium and the silica, showed up strongly on the films. The introduction of thin silver foil between the filings and the walls of the capillary was not an effective solution to this problem.

3. EXPERIMENTAL RESULTS

(a) *Transition temperatures*

Average values for a series of runs by each of the methods listed are given in Table 1. Agreement between the various methods is good for the $\beta \rightarrow \gamma$ and $\gamma \rightarrow$liquid transitions, but wider variation occurs in the case of the $\alpha \rightarrow \beta$ transition. However, the start of this particular transition is somewhat obscured by an extensive lead-in stage, and thus the value obtained depends upon the method of interpretation of the results. The most probable values for the transition temperatures are: $\alpha \rightarrow \beta$ 280±5°C; $\beta \rightarrow \gamma$ 577±3°C; $\gamma \rightarrow$liquid 637±2°C.

A typical dilatometer run is shown in Fig. 1. The values of the coefficient of linear expansion were $27{\cdot}5 \times 10^{-6}$°C for the α phase (40–240°C) and 41×10^{-6}°C for the β phase (300–540°C). Because of creep, no reliable value is available for the γ phase.

Measurements of the density of the sample at room temperature gave 20·18 g/cc before arc-melting and 20·25 g/cc after arc-melting. The latter figure yields values of 19·31 and 18·55 g/cc for the β and γ phases at 290 and 580°C, respectively. The values for the α and β phases are in good agreement with the calculated crystallographic values of 20·48 and 19·40 g/cc, but the calculated value for the γ phase, assuming it to

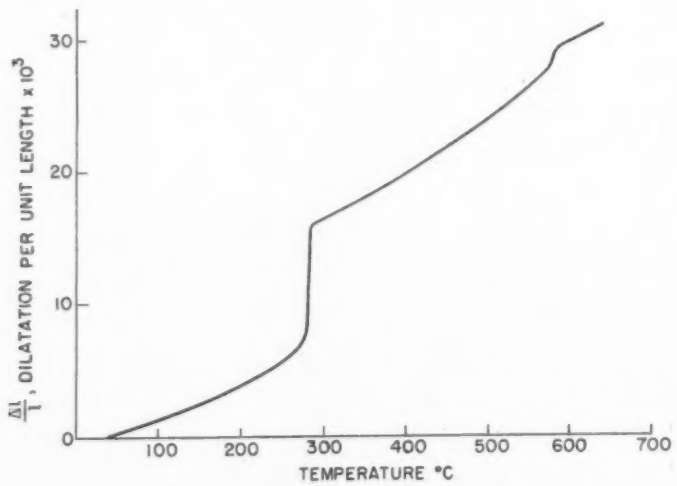

FIG. 1. Thermal expansion of neptunium metal.

be body-centred cubic, is only 18·04 g/cc. However the dilatometric work shows that creep occurs during the $\beta \rightarrow \gamma$ transformation and this may explain the discrepancy.

(b) *X-ray studies*

The results of the present investigation are essentially in agreement with those of ZACHARIASEN.[1] Table 2 gives a comparison of the low-angle lines observed at A.E.R.E. and by ZACHARIASEN for the α phase. The advantages of the focussing camera over a straight powder camera are shown by the better fit between the observed and calculated $\sin^2\theta$ values in the case of the former and by the presence of several of the weaker lines not observed by ZACHARIASEN. The results of a determination of the unit cell by a least-squares method give close agreement with U.S. values.

Calculated unit cell, α-neptunium:

	HARWELL	ZACHARIASEN
a	4·721±0·002 Å	4·723±0·001 Å
b	4·888±0·002 Å	4·887±0·002 Å
c	6·661±0·002 Å	6·663±0·003 Å

High-temperature powder photographs were only taken in the β and γ phase fields. The β pattern taken at 312°C gave lines in agreement with ZACHARIASEN's primitive tetragonal cell with lattice parameters of $a = 4{\cdot}895$, $c = 3{\cdot}386$ Å, the U.S. values at this temperature being $a = 4{\cdot}897$, $c = 3{\cdot}388$ Å.

As mentioned previously, oxidation proved to

Table 2. Observed reflections for α-neptunium

Indices $h\,k\,l$	Harwell values		ZACHARIASEN values	
	Intensity	$\sin^2\theta$obs.*	$\sin^2\theta$obs.	$\sin^2\theta$calc.
100	VW	0·0270		0·0266
110	W	0·0512		0·0514
002	W	0·0531		0·0534
111	VS	0·0647	0·0654	0·0648
012	VS	0·0780	0·0792	0·0782
102	VW	0·0805		0·0800
020	S	0·0992	0·1004	0·0994
112	VVS	0·1050	0·1058	0·1048
200	VS	0·1063	0·1077	0·1064
021	S	0·1126	0·1139	0·1128
121	VS	0·1395	0·1406	0·1394
013	S	0·1450	0·1453	0·1450
022	M	0·1530	0·1526	0·1528
202	VW	0·1610		0·1598
122	VW	0·1782		0·1794
212	VS	0·1847	0·1859	0·1846
220	S	0·2059	0·2077	0·2058
004	W	0·2139		0·2138
221 023	S	0·2194	0·2208	0·2192 0·2196
031				0·2370
104	VS	0·2407	0·2420	0·2404
123	M⁻	0·2464	0·2482	0·2462
130 213	S	0·2510	0·2523	0·2502 0·2516
222	M⁻	0·2593	0·2611	0·2592
131 310	VS	0·2640	0·2653	0·2636 0·2641

*Mo $K\alpha$ radiation used in practice. Observed values converted to equivalent values for Cu $K\alpha$.

be serious at temperatures above 500°C, and no definite solution could be obtained for the structure of γ-neptunium. ZACHARIASEN has suggested that, owing to an unfortunate geometrical relationship, the lines of NpO may obscure the lines of γ-neptunium if it is body-centred cubic, as would seem a strong possibility. The only exception to this would be the γ-neptunium line with indices 321, and such a line was observed both by ZACHARIASEN and the present workers. However, the Harwell pattern also contains one or two weak lines which do not fit such a structure.

4. DISCUSSION

The present work has confirmed that neptunium exists in three allotropic modifications. The transition from the β to the γ phase shows some interesting features; thus on thermal analysis it sometimes appears to be two very close overlapping arrests on heating, whilst at other times this phenomenon shows up only as a discontinuity in the shape of the "kick". The dilatometric behavior also shows a discontinuous change of slope in the middle of the transition during heating runs, and the temperature spread of the transition is rather large. These effects may be due to impurities in the metal, but it is noticeable that there are only two major impurities reported, calcium and uranium; the former was probably removed in the preliminary arc-melting process and besides, if one judges from the case of plutonium, it is unlikely to have any effect on the neptunium transformations, whilst investigations into the neptunium–uranium system[6] have shown that the $\beta \rightarrow \gamma$ arrest becomes sharper as more uranium is added. This behaviour therefore suggests that a fourth phase may exist over a small temperature range in the pure metal and, like δ'-plutonium, is very sensitive to certain impurities[7] and has been suppressed in the comparatively impure metal used in the present work. Against this, the $\gamma \rightarrow \beta$ transformation on cooling is clear-cut on both thermal analysis and dilatometry. This problem clearly cannot be solved until pure neptunium is available.

A second interesting problem is the crystal structure of the γ phase. ZACHARIASEN's suggestion that it is body-centred cubic is reasonable from certain points of view. Thus it explains why virtually no lines are seen on the pattern other than those of NpO and it would make the γ phase isomorphous with the highest-temperature allotropes of plutonium and uranium. Initial investigations into the neptunium–uranium system[8] suggested that complete solid solubility occurs between γ-neptunium and γ-uranium, but recently the same investigators have shown that there is a small miscibility gap between the phases at the uranium-rich end. If γ-neptunium is body-centred cubic, it is surprising that such a solubility gap should occur, since the size-factor for the two phases would be extremely favourable (less than 1 per cent), whilst in the plutonium-uranium system, in which a limiting case of solid solubility occurs,[9,10] the size-factor is considerably greater (around 3 per cent). It is possible, however, that the neptunium–uranium alloy has become contaminated as a result of the frequent remelting necessary to allow one basic alloy to span a wide range of compositions. An attempt has been made to determine the structure of the γ phase in a 50:50 neptunium–uranium alloy by quenching it from the γ field, but this treatment failed to prevent the material from transforming to its room-temperature structure.

In view of these observations, the authors feel that the obtaining of a definite structure for γ-neptunium depends upon finding a method of reducing the oxidation at high temperatures, and further work will be conducted on this premise.

Acknowledgement—The authors wish to thank Mr. J. A. C. MARPLES, who carried out the X-ray studies on the Guinier camera.

REFERENCES

1. ZACHARIASEN W. H., *Acta. Cryst., Camb.* **5,** 660, 664 (1952).
2. WESTRUM E. F. and EYRING LEROY, *J. Amer. Chem. Soc.* **73,** 3399 (1951).
3. EVANS J. P. and MARDON P. G., *J. Phys. Chem. Solids* **10,** 311 (1959).
4. BALL J. G., LEE J. A., MARDON P. G. and ROBERTSON J. A. L., *Rev. Métall.* (to be published).
5. WILLIAMSON G. K., POOLE D. M. and MARPLES J. A. C., *J. Inst. Met.* **85,** 431 (1957).
6. MARDON P. G., PEARCE J. H. and MARPLES J. A. C. Unpublished work.
7. ELLIOTT R. O., *The Delta-Prime Phase,* Plutonium Session, 2nd World Metallurgical Congress, Chicago (November, 1957).

8. MARDON P. G., private communication to M. B. WALDRON reported in *The Chemistry and Metallurgy of Neptunium*, 2nd International Conference on the Peaceful Uses of Atomic Energy, A/Conf 15/P/304 (1958).
9. SCHONFELD F. W., *Phase Diagrams Studied at Los Alamos*, Plutonium Session, 2nd World Metallurgical Congress, Chicago (November, 1957).
10. MARDON P. G., private communication to M. B. WALDRON reported in *Phase Diagrams Studied at A.E.R.E. Harwell*, Plutonium Session, 2nd World Metallurgical Congress, Chicago (November, 1957).

VOL.
11
1959

J. Phys. Chem. Solids Pergamon Press 1959. Vol. 11. pp. 182–189. Printed in Great Britain.

PENETRATION DEPTH OF SURFACE EFFECTS IN MOLECULAR CRYSTALS

B. J. ALDER, J. R. VAISNYS, and G. JURA

University of California, Lawrence Radiation Laboratory, Livermore, California, and Department of Chemistry, Berkeley, California

(*Received* 27 *March* 1959)

Abstract—In the semi-infinite molecular crystal the interplanar distances perpendicular to the surface are allowed to assume their equilibrium value. By minimizing the energy of the system it is shown that the first interplanar distance increases by 2·5 per cent, the second by 0·6 per cent, the third by 0·2 per cent, and the fourth by 0·08 per cent. It can be shown that this expansion over the normal distance in an infinite crystal falls off as one over the cube of the distance from the surface. On the other hand, the surface energy is shown to be only slightly affected by these deeper distance perturbations. The change in interplanar distances is also calculated for various uniformly distorted semi-infinite crystals.

VOL
11
195

1. INTRODUCTION

It has not been possible up to now to determine experimentally the structure of solids in the neighborhood of surfaces or defects. Hence, in order to study lattice distortions in the vicinity of discontinuities in the periodic arrangements of atoms, theoretical models have to be investigated. Although such calculations can be considered as only qualitatively significant, they might aid in answering such problems as how two holes in an otherwise perfect lattice attract each other, what the stable configuration of a cluster of holes in a lattice is, what the potential field experienced by a charged particle in the neighborhood of a hole in an ionic lattice is, and, as a final example, what the potential is with which a foreign atom is attracted to a surface and how that surface is distorted because of the presence of that foreign atom.

The problem investigated here is the simplest of its class, namely, the surface effects on a perfect semi-infinite molecular crystal. What makes this particular problem simple is that the perturbation of the surface on the crystal can be entirely characterized by a variation of the interplanar distances normal to the surface. Because of the symmetry of this discontinuity, it can be shown that in-plane distances between the molecules do not change. Although in the presence of a single hole in an infinite crystal symmetry requirements still restrict the way in which intermolecular distances can relax, the number of relaxation parameters required to describe the system is much larger. A further simplifying feature is that in a molecular crystal, as opposed to an ionic crystal, one deals with a single species of molecules and with faster convergence of energy sums due to the short-range nature of the potential.

The surface effects on a molecular crystal have been previously examined.[1] In that calculation only the first interplanar distance was allowed to relax. The conclusion was drawn that changes in the spacing of further layers affected the surface energy by less than 0·1 per cent. This is confirmed by the present calculation and, in addition, the variation in further interplanar distances will be calculated. In previous investigations[2,3] of ionic crystals again only a small number of relaxations in distances have been allowed for. Relaxations around a vacancy in a molecular crystal has also been investigated.[4–6]

2. THE METHOD

The model adopted for the semi-infinite crystal is that it has a perfectly planar surface, that all quantum effects can be neglected, and hence,

VOL. 11 1959

also all vibrational effects at the absolute zero of temperature, and that the atoms are point particles interacting with a LENNARD-JONES potential:

$$V(x_{ij}) = \frac{\alpha}{a_0{}^{12}x_{ij}{}^{12}} - \frac{\beta}{a_0{}^{6}x_{ij}{}^{6}}, \qquad (1)$$

where $a_0/\sqrt{2}$ is the equilibrium interatomic distance in the crystal, since (see Fig. 1) for the face-centered cubic lattice considered the interplanar distance has been taken as the unit of distance. It is further assumed that a total energy, E_T, of the crystal can be obtained by pair-wise summation of this potential:

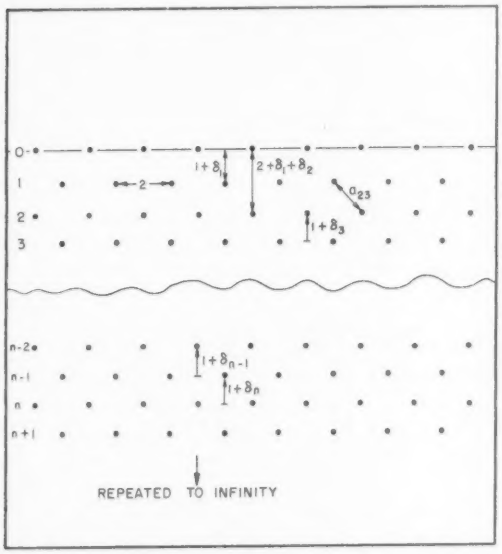

FIG. 1. Schematic diagram of semi-infinite crystal with various distances marked off.

$$-E_T = \tfrac{1}{2}\,\Sigma\, V(x_{ij}), \qquad (2)$$

where the summation runs over all possible pairs of particles consistent with the lattice under consideration. The ratio of the constants α to β is uniquely determined by the fact that for an infinite crystal the total potential energy must be a minimum at the equilibrium distance of separation. Thus

$$\frac{12A_{12}\alpha}{a_0{}^{13}} = \frac{6A_6\beta}{a_0{}^{7}},$$

where

$$A_n = \sum_{\substack{x,\,y,\,z \\ -\infty \\ x+y+z=\text{even.}}}^{\infty} \frac{1}{(x^2+y^2+z^2)^{n/2}}.$$

A_{12} has been calculated[7] to be 0·1895606 and A_6 to be 1·8067401, so that

$$\frac{a_0{}^{6}\beta}{2\alpha} = 0{\cdot}1049188. \qquad (3)$$

The total energy expression for a semi-infinite crystal in which the first two interplanar distances perpendicular to the surface (z-direction) are allowed to change by δ_1 and δ_2 respectively, all others remaining at the bulk interplanar spacing ($\delta_i = 0\ i>2$), will illustrate the nature of the problem encountered (see Fig. 1). If $\theta(z+\delta_i)$ is defined as

$$\theta(z+\delta_i) = \frac{\alpha}{a_0{}^{12}}\phi_{12}(z+\delta_i) - \frac{\beta}{a_0{}^{6}}\phi_6(z+\delta_i),$$

where

$$\phi_n(z+\delta_i) = \sum_{\substack{x,\,y \\ -\infty \\ x+y+z=\text{even}}}^{\infty} \frac{1}{[x^2+y^2+(z+\delta_i)^2]^{n/2}} \qquad (4)$$

then the energy of the top layer is $\theta\,(0)$ and its interaction with the rest of the layers is

$$\theta(1+\delta_1)+\sum_{z=2}^{\infty}\theta(z+\delta_1+\delta_2).$$

Thus the total interaction energy of the first layer is

$$\theta(0)+\theta(1+\delta_1)+\sum_{z=2}^{\infty}\theta(z+\delta_1+\delta_2).$$

Similarly for the second layer, the total energy is

$$\theta(0)+\theta(1+\delta_1)+\sum_{z=1}^{\infty}\theta(z+\delta_2),$$

and for the third layer

$$\theta(0)+\theta(2+\delta_1+\delta_2)+\theta(1+\delta_2)+\theta(1)+\theta(2)+\ \ldots\ .$$

The fourth and all subsequent layers have the same form of the interaction energy, and thus for the $N+1$st layer

$$\theta(0)+\theta(N+\delta_1+\delta_2)+\theta(N-1+\delta_2)+ \\ +\theta(N-2)+ \ldots \theta(1)+\theta(1)+\theta(2)+ \ldots .$$

The sum of the contributions for all the layers beyond the second is then

$$(N-2)\theta(0)+\sum_{z=2}^{N}\theta(z+\delta_1+\delta_2)+ \\ +\sum_{z=1}^{N-1}\theta(z+\delta_2)+(2N-5)\theta(1)+(2N-6)\theta(2)+ \ldots \tag{5}$$

in as much as $(N-2)+(N-3)\theta(1)$'s occur and $(N-2)+(N-4)\theta(2)$'s &c. Adding the first two layers and taking the limit of an infinite system yields then twice the total energy of the semi-infinite crystal, E_T.

$$-2E_T = 2\sum_{z=2}^{\infty}\theta(z+\delta_1+\delta_2)+2\sum_{z=1}^{\infty}\theta(z+\delta_2)+ \\ +2\theta(1+\delta_1)+\lim_{N\to\infty}[N\theta(0)+2N\sum_{z=1}^{\infty}\theta(z)- \\ -\sum_{z=1}^{\infty}(z+4)\theta(z)], \tag{6}$$

where the explicitly written-down series in equation (5) has been rewritten as the last two sums in equation (6).

It is this expression for the total energy which has to be minimized with respect to δ_1 and δ_2 in order to obtain their equilibrium values. This minimization results in this case in two simultaneous equations which have to be solved numerically. Once these simultaneous equations have been solved, the δ values can be substituted into equation (6) to obtain the total energy of the semi-infinite crystal, and perhaps more interestingly the surface energy, E_s, can be evaluated. The surface energy is defined as one-half the energy required to split an infinite crystal (of total energy E_T^{∞}) into two infinitely separated semi-infinite crystals.

$$E_s = \tfrac{1}{2}(E_T^{\infty}-2E_T). \tag{7}$$

E_T^{∞} can be evaluated by summing layer energies as was done for the semi-infinite crystal. Each layer has an energy

$$\theta(0)+2\theta(1)+2\theta(2)+ \ldots$$

and since all layers are equivalent, twice the total energy for a crystal of $2N$ layers is, in the limit of an infinite crystal

$$-2E_T^{\infty} = \lim_{N\to\infty} 2N[\theta(0)+2\sum_{z=1}^{\infty}\theta(z)]. \tag{8}$$

$2N$ layers have to be considered, since this crystal is split up into two semi-infinite crystals of N layers each. According to the definition in equation (7) and by the use of equations (6) and (8),

$$-E_s = \tfrac{1}{2}\sum_{z=1}^{\infty}z\theta(z)+\sum_{z=2}^{\infty}[\theta(z)-\theta(z+\delta_1+\delta_2)]+ \\ +\sum_{z=1}^{\infty}[\theta(z)-\theta(z+\delta_2)]+[\theta(1)-\theta(1+\delta_1)], \tag{9}$$

where the sums have been arranged for calculational convenience to take advantage of difference procedures. When δ_1 and δ_2 are zero, that is when all interplanar distances are the same as in the bulk crystal, the surface energy reduces to

$$-E_s = \tfrac{1}{2}\sum_{z=1}^{\infty}z\theta(z)$$

as previously derived,[1] and the further terms in equation (9) represent the correction to the surface energy due to the relaxation of the surface layers. Since the surface energy and the total energy of a semi-infinite crystal differ only by a constant (see equation (7)), it would have been equally justified in a minimization procedure to use the surface energy expression.

VOL. 11 1959

3. CALCULATIONS

Because the surface perturbations destroy the periodicity of the lattice, the elegant mathematical methods to evaluate lattice sums become inapplicable. In the minimization process of the total energy (equation (6)), the basic term that is needed is the derivative of θ with respect of δ and that involves

$$\frac{\partial\phi_n(z+\delta_i)}{\partial\delta_i} = \sum_{\substack{x,y \\ -\infty}}^{\infty} \frac{-n(z+\delta_i)}{[x^2+y^2+(z+\delta_i)^2]^{n/2+1}}. \qquad (10)$$

$x+y+z = \text{even}.$

No matter how many different interplanar distances are varied, the simultaneous equations for the solution of the δ's are all of the same form. The summations over z of θ start at different values and different sums of δ occur. Hence one way to proceed is to evaluate

$$\sum_{z=i}^{\infty} \sum_{\substack{x,y \\ -\infty}}^{\infty} \frac{(z+\delta_i)}{[x^2+y^2+(z+\delta_i)^2]^{n/2+1}}. \qquad (11)$$

$x+y+z = \text{even}$

for the first few intergers in i and a series of values of δ. This was done with the aid of an IBM 650 electronic computer for i between 1 and 20, taking every value of i between 1 and 10 and every other value between 10 and 20. The values of δ computed ranged between $-0{\cdot}09$ and $+0{\cdot}09$ in steps of $0{\cdot}01$ and a few additional values near the equilibrium solutions for the various δ's. The range in x and y was determined by $x^2+y^2<6400$ and z ranged up to 80. The results are tabulated in Appendix II of UCRL report No. 5502-T. With these sums the calculations were carried out in a step-wise manner by allowing variations in the first interplanar distance, then in the first and second interplanar distance, &c., up to a maximum of five interplanar spacings. To solve the simultaneous equations for the δ's, a process of iteration was employed using Newton's method to interpolate the tabulated $(\partial\phi_n/\partial\delta_i)$'s. In these equations the same combination of α and β as in equation (3) occurs.

An alternative procedure, making use of the fact that the δ's are small, is to expand θ in powers of δ. The coefficients of the powers of δ in this expansion were again obtained by machine methods. In this case the summations were again carried out over a cylinder but determined by $x^2+y^2<1800$ and z ranged up to 51. The results were as follows for the first four layers:

(First layer)

$$\phi_6(1+\delta) = \frac{4}{[1+(1+\delta)^2]^3} + 0{\cdot}0469605 - 0{\cdot}04143580\delta + 0{\cdot}0054306\delta^2 + \\ + 0{\cdot}0120028\delta^3 - 0{\cdot}0077049\delta^4 + 0{\cdot}0002659\delta^5 + \ldots,$$

where the dominant first term was not expanded in Taylor series.

(Second layer)

$$\phi_6(2+\delta) = 0{\cdot}0496600 - 0{\cdot}1015312\delta + 0{\cdot}1327936\delta^2 - \\ - 0{\cdot}1434358\delta^3 + 0{\cdot}1403090\delta^4 - 0{\cdot}1108712\delta^5 + \ldots$$

(Third layer)

$$\phi_6(3+\delta) = 0{\cdot}0096938 - 0{\cdot}0129167\delta + 0{\cdot}0107425\delta^2 - \\ - 0{\cdot}0071261\delta^3 + 0{\cdot}0041126\delta^4 - 0{\cdot}0661448\delta^5 + \ldots \qquad (12)$$

(Fourth layer)

$$\phi_6(4+\delta) = 0{\cdot}0030677 - 0{\cdot}0030680\delta + 0{\cdot}0019176\delta^2 + \\ + 0{\cdot}0009590\delta^3 + 0{\cdot}0004198\delta^4 - 0{\cdot}0050764\delta^5 + \ldots.$$

For the repulsive part of the potential the corresponding terms are:

$$\left.\begin{aligned}
&\text{(First layer)}\\
&\phi_{12}(1+\delta) = \frac{4}{[1+(1+\delta)^2]^6} + 0{\cdot}0001768 - 0{\cdot}0003488\delta + \\
&\qquad + 0{\cdot}0002296\delta^2 + 0{\cdot}0000464\delta^3 - 0{\cdot}0001678\delta^4 + \ldots\\
&\text{(Second layer)}\\
&\phi_{12}(2+\delta) = 0{\cdot}0003477 - 0{\cdot}0018582\delta + 0{\cdot}0055477\delta^2 - \\
&\qquad - 0{\cdot}0121993\delta^3 + 0{\cdot}0219904\delta^4 + \ldots\\
&\text{(Third layer)}\\
&\phi_{12}(3+\delta) = 0{\cdot}0000053 - 0{\cdot}0000175\delta + 0{\cdot}0003184\delta^2 - \\
&\qquad - 0{\cdot}0004183\delta^3 + 0{\cdot}0004434\delta^4 + \ldots\\
&\text{(Fourth layer)}\\
&\phi_{12}(4+\delta) = 0{\cdot}0000003 - 0{\cdot}0000007\delta + 0{\cdot}0000112\delta^2 - \\
&\qquad - 0{\cdot}0000103\delta^3 + 0{\cdot}0000084\delta^4 + \ldots .
\end{aligned}\right\} \quad (13)$$

With these expressions plus the additional terms for the remainder of the layers, the total energy can again be formed as given in equation (6). The differentiation can be carried out explicitly and the values of δ solved for.

Both methods give essentially the same results, the slight differences being accounted for by the use of different values of x, y and z in terminating the sums. The sums were carried out to eight significant figures, and the values are given to seven significant figures because of round-off errors of the machine. The remainder, R, due to terminating the sums at 80 instead of infinity in $(1/n)(\partial\phi/\partial\delta)$ for $\delta = 0$, can be estimated by replacing the sums by integrals:

$$R = \tfrac{1}{2}\int_{0{\cdot}5}^{\infty} dz \int_{80{\cdot}5}^{\infty} r\,dr \int_{0}^{2\pi} d\phi \frac{z}{(r^2+z^2)^{n/2+1}} + \\ + \tfrac{1}{2}\int_{80{\cdot}5}^{\infty} dz \int_{0{\cdot}5}^{80{\cdot}5} r\,dr \int_{0}^{2\pi} d\phi \frac{z}{(r^2+z^2)^{n/2+1}},$$

where the first term is the contribution due to the neglect of terms outside the cylinder $x^2+y^2<6400$ and the second term represents the terms in the cylinder $x^2+y^2<6400$ but above $z = 80$. The factor of $\frac{1}{2}$ in front represents the density per unit volume for a face-centered lattice, and since the integration is over a continuous medium, the atoms have been spread over half layers, accounting for the half interger limits. The result for $n = 6$ for R is $5{\cdot}45\times10^{-9}$, so that seven significant figures are justified. For the numerical values of δ only six decimal numbers are given, since the solution of the simultaneous equations incurs further errors.

The functions ϕ_{12} and ϕ_6 have been tabulated in order to evaluate the surface energy once the δ's are known. The values are given in Appendix I of the UCRL report #5502-T for the same values of i and δ and for the same range of x, y and z as the derivative of that function. From the values at $\delta = 0$, it is possible to check on the calculation by evaluating A_{12} and A_6 (equation (8)). A_{12} came out to be 0·1895606 and A_6 1·8067405 after the correction for the remainder had been added on to the latter value ($2{\cdot}92\times10^{-6}$). The agreement is within the seven significant figures expected.

The remainder for the surface-energy expression due to terminating the sums at 80 is considerably larger. The slower convergence of this expression due to the extra power of z in the numerator leads to a remainder value for the attractive term of $9{\cdot}089\times10^{-5}$ at $\delta = 0$. Hence the surface energy is given only to five significant figures, although

the correction to the surface energy due to the relaxation of the surface layers are more accurate since they involve differences.

4. RESULTS

The results of these computations for the normal face-centered cubic crystal with the surface in the 100 plane are shown in Table 1. The results agree with the previous calculation[1] when one surface layer was allowed to relax for both the value of δ and the surface energy. The surface energy is given in units of the total energy of the infinite crystal by taking advantage of the relation in equation (3). The effect of surface-layer perturbations on the surface energy is less than 1 per cent. As deeper layers are allowed to relax, only small changes in the surface energy result and the change in surface energy, due to the variation of deeper layers, rapidly converges to a constant value.

Table 1. *The differences in surface energy,* ΔE_s, *and in distances between crystal planes,* δ, *of a semi-infinite crystal where successive planes from the surface are allowed to assume their equilibrium distances and of a perfect semi-infinite crystal* $[(E_s/E_T^{\infty} = 0{\cdot}44813]$

δ_1	δ_2	δ_3	δ_4	δ_5	$-\frac{\Delta E_s}{E_T^{\infty}}$
0·025496	0	0	0	0	0·003723
0·025766	0·005792	0	0	0	0·003929
0·025780	0·005885	0·001937	0	0	0·003952
0·025782	0·005891	0·001977	0·000829	0	0·003957
0·025782	0·005892	0·001981	0·000849	0·000420	0·003958

Also, the perturbation in the first interplanar distance rapidly approaches a constant value as deeper variations are considered. It is seen that the value of a given layer separation is affected only by the value of a few interplanar distances surrounding the two layers under consideration. However, the perturbations of the interplanar distances themselves decrease only relatively slowly with distance into the crystal from the surface. In fact, it can be shown analytically that the value of δ falls off as the inverse cube of the distance to the surface, rather than exponentially as sometimes thought.

Since the value of δ for a given interplanar spacing seems to be affected only slightly by the values of δ of the surrounding layers, no qualitative error shall be incurred if it is assumed that all δ's are zero except the one under consideration, δ_n, deep in the crystal. For such a model of a semi-infinite crystal the part of the total energy which depends on δ_n, U can be written using identical considerations as in equation (6) as (the constant terms will drop out in the minimization process anyway):

$$U = \sum_{z=1}^{\infty} \theta(z+\delta_n) + \sum_{z=2}^{\infty} \theta(z+\delta_n) + \ldots \sum_{z=n}^{\infty} \theta(z+\delta_n)$$

$$= \sum_{z=1}^{n} z\theta(z+\delta_n) + n \sum_{z=n+1}^{\infty} \theta(z+\delta_n). \qquad (14)$$

Differentiating this expression with respect to δ_n (indicated by primes) results in the following equation to be solved for the equilibrium value of δ_n,

$$\sum_{z=1}^{n} z\theta'(z+\delta_n) + n \sum_{z=n+1}^{\infty} \theta'(z+\delta_n) = 0.$$

Since δ_n is small, a linear Taylor expansion in δ_n is justified resulting in

$$\sum_{z=1}^{n} z\theta'(z) + n \sum_{z=n+1}^{\infty} \theta'(z)$$

$$= -\delta_n \left[\sum_{z=1}^{n} z\theta''(z) + n \sum_{z=n+1}^{\infty} \theta''(z) \right]. \qquad (15)$$

In the case that the single perturbed interplanar distance is infinitely deep inside the crystal, it is surely true that

$$\lim_{n\to\infty} \delta_n \to 0.$$

In that case also

$$\lim_{n\to\infty} U = \lim_{n\to\infty} \sum_{z=1}^{n} z\theta(z+\delta_n).$$

Thus in this limit it can be shown that

$$\lim_{n\to\infty} U' = \lim_{n\to\infty} \sum_{z=1}^{n} z\theta'(z+\delta_n) = 0$$

or

$$\sum_{z=1}^{\infty} z\theta'(z) = 0.$$

Hence, by rearranging the first term in equation (15), the expression can be rewritten as

$$-\sum_{n}^{\infty} z\theta'(z)+n\sum_{z=n+1}^{\infty}\theta'(z)$$

$$= -\delta_n\left[\sum_{z=1}^{n} z\theta''(z)+n\sum_{z=n+1}^{\infty}\theta''(z)\right].$$

Since n is large, the errors incurred by replacing the sums by integrals (see remainder calculations) will be small except in the term where the summation starts at one. In that case the first four terms were evaluated by using the numerical series in equations (12) and (13) and from then on in the integral representation was used. Utilizing the constant of equation (3), the following

Table 2. The differences in distances, δ, between crystal planes of a semi-infinite crystal where the first four planes are allowed to assume their equilibrium distances and of a perfect crystal constrained at various intermolecular separations including the equilibrium one (first row). The first column gives the volume relative to the equilibrium volume for the various cases.

v/v_0	δ_1	δ_2	δ_3	δ_4
1·000000	0·025787	0·005897	0·001980	0·000832
0·926179	0·078152	0·059997	0·055899	0·052290
0·931310	0·074342	0·056047	0·051979	0·048571
0·936414	0·070584	0·052155	0·048113	0·044898
0·941489	0·066876	0·048318	0·044299	0·041269
0·946537	0·063214	0·044533	0·040534	0·037682
0·951558	0·059597	0·040796	0·036814	0·034135
0·956554	0·056022	0·037106	0·033139	0·030626
0·961521	0·052489	0·033459	0·029505	0·027155
0·966467	0·048995	0·029854	0·025910	0·023720
0·971384	0·045539	0·026288	0·022352	0·020318
0·976279	0·042119	0·022760	0·018831	0·016950
0·981147	0·038735	0·019267	0·015343	0·013615
0·985994	0·035384	0·015809	0·011889	0·010310
0·990814	0·032066	0·012383	0·008465	0·007035
0·995612	0·028780	0·008989	0·005072	0·003789
1·000387	0·025524	0·005625	0·001708	0·000572
1·005139	0·022298	0·002290	−0·001629	−0·002618
1·009869	0·019100	−0·001017	−0·004938	−0·005782
1·014579	0·015931	−0·004298	−0·008222	−0·008919
1·019264	0·012788	−0·007552	−0·011481	−0·012032
1·023929	0·009672	−0·010782	−0·014716	−0·015120
0·028573	0·006581	−0·013987	−0·017927	−0·018184
1·033195	0·003515	−0·017169	−0·021116	−0·021225
1·037798	0·000473	−0·020329	−0·024283	−0·024243

Table 3. Comparison of the intermolecular distances between nearest neighbors in two adjacent planes in the first four surface layers for the constrained (indicated in the first columns by the volume relative to the normal volume) and the equilibrium lattice.

v/v_0	a_{12}	a_{23}	a_{34}	a_{45}	a_{interior}
0·926179	1·434846	1·421578	1·418598	1·415978	1·378521
1·000000	1·432564	1·418389	1·415614	1·414802	1·414214
1·037798	1·432146	1·417510	1·414746	1·414773	1·431812

value of δ_n resulted keeping only the leading power in n in the numerator and denominator

$$\delta_n = -\frac{\dfrac{\beta\pi}{-12n^3a_0^6}}{\dfrac{2\cdot2746\alpha}{a_0^{12}} - \dfrac{5\cdot1372\beta}{a_0^6} + \dfrac{\beta\pi}{4n^4}}$$

or

$$\delta_n = \frac{1}{21\cdot8n^3}.$$

The values of δ in Table 1 indicate that

$$\delta_n = \frac{1}{19\cdot7n^3} \text{ for } n > 1$$

represents the average fall-off of the δ's with distance from the surface very well. The difference between these two can be accounted for if neighboring interplanar distances in the interior are allowed to relax also, since, as Table 1 shows, the value of δ is too small if these neighboring layers are kept at the bulk interatomic distance.

Values of the first four interplanar separations were also computed for various crystals which are uniformly constrained under pressure or tension. In that case the constant used in equation (3) is no longer applicable, and the new equilibrium bulk interplanar distance, a_0' can be calculated from

$$\frac{a_0^6}{a'_0{}^6} = \frac{0\cdot1049188}{C},$$

where C is the new value of the constant assumed in the calculation. The results are given in Table 2 and show that the δ's change greatly as the material is either compressed or expanded including even negative values of δ.

This is misleading, however, since if the interplanar distances are allowed to relax near the surface, they should adjust themselves so that the interatomic distances are near the equilibrium value. That this is indeed so is illustrated in Table 3, where the interatomic distances between atoms in adjacent planes are calculated for the normal crystal in the first four layers and also for the most compressed and expanded crystal considered. It is seen that these interatomic distances for a given layer are very nearly independent of the degree of distortion. The in-plane interatomic distances are not allowed to relax, and hence they are unchanged from those in the interior crystal as given in the last column of Table 3. As might be expected, the compressed crystal has slightly larger perturbations than the normal crystal because the larger repulsive forces cause the outer layers to be pushed out even further. For the expanded crystal the opposite is true, and it is interesting to note that a_{45} is larger than a_{34}, since the value of a_{ij} eventually must approach the value it has in the interior.

Acknowledgements—Mr. R. SHAFER and Mr. D. FREEMAN greatly aided this project by their coding help.

REFERENCES

1. SHUTTLEWORTH R., *Proc. Phys. Soc.* **A62,** 167 (1949).
2. LENNARD-JONES J. E. and DENT B. M., *Proc. Roy. Soc.* **A121,** 247 (1928).
3. VERVEY E. J. W., *Rec. Trav. Chim. Pays Bas* **65,** 521 (1946).
4. KANZAKI H., *J. Phys. Chem. Solids* **2,** 24 (1957).
5. HALL G. L., *J. Phys. Chem. Solids* **3,** 210 (1957).
6. GIRIFALCO L. A. and STREETMAN J. R., *J. Phys. Chem. Solids* **4,** 182 (1958).
7. LENNARD-JONES J. E. and INGHAM A. E., *Proc. Roy. Soc.* **A107,** 636 (1925).

J. Phys. Chem. Solids Pergamon Press 1959. Vol. 11. pp. 190–194. Printed in Great Britain.

INFRARED REFLECTIVITY OF ZINC OXIDE

R. J. COLLINS and D. A. KLEINMAN

Bell Telephone Laboratories, Murray Hill, New Jersey

(*Received* 4 *March* 1959)

Abstract—The reflection spectra of single crystals of ZnO were studied between 1 and 45μ. In samples with free-carrier concentration below 10^{16} cm^{-3}, the usual reflection spectrum of an ionic crystal was observed. An excellent fit to the data is achieved by using a value of the high-frequency dielectric constant $\epsilon_0 = 2{\cdot}0$, a static dielectric constant $\epsilon_s = 8{\cdot}15$, and a transverse optical mode frequency $\nu_t = 414$ cm^{-1}. The contribution to the optical constants by the free carriers becomes significant in the reflection spectra for carrier concentrations larger than $\sim 1 \times 10^{17}$ cm^{-3}. Using a method similar to that of SPITZER and FAN an effective mass of $m^* = 0{\cdot}06$ has been measured. The reflection of ZnO containing carriers can be fitted remarkably well over the range 1–45μ by the classical theory for free carriers and a lattice oscillator. The effective charge per ion site, as defined by SZEGETTI, is found to be $q^* = 1{\cdot}06\epsilon$.

1. INTRODUCTION

IN recent years optical measurements have been used in the study of semiconductors to gain knowledge concerning: width of energy gap, effective mass of carriers, shapes of energy bands, and details of shallow impurity levels. The results of such studies in germanium, silicon, and $A^{III}B^{V}$ compounds have been discussed in review articles most recently by FAN and HROSTOWSKI[1]. The oxides, and in particular zinc oxide, have not received as much attention as the valence semiconductors, largely due to the lack of single crystals of controlled impurity content. Work at this laboratory on the preparation of zinc oxide by D. G. THOMAS and J. J. LANDER has now reached the point where optical experiments are feasible.

The infrared reflection spectrum of ZnO was observed by STRONG[2], using natural zincite, and PARODI[3], using evaporated films. In both cases residual-ray monochromators were used which gave widely spaced points and only qualitative values of the reflectivity. In addition to the reflectivity, TOLKSDORFF[4] (also using evaporated films of ZnO) reported the transmission spectra between 1 and 20μ. Her data showed a large number of bands that are not observed in the single-crystal data in this paper. Based on the work of STRONG, PARODI and TOLKSDORFF, an estimate of the transverse optical mode frequency of 343 cm^{-1} was made by KRÖGER and MEYER[5].

In the present paper the absolute reflectivity of single crystals with different concentrations of free charge carriers in the range 1→40μ are given. From the data values for the optical mode frequencies, the effective charge per ion site and the carrier mass will be found. Also a slight modification of the SPITZER and FAN[6] susceptibility method for determining the effective mass will be discussed.

2. EXPERIMENTAL

The reflection spectra were taken on single crystals of zinc oxide from two sources: (*a*) crystals grown in our own laboratory in the form of ribbons ($\sim 1{\cdot}0 \times 0{\cdot}1 \times 0{\cdot}01$ cm) and used both in an "as-grown" condition and after being etched in HF, and (*b*) samples obtained from the cinder piles of the New Jersey Zinc Company and optically polished by conventional methods.

Most of the crystals obtained from either source contained a sufficiently high electron concentration to affect the reflectivity. Free-carrier effects, however, could be reduced to a negligible value by the diffusion of lithium, which acts as an acceptor. The introduction of lithium was accomplished by allowing a solution of lithium hydroxide to dry on the crystal surface, followed by baking in air at 700°C for 1 hr. For the samples used in the free-carrier mass determinations, where some control over the carrier concentration

VOL. 11 1959

was desired, indium was used as the impurity.[7] In this case a similar diffusion technique was used which differed only in that the baking temperature allowed the amount of indium in the sample to be controlled. Following the diffusion process, the thin ribbons were etched to remove surface contamination and the larger crystals were ground and polished. In the case of the indium-doped samples, several microns had to be removed before steady-state surface conditions were reached. The actual carrier concentration was found from Hall-effect measurements. Current contacts to the ends of the sample were made with pools of gallium, and the Hall probes were pressure contacts of phosphor-bronze wire.

The reflectivity measurements were made with a double-pass Perkin–Elmer monochromator equipped with prisms of NaCl, KBr and CsI. A toroidal mirror was used to form a 1 : 1 image of the exit slit in the plane of the sample with the center ray 8° from the normal. The reflected beam from the sample or the reference, a freshly evaporated aluminum film, was then imaged onto a wide-area thermocouple. Previous measurements had shown that the absolute reflectance of a fresh aluminum film is >96 per cent in the wavelength region of interest. As could be expected from the small size of the samples, energy limitations in the far infrared made the measurements somewhat uncertain. It was not possible to employ microscope optics to alleviate this situation, since reflectance measurements should be made at a well-defined angle of incidence.

3. LATTICE REFLECTION

The dominant feature in the reflection spectrum of an ionic crystal is the residual ray band of the fundamental lattice absorption. According to the classical dispersion theory[8] of Lorentz, the susceptibility χ and the conductivity σ of the lattice are given by:

$$\chi = \frac{N_0 e^2}{4\pi^2 M} \frac{\nu_0^2 - \nu^2}{(\nu_0^2-\nu)^2+\gamma^2\nu^2} \tag{1}$$

and

$$\sigma = \frac{N_0 e^2}{4\pi^2 M} \frac{2\pi\gamma\nu^2}{(\nu_0^2-\nu^2)^2+\gamma^2\nu^2} \tag{2}$$

where N_0 is the ion pair concentration, M the reduced mass of the oscillator, γ the width of the resonance at half maximum, and ν_0 is the resonance frequency. These quantities and the high-frequency dielectric constant, ϵ_0, completely determine the optical constants n and k, and the reflectivity R through the expressions:

$$n^2-k^2 = \epsilon_0+4\pi\chi$$

$$nk = \sigma/\nu$$

and

$$R = \frac{(n-1)^2+k^2}{(n+1)+k^2} \tag{3}$$

The observed reflectivity at 300°K of zinc oxide for unpolarized light is shown by the points in

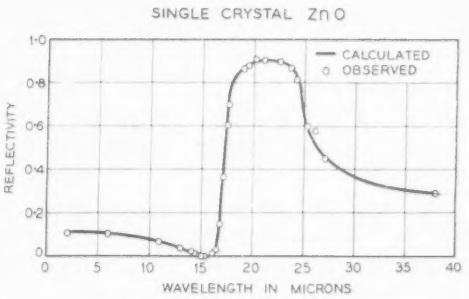

FIG. 1. Reflectivity of single crystal ZnO.

Fig. 1. The solid curve is calculated from the parameters

$$\frac{N_0 e^2}{4\pi^2 M} = 5{\cdot}1\times 10^{25}$$

$$\gamma = 3{\cdot}1\times 10^{11}\ \text{sec}^{-1}$$

and

$$\hat{\nu}_0 = 414\ \text{cm}^{-1}(\lambda_0\ 24{\cdot}2\ \mu).$$

For the trial-and-error method of selecting the best values for the three parameters, the equations were programmed for an IBM 650 calculator. It is clear from the agreement in Fig. 1 between the data and the calculated curve that the estimate of KRÖGER and MEYER[5] for the ZnO residual-ray frequency of 343 cm^{-1} was too low. The value of the static dielectric constant corresponding to the theoretical fit is $\epsilon_s = 8{\cdot}15$, which compares with the value of 8·5 measured at 1 cm by HUTSON[9].

Since zinc oxide has the wurtzite structure, it would be expected to have two distinct lattice frequencies. Using light polarized along (extraordinary ray) and perpendicular (ordinary ray) to the c-axis, these two frequencies are separately excited. These experiments showed only very slight differences, the shift being less than $0{\cdot}1\mu$, and hence the frequencies are nearly equal. According to the LYDDANE–SACHS–TELLER[10] relation, the longitudinal optical mode frequency is

$$\hat{\nu}_1 = \left(\frac{\epsilon_s}{\epsilon_0}\right)^{\frac{1}{2}} \hat{\nu}_0 = 591 \text{ cm}^{-1}.$$

The effective charge per ion site can be deduced from the parameters of the resonance by means of the SZIGETTI[11] relation:

$$\frac{q^*}{e} = \left\{(\epsilon_s - \epsilon_0)\frac{9}{(\epsilon_0+2)^2}\frac{M}{N_0}\frac{\pi\nu_0^2}{e^2}\right\}^{\frac{1}{2}}$$

which gives $q^* = 1{\cdot}06e$.

In the lattice absorption of an ionic crystal the first-order and strongest absorption will take place at the transverse optical frequency and second-order or two-phonon processes will take place with combinations between branches of the optical modes or between one optical and one acoustical mode. Fig. 2 shows the lattice absorption spectrum of ZnO. The points from 6 to 14μ represent data obtained from transmission measurements on thin samples, while the points at longer wavelengths are calculated from the residual-ray band reflection. Aside from the main absorption at $24{\cdot}2\mu$, only two strong absorption lines are present in the spectrum of zinc oxide, one at $11{\cdot}4\mu$ and the other at $10{\cdot}2\mu$. The assignment of twice the transverse optical mode for the $11{\cdot}4\mu$ band and the combination of the transverse optical and longitudinal optical for the $10{\cdot}2\mu$ band is suggested. Higher-order combinations are probably present, but will be of a much lower magnitude. In the early work of TOLKSDORFF[4] on evaporated films of zinc oxide, many bands were present which were not observed in the single-crystal specimens, and speculation on their origin would not be fruitful. The reflection data STRONG[2] obtained from natural zincite, although not in complete agreement with our own work, probably differ only because of the effect of carriers in his samples.

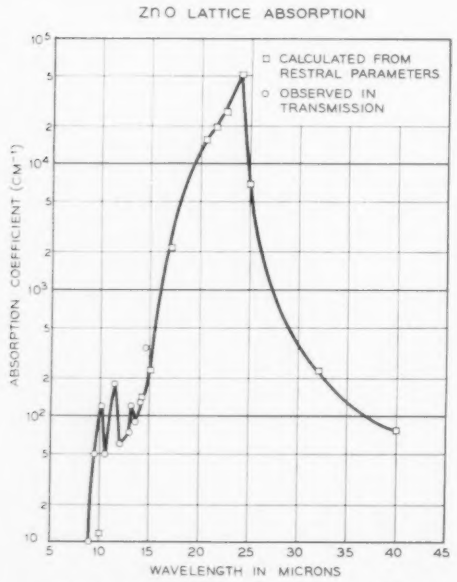

FIG. 2. Lattice absorption spectra of ZnO.

4. FREE-CARRIER EFFECTS

The presence of free charge carriers affects both the real and imaginary parts of the index of refraction. In valence semiconductors, i.e. germanium and silicon, the free-carrier absorption has been studied in detail both theoretically and experimentally, with the result that no present theory seems adequate to allow measurement of the effective mass from absorption data. SPITZER and FAN[6] showed, however, that under the condition $\omega\tau > 1$ a value of effective mass could be deduced in a straightforward manner from the free-carrier susceptibility without knowledge or assumptions concerning the relaxation time. Using the values of susceptibility determined from absolute reflectivities, they obtained effective masses for carriers in germanium, silicon, InS, and InAs which are in good agreement with the cyclotron-resonance values.

In the case of zinc oxide the free-carrier absorption has been reported[12] with marked deviations from theory and therefore cannot be used to determine the carrier effective mass. The susceptibility method can be applied, however, if enough carriers are present to produce a

well-defined minimum in the reflectivity. If the minimum reflectivity is very low, the extinction co-efficient k is very small, and the reflectivity minimum therefore corresponds to the condition $n(\lambda) = 1$. The contribution of the carriers to the susceptibility χ may be found from equation (1) by setting $\nu_0 = 0$ and interpreting N_0 as the carrier density, M as the carrier effective mass, and $(2\pi\gamma)^{-1}$ as the carrier relaxation time τ. Therefore if N_0 is known from independent Hall-effect experiments, the effective mass can be calculated from the position of the reflectivity minimum by the relation:

$$m^* = \frac{e^2 N_0 \lambda^2_{\min}}{\pi(\epsilon - 1)c^2} \tag{4}$$

It is not essential to measure accurately the absolute reflectivity, which may be difficult at low reflectivities.

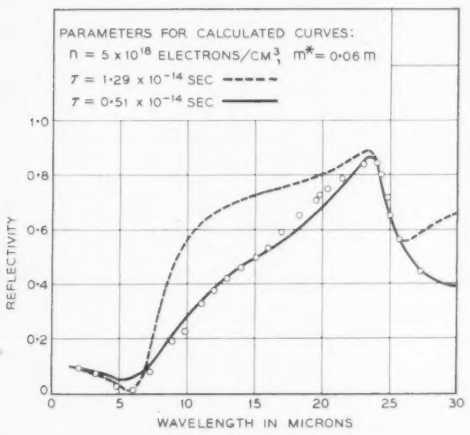

FIG. 3. Reflectivity of ZnO containing 5×10^{18} electron/cm^3.

Fig. 3 (points) shows the reflectivity of an indium-doped sample of zinc oxide containing $5{\cdot}0 \times 10^{18}$ electrons/cm^3. The reflectivity has been modified by the carriers even in the region of the residual-ray band. From the minimum at $6{\cdot}0\mu$, the point where the susceptibility of the carriers has caused the total dielectric constant to equal unity, one calculates $m^* = 0{\cdot}06$ m. For one sample it was verified that the reflectivity on the short-wavelength side of the minimum obeys the classical equations for $\omega\tau \gg 1$.

Experiments in which the light was polarized parallel and perpendicular to the c-axis revealed differences in the carrier mass which were not significantly larger than the experimental error.

In principle, to calculate the total reflection from an ionic lattice containing free carriers, a knowledge of the wavelength-dependence of each dispersion mechanism is needed. For zinc oxide the lattice dispersion seems to be well accounted for by the classical relations (1) and (2), but the free-carrier contribution is not so well understood. However, the simplest assumption which can be made for the carrier absorption is a constant relaxation time, which leads to equations of the form of (1) and (2) with $\nu_0 = 0$. In this model the only adjustable parameters for the free carriers are the effective mass and the relaxation time. Fig. 3 shows the calculated reflectivity for a sample containing 5×10^{18} carriers/cm^3 with the effective mass as determined above and for two values of relaxation time. The fit obtained for the shorter relaxation time is quite good over most of the range. It is interesting to note that a long relaxation time $\tau = 1{\cdot}2 \times 10^{-14}$ sec gives a very good fit on the short-wavelength side of the minimum, but fails completely on the long-wavelength side, suggesting that near the frequency of the minimum an additional relaxation process may become effective. The same type of change in relaxation time has been observed $\sim 40\mu$ for a sample containing $3{\cdot}7 \times 10^{17}$ electrons/cm^3.

At low frequencies the coulomb field of carriers in an ionic crystal causes a polarization of the lattice to accompany the carrier; the combination of carrier and polarization is called the *polaron*. The polaron effective mass[13] m_p, is given in terms of the bare electron mass m^* by:

$$m_p = m^*(1 + \alpha/6)$$

where

$$\alpha = \frac{e^2}{\hbar}\left[\frac{m^*}{4\hbar\pi\nu_l}\right]^{\frac{1}{2}}\left(\frac{\epsilon_s - \epsilon_0}{\epsilon_0\epsilon_s}\right)\left(\frac{m}{m^*}\right)^{\frac{1}{2}}$$

is the coupling constant between the carriers and the lattice. Since the coupling of the electron to the lattice responsible for the polaron takes place through the longitudinal optical mode, the polaron mass will be observed for $\nu < \nu_l$ and the "bare" electron mass for $\nu > \nu_l$. Unfortunately,

zinc oxide does not offer an easy way of checking this prediction, since an $\alpha \approx 0{\cdot}5$ will produce only $\sim$8 per cent increase in effective mass on passing through ν_l.

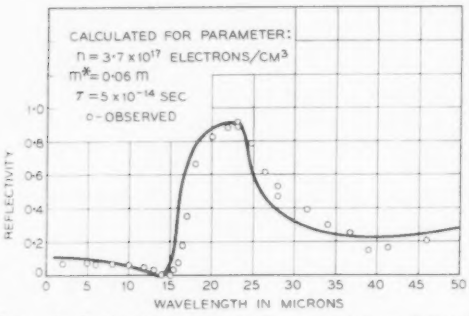

FIG. 4. Reflectivity of ZnO containing $3{\cdot}7 \times 10^{17}$ electron/cm^3.

Using the method described to determine the carrier effective mass from the location of the reflectivity minimum, for a sample containing $3{\cdot}7 \times 10^{17}$ electrons/cm^3, a value of $m^* = 0{\cdot}06\, m$ is obtained. The value of the effective mass for $\nu < \nu_l$ represents the polaron mass and is consistent with prediction of a small α. In Fig. 4 the points show the measured reflectivity of the sample, and the solid curve is the calculated reflectivity.

Acknowledgements—The authors wish to thank Dr. D. G. THOMAS for supplying the crystals used in this work.

REFERENCES

1. FAN H. Y., *Rep. Progr. Phys.* **19,** 107 (1956). HROSTOWSKI H. J., *Semiconductors* (Ed. B. HANNAY) Reinhold, New York.
2. STRONG J., *Phys. Rev.* **38,** 1818 (1931).
3. PARODI M., *C.R. Acad. Sci., Paris* **204,** 1111 (1937).
4. TOLKSDORFF S., *Z. Phys. Chem.* **132,** 161 (1928).
5. KRÖGER F. A. and MEYER H. J. G., *Physica's Grav.* **20,** 1149 (1954).
6. SPITZER W. G. and FAN H. Y., *Phys. Rev.* **106,** 882 (1957).
7. THOMAS D. G., *J. Phys. Chem. Solids* **9,** 31 (1958).
8. SEITZ F., *Modern Theory of Solids* 633, McGraw Hill, New York (1940).
9. HUTSON A. R., *Phys. Rev.* **108,** 227 (1957).
10. LYDDANE R. H., SACHS R. G. and TELLER E., *Phys. Rev.* **59,** 673 (1941).
11. SZIGETTI B., *Trans. Faraday Soc.* **45,** 155 (1949).
12. THOMAS D. G., *J. Phys. Chem. Solids* **10,** 47 (1959). ARNETH R., *Naturwissenschaften* **45,** 282 (1958).
13. LEE, T. D., LOW F. E. and PINES D., *Phys. Rev.* **90,** 297 (1953).

J. Phys. Chem. Solids Pergamon Press 1959. Vol. 11. pp. 195–204. Printed in Great Britain.

ADSORPTION ON CLEAN GERMANIUM SURFACES

MINO GREEN and K. H. MAXWELL

Zenith Radio Corporation, Chicago 39, Illinois

(*Received* 10 *March* 1959)

Abstract—The adsorption of various gases on clean germanium surfaces has been investigated. At room temperature and for $(p/p_s) \lesssim 5 \times 10^{-3}$, the gases found to be adsorbed were H_2O, CH_3OH, $(CH_3)_2O$, CH_3COOH, $(CH_3)_2CHCH_2NH_2$, C_5H_5N, and *p*-dioxan, while H_2, N_2, CO, CO_2, CH_4, C_2H_4, CCl_4, $CHCl_3$, $(C_2H_5)_2O$, C_6H_6 and C_6H_5Cl were found not to be adsorbed within the limits of our experimental error. For those gases that were adsorbed, the adsorption was extremely rapid, and the extent of take-up was equivalent to about a monolayer coverage.

The various classes of adsorbent–adsorbate binding forces have been examined with a view to identifying the type of binding force predominant in the adsorption. For H_2O, CH_3OH, $(CH_3)_2O$ in its enolic modification, CH_3COOH, and $(CH_3)_3CNH_2$, electrostatic interaction between the permanent charge distributions of the adsorbent and the adsorbate was found to account for adsorption; the nature of the binding for these systems can be described as a form of "hydrogen bond". The adsorption of pyridine and *p*-dioxan cannot readily be explained on the basis of a simple classical electrostatic interaction picture. The non-adsorption of the gases listed above is shown to be expected if only classical electrostatic interaction is considered. However, it is not suggested that this electrostatic criterion is by itself the only criterion for non-adsorption.

1. INTRODUCTION

In recent years several groups have studied the adsorptive properties of clean germanium surfaces. The reported results are, in some instances, contradictory and have been confined to a few gases only. It seemed to us that a broader study should be made of the surface chemistry of germanium, and that not only the "permanent" gases and water, but also a number of the more common organic compounds merited attention.

(a) *Preparation of clean surfaces*

The cleanness of the adsorbent surface is of extreme importance in adsorption studies (cf., e.g., adsorption on tungsten[1]), and germanium is no exception. Other workers have prepared germanium surfaces for adsorption studies in various ways. Law[2] used the flash filament technique in which a germanium filament, previously treated with C.P.4 etch,[3] was heated electrically for short periods at 800–900°C in a vacuum system. This technique is probably ineffective as a cleaning method, since Kafalas[4] was unable to measure any oxygen adsorption on etched germanium after many hours' heating in vacuum at 800°C, and furthermore Schlier and Farnsworth[5] did not obtain surface electron-diffraction patterns from etched germanium which had been heated for 24 hr in vacuum at just below the melting point. Farnsworth and co-workers[6] have produced clean germanium surfaces, as evidenced by electron-diffraction patterns[7] and oxygen adsorption,[8] by a combination of argon-ion bombardment and high-temperature annealing. Dell[9] has produced clean germanium surfaces by reducing germanium dioxide with hydrogen and has substantiated his claim for their cleanness by oxygen-adsorption studies. Green *et al.*[10] produced virgin germanium surfaces by crushing crystals of germanium in an all-glass vacuum system, and the cleanness of the surfaces produced was substantiated by the fact that both the kinetics and extent of oxygen adsorption were the same for either crushing in the presence of oxygen or crushing in vacuum with oxygen being admitted some time later.

(b) *Previous adsorption studies*

Gases, other than oxygen, whose adsorptive properties on germanium surfaces have been studied are:

Hydrogen. Schlier and Farnsworth[5] observed

the adsorption of a monolayer of hydrogen in the presence of a hot tungsten filament (i.e. atomic hydrogen present), and no adsorption in the absence of a hot filament.[11,12] LAW[2] measured the adsorption of ~0·05 of a monolayer at 300°K (hot filament present). DELL[9] could detect no hydrogen adsorption at room temperature (i.e. $<10^{-4}$ of a monolayer).

Nitrogen. LAW[2] has reported the reversible adsorption of nitrogen. At a pressure (p) of 10^{-4} mm Hg and a temperature (T) of 195°K, (this corresponds to $(p/p_s)_T = 3\times10^{-7}$, where p_s is the saturation vapour pressure at T°K) adsorption to the extent of 0·03 of a monolayer was found.

Carbon Dioxide. LAW[2] measured the reversible adsorption at 195 and 300°K; for the latter temperature at $p = 2\times10^{-4}$ mm Hg, $(p/p_s)_T = 5\times10^{-9}$, the coverage was 0·008 of a monolayer.

Carbon Monoxide. LAW[2] observed reversible adsorption at 77 and 300°K. At the higher temperature and at $p = 10^{-4}$ mm Hg, the coverage was about 0·007 of a monolayer for $(p/p_s)_T = 10^{-11}$. DELL[9] on the other hand, could measure no adsorption (i.e. $<10^{-4}$ monolayer) on either bare or partially oxygenated germanium surfaces at 300°K at $p = 4\times10^{-4}$ mm Hg or at $p = 0{\cdot}3$ mm Hg.

Krypton. ROSENBERG[13,14] has carried out extensive measurements of the adsorption of krypton on germanium powders produced by crushing. Typical physical adsorption isotherms were obtained at 78°K.

Water. The adsorption of water on what was probably a partially regenerated germanium surface[15] has been investigated by LAW[16]. Strong localized binding of water to germanium was found up to monolayer coverage, and multilayer physical adsorption was observed over the range of $(p/p_s)_{T=30°C}$ from 0·1 to 0·9.

Only for oxygen interaction with germanium surfaces is there substantial agreement amongst different workers as to the kinetics and extent of adsorption (cf. GREEN *et al.*[10], WOLSKY[8], DELL[9] and SPARNAAY[17]). It is clear that this situation does not prevail when other germanium/gas systems are considered. Of the work quoted above, that of LAW[2] concerning N_2, CO, and CO_2 must be regarded with suspicion, since it is unlikely that LAW had a clean surface.

Scope of the present investigation

The interaction of clean germanium surfaces with a variety of gases was investigated. The conditions under which the experiments were carried out were such that the extent of physical adsorption was insignificant and only adsorption involving strong adsorbent–adsorbate interactions was observable. Various adsorbent–adsorbate forces are considered with a view to explaining the observed adsorption phenomena.

2. EXPERIMENTAL TECHNIQUE

The single-chamber method of GREEN *et al.*[10] was closely followed. A wafer of germanium was crushed by a magnetically operated glass-encased iron drop-hammer in the presence of a known quantity of the gas being studied. The vacuum system was a conventional one with a rotary oil pump, a mercury diffusion pump, and a trap immersed in liquid nitrogen. After the usual bake-out procedure, the vacuum system could be pumped down to better than 10^{-6} mm Hg. The pressure-measuring device was a thermistor bead operating as a non-linear Pirani gauge. For the "permanent" gases which do not attack mercury, the calibration was against a McLeod gauge. For condensible vapours, the control of the vapour pressure* and calibration of the thermistor was effected by varying the temperature of some of the liquid contained in a side arm. An acetone–solid CO_2 bath was used for this purpose. The experimental method used in this study was limited to substances with $(p_s)_{T=25°C} \gtrsim 20$ mm Hg. The reason for this limitation is that the useful range of the thermistor gauge centres around 0·1 mm Hg, and it is necessary that $(p/p_s)_{T=25°C} \lesssim 5\times10^{-3}$ if significant physical adsorption of the gases studied is to be avoided.

The experimental sequence was as follows: The sample chamber was filled to the desired pressure

*Vapour-pressure data were obtained from the following sources: *International Critical Tables* Vol. 3. McGraw-Hill, New York (1928); TIMMERMANS J., *Physico-Chemical Constants of Pure Organic Compounds* Elsevier Publishing Co., New York (1950); and directly from the literature via references given by STULL D. R., *Industr. Engng. Chem.*, **39**, 517 (1947).

The vapours used in this study were assumed to be essentially monomeric at the pressures employed; this is consistent with the available thermodynamic data.

VOL
11
195

VOL. 11 1959

(0·1–0·3 mm Hg) with the gas being studied and then sealed off from the rest of the apparatus. The germanium wafer was crushed and the pressure recorded as a function of time.

This technique requires that the surface area of the germanium powder be known. We thought it likely that the crushing procedure could be standardized so that a more or less constant surface area could be produced for each experiment. To this end, several trial experiments were performed with oxygen as adsorbate, since the kinetics of the interaction of O_2 with crushed germanium have been extensively investigated.[10] Using germanium wafers of a uniform size (squares $7\times7\times0{\cdot}7$ mm) and a standard crushing procedure (i.e. constant drop height and a fixed number of strokes of the hammer), the surface areas produced were approximately the same. Three experiments yielded surface areas of 71, 74 and 68 cm^2, as estimated from O_2 adsorption. Two other runs using germanium from another crystal gave 70 and 73 cm^2. Thus a surface area of approximately 71 cm^2 can be produced by this technique to an experimental accuracy of about ±5 per cent and an absolute accuracy of about ±15 per cent. Crushing a germanium square about one-half the size of those described above produced ~50 cm^2. However, the larger wafer size was used in all the experiments described in this paper.

The germanium used in all the experiments was cut from a 2·4-Ω-cm *n*-type single crystal. Before being introduced into the sample chamber, the wafers were boiled in distilled water for 15 min. The volume of the sample chamber was determined at the end of each run by measuring the volume of water required to fill it; typically it was 25 cm^3. All adsorptions were first carried out at room temperature (25 ± 2°C). Some systems were later heated to 100°C in boiling water if no reaction occurred at room temperature. The amount of gas adsorbed could be determined to about 1 per cent accuracy, assuming that the vapour-pressure data were sufficiently accurate.

3. RESULTS

Table 1 contains a summary of our results. In those cases where adsorption occurred, the systems had this in common: there was an immediate extensive gas take-up when fresh surface was exposed to the gas, but there was no substantial slow take-up subsequently. The immediate take-up was, except for pyridine and *p*-dioxan, equivalent to monolayer coverage. The values indicated are the average of several runs and appear to be independent of the initial pressure of gas (which was usually varied over the range 0·1–0·25 mm Hg).

Table 1. Extent of adsorption of various gases on a clean germanium surface at 25°C assuming a germanium surface area of 71 cm^2 and $7{\cdot}7\times10^{14}$ sites per cm^2. The extent of adsorption is in units of $\sigma/7{\cdot}7\times10^{14}$, where σ is the number of molecules adsorbed per cm^2 of germanium surface.

Gas	Extent of Adsorption ($\sigma/7{\cdot}7\times10^{14}$)
Hydrogen*	0
Nitrogen	0
Carbon Monoxide*	0
Carbon Dioxide	0
Methane	0
Ethylene	0
Methanol	1·05
Acetone	1·06
Water	0·98
Benzene	0
Chlorobenzene	0
Carbon tetrachloride	0
Chloroform*	0
Diethyl ether*	0
Acetic acid	0·94
Pyridine	0·77
p-Dioxan*	0·72
iso-Butylamine	1·06

*These results also apply to the system heated to 100°C.

The adsorptions of pyridine and *p*-dioxan were somewhat anomalous. For both these gases the rapid take-up was followed by a slow monotonic pressure *increase* (assuming no change in the heat-conducting properties per molecule of the gas which was measurable for a period of about 6 hr. With only a thermistor as a pressure-measuring device, it is impossible to say how much material was involved in the pressure change. If it is assumed that the pressure rise is due to a gas with the same heat-conducting properties per molecule as the initial gas, then for pyridine $\sim10^{15}$ extra

molecules appeared in the gas phase and for *p*-dioxan 3×10^{15} extra molecules appeared in the gas phase. In the case of *p*-dioxan adsorption, the adsorbent–adsorbate system was heated at 100°C for about ½ hr, whereupon a further increase in pressure (as registered by the thermistor) was observed, which, on the above criterion, corresponded to 10^{15} extra molecules entering the gas phase.

4. DISCUSSION

In the discussion which follows various gas/solid interaction forces are considered with a view to explaining the adsorption or non-adsorption of the gases investigated in this study.

Adsorbent surface

In considering adsorbent–adsorbate interaction, we require an atomic model of the clean germanium surface. For such a model we draw in large measure on the work of FARNSWORTH *et al.*,[6,7] who have used low-speed electron diffraction to study the spatial arrangement of the surface atoms on the three major crystal faces of germanium. The main conclusion of their work is that the ideal (i.e. as built up from the bulk crystal) surface array does not exist on the surface of a real crystal. There is a slight distortion of the surface which takes the form of an ordered pairing of adjacent surface atoms in such a way as to give rise to a surface grating with a double spacing in addition to the expected single spacing. Thus, from a spatial point of view, we are probably justified, for rough calculations, in retaining the ideal surface geometry, but we must modify the notion that there are unperturbed directed surface sp^3 valence electrons (sometimes called "dangling bonds") in the ideal positions. Instead, the unpaired surface valence electrons are imagined to be considerably localized between neighboring surface germanium atoms, leading to a kind of surface Ge–Ge bond.

There is a certain measure of support for the above view of the germanium surface. For example, if the germanium surface contained one [(111) or (110) plane] or two [(100) plane] unpaired electrons per surface germanium atom (these unpaired electrons constituting acceptor-type surface states), we would expect to find $\sim 10^{15}$ surface states cm^{-2}. Instead, the work of BARNES and BANBURY[18] on cleaved single crystals of germanium has shown that the surface concentration of acceptor-type states in the forbidden gap is $\sim 10^{11}$ cm^{-2}. It seems likely that the higher concentration of surface states reported by workers examining surfaces cleaned by the ion-bombardment method[19] can be ascribed to imperfect surface pairing at surface imperfections, a likely occurrence with such a drastic cleaning method. Support for the above model comes from recent low-temperature ($\sim 4{\cdot}2$°K) electron magnetic-resonance studies on clean germanium powders.[20] These experiments have failed to show an absorption which could be identified with unpaired electron states. While such studies are not conclusive, they do support the proposal that free surface valences do not exist in high concentration on a clean germanium surface.

Adsorption forces

Adsorbent–adsorbate interactions usually fall into one of two main groups: (i) short-range interactions involving electron exchange or electron transfer and generally associated with chemisorption, or (ii) long-range interactions involving dipole–dipole forces, van der Waals forces, &c., which are generally regarded as causing physical adsorption. The discussion which follows is concerned with determining what adsorption forces predominate in the systems we have studied.

Ion formation. Adsorption by ion formation, involving the transfer of an electron to or from the bulk of the semiconductor, has been extensively discussed in the literature.[21] Such a mechanism cannot apply where adsorption to the extent of about a monolayer occurs, as is the case for the systems reported above. A monolayer of a fully-ionized singly-charged adsorbate species would give rise to an electrostatic repulsion energy in excess of 200 kcal/mole (cf. GREEN[22]), while the energy gained from electron transfer processes is at most about one-fifth of this figure.

Covalent binding. A model involving the formation of simple electron-pair bonds between adsorbent and adsorbate can be rejected for the substances which have been found to adsorb to the extent of a monolayer on germanium. Such a mechanism of adsorption would require that the adsorbate species should dissociate, either before

or during adsorption, and this must lead to values of the amount adsorbed (as measured by the pressure change) different from those found. However, the formation of an adsorbent–adsorbate complex in which the excess electron can be treated as a molecular orbital electron, requires further consideration. For example, consider that the surface complex between germanium and pyridine can be represented by

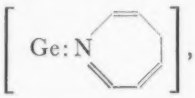

where the electron denoted outside the square bracket extends over the surface complex. In the absence of a full quantal treatment, it is difficult to say if this type of surface complex can be stable. We note, however, that $(C_2H_5)_2O$, CO, and CO_2 all contain lone-pair electrons, necessary for the formation of the above type of complex, and yet these substances do not react with the germanium surface. Therefore we tentatively reject the formation of the kind of surface complex just described.

van der Waals forces. It is certain that dispersion-force interaction must occur between adsorbent and adsorbate. But we know that the extent of adsorption (at $p/p_s \lesssim 10^{-3}$) is insensitive to pressure and, therefore, that van der Waals forces cannot predominate in those cases where adsorption has been observed. For the substances investigated, van der Waals forces will range from 0·5 to ~5 kcal/mole at adsorbent–adsorbate separations corresponding to the equilibrium van der Waals radii.

Electrostatic interactions. Since we cannot account for the observed adsorptions by any of the interaction forces examined thus far, we must consider the possibility of electrostatic interactions. Here we are confronted with our lack of exact knowledge of the nature of the germanium surface. At best we can use a crude model of the surface and the adsorbing species and obtain correspondingly rough estimations of the adsorbent–adsorbate electrostatic interaction energies. Such a procedure will at least tell us if we are moving in the right direction. Two types of electrostatic interaction are considered. (i) The inductive effect; the electric field due to the adsorbate is taken to induce a dipole in the adsorbent and the electrostatic interaction energy of the induced dipole with the adsorbate molecule is estimated.* (ii) Permanent charge interaction; the interaction energy of the charge distribution of the adsorbent with the charge distribution of the adsorbate is estimated.

The calculation of the inductive interaction using the image force interaction formalism must be discarded for several reasons. The classical theory of images does not apply to metals at adsorbent–adsorbate separations of several Ångstroms or to semiconductors probably at separations of several hundred Ångstroms.[23,24] If the classical theory of images is retained down to molecular dimensions, strong adsorbent–adsorbate interactions are predicted, e.g. water on a metal would have an image binding energy of about 20 kcal/mole. But KEMBALL[25] has shown that the adsorption of water on mercury is reversible; this is taken as experimental evidence for rejecting image interaction as an important adsorption force.

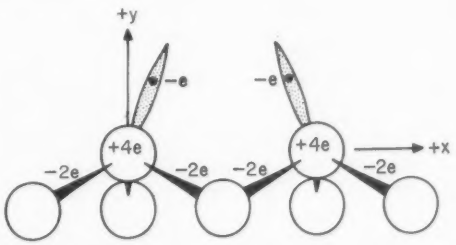

FIG. 1. Representation of the charge distribution on a pair of surface germanium atoms in the (111) plane. The y-direction is normal to the (111) plane and the x-direction is in a line connecting the pair of surface germanium atoms.

In calculating the inductive and permanent-charge electrostatic interactions, we will consider only the (111) crystal plane of germanium, the cleavage plane, and assume a point-charge model

*The inductive interaction arising from the dipole induced in the adsorbate molecule by the permanent charge distribution of the adsorbent is not considered here. We have neglected this interaction because, for those substances examined in this paper, the only significant inductive interaction occurs for groups with comparatively small bond polarizabilities, i.e. substances with OH or NH groups.

for the charge distribution on the surface atoms. The charge is taken to be disposed in the following manner (cf. Fig. 1). The germanium core has a central charge of $4\,e^+$; each Ge–Ge bond (normal sp^3 binding) has $2\,e^-$ half-way along the bond; the electron orbital projecting up from the surface germanium atom, which is partially paired to an adjacent germanium surface atom, has $1\,e^-$ in a plane normal to the surface which contains the two surface germanium atoms. The charge in the surface orbital is taken to be 1·2 Å from the germanium nucleus (i.e. a distance equal to the covalent radius of the germanium atom) and along a line which makes an angle of 20° with the normal to the surface (20° is about the maximum that most bonds can be distorted without bond rupture).

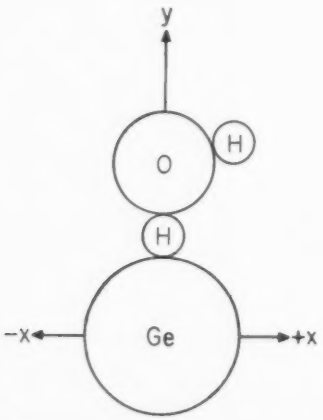

FIG. 2. H_2O over a surface germanium atom in "pirouette" position: upper H and projecting electron of Ge atom are both on the $+x$ side. The x-y plane corresponds to the x-y plane of Fig. 1.

A point-charge model is also used for the adsorbate molecules. The inductive interaction is calculated, for the sake of illustration, for two kinds of adsorbate species: water, which was adsorbed, and carbon tetrachloride, which was not adsorbed. We use an effective point-charge model for H_2O and CCl_4. For water we use the model provided by ROWLINSON[26]. For CCl_4 we must use the cruder model given by PAULING[27]. In the latter case, knowing the bond length and the bond dipole moment[27] and placing the

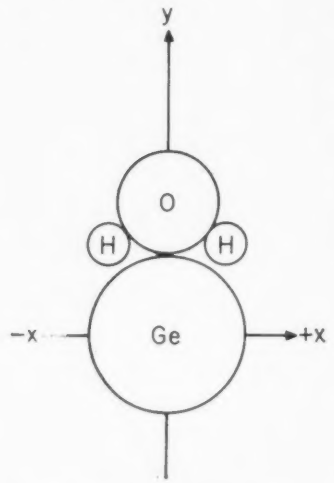

FIG. 3. H_2O over a surface germanium atom in astride position. The H–O–H chain is in the x-y plane.

charge at the centre of the atoms, we have $0{\cdot}6\,e^+$ on the carbon atom and $0{\cdot}15\,e^-$ on each of the chlorine atoms.

Several likely dispositions of the adsorbate molecule with respect to the adsorbent molecule are shown on Figs. 2–4. In each case the van der Waals radius for adsorbent and adsorbate is used. Germanium is taken to have about the same

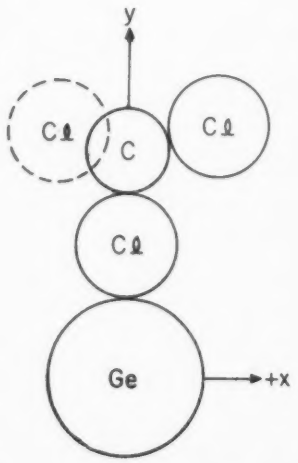

FIG. 4. CCl_4 over a surface germanium atom: one of the upper Cl atoms is in the x-y plane.

van der Waals radius as krypton,[28] i.e. 2 Å.* The radius of water [29] is taken as 1·35 Å and that of carbon tetrachloride[29] as 2·95 Å; the centres of the molecules (which are treated as spheres) are taken at the Ge, O, and C nucleus respectively.

Several assumptions must be made in order to estimate the inductive interaction. The polarizability of the surface germanium atom is taken to reside mainly in the bonding electrons. The polarizability α of the bonding electrons and the surface electron is taken to act along the direction of the bond and the transverse polarizability is taken to be negligibly small. This gives a value of $\sim 22 \times 10^{-25}$ cm^3 per bond, given the experimental value of $\sim 44 \times 10^{-25}$ cm^3 for crystalline germanium (obtained from its refractive index[30]). The method of computation of the inductive interaction at a bond of a surface germanium atom is as follows. The electric field, F, due to the adsorbate molecule, at the position where the point charge of the bond has been sited, and along the bond direction, is calculated. The induced dipole is obtained from the relation $\mu = \alpha F$. The dipole is taken to be a point dipole, whence the potential at any point due to the induced dipole is given by $V = \mu \cos\theta / r^2$, where $\mu \cos\theta$ is the dipole strength along the line connecting the dipole with the point in question and r is the distance to that point. The potential, V, due to the induced dipole, is calculated at each of the charges of the adsorbate molecule. The interaction energy with each of the charges is given by the product qV, where q is the magnitude of the adsorbate charge being considered. The sum of these interactions is the estimated inductive interaction energy with the bond in question. This is carried out for the four bonds associated with each surface germanium atom. When this is done, it at once becomes apparent that only the interaction with the projecting surface electron is of any consequence; the lower bonds give an interaction energy of $\sim 0{\cdot}1$ kcal/mole^{-1} or less. The interaction energy of water with the projecting electron (for the configuration of Fig. 2) is the largest calculated quantity and is +3·7 kcal/mole (the positive sign signifying net attraction). We would expect a similar value for the inductive interaction energy for other substances possessing an OH group, i.e. CH_3OH, CH_3COOH, &c., CCl_4 in the configuration shown in Fig. 4 gives $<0{\cdot}5$ kcal/mole. In view of the smallness of the estimated inductive interactions, this effect need not be considered further; it cannot, by itself, account for our experimental observations.

The interaction between the permanent-charge distributions is calculated according to classical electrostatics, using the model described above. Here, however, the charge on the bonds between the surface germanium atom and the lower-lying atoms, the sp^3 bonds, is taken to be 1 e^-, rather than 2 e^-, since one of the electrons of the bond is donated from the lower germanium atom, and we should have to include the whole of the lower germanium atom if we included one of its electrons.

Detailed calculations of the permanent-charge interaction energy have been carried out for water/germanium and methanol/germanium for the "pirouette" configuration (Fig. 2). These calculations show clearly that it is only because the hydrogen atom can approach close to the projecting surface electron *and* because the OH group has a high dipole moment, with the positive end of the dipole on the hydrogen atom, that strong electrostatic interaction occurs with germanium. Essentially the same conclusion applies to hydrogen bonding in liquid systems, where the simple classical electrostatic approach has attained a great deal of success in explaining intermolecular attraction involving positively charged hydrogen groups.[31] Our results for H_2O on germanium give U_e, the permanent electrostatic interaction energy, equal to +12·5 kcal/mole, using DUNCAN and POPLE's[32] model for H_2O. (Using ROWLINSON's model, we obtain +11·5 kcal/mole.) For methanol on germanium, we obtain $U_e = +14{\cdot}3$ kcal/mole. The charge distribution on methanol was obtained by using DUNCAN and POPLE's model for water, replacing one of the hydrogen atoms by a CH_3 group (C–H dipole taken = 0) and adjusting the mean position of the bonding electrons of the O–C bond until the final charge distribution of the molecule yielded the

*Germanium is compared with krypton because of their relative positions in the Periodic Table. Furthermore, an analysis (GREEN, MAXWELL and SEIWATZ, unpublished work) of the heat of adsorption of krypton on Germanium leads to a value of about 1·9 Å for the effective van der Waals radius of the surface germanium atom.

experimental dipole moment of methanol, i.e. 1·68 *D*. On the basis of the above calculations, and the known polar character of acetic acid and *iso*-butylamine (this latter substance taken to be similar to ammonia), we can confidently expect these two substances to give U_e values of 13 kcal/mole to within ±20 per cent. We would expect acetone, *in its enolic modification*, to give a similar value for U_e.

The net heat of adsorption, U, i.e. the adsorbent–adsorbate binding energy, will be approximately equal to or greater than $U_e+U_v+U_i$ (U_v and U_i are the van der Waals and inductive interaction energy, respectively), where U_e, U_v and U_i have been calculated for an adsorbent–adsorbate separation corresponding to the maximum van der Waals energy. For U in excess of about 12 kcal/mole, the adsorption is generally irreversible and has the characteristics associated with chemisorption. Chemisorption is, amongst other things, characterized by the presence of adsorption sites; this site characteristic is displayed in electrostatic interaction, where the value of U_e is a maximum approximately over a surface germanium atom.

In equating U_e to the permanent-charge interaction energy between adsorbent and adsorbate *for monolayer coverage*, it is tacitly assumed that an adsorbate molecule interacts only with the adsorbent molecule immediately beneath it. Furthermore, it is assumed that lateral interaction between adsorbate molecules in the monolayer is insignificant. The first of these assumptions seems justifiable when it is noted that the hydrogen atom of an adsorbate molecule must approach close to the surface projecting electron for a significant permanent-charge interaction energy to result. The second assumption is more difficult to justify by a calculation and here we can appeal to experiment. KEMBALL[25] has shown, in an investigation of the adsorption of water and the simple aliphatic alcohols on mercury surfaces, that the heat of adsorption is independent of coverage (up to a monolayer). In the case of water, KEMBALL[25] concludes that water is probably in a "pirouette" position on the mercury surface and that localized adsorption has occurred; this is the same model that we have used. These results would seem to militate against the need to consider lateral interactions.

The adsorption of pyridine and *p*-dioxan cannot be readily accounted for by electrostatic interaction, and we are not in a position to explain the nature of the binding. We note, however, that in both cases there is an unusual pressure change after the initial fast adsorption, which may be due to a decomposition reaction. It would seem that an experimental study involving a system for identifying the species in the gaseous phase is called for.

From an electrostatic viewpoint, all those substances listed in Table 1 as not adsorbing should not have adsorbed. In some cases it is clear from the small polar character of the intended adsorbate molecule that the electrostatic interaction would be trivial. Thus, CO has a dipole moment of 0·1 *D*; H_2 and C_2H_4 have essentially no polar character.[33] In other cases, e.g. CH_4, CCl_4 and CCl_3H, the central atom is positive: C–H with sp^3 bonding is estimated[33] to have a dipole moment of about 0·4 *D*, with the hydrogen as the negative end of the dipole. In yet other cases, it is not immediately clear that electrostatic interaction would be small, and these cases have been treated numerically, using our model for the germanium surface. The results of these calculations follow below.

CO_2. For CO_2 we take a configuration where the C atom is directly over a surface Ge atom and the O=C=O is in the *x*–*y* plane (cf. Fig. 1). The van der Waals radius for the carbon atom is taken as 1·2 Å. The charge distribution is calculated from WALSH's[34] estimate of 9 per cent polar character for CO_2, whereupon we obtain $U_e \simeq 0{\cdot}2$ kcal/mole.

C_6H_5Cl. The Cl atom is placed over a surface Ge atom and the plane of the benzene ring in the *x*–*y* plane (Fig. 1). The van der Waals radius for the Cl atom is taken as 1·19 Å. The charge distribution is estimated assuming the following: that the Cl atom is positive, that the excess charge on the Cl atom is balanced against the excess negative charge in the benzene ring, and that this negative charge is equally distributed over the 1, 3, 4, and 6 positions of the ring. The measured dipole moment of C_6H_5Cl is 1·73 *D* and the dimensions of the molecule are C–C = 1·39 Å and C–Cl = 1·69 Å. U_e is found to be $<0{\cdot}5$ kcal/mole.

C_6H_6. The carbon–hydrogen bonds of benzene

are polar,[33] $\bar{C}$–$\dot{H}$≃0·4 *D*. In estimating the permanent charge interaction, benzene is placed in the same configuration as C_6H_5Cl above, and the van der Waals radius of the hydrogen atom is taken as 0·35 Å, whereupon we estimate that U_e≃1 kcal/mole.

$(C_2H_5)_2O$. The polarity of the C–H bond in diethyl ether is not known, and this makes it difficult to estimate the charge distribution from the dipole moment. However, assuming the

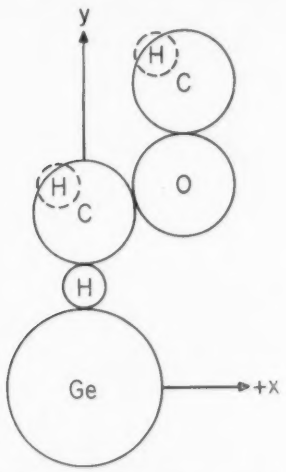

FIG. 5. Diethyl ether, $[(C_2H_5)_2O]$, over a surface germanium atom; the terminal CH_3 groups are not shown since these were not taken into account for the calculations. The C–O–C chain is in the *x*-*y* plane.

C–C and the C–H dipole≃0, the effective excess charge on the C and O atoms can be estimated from the dipole moment. The $(C_2H_5)_2O$ is placed over the surface as shown in Fig. 5, with the C–O–C chain in the *x*–*y* plane (cf. Fig. 1). We obtain U_e≃0·1 kcal/mole.

5. CONCLUSIONS

The results of our electrostatic calculations show that, apart from pyridine and *p*-dioxan, the adsorption or non-adsorption of the substances investigated can be explained on a purely electrostatic basis. It is important to note that only where one would expect a form of hydrogen bonding does a formal electrostatic calculation yield U_e values which are probably high enough to account for "chemisorption". We have yet to deduce a criterion for non-adsorption on germanium surfaces; the above findings for non-adsorption on an electrostatic basis, while they are gratifying, are not by themselves sufficient.

REFERENCES

1. MILLER A. R., *The Adsorption of Gases on Solids* Cambridge University Press (1940).
2. LAW J. T., *J. Phys. Chem.* **59,** 543 (1955).
3. HEIDENREICH R. H., *Phys. Rev.* **81,** 838 (1951).
4. KAFALAS J. A., *Lincoln Laboratory, Lexington, Mass. Quart. Progr. Rep. Group* 35, p. 21 (1 May 1957).
5. SCHLIER R. E. and FARNSWORTH H. E., *Semiconductor Surface Physics* (Ed. R. H. KINGSTON) p. 11 University Pennsylvania Press (1957).
6. FARNSWORTH H. E., SCHLIER R. E., GEORGE T. H. and BURGER R. M., *J. Appl. Phys.* **26,** 252 (1955).
7. FARNSWORTH H. E., SCHLIER R. E., GEORGE T. H. and BURGER R. M., *J. Appl. Phys.* **29,** 1150 (1958).
8. WOLSKY S. P., *Phys. Rev.* **108,** 1131 (1957).
9. DELL R. M., *J. Phys. Chem.* **61,** 1584 (1957).
10. GREEN M., KAFALAS J. A. and ROBINSON P. H., *Semiconductor Surface Physics* (Ed. R. H. KINGSTON) p. 349. University of Pennsylvania Press (1957).
11. FARNSWORTH H. E., SCHLIER R. E. and TUUL JOHANNES. To be published.
12. LAW J. T., *J. Chem. Phys.* **28,** 511 (1958).
13. ROSENBERG A. J., *J. Amer. Chem. Soc.* **78,** 2929 (1956).
14. ROSENBERG A. J., *J. Phys. Chem.* **62,** 1112 (1958).
15. ROSENBERG A. J., ROBINSON P. H. and GATOS H. C., *J. Appl. Phys.* **29,** 771 (1958).
16. LAW J. T., *J. Phys. Chem.* **59,** 67 (1955).
17. SPARNAAY M. J., *Proceedings of the International Conference of Solid State Physics and its Application to Electronics and Telecommunications* (Brussels, June 2–7, 1958) to be published by Academic Press.
18. BARNES G. A. and BANBURY P. C., *Proc. Phys. Soc.* **71,** 1020 (1958).
19. HANDLER P., *Semiconductor Surface Physics* (Ed. R. H. KINGSTON) p. 23 University of Pennsylvania Press (1957).
    DILLON J. A. and FARNSWORTH H. E., *J. Appl. Phys.* **28,** 174 (1957).
20. KINGSTON R. H. Private communication.
21. AIGRAIN P. and DUGAS C., *Z. Elektrochem.* **56,** 363 (1952).
    WEISZ P. B., *J. Chem. Phys.* **21,** 1531 (1953).
    HAUFFE K., *Advances in Catalysis* Vol. 7, p. 213. Academic Press, New York (1955).
22. GREEN M., *Semiconductor Surface Physics* (Ed. R. H. KINGSTON) p. 362. University of Pennsylvania Press (1957).
23. CUTLER P. H. and GIBBONS J. J., *Phys. Rev.* **111,** 394 (1958).

24. SACHS R. G. and DEXTER D. L., *J. Appl. Phys.* **21,** 1304 (1950).
25. KEMBALL C., *Proc. Roy. Soc.* A**190,** 117 (1947).
26. ROWLINSON J. S., *Trans. Faraday Soc.* **47,** 120 (1951).
27. PAULING L., *The Nature of the Chemical Bond,* p. 74. Cornell University Press, Ithaca (1940).
28. BEATTIE J. A., BARRIAULT R. J. and BRIERLEY J. S., *J. Chem. Phys.* **19,** 1222 (1951).
29. HIRSCHFELDER J. O., CURTISS C. F. and BIRD R. B., *Molecular Theory of Gases and Liquids,* pp. 218, 227 and 1111. John Wiley & Sons, New York (1954).
30. SALZBERG C. D. and VILLA J. J., *J. Opt. Soc. Amer.* **47,** 244 (1957).
31. COULSON C. A., *Valence,* p. 302 Oxford University Press (1952).
32. DUNCAN A. B. F. and POPLE J. A., *Trans. Faraday Soc.* **49,** 217 (1953).
33. GENT W. L. G., *Quart. Rev. Chem. Soc.* (*Lond.*) **2,** 383 (1948).
34. WALSH A. D., *Trans. Faraday Soc.* **43,** 158 (1947).

VOL
11
195

J. Phys. Chem. Solids Pergamon Press 1959. Vol. 11. pp. 205–214. Printed in Great Britain.

PHOTOELECTRIC EMISSION AND WORK FUNCTIONS OF InSb, GaAs, Bi_2Te_3 AND GERMANIUM

D. HANEMAN*

Physics Research Laboratory, University of Reading

(*Received* 16 *March* 1959; *revised* 10 *April* 1959)

Abstract—Measurements have been made of the energy distributions of photoelectrons emitted by various semiconductor surfaces freshly exposed by breaking in high vacuum ($\sim 10^{-8}$ mm). The data have been used to obtain the variation with energy of the density of states in the valence band, multiplied by a photoelectric excitation probability. Spectral distributions of the photoelectric yield and accelerating field characteristics were also measured. Marked differences were found between the energy-dependence of the photoemission of the hexagonal structure Bi_2Te_3 on the one hand, and the three diamond-structure semiconductors on the other. Work functions found were: 4·57 eV for InSb, 4·69 eV for GaAs, and 4·75 eV for germanium, the clean faces being composed of (110) facets for the intermetallic semiconductors and of (111) facets for the germanium. For Bi_2Te_3, mirror-like (0001) cleavage planes had a work function of 5·30 eV.

1. INTRODUCTION

THERE is much interest in the valence bands of certain semiconductors, including germanium and the intermetallic semiconducting compounds. Experimental evidence concerning the density of states in the valence bands of these materials, for a depth of more than a few times kT below the top of the band, has not been obtained, and few methods are available. Because of the difficulties of interpreting the results of soft X-ray emission studies on materials of high atomic number (see e.g. TOMBOULIAN[1]), it was considered worthwhile to gain information by measuring the external photoelectric emission from the materials.

APKER *et al.*[2] showed that the energy distribution of external photoelectrons could be analysed, using certain simplifying assumptions, to deduce the product of the photoelectric excitation probability and the density of states in the valence band. Subject to a knowledge of the former quantity, the density of states can thus be obtained. In addition, the photoelectric method leads to the determination of the work function of the surface examined, and also an estimate of the valence band edge separation from the Fermi level in the surface region, both of which parameters are of interest.

2. THEORY OF METHOD

The well-known retarding potential method of determining energy distributions of photoelectrons was used. The theory of this method, and a theoretical scheme for analysing the results of the photoemission from semiconductors using monochromatic incident light, were given by APKER *et al.*[2] For convenience of discussion, we include here some important points, with special emphasis on electron–electron collisions.

An internal electron of energy ϵ excited by a photon $h\nu$ becomes an external photoelectron of energy E after passing through the surface barrier of height $\mu+\phi$, where μ is the Fermi energy and ϕ the work function for the surface concerned. As will be discussed further in Section 8(c), we consider a volume photoelectric process in which the electrons are excited internally and then travel to the surface, suffering possible collisions. Recent experiments on avalanche effects in reverse-biased p–n junctions (CHYNOWETH and MCKAY[3], and references to earlier work) indicate that highly excited electrons lose energy mainly by electron–electron collisions, the minimum loss being somewhat greater

* Now at Barus Research Laboratory, Brown University, Providence, Rhode Island, U.S.A.

than the forbidden energy gap, though most losses are considerably higher. One may thus assume that the more energetic external photoelectrons have suffered no internal electron–electron collisions. The further assumption is made, as in the work of FOWLER[4], DUBRIDGE[5], and APKER *et al.*[2], that the probability of an excited electron passing through the surface barrier is proportional to E. It was shown by APKER *et al.*[2] that the product sn of the photoelectric excitation probability $s(\nu, \epsilon)$ and the density of states $n(\epsilon)$ is proportional to $N(E)/E$, where $N(E)$ is the energy distribution of the photoelectrons, and is the quantity obtained by differentiating experimental retarding potential plots. By further assuming that sn varied as $(\epsilon_0-\epsilon)^m$ in the range of interest, where ϵ_0 is the top of the valence band and m is an arbitrary parameter, APKER *et al.*[2] derived a theoretical expression for retarding potential curves from semiconductors. This expression contained the parameter m and also Δ, the distance between the top of the valence band and the Fermi level in the surface region.

The quantity Δ is of great interest. It can be determined from the photoelectric data by using the relation

$$\Delta = e(V_0 - V_0') \qquad (1)$$

where V_0 is the retarding potential which just prevents electrons coming from the Fermi level of the emitter reaching the collector, and V_0' is the retarding potential which just stops electrons coming from the top of the valence band. The potential V_0 is equal to $h\nu-\phi_c$, where ϕ_c is the collector work function, which can be found by studying the emission from a metal emitter, using the analysis of FOWLER and DUBRIDGE. If a semiconductor is then substituted for the metal emitter, its work function ϕ can be found from the contact potential between it and the surrounding collector of determined work function ϕ_c. This contact potential is equal to the voltage V_s—which should be independent of $h\nu$—at which the photoelectric current saturates

$$eV_s = \phi_c - \phi \qquad (2)$$

The voltage V_s can be satisfactorily determined by using parabolic extrapolation techniques.[6]

3. EXPERIMENTAL DETAILS

(a) *Surface preparation*

To avoid spurious effects due to emission from surface layers of foreign atoms, it is desirable to study surfaces having less than a monolayer of contamination.

The three most widely used methods for producing clean surfaces involve heating, the formation of evaporated films, and ion bombardment of the surfaces. The heating method of cleaning is not promising for some of the materials studied here, owing to their low melting point. Evaporated films of compound semiconductors are difficult to prepare and are unsatisfactory, as they generally have

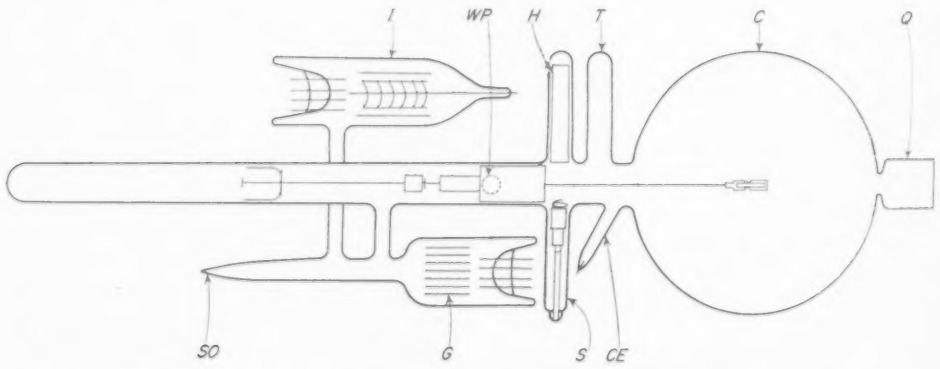

FIG. 1. Diagram of phototube. *Q*—quartz-to-glass seal with quartz window; *C*—spherical collector; *CE*—electrode making contact to collector surface; *T*—trap for fragments of broken crystal; *H*—hammer; *S*—side tube containing tungsten spring; *WP*—tungsten pin connected to crystal holder (tube containing this pin is underneath); *I*—ionization gauge *G*—getter tube containing molybdenum wires and *SO*—seal-off constriction.

properties differing appreciably from those of the bulk specimens (see e.g. PAPARODITIS[7]). There is reason also to suspect evaporated surfaces, as the work-function values may differ from those obtained for solid-specimen surfaces.[8] The third method is the ion-bombardment cleaning technique of FARNSWORTH *et al.*[9] The efficacy of this method has not to date been demonstrated for all the semiconductors used here.

In view of the above considerations, fresh surfaces were produced by breaking and cleaving the materials in high vacuum. The surfaces so produced are expected to be initially clean, and free of the objections applicable to surfaces produced by the other techniques.

Sealed-off phototubes were used, gettered by Alpert ionization gauges and freshly evaporated molybdenum films. A sketch of the type of phototube used is shown in Fig. 1. Ultraviolet light was admitted through a polished 1-mm. quartz window attached by a graded seal to the 1 litre collector sphere, which was coated internally with a conducting layer of graphite. The breaking mechanism is

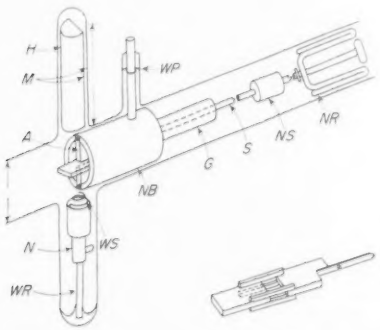

FIG. 2. Crystal-breaking assembly. *H*—hammer; *M*—matching flat surfaces; *A*—anvils; *N*—nickel cup; *WR*—3-mm tungsten rod; *WS*—tungsten spring; *NB*—nickel barrel; *G*—guide into barrel; *S*—support rod; *NS*—nickel slider; *NR*—nickel rod; and *WP*—tungsten pin to barrel.

shown in detail in Fig. 2. Most crystals were about 20 mm long × 8 mm wide × 2 mm thick. For breaking, the crystal was supported on either side by nickel anvils screwed to a nickel barrel which was itself a sliding fit in the surrounding glass tube. This arrangement distributed the shock when the tungsten-loaded hammer was jerked on to the crystal to break it. This method of breaking was successful for germanium, InSb, and GaAs crystals, not all of which could be obtained suitably oriented for cleavage. For bismuth telluride, which is soft and cleaves easily, a somewhat different method was adopted. A piece of razor blade was driven by magnetic control a distance of 0·5 mm into the side of the crystal, whose front face was (0001). The crystal was then pulled back in such a way that a piece of the material was flicked off, exposing a mirror-like cleavage plane of dimensions 5 × 5 mm.

In all cases the crystals were clamped in a suitably shaped nickel fork welded to the end of a polished 2-mm-dia. tungsten rod which was a sliding fit in the guide tail of the nickel barrel. This rod could be slid to any desired position by tilting the sealed phototube or by magnetically forcing the nickel slider (Fig. 2) against the stops welded to the rod. The assembly could be rotated by magnetic control of the nickle **U** piece attached to the end of the rod. Broken crystal fragments were accommodated in a separate chamber shown in Fig. 1.

Electrical contact to the crystal was made through the 3-mm tungsten pin which held the barrel in position. The collector contact was a piece of nickel wire pressed against the graphite and held by a small pinch at the neck of the tube.

(b) *Vacuum procedures*

Prior to assembly of the tube, metal parts were degassed to near melting point by r.f. heating in high vacuum. The assembled tube was connected via a seal-off constriction to a vacuum system consisting of a two-stage backing pump followed by a mercury diffusion pump and three liquid-air traps. The top trap and the phototube were baked for 50 hr at 400°C, with liquid air in two traps. Before seal-off, the ionization gauge, molybdenum getter filaments, and seal-off constriction were thoroughly degassed at 10^{-8} mm. After seal-off, pumping with the ionization gauge and evaporated molybdenum getter films gave recorded pressures of 10^{-8}–10^{-9} mm. A fresh molybdenum getter film was evaporated just before breaking a crystal.

(c) *Measuring procedures*

The tubes were assembled with platinium caps fitting over the crystals. Each cap had a similar shape to the crystal, but was in contact only near

the crystal support. The first measurements were made on the cap. They included the spectral distribution of the photoelectric yield, retarding potential characteristics taken at several different photon energies, and the increase of photocurrent with accelerating field. The cap was then dislodged and measurements made on the ground front face of the crystal. After this the crystal was broken and slid into the centre of the sphere, and measurements were made as soon as possible on the freshly exposed face. The first yield measurement was usually complete about 15 min after breaking the crystal. Yield measurements could be taken in 2 or 3 min and retarding potential characteristics in about 5 min. A full set of measurements could be taken and repeated within an hour of breaking the crystal.

Low- and medium-pressure mercury discharge lamps and low-pressure zinc and cadmium discharge lamps were used as light sources. Photoelectric currents were measured with a d.c. electrometer amplifier. During measurements, the phototube was shielded from stray fields and the earth's magnetic field by three concentric Mumetal shields.

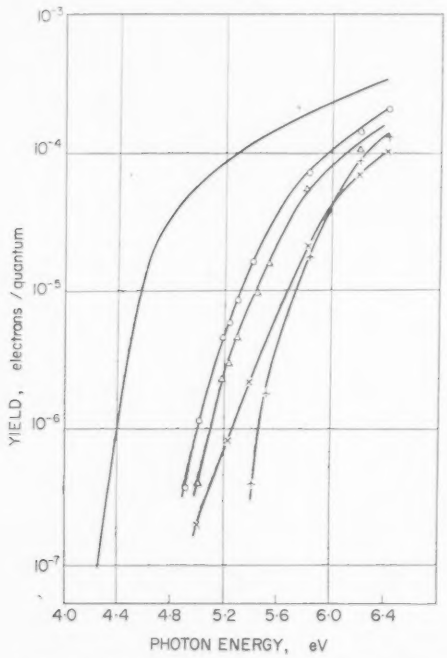

FIG. 4. Yield curves for freshly broken crystals.

KEY

O——O——O InSb; Δ——Δ——Δ Ge;
×——×——× GaAs; +——+——+ Bi_2Te_3;
———— FOWLER curve

4. EXPERIMENTAL RESULTS

(a) *InSb*

Single crystals with 10^{15} donor atoms/cc were used.* They were examined in three tubes, in two of which broken faces were measured. After the baking at 400°C the specimens were *n*-type degenerate. Some decomposition was also evident on the ground faces. A photograph of one of the crystals as it appeared after breaking is shown in Fig. 3. The main face, which was (110), the cleavage plane for InSb, is just visible in the photograph.

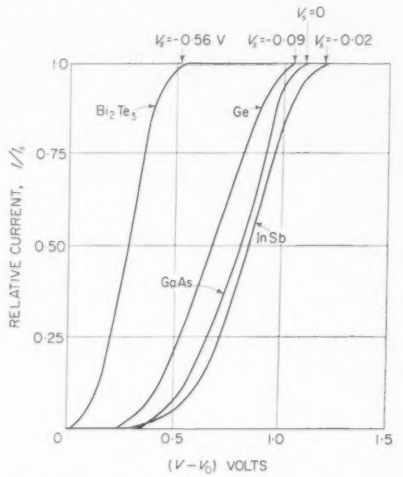

FIG. 5. Retarding potential characteristics for freshly broken crystals and for an incident photon energy $h\nu$ = 5·80 eV. The current is plotted against $(V-V_0)$, so that in all cases the origin corresponds to the Fermi level. The values of V_0 were: Bi_2Te_3 = −1·08 V; Ge = −1·14 V; GaAs = −1·11 V; and InSb = −1·25 V.

The orientation was found by X-ray diffraction, using the back-reflection Laue technique. A second broken face consisted mainly of (110) facets with small areas of damage also present. Photoelectric yields are shown in Fig. 4, and retarding potential characteristics in Figs. 5 and 6 for three surfaces of

* Kindly supplied by Dr. D. G. AVERY of the Royal Radar Establishment, Malvern.

VOL.
11
1959

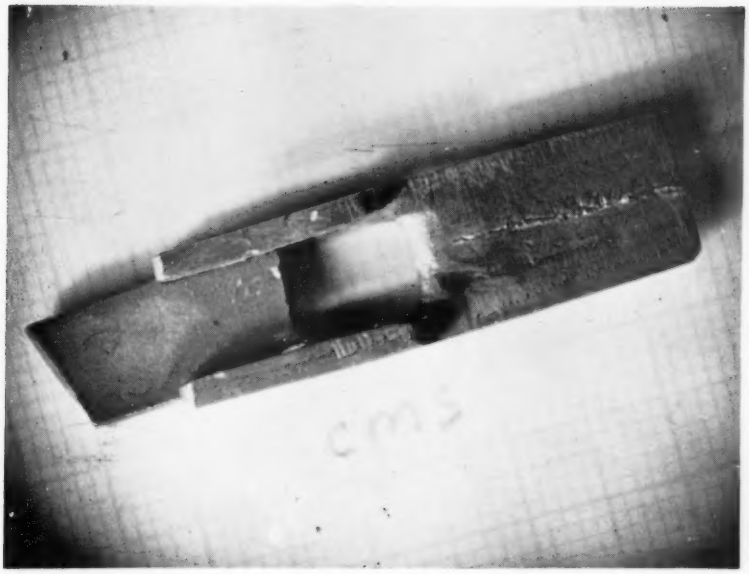

FIG. 3. Photograph of a broken InSb crystal in its holder.

[*facing page* 208

VOL
11
195

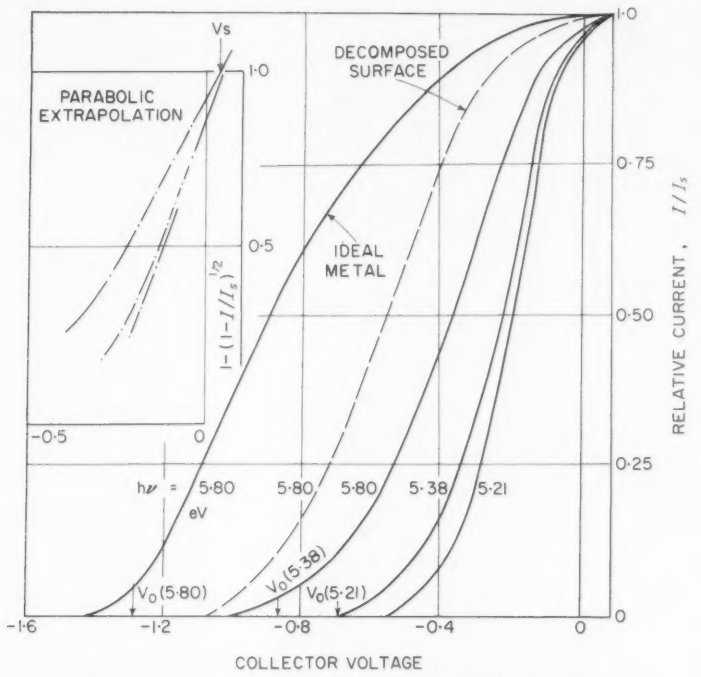

FIG. 6. Retarding potential characteristics at three photon energies (5·80, 5·38, and 5·21 eV) for a freshly broken InSb surface. The positions of the Fermi level are marked by arrows. A characteristic for a partially decomposed surface is also shown, together with a DUBRIDGE theoretical curve for an ideal metal having the same work function as the clean InSb. The inset shows the parabolic extrapolation used to find the saturation point V_s.

interest. An example of parabolic extrapolation to determine the saturation voltage V_s is given in Fig. 6. Also shown for comparison are the retarding potential characteristic from an ideal metal having the same work function as InSb crystal B, for an incident photon energy of $h\nu = 5{\cdot}80$ eV. This characteristic is computed from DUBRIDGE's theoretical formula. The difference between the metal and semiconductor characteristics is clearly apparent, as seen by the absence of photocurrent for the semiconductor at retarding potentials in the vicinity of V_0, the stopping potential for electrons coming from the Fermi level. This suggests the relatively low density of states in the semiconductor at the Fermi level. The characteristic of the front ground surface which showed decomposition is intermediate between those from the broken surface and the metal.

Energy distributions $N(E)$ were computed by differentiating curves such as those in Fig. 6, and the value of $N(E)/E$ was found. This should be proportional to $s(\nu, \epsilon)n(\epsilon)$. Such curves are shown in Fig. 8 for various surfaces. Comment on the curves will be made in Section 8(b).

The work function for the broken face of InSb crystal A was $4{\cdot}57 \pm 0{\cdot}03$ eV, decreasing after a week to 4·48 eV. The value for the second crystal face, 4·46 eV, showed no appreciable change after a week. In the tube containing the latter crystal the recorded pressure did not fall below about 10^{-7} mm, owing to a possible trace leak. Possible contamination present on the surface will be discussed in Section 5.

(b) *GaAs*

An *n*-type GaAs block, which was mainly

single-crystal, was used.* The material contained small cavities formed during the growing process. Ohmic contact could be established at these holes by probing. The metallic nature of the surfaces of the cavities was confirmed by measuring energy distributions of the photoelectric emission, which were characteristic of the emission from a metal.

No decomposition was noted after baking the crystal, and the photoemission data from ground surfaces of two differently oriented crystal faces were characteristic of a semiconductor, with a value of Δ, or $e(V_0-V_0')$, of $\sim 0{\cdot}3$ eV.

The broken GaAs surface consisted mainly of (110) cleavage plane facets. Yield data, taken within an hour of breaking, are shown in Fig. 5, and a retarding potential characteristic, part of the full photoelectric data taken the following day, is shown in Fig. 6. It was found that the interval between V_0 and the point V_0', where the curve meets the voltage axis, was similar for both broken and ground surfaces, thus indicating a similar separation of the valence band edge from the Fermi level for the surface regions. The work function for the broken face was 4·69 eV.

(c) *Bi_2Te_3*

Oriented single crystals of this material were used.† After baking at 400°C on the vacuum system, some surface decomposition was noted for this material. Separate tests indicated that a degree of evaporation took place which seemed to keep the recorded pressure in the sealed tube up to $\sim 5\times 10^{-7}$ mm. Measurements were made of the emission from the etched crystal face and from two mirror-like (0001) cleavage surfaces produced by the method described in Section 3(a). The photoemission characteristics for two fresh surfaces were similar, the work function being 5·28 eV in one case and 5·31 eV in another. The yield is shown in Fig. 4. Retarding potential data for the fresh and etched surfaces indicated that for both surfaces V_0' was close to V_0, thus showing that the top of the valence band was approximately at the Fermi level.

(d) *Germanium*

Single-crystal *n*-type material was used. Two broken surfaces were examined. For the first surface, concoidal in shape, only the spectral distribution of the photoelectric yield was measured. For the second surface, full photoelectric data were obtained. The major surface was (110), with small irregularities present. The yield is shown in Fig. 4 and a typical retarding potential curve in Fig. 5. The work function for a surface cleft in air and baked in high vacuum was 4·12 eV, with a value of Δ of 0·20, and the work function for a surface broken in high vacuum ($\sim 10^{-9}$ mm) was 4·75 eV, in good agreement with the values found for a (111) face by DILLON and FARNSWORTH[10] and for polycrystalline films.[2,11]

5. CONTAMINATION

Assuming a sticking coefficient of unity, a monolayer of gas would form on a clean surface at 10^{-8} mm in ~ 4 min. Since the recorded pressures when most of the surfaces were broken were $\sim 10^{-8}$–10^{-9} mm and the first measurements were made after 15 min, a monolayer of adsorbed gas atoms could conceivably have been present. However, reasons are given in the following paragraph for believing that this possibility is unlikely to occur.

Firstly, at 10^{-8} mm the total quantity of gas in the sealed tube is sufficient to form only 1/100th of a monolayer on the fresh surfaces. Pumping effects corresponding to adsorption taking place on the fresh surfaces were not detected. Secondly, the number of active gas atoms present is likely to be considerably lower than the recorded pressure owing to the presence of the fresh molybdenum getter films, which are known to getter active gases efficiently. Thirdly, the available evidence, although meagre, indicates that sticking coefficient at room temperature are probably less than unity.[12] In these circumstances, surfaces produced under the conditions described here could stay substantially clean for days or weeks. In agreement with this, no change was detected in the work function of germanium for over a week, the value after that time still corresponding to the clean-surface value found by DILLON and FARNSWORTH[10].

6. STRAY FIELDS AT THE EMITTER

The surfaces produced by the methods described here are subject to stray fields caused by the

* Kindly supplied by Dr. J. T. EDMOND of Services Electronics Research Laboratory, Baldock, Herts.

† Kindly supplied by Dr. D. A. WRIGHT of The General Electric Co. Ltd., Wembley, Middlesex.

VOL. 11 1959

contact potential difference between the emitter surface and the other crystal surfaces, arising from their differing work functions. Patch fields on the emitter face itself are also present on most surfaces. Checks can be made to discover whether the distortion to photoelectron paths introduced by these stray fields is sufficient to affect seriously the measured retarding potential characteristics.

A direct method of checking involves the application of accelerating fields F. According to the Schottky theory, the photocurrent should increase linearly with $F^{\frac{1}{2}}$. The slope at comparatively low fields, such as those obtained by applying voltages V of up to $+1000$ V to the collector may not be the true Schottky slope for a uniform surface, but will probably be similar to this owing to the dominance of low-work-function patches (case II collecting fields, HERRING and NICHOLS[13]).

At the low accelerating fields, electrons of low energy, whose paths are easily distorted, are prevented from reaching the collector. At high collecting fields these electrons reach the collector, so that the recorded photocurrent increases more than linearly. The degree to which this occurs gives an indication of the stray field disturbance. Examples of accelerating field characteristics are shown in Fig. 7, where the initial non-linear region is clearly in evidence for some surfaces. To avoid superposition of curves, the yields are given in arbitrary units. The fourth curve from the top applies to a surface on which a metal clip was placed to increase the stray-field distortion. The effect on the low-voltage region is evident. It is interesting to note that since the relative number of slow electrons is less the more $h\nu$ exceeds ϕ, distortion effects can be minimized by using larger incident photon energies. The Schottky slopes also decrease as $(h\nu-\phi)$ increases. Values of $(h\nu-\phi)$ for the curves in Fig. 7 are shown in brackets.

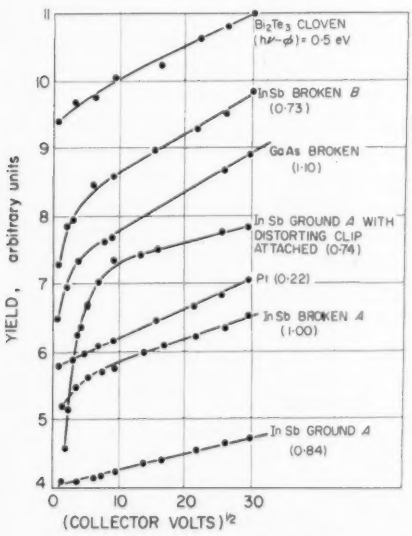

FIG. 7. Relative increase of photoelectric current as a function of the square root of the applied accelerating voltage. Values of $(h\nu-\phi)$ are shown in brackets.

Safe limits of distortion for retarding potential characteristics can be estimated from the following criteria. If distortion is not severe, the saturation voltage V_s found by parabolic extrapolation of the low-energy part of a retarding potential curve should be the same to within a few hundredths of an electron volt for all the curves taken at different values of $h\nu$ for a particular emitting surface. The second criterion is derived from comparison with the emission from clean metals where the undistorted form of the tail regions of retarding potential curves is known, being given by DUBRIDGE's expression. To compare curves, it is necessary to have some parameter specifying the distortion. For convenience we define the distortion parameter β as the percentage increase in the photoemission caused by accelerating fields, which is over and above that caused by the normal Schottky effect. In plots like those in Fig. 7, β is obtained by extrapolating the straight-line Schottky slopes back to intersect the line $V^{\frac{1}{2}}=1$, at a point which will correspond to $I'+\beta I'$, where I' is the recorded photocurrent at $V=+1$ V. In this work it has been found for a variety of platinium emitters that the photoemission obeyed DUBRIDGE's form for several tenths of an electron volt in the tail region of retarding potential curves, even in the presence of stray distorting fields sufficient to result in values of β up to about 0·1 at values of $(h\nu-\phi)$ in the region of 1 eV. From such results it would appear that this degree of distortion is tolerable. Endorsement of this conclusion is obtained from comparison of the emission from the two InSb crystals discussed in Section 4(a). The retarding potential curves at $h\nu=5{\cdot}80$ eV for InSb crystal A one week after breaking ($\phi=4{\cdot}48$ eV) and for InSb crystal B ($\phi=4{\cdot}46$ eV) were almost identical, though the values of β were 0·06

and 0·09 respectively. (The difference in distorting fields is probably due to the different geometry over the broken faces.)

On the above criteria the retarding potential curves which are presented in this report would be relatively little affected by stray distorting fields with the possible exception of the very low-energy regions.

7. ANALYSIS OF RESULTS

As described in Section 2, the quantity of interest $s(\nu, \epsilon)n(\epsilon)$ is proportional to $N(E)/E$. This function is readily obtained graphically by differentiating retarding potential plots like those in Fig. 5 to obtain $N(E)$, and then determining $N(E)/E$, to give the curves shown in Fig. 8.

The important parameter Δ is determined from a knowledge of V_0 and V_0'. The latter quantity is the point where the retarding potential curve meets the voltage axis. Since currents can be measured only down to the detection limit, the curve must be extrapolated to $I = 0$. A possible method of extrapolation would be to fit the theoretical formula of APKER *et al.*, mentioned in Section 2, to the curve. This formula however contains, in addition to Δ, an undetermined parameter m. APKER *et al.* considered several arbitrary methods of extrapolation leading to values of Δ differing by up to 100 per cent. We have here adopted the following particular method of extrapolation.

Referring to the plots of $N(E)/E$ versus E in Fig. 8, it is noted that the curves exhibit a fairly smooth curvature, and may, for a distance of $\sim 0{\cdot}5$ eV from the maximum energy E_m, be fitted by a power-law expression of the form $(E_m - E)^m$, where m is a suitable number. This empirical fact is in accord with the theoretical assumption of APKER *et al.*, mentioned in Section 2, that $s(\nu, \epsilon)n(\epsilon)$ varies as $(\epsilon_0 - \epsilon)^m$. Putting $N(E)/E = Z$, the quantity $(1/Z)(dZ/dE)$ can be plotted against E, giving a straight line of slope $1/m$ intersecting the E axis at E_m, which quantity determines V_0'.

In this way both m and Δ can be uniquely determined. This analysis was used on the data obtained in the work reported here.

8. INTERPRETATION OF RESULTS

(a) *The valence band edge separation from the Fermi level*

In assessing the significance of the quantity Δ, (the valence band edge separation from the Fermi level in the surface region), the possibility of a surface space-charge barrier must be considered. If a barrier is present, Δ varies near the surface, and the value obtained represents some average over the depth from the surface from which photoelectrons emerge. The interpretation of retarding potential curves would also be affected. If, however, the semiconductor has a high free-carrier concentration of the order of 10^{17} cm^{-3} or more, the surface barrier would vary appreciably over only a very narrow region which may be less than the photoelectron mean free path.

The results from InSb and Bi_2Te_3 give some support for the last conclusion. The InSb crystals after baking were n-type degenerate at room temperature, with the Fermi level at the bottom of the conduction band. For no surface barrier effects the theoretically expected value of Δ is thus equal to the band gap, which at room temperature is 0·17 eV. The experimental value of Δ of about 0·2 eV, as in Fig. 6, is in agreement with this. (The error due to the extrapolation method used to determine Δ is about $\sim \pm 0{\cdot}05$ eV.) The Bi_2Te_3 crystals after baking were p-type degenerate, so that the expected value of Δ is zero, in good agreement with the estimate of $\Delta \approx 0$ found from the retarding potential data, as seen in Fig. 5.

For the n-type GaAs, which has a band gap at 300°K of 1·6 eV, the experimental value of Δ of $\sim 0{\cdot}3$ eV would indicate a high surface barrier. A similar value of Δ was also found for the ground surface of this material, indicating a similar high barrier for this surface. Such a barrier would account for the well-known excellent point-contact rectification properties of GaAs. Even contacts of several square mm area on ground surfaces show rectification.

For n-type germanium the value of Δ was $\sim 0{\cdot}20$ eV, which indicates a high surface barrier in this case, since the band gap at 300°K is 0·75 eV.

(b) *Density of states*

The functions $N(E)/E$ computed from the photoemission from the different fresh crystal surfaces are plotted in Fig. 8. On the assumptions mentioned in Section 2, these functions are proportional to the product of the photoelectric excitation probability $s(\nu, \epsilon)$ and the density of states $n(\epsilon)$. If $s(\nu, \epsilon)$ does not vary sharply in the energy

VOL 11 195

range considered, then the forms of the functions shown in Fig. 7 are proportional to the density of states, the point at $(E_m - E) = 0$ corresponding to the top of the valence band. This applies for all but the very low-energy regions of the curves (i.e. $(E_m - E)$ is large), as these regions may not be fully

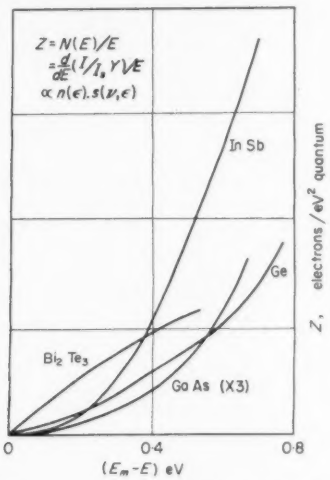

FIG. 8. Experimental curves for the product of the density of states and the excitation probability as a function of energy. (GaAs results were smaller than shown by a factor of three.)

trustworthy, since low-energy electrons are most susceptible to possible stray distorting fields at the emitter face. Note that in this type of plot absolute values of the ordinates are not of great significance, as they contain the photoelectric yield, the magnitude of which may vary from surface to surface.

The curvatures of the functions for InSb, GaAs, and germanium are similar for several tenths of an electron volt from the edge. The curves approximately obey a power law of the form $(E_m - E)^2$. In contrast, the function for Bi_2Te_3 is more nearly of the form $(E_m - E)^1$. These features are in agreement with predictions based on our knowledge of the band structures of the materials. The valence bands of InSb and GaAs are expected to be similar to that of germanium.[14,15] This similarity is not likely to extend to Bi_2Te_3, which has a hexagonal structure and is highly anisotropic. It can be considered that the influence of the density of states on the function $s(\nu, \epsilon)n(\epsilon)$ is sufficiently marked for the broad similarity between the valence bands of germanium, InSb, and GaAs to be revealed in the photoemission characteristics. The different form of $N(E)/E$ for Bi_2Te_3 would indicate that the density of states does not vary as rapidly with energy as for the other materials in the range of −0·5 eV from the top of the valence band. A comparison is particularly noteworthy between the InSb and Bi_2Te_3, in which, because of high carrier concentrations, possible surface barrier effects are less important.

(c) *The photoelectric process*

The results described here can be considered in relation to the nature of the photoelectric process. Evidence relevant to this point has been obtained from recent measurements on the photoemission from evaporated potassium films of controlled thickness[16] and from insulators.[17] The results on potassium would indicate that for this alkali metal the photoelectrons originate mainly internally by a volume process, and not by a surface mechanism. For insulators such as Cs_3Sb, APKER *et al.*[17] have explained the energy distributions found for external photoelectrons by postulating certain bulk processes involving electron–electron collisions, for the production of photoelectrons. These results for metals and non-conductors can be combined with the results reported here for semiconductors.

If a volume photoelectric effect were dominant, one would expect agreement between the experimental values of Δ for the degenerate InSb and Bi_2Te_3 crystals, and the corresponding known distance between the valence band edge and the Fermi level in the interior of these materials. As described in Section 8(a), such agreement was found. Thus the features of the external photoelectric emission noted for the three classes of materials—metals, semiconductors, and insulators—can be satisfactorily accounted for by assuming that the photoelectric effect takes place mainly as a volume process. This would lessen the significance of much of the theoretical work that has been published on the photoelectric effect. With the exception of the work of FAN[18], nearly all theories in the literature have considered a surface-effect model in which the light wave interacts with the surface field of the solid. It would appear, however, that considerations of photon-induced interband transitions may be more appropriate. As yet

there is insufficient knowledge of the upper-lying energy states of most solids for any but the most general considerations to be used. However, the above evidence supports the interpretation in Section 8(b) of the quantity $n(\epsilon)$ as a bulk density of states and the excitation probability $s(\nu, \epsilon)$ as a quantity averaged over the appropriate excited states of the solid.

Acknowledgements—The author is grateful to Dr. E. W. J. MITCHELL for suggesting the problem and for the benefit of valuable discussions throughout the course of the work, and wishes to thank Professor R. W. DITCHBURN for his interest and support. Thanks are due to Mr. W. DIXON for assistance with glassblowing, and to the Admiralty for financial support and permission to publish this work.

REFERENCES

1. TOMBOULIAN D. H., *Handbuch der Physik* Vol. 30. Springer, Berlin (1957).
2. APKER L., TAFT E. and DICKEY J., *Phys. Rev.* **74,** 1462 (1948).
3. CHYNOWETH A. G. and MCKAY K. G., *Phys. Rev.* **108,** 29 (1957).
4. FOWLER R. H., *Phys. Rev.* **38,** 45 (1931).
5. DUBRIDGE L. A., *Phys. Rev.* **43,** 727 (1933).
6. APKER L., TAFT E. and DICKEY J., *Phys. Rev.* **73,** 46 (1948).
7. PAPARODITIS C., *C.R. Acad. Sci., Paris* **245,** 1525 (1957).
8. FARNSWORTH H. E., *Proc. Phys. Soc.* **71,** 703 (1958).
9. FARNSWORTH H. E., SCHLIER R. E., GEORGE M. and BURGER R. M., *J. Appl. Phys.* **26,** 252 (1955).
10. DILLON J. A. and FARNSWORTH H. E., *J. Appl. Phys.* **28,** 174 (1957).
11. MITCHELL E. W. J. and MITCHELL J. W., *Semiconducting Materials* (Ed. H. K. HENISCH). Butterworths, London (1951).
12. SCHLIER R. E. and FARNSWORTH H. E., *Semiconductor Surface Physics.* University of Pennsylvania Press, Philadelphia (1956).
13. HERRING C. and NICHOLS M. H., *Rev. Mod. Phys.* **21,** 185 (1949).
14. HERMAN F., *J. Electronics* **1,** 153 (1955).
15. KANE E. O., *J. Phys. Chem. Solids* **1,** 249 (1957).
16. THOMAS H., *Z. Phys.* **147,** 395 (1957).
17. APKER L., TAFT E. and DICKEY J., *J. Opt. Soc. Amer.* **43,** 78 81 (1953).
18. FAN H. Y., *Phys. Rev.* **68,** 43 (1945).

VOL.
11
195

J. Phys. Chem. Solids Pergamon Press 1959. Vol. 11. pp. 215–219. Printed in Great Britain.

PURE QUADRUPOLE RESONANCE OF N_2 IN β QUINOL CLATHRATES

HORST MEYER† **and THOMAS A. SCOTT**‡

Gordon McKay and Lyman Laboratories, Harvard University, Cambridge, Mass.

(*Received* 4 *May* 1959)

Abstract—Pure quadrupole resonance of $^{14}N_2$ molecules trapped in β quinol clathrates has been observed at temperatures below 25°K. The resonance occurs at about 3·6 Mc/s and there is an extensive fine structure of at least seven lines. The relative intensity, but not the frequency of these lines, was found to vary for samples under different conditions of annealing and concentration of trapped molecules. Studies of the Zeeman splitting of the resonance lines were made, and it was found that at these low temperatures the axes of the trapped molecules oscillate around the trigonal crystalline axis of the β quinol. The frequency of these oscillations was found to be $1{\cdot}55 \times 10^{12}\text{sec}^{-1}$ from preliminary measurements of the temperature-dependence of the pure quadrupole resonance. Measurement of the resonance under a hydrostatic pressure of 1790 lb./in.^{2} showed only a very small frequency increase.

1. INTRODUCTION

H. M. POWELL and his collaborators[1] have shown that in certain compounds, called clathrates, which crystallize in lattices with an open structure, foreign molecules of suitable dimensions can be trapped in the regularly spaced lattice holes. In the β quinone clathrates, which have a trigonal symmetry,[1] at most one molecule can be trapped in each hole. The chemical formula is $3C_6H_4(OH)_2 + + xM$, where M is the trapped molecule and x the concentration of the filled holes. It was found[2,3] that certain enclosed molecules, such as O_2, HCN and NO behave at room temperature like a free gas, but susceptibility measurements of O_2 in the clathrate suggested that at low temperatures the molecules are no longer free to rotate in their cages.[4] O'BRIEN and VAN VLECK[5] devised then a theory explaining the susceptibility results in terms of oscillations of the molecule around a fixed axis, and this theory was confirmed by further susceptibility measurements on O_2 clathrates below 1°K[5] and by electron spin-resonance experiments.[6]

It seemed interesting, on the other hand, to place a diamagnetic molecule possessing a nuclear quadrupole moment Q in the clathrate for the purpose of probing the environment by means of nuclear-resonance techniques. It is known that when a molecule with a nuclear quadrupole moment rotates freely, pure quadrupole resonance cannot be observed, since the electric field gradient is averaged to zero over all spatial directions. On the other hand, when the molecule is exposed to surroundings which are able to make the expectation direction of its axis an anisotropic one, resonance can be obtained. A study of the resonance-line structure in a clathrate could provide information on the crystalline potential, while the temperature-dependence of the resonance frequency allows an evaluation of the mean oscillation frequency of the molecule inside the cage.

Nitrogen N_2 seemed particularly suitable for this purpose. It is relatively simple and ^{14}N (96·6 per cent abundant, $I = 1$) gives an intense pure quadrupole resonance line at 4·2°K in solid N_2 at the frequency of 3·5 Mc/s.[7] Since the field gradient at the nucleus is chiefly molecular one expects nearly the same frequency in the clathrate. The expected line intensity is lower, however, since the density of nitrogen in the clathrates is

† Now at Department of Physics, Duke University, Durham N.C.

‡ Now at Department of Physics, University of Florida, Gainesville, Fla.

of the order of 5 per cent of the density in solid nitrogen.

2. EXPERIMENTAL RESULTS

We have observed pure quadrupole resonance at low temperatures in the region of 3·6 Mc/s, using a Pound–Watkins radiofrequency spectrometer with Zeeman modulation. Measurements were largely made in the temperature region between 4·2 and 1·5°K. The resonance frequencies were independent of temperature in this range within experimental accuracy. Instead of the single absorption line of ^{14}N observed by SCOTT[7] in solid nitrogen, we found a group of at least seven lines with the following frequencies:

kc/s

$$\nu_1 = 3580{\cdot}2 \pm 0{\cdot}2$$
$$\nu_2 = 3581{\cdot}8 \pm 0{\cdot}2$$
$$\nu_3 = 3585{\cdot}0 \pm 0{\cdot}2$$
$$\nu_4 = 3586{\cdot}8 \pm 0{\cdot}3$$
$$\nu_5 = 3588{\cdot}4 \pm 0{\cdot}3$$
$$\nu_6 = 3592{\cdot}3 \pm 0{\cdot}3$$
$$\nu_7 = 3594{\cdot}0 \pm 0{\cdot}3$$

These values represent an average over several runs. Within experimental accuracy their positions are symmetric about ν_4, but their shapes are not. A careful recording of the pattern is shown in Fig. 1.

Systematic experiments were undertaken to study the effect on the resonance pattern of the concentration of holes filled with nitrogen. This concentration could be varied between 0·2 and 0·8 by changing the nitrogen gas pressure under which these crystals were grown from their solution. The method of EVANS and RICHARDS[2] was used to grow eight different batches of crystals from solutions of quinol in *n*-propanol and in water. The peak frequencies were the same for all crystals, and this is considered a very significant fact for the interpretation of the experiment. However, the line intensities varied in an erratic way for these eight samples and therefore it has not been possible to relate the line structure in any certain way to the differences in population of the holes.

Studies of line intensity were carried out on the same sample as a function of storage time at room-temperature and annealing time at 65°C. This batch of crystals was grown at a pressure of 2000 lb/in.^{2} and chemical analysis before and after annealing showed a decrease of N_2 of up to 13 per cent. Thus some nitrogen molecules must be capable of escaping from the holes and diffusing through the clathrate (possibly by means of empty holes or dislocations). The resulting change in line structure for these crystals was very marked (Fig. 2). Line ν_1 and ν_2 become continuously more

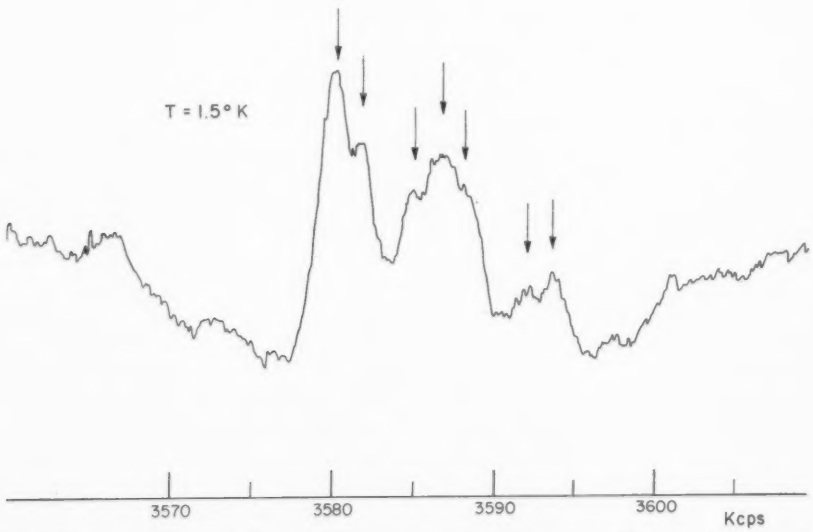

FIG. 1. Line structure recording of the pure quadrupole resonance of N_2 in β quinol. Sample grown under 1350 lb/in.^{2} $T = 1{\cdot}5$°K. Arrows show the seven peaks.

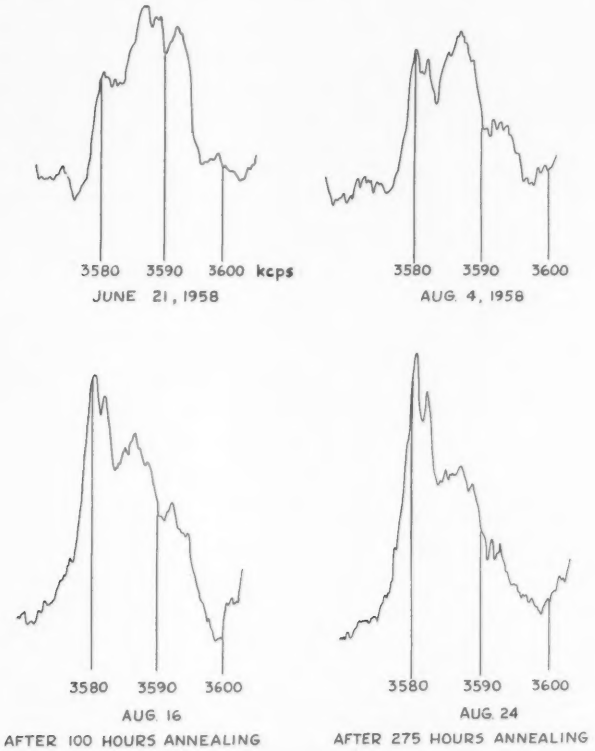

FIG. 2. Effect of storage and annealing on a sample of N_2 clathrate grown under 2000 lb/in.^{2} on 20 June 1958.

intense at the expense of the other lines. After 275 hr of annealing, lines ν_6 and ν_7 have almost completely disappeared.

At the present time these phenomena are not fully understood. Dipole–dipole interactions are too small to account for the structure and merely produce line-broadening. The annealing experiments and the constancy of the resonance frequencies eliminate the possibility of the structure being due to a coupling of the type $J\, I_1 \cdot I_2$. The X-ray data of PALIN and POWELL[1] show that all the holes are equivalent, but it is felt that the only satisfactory explanation of our data is that, owing to slight distortions of the cages by the trapped molecules, the electric environments are not quite equivalent at all holes. Each cavity has two nearest-neighboring holes located respectively above and below it on the hexagonal axis at a distance of 5·6 Å. There are essentially 12 next-nearest-neighboring holes located in four planes perpendicular to the trigonal axis containing three cavities each. Six of these are at a distance of 9·5 Å and six at 10·1 Å. The lines probably arise from different field gradients resulting from various statistical combinations of filled and unfilled neighboring holes around a molecule in a given cavity with the consequently different lattice distortions. The changing of the pattern on annealing may represent the relieving of strains by diffusion and loss of nitrogen as well as by possible annealing of the lattice itself. If this is true, it is likely that the resonance consists of more than seven lines with finer details not resolved. More experiments will be undertaken towards the understanding of the resonance structure.

A study of the Zeeman splitting of the quadrupole lines was made at 1·5°K in order to determine the orientation of the field-gradient symmetry axis

in the crystal. Since nearly all of the field gradient is molecular in origin, this determines the orientation of the diatomic molecule as well. About eight of our best crystals (for signal-to-noise reasons the sample always consisted of a number of individual crystals) were aligned parallel to each other in the resonant coil with their axes perpendicular to the coil axis. A d.c. magnetic field H of 112 gauss was applied from a pair of Helmholtz coils in a direction making an angle θ between 90° and −90° with the crystalline axis. For such a small field the Zeeman splitting is given by first-order perturbation theory for $I = 1$ as

$$\nu = \frac{3}{4} \cdot \frac{e^2qQ}{h} \pm (\mu H \cos\theta)/h \qquad (1)$$

with $\mu = 0{\cdot}4036$ nuclear magnetons.[8] This formula assumes that the electric field gradient tensor is cylindrically symmetric with q as its axial component. θ is the angle between the direction of H and the tensor axis.

A simple splitting was observed, which was the same for each component of the structure and was maximum for $\theta = 2° \pm 3°$. The uncertainty comes from a possible small misalignment of the crystals and the error in the measurement of the Zeeman splitting. The experimental results are presented in Fig. 3, where $\Delta\nu = (2\mu H \cos\theta)/h$. For θ near 90°, the scatter is large owing to overlapping of some lines in the structure. The agreement of experiment with theory is good, and it is thus seen that the field gradient tensors are axially symmetric and are parallel to the crystalline axis of the clathrate compound. The diatomic molecule oscillates around this spin quantization direction with a frequency ν_0 which is considerably larger than the spin-precession frequency. The effect of this oscillation is to reduce the electric field gradient at the nucleus. As the temperature increases, the oscillation amplitude increases and this results in a decrease of the quadrupole resonance frequency, $\nu(T)$. From this frequency shift, one can derive the frequency of oscillation. Using the theory of BAYER, one has for a molecule vibrating in two directions

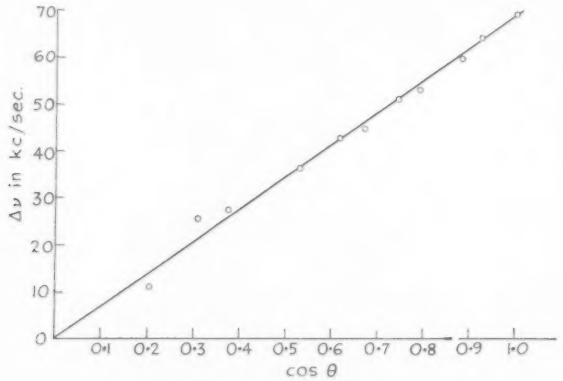

FIG. 3. Plot of the Zeeman splitting $\Delta\nu$ as a function of $\cos\theta$. ○ experimental points, drawn line: calculated from equation (1).

$$\left.\begin{aligned} \nu(T) &= \nu(T=0) - \frac{3}{4} \cdot \frac{h\nu_f}{\pi\nu_0 I} \frac{1}{\exp\left(\dfrac{h\nu_0}{kT}\right) - 1} \\ \nu(T=0) &= \nu_f\left(1 - \frac{3}{8}\frac{h}{\pi\nu_0 I}\right) \end{aligned}\right\} \qquad (2)$$

where ν_f is the pure quadrupole frequency when the molecule is fixed in the cavity, and I is the momentum of inertia of the molecule $I = 1{\cdot}39 \times \times 10^{-39}$ cgs.

In an effort to determine ν_0, preliminary experiments were made of the temperature-dependence of the quadrupole resonance frequency. The results presented in Fig. 4 are not very accurate

because of the low signal-to-noise ratio. By fitting equation (2) to the experiments, a value of $\nu_0 = (1{\cdot}55 \pm 0{\cdot}10) \times 10^{12}$ was obtained, which can be compared to $\nu_0 = 0{\cdot}50 \times 10^{12}$ for the vibration of O_2 in the clathrates, as one can calculate from

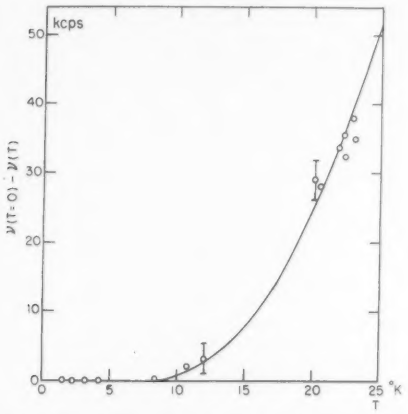

FIG. 4. Temperature-dependence of the pure quadrupole resonance frequency. $\nu(T=0) - \nu(T)$ plotted versus T. ○ experimental points, drawn line: calculated from equation (2) with $\nu_0 = 1{\cdot}55 \times 10^{12} \text{sec}^{-1}$.

susceptibility measurements.[5] These frequencies are in the same order of magnitude as the hindered rotation of groups in some organic molecules.[9,10] ν_f was found to be 4·040 Mc/s as average value for the line structure.

Resonance measurements were also made at 4·2°K, while the sample was subjected to hydrostatic pressure of 1790 lb/in². The resonant frequency was found to increase by about 2 kc, but accurate measurements could not be made because of the low signal-to-noise ratio in the high-pressure assembly at 4·2°K.

Acknowledgements—The authors wish to acknowledge the interest of Professors VAN VLECK, POUND, BLOEMBERGEN and PURCELL in these experiments and their helpful suggestions. They also thank Professor H. M. POWELL for supplying a clathrate sample on which some preliminary experiments were done.

This research was supported by a joint contract of the Office of Naval Research and the Atomic Energy Commission Nonr 1866(19) and by a joint contract of the Office of Naval Research and the National Security Agency Nonr 1866(33).

REFERENCES

1. PALIN D. E. and POWELL H. M., *J. Chem. Soc.* p. 815 (1948).
   POWELL H. M., *J. Chem. Soc.* p. 61 (1948).
2. EVANS D. F. and RICHARDS R. E., *J. Chem. Soc.* p. 3295 (1952).
3. DRYDEN J. S. and MEAKIN R. J., *Nature, Lond.* **169,** 324 (1952).
4. COOKE A. H., MEYER H., WOLF W. P., EVANS D. F. and RICHARDS R. E., *Proc. Roy. Soc.* A**225,** 112 (1954).
5. MEYER H., O'BRIEN M. and VAN VLECK J. H., *Proc. Roy. Soc.* A**243,** 414 (1957).
6. FONER S. and MEYER H., to be published.
7. SCOTT T. A., Thesis, Harvard (1959).
   TERMAN F. and SCOTT T. A., *Bull. Amer. Phys. Soc.* Ser. 2 **3**, 23 (1958).
8. PROCTOR W. G. and YU F. C., *Phys. Rev.* **77,** 716 (1950).
9. BAYER H., *Z. Phys.* **130,** 227 (1951). See also DAS T. P. and HAHN E. L., *Nuclear Quadrupole Resonance Spectroscopy* (Supplement I to *Solid State Physics*) Academic Press, New York (1958).
10. DEAN C., Thesis, Harvard (1952) (unpublished).

VOL. 11 1959

J. Phys. Chem. Solids Pergamon Press 1959. Vol. 11. pp. 220–225. Printed in Great Britain.

EXCHANGE ANISOTROPY IN DISORDERED NICKEL–MANGANESE ALLOYS

J. S. KOUVEL and C. D. GRAHAM, Jr.

General Electric Research Laboratory, Schenectady, New York

(*Received* 5 *March* 1959)

Abstract—Disordered polycrystalline nickel–manganese alloy specimens of about 20, 25 and 30 atomic per cent manganese were cooled from 300 to 1·8°K in a magnetic field, and their magnetic hysteresis loops measured parallel to this field are found to be displaced from their symmetrical positions about the origin. Upon warm-up, the displacement of the loops decreases monotonically, vanishing at about 25, 35 and 75°K for the 20, 25 and 30 atomic per cent manganese specimens, respectively. The disappearance of this asymmetry with increasing temperature is accompanied by large hysteresis losses. Torque measurements were made on the same specimens cooled to 4·2°K in a field perpendicular to the axis of rotation. For all compositions, the predominant anisotropy is unidirectional, with the easy direction the same as the direction of the field applied during cooling. The magnitude of this anisotropy decreases monotonically with increasing temperature, vanishing at the same temperatures as the asymmetry of the hysteresis loops. At these temperatures, the rotational hysteresis rises to a maximum. These effects are believed to be due to exchange-anisotropy interactions between very small regions of ferromagnetic and antiferromagnetic spin order in these alloys at low temperatures.

1. INTRODUCTION

THE development of strong ferromagnetism with increased atomic order in the nickel–manganese alloy Ni_3Mn has been a subject of considerable investigation.[1] However, it was only recently discovered that this alloy in a disordered state has unusual magnetic properties at low temperatures.[2] Most strikingly, the magnetization of this disordered alloy for any field up to 7550 Oe was found to have a maximum value at about 25°K. Furthermore, at any temperature down to 1·5°K, its magnetization at the maximum field did not appear to be approaching a saturation value, although its estimated ferromagnetic Curie point was about 130°K. VOLKENSHTEIN *et al.*[3] subsequently presented similar results for measurements made on disordered Ni_3Mn in fields up to 18,000 Oe. More recent experiments[4] revealed that in varying degree these peculiar magnetic properties were characteristic of disordered nickel–manganese alloys at least over the composition range of $\sim$20–30 atomic per cent manganese; moreover, at any temperature down to that of liquid helium, the magnetizations of these alloys were still increasing with field at 100,000 Oe.

This anomalous magnetic behavior suggested the existence of antiferromagnetically as well as ferromagnetically aligned moments in these alloys at low temperatures. This interpretation was further supported by the discovery that the hysteresis loop of the 26·5 per cent manganese specimen, when cooled to 4·2°K in a magnetic field, was shifted from its symmetrical position about the origin.[4] A displaced hysteresis loop of this kind was first obtained for a compact of partially oxidized fine particles of cobalt that had been cooled in a magnetic field;[5] similar results have since been reported for UMn_2 cooled in a field.[6] MEIKLEJOHN and BEAN[5] attributed their results to exchange interactions across the interfaces between the ferromagnetic cobalt and the antiferromagnetic cobaltous oxide. They proposed that these interactions give each cobalt particle an easy direction (rather than axis) of magnetization; furthermore, these directions take on a preferred orientation about the direction of the magnetic field in which the specimen is cooled, but are oriented at random when the cooling is done in zero field. Since this anisotropy is produced by exchange interactions, it was called an exchange

anisotropy. The unidirectionality of this anisotropy in the cobalt–CoO system was demonstrated not only by the displaced hysteresis loop but also by a $\sin\psi$ variation of the torque on the specimen suspended in a field (whose direction makes an angle ψ with the direction of the field during cooling).[5]

We have recently reported on some magnetic hysteresis-loop and torque measurements made on disordered Ni_3Mn cooled to liquid-helium temperatures in a magnetic field.[7] Although the results strongly support the existence of an exchange-anisotropy mechanism in this alloy, they differ in important details from the predictions of the simple exchange-anisotropy model discussed above. These measurements have now been extended to a range of disordered alloys (centered at about Ni_3Mn) under a wider variety of experimental conditions.

VOL. 11 1959

2. HYSTERESIS-LOOP MEASUREMENTS

The three disordered polycrystalline alloys of the present work are the 21·6, 26·5 and 31·1 atomic per cent manganese specimens of reference 4 (which had been quenched into water from 900°C). For the hysteresis-loop measurements, the apparatus and techniques described previously were used.[2,4] Each of the specimens was cooled from 300 to 1·8°K under three different conditions: in a 5000-Oe field applied parallel to the axis of magnetization measurement (the cylindrical axis of the specimens), in a 5000-Oe field applied perpendicular to this axis, and in zero field. The hysteresis loops measured at 1·8°K for maximum fields of ±8000 Oe are given in Fig. 1 as curves of magnetization versus internal field, obtained after making appropriate corrections for demagnetization. For the case where the field during cooling was applied parallel to the measurement axis, it is evident that the hysteresis loops of all three alloys (solid curves, left in Fig. 1) have been displaced from their symmetrical positions about the origin. In fact, for each of the alloys, this displacement is so large compared to the thickness of the loop that both remanent magnetizations are positive (where the positive direction is that of the field during cooling). It follows that the two coercive fields are negative; both branches of the loop cross the H axis at about −200, −500 and −6000 Oe for the 21·6, 26·5 and 31·1 per cent manganese alloys, respectively.

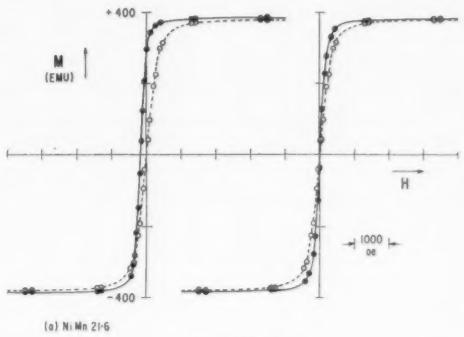

FIG. 1(a)

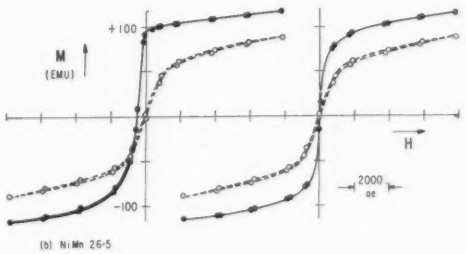

FIG. 1(b)

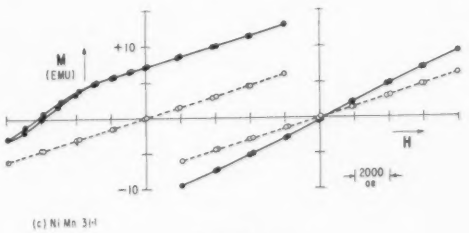

FIG. 1(c)

FIG. 1. Hysteresis loops of disordered alloys containing (a) 21·6, (b) 26·5 and (c) 31·1 atomic per cent manganese, measured at 1·8°K. Solid curves, left: specimens cooled in +5000-Oe field applied parallel to axis of measurement. Solid curves, right: specimens cooled in 5000-Oe field applied perpendicular to axis of measurement. Dashed curves, left and right: specimens cooled in zero field.

This displaced-hysteresis-loop behavior is qualitatively consistent with the unidirectional exchange-anisotropy model. Moreover, this model predicts that a field applied perpendicular to the measurement axis during cooling would align the easy directions of magnetization preferentially about this perpendicular direction and give rise to

zero remanent magnetization along the measurement axis. This is experimentally borne out by the solid curves, right in Fig. 1 for all the alloy specimens. Similarly, for the specimens cooled in zero field, the simple exchange-anisotropy model predicts a random alignment of easy directions of magnetization and, hence, zero remanence. The dashed curves in Fig. 1 are clearly in agreement with this prediction.

In detail, however, the hysteresis loops of Fig. 1 suggest a serious departure from the simple exchange-anisotropy model. We note that the solid curves on the left give larger magnetizations than the corresponding dashed curves for all positive fields and for sufficiently large negative fields (except for the 31·1 per cent manganese specimen, where the negative fields required exceed the 8000 Oe available for these measurements). This is reasonable because positive and negative fields for the former loops represent the easiest and hardest directions of magnetization, respectively, and because even along this hard direction, in fields exceeding the effective anisotropy field, the magnetization should be larger than in the latter cases where presumably the anisotropy directions are randomly oriented. Under these circumstances, however, these two sets of hysteresis loops would be expected to converge much more rapidly at large positive and negative fields than is indicated in Fig. 1. Moreover, the loops for the field during cooling applied perpendicular to the axis of measurement (solid curves, right) show larger magnetizations at all fields than the corresponding loops for zero field during cooling. The higher magnetizations in the directions midway between the easiest and hardest directions are not even qualitatively consistent with a simple anisotropy model.

Each specimen, after being cooled from 300 to 1·8°K in a 5000-Oe field applied in the direction of measurement, was allowed to warm up slowly, and its hysteresis loop (for maximum fields of ± 8000 Oe) was measured at frequent temperature intervals. In Fig. 2(a), we define the average values of remanent magnetization and coercive field, $\overline{M}_r$ and $\overline{H}_c$, both of which are measures of the displacement of the hysteresis loop from the origin; we also define ΔM_r and ΔH_c as difference values of remanence and coercive field, which give some measure of the thickness of the loop. All these quantities taken from the measured hysteresis loops are plotted against temperature in Figs. 2(b) and (c) for the different specimens. We note that $\overline{M}_r$ and $\overline{H}_c$ decrease monotonically with increasing temperature, vanishing at about 25, 35 and 75°K

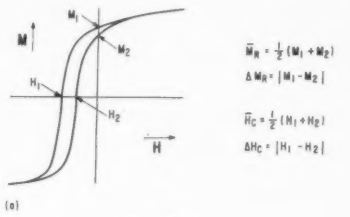

FIG. 2(a)

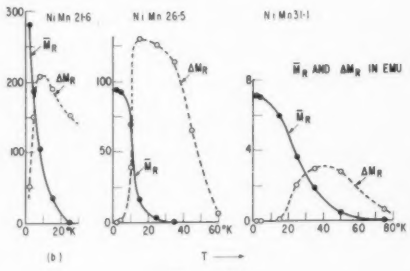

FIG. 2(b)

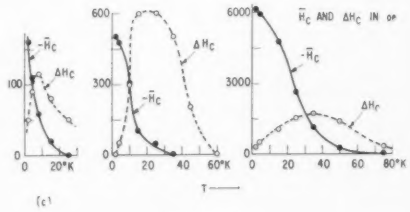

FIG. 2(c)

FIG. 2. Average and difference values of remanence and coercive field, as defined in (a), plotted against temperature in (b) and (c) for the 21·6, 26·5 and 31·1 atomic per cent manganese alloys cooled to 1·8°K in +5000-Oe field applied parallel to axis of measurement.

for the 21·6, 26·5 and 31·1 per cent manganese alloys, respectively. It is also evident that for each specimen both ΔM_r and ΔH_c rise from essentially zero at 0°K, reach a peak at a temperature where $\overline{M}_r$ and $\overline{H}_c$ have dropped to relatively small values and then decrease gradually at higher temperatures.

According to the simple exchange-anisotropy model, if the antiferromagnetically aligned

moments, with which ferromagnetically aligned moments are interacting, are coupled rigidly to the crystal by large magnetocrystalline anisotropy forces, such a system when cooled in a field would exhibit a shifted hysteresis loop with practically no hysteresis losses. This appears to be a reasonable explanation of the thin but shifted hysteresis loops observed at the lowest temperatures. Moreover, let us suppose that at some higher temperature the crystal anisotropy energy of the antiferromagnetically aligned moments has decreased and become comparable with their energy of interaction with the ferromagnetically aligned moments. Then, the latter moments when turned by a reverse field would also reverse the former moments, resulting in a rapid decrease of the displacement of the hysteresis loop from the origin. At that temperature, the reversals of the antiferromagnetically coupled moments can be expected to be discontinuous and thus give rise to increased hysteresis losses. At still higher temperatures, if the crystal anisotropy decreases further, these reversals would become continuous and lossless. This suggested sequence of events can account for the experimental fact that for each alloy specimen the decrease of the shift of the hysteresis loop with increasing temperature was accompanied by a rapid rise and then a gradual decrease of the thickness of the loop, as shown in Fig. 2. A similar variation of the thickness of the hysteresis loops with temperature has been previously observed for the same specimens cooled in zero field.[4] In the mechanism proposed above for these hysteresis losses, only the relative strengths of the exchange and crystal anisotropy forces are involved; the cooling in a field affects primarily the orientation of these forces and hence would not alter the hysteresis losses.

Hysteresis-loop measurements were also made on the specimens cooled from 300 to 4·2°K in a number of different fields applied along the axis of measurement. The results are shown in Fig. 3, where we have plotted the average values of remanence and coercive field, as defined in Fig. 2(a), and the magnetizations at +4000 and +8000 Oe against H_{cooling}, the field applied in the plus direction during cooling. It is clear that $\overline{H}_c$ does not increase indefinitely with increasing H_{cooling} for any of the alloys; instead, it appears to reach a steady value or, in the 31·1 per cent manganese alloy, actually decreases at large values of H_{cooling}. The variation of $\overline{M}_r$ with H_{cooling}, however, seems to depend more systematically on the composition of the alloy. For the 21·6 per cent manganese specimen, $\overline{M}_r$ is evidently close to a limiting value at an

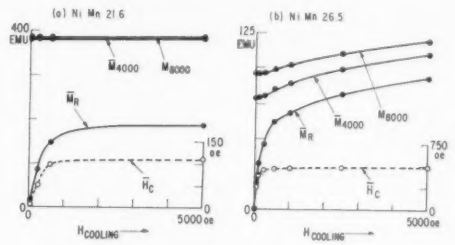

FIG. 3(a) FIG. 3(b)

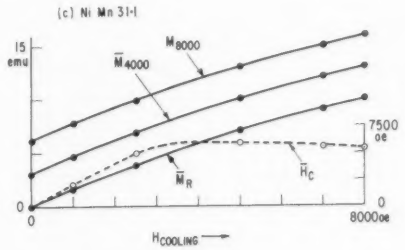

FIG. 3(c)

FIG. 3. Average values of remanence and coercive field, as defined in Fig. 2(a), and the magnetizations at +4000 and +8000 Oe for the (a) 21·6, (b) 26·5 and (c) 31·1 atomic per cent manganese alloys cooled to 4·2°K in various positive fields applied parallel to axis of measurement.

H_{cooling} of 5000 Oe. The $\overline{M}_r$ versus H_{cooling} plots for the other two compositions may be interpreted as indicative of a similar but slower saturating behavior of $\overline{M}_r$ with increasing H_{cooling}. With increasing H_{cooling}, the magnetizations at +4000 and +8000 Oe also appear to be approaching limiting values at a rate that decreases as the manganese content of the alloy increases.

3. MAGNETIC TORQUE MEASUREMENTS

Torque measurements were made on the same specimens; each was suspended so that it could be rotated about its cylindrical axis in a magnetic field perpendicular to this axis. The results are shown in Fig. 4 for the specimens cooled from 300 to 4·2°K in a 5000-Oe field. The most striking feature

of the torque curves (L versus ψ) is their predominant $\sin\psi$ component, the single easy direction of magnetization being along $\psi = 0$, the direction of the field applied during cooling. The amplitude of this unidirectional torque component, L_1,

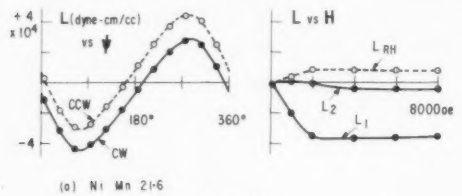

(a) Ni Mn 21·6

FIG. 4(a)

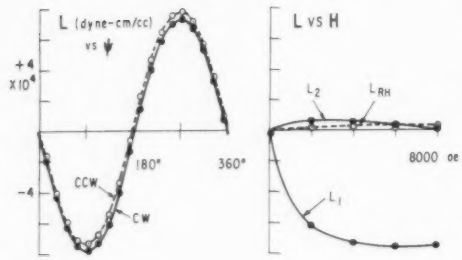

(b) Ni Mn 26·5

FIG. 4(b)

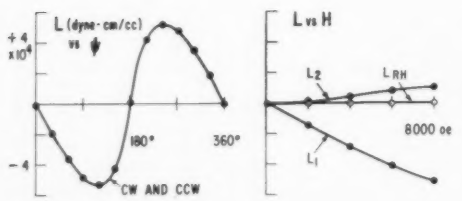

(c) Ni Mn 31·1

FIG. 4(c)

FIG. 4. Torque, L, on the (a) 21·6, (b) 26·5 and (c) 31·1 atomic per cent manganese specimens cooled to 4·2°K in 5000-Oe field applied along $\psi = 0$. Left: L versus ψ for clockwise (cw) and counterclockwise (ccw) rotation of specimen in 8000-Oe field. Right: amplitudes of $\sin\psi$, $\sin 2\psi$ and rotational hysteresis components of torque (L_1, L_2 and L_{RH}, respectively) plotted against field of measurement.

has been plotted in Fig. 4 against the field of measurement. For the 21·6 and 26·5 per cent manganese alloys, it appears to have reached a steady value at a field less than 8000 Oe; presumably, for the 31·1 per cent manganese alloy, higher fields are necessary for this to happen. In Fig. 4, the relatively small amplitude of the $\sin 2\psi$ torque component (L_2) and half the mean separation between the torque curves for clockwise and counterclockwise rotation of the specimen (L_{RH}, where $2\pi L_{RH}$ is the rotational hysteresis loss per revolution) are also plotted against the field of measurement. Higher harmonic components of the torque curves were found to be negligible.

Similar experiments with the same specimens cooled to 4·2°K in zero field showed no variation of torque with the position angle ψ in any field of measurement. Hence, all the variations of torque with ψ shown in Fig. 4 are entirely due to the field applied on the specimens during cooling. However, the rotational hysteresis torque, L_{RH}, measured in any given field, was essentially the same whether the specimen was cooled in zero field or in 5000 Oe. This behavior is undoubtedly related to the fact that the losses associated with the hysteresis loops of these alloys are also independent of the field applied during cooling. In the preceding section, this latter observation was shown to be consistent with the simple exchange-anisotropy model. Furthermore, according to this model, magnetic losses arise when the exchange coupling between the ferromagnetically and antiferromagnetically aligned moments is comparable to the crystal anisotropy forces on the latter moments. These losses should then be independent of the applied field as long as it is large enough to turn all the ferromagnetically aligned moments. As shown in Fig. 4, this consequence of the exchange-anisotropy model is experimentally borne out for these alloys whose rotational hysteresis torque at 4·2°K does not decrease with increasing field even at 8000 Oe.

After each specimen had been cooled from 300 to 4·2°K in a 5000-Oe field, its temperature was allowed to rise slowly, and its torque curves were measured in 2000 Oe. The temperature-dependence of the amplitude of the $\sin\psi$ component of torque, L_1, and of the rotational hysteresis loss, W_{RH} or $2\pi L_{RH}$, taken from these torque curves, is shown in Fig. 5. For each specimen, it is evident that L_1 decreases monotonically with increasing temperature, and, at the temperature where it has dropped to a relatively small value, W_{RH} has risen to a maximum value. There is an obvious analogy between Fig. 5 and Figs. 2(b) and (c). This is

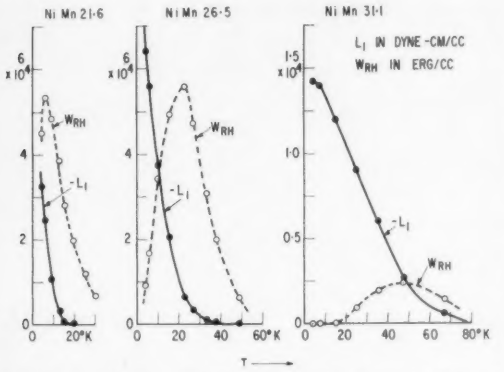

FIG. 5. Amplitude of sin ψ component of torque, L_1, and rotational hysteresis loss from torque curves measured at 2000-Oe versus temperature for the (a) 21·6, (b) 26·5 and (c) 31·1 atomic per cent manganese alloys cooled to 4·2°K in 5000 Oe.

reasonable because L_1, like $\overline{M}_r$ and $\overline{H}_c$, is a measure of the unidirectional anisotropy produced by cooling the specimens in a field, while W_{RH}, like ΔM_r and ΔH_c, is a measure of the lossiness of the magnetization process.

4. CONCLUSIONS

The results of our magnetic hysteresis-loop and torque measurements strongly suggest an exchange-anisotropy mechanism and, hence, a coexistence of ferromagnetism and antiferromagnetism in nickel–manganese alloys at low temperatures. However, contrary to the predictions of the simple exchange-anisotropy model proposed by MEIKLEJOHN and BEAN for the cobalt–CoO system, the magnetic field applied to the alloy specimens during cooling does not simply give the exchange anisotropy a preferred orientation. Quite likely, this field also affects the type and degree of magnetic order in what presumably are very small regions of ferromagnetic and antiferromagnetic spin alignment. Some recent neutron-diffraction experiments[8] did not reveal any clear evidence for longe-range antiferromagnetic order in these alloys at low temperatures; this indicates that the antiferromagnetic regions, if present, must be very small.

HAHN and KNELLER[9] interpret the results of their recent magnetic measurements on nickel–manganese alloys subjected to different heat treatments as indicative of very small regions of ordered Ni_3Mn phase in a matrix of disordered material. They report that this is the case even for the specimens quenched from well above the ordering temperature, for which they deduce an average diameter of about 20 Å for the ordered regions. An exchange coupling between the ferromagnetically aligned spins of these small ordered regions and an antiferromagnetic matrix would provide a plausible basis for exchange anisotropy in these imperfectly disordered alloys. Alternatively, we may suppose that our specimens, which were rapidly quenched from well above the ordering temperature, have no long-range atomic order and that normal statistical composition fluctuations give rise to extremely small regions of ferromagnetic and antiferromagnetic spin order. The type of magnetic order of a given region presumably would be decided by a competition between antiferromagnetic interactions of Mn–Mn nearest-neighbor atoms and ferromagnetic interactions of Ni–Ni and Ni–Mn atom pairs, and would therefore depend on the local composition.[4]

Acknowledgements—We gratefully acknowledge helpful discussions with J. J. BECKER, I. S. JACOBS, J. S. KASPER and W. H. MEIKLEJOHN and the continued stimulating interest of G. W. RATHENAU in this work.

REFERENCES

1. KAYA S. and KUSSMANN A., *Z. Phys.* **72,** 293 (1931). THOMPSON N., *Proc. Phys. Soc.* **52,** 217 (1940). GUILLAUD C., *C.R. Acad. Sci., Paris* **219,** 614 (1944). PIERCY G. R. and MORGAN E. R., *Canad. J. Phys.* **31,** 529 (1953).
2. KOUVEL J. S., GRAHAM C. D., Jr. and BECKER J. J., *J. Appl. Phys.* **29,** 518 (1958).
3. VOLKENSHTEIN N. V., TURINSKAYA M. I. and GALOSHINA E. V., *Zh. éksper. teor. Fiz.* **35,** 1312 (1958).
4. KOUVEL J. S., GRAHAM C. D., Jr. and JACOBS I. S., *J. Phys. Radium* **20,** 198 (1959).
5. MEIKLEJOHN W. H. and BEAN C. P., *Phys. Rev.* **102,** 1413 (1956); **105,** 904 (1957).
6. LIN S. T. and KAUFMANN A. R., *Phys. Rev.* **108,** 1171 (1957).
7. KOUVEL J. S. and GRAHAM C. D., Jr., *J. Appl. Phys.* **30,** 312*s* (1959).
8. KASPER J. S., private communication.
9. HAHN R. and KNELLER E., *Z. Metallk.* **49,** 426 (1958).

J. Phys. Chem. Solids Pergamon Press 1959. Vol. 11. pp. 226–230. Printed in Great Britain.

ON THE CALCULATION OF CRYSTAL FIELD PARAMETERS*

J. C. PHILLIPS†

Department of Physics, University of California, Berkeley 4, California

(*Received* 16 *March* 1959; *revised* 27 *April* 1959)

Abstract—A new method is presented for calculating crystal field splittings. The method includes the effect of orthogonalization to ligand orbitals by grouping the latter terms into an effective repulsive potential. It is shown by a very general argument that this repulsive potential should cancel to high accuracy the excess attractive potential obtained when point-ion ligands are replaced by distributed-charge ligands. This result therefore provides a qualitative justification for the empirical success of the VAN VLECK point-ion approximation for crystal fields.

VOL
11
195

1. INTRODUCTION

IN recent years crystal (ligand) field theory has been used with considerable success to interpret magnetic and spectroscopic data on transition and rare-earth metal ions.[1] This success has been achieved by determining the crystal field splitting parameter, usually called Dq, empirically. Only a few *a priori* estimates of this parameter have been made. Most of the early investigators (e.g. VAN VLECK[2]) have merely computed the fields due to point charges or point dipoles at the positions of the ligands. These calculations have usually yielded good agreement with experiment. A more refined calculation was carried out by KLEINER[3] for $Cr^{+++} \cdot 6H_2O$. KLEINER tried to take account of the finite charge distribution of the O^{--} ion. His result was in contradiction with experiment and he concluded that the approach based on free-atom wave functions was invalid.

The purpose of this note is to provide a formal justification for HERRING's suggestion[4] that this result is a consequence of neglecting orthogonalization terms. We shall see that all effects due to the finite distribution of charge cancel to a good first approximation and that the usual estimates based on point ions are indeed well justified.

Orthogonalization terms can be included by representing them as an effective potential calculated from free-atom wave functions and term values. The method used for doing this here is similar to the one already proposed by KLEINMAN and the author[5] for calculating wave functions in metals and semiconductors. A description of the formalism is given in Section 2. A semi-quantitative discussion of the effective potential and the resulting values of Dq is given in Section 3.

2. DERIVATION OF EFFECTIVE CRYSTAL FIELD

We adopt here the ionic model for the crystal wave functions. The derivation of the effective crystal field is obtained by orthogonalizing the metal-ion wave function to the ligand wave functions. The metal-ion wave functions may be chosen to be orthogonal among themselves, as may the ligand wave functions. (Overlap of wave functions centered on different ligands may be neglected.) In this way we obtain an orthogonal set of wave functions; when Slater determinants are formed from these, only the usual direct and exchange terms will appear in the one-electron energies. In the derivation presented below, only the direct terms will be included explicitly; at the end of the section, the exchange terms will be discussed.

Let the Hamiltonian for the free ion be $\mathscr{H}_0$ and the perturbing crystal potential be V_C. As a concrete example, consider Cr^{+++} surrounded octahedrally by O^{--}; for simplicity other ligands will

* This work was supported in part by the National Science Foundation.

† National Science Foundation Postdoctoral Fellow.

be neglected. Then let ψ denote a wave function of a d-electron centered on the Cr ion. To a good approximation (it will be seen later that the result is insensitive to small errors here), we have:

$$\psi = \psi_{Cr} + \sum_{j,n,l,m} a_{jnlm}\phi_{jnlm} \tag{1}$$

where ψ_{Cr} denotes a free-ion Cr^{+++} d wave function, ϕ_{jnlm} denotes a free-ion O^{--} wave function of quantum numbers n, l and m centered on the jth ligand, and

$$a_{jnlm} = -(\psi_{Cr}, \phi_{jnlm}), \tag{2}$$

the last equation resulting from the requirement discussed above that the metal d wave function be orthogonal to all occupied orbitals of the ligands. The Schrödinger equation for ψ in terms of the complete crystal Hamiltonian $\mathcal{H}$ now reads

$$\begin{aligned}\mathcal{H}\psi &= \mathcal{H}\psi_{Cr} + \sum_{j,n,l,m} a_{jnl}\mathcal{H}\phi_{jnlm}, \\ &= (\mathcal{H}_0 + V_C)\psi_{Cr} + \sum_{j,n,l,m} a_{jnl}E_{nl}\phi_{jnlm} \\ &= E(\psi_{Cr} + \sum_{j,n,l,m} a_{jnlm}\phi_{jnlm}),\end{aligned} \tag{3}$$

where we have taken advantage of the usual assumption that one can use free-atom wave functions in the crystal. Now equation (3) can be rewritten as

$$(\mathcal{H}_0 + V_C + V_R)\psi_{Cr} = E\psi_{Cr} \tag{4}$$

where

$$\begin{aligned}V_R &= \sum_j V_R{}^j \\ &= \sum_{j,n,l,m} (E - E_{nl})(\psi_{Cr}, \phi_{jnlm})\phi_{jnlm}/\psi_{Cr}.\end{aligned} \tag{5}$$

The result displayed in equation (4) has a simple physical interpretation. It states that crystal field splittings may be calculated from free-ion wave functions providing the ligand potential V_C is augmented by the effective repulsive potential V_R. From equation (5) we can see that the repulsive potential will have the ligand symmetry and that it is small outside the ligands. It is important to notice also that the orthogonalization terms closely resemble a physical potential; in particular they are independent of the normalization of ψ_{Cr}. Stated somewhat differently, if the spatial variation of ψ_{Cr} is neglected compared to that of the occupied O^{--} orbitals (and this is a good approximation in the region of the ligand cores where the repulsive potential is large) then the repulsive potential is a linear operator.

Let us consider the effective potential in the neighborhood of a ligand in more detail. Let

$$V_C = \sum_j \frac{Ze}{|r - r_j|} + V_L{}^j \tag{6}$$

where $V_L{}^j$ represents the difference between the point-ion potential and the "distributed potential" of the O^{--} ligand. Then the effective crystal potential near a ligand is

$$V_{eff} = \frac{Ze}{|r - r_j|} + V_L{}^j + V_R{}^j, \tag{7}$$

and the last two terms are large only in the region of the ligand core. From equation (7) we see that the perturbing crystal potential, *including* the effect of orthogonalization terms, can be calculated directly from the free-ion wave functions, with very little information required about the metal-ion wave function.

Let us now consider the effect of the metal-ion wave function on the repulsive potential in somewhat more detail. For this purpose we imagine the ligand potential to be large and spherically symmetric within a sphere of radius R centered at the ligand. (Presumably R can be taken as the radius of the ligand ion.) Then all wave functions, including ψ_{Cr}, in this region can be expanded in spherical harmonics with origin at the ligand:

$$\psi_{Cr}{}^R = \sum_{l,m} f_{lm}(r)\, Y_{lm}(\theta, \phi) \tag{8}$$

where the superscript R has been added as a reminder that we are in the region of the ligand core. (The advantage of this artifice is that no interference terms between different l's will appear.) It is easy to show that only values of l which appear in the ligand orbitals need be included in the expansion; thus for an O^{--} ligand $l = 0, 1$.

Suppose first that only one of the f_{lm}'s is appreciable and that the others can be neglected. Then

$$V_R{}^{jlm} = \sum_n (E_{nl}-E)a_{nlm}\frac{\phi_{nlm}}{f_{lm}(r)Y_{lm}(\theta,\phi)}, \quad (9)$$

$$\phi_{nlm} = g_{nl}(r)Y_{lm}(\theta,\phi), \quad (10)$$

$$V_R{}^{jlm} = \sum_n (E_{nl}-E)a_{nlm}g_{nl}(r)/f_{lm}(r). \quad (11)$$

Thus the repulsive potential in this case is a function of $|r-r_j|$ only. We shall investigate the analytic form given by equation (11) in more detail in the next section.

In general more than one of the f_{lm}'s will be large and in this case the repulsive terms are the sum of the separate terms for each l and m. To show this we return to equation (4) and compute $(\psi_{Cr}\mathcal{H}\psi_{Cr})$, which is what is required in calculations of Dq. From equations (8) and (10) we find:

$$(\psi_{Cr}V_R{}^j\psi_{Cr}) = \sum_{n,l,m}(E-E_{nl})\{g_{nl}(r)f_{lm}(r)\}^2, \quad (12)$$

$$= \sum_{l,m}\{f_{lm}(r)V_R{}^{jlm}f_{lm}(r)\}, \quad (13)$$

where $V_R{}^{jlm}$ is defined in equation (11). By taking advantage of the orthogonality of the spherical harmonics in the region R, we also obtain:

$$(\psi_{Cr}V_L{}^j\psi_{Cr}) = \sum_{l,m}\{f_{lm}(r)V_L{}^jf_{lm}(r)\}. \quad (14)$$

Combining equations (13) and (14), we find:

$$(\psi_{Cr}(V_R{}^j+V_L{}^j)\psi_{Cr})$$

$$= \sum_{l,m}\{f_{lm}(r)(V_R{}^{jlm}+V_L{}^j)f_{lm}(r)\}. \quad (15)$$

We have arranged the terms in the way shown by equation (15) in order to display explicitly the large cancellation which takes place between the attractive potential V_L and the repulsive potential V_R. This cancellation will be discussed in more quantitative terms in the next section.

We must now consider the effect of exchange terms on the above formulation. It is evident that our approach attempts to convert all the terms which arise from forming determinantal wave functions into an effective one-electron potential. Our "effective repulsive potential" represents just this for the terms which can be eliminated by orthogonalization. There remain the exchange terms which are not eliminated. However, SLATER[6] has shown that the exchange terms can also be approximated quite well, especially in core regions, by an average exchange potential. Using his arguments, we assume that the average exchange potential has been included in $V_L{}^j$; with this modification all the above results are valid with exchange included.

3. QUANTITATIVE ESTIMATES OF V_R

No calculations have been carried out for O^{--}. However KLEINMAN and the author[5] have constructed an effective potential for the valence electrons in silicon in connection with a calculation of the energy bands of that crystal. These results will be presented so that the reader may have a concrete example of the very general argument we shall offer later concerning the order of magnitude of V_C+V_R. A detailed description of the method used to derive the potential is presented elsewhere.[5]

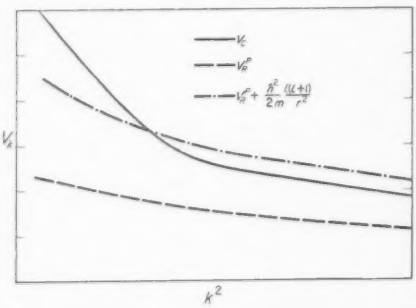

FIG. 1. A schematic plot of the Fourier transforms of the attractive and repulsive s-potentials for silicon.

We plot in Figs. 1 and 2 the Fourier transforms,

$$V_k = \frac{1}{\Omega}\int V(r)\exp(ik\cdot r)\,d^3r, \quad (16)$$

of V_C and $V_R{}^l$ for $l=0, 1$ in silicon. Here Ω is the volume of an atomic cell in silicon. We plot the Fourier transform because small values of k

correspond to a slowly-varying ψ_{Cr}. The core levels in silicon have $E_{1s} = -135\ R$, $E_{2s} = -11\ R$ and $E_{2p} = -8\ R$. For the energy of the valence electron we have taken $E = -2\ R$.

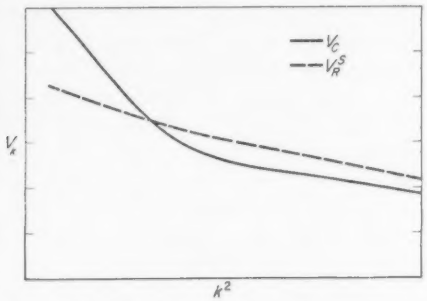

FIG. 2. A schematic plot of the Fourier transforms of the attractive and repulsive p-potentials for silicon.

The effective potential for $l = 0$ is given by the difference of the two potentials shown in Fig. 1. The situation of valence electrons in neutral silicon outside the core is somewhat different from that of an electron outside an O^{--} because the point-ion term in equation (7) is attractive rather than repulsive. Thus the electrostatic potential for O^{--} would bend down rather than up on the left-hand side of Fig. 1. However, in the case of neutral silicon also, the excess attractive potential due to the distributed charge is readily identified as the flat portion of the V_C curve on the right-hand side of Fig. 1. It will be observed that the repulsive potential cancels this potential to within about 10 per cent. (Actually the repulsive potential is somewhat larger.)

The case is somewhat different when $l = 1$. The results are shown in Fig. 2, and it can be seen that $V_R{}^p$ alone does not produce nearly so good a cancellation as $V_R{}^s$ did. The reason for this is that the repulsive potential represents a means of including the kinetic energy arising from the radial nodes of the wave function in the core region. The angular energy in the core region is also large, however, and if it is included the resulting repulsive potential is strikingly similar to the s-repulsive potential (see Fig. 2).

From equation (15) we see that the cancellation just described for s-states will make the right-hand side of equation (15) small for $l = 0$. This shows that the radial kinetic energy of the s-part of ψ in the ligand core region (which has been transformed into $V_R{}^{J0}$) largely cancels the attractive potential of the ligand core. On the other hand for the p-part of the wave function we conclude that the radial plus the angular kinetic energy will again cancel the excess attractive energy in the core region.

It seems very unlikely that the cancellation that we have just described is fortuitous, especially since such cancellation is required to obtain the observed rapid convergence in orthogonalized plane wave calculations. (For a more complete discussion of this point see ref. 5.) In fact it is easy to see that such cancellation must occur. The core levels E_n of all atoms heavier than carbon are known from X-ray data to satisfy the following relationship to a good approximation:

$$E_{n-1}/E_n \cong 10. \tag{17}$$

Now the only effect that prevents ψ_{nl} from collapsing towards ψ_{n-1l} is the exclusion principle, which is reflected in the requirement that ψ_n be orthogonal to ψ_{n-1}. This in turn leads to an effective repulsive potential for ψ_n, and if this potential did not cancel V_C to within about 10 per cent the experimental result (17) could not hold.

We now apply this conclusion to the calculation of crystal field splittings, taking as an example KLEINER's[3] calculation of Dq for $Cr^{+++} \cdot 6H_2O$. If only the first term is included in equation (7), one obtains, with VAN VLECK[2],

$$Dq \cong 1000\ \text{cm}^{-1}, \tag{18}$$

a result in good agreement with experiment.[3] KLEINER has shown that the second term in equation (7) contributes about $-1500\ \text{cm}^{-1}$, which completely spoils the agreement. We have just shown, however, that the third term of equation (7), which is positive, should be about equal to the second in magnitude, or perhaps 10 per cent larger. For the third term then we have $1700 \pm 400\ \text{cm}^{-1}$, where the uncertainty quoted represents our estimate of the probable error associated with our general argument. Thus we find

$$Dq \cong 1200 \pm 400\ \text{cm}^{-1}, \tag{19}$$

in good agreement with VAN VLECK's original result.

Recently TANABE and SUGANO[7] have attempted to correct KLEINER's calculation by including overlap integrals in the tight-binding formalism. They

obtain $Dq = 4700$ or $3800\ cm^{-1}$ after a correction has been applied.* They also quote an experimental value of $1700\ cm^{-1}$ which is much closer to our value (19).

We now assert that, although their calculation is more elaborate, our results may be expected to be much more accurate. The reason for this can be seen if one imagines the repulsive potential expanded in spherical harmonics about the metal ion. Terms in $l = 0, 2, 4, \ldots$ will appear. The terms in $l = 0$ and 2 shift e_g and t_{2g} levels equally, and the largest contribution to the crystal field splitting of the levels comes from the term $l = 4$. In TANABE and SUGANO's calculation this contribution appears as a small difference between two large terms consisting chiefly of $l = 0$ and 2 shifts and is therefore quite sensitive to calculational errors. They also calculate the repulsive and attractive terms (the last two terms of equation (7)) separately and then take the difference. We have calculated directly the difference between the two $l = 4$ terms thus explicitly taking into account the cancellation depicted in Figs. 1 and 2. (From orthogonalized plane wave calculations of energy bands in crystals (see, e.g., WOODRUFF[8]), it is well known that great care must be taken to ensure the required cancellation between the attractive distributed potential and the repulsive potential. This cancellation will not hold in general, e.g. for the SLATER ligand wave functions used by TANABE and SUGANO. (A more quantitative discussion of the inadequacy of SLATER wave functions has been given by MUKHERJI and DAS[9]). This argument suggests that the agreement between our value and the experimental value may not be fortuitous.

We conclude with some comments regarding the significance of the foregoing results. The complete calculation of self-consistent wave functions and potentials for crystals containing metal-ion complexes represents a problem well beyond the limits of this paper. In spite of the apparent complexity of the problem, the point-ion approach has yielded remarkably good values for crystal field splittings. We have tried to show here that this agreement is not accidental, but can be expected to follow from quite general arguments concerning the effective one-electron eigenvalue problem. In so doing we have arrived at rough conclusions concerning the cancellation which must take place if the point-ion approximation is to be valid.

These conclusions are also of interest in connection with spin-orbit splittings and hyperfine interactions. MARSHALL[10] has recently shown that the observed values of these quantities can be understood if the metal-ion wave function ψ is imagined to be more extended in the crystal than in the free atom; this explanation is also supported by neutron form factors. (It appears that a similar explanation was previously proposed, for empirical reasons, by KURODA and ITOH[11].) MARSHALL[10] has proposed that this dilatation results from "screening", while the "Fermi principle" has an opposite, but small, effect. These effects are readily recognized as our terms V_L and V_R, respectively. This suggests that the observed dilatation may have a somewhat more complicated origin, since the considerations presented above suggest that V_R is, if anything, slightly larger than V_L.

Acknowledgements—It is a pleasure to acknowledge that this problem was suggested to the author by Dr. C. HERRING. The author has benefited from conversations with Professor J. H. VAN VLECK, Dr. P. W. ANDERSON, Dr. A. D. LIEHR and Dr. W. MARSHALL.

REFERENCES

1. MOFFITT W. and BALLHAUSEN C. J., *Ann Rev. Phys. Chem.* **7,** 107 (1956).
2. VAN VLECK J. H., *J. Phys. Chem.* **41,** 67 (1940).
3. KLEINER W. H., *J. Chem. Phys.* **20,** 1784 (1952).
4. HERRING C., *Photoconductivity Conference, Atlantic City* (1954). John Wiley, New York (1956).
5. PHILLIPS J. C. and KLEINMAN L. (submitted to *Phys. Rev.*).
6. SLATER J. C., *Phys. Rev.* **81,** 385 (1951).
7. TANABE Y. and SUGANO S. J., *J. Phys. Soc. Japan* **11,** 864 (1956).
8. WOODRUFF T. O., *Solid State Physics* (Ed. F. SEITZ and D. TURNBULL). Vol. 4. Academic Press, New York (1957).
9. MUKHERJI A. and DAS T. P., *Phys. Rev.* **111,** 1479 (1958).
10. MARSHALL W., *Bull. Amer. Phys. Soc.* **4,** 142 (1959).
11. KURODA Y. and ITOH K., *Nippon Kagaku Kaishi* **76,** 545, 762, 766, 934 (1955).

* The correction attempts to take into account the difference between $\psi_{Cr^{++}}$ and $\psi_{Cr^{+++}}$. The correction is only half as large as that quoted by TANABE and SUGANO because the term proportional to the square of the overlap integral changes in such a way as to cancel half the correction from the "resonance" integral, which was the only correction included by them.

J. Phys. Chem. Solids Pergamon Press 1959. Vol. 11. pp. 231–238. Printed in Great Britain.

THE ANTIFERROMAGNETIC STRUCTURE OF NiMn*

J. S. KASPER and J. S. KOUVEL

General Electric Research Laboratory, Schenectady, New York

(*Received* 7 *May* 1959)

Abstract—The ordered alloy NiMn is found to be an antiferromagnet with a very high Néel temperature (> 600°K) on the basis of neutron-diffraction and magnetic-susceptibility measurements. The magnetic unit cell has lower symmetry than the tetragonal chemical cell; the moment directions are normal to the *c*-axis. The moments of nearest-neighbor manganese atoms (in planes normal to the *c*-axis) are antiparallel to each other. A detailed discussion of possible magnetic models is given; for all of them, $\mu_{Mn} = 4{\cdot}0 \pm 0{\cdot}1$. It is inferred that μ_{Ni} is probably much less than 0·6. The magnetic anisotropy is discussed and compared to that of γ-manganese.

1. INTRODUCTION

WE have found that the *ordered* alloy NiMn (Fig. 1) is an antiferromagnet, and have established essential features of its magnetic structure. This investigation was undertaken not only because of a general interest in the magnetic structures of metallic systems, but also to obtain further knowledge regarding the magnetic interactions of nickel and manganese specifically. Disordered nickel–manganese alloys containing 20–30 per cent manganese have been recently found to have unusual low-temperature magnetic properties[1] which can be attributed to competing antiferromagnetic (Mn–Mn) and ferromagnetic (Ni–Mn and Ni–Ni) exchange interactions. Unfortunately, the neutron-diffraction effects—studied by us (unpublished)—are very small and subtle for these *disordered* alloys. No evidence of long-range magnetic ordering could be found at 4·2°K, nor could there be discerned any changes in the nature of the diffuse scattering between 4·2 and 298°K. Accordingly, *ordered* alloys seemed more promising, from the standpoint of neutron diffraction, for providing definite information about the magnetic state in the nickel–manganese system.

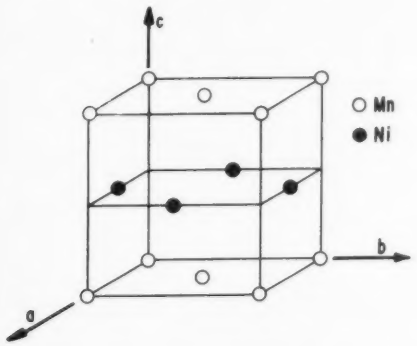

FIG. 1. The tetragonal structure of NiMn.
$a_0 = 3{\cdot}174$ Å $c_0 = 3{\cdot}524$ Å $c_0/a_0 = 0{\cdot}948$

A neutron-diffraction study of ordered Ni_3Mn has already been made,[2] the results of which suggest that all the atomic magnetic moments of this alloy are ferromagnetically aligned. It should be noted that in perfectly ordered Ni_3Mn there are only Ni–Ni and Ni–Mn nearest neighbors. However, the alloy NiMn, which occurs in an ordered form,[3] also has Mn–Mn nearest neighbors whose presumably antiferromagnetic interactions can be expected to play a significant role. Consequently, a neutron-diffraction study and a magnetic investigation of ordered NiMn were undertaken.

2. SAMPLE PREPARATION AND ANALYSIS

Equiatomic proportions of nickel and manganese were induction-melted in an argon atmosphere. From each of two ingots, a cylindrical

* The neutron-diffraction work was performed at the Brookhaven National Laboratory, Upton, N.Y.

specimen, 0·50 in. long and 0·25 in. in diameter, was machined out for magnetic-susceptibility measurements. The remainder of each ingot was milled to give small chips for the neutron-diffraction work. The chips, sealed in quartz, and the cylindrical specimens were then given the following heat treatment: 3 hr at 900°C, 1 hr each at 800, 700, 650 and 600°C, furnace-cooled to room temperature. This heat treatment should result in well-ordered face-centered tetragonal[3] NiMn. Chemical analyses of the two ingots gave 49·4 atomic per cent manganese for the composition in both cases, indicating only a slight loss of manganese in the preparation.

The X-ray diffraction data with CuK_α radiation showed only the pattern of a tetragonal phase with lattice parameters differing but slightly from the values inferred for the above composition from the work of KÖSTER and RAUSCHER[4]. These were $a_0 = 3{\cdot}714$ Å, $c_0 = 3{\cdot}524$ Å, ($\pm 0{\cdot}003$ Å for both), $c_0/a_0 = 0{\cdot}948$ for the 4-atom C-centered cell of Fig. 1. There was no evidence of superlattice reflections in the X-ray photographs taken with CuK_α, as is to be expected from applying Hönl corrections. The most advantageous radiation for exhibiting the superlattice reflections is FeK_α, which depresses the scattering factor of manganese considerably more than that of nickel. Photographs taken with FeK_α did show all possible superlattice reflections quite sharply and established that the ordered structure consisted of planes parallel to (001) alternately all nickel or all manganese; the rules governing these reflections were h, k, l not all odd and not all even but with $h+k$ even.

3. MAGNETIC-SUSCEPTIBILITY MEASUREMENTS

Prior to the neutron-diffraction study, the magnetization of one of the cylindrical polycrystalline specimens was measured in fields up to 8000 Oe from 1·8°K to room temperature. Over this entire temperature range, the volume susceptibility was found to have an essentially constant and field-independent value of approximately 6×10^{-5} e.m.u. Since this value is abnormally high for Pauli paramagnetism, we inquired into the possibility that this susceptibility behavior is theoretically consistent with an antiferromagnetic state having a Néel temperature substantially above room temperature.

If we assume that the magnetic state of ordered NiMn is governed primarily by a strong antiferromagnetic exchange coupling between the moments of nearest-neighbor manganese atoms and that these moments form a two-sublattice system, we can express the volume susceptibility of a polycrystalline specimen at 0°K as[5]

$$\chi = Ng^2\mu_B^2/6z_0J, \tag{1}$$

where N is the number of manganese atoms per unit volume, g the Landé factor, μ_B the Bohr magneton, z_0 the number of nearest neighbors of the opposite sublattice and J the exchange interaction coefficient. Furthermore, from molecular-field considerations, we may write for the Néel temperature

$$T_N = 2(z_0 - z_s)JS(S+1)/3k, \tag{2}$$

where z_s is the number of nearest neighbors of the same sublattice, S the spin quantum number for manganese, and k the Boltzmann constant. Our neutron-diffraction results, discussed in the next section, suggest an extremely small moment for nickel in this alloy, which would justify the neglect of nickel in this computation. Moreover, these measurements reveal a two-sublattice antiferromagnetic arrangement of manganese moments such that $z_0 = 4$ and $z_s = 0$. Substituting these values of z_0 and z_s into equations (1) and (2) and then combining these equations, we obtain

$$T_N = Ng^2\mu_B^2S(S+1)/9k\chi. \tag{3}$$

From the lattice-parameter values given in the previous section, $N = 4{\cdot}12 \times 10^{22}$ manganese atoms/cm^3. When this value for N, the experimental value given above for χ and $g = 2$ are substituted into equation (3), it is found that

$$T_N \simeq 190S(S+1). \tag{4}$$

Hence, if the number of Bohr magnetons per manganese atom, gS (i.e. $2S$ in this approximation), is 2, 3 or 4, the Néel temperature should be about 380, 710 or 1140°K, respectively.

Although any speculations based on equations (1) and (2) cannot be very reliable quantitatively, the results of this computation are probably meaningful to the extent that they predict a Néel temperature that is well above room temperature. This prediction is consistent with the original observation of a constant susceptibility between

liquid-helium and room temperatures for our polycrystalline specimen of ordered NiMn.

4. NEUTRON-DIFFRACTION RESULTS

The neutron-diffraction data were obtained at three temperatures (77, 298 and 600°K) for the polycrystalline chips, packed into aluminum cylinders. The patterns were the same with regard to the relative intensities of Bragg peaks, allowing for the effects of thermal motion. At 600°K, where the data are least accurate, a 10 per cent variation in intensity ratios could exist. Also, at all three temperatures, the background intensity was flat and free of any suggestion of special diffuse scattering effects. Fig. 2 shows a trace obtained at 77°K.

It is apparent from Fig. 2 that in addition to the peaks due to the ordered NiMn structure, for which $h+k=2n$, there occur peaks for which $h+k=2n+1$; namely (100), (101), (102) and (211). The latter appear, then, to be of magnetic origin, and in support of this they indicate a form factor dependence with angle as expected for magnetic reflections. The interpretation of the intensities of these reflections constitutes the major part of this contribution and is given in the next section. It should be noted that since these intensities up to 600°K diminished only in accordance with thermal motion, the magnetic transformation temperature is presumably well above this temperature.

In regard to the nuclear reflections, quite satisfactory agreement was obtained for the ordered model, as may be judged from the data listed in Table 1. The superlattice reflections are much stronger than the fundamentals because of the opposite signs of the scattering factors of nickel and manganese ($b_{Ni}=1{\cdot}03$, $b_{Mn}=-0{\cdot}36$). For the superlattice reflections, $I\sim(b_{Ni}-b_{Mn})^2$, and for the fundamentals $I\sim(b_{Ni}+b_{Mn})^2$. Also, there is a great sensitivity of the intensity ratios to variation of composition. The best fit of calculated to observed intensities was obtained for a composition of 49 atomic per cent manganese, assuming that one layer of the structure is 100 per cent nickel and the other is 98 per cent manganese and 2 per cent nickel. This composition is in satisfactory

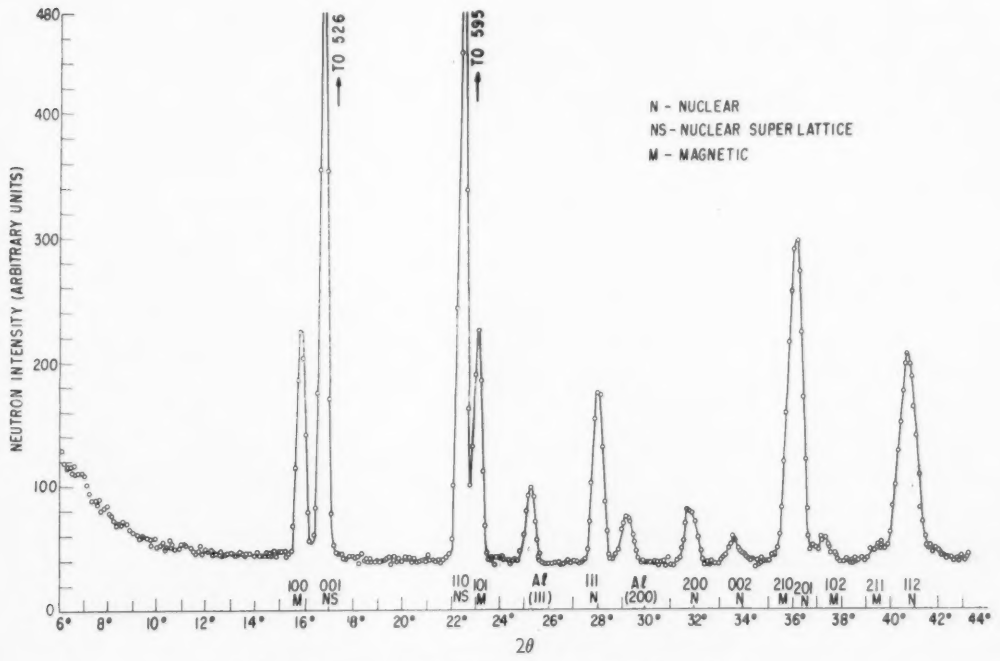

FIG. 2. Neutron-diffraction pattern of NiMn at 77°K.

Table 1. *Neutron intensities for NiMn at* 77°K (*arbitrary units*)

hkl	Calculated*			Observed
	Nuclear	Magnetic†	Total	
100		198	198	192
001	456		456	459
110	512		512	492
101		186	186	189
111	178		178	185
200	65		65	64
002	31		31	26
210		17		
201	420		437	487
102		24	24	28
211		21		
112	324		345	386

* Calculated intensities are for P_cman with $\mu_{Mn} = 4{\cdot}0$, $\mu_{Ni} = 0$.

† Based on the form factor for Mn^{++} (Ref. 6).

agreement with that from chemical analyses (49·4 per cent) made on small portions of the large ingot which were used subsequently for the neutron-diffraction experiments.

The intensities were calculated from the expression $I_{hkl} = K\ (\sin\theta \sin 2\theta)^{-1}\ j_{hkl}|F_{hkl}|^2$, where K is a normalizing factor, $(\sin\theta \sin 2\theta)^{-1}$ is the angular correction for a cylindrical specimen, j_{hkl} is the multiplicity and F_{hkl} is the structure factor. In the case of the magnetic intensities, $|F_{hkl}|^2$ was computed in the following way[7]

$$|\boldsymbol{F}|^2 = |\boldsymbol{K}|^2 - |(\epsilon \cdot \boldsymbol{K})|^2,$$

$$\boldsymbol{K} = \sum_i \boldsymbol{K}_i \exp[-2\pi i(hx_i + ky_i + lz_i)].$$

No absorption correction was applied, since its variation over the range of angles used was less than 1 per cent. Also, no temperature-factor correction was made for the data at 77°K, because it was indicated to be considerably less than the error in the measured intensity. Such a correction was indicated particularly for the measurements at 600°K, but it could not be evaluated reliably. The error in the intensities given in Table 1 is variable, but up to $2\theta = 33°$, i.e. through (200), it is estimated to be ~ 5 per cent. For the rest of the intensities, where there were not as many repeated measurements, the error is approximately 10 per cent.

5. THE MAGNETIC STRUCTURE

The reflections with $h+k = 2n+1$, considered as magnetic, immediately suggest the antiparallelism of moments for atoms related by the C-centering, i.e. atomic moments in planes parallel to (001) are antiparallel to their nearest neighbors in the same planes. The simplest magnetic structures, of tetragonal symmetry, would be those wherein the moments are parallel or antiparallel to [001]. Considerations of the magnetic intensities, however, exclude this possibility. For example, the relative intensities of (101) and (100) would be in the ratio of 1:2 rather than of essentially equal

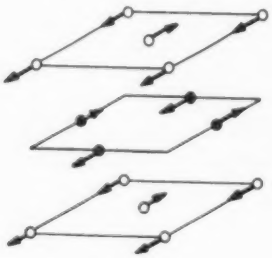

P_c man

$a_0 = b_0 = 3.714$ Å, $c_0 = 3.524$ Å

(a)

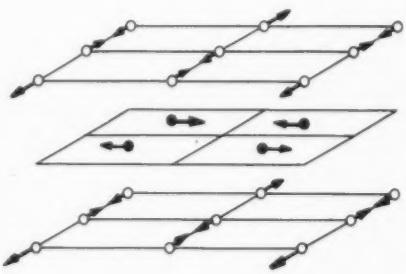

C_a mma

$a_0 = b_0 = 3.714 \times \sqrt{2}$ Å $c_0 = 3.524$ Å

(b)

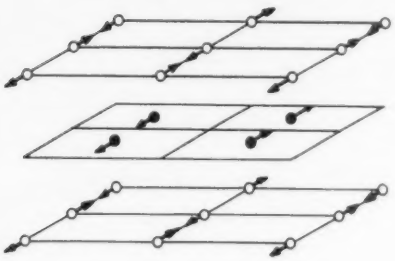

Pmab'

$a_0 = b_0 = 3.714 \times \sqrt{2}$ Å, $c_0 = 3.524$ Å

(c)

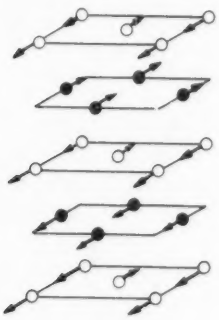

Pmm'2'

$a_0 = b_0 = 3.714$ Å, $c_0 = 3.524 \times 2$ Å

(d)

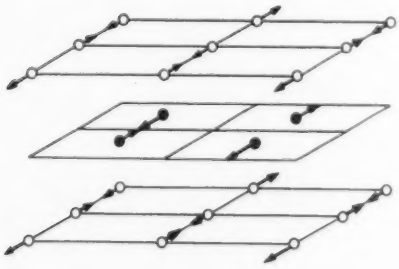

$P_a 2/b$

$a_0 = b_0 = 3.714 \times \sqrt{2}$ Å, $c_0 = 3.524$ Å

(e)

FIG. 3. Possible magnetic structures of NiMn.

magnitude as observed. The magnetic unit cell, therefore, is not tetragonal.

On the other hand, several magnetic models of orthorhombic symmetry with the moments lying in planes parallel to (001) give very satisfactory intensity agreement. They differ principally as to the specific direction of the moments. They are depicted in Fig. 3, examples (a) through (d), and described in Table 2. The space-group designations are those of the Schubnikov groups[8] for black and white objects, which groups are appropriate for describing magnetic structures as well.[9,10] It is noteworthy that all the orthorhombic structures have in common the result that $\mu_{Mn} = 4{\cdot}0 \pm 0{\cdot}1 \mu_B$ and also that only small or zero magnitudes are allowed for μ_{Ni}. A rigorous solution of the intensity relationships, mainly for (100) and (101), yields the result that $\mu_{Ni} = 0{\cdot}06$ for P_C *man* and C_a *mma*. The small intensity differences responsible for this result are not beyond experimental error, so that $\mu_{Ni} = 0$ is quite acceptable. Furthermore, from our magnetic-susceptibility measurements, we can set an upper limit of 10^{-4} Bohr magneton per atom to any ferromagnetic component in ordered NiMn. Hence, if μ_{Ni}, though very small, exceeds this value, then the moments of nickel (as well as of manganese) must be arranged antiferromagnetically, as shown in Fig. 3.

The individual moments reported[2] for ordered Ni_3Mn are $\mu_{Mn} = 3{\cdot}2$ and $\mu_{Ni} = 0{\cdot}3$. Hence, our value of 4·0 Bohr magnetons for the moment of manganese in ordered NiMn is quite reasonable. Moreover, since the moment of nickel in ordered Ni_3Mn is about half that of pure nickel, it is not too strange that the moment of nickel in the more manganese-rich NiMn should be exceedingly small. This would suggest, incidentally, that the rapid decrease in the magnetization of the disordered alloys with an increase of manganese concentration from 20 to 30 per cent[1] is due not only to antiferromagnetic alignment of moments but also to a decrease of μ_{Ni} in these alloys.

The structure with space-group P_C *man* appears to be the simplest high-symmetry one in accord with the data. It is also the only one where the magnetic unit cell is the same as the chemical cell. It might be argued that in those circumstances it be taken as the solution of the magnetic structure. It is quite possible, however, for the magnetic structure

Table 2. Possible magnetic structures for NiMn

Space-group	z†	Cell dimensions	μ_{Mn}	μ_{Ni}	Direction of moments*
		I—*Orthorhombic Models*			
$P_C\,man$	2	$a_0 = 3{\cdot}714$, $c_0 = 3{\cdot}524$	4·0	$< 0{\cdot}1$	[100]
$C_a\,mma$	4	$a_0' = (\sqrt{2})\,a_0$, $c_0' = c_0$	4·0	$< 0{\cdot}1$	[100] for Mn [010] for Ni
$P\,mab'$	4	$a_0' = (\sqrt{2})\,a_0$, $c_0' = c_0$	4·0	$< 0{\cdot}3$	[100]
$P\,mm'2'$	4	$a_0' = a_0$, $c_0' = 2c_0$	4·0	$< 0{\cdot}2$	[100]
		II—*Monoclinic Model*			
P_a2/b	4	$a_0' = (\sqrt{2})\,a_0$, $c_0' = c_0$	$\mu_{Mn}^2+\mu_{Ni}^2 = 16{\cdot}1$		[100]

* Note that directions are for the specific unit cell indicated.
† Formula weights per unit cell.

to be of lower symmetry than that consistent with the information obtained from polycrystalline material. Accordingly, we have considered other alternatives of a simple nature.

If the moment direction is chosen at 45° to the one for $P_C\,man$, then for the structure to be orthorhombic, the moments on the two kinds of atoms cannot be collinear but are at right angles. A C-centered cell of twice the volume of the chemical cell is the proper one and the space-group is $C_c\,mma$ (Fig. 3(b)). The result as to magnitude of the nickel moment is the same as for $P_C\,man$—either $\mu_{Ni} = 0{\cdot}06$ or $\mu_{Ni} = 0$. If for both atoms a single-axis model is desired, with the moment direction along [110] (of the chemical cell), then the cell becomes monoclinic with space-group P_a2/b (Fig. 3(e)). There is now indefiniteness as to the respective moments of the two kinds of atoms, the relationship between them being $\mu_{Mn}^2+\mu_{Ni}^2 = 16{\cdot}1$. We wish to remark that the indefiniteness is mainly concerning the value of μ_{Ni}, but that μ_{Mn} cannot deviate appreciably from $4{\cdot}0\,\mu_B$. For example, if we assume $\mu_{Ni} = 0{\cdot}6$ as in pure nickel, then $\mu_{Mn} = 3{\cdot}95$. We believe it very unlikely that μ_{Ni} exceeds this value, and that it probably is substantially lower.

A still different way of making an antiparallel arrangement of nickel atoms and preserving orthorhombic symmetry is given by $P\,mab'$ (Fig. 3(c)). This model calls for the presence of reflections which are not observed. For $\mu_{Ni} < 0{\cdot}3$—not an impossibility—such reflections could escape detection; the value of μ_{Mn} would still be 4·0.

In all the models discussed so far, the nickel atoms are made to be antiparallel within a layer parallel to (001) or to have no moment. Since the Ni–Ni exchange coupling is generally a ferromagnetic one, it is reasonable to inquire about the possibility that nearest neighbors of nickel within a (001) layer are parallel. The net moment may be made zero by choosing alternate ferromagnetic layers of nickel atoms with moments oriented in opposite directions. $P\,mm'2'$ (Fig. 3(d)) represents this situation. Again, reflections that have not been observed are called for, because of the doubling of the c-axis, but if $\mu_{Ni} < 0{\cdot}2$, then such reflections would escape detection.

So far we have taken the moment directions to be normal to the c-axis. It should be remarked that consideration has been given to the possibility that the moment directions are inclined at some other angle to the c-axis. Generally, the calculated intensities for such models are in serious disagreement with the observed ones. We have found only one possible solution. If the moments are oriented along [101] of the chemical cell, there is the special solution $\mu_{Mn} = \mu_{Ni} = 2{\cdot}8$. We consider this an implausible result on physical grounds and consequently aver that it is essentially established that the moment directions are normal to the c-axis.

VOL
11
195

VOL. 11 1959

6. NÉEL TEMPERATURE AND MAGNETIC ANISOTROPY

Since the intensities of the neutron-diffraction reflections attributed to magnetic sources suggest essentially no loss of magnetization between 77 and 600°K, it is presumed that the Néel temperature of this antiferromagnetic structure is well above 600°K. When we substitute $\mu_{Mn} = 2S = 4$ into equation (4), a Néel temperature value of 1140°K is obtained. Hence, both our neutron-diffraction and magnetic-susceptibility measurements offer indirect but consistent evidence for a very high Néel temperature.

This high Néel temperature is presumably due to strong antiferromagnetic exchange interactions between the moments of nearest-neighbor manganese atoms. Let us further suppose that these interactions are not entirely isotropic and that, in addition to the usual isotropic Heisenberg term, the expression for the exchange energy contains an anisotropic pseudo-dipolar term. Specifically, we write

$$E = 2J \sum_{i,j} \{\boldsymbol{S}_i \cdot \boldsymbol{S}_j + \alpha(\boldsymbol{S}_i \cdot \boldsymbol{r}_{ij})(\boldsymbol{S}_j \cdot \boldsymbol{r}_{ij})/r_{ij}^2\}, \quad (5)$$

where α is an arbitrary dimensionless quantity and i and j refer to nearest-neighbor atoms and $\boldsymbol{r}_{ij}$ to the vector distance between them. If we now consider a sheet of manganese atoms perpendicular to the tetragonal axis of ordered NiMn and let the magnetic axis have the three simple orientations

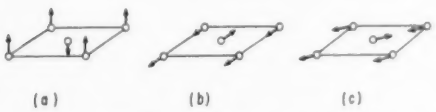

FIG. 4. Models considered for the magnetic anisotropy of NiMn.

shown in Figs 4(a), (b) and (c), we find from equation (5) that the exchange energies (per manganese atom) are

$$E(a) = -4JS^2$$

$$E(b) = E(c) = -4JS^2(1+\alpha/2).$$

Thus, configurations (b) and (c) in Fig. 4, to which all the magnetic structures in Fig. 3 correspond, have the same energy. Furthermore, in order that this energy be lower than that of configuration (a), α must be positive.

In a recent study of the manganese–copper system, BACON *et al.*[11] conclude that the face-centered tetragonal alloys of 80–95 per cent manganese, although atomically disordered, have an ordered antiferromagnetic structure. In this structure, for each plane of atoms perpendicular to the tetragonal axis, the moments are parallel to each other and antiparallel to those in adjacent planes. The magnetic axis was found to coincide with the tetragonal axis, as shown in Fig. 5(a). Let

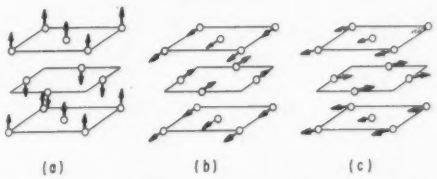

FIG. 5. Models considered for the magnetic anisotropy of γ-manganese.

us now compare this configuration (which by extrapolation can be expected to hold for pure γ-manganese) with the configurations shown in Figs. 5(b) and (c), in which the magnetic axis is perpendicular to the tetragonal axis. If we assume, as we did for ordered NiMn, that the predominant exchange interactions are between nearest-neighbor manganese atoms and compute the exchange energies of these configurations (per manganese atom) on the basis of equation (5), we find that

$$E(a) = -4JS^2(1+\alpha)$$

$$E(b) = E(c) = -4JS^2.$$

Hence, in order that the experimentally deduced configuration for γ-manganese have the lowest energy, α must once again be taken as positive. Since equation (5) with positive α successfully predicts that in ordered NiMn and γ-Mn the magnetic axis is respectively perpendicular and parallel to the tetragonal axis, it is possible that this equation is a fairly general expression for the anisotropic exchange interaction between the moments of nearest-neighbor manganese atoms in a metallic system.

7. CONCLUSIONS

We conclude from the analysis of the neutron-diffraction data on ordered NiMn that the moments are normal to the c-axis, that $\mu_{Mn} = 4{\cdot}0 \pm \pm 0{\cdot}1$, that the moments of nearest-neighbor manganese atoms are antiparallel to each other, and that the magnetic structure is of no higher symmetry than orthorhombic. Less definitely, we state that the specific direction for manganese moments is either [100] or [110], referred to the chemical cell, and that μ_{Ni} is substantially less than 0·6. Both neutron-diffraction and magnetic-susceptibility measurements indicate a very high Néel temperature. Although the magnetic anisotropy is different from that of γ-manganese, they can both be qualitatively deduced from the same energy expression.

Acknowledgements—We are grateful to C. P. BEAN and I. S. JACOBS for helpful discussions of this work, to A. ABRAHAMSEN for assistance in obtaining the neutron-diffraction data, and to R. LEWINSKI and W. G. MARTIN for assistance with the X-ray diffraction study.

REFERENCES

1. KOUVEL J. S., GRAHAM C. D., Jr. and BECKER J. J., *J. Appl. Phys.* **29,** 518 (1958).
   KOUVEL J. S., GRAHAM C. D., Jr. and JACOBS I. S., *J. Phys. Radium* **20,** 198 (1959).
2. SHULL C. G. and WILKINSON M. K., *Phys. Rev.* **97,** 304 (1955).
3. COLES B. R. and HUME-ROTHERY W., *J. Inst. Metals* **80,** 85 (1951).
4. KÖSTER W. and RAUSCHER W., *Z. Metallk.* **39,** 178 (1948).
5. KITTEL C., *Introduction to Solid State Physics* 2nd edn., pp. 439–442. John Wiley, New York (1956).
6. CORLISS L. M., ELLIOTT N. and HASTINGS J. M., *Phys. Rev.* **104,** 924 (1956).
7. CORLISS L. M., HASTINGS J. M. and BROCKMAN F. J., *Phys. Rev.* **90,** 1013 (1953).
8. BELOV N. V., NERONOVA N. N. and SMIRNOVA T. S. *Kristallografiya* **2,** 315 (1957).
9. DONNAY G., CORLISS L. M., DONNAY J. D. H., ELLIOTT N. and HASTINGS J. M., *Phys. Rev.* **112,** 1917 (1958).
10. LECORRE Y., *J. Phys. Radium* **19,** 750 (1958).
11. BACON G. E., DUNMUR I. W., SMITH J. H. and STREET R., *Proc. Roy. Soc.* A**241,** 223 (1957).

J. Phys. Chem. Solids Pergamon Press 1959. Vol. 11. pp. 239–245. Printed in Great Britain.

SOLID SOLUBILITIES OF ALUMINUM AND GALLIUM IN GERMANIUM*

F. A. TRUMBORE, E. M. PORBANSKY, and A. A. TARTAGLIA

Bell Telephone Laboratories, Inc., Murray Hill, New Jersey

(*Received* 15 *April* 1959)

VOL. 11 1959

Abstract—Crystal-pulling and thermal-gradient crystallization techniques have been used to determine the solid solubilities of aluminum and gallium in germanium in the ranges from 500 and 300°C, respectively, to the melting point of germanium. Both elements have maximum solubilities of the order of 1 atomic per cent. In addition, these systems are characterized by a relatively rapid variation of the distribution coefficient with temperature near the melting point of germanium. The form of the temperature-dependence of the distribution coefficient can be interpreted qualitatively in terms of departures from ideality in the liquid phase and of the effects due to ionization of these acceptor impurities in solid solution.

1. INTRODUCTION

In previous work[1,2] crystal-pulling and thermal-gradient techniques were used to determine the solid solubilities of tin in germanium and silicon. The present paper contains the results of similar studies on the solubilities of aluminum and gallium in germanium. Earlier work on the aluminum– and gallium–germanium systems includes the solidus-curve estimates of THURMOND and KOWALCHIK reported by THURMOND *et al.*[3] These estimates were obtained from the analysis of crystals recovered from slowly cooled melts. The reliability of the slow-cooling technique, as well as the thermal-gradient technique, has been questioned by HALL[4], who presented experimental evidence that the slow-cooling measurements on the indium–germanium system[3] were in error. It is evident from the data presented in this paper, and from the other experiments on the indium–germanium system,† that HALL's criticism of the slow-cooling results is justified. However, the present data support the earlier conclusion[2] that the thermal-gradient technique can be used to give reliable solubility data.

2. EXPERIMENTAL

(a) *Materials*

The germanium, obtained from the Western Electric Company, was zone-refined material from which single crystals of near-intrinsic resistivity ($> 40\ \Omega$-cm) could be grown. The gallium was Eagle-Picher electronic-grade material of $> 99{\cdot}999$ per cent purity. The aluminum used in most of these experiments was of unknown origin and was found by spectrochemical analysis to be $> 99{\cdot}98$ per cent pure. Although relatively impure, neither the aluminum nor the aluminum-doped germanium contained detectable boron ($< 0{\cdot}005$ per cent), the only element which would interfere significantly with the solid-solubility measurements.

(b) *Crystal-pulling experiments*

A conventional crystal-pulling machine was used

* Presented in part at the Electrochemical Society Meeting, New York, N.Y., 28 April, 1958.

† We have performed thermal-gradient and crystal-pulling experiments on the indium–germanium system which yield appreciably lower solubilities than those obtained from the slow-cooling measurements.[3] Unfortunately, our results are rather ambiguous insofar as the actual values of the solid solubility are concerned However, the available data indicate that the temperature-dependence of the distribution coefficient is not described by the linear log k versus $1/T$ plot suggested by HALL[4]. It appears more probable that HALL's experimental points are fair approximations to the true solid solubility and not merely maximum values as he suggests.

continued at foot of next column

to pull nine germanium single crystals from melts containing initially between 0·01 and 10 atomic per cent gallium. The crystals, rotated at 144 rev/min, were pulled at a rate of 0·5 cm/hr in the [111] direction under a hydrogen atmosphere. Growth of crystals of uniform diameter was encouraged by the use of a seed crystal of the same diameter (12–25 mm) as the desired grown crystal. There was no significant evaporation of gallium from the melt during the growth of the crystals.

For the aluminum-doped crystals it was necessary to use the vacuum crystal-pulling machine described by BRIDGERS and KOLB[5]. Six germanium crystals, rotated at 125 rev/min, were pulled at 0·5–0·7 cm/hr in the [111] direction from melts containing initially between 0·25 and 8 atomic per cent aluminum. In spite of the presence of a slight surface contamination due to aluminum oxide, single crystals were obtained except in the case of the melt containing 8 per cent aluminum.

Two experiments were performed in which both aluminum and gallium were added to the melt in an effort to determine whether the solid solubility of one element was affected by the presence of the other. These crystals were grown under vacuum in the [111] direction at a rotation rate of about 120 rev/min and a pull rate of 0·5 cm/hr. Equal melt concentrations of aluminum and gallium of 0·1 and 1 atomic per cent were used in the two experiments. However, no effect was observed.

(c) *Thermal-gradient experiments*

A thermal-gradient technique, described in detail elsewhere,[1,2] was used with slight modifications to grow gallium- and indium-doped germanium crystals. The temperature gradients ranged from about 2 to 10°C/cm, depending on the temperature, the larger gradients being used at lower temperatures to speed up the rate of growth. Leeds and Northrup Speedomax controllers were used to control the temperatures to within about ±2–5°C over growth times ranging from about 1 week to 3 months. The most spectacular growth was obtained in one experiment lasting for 3 months at 300°C. Fig 1 shows a crystal grown from an indium–germanium melt in this experiment.

Two factors complicated the growth of the aluminum-doped germanium crystals. First, the fact that aluminum reacts with silica necessitated the use of graphite or alumina crucibles. Second, since germanium sinks instead of floating in liquid aluminum, the temperature had to be kept lower in the top of the tube instead of in the bottom, as in previous experiments. This was necessary to prevent spurious nucleation and growth. Two successful experiments were performed. The method used in one of these experiments is illustrated schematically in Fig. 2. Here

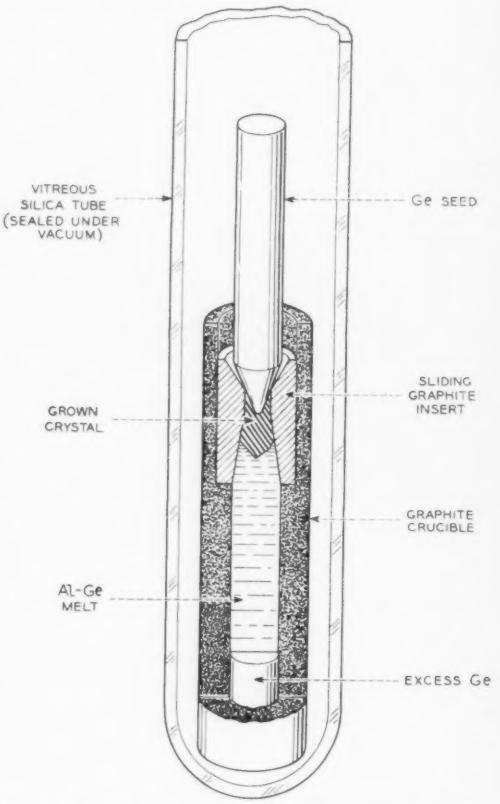

FIG. 2. Schematic diagram of one arrangement used for growing germanium from aluminum–germanium melt. The large germanium seed and the sliding graphite insert served as weights pushing the seed into contact with the liquid after melting of the aluminum.

the germanium dissolves in the hotter, lower portion of the melt, diffuses up to the top where it precipitates and grows in the constriction in the upper portion of the crucible.

In a third experiment, a modification of the

VOL.
11
1959

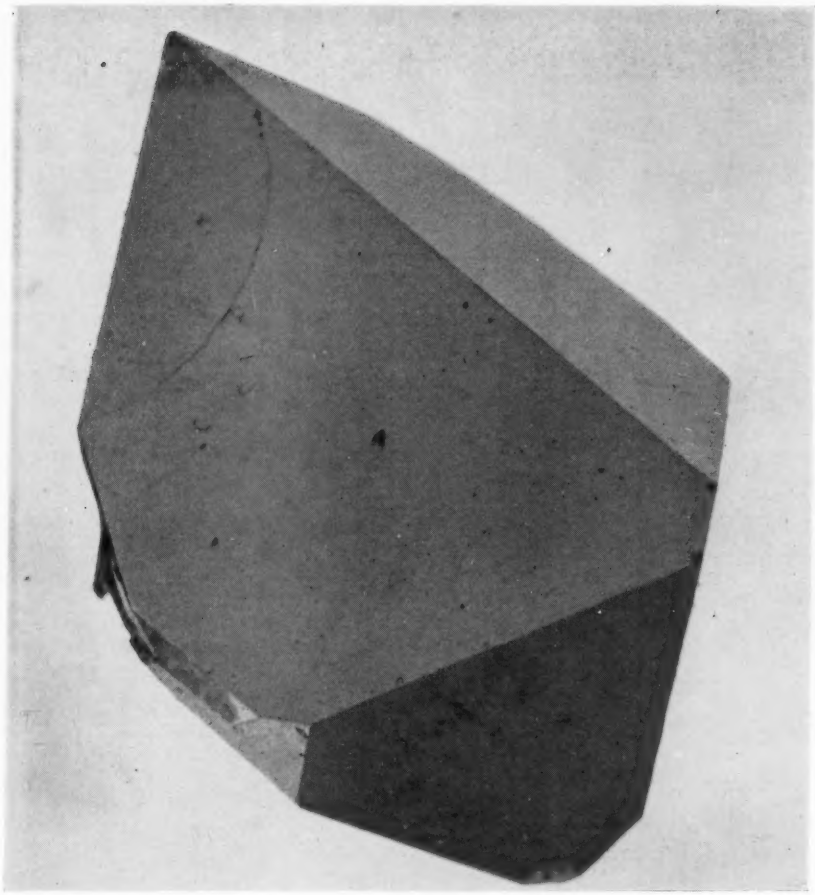

FIG. 1. Germanium single crystal grown by the thermal-gradient method from an indium–germanium melt at about 300°C. The growth time was 3 months at a thermal gradient of about 10°C/cm. The natural growth faces are shown here. The crystal is about 1 cm in its longest dimension.

[*facing page 240*

FIG. 4. Germanium single crystal grown by the method of Fig. 3. A slice has been removed to reveal more clearly the grown material at the lower end of the seed crystal. The growth took roughly 15 hr.

VOL
11
195

thermal-gradient method by stirring was used to obtain a single crystal of germanium from an aluminum–germanium melt. This method is illustrated in Fig. 3. Here, the vacuum crystal-pulling machine was used in the normal way with

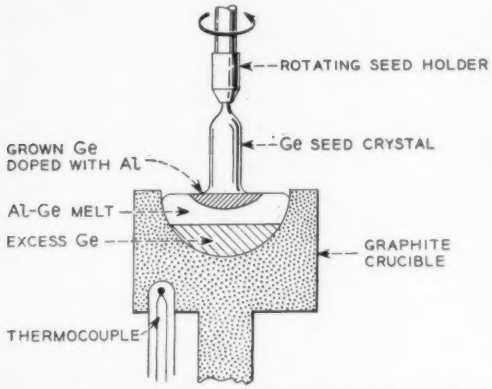

FIG. 3. Schematic diagram of the modification of the crystal-pulling apparatus for the growth of germanium from aluminum–germanium melts. The seed crystal is rotated, but is not withdrawn from the melt.

two important modifications. The large quantity of germanium, in excess of that needed to saturate the aluminum at the desired temperature, remains at the bottom of the crucible on melting the aluminum. After the melt has been heated to the desired temperature, a germanium seed is lowered into it. If the melt is not yet saturated with germanium (due to the time required for the dissolution of the original germanium) part of the seed will dissolve and further lowering of the seed is necessary. After the melt has become saturated, however, the natural thermal gradient leads to solution of the excess germanium and growth on the cooler, rotating seed crystal. No pulling is necessary. An example of the type of growth is shown in Fig. 4. Unfortunately, measurement of the actual growth temperature in the vacuum machine was not possible, so that this particular crystal was used only in the electrical measurements and not for solid-solubility measurements.

(d) *Chemical analyses*

In all cases two sections of the pulled and thermal-gradient crystals were analyzed for aluminum or gallium by spectrophotometric techniques.[6] Prior to analysis, the thermal-gradient crystals were crushed and digested in hydrochloric acid to remove any occluded metal. The analyses are believed to be accurate to better than $\pm$ 10 per cent in most cases. For the least heavily gallium-doped crystals, the analyses did not appear to be reliable. Possible reasons for this lack of reliability are discussed later.

(e) *Electrical measurements*

Hall-effect and resistivity measurements were made on a majority of the crystals grown in these experiments. The results of these measurements have been presented elsewhere.[7] The importance of these measurements here is that the very good internal consistency of the electrical and chemical measurements is strong evidence in support of the reliability of the solid-solubility measurements on aluminum and gallium.

3. RESULTS

The results of the crystal-pulling experiments on the aluminum–germanium and gallium–germanium systems are summarized in Table 1, which contains the distribution coefficient, $k(=x^S/x^L)$, as a function of the atom fraction of impurity in the melt, x^L. The results of the thermal-gradient experiments are summarized in Table 2, which contains the solid solubility as a function of the growth temperature. Unless noted otherwise, the values of k in Tables 1 and 2 were obtained from chemical analyses. The solidus curves derived from these data are shown in Fig. 5. For the crystal-pulling measurements, the temperatures were calculated from the corresponding melt compositions, assuming ideal-solution behavior for the germanium in the liquid and solid alloys. For the freezing-point lowering constant, we used the expression $(1-k)RT_f^2/\Delta H_f$, where R is the gas constant, T_f is the melting point of germanium (1210°K)[8,9] and ΔH_f is the heat of fusion of germanium (8·1 kcal/g-atom).[10]

It is evident from Table 1 that the four chemical analyses on the two most lightly doped crystals scattered appreciably. These samples contained only of the order of 0·001–0·01 atomic per cent gallium. Aside from any difficulties encountered in the chemical analyses themselves, other possible sources of error include the presence of micro-occlusions of gallium during crystal growth and contamination during the etching and crushing

Table 1. Results of crystal-pulling experiments on the aluminum– and gallium–germanium systems

(a) *Aluminum*

x^{L}_{Al}	k	x^{L}_{Al}	k
$0{\cdot}0029_6$	0·071	0·0423	0·053
$0{\cdot}0030_8$	0·077	0·0427	0·050
$0{\cdot}0097_8$	$0{\cdot}060_5$	0·0444	0·049
$0{\cdot}0101_8$	0·069	0·0452	$0{\cdot}050_5$
0·0185	0·058	0·0792	0·047
0·0232	0·054	0·0831	0·045

(b) *Gallium*

x^{L}_{Ga}	k	x^{L}_{Ga}	k
0·000089	0·084*	0·0227	0·073
0·000093	0·085*	0·0295	0·078
0·00103	—*	0·0335	$0{\cdot}077_5$
0·00132	0·092*	0·0416	0·070
0·00307	0·085	0·0420	0·069
0·00320	$0{\cdot}094_5$	0·0594	0·063
$0{\cdot}0105_0$	0·085	0·0607	0·063
$0{\cdot}0115_2$	0·072	0·0989	0·054
$0{\cdot}0202_5$	0·076	0·1032	$0{\cdot}052_5$

* These values of k were based on resistivity and Hall-effect measurements which were deemed more reliable than the chemical analyses (see text). The values of k from chemical analyses for these four samples were 0·13, 0·16, 0·10 and 0·11 respectively, showing the erratic nature of these results.

Table 2. Results of thermal-gradient experiments on the aluminum– and gallium–germanium systems

System	Temp. (°C)	x^{S}_{Al} or x^{S}_{Ga}	k
Al–Ge	496±10	0·0091	0·014
Al–Ge	675±25	0·0098	0·021
Ga–Ge	303±10	$0{\cdot}0062_5$	0·0064
Ga–Ge	505±10	0·0097	$0{\cdot}011_5$
Ga–Ge	708±10	0·0108	0·020
Ga–Ge	799±10	0·0095	0·027

treatment prior to analysis. (The magnitude of such occlusions or contamination, if present, would of course be negligible at the higher concentrations, assuming they remained of the same order of magnitude.) In view of these possible

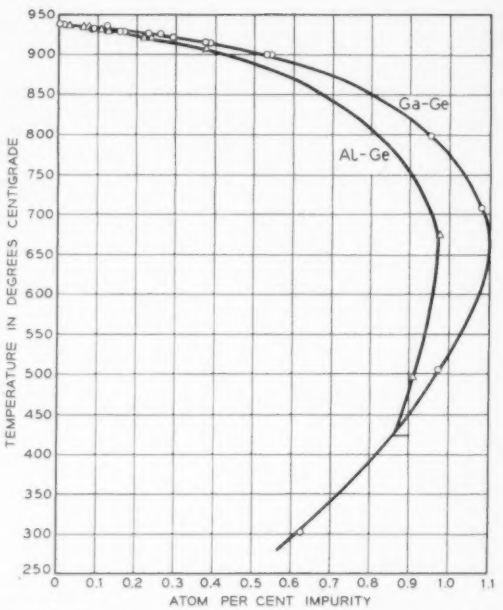

FIG. 5. Aluminum–germanium and gallium–germanium solidus curves.

sources of error, a more reliable estimate of impurity concentration should be obtained by using the resistivities of these crystals in conjunction with the resistivity/concentration curve of reference (7). The k values calculated from the resistivity data fit in quite reasonably with the chemical data for the more heavily doped crystals. It should be noted, however, that at these relatively low concentrations there is some question as to whether or not the degenerate formula for the Hall effect used in reference (7) applies, i.e. there is apparently no exact information available concerning the concentrations at which degeneracy sets in.*

The temperature-dependence of the distribution coefficient for these systems is shown in Fig. 6 in the form of $\log k$ versus $1/T$ plots. For the

* The situation in p-type germanium is complicated by the contributions of two different types of holes with different mobilities. If the magnetic field of 4600 G used in the Hall-effect measurements of reference (7) is not sufficiently large, the degenerate formula would not be expected to be valid unless the hole mobilities were fortuitously equal (C. HERRING, private communication). For a discussion of the interpretation of Hall-effect measurements see, for example, CONWELL[19].

thermal-gradient data, the liquidus compositions were obtained from the growth temperatures and the phase diagrams.[11] By extrapolation of the log k versus $1/T$ data, the most probable values of

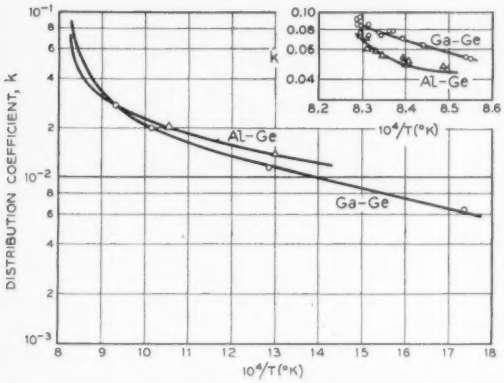

FIG. 6. Plots of log k versus $1/T$ for the aluminum–germanium and gallium–germanium systems. The crystal-pulling data are shown in the expanded plot of the region near the melting point of germanium.

k^0, the distribution coefficient at the germanium melting point, have been obtained. These values are 0·073 for aluminum and 0·087 for gallium, and are thought to be accurate to within ± 10 per cent. (This estimate of the error assumes that the degenerate formula for the Hall effect is valid for the two lightly doped crystals, as discussed above.)

In general, the solid solubilities obtained in the present study are lower than those reported by earlier workers. In the case of gallium, the value for k^0 of 0·087 compares favorably with the value of 0·10 quoted by BURTON[12] and HALL[13]. The agreement here is within the experimental errors claimed for these measurements. THURMOND and KOWALCHIK[3], GREINER and BREIDT[8] and DE ROCHE[14] have considered the solid solubilities of gallium at lower temperatures. Qualitatively, these data are in agreement with our data in that the maximum solid solubility is of the order of 1 atomic per cent. At certain temperatures discrepancies are observed which appear to amount to differences of less than a factor of two. In the case of aluminum the value for k^0 of 0·073 is in only fair agreement with the value of 0·10 quoted by BURTON[12]. In addition, the low-temperature data reported here differ appreciably from the slow-cooling measurements of THURMOND and KOWALCHIK[3], the discrepancy at some temperatures being about a factor of four. The very good consistency of the electrical and chemical measurements reported earlier[7] provides strong evidence in support of the greater reliability of the solubility data reported here.*

4. DISCUSSION

Although the temperature-dependence of k for the aluminum–germanium and gallium–germanium systems is very similar in form to the results obtained for the tin–germanium and tin–silicon systems,[2] the relatively rapid rise in k with temperature near the semiconductor melting points cannot reasonably be attributed to the same cause in all four cases. For the tin–germanium and tin–silicon systems, this behavior was explained in terms of the presence of significant positive departures from ideality (Raoult's law) in the liquidus alloys at the higher temperatures and impurity concentrations. However, this explanation does not apply to the gallium–germanium system since the liquidus alloys appear to be nearly ideal, while in the aluminum–germanium system negative, instead of positive, departures from ideality are expected.[11,15]

The failure of liquid-phase interactions to account for the observed variation of k with temperature indicates the presence of departures from

* Recently, JOHN[20] has discussed some crystal-pulling experiments in which he grew germanium crystals from melts containing 63 and 55 atomic per cent gallium and aluminum, respectively. His resistivity measurements on these two crystals may be interpreted in terms of recent liquidus-curve[11] and resistivity[7] data to give values of k of 0·01 at $\sim$ 660°C for gallium and 0·002 at $\sim$ 610°C for aluminum. (These figures differ from those quoted by JOHN, who used different liquidus data and assumed an arbitrary figure for the hole mobility, lacking experimental data.) In the case of gallium, JOHN's data point to a value of $k \sim 40$ per cent lower than our work indicates at the same temperature. This lack of agreement may well be due to experimental error. In the case of aluminum, however, the value of k inferred from JOHN's data is lower by a factor of 8 than our data would indicate. The source of this discrepancy is not obvious. While our aluminum data appear to be more consistent with the gallium solubility results and with the resistivity data,[7] it would certainly be desirable to repeat JOHN's crystal-pulling experiments. There is the slight possibility that, at the higher growth rates used by JOHN, a solubility lower than the equilibrium value would result if a rate-limiting step was present at the growing interface (C. D. THURMOND, private communication).

ideal dilute-solution behavior (Henry's law) in the solid solutions of aluminum and gallium in germanium. Indeed, departures from Henry's law in even very dilute solid solutions of donors or acceptors in germanium are to be expected from the work of REISS[16], who considered the effect of ionization of the donor or acceptor on the equilibrium between the impurity in the solid solution and that in an external phase. If we assume that REISS's treatment is applicable here, the equilibria in question are, for an acceptor element, M,

$$M(\text{in liquidus alloy}) \rightleftarrows M(\text{in solidus alloy}) \rightleftarrows \rightleftarrows M^- + e^+(\text{in solidus alloy}) \quad (1)$$

where e^+ represents a free hole. The source of the departures from Henry's law is apparent if the above equilibria are considered in terms of the activity of the impurity in the liquidus alloy, a_L, the atom fractions of the neutral and ionized acceptor, x_n and $x_i (x_S = x_n + x_i)$, and the activity coefficients, γ_L, γ_S and γ_n defined by the relations

$$a_L = \gamma_L x_L = \gamma_S x_S = \gamma_n x_n \quad (2)$$

which are valid as long as the same standard state is used for both liquid and solid solutions.* It follows from equation (2) that γ_S, which relates the total impurity concentration, x_S, to the activity in the liquid alloy, can be written as

$$\gamma_S = \gamma_n (x_n/x_S) = \gamma_n F_n \quad (3)$$

where we let $F_n = (x_n/x_S)$, the fraction of the impurity atoms which remain electrically neutral. If, as REISS assumed, the neutral impurity obeys Henry's law (γ_n is constant at a given temperature), any variation of F_n with the impurity concentration will result in a like variation of γ_S. Hence, the impurity concentration, x_S, would not be directly proportional to a_L and there would result a departure from Henry's law owing to the ionization of the acceptor.

The effect of ionization on the magnitude and temperature-dependence of k can be obtained by combining equations (2) and (3) to give:

$$k \equiv x_S/x_L = \gamma_L/\gamma_S = \gamma_L/\gamma_n F_n \quad (4)$$

or

$$\frac{\partial \ln k}{\partial 1/T} = \left(\frac{\partial \ln \gamma_L}{\partial 1/T}\right)_{\text{liquidus}} - \left(\frac{\partial \ln \gamma_n}{\partial 1/T}\right)_{\text{solidus}} - \left(\frac{\partial \ln F_n}{\partial 1/T}\right)_{\text{solidus}} \quad (5)$$

Thus, the temperature-dependence of k depends on: (1) the variation of γ_L along the liquidus curve, (2) the variation of γ_n along the solidus curve and (3) the change in the degree of ionization, as represented by F_n, along the solidus curve. Unfortunately, no quantitative experimental data are available on any of these three quantities. However, certain reasonable assumptions and approximations can be made which allow one to predict at least qualitatively the general form of the change in k with temperature. The assumption that the neutral impurity obeys Henry's law permits the approximation to be made that

$$\left(\frac{\partial \ln \gamma_n}{\partial 1/T}\right)_{\text{solidus}} \approx \left(\frac{\partial \ln \gamma_n}{\partial 1/T}\right)_{x_n} = \frac{\bar{H}_n - H^0}{R} \quad (6)$$

where $(\bar{H}_n - H^0)$ is the differential heat of solution of the neutral impurity in the solid solution. [Selecting as our standard state the pure liquid impurity, $(\bar{H}_n - H^0)$ corresponds to the heat of the reaction M (pure liquid) $= M$ (neutral, in solid solution).] Furthermore, we may reasonably expect that $(\bar{H}_n - H^0)$ will vary only slightly with temperature, in which case the terms in equation (6) would be essentially constant. Therefore, if no ionization effects were present and if the liquid-phase departures from ideality were negligible, we would expect a $\log k$ versus $1/T$ plot to be linear. Thus, we may consider the $(\partial \ln \gamma_L/\partial 1/T)$ and $(\partial \ln F_n/\partial 1/T)$ terms in equation (5) as perturbations causing the $\log k$ versus $1/T$ plots to deviate from linearity.

Let us now apply the above considerations to a specific case, the gallium–germanium system. The situation for this system is simplified by the fact that the liquidus alloys appear to be nearly ideal,[11,15] so that the term $(\partial \ln \gamma_L/\partial\, 1/T)$ can be neglected. Hence, if our assumptions are correct, the observed departures from linearity of the

* These relations follow from the requirement that at equilibrium the chemical potentials of a given component must be equal in the different phases. The activity a_L is defined by the relation $\mu_L = \mu^0 + RT \ln a_L$, where μ_L and μ^0 are the chemical potentials of the impurity in the liquidus alloy and in the standard state (e.g. pure liquid or pure solid impurity).

VOL 11 195

log k versus $1/T$ plot for the gallium–germanium system must be due to ionization as expressed in the $(\partial \ln F_n/\partial\, 1/T)$ term. The calculation of F_n for both the gallium–germanium and aluminum–germanium systems is complicated by the fact that the solid solutions, which contain as many as 5×10^{20} impurity atoms/cm^3, are highly degenerate over much of the temperature range. In addition, little is known about the band structure of germanium at high temperatures. However, as a first approximation, estimates of F_n have been made by the method of BLAKEMORE[17], who calculated the variation of the Fermi level in germanium with temperature and impurity concentration on the basis of a very simple band model and simple Fermi–Dirac statistics. With this approach, the results indicate that in the range 300–800°C, where the solidus alloys are highly degenerate, F_n varies only slightly in the range 0·85–0·9, while above 800°C, F_n falls relatively rapidly to a value of about 0·4 at the melting point of germanium, where the solid solubility goes to zero.* From these estimates of F_n and equations (4) and (5), one would predict that the log k versus $1/T$ plot would depart only slightly from linearity between 300 and 800°C, while at higher temperatures k would rise relatively rapidly. It is evident from Fig. 6 that this prediction is at least qualitatively in agreement with the experimental results. Quantitatively, the magnitude of the predicted rise in k is within a factor of two of the observed rise at the high temperature. Similar agreement is found for the aluminum–germanium system when the non-ideality of the liquid solutions is considered. A detailed analysis of the available solid-solubility data for a number of germanium alloy systems, including aluminum–germanium and gallium–germanium, in terms of ionization and liquid-phase interactions is in preparation and will be published elsewhere.[18]

* Since BLAKEMORE assumes that the valence band overlaps the impurity band at high impurity concentrations, it follows that, although F_n may be nearly unity, each acceptor impurity essentially contributes a hole to the valence band. Thus, the distinction between a "neutral" and an "ionized" impurity becomes, perhaps, a matter of definition, and it should be emphasized that here F_n is simply the fraction of empty acceptor levels as given by BLAKEMORE's treatment.

Acknowledgements—The authors are indebted to Mrs. M. E. BOTT and C. L. LUKE for the spectrophotometric analyses, to D. BABUSCI for the spectroscopic analyses and to M. KOWALCHIK for assistance in certain experiments. Numerous stimulating discussions with C. D. THURMOND are gratefully acknowledged. The comments of M. TANENBAUM are also appreciated.

REFERENCES

1. TRUMBORE F. A., *J. Electrochem. Soc.* **103,** 597 (1956).
2. TRUMBORE F. A., ISENBERG C. R. and PORBANSKY E. M., *J. Phys. Chem. Solids* **9,** 60 (1959).
3. THURMOND C. D., TRUMBORE F. A. and KOWALCHIK M., *J. Chem. Phys.* **25,** 799 (1956).
4. HALL R. N., *J. Phys. Chem. Solids* **3,** 63 (1957).
5. BRIDGERS H. E. and KOLB E. D., *J. Chem. Phys.* **25,** 648 (1956).
6. See, for example, LUKE C. L., *Analyt. Chem.* **28,** 1276 (1956).
7. TRUMBORE F. A. and TARTAGLIA A. A., *J. Appl. Phys.* **29,** 1511 (1958).
8. GREINER E. S. and BREIDT P., *J. Metals* **7,** 187 (1955).
9. HASSION F. X., THURMOND C. D. and TRUMBORE F. A., *J. Phys. Chem.* **59,** 1076 (1955).
10. GREINER E. S., *J. Metals* **4,** 1044 (1952).
11. THURMOND C. D., HASSION F. X. and KOWALCHIK M., American Chemical Society Meeting, New York, N.Y. (Sept. 1957).
12. BURTON J. A., *Physica's Grav.* **20,** 845 (1954).
13. HALL R. N., in *Fortschritte der Hochfrequenztechnik* (to be published).
14. DE ROCHE N., *Z. Metallk.* **48,** 59 (1957).
15. THURMOND C. D., *J. Phys. Chem.* **57,** 827 (1953).
16. REISS H., *J. Chem. Phys.* **21,** 1209 (1953).
17. BLAKEMORE J. S., *Proc. Phys. Soc.* **71,** 692 (1958).
18. TRUMBORE F. A. and THURMOND C. D. (to be published).
19. CONWELL E., *Proc. Inst. Radio Engrs.* **46,** 128 (1958).
20. JOHN H., *J. Electrochem. Soc.* **105,** 741 (1958).

J. Phys. Chem. Solids Pergamon Press 1959. Vol. 11. pp. 246–248. Printed in Great Britain.

ON THE THERMAL EXPANSION AND GRÜNEISEN FACTOR OF VITREOUS SILICA

D. F. GIBBONS

Bell Telephone Laboratories, Murray Hill, New Jersey

(*Received* 13 *April* 1959)

Abstract—The expansivity and linear thermal-expansion coefficient of vitreous silica have been measured between 4·2 and 140°K. Below 130°K the expansivity $\Delta l/l_{273\cdot2}$ is somewhat greater than the value from previous measurements. This difference may be due to variations in manufacture of such a noncrystalline solid. The Grüneisen factor, γ, is calculated and its variation with reduced temperature T/θ_∞ is compared with that of silicon and indium antimonide. In contrast to these crystalline solids, the temperature variation of γ for vitreous silica is dictated by the $1/C_v$ term in the temperature region investigated.

THE variation of the Grüneisen factor with temperature can give information about the lattice-vibration spectrum of solids. Recently, both BARRON[1] and BLACKMAN[2] have considered the theoretical aspects of this problem. In particular, solids for which the Grüneisen factor has negative values (i.e. solids for which the volume coefficient of thermal expansion is negative) have been considered by the above authors. The validity of BARRON's general arguments was demonstrated[3] by comparison with measurements on germanium, silicon, indium antimonide and vitreous silica, a noncrystalline solid. However, thermal-expansion data were not available for vitreous silica below 123°K, the beginning of the interesting region. The purpose of the present work was to obtain data on the coefficient of linear thermal expansion of vitreous silica between 4 and 130°K and to evaluate Grüneisen's factor over the interesting temperature range.

The specimens, after grinding from optical-quality vitreous silica (Amersil Co.), were annealed at 800°C to remove internal stresses before the measurements were made. The expansivity β, $[\Delta l/l_{273\cdot2}]$ was measured by an optical interferometer described elsewhere.[3] Temperatures could be controlled to within $\pm 0\cdot05$°K. The minimum in the expansivity, β, from the present investigation was calculated to be $-17\cdot5\times10^{-6}$, which agrees well with the value of $-18\cdot0\times10^{-6}$ reported by BEATTIE *et al.*[4] and is certainly within the experimental accuracy.*

Fig. 1 shows the values of expansivity, β, obtained in the present work and also those of

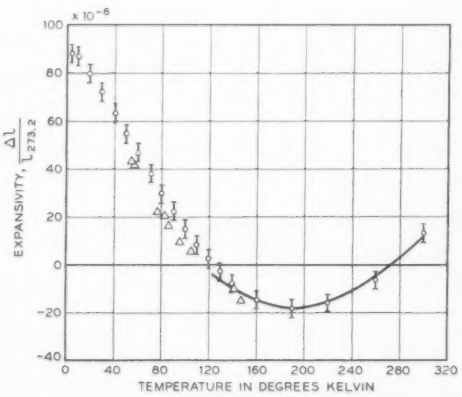

FIG. 1. Expansivity of vitreous silica. The full curve is that reported by BEATTIE *et al.*[4] The points △, below 130°K, are taken from BEATTIE's Table 1, p. 375, and were not used in calculating the full curve. The points ○ are for the present work.

* In both this work and that of BEATTIE, changes in length could be measured to an accuracy of better than 0·05 of a fringe spacing, giving a resolution of ~ 150 Å.

BEATTIE *et al.* Below 140°K there is some deviation between the present results and those of BEATTIE; however, since vitreous silica is a noncrystalline solid, the origin of this deviation may be inherent in the specimens, as they were from different suppliers and twenty years apart in manufacture. Table 1, which contains the average of three separate runs, gives values for expansivity, β, and linear thermal-expansion coefficient $\alpha[(1/l)(dl/dT)_p]$ between 10 and 140°K. It is of interest to note that the maximum in the thermal-expansion coefficient occurs at approximately 40°K, and at 4·2°K the volume of vitreous silica is 0·024 per cent greater that at 273·2°K.

Table 1. *Expansivity and coefficient of linear thermal expansion of vitreous silica*

T(°K)	$\beta = \dfrac{\Delta l}{l_{273\cdot2}}$	$\alpha = -\dfrac{1}{l}\left(\dfrac{dl}{dT}\right)_p$
	$\times 10^{-6}$	$\times 10^{-8}$
5	+87·5	—
10	+86·2	−40·9
20	+79·7	−74·7
30	+71·9	−85·4
40	+63·0	−86·7
50	+54·7	−84·6
60	+46·4	−82·9
70	+38·0	−80·1
80	+30·2	−76·7
90	+22·4	−72·7
100	+15·4	−67·9
110	+ 8·3	−62·1
120	+ 2·9	−55·6
130	− 2·6	−48·5
140	− 7·6	−41·2

The Grüneisen factor, γ, is given by the expression

$$\gamma = \frac{\alpha V}{\chi C_v}.$$

The data of FINE[5] for compressibility, χ, and of WESTRUM[6] for C_p used in calculating γ were for vitreous silica from the same supplier; V was taken as 27·4 cm^3 mole^{-1}. Fig. 2 shows γ as a function of reduced temperature T/θ_∞, where θ_∞ is the high-temperature Debye limit and is 495°K. The curves for γ versus T/θ_∞ for silicon and indium antimonide are shown for comparison. The value of γ for vitreous silica starts to decrease rapidly in the region of $T/\theta_\infty = 0{\cdot}2$, the change being similar to that for silicon and indium antimonide. In crystalline silicon and indium antimonide, the rate of change of C_v with temperature is considerably less (by a factor of approximately 15) than that of α, and so the minimum in α is exhibited in the Grüneisen factor γ. In the case of vitreous silica, however, the reverse is true, and so the minimum in α is masked. As has been pointed out by ANDERSON[7], up to 80 per cent of the thermal energy below 50°K arises from non-acoustic sources, and this is responsible for the strong temperature-dependence of C_v below 50°K. In the temperature region investigated, therefore, the $1/C_v$ term dominates the expression for the Grüneisen factor.

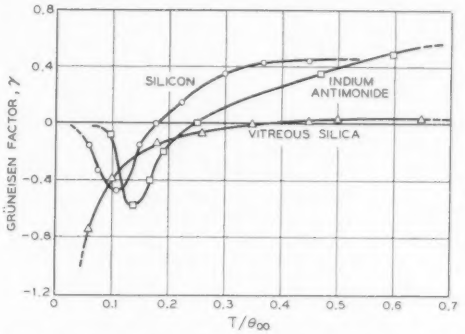

FIG. 2. Grüneisen's factor γ as a function of T/θ_∞. Silicon, $\theta_\infty = 674$°K; indium antimonide, $\theta_\infty = 214$°K; vitreous silica, $\theta_\infty = 495$°K.

The results on Grüneisen's factor, γ, show agreement with BARRON's general expectation that it will fall off most rapidly in the region below $T/\theta_\infty \sim 0{\cdot}3$, but they do nothing to clear up the confusion which exists in the understanding of vitreous silica at low temperatures; there is an enormous discrepancy between the Debye temperature, θ_∞, obtained from acoustic techniques (495°K) and that obtained from thermal measurements (374°K).[8]

Acknowledgements—I would like to thank Dr. O. L. ANDERSON for providing the samples and for many stimulating discussions and Mr. V. G. CHIRBA for his help in making the measurements.

REFERENCES

1. Barron T. H. K., *Phil. Mag.* **46,** 720 (1955).
2. Blackman M., *Phil. Mag.* **3,** 831 (1958).
3. Gibbons D. F., *Phys. Rev.* **112,** 136 (1958).
4. Beattie J. A., Blaisdell B. E., Kaye J., Gerry H. T. and Johnson C. A., *Proc. Amer. Acad. Arts Sci.* **74,** 371 (1940–42).
5. Fine M. E., Van Duyne H. and Kenney N. T., *J. Appl. Phys.* **25,** 402 (1954).
6. Westrum E. F., Jr., Private communication.
7. Anderson O. L. and Dienes J., *Transactions of the Conference on Noncrystalline Solids* John Wiley, New York (1959).
8. Morrison J. A., Submitted to *J. Phys. Chem. Solids.*

VOL
11
195

J. Phys. Chem. Solids Pergamon Press 1959. Vol. 11. pp. 249–256. Printed in Great Britain.

ON THE ANOMALOUS THERMODYNAMIC PROPERTIES OF ICE*

P. A. GIGUÈRE

Department of Chemistry, Laval University, Quebec, Canada

(*Received* 19 *May* 1959

VOL. 11 1959

Abstract—Comparison of the measured heat capacity of ice with that of crystalline hydrogen peroxide reveals some unusual features in the former. For instance, the translational heat capacity of ordinary ice below 100°K bears no resemblance to a Debye curve. In that range the values of θ_D increase considerably with temperature: from 192° at 10°K up to 318° at ~ 100° K for ordinary ice, and from 180° at 15°K up to 300° at ~ 80°K for heavy (D_2O) ice. Various criteria point to the high-temperature limiting values of θ_D as the normal ones. Like the zero-point entropy, the anomalously large heat capacity of ice below 100°K must be a consequence of frozen-in disorder. Calculations of the thermodynamic functions of ice and crystalline hydrogen peroxide, based partly on spectroscopic data, support the view that the order–disorder transition in ice would be of the λ type, with a λ point in the neighbourhood of 80°K. On structural grounds, the occurrence of Bjerrum defects in ice is ruled out.

1. INTRODUCTION

THE exceptional behaviour of certain physical properties of ordinary ice has been generally interpreted as an indication of disorder in its crystal structure. From recent discussions of that much-debated problem, it appears that disorder in ice must be of two different kinds: one, due to the statistical positions of the hydrogen atoms,[1] which is responsible for the zero-point entropy and also, presumably, for the glass-like appearance of the molecular spectra[2]: the other, related to an apparent mobility of the H_2O molecules in the temperature range just below the melting point, which could account for such phenomena as the unusually large dielectric constant of ice down to about —70°C,[3] the streaking of X-ray diffraction patterns,[4] the so-called "slickness" of ice[5] &c. Intuitively one would expect such major disorder to be reflected in the thermodynamic properties. Since accurate heat-capacity data are available for ordinary ice down to 10°K[6] and for D_2O ice down to 15°K,[7] the question arises: In what respect are these quantities unusual if so?

2. THE HEAT CAPACITY OF ICE

The existing theories of the heat capacity of solids have been quite successful in the case of simple atomic and ionic crystals. For molecular crystals the situation is much less advanced because of the lack of experimental data and the great diversity of structures encountered. What is usually done is to make an attempt to calculate the translational contributions by means of a Debye function, using a single characteristic temperature θ_D (generally from calorimetric measurements), and the vibrational contributions through Planck–Einstein functions, using experimental (infrared and Raman) frequencies. The contribution of the internal modes is estimated as for the free molecules. Agreement between the calculated and the measured heat-capacity curves is often surprisingly good under the circumstances. However, this is no proof of the correctness of the method, but rather a consequence of the fact that the calculated thermodynamic functions are not very sensitive to a particular choice of frequencies.

Nevertheless, in the case of ice the above procedure turns out to be entirely inapplicable. Indeed, the translational heat capacity—the only one appreciably active below 100°K in ordinary ice—cannot be assimilated even roughly to a

* Presented in part at the Fourth Congress of the International Union of Crystallography in Montreal, July 1957.

Table 1. *Comparison of the translational heat capacity of ice and hydrogen peroxide with Debye functions*

H_2O ice				D_2O ice				H_2O_2		
T(°K)	Obs.	$\theta_D = 192°$	$\theta_D = 318°$	T(°K)	Obs.	$\theta_D = 180°$	$\theta_D = 300°$	T(°K)	Obs.	$\theta_D = 234°$
10	0·066	0·066	0·015	15	0·270	0·267	0·058	12	0·062	0·062
20	0·490	0·50	0·12	20	0·532	0·60	0·14	20	0·295	0·298
30	0·984	1·39	0·39	30	1·043	1·58	0·46	30	0·872	0·88
40	1·466	2·34	0·85	40	1·524	2·57	0·96	40	1·648	1·65
50	1·896	3·14	1·42	50	1·977	3·36	1·58	50	2·40*	2·43
100	3·796	4·99	3·79	80	3·234	4·69	3·23			

* Corrected for the librational heat capacity.

Debye curve with a single value of θ_D. If the latter be taken as 192° (from the calorimetric data at 12°K) then the calculated value of C_v becomes altogether too large at higher temperatures (Table 1); conversely, a much higher value of θ_D, 318°, yields the correct value of C_v at about 100°K, but too small values at lower temperatures. A similar situation obtains in heavy ice, for which the corresponding values of θ_D are 180° and 300°. Whether or not this peculiarity is specific to ice may be inferred from comparison with related compounds. Without doubt hydrogen peroxide is the substance *par excellence* for comparison with water, since both have the same type of crystal structure, namely a three-dimensional lattice of hydrogen bonds of the same strength and length.[8] On the other hand, hydrogen peroxide shows none of the anomalies of the water substance such as residual entropy, expansion on freezing, temperature of maximum density of the liquid, &c. Therefore, it is of great interest that the measured heat capacity of crystalline hydrogen peroxide[9] follows quite closely a Debye curve, with the calorimetric $\theta_D = 234°$ up to 50°K (Table 1) and even higher when appropriate correction for the contribution of other modes is made as explained below.

A plot of θ_D against temperature illustrates further the singularity of ice in that respect. As shown in Fig. 1, for various hydrides of the first-row elements, θ_D is fairly constant at low temperatures, i.e. for translation only, until other degrees of freedom come into play, whereupon θ_D begins to decrease. In striking contrast, for ice and heavy ice θ_D increases regularly from the low-temperature limiting value up to a maximum in the neighbourhood of 100°K. For D_2O ice, the maximum value

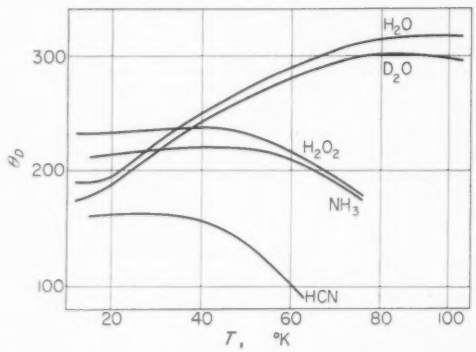

FIG. 1. Variation of θ_D with temperature for a few simple hydrides.

of θ_D is reached at ~ 80°K; because of the larger moments of inertia of the isotopic molecule, the vibrational contribution becomes noticeable at 100°K. Again, considering the great similarity of ice and hydrogen peroxide, the former, because of its smaller molecular mass, should have the lower

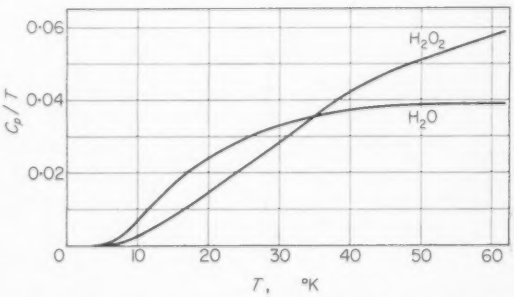

FIG. 2. Low-temperature heat capacity of ice and crystalline hydrogen peroxide.

translational heat capacity at all temperatures, contrary to observation (Fig. 2). In fact both crystals have the same value of the calorimetric entropy at $\sim 55°$.

3. THE θ VALUES OF ICE

A number of relationships have been proposed to calculate θ, the characteristic temperature of a crystal, from various physical properties. As pointed out by BLACKMAN[10], these various values of θ cannot be expected to be equal. Most of the relationships have been derived for simple metallic or ionic lattices (cubic system only) and some include semi-empirical constants. Therefore their application to other types of crystals must be viewed with caution.* An early attempt to calculate the heat capacity of ice by means of one of these equations had led NERNST[13] to postulate double molecules, $(H_2O)_2$, in the solid state. More recently, a set of acoustic frequencies was derived from the elastic constants of ice,[14] which led to the improbable value $\theta \simeq 100°$.[15] In the following paragraphs some of these relationships are used in a comparative manner only.

(a) *Lindemann's equation*

According to LINDEMANN, θ for a crystal is related to its melting point T_m as follows:

$$\theta = B\sqrt{\left(\frac{T_m}{MV^{\frac{2}{3}}}\right)},$$

where B is a constant for crystals of the same kind, M the molecular weight and V the molecular volume. Since ice and crystalline hydrogen peroxide have very nearly the same melting point and molecular volume,[16] their θ values should be in the inverse half-power ratio of the molecular weight; hence $\theta_{H_2O} = \theta_{H_2O_2}\sqrt{(34/18)} = 320°$, in good agreement with the maximum value of the calorimetric θ_D (Fig. 1). The near coincidence of the two values of θ is all the more remarkable as both the melting point and density of ice are abnormal. Incidentally, it follows from LINDEMANN's equation that the θ values of D_2O ice and of ordinary ice should be in the ratio 1 : 1·05.

(b) *Intermolecular force constants*

Through correlation of the vibrational spectra with the symmetry properties of molecular crystals, it is possible to calculate with fair accuracy the intermolcular force constants. From a normal co-ordinate treatment, MILLER[17] found for k', the principal force constant for ice, values ranging from 0·24 to $0{\cdot}3\times10^5$ dynes/cm, depending on various possible assignments, and for crystalline hydrogen peroxide, the unique value $0{\cdot}25\times10^5$ dynes/cm. The latter may be used safely for both solids in view of the near equality of their O–H ... O bonds (2·76 Å in ice and 2·78 Å in hydrogen peroxide). Now, for three-dimensional hydrogen-bonded lattices, such as exist in these two crystals, the mean translational frequency of the molecules ν_T may be estimated roughly from the usual expression for the simple harmonic oscillator:

$$\nu_T = \frac{1}{2\pi}\sqrt{\left(\frac{k'}{\mu}\right)}$$

where μ is the reduced mass of the system, in this case a pair of adjacent molecules undergoing oscillations with respect to each other. This leads to the value $\nu_T = 218$ cm^{-1} and, therefrom, $\theta = 314°$ for ice. For hydrogen peroxide, $\nu_T = 156$ cm^{-1} and $\theta = 225°$, the latter quite close to the calorimetric value of θ_D.

(c) *Lattice frequencies*

The above calculated values of ν_T are merely average values, since one may normally expect a whole spectrum of lattice frequencies in these crystals. For instance, in the Raman spectrum of the single crystal of hydrogen peroxide,[18] four or five bands have been found below 200 cm^{-1}, none of which corresponds exactly to the above value of $\nu_T = 156$ cm^{-1}. In the case of ice, the molecular spectra, in both the Raman and infrared ranges, are very diffuse because of hydrogen bonding and the disordered structure. The region below 300 cm^{-1} has not yet been explored systematically in

* The reverse procedure was followed by OWSTON[11], who estimated the mean amplitude of thermal motions of the molecules from θ_D. Using the values 192° for ordinary ice and 163° for D_2O ice, he obtained r.m.s. amplitudes considerably larger than those found in a neutron-diffraction study of D_2O ice.[12] Substitution of the high-temperature limiting values of θ_D in the Debye–Waller relationship leads to much better agreement with the neutron-diffraction results.

the infrared range,* but a number of Raman studies have revealed a strong, fairly wide band centering around 200–220 cm^{-1} (cf. OCKMAN[19] for a recent review). The slightly prominent maximum at 213 cm^{-1} reported by NARAYANASWAMY[20] may reasonably be taken as the average translational frequency of the H_2O molecules in ice. WHALLEY[21] has used it to evaluate the zero-point translational energy, 685 cal/mole; as this quantity is equal to $9/8\ R\theta$ in the Debye equation, one finds $\theta = 306°$ for ice.

(d) *Isotope effect in* D_2O_2 *ice*

Since the heat-capacity curve of heavy ice is known with the same accuracy as that of ordinary ice, the difference between the two may be used to evaluate the effect of isotope substitution on the rotational heat capacity, and hence to differentiate between the latter and the translational heat capacity at low temperatures. Such computations have been made by BLUE[22], who found $\theta = 315°$ for the translation heat capacity. BLUE has remarked that a Debye curve (with $\theta = 315°$) fits rather poorly the measured heat capacity, at low temperatures and has suggested that it might be due in part to failure of the Debye theory. However, the anomalies found in the case of ice are certainly too large to be accounted for in terms of uncertainties in that theory, even granting its approximate nature.

Summing up, the excellent agreement among the various values of θ derived from quite different sources, namely

(i) Maximum value from calorimetric data	318°
(ii) LINDEMANN's relationship,	320°
(iii) Crystalline force constants,	314°
(iv) Average translational frequency	306°
(v) Isotope effect in heavy ice,	315°

is strong evidence for the characteristic temperature to be expected for the ice crystal.

4. THE CALCULATED HEAT CAPACITY OF ICE

Using the above "normal" value of θ for ice, one may calculate, by the method already described in Section 2, its entropy and heat capacity as a function of temperature for comparison with the actual values. It has been rightly said that such calculations cannot inspire much confidence unless they are based entirely on spectroscopic data, and our knowledge of the lattice frequencies of ice is rather scanty, as mentioned above. Yet, again, the main purpose sought here is a correlation with hydrogen peroxide. For expediency an extremely simplified model was assumed, with molecules essentially unaffected by their neighbours in their oscillations about equilibrium positions in the crystal lattice (the Einstein approximation). The contribution of the internal modes was evaluated with Planck–Einstein functions, using the well-known frequencies: $\nu_2 = 1640\ cm^{-1}$ for H_2O, and $\nu_2 = 1405$, $\nu_3 = 880$, $\nu_4 = 690$ and $\nu_6 = 1385$ for H_2O_2 (the O–H stretching modes do not contribute appreciably to C_v in the crystals). The same functions were used for the librational modes[2,23] with $\nu_R = 800$–$820\ cm^{-1}$ for ice and $\nu_A = 656\ cm^{-1}$, $\nu_B = 289$, and $\nu_C = 245\ cm^{-1}$ for hydrogen peroxide. The last two, from Raman spectrum of the single crystal,[18] are roughly in the correct ratio to ν_A with respect to the moments of inertia of the H_2O_2 molecule. As may be judged from the results in Table 2, the thermodynamic properties of the hydrogen peroxide crystal, in striking opposition to those of ice, can be estimated with fair accuracy from the calorimetric value of θ_D and appropriate optical data.

5. THE ZERO-POINT ENTROPY OF ICE

An interesting feature of the above results is the fact that the calculated entropy of ice in the neighbourhood of 100°K is smaller than the experimental quantity by about the same amount (0·8 e.u.) as the residual entropy.† From this one might speculate that the disorder in ice contributes equally to the zero-point entropy and the "excess" calorimetric entropy over the range 0–100°K. PAULING[1] has calculated by two different methods the residual entropy for his random structure of ice as $R \ln (3/2) = 0{\cdot}806$ e.u. These are to be compared with the observed quantities, viz. 0·82 e.u.

* *Note added in proof*: A very recent investigation of that spectrum as far as 200 cm^{-1} has, indeed, detected a distinct absorption band near 220 cm^{-1} in agreement with the Raman spectrum. (G. C. PIMENTEL, private communication.)

† A smaller difference (0·65 e.u.) is found in the case of D_2O ice, using $\theta_D = 305°$ and vibrational frequencies of 600–620 cm^{-1} for the D_2O molecules.[23]

for H_2O ice and 0·77 e.u. for D_2O ice. Various authors have re-examined critically PAULING's original derivations, particularly as regards the assumption of equal probability of the $(3/2)^N$ possible configurations.[24–26] More recently MEIJERING[27] has pointed out that in PAULING's calculations probabilities are assumed without justification to be mutually independent. However, after an elaborate recalculation he arrived at a value only some 5 per cent higher than PAULING's original result. It was also suggested at one time[15] that the T^3 region in ice might start well below 10°K, so that the now-accepted value of the calorimetric entropy, including extrapolation using $\theta_D = 192°$, is too small by at least 0·82 e.u. (or conversely the zero-point entropy is too large by the same amount). However, this is rather unlikely in view of the narrow temperature range involved. Furthermore, MACDOUGALL and GIAUQUE[28] have shown experimentally that "the heat capacity of ice between 0 and 4°K is zero within an accuracy of 0·01 cal/deg".

More plausible is the suggestion of PITZER and POLISSAR[29] of an unrealized λ transition in ice at some temperature below 100°. From the energy change involved, and assuming a dielectric constant of 3, these authors estimated the λ point as $T_\lambda \simeq 60$°K. This agrees well with the data in Table 2, possibly with a slightly higher T_λ (80°). In that conjecture an hypothetical, perfectly ordered ice crystal at very low temperature would exhibit on warming a heat-capacity increase following approximately a Debye curve with $\theta \simeq 310°$ up to about 70°K, followed by a rapid rise due to a

Table 2. Calculated and observed thermodynamic functions of ice and hydrogen peroxide

	Heat capacity					Entropy				
T(°K)	Transl.	Vibr.	Intra.	Total (C_v)	Obs. (C_p)	Transl.	Vibr.	Intra.	Total	Obs.
					Ice ($\theta = 320°$)					
10	0·015			0·015	0·065					0·02
20	0·115			0·115	0·490	0·04			0·04	0·177
30	0·37			0·37	0·984	0·124			0·124	0·464
40	0·83			0·83	1·466	0·292			0·292	0·811
50	1·39			1·39	1·896	0·535			0·535	1·18
60	2·01			2·01	2·304	0·852			0·852	1·57
80	3·01			3·01	3·075	1·55			1·55	2·33
100	3·75			3·75	3·796	2·31			2·31	3·10
120	4·28	0·03		4·31	4·434	3·05			3·05	3·85
160	4·90	0·20		5·10	5·550	4·37	0·03		4·40	5·28
200	5·27	0·55		5·82	6·744	5·50	0·11		5·61	6·65
240	5·48	1·08	0·01	6·57	8·013	6·50	0·26		6·76	7·99
270	5·57	1·57	0·025	7·16	8·960	7·11	0·45		7·56	8·99
					Hydrogen peroxide ($\theta_D = 234°$)					
10	0·062			0·062	0·062	0·02			0·02	0·02
20	0·298			0·298	0·295	0·096			0·096	0·099
30	0·88			0·88	0·872	0·310			0·31	0·318
40	1·65	0·02		1·67	1·648	0·676			0·67	0·670
50	2·43	0·11		2·54	2·505	1·12	0·01		1·13	1·126
60	3·11	0·28		3·39	3·372	1·62	0·05		1·67	1·66
80	4·03	0·79		4·82	4·895	2·64	0·21		2·85	2·83
100	4·60	1·34	0·01	5·95	6·144	3·61	0·43		4·04	4·06
120	4·97	1·84	0·04	6·85	7·164	4·47	0·77	0·01	5·25	5·27
160	5·37	2·70	0·21	8·28	8·822	5·97	1·38	0·04	7·39	7·57
200	5·58	3·36	0·51	9·45	10·283	7·19	2·06	0·23	9·36	9·70
240	5·68	3·85	0·92	10·45	11·86	8·22	2·73	0·23	11·18	11·71
270	5·74	4·45	1·26	11·45	13·02	8·89	3·19	0·36	12·44	13·18

co-operative disordering process (Fig. 3). Some indication of a trend towards a more ordered structure may be seen in the observation of GIAUQUE and STOUT[6] that ordinary ice is very sluggish in reaching thermal equilibrium upon cooling from

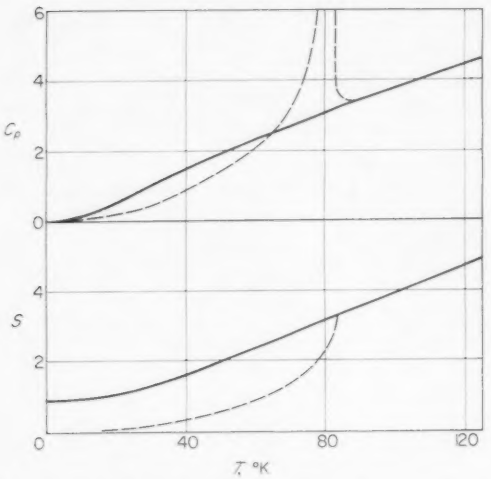

FIG. 3. Hypothetical warming curves for a perfectly ordered ice crystal – – – – – –, compared with the experimental curves ——— for ordinary ice.

100 to 80°K. No such phenomenon was detected in the case of D_2O ice,[7] but this is not surprising as substitution of hydrogen by deuterium is bound to shift the λ point markedly. It may be worth noting here that a large-scale plot of the difference between the measured heat capacities of ordinary ice and heavy ice against temperature indicates a noticeable change of slope near 100°K.

6. STATIC AND DYNAMIC DISORDER IN ICE

Although the ice crystal may be considered as completely disordered—in the PAULING sense—at all temperatures, the nature of the disorder must change from the static at low temperatures to the dynamic in the neighbourhood of the melting point. Because changes of configuration are unlikely in an ideal crystal,[30] some defects are needed at which reorientation of the H_2O molecules can take place. The most obvious types of lattice defect are the ionized species H_3O^+ and OH^-, as pointed out by BJERRUM[25]. Their low equilibrium concentration in ice* is compensated by their high rate of diffusion through proton jumps along the O–O lines, mostly by quantum-mechanical tunnelling.[32]

However, the explanation of the high dielectric constant of ice solely by this mechanism[33–35] has been rejected by BJERRUM[25], who showed the need for other types of defects of the so-called orientational type. For these he postulated doubly-occupied bonds (*D*-defects), and vacant bonds (L-defects). Now the existence of such defects raise considerable difficulty from the structural viewpoint. Indeed, a doubly-occupied bond O–H H–O could not possibly be linear, as the two hydrogen atoms would be as near together (0·74 Å) as in the H_2 molecule. The diagrams used to depict such configurations are certainly unrealistic. Even taking into account thermal motions, for instance near the melting point, in the most favorable conditions there can be but one H atom per O–O bond. As for bent O–H H–O bonds, they are also ruled out because in their equilibrium positions the hydrogen atoms of adjacent water molecules are almost within van der Waals contact, 2·3 Å.† Consequently, rotation of H_2O molecules at large angle about one hydrogen bond in ice, whether by the classical mechanism or by "rotational proton jump", can only take place next to vacant sites, such as Schottky or Frenkel defects, or by a simultaneous process. Doubly-occupied bonds have been suggested for the H_2S crystal,[36] but there the intermolecular distances (5·76 Å) are more than twice as long as in ice, and the coordination number is high (12 compared to 4

* From electrical-conductivity measurements, the equilibrium concentration of each ion in pure ice is known to be of the order of one in 10^{13} H_2O molecules at −10°C.[31] No data are available for lower temperatures, but a very rough estimate based on the same value of the heat of self-dissociation as in liquid water indicates a maximum concentration of one in 10^{21} molecules at about −180°C.

† The nearness of the H_2O molecules in ice may account for the abnormally high librational frequencies, 800–850 cm^{-1}. By comparison with the hydrogen peroxide crystal, frequencies of about 650 cm^{-1} would be expected, as explained elsewhere.[2]

Note added in proof: Lately MUTTER, MECKE and LÜTTKE (*Z. Phys. Chem. N.F.* **19**, 83 (1959) have reported a new infrared spectrum of ice in which the librational frequency occurs precisely at 649 cm^{-1}. The nature of that spectrum has not been elucidated yet.

VOL. 11 1959

in ice) so that the position of the hydrogen atoms has little effect on the crystal packing. It is noteworthy that, in spite of the absence of hydrogen bonds and the rather open structure, molecular rotation does not seem to occur at either of the two λ points in the H_2S crystal.[37]

The existing data on the proton conductance in ice indicate that quantum-mechanical tunnelling is the rate-determining step.[38] Finally, it is worth emphasizing here that from a recent analysis of the mechanical relaxation in single crystals of ice,[39] a mechanism based on diffusion of *D*- and *L*-defects is entirely inconsistent with the experimental evidence, whereas, on the contrary, rearrangement of the hydrogen atoms among various possible configurations not only agrees qualitatively with the observations, but even predicts the right order of magnitude for the decrement. Since the dielectric relaxation in ice shows the same activation energy as the mechanical relaxation, it is logical to assume that both proceed via the same mechanism.

7. THE MOLECULAR SPECTRA OF ICE

As explained elsewhere,[2] the close resemblance of the infrared spectrum of ordinary polycrystalline ice to that of vitreous hydrogen peroxide—as distinct from that of the crystalline peroxide—appears as a consequence of the random distribution of the hydrogen atoms (the Pauling model). In particular, the 3μ region shows hardly any sign of resolution of the two O–H stretching frequencies otherwise known to lie approximately at 3140 and 3250 cm^{-1}. For hydrogen peroxide, where the splitting is roughly the same, both components are clearly separated in the crystalline spectrum but not in the amorphous spectrum; there also a single broad maximum is observed at intermediate frequency. Again, in the ice spectrum the overtone bands $2\nu_2$ and $2\nu_R$ are submerged in the diffuse fundamentals ν_3 and ν_2. It had been suggested by BORN[40] that the diffuseness of the ice bands could be due to proton jumps, but this explanation is ruled out by the fact that the infrared spectrum of ice is not appreciably altered on cooling down to liquid-air or even liquid-helium temperature.[41] Therefore, the glass-like nature of the ice spectra must be related to the static, not the dynamic disorder. In that connection it is worth noting here that the polarized infrared reflection spectrum of a crystal of ordinary ice shows a significant change in the 3μ region on cooling.[42] The broad band with a slight shoulder found at —26°C is resolved at —134°C into two distinct, fairly sharp peaks at 3137 and 3233 cm^{-1}. This is of interest in view of the well-known suggestion that, in the temperature range not too far below its melting point, ordinary ice is always covered with a film of liquid, which may account for the possibility of skating on ice.[5]

Like the infrared spectrum, the Raman spectrum of ice is characterized by rather diffuse bands, even for the single crystal.[19] In the O–H stretching region, the depolarization ratio was found to remain constant across each of the bands,[43] a further argument for the disordered structure. The contrast with the case of hydrogen peroxide is particularly striking in the low-frequency region; whereas in the latter crystal some eight distinct Raman shifts have been detected below 300 cm^{-1},[18] in ice the main feature is a very broad band extending from around 150 to 350 cm^{-1}. A number of very weak peaks have also been reported, but except for a few of them, notably that at 52 cm^{-1},[20,44] they have not been duplicated in the various investigations. The explanation for the different appearance of the low-frequency spectra must be sought in the structure of the two crystals. In ice, the packing is realized entirely through a regular three-dimensional lattice of hydrogen bonds, giving complete 4-co-ordination with almost perfect tetrahedral symmetry of the H_2O sites. On the other hand, in the hydrogen peroxide crystal,[8] neighbouring H_2O_2 molecules are linked through short hydrogen bonds (2·78 Å) forming infinite helices which, in turn, are held together by weaker hydrogen bonds (2·90 Å).

8. CONCLUSIONS

From the above considerations it is obvious that a satisfactory explanation of the thermodynamic properties of ice will require more experimental work. In particular, the calorimetric measurements should be extended down to 2 or 1°K for both ordinary and heavy ice, and the effect of added impurities (such as HF) investigated, for this is one way of introducing lattice defects with temperature-independent concentration.[30] Likewise the heat capacity of cubic ice[45] should be measured and its range of thermodynamic stability ascertained. The properties of an ice condenser charged

at liquid-air temperature[46] also seem to deserve further attention.

Much valuable information on the anomalies of the water substance may be gathered from comparison with hydrogen peroxide, as shown here. For instance, a clear indication of disorder in ice is its low entropy of melting, 5·26 e.u., as compared with 10·95 e.u. for hydrogen peroxide. Unfortunately, investigation of the physical properties of pure hydrogen peroxide in the solid state is hampered by its chemical instability. Measurements of electrical conductivity and dielectric behaviour would throw light on the problem of molecular mobility in ice in the temperature range just below the melting point. No streaking of the X-ray diffraction patterns has been observed,[47] although the temperature of the H_2O_2 crystal may have been too low. Lastly, there is no evidence for surface wetness or "slickness" of solid hydrogen peroxide as is the case for ice. For that purpoes the ingenious test devised by NAKAYA and MATSUMOTO[48] would no doubt be much easier than attempting to skate on pure, frozen hydrogen peroxide.

REFERENCES

1. PAULING L., *J. Amer. Chem. Soc.* **57,** 2680 (1935).
2. GIGUÈRE P. A. and HARVEY K. B., *J. Molecular Spectroscopy* **3,** 36 (1959).
3. SMYTH C. P., *Dielectric Behavior and Structure.* Chap. V. McGraw-Hill, New York (1957).
4. OWSTON P. G. and LONSDALE K., *J. Glaciol.* **1,** 118 (1951).
5. WEYL W. A., *J. Colloid Sci.* **6,** 389 (1951).
6. GIAUQUE W. F. and STOUT J. W., *J. Amer. Chem. Soc.* **58,** 1144 (1936).
7. LONG E. A. and KEMP J. D., *J. Amer. Chem. Soc.* **58,** 1829 (1936).
8. ABRAHAMS S. C., COLLIN R. L. and LIPSCOMB W. N., *Acta Cryst., Camb.* **4,** 15 (1951).
9. GIGUÈRE P. A., LIU I. D., DUGDALE J. B. and MORRISON J. A., *Canad. J. Chem.* **32,** 117 (1954).
10. BLACKMAN M., *The Specific Heat of Solids* in *Handbuch der Physik* Vol. VII, Part I. Springer, Berlin (1955).
11. OWSTON P. G., *Quart. Rev. Chem. Soc.* **5,** 344 (1951).
12. PATTERSON S. W. and LEVY H., *Acta Cryst., Camb.* **10,** 70 (1957).
13. NERNST W., *Theory of the Solid State.* Wolfskehlstiftung, Göttingen (1914).
14. FORSLIND E., *Swedish Cement and Concrete Res. Inst. Proc.* No. 21 (1954).
15. GRÄNICHER H., *Helv. Phys. Acta* **29,** 212 (1956.)
16. SCHUMB W. C., SATTERFIELD C. N. and WENTWORTH R. L., *Hydrogen Peroxide.* Reinhold, New York (1955).
17. MILLER R. L., Ph.D. Thesis, Brown University (1954).
18. TAYLOR R. C., *Symposium on Molecular Structure and Spectroscopy.* Columbus, Ohio (1957).
19. OCKMAN N., *Advances in Phys.* **7,** 199 (1958).
20. NARAYANASWAMY P. K., *Proc. Indian Acad. Sci.* **A27,** 311 (1948).
21. WHALLEY E., *Trans. Faraday Soc.* **53,** 1578 (1957).
22. BLUE R. W., *J. Chem. Phys.* **22,** 280 (1954).
23. GIGUÈRE P. A. and HARVEY K. B., *Canad. J. Chem.* **34,** 798 (1956).
24. ROWLINSON J. S., *Trans. Faraday Soc.* **47,** 120 (1951).
25. BJERRUM N., *Science* **115,** 285 (1952).
26. RUNDLE R. E., *J. Phys. Chem.* **59,** 680 (1955).
27. MEIJERING J. L., *Philips Res. Rep.* **12,** 333 (1957).
28. MACDOUGALL D. P. and GIAUQUE W. F., *J. Amer. Chem. Soc.* **58,** 1032 (1936).
29. PITZER K. S. and POLISSAR J., *J. Phys. Chem.* **60,** 1140 (1956).
30. GRÄNICHER H., *Z. Krist.* **110,** 432 (8).
31. EIGEN M. and DE MAEYER L., *Proc. Roy. Soc.* **A247,** 505 (1958).
32. CONWAY B. E., BOCKRIS J. O'M. and LINTON H., *J. Chem. Phys.* **24,** 834 (1956).
33. HUGGINS M. L., *J. Phys. Chem.* **40,** 723 (1936).
34. KAUZMAN W., *Rev. Mod. Phys.* **14,** 40 (1942).
35. LATIMER W. M., *Chem. Rev.* **44,** 59 (1949).
36. REDING F. P. and HORNIG D. F., *J. Chem. Phys.* **27,** 1024 (1957).
37. ALPERT N. L., *Phys. Rev.* **76,** 398 (1949).
38. CONWAY B. E. and BOCKRIS J. O'M., *J. Chem. Phys.* **28,** 354 (1958).
39. BASS R., *Proc. Roy. Soc.* **A247,** 462 (1958).
40. BORN M., *Nature, Lond.* **158,** 830 (1946).
41. HARVEY K. B., private communication.
42. OCKMAN N., Ph.D. Thesis, University of Michigan (1957).
43. MAISCH W., Ph.D. Thesis, Brown University (1956).
44. RASETTI F., *Nuovo Cimento* **9,** 72 (1932).
45. BLACKMAN M. and LISGARTEN N. D., *Proc. Roy. Soc.* **A239,** 93 (1957).
46. MURPHY E. J., *Trans. Amer. Electrochem. Soc.* **65,** 133 (1931).
47. LIPSCOMB W. N., private communication.
48. NAKAYA U. and MATSUMOTO A., *J. Colloid Sci.* **9,** 41 (1954).

J. Phys. Chem. Solids Pergamon Press 1959. Vol. 11. pp. 257–262. Printed in Great Britain.

NUCLEAR MAGNETIC RESONANCE IN GALLIUM ANTIMONIDE

D. J. OLIVER

Services Electronics Research Laboratory, Baldock, Herts, England

(*Received* 8 *May* 1959)

VOL. 11 1959

Abstract—The effects of both *n*-type and *p*-type impurities on the resonances of ^{69}Ga, ^{71}Ga and ^{121}Sb have been studied. *P*-type impurity concentrations of approximately 10^{19} cm^{-3} reduce the resonance intensity by $\sim$ 60 per cent in ^{69}Ga and ^{71}Ga and by 75 per cent in ^{121}Sb. This reduction is attributed to the quadrupolar interaction between the nuclei and the charged impurity centres and implies fairly large "antishielding factors". The values deduced are 49 for ^{121}Sb, 175 for ^{69}Ga and 321 for ^{71}Ga. A negative frequency shift of 1·3 kc/s was observed in the ^{121}Sb resonance for a *p*-type impurity concentration of 6×10^{19} cm^{-3}, and a similar shift was observed in an *n*-type sample (impurity concentration 2×10^{18} cm^{-3}). Both these displacements are ascribed to a second-order quadrupolar effect. No frequency shifts were observed for the gallium resonances.

1. INTRODUCTION

NUCLEAR magnetic resonance has been applied extensively, in recent years, to problems in solid-state physics. The technique has proved particularly valuable in the study of imperfections of various kinds, because the details of the nuclear resonance lines, exact frequency, width, shape, &c., are sensitive to the nuclear environment. Since imperfections play an important role in determining the properties of semiconductors, it might be expected that nuclear resonance would be especially useful in this field. Unfortunately germanium and silicon are not suited to this kind of study, because of the low abundance of the isotopes which possess magnetic moments. The situation is more favourable in the case of the III–V intermetallic compounds, and some work on these materials has already been published.

Pure indium antimonide and gallium antimonide have been studied by SHULMAN *et al.*[1], who found that the line widths were greater than the values calculated by dipolar effects and who explained the broadening in terms of an indirect exchange interaction. RHODERICK[2] has investigated the effects of impurities on the resonance of ^{115}In in indium antimonide and found that a small impurity concentration ($\sim 10^{19}$ cm^{-3}) produces a marked reduction in the intensity of the resonance. The effect was attributed to the quadrupolar interaction between the nuclei and the electrostatic field gradients produced by ionized impurities. To secure quantitative agreement with experiment, it was necessary to suppose that the field gradients were greater by a factor of $\sim$ 1000 than those calculated by ordinary electrostatic theory (the so-called "antishielding effect" (see FOLEY *et al.*[3])). The present work is concerned with a similar study on gallium antimonide, which is also a semiconductor having the zinc blende structure but with a larger energy gap of approximately 0·77 eV. Gallium and antimony each have two stable isotopes which occur in reasonable abundances and which possess both magnetic and electric quadrupole moments, so that gallium antimonide is a suitable material in which to study impurity effects. This semiconductor was also of interest because rough calculations indicated that a Knight shift might be observable in highly doped *n*-type material.

2. APPARATUS AND EXPERIMENTAL METHOD

Most of the experiments were carried out with a conventional Pound–Watkins spectrometer and a permanent magnet giving a field of 4800 Oe. The resonances were displayed on a pen recorder as the derivative of the absorption. Usually curves were

obtained by sweeping the frequency, and when necessary frequency markers were superposed on the recording with the aid of a B.C.221 frequency meter. The resonance frequency of a nucleus in an impure sample was compared with that in a pure sample by recording both resonances alternately a number of times and making a correction where necessary for the small temperature drifts in the magnet.

3. EXPERIMENTAL RESULTS

(a) *Pure materials*

Of the four isotopes in gallium antimonide, ^{123}Sb has a rather broad resonance,[1] and no observations were made on this isotope. A list of the properties of the other nuclei is given in Table 1.

The ^{121}Sb and ^{69}Ga resonances are sufficiently close to overlap, but in interpreting the curves it has been assumed that the low-frequency half of the ^{121}Sb resonance and the high-frequency half of the ^{69}Ga resonance are practically undistorted.

Table 1

Nucleus	Magnetic moment (nuclear magnetons)	Electric quadrupole moment (10^{-24} cm^2)	Spin	Abundance (per cent)	Resonance width (Oe)
^{69}Ga	2·01	0·23	3/2	60·2	7·1
^{71}Ga	2·55	0·15	3/2	39·8	6·6
^{121}Sb	3·34	−0·8	5/2	57·25	5·5

The width represents the separation of the points of maximum slope.

The purest material available in these experiments was *p*-type with a hole concentration of $1{\cdot}2\times10^{17}$ cm^{-3} (the intrinsic concentration at room temperature is approximately 10^{13} cm^{-3}). Impure samples were prepared by doping with zinc, which acts as an acceptor, and with tellurium, which acts as a donor, and although no difficulty was encountered in producing a wide range of hole concentrations, it was not found possible to achieve an electron concentration greater than 2×10^{18} cm^{-3}.

All the material used was polycrystalline. A sample of pure material, used as a reference with which to compare the doped specimens, was made up of slices approximately $1\times0{\cdot}1\times0{\cdot}1$ cm. All the other samples were powders prepared by crushing the solid and selecting particles of roughly uniform size by sieving. The object of this procedure was to produce particles of dimensions smaller than the penetration depth, so as to ensure complete penetration of the radio-frequency field. An experiment carried out with the pure material showed that crushing reduced the resonance intensity slightly, no doubt as a result of the introduction of dislocations, but the magnitude of the reduction was very much less than that produced by impurities.

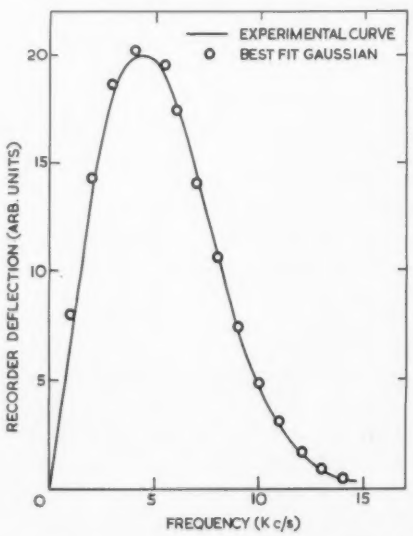

FIG. 1. ^{71}Ga resonance in pure GaSb at 90°K. The full line is the high-frequency half of the experimental record which is proportional to the derivative of the absorption. The circles are obtained from the gaussian curve of best fit.

This assumption is justified by the fact that the separation between the resonances is about 13 kc/s, whereas in both ^{69}Ga and ^{121}Sb the deflection at 13 kc/s from the resonance centre is negligible. A gaussian curve can be fitted accurately to the recording of the ^{71}Ga resonance (Fig. 1), but can not be fitted to the curves for ^{69}Ga and ^{121}Sb, the latter exhibiting a long "tail". The ratio of the integrated

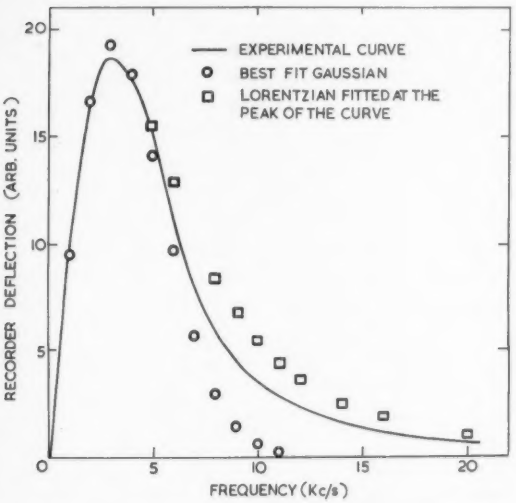

FIG. 2. ^{121}Sb resonance in pure GaSb at 90°K. The full line is the experimental curve. Circles follow the gaussian curve which is the best fit over the whole range. Squares follow a Lorentzian curve fitted at the peak.

intensity of the ^{121}Sb resonance to that of ^{69}Ga, equal to 1·33, is much less than the theoretical value of 2·22 deduced from the spins and relative abundances of the two isotopes. In addition, assuming that the indirect exchange interaction is responsible for the broad lines observed in the pure samples, the line widths (in oersteds) should be the same for isotopes of the same element, although experimentally the ^{69}Ga resonance appears broader than the ^{71}Ga resonance. These facts taken together suggest that even in the purest of our samples the resonances are affected by quadrupolar broadening which could arise from residual impurities or strains. The magnitude of the effect would be proportional approximately to Q/I, which, in appropriate units, is 0·32 for ^{121}Sb, 0·15 for ^{69}Ga and 0·1 for ^{71}Ga, and so would be most apparent in ^{121}Sb and least in ^{71}Ga.

(b) *Impure materials*

(i) *Intensity measurements and line shape.* Fig. 3 shows the effect of adding impurities to gallium antimonide. The curves relate to the zinc-doped samples and in all three cases the intensity of the

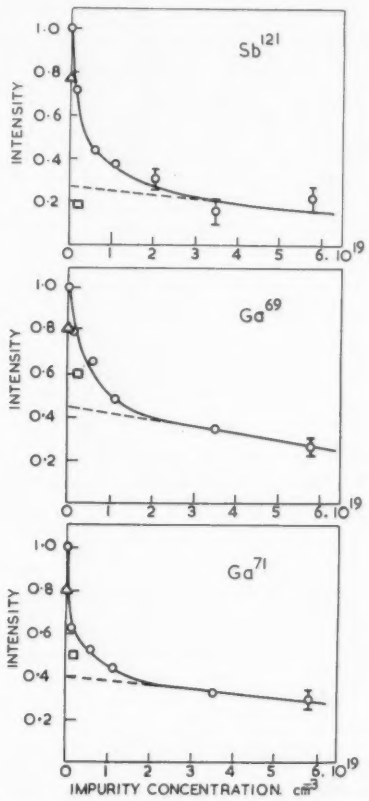

FIG. 3. Intensity of resonances in impure samples. In all cases the intensity of a sample of pure material cut into 1-mm slices is taken as unity. The triangle shows the effect of crushing the pure sample. Circles show the intensity variation in zinc-doped materials. Squares show the intensity of a tellurium-doped (*n*-type) sample.

resonance, as indicated by the peak recorder deflection, dropped sharply for small impurity concentrations, the curve flattening off as further impurities were added. This behaviour is qualitatively similar to that observed by RHODERICK[2] for ^{115}In in doped indium antimonide, and a similar explanation can be given, namely that the reduction in intensity is caused by the quadrupolar

interaction between the nuclei and the field gradients produced by the charged impurities.

On the other hand the intensity loss of the ^{71}Ga resonance does not appear to be accompanied by a change of shape, and for two different impurity concentrations ($1{\cdot}2\times10^{18}$ and 6×10^{18} cm^{-3}) the line was found to be gaussian. For the other two resonances the "tail" observed in the pure specimens was not present in the lines obtained from doped specimens, the line shapes in this case being also gaussian.

The results for the one *n*-type sample are indicated by squares in Fig. 3. The most interesting feature of these results is the sharp reduction in intensity suffered by the ^{121}Sb resonance compared with the other resonances.

The difference in the behaviour of ^{121}Sb and that of ^{69}Ga is particularly obvious because these two resonances almost overlap. In heavily doped *p*-type samples the ^{121}Sb resonance is more intense than that of ^{69}Ga, but the ratio is inverted in the *n*-type sample.

(ii) *Frequency measurements.* Careful measurements were made of the resonance frequencies in the most highly doped samples, and it was found that for a zinc concentration of 6×10^{19} cm^{-3} the ^{121}Sb resonance was displaced to a lower frequency by an amount $\Delta\nu(^{121}\text{Sb}) = -1{\cdot}3\pm0{\cdot}2$ kc/s relative to the pure sample. No change was observed in the frequencies of the gallium resonances.

A similar frequency shift of $-1{\cdot}6$ kc/s was observed for ^{121}Sb in the tellurium-doped specimen.

4. DISCUSSION OF RESULTS

(a) *P-type materials*

The results for the doped samples will be discussed in terms of the theory of the quadrupolar interaction between the nuclei and the electric field gradients produced by charged centres. This theory is discussed in detail by COHEN and REIF[4], and only a brief description of the salient features need be given here. The interaction is treated by perturbation theory and the first-order effect is to split up the single resonance line into $2I$–1 satellites (I half integral) symmetrically disposed about an undisplaced central line, the separation between the components being proportional to the strength of the interaction. If the field gradients vary randomly from nucleus to nucleus, the satellites are not resolved, but the original line becomes broader and less intense. Ultimately, as the strength of the interaction increases, the satellites are so smeared out as to be unobservable, and only the central component remains. When carried to second order, the theory shows that the central component is also broadened if the interaction is sufficiently strong and is, in addition, displaced to lower frequencies.

The curves for the *p*-type samples shown in Fig. 3 can thus be interpreted as follows. The sharp initial drop in intensity is due to the removal of the satellites described by the first-order theory, and the more gradual decrease which follows a further increase in impurity concentration is due to the broadening of the central component. The latter part of the curve, when extrapolated to cut the intensity axis, indicates the contribution of the central component to the intensity of the line in the purest sample. For ^{71}Ga the value is 40 per cent, which is the theoretical figure for $I = 3/2$, assuming that the line obtained for the purest specimen represents the complete resonance. For ^{69}Ga and ^{121}Sb the extrapolated values are slightly larger than the theoretical ones (40 and 26 per cent respectively), implying that a fraction of these resonances is unobservable owing to quadrupolar broadening even in the purest specimens. However, neither the intensity measurements nor the determinations of impurity concentration by means of the Hall effect are accurate over the flat part of the curve.

It is surprising that the reduction in the intensity of the resonances due to the splitting into satellites is not accompanied by an observable change in shape such as was observed in indium antimonide.[2] This may arise because the central component, which is not affected in first-order effects, represents in the case of ^{69}Ga and ^{71}Ga 40 per cent of the total intensity of the resonance. It is possible that the quadrupolar broadening may not produce a change in shape which is observable over the region where the central component makes an appreciable contribution to the deflection. A change might exist in the wings of the curve, but this would be difficult to observe, especially in a recording of the derivative.

The field gradients produced at the nuclear sites by the impurities differ from the free space values because of the presence of free charge carriers, the polarization of the surrounding medium and the

distortion of the electron shells at the particular nuclear site of interest. Approximate theoretical treatments can be given of the first two effects, but not of the last, the so-called "anti-shielding effect". One result of the experiments is, therefore, to provide an estimate of the antishielding factor written conventionally as $(1+\gamma)$. Values for the nuclei in gallium antimonide have been obtained in the following way.

For the satellite component $m \rightarrow m-1$, the frequency shift due to the first-order quadrupole effect resulting from an impurity atom of charge e at a distance r is, apart from an angular factor

$$\Delta\nu = (2m-1)(1+\gamma)\frac{2\epsilon+3}{5\epsilon}\cdot\frac{3e^2Q}{2I(2I-1)h}\cdot\frac{f(qr)}{r^3} \qquad (1)$$

(see, for example, COHEN and REIF[4]). In this equation, ϵ is the dielectric constant and the term $f(qr)$ takes account of the screening by free carriers.[5] In the experimental records the frequency at which the maximum in the derivative occurs remains constant ($=\nu_1$ say) as the impurity concentration varies. Consequently, when the smallest first-order splitting reaches a value $k\nu_1$, where k is some small multiplier, the satellite will no longer contribute appreciably to the derivative at ν_1. This is the point at which the slope of the intensity/concentration graph changes markedly, and the maximum distance R separating any nucleus from an impurity can be obtained by substituting this value of concentration in the relation $4\pi R^3/3 = N^{-1}$. Values of $(1+\gamma)$ can thus be obtained from equation (1) by putting $r = R$ and $\Delta\nu = k\nu_1$. The constant k was put equal to 4 by reference to the results of RHODERICK[2] on ^{115}In in indium antimonide. In this work a value of γ for ^{115}In was calculated from the change in the second moment observed on doping. Since the variation of intensity versus concentration was qualitatively similar to that observed in GaSb, the preceding argument can be applied to the results on ^{115}In and, knowing the values of $(1+\gamma)$, can be used to obtain a value of k. The final values of $1+\gamma$ are listed in Table 2. Because of the crude nature of the analysis, no accuracy better than a factor of 2 or so is claimed for these values, but they are significantly less than the value of 1000 deduced for ^{115}In by RHODERICK[2]. This difference is probably associated with the difference in energy gap. If the antishielding effect in III–V compounds is ascribed to a distortion of the valence-band wave functions, it is likely that this distortion will take place more readily the smaller the energy gap. On the other hand, too close a comparison cannot be justifiably made between the two results in view of the different elements involved.

Table 2

Nucleus	Impurity concentration for the disappearance of the satellites (cm^{-3})	Antishielding factor
^{69}Ga	$1{\cdot}4\times10^{19}$	175
^{71}Ga	$1{\cdot}5\times10^{19}$	321
^{121}Sb	2×10^{19}	49

(b) *N-type materials*

The results for the n-type sample are indicated in Fig. 3 by squares. Because of the difference in the effective mass between holes and electrons, the shielding due to free carriers differs in the two cases. This can account for the fact that for ^{69}Ga and ^{71}Ga the intensity of the resonance in the n-type sample was about 85 per cent of that for a corresponding concentration of p-type impurity. Such an explanation does not account for the behaviour of the ^{121}Sb resonance, whose intensity was only about 25 per cent of that for a p-type sample of the same concentration.

Thus the simple theory of screening based on the modified Coulomb potential does not account for the difference in behaviour between n-type and p-type materials. The results indicate that the electron wave functions around the nuclei must be quite different in the two cases.

(c) *Frequency shifts*

The negative frequency shifts observed for ^{121}Sb in the highly doped p-type sample and in the n-type specimen probably arise from the second-order quadrupolar effects which displace the central component to lower frequencies. No similar

shifts were observed for the gallium nuclei. The frequency displacement of the central component is given by:

$$\Delta\nu = -\frac{{\nu_Q}^2}{16\nu_L}(a-\tfrac{3}{4})(1-\mu^2)(9\mu^2-1) \qquad (2)$$

where

$$\nu_Q = \frac{3e^2qQ}{2I(2I-1)h},$$

$a = I(I+1)$, $\mu = \cos\theta$ and the field gradient is $eq = 2\beta e/r^3$; θ is the angle between the magnetic field and the line joining the impurity to a nucleus. The factor β includes all the effects of screening, antishielding, etc. In principle it should be possible to determine β from the experimental results, but it has not been found possible to derive a relation between the measured shift, which is the displacement of the zero in the derivative of the absorption, and the $\Delta\nu$ of equation (2).

In metals the resonance frequency of a nucleus is often displaced in a positive sense, the so-called Knight shift,[6] owing to the polarization of the free electron spins which produces an enhanced local magnetic field at the nuclei. A similar effect could occur in semiconductors with a large number of free carriers. Rough calculations indicated that a Knight shift might be observable in samples with an electron concentration $\sim 10^{19}$ cm^{-3}, but it was unfortunately not found possible to prepare specimens with electron concentrations of this order. In any event, if a high concentration of carriers is produced by doping, any Knight shift may be obscured by frequency shifts due to second-order quadrupolar effects.

5. CONCLUSIONS

The reduction in intensity produced by impurities is due to quadrupolar interactions between the ionized centres and the nuclei. Because of large antishielding factors, the interaction is long-range and is not therefore particularly useful in elucidating the nature of impurity sites, for example, whether these are interstitial or substitutional. Measurements of the Knight shift in semiconductors are potentially useful in yielding information about the electron wave functions. It has not been found possible to obtain a sufficiently high electron concentration in gallium antimonide in which to look for the effect. There is also a danger of the positive shifts due to electron spin paramagnetism being to some extent offset by negative shifts due to second-order quadrupolar interactions.

Acknowledgements—The author is indebted to Dr. E. H. RHODERICK for his continued advice and encouragement throughout the course of the work and to Dr. O. SIMPSON, who read and commented on the manuscript. The gallium antimonide was prepared by Mr. J. T. EDMOND and Dr. F. A. CUNNELL. Acknowledgement is made to the Admiralty for permission to publish this paper.

REFERENCES

1. SHULMAN R. G., MAYS J. M. and MCCALL D. W., *Phys. Rev.* **100,** 692 (1955).
2. RHODERICK E. H., *Phil. Mag.* **3,** 545 (1958).
3. FOLEY H. M., STERNHEIMER R. M. and TYCKO D., *Phys. Rev.* **93,** 734 (1954).
4. COHEN M. H. and REIF F., *Solid State Physics* (Ed. F. SEITZ and D. TURNBULL) Vol. 5. Academic Press, New York (1957).
5. MANSFIELD R., *Proc. Phys. Soc.* B **69,** 76 (1956).
6. KNIGHT W. D., *Phys. Rev.* **76,** 1259 (1949).

J. Phys. Chem. Solids Pergamon Press 1959. Vol. 11. pp. 263–267. Printed in Great Britain.

INTERACTIONS AND DISTRIBUTIONS OF MAGNETIC IONS IN SOME GARNET SYSTEMS

R. M. BOZORTH and S. GELLER

Bell Telephone Laboratories, Inc., Murray Hill, New Jersey

(*Received* 11 *May* 1959)

Abstract—The tetravalent ions of silicon, germanium and tin have been substituted in the garnet structure as, for example, in the solid solutions $\frac{1}{3}Ca_3Fe_2M_3^{4+}O_{12}$–$\frac{2}{3}Y_3Fe_2Fe_3O_{12}$. Measurements of the spontaneous magnetizations at low temperatures indicate that in these solid solutions about 95 per cent of the small Si^{4+} ions and 85 per cent of the somewhat larger Ge^{4+} ions go into tetrahedral sites. On the other hand the much larger Sn^{4+} ions greatly prefer the octahedral sites. In the garnets $Ca_3Fe_2Ge_3O_{12}$ and $Mn_3Fe_2Ge_3O_{12}$ there are indications of antiferromagnetism: in the former, the $1/\chi$ versus T curve becomes horizontal at low temperatures and in the latter there is a maximum in χ at about 6°K. In the compounds $Gd_3Co_2GaGe_2O_{12}$ and $Gd_3Ni_2GaGe_2O_{12}$ we observe only paramagnetism with a negative intercept of the $1/\chi$ versus T curve, whereas $Gd_3Mn_2GaGe_2O_{12}$ has previously been found to be ferrimagnetic. In comparison with the latter compound, it is surprising to find only a slight spontaneous magnetization of 0·1–0·2 μ_B in $Mn_3Fe_2Si_3O_{12}$.

1. INTRODUCTION

SEVERAL recent reports have been concerned with the crystal chemistry and interactions of magnetic ions in the garnets. In the present paper the distributions of the Group IV ions of silicon, germanium and tin deduced from magnetic measurements at low temperatures are compared in the systems

$$\frac{2}{3}(Y_3Fe_2Fe_3O_{12})–\frac{1}{3}(Ca_3Fe_2M_3O_{12})$$

and

$$\frac{2}{3}Gd_3Fe_2Fe_3O_{12}–\frac{1}{3}Ca_3Fe_2Si_3O_{12}.$$

The solid solutions

$$\frac{4}{5}Y_3Fe_2Fe_3O_{12}–\frac{1}{5}Ca_3Al_2Si_3O_{12}$$

and

$$\frac{4}{5}Gd_3Fe_2Fe_3O_{12}–\frac{1}{5}Ca_3Al_2Si_3O_{12}$$

have also been investigated.

Measurements of $Ca_3Fe_2Ge_3O_{12}$ were made to compare the interaction between Fe^{3+} ions in octahedral positions with that previously observed[1] between Mn^{2+} ions. The dodecahedral–tetrahedral interactions were studied in

$Mn_3Fe_2Ge_3O_{12}$,[2,3] $Mn_3Fe_2Si_3O_{12}$,[4,5]

$Gd_3Co_2GaGe_2O_{12}$[2] and $Gd_3Ni_2GaGe_2O_{12}$[2]

for comparison with $Gd_3Mn_2GaGe_2O_{12}$.

2. EXPERIMENTAL

(a) *Preparation of compounds*

The garnet $Mn_3Fe_2Si_3O_{12}$, a high-pressure phase, was kindly supplied to us by L. COES of the Norton Company. The details of the preparation of most of the other specimens have already been given elsewhere.

(b) *Magnetic measurements*

Measurements of magnetic moment per mole, σ_m, were made in the temperature range 1·3–300°K in fields up to $H = 12{,}500$ Oe, by means of the pendulum magnetometer previously described.[6]

The spontaneous magnetization per mole, σ_0, was normally determined by extrapolation of the magnetic moment to $H = \infty$, assuming a linear relation between σ_m and $1/H^2$; such a relation was normally followed for $H = 8000$–$12{,}500$. However, when the measured value of σ_m was relatively small, it was usually found that the moment was given by:

$$\sigma_m = \sigma_0 + \chi' H$$

for $H = 2000$–$12{,}500$ and σ_0 was then determined by extrapolation to $H = 0$. The latter method was justified when the plot of $1/\chi'$ versus T was a straight line corresponding nearly in slope to the

Table 1. *Lattice constants of the garnet systems studied*

Garnet	a_0(Å)	Reference
$\frac{1}{3}Ca_3Fe_3Si_3O_{12}$–$\frac{2}{3}Y_3Fe_2Fe_3O_{12}$	12·290	This work
$\frac{1}{3}Ca_3Fe_3Ge_3O_{12}$–$\frac{2}{3}Y_3Fe_2Fe_3O_{12}$	12·370	This work
$\frac{1}{3}Ca_3Fe_3Sn_3O_{12}$–$\frac{2}{3}Y_3Fe_2Fe_3O_{12}$	12·502	(7)
$\frac{1}{3}Ca_3Fe_3Si_3O_{12}$–$\frac{2}{3}Gd_3Fe_2Fe_3O_{12}$	12·36	This work
$\frac{1}{5}Ca_3Al_2Si_3O_{12}$–$\frac{4}{5}Y_3Fe_2Fe_3O_{12}$	12·35	(8)
$\frac{1}{5}Ca_3Al_2Si_3O_{12}$–$\frac{4}{5}Gd_3Fe_2Fe_3O_{12}$	12·402	(8)
$Ca_3Fe_2Ge_3O_{12}$	12·312	(2)
$Mn_3Fe_2Ge_3O_{12}$	12·087	(2)
$Mn_3Fe_2Si_3O_{12}$	11·82	(5)
$Gd_3Co_2GaGe_2O_{12}$	12·446	(2)
$Gd_3Ni_2GaGe_2O_{12}$	12·401	(2)

effective moments of the magnetic ions known to be present, using the usual relation $\mu_{\text{eff}} = 2{\cdot}83\sqrt{C}$, $C = \Delta T/\Delta(1/\chi')$. In some intermediate cases the method of extrapolation was not surely known, and some uncertainty in the value of σ_0 remained.

Magnetic data are given in Figs. 1–5 and are discussed below.

(c) *Crystallographic data*

Some of the lattice constants have been reported elsewhere, but are summarized in Table 1 for the sake of completeness.

3. DISCUSSION

(a) $\frac{1}{3}Ca_3Fe_2M_3^{4+}O_{12}$–$\frac{2}{3}Y_3Fe_2Fe_3O_{12}$(M = Si, Ge *or* Sn)

In these solid solutions, with M = Si, Ge or Sn, we may infer the ionic distributions from the Bohr magneton numbers (Fig. 1) if we assume that the moments of the ions in the octahedral and tetrahedral positions are strictly antiparallel. The Bohr magneton numbers and inferred distributions of these three materials may then be represented as follows, the sites being indicated in the usual order: {dodecahedral}, [octahedral] and (tetrahedral):

$0{\cdot}5\ \mu_B$, $\{CaY_2\}[Fe_{1{\cdot}95}Si_{0{\cdot}05}](Fe_{2{\cdot}05}Si_{0{\cdot}95})O_{12}$

$1{\cdot}5\ \mu_B$, $\{CaY_2\}[Fe_{1{\cdot}85}Ge_{0{\cdot}15}](Fe_{2{\cdot}15}Ge_{0{\cdot}85})O_{12}$

$5{\cdot}2\ \mu_B$, $\{CaY_2\}[Fe_{1{\cdot}48}Sn_{0{\cdot}52}](Fe_{2{\cdot}52}Sn_{0{\cdot}48})O_{12}$.

Thus the magnetic measurements indicate that silicon *does* act ionically in the garnets, but prefers tetrahedral sites because of its small size. The Ge^{4+} ion shows somewhat more preference for octahedral sites than does Si^{4+} because of its larger size; the Sn^{4+} ion—much larger than the Ge^{4+} ion—shows the greatest preference for octahedral sites. This behavior is similar to that of the trivalent nonmagnetic ions.

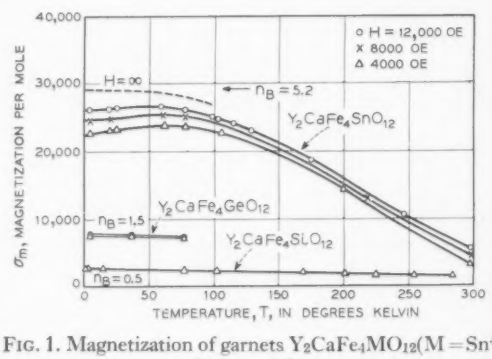

FIG. 1. Magnetization of garnets $Y_2CaFe_4MO_{12}$(M = Sn^{4+} Ge^{4+} or Si^{4+}).

In the case of M = Sn^{4+}, however, the assumed model of interaction of Fe^{3+} moments is probably not correct. X-ray studies on this specimen[7] indicate that perhaps 90 per cent or more of the Sn^{4+} ions occupy octahedral sites and that the formula describing the specimen should more likely be written $\{CaY_2\}[FeSn](Fe_3)O_{12}$ than as above. A detailed study of the $Ca_3Fe_2Sn_3O_{12}$–$Y_3Fe_2Fe_3O_{12}$ system is described in another paper.[7]

Recently, definite evidence has been obtained of the existence of defect structures in some garnets

containing the Ge^{4+} ion.[2] In these cases a deficiency of the Ge^{4+} ion, but not of the O^{2-} ion, is implied. Moreover, it appears that an increase of cell size (over the predicted value) is associated with the deficiency.

The specimen $\frac{1}{3}Ca_3Fe_2Ge_3O_{12}$–$\frac{2}{3}Y_3Fe_2Fe_3O_{12}$ discussed above was made in such manner as to assure the proper stoichiometry. However, another specimen was made from which it was definitely known that GeO_2 was lost. This specimen had a lattice constant 12·386 Å, which is 0·016 Å greater than that of the specimen having the full amount of GeO_2. Thus apparently even a deficiency of *both* Ge^{4+} and O^{2-} ions causes an increase in volume.

The saturation magnetization at 0°K of the GeO_2-deficient specimen was only 0·7 μ_B; this indicates a more nearly equal distribution of Fe^{3+} ions over the two types of sites than for the specimen of proper stoichiometry. It is possible that the deficiency of GeO_2 causes a smaller available average volume for tetrahedral ions and/or a larger available average volume for octahedral ions, and that this accounts for the increase in the number of Fe^{3+} ions occupying octahedral sites.

(b) $\frac{1}{3}Ca_3Fe_2Si_3O_{12}$–$\frac{2}{3}Gd_3Fe_2Fe_3O_{12}$

In this solid solution the saturation magnetization (Fig. 2) is 13·5 μ_B and the indicated distribution of ions may be expressed by the formula:

13·5 μ_B, $\{CaGd_2\}[Fe_{1.95}Si_{0.05}](Fe_{2.05}Si_{0.95})O_{12}$.

This corroborates the previous finding, in which Y was present instead of Gd.

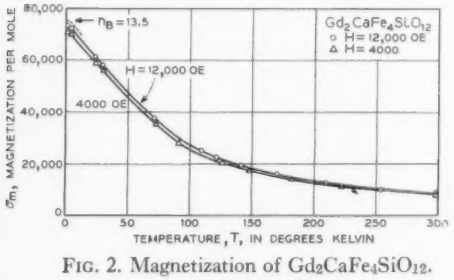

FIG. 2. Magnetization of $Gd_2CaFe_4SiO_{12}$.

(c) $\frac{1}{5}Ca_3Al_2Si_3O_{12}$–$\frac{4}{5}R_3^{3+}Fe_2Fe_3O_{12}$, (R = Y or Gd)

The saturation magnetizations at 0°K and the inferred ions distributions are:

1·4 μ_B,

$\{Y_{2.4}Ca_{0.6}\}[Fe_{1.86}Al_{0.14}](Fe_{2.14}Al_{0.26})Si_{0.6}O_{12}$

14·2 μ_B,

$\{Gd_{2.4}Ca_{0.6}\}[Fe_{1.74}Al_{0.26}](Fe_{2.26}Al_{0.14}Si_{0.6})O_{12}$.

There may be some octahedral Si^{4+} ions, but the exact amount is not determinable from these measurements. The results are somewhat anomalous in that if the octahedral sites of either one of these specimens contained more Fe^{3+} than the other, it would seem that it should be the R = Gd specimen that contained more, since Gd^{3+} is larger than Y^{3+}, thus possibly making the octahedral holes larger. The results imply, however, that in this case the Gd^{3+} ion has the effect of increasing the average volume available to an ion entering a tetrahedral position.

In the two garnets

$\frac{1}{3}Ca_3Fe_2Si_3O_{12}$–$\frac{2}{3}Gd_3Fe_2Fe_3O_{12}$

and

$\frac{1}{5}Ca_3Al_2Si_3O_{12}$–$\frac{4}{5}Gd_3Fe_2Fe_3O_{12}$,

the results indicate that the tetrahedral–octahedral and tetrahedral–dodecahedral interactions are antiferromagnetic, in accord with expectation.[9,10]

(d) $Ca_3Fe_2Ge_{31}O_2$

From results given earlier, one would guess that some of the Fe^{3+} ions in this garnet are in tetrahedral sites. However, as might be expected, no spontaneous magnetization is observed here. The

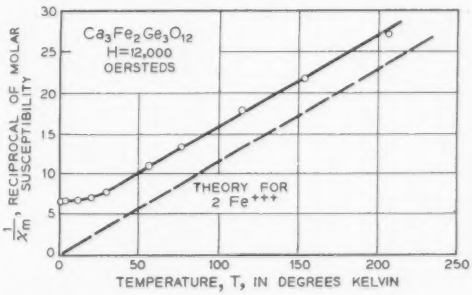

FIG. 3. Inverse susceptibility, showing tendency toward antiferromagnetism.

curve obtained by plotting reciprocal molar susceptibility $1/\chi_m$ versus T (Fig. 3) is a straight line above about 40°K, and there has a slope corresponding to the normal value of $\mu_{eff} = 4{\cdot}9$ Bohr magnetons per Fe^{3+} ion. Below 30°K, the curve becomes almost horizontal. This tendency toward

antiferromagnetic behavior is also indicated by the negative intercept on the temperature axis of the straight-line portion of the curve.

Weak antiferromagnetic interaction among magnetic ions in octahedral positions has also been observed in the garnet $\{CaY_2\}[Mn_2](Ge_3)O_{12}$.[1]

(e) $Mn_3Fe_2Ge_3O_{12}$

We had hoped to observe in this garnet a spontaneous magnetization greater than or equal to 5 μ_B as a result of interactions between the magnetic ions in dodecahedral and octahedral positions. No spontaneous magnetization was observed; however, the $1/\chi_m$ versus T (Fig. 4) and χ_m versus T (Fig. 5) curves* indicate antiferromagnetic ordering. The former curve becomes concave upwards below about 20°K, and there are maxima in the latter at about 6°K. There are several possible causes of the absence of ferrimagnetism: (1) weak interaction because of unfavorable geometry, (2) distribution of Fe^{3+} ions over the octahedral and tetrahedral sites, resulting in a marked weakening of interaction and (3) inherently weak interaction between Mn^{2+} and Fe^{3+} ions. We believe that the last is the least likely contributor, since, as mentioned below, one would expect magnetic interactions between Gd^{3+} and Mn^{2+} ions to be inherently weaker than those between Mn^{2+} and Fe^{3+} ions, yet $Gd_3Mn_2GaGe_2O_{12}$ is ferrimagnetic.[1]

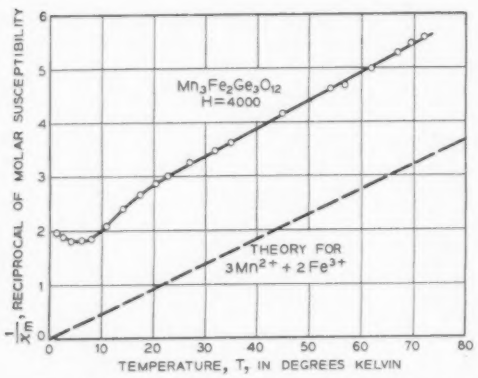

FIG. 4. Inverse susceptibility of $Mn_3Fe_2Ge_3O_{12}$.

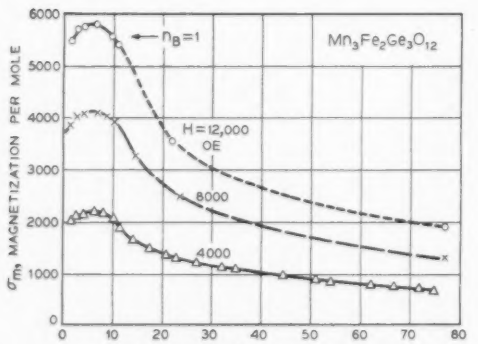

FIG. 5. Antiferromagnetism of $Mn_3Fe_2Ge_3O_{12}$.

* The slope of the linear portion of the $1/\chi_m$ versus T curve corresponds to an effective Bohr magneton number per magnetic ion of about $\mu_{eff} = 5{\cdot}6$, to be compared with the theoretical value of 5·9.

(f) $Mn_3Fe_2Si_3O_{12}$

This garnet could not be synthesized directly at ordinary pressures.[5] The sample obtained from COES (see above) proved to have a small spontaneous magnetization characteristic of "weak" or "parasitic" ferrimagnetism. Because it would hardly be expected that more than 5 per cent of the octahedral sites would have Si^{4+} ions in them, it is unlikely that the ionic distribution is responsible for the unexpected result of the magnetic measurements. Because it is likely that under the same geometric arrangement of bonds, the dodecahedral–octahedral Gd^{3+}–O^{2-}–Mn^{2+} superexchange interaction would be weaker than that of Mn^{2+}–O–Fe^{3+}, it would seem that the geometry in $Mn_3Fe_2Si_3O_{12}$ is significantly different from that of $Gd_3Mn_2GaGe_2O_{12}$ and unfavorable to superexchange. Comparison of the results of structure

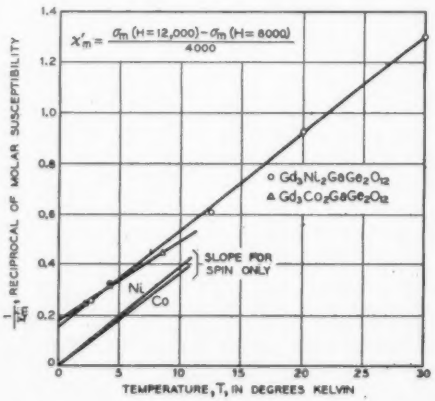

FIG. 6. Inverse susceptibility, showing negative intercept on temperature axis.

refinement of $Y_3Fe_2Fe_3O_{12}$[10] and $Ca_3Al_2Si_3O_{12}$[11] (the only garnets whose structures have been very accurately determined) indicates that differences in arrangement can be rather large.

(g) $Gd_3Co_2GaGe_2O_{12}$ *and* $Gd_3Ni_2GaGe_2O_{12}$

These were measured to compare Gd^{3+}–O^{2-}–Co^{2+}, Gd^{3+}–O^{2-}–Ni^{2+} and Gd^{3+}–O^{2-}–Mn^{2+} interactions. The garnet $\{Gd_3\}[Mn_2](GaGe_2)O_{12}$ has previously been found to be ferrimagnetic, with a Curie temperature of 8°K.[1] The former are paramagnetic only down to 1·3°K with a negative intercept of the $1/\chi_m$ versus T curve (Fig. 6). Thus the interactions between Gd^{3+} and Co^{2+} and between Gd^{3+} and Ni^{2+} are weaker than those between Gd^{3+} and Mn^{2+}, as one would expect.

Acknowledgements—The authors wish to thank D. D. Davis, C. E. Miller and A. J. Williams for assistance in various phases of the experiments.

VOL. 11 1959

REFERENCES

1. Gilleo M. A. and Geller S., *J. Appl. Phys.* **30,** 297S (1959); *J. Phys. Chem. Solids* **10,** 187 (1959).
2. Geller S. and Miller C. E., *Acta. Cryst., Camb.* (in the press).
3. Tauber A., Banks E., and Kedesdy H., *J. Appl. Phys.* **29,** 385 (1958).
4. Coes L., *J. Amer. Ceram. Soc.* **38,** 298 (1955).
5. Geller S. and Miller C. E., *Amer. Min.* **44,** 665 (1959).
6. Bozorth R. M. and Walsh D., *J. Phys. Chem. Solids* **5,** 299 (1958).
7. Geller S., Bozorth R. M., Gilleo M. A. and Miller C. E. *J. Phys. Chem. Solids* (to be published).
8. Geller S. and Miller C. E., *Amer. Min.* (in the press).
9. Pauthenet R., *C.R. Acad. Sci., Paris* **243,** 1449 (1956).
10. Geller S. and Gilleo M. A., *J. Phys. Chem. Solids* **3,** 30 (1957).
11. Abrahams S. C. and Geller S., *Acta Cryst., Camb.* **11,** 437 (1958).

J. Phys. Chem. Solids Pergamon Press 1959. Vol. 11. pp. 268–273. Printed in Great Britain.

THE SEEBECK COEFFICIENT OF BISMUTH SINGLE CRYSTALS

B. S. CHANDRASEKHAR

Westinghouse Research Laboratories, Pittsburgh 35, Pennsylvania

(*Received* 18 *May* 1959)

Abstract—The Seebeck coefficient S of single crystals of bismuth has been measured between room temperature and about 250°C. The results are used to resolve a discrepancy in the data on the Seebeck coefficient of polycrystalline bismuth as given by SATO and by SAVORNIN and POGGI; the values given by the latter workers are shown to be more reasonable. The anisotropy in S at 300°K is analyzed in terms of the current model for the carriers in bismuth. ABELES and MEIBOOM's results from magnetoresistance measurements and the present data are used to calculate the density-of-states effective masses of the electrons and holes respectively. The value for the electrons agrees well with that deduced from de Haas–van Alphen-effect and cyclotron-resonance experiments. The value for the holes is very close to that deduced from cyclotron resonance, but much smaller than is suggested by electronic heat-capacity data.

VOL
11
195

1. INTRODUCTION

RECENT experiments on the de Haas–van Alphen effect,[1] cyclotron resonance[2,3] and magnetoresistance[4] in bismuth have provided information about the band structure in this element, and it is now feasible to attempt an understanding of other transport phenomena, such as the thermoelectric effects.

BOYDSTON[5] did some early experiments on the thermoelectric properties of single-crystal bismuth, but his results were criticized by BRIDGMAN[6] because of the low purity of the samples used. It is well known that the electronic properties of bismuth are very sensitive to minute amounts of dissolved impurities. BRIDGMAN's own work on the Seebeck coefficient* S was limited to the vicinity of room temperature, as he was primarily concerned with the relation between thermoelectric effects and crystal symmetry.

Recently SATO[7] reported measurements of S made on polycrystalline bismuth against platinum between room temperature and the melting point. He found that the magnitude of S went through a pronounced maximum as a function of temperature, at about 50°C, attaining a value of about 220 μV/°K. More recent work by SAVORNIN and POGGI[8], who measured bismuth against copper, contradicted SATO's results; they observed no maximum in the S versus temperature curve, after allowance had been made for the Seebeck coefficient of copper against platinum, and the magnitude of S was found to be much smaller than the value SATO found in the same temperature range. Fig. 1 shows the results of these two sets of measurements. One possible explanation of this discrepancy is that the polycrystalline samples used in the two sets of experiments had in fact different textures; then different dependences of S on T along different crystal axes might account for the discrepancy. Thus a measurement of S as a function of crystal orientation and temperature should indicate whether this is the correct explanation.

There has also been disagreement in a somewhat different region, relating to the electronic band structure of bismuth. The cyclotron-resonance experiments of GALT *et al.*[3] indicated, in addition to electrons, the existence of a band of light holes, with a density-of-states effective mass of 0·16 m_0, where m_0 is the normal electronic mass. The de Haas–van Alphen effect[1] has, on the other

* The term Seebeck coefficient is used here for the quantity which is also known as the thermoelectric power in order to keep the terminology consistent (cf. Peltier coefficient, Thomson coefficient, &c.).

hand, shown oscillations due only to the electrons, and none due to the holes. The data on the electrons from the two sets of measurements are in quantitative agreement. HEINE[9] has suggested

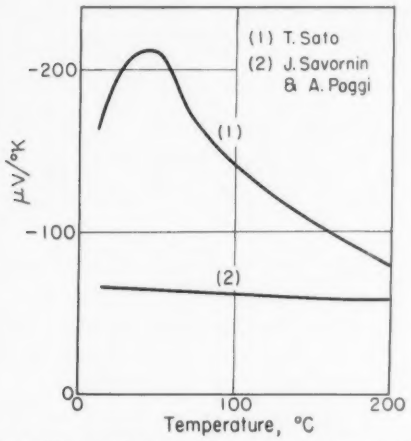

FIG. 1. The Seebeck coefficient of polycrystalline bismuth, against platinum as measured by SATO[7] (curve 1), and against copper by SAVORNIN and POGGI[8] (curve 2).

that the holes have a high effective mass, and therefore do not contribute appreciably to the de Haas–van Alphen effect; an estimate of their mass can be made by assuming that they make the major contribution to the electronic heat capacity. Using these ideas, AUBREY and CHAMBERS[2] estimated the density-of-states mass of the holes to be 2·2 m_0 (contrasted with 0·16 m_0 from cyclotron resonance). As will be shown below, the present measurements shed some light on this problem.

2. EXPERIMENTAL

Single crystals of about 0·5 cm square cross-section and over 10 cm long were grown in a graphite mould in vacuum, using a modified BRIDGMAN technique. The bismuth, of 99·999 per cent purity, was obtained from The American Smelting and Refining Company. The crystals as grown had a ratio of room-temperature to liquid-helium-temperature resistivities of 90, which compares favourably with a value of about 50 for zone-refined bismuth,[10] and 80–105 for the bismuth used in cyclotron-resonance experiments.[2] Some of the crystals were grown without seeding, and these tended to have the sample axis make a large angle with the three-fold axis. Orientations closer to the three-fold axis were obtained by suitable seeding. The orientations of the crystals were determined by back-reflection Laue photographs, using two recent compilations[11,12] of crystallographic angles in bismuth.

The sample was supported lightly at each end by a beryllium–copper spring, mounted on an insulating base. The temperatures at two points along the crystal were measured with copper/Constantan thermocouples, and the copper leads were used to determine the thermo-e.m.f. between these points. Each thermocouple junction was fused into the crystal by laying it on the surface and then pressing on it with a clean hot soldering-iron tip, using a trace of bismuth as the solder. With practice, it is possible to do this without introducing any new grains of bismuth around the junction. This method of attaching the thermocouples ensures that (1) the crystal remains single, and (2) the electrical and thermal contacts between each junction and the crystal are at the same temperature.

The sample assembly went into an evacuated Pyrex tube placed in a cylindrical furnace. The temperature difference between the thermocouples could be varied by varying the position of the tube along the axis of the furnace, and was 10–20°C in these experiments. The various voltages were measured on a Rubicon type-B potentiometer, and the Seebeck coefficient of bismuth relative to copper was calculated. When necessary, these values could be converted to absolute values by the use of the absolute Seebeck coefficient of copper as given by NYSTROM[13].

3. RESULTS AND DISCUSSION

(a) S *for polycrystalline bismuth*

On Fig. 2 is shown the Seebeck coefficient, relative to copper, for different values of ϕ (the angle between the sample axis and the three-fold axis) and temperature. For a crystal such as bismuth with a three-fold axis of symmetry, S, which

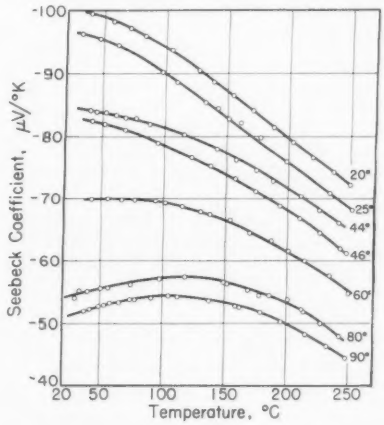

FIG. 2. The Seebeck coefficient, against copper, of single crystals of bismuth. The angle ϕ between the sample axis and the three-fold axis is indicated at the right-hand end of each curve.

in the general case is a second-rank tensor, reduces to two components $S_{\parallel}$ and $S_{\perp}$, which are respectively parallel and perpendicular to the three-fold axis.

If the direction of the temperature gradient is the same as the direction along which the Seebeck voltage is measured, making an angle ϕ with the three-fold axis, then it is easy to show that the Thomson–Voigt relation[14] holds:

$$S_{\phi} = S_{\parallel} \cos^2\phi + S_{\perp} \sin^2\phi \qquad (1)$$

where $V = S_{\phi}(T_2 - T_1)$, and T_1 and T_2 are the temperatures at the two points between which the Seebeck voltage V appears. Equation (1) indicates that a plot of S_{ϕ} against $\cos^2\phi$ should be a straight line. Such a plot, at 300°K, is shown in Fig. 3, where the ordinate now represents the absolute Seebeck coefficient of bismuth. From here on, S will stand for the absolute value.

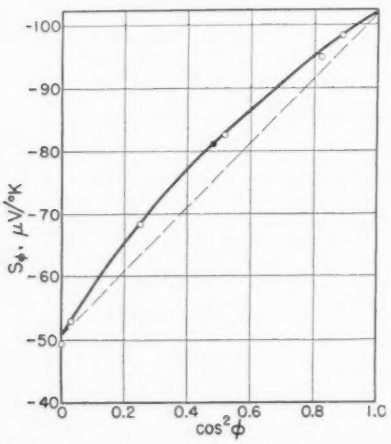

FIG. 3. A plot of the absolute Seebeck coefficient against $\cos^2\phi$, at 300°K, where ϕ = angle between the sample axis and the three-fold axis. The open circles denote samples made from as-received 99·999 per cent pure bismuth. The filled circle denotes a zone-refined sample. The broken line represents the Thomson–Voigt relationship.

It is clear from Fig. 3 that the Thomson–Voigt relation is not valid for bismuth. This was first pointed out by BRIDGMAN, but it was left to KOHLER[15] to account for the anomaly. A careful examination of the experimental conditions shows that it is the heat flow, and not the temperature gradient, which is forced to be along the sample axis. Since the thermal conductivity of the material is also anisotropic, this heat flow will in general produce a temperature gradient in a direction different from the sample axis. Let S_{ϕ} be the ratio of the voltage difference to the temperature difference along the sample axis (this is the experimentally measured quantity) making an angle ϕ with the three-fold axis. Then a solution of the equations to the heat flow and the Seebeck voltage with the appropriate boundary conditions leads to:

$$S_{\phi} = S_{\parallel} \cos^2\phi + S_{\perp} \sin^2\phi + \frac{(\lambda-1)(S_{\parallel} - S_{\perp})}{\sin^2\phi + \lambda \cos^2\phi} \sin^2\phi \cos^2\phi \qquad (2)$$

where $\lambda = \Lambda_{\perp}/\Lambda_{\parallel}$, the ratio of the thermal conductivities perpendicular and parallel to the three-fold axis respectively. For bismuth $\lambda > 1$, and one would expect the curve of S_{ϕ} against $\cos^2\phi$ to be concave to the $\cos^2\phi$ axis, as is indeed seen to be the case. The actual value of λ is in some doubt, the values reported in the literature[16,17] ranging from 1·39 to 1·77. Bismuth cleaves easily in the plane perpendicular to the three-fold axis, and there is a suspicion that some of the measured values of λ may be too high because of minute cracks parallel to the cleavage plane. Therefore $\lambda = 1{\cdot}39$ has been used in the present analysis. This uncertainty in λ is not too serious, since it appears only in a correction term, and the final conclusions that are drawn are not at all sensitive to its exact value.

The measured values of S_{ϕ} at 300°K have been used to solve equation (2) by the method of averages, to give

$$S_{\parallel} = -102{\cdot}7\ \mu\text{V/°K}, \quad S_{\perp} = -51{\cdot}4\ \mu\text{V/°K}. \qquad (3)$$

The uncertainty in these values is not greater than a few per cent; this is insignificant for the purposes of the subsequent discussion. The calculation of S for a polycrystalline sample from single-crystal parameters involves a knowledge of the electrical- and thermal-conductivity tensors,[18] for which complete data above 300°K are not available. Nevertheless, it is amply evident from a comparison of Figs. 1 and 2, along with equation (2), that no possible texture in polycrystalline bismuth could yield a curve of the type obtained by SATO[7]. The present results indeed favour the data of

SAVORNIN and POGGI[8]. The explanation of SATO's curve must lie either in the effect of impurities or in unknown experimental errors.

(b) *The anisotropy of* S *for single-crystal bismuth*

The Jones zone for bismuth is capable of accommodating exactly five electrons per atom. It is believed that the unusual electrical and magnetic properties of bismuth are due to a small number of electrons which spill over into a higher zone, leaving an equal number of holes in the first zone, even at 0°K. This implies an overlap between the electron and the hole bands, sometimes referred to as the conduction and valence bands, by analogy with semiconductor terminology. The following model for the carriers in bismuth represents a synthesis of the data from de Haas–van Alphen, magnetoresistance and cyclotron-resonance experiments.

(1) The electrons are in a group of ellipsoids in $\boldsymbol{k}$-space, the equation to a single ellipsoid being

$$\frac{2m_0E}{\hbar^2} = \alpha_1k_1^2+\alpha_2k_2^2+\alpha_3k_3^2+2\alpha_4k_2k_3 \qquad (4)$$

where the energy E and the components of crystal momentum k_i are measured from the band edge, and the subscripts 1, 2 and 3 refer to a binary, a bisectrix and the three-fold axes respectively. The α_i are the components of the reciprocal mass tensor.

Equation (4) indicates that one axis of the ellipsoid is along the k_1 axis, and the other two axes are respectively inclined to the k_2 and k_3 axes at an angle θ, where $\tan 2\theta = 2\alpha_4/(\alpha_2-\alpha_3)$. If the band edge is on a binary axis, then the symmetry operations of the lattice yield a total of either three or six ellipsoids, according as the edge lies on the zone boundary or not.

(2) The holes are in a spheroid centred at the origin of $\boldsymbol{k}$-space, and overlap the electrons by an energy E_0:

$$\frac{2m_0(E_0-E)}{\hbar^2} = \beta_1(k_1^2+k_2^2)+\beta_3k_3^2 \qquad (5)$$

where the β_i are the components of the reciprocal mass tensor for the holes.

Only the results at 300°K are discussed, and therefore pure lattice scattering is assumed, with different relaxation times for the electrons and the holes, each being expressible in terms of components parallel and perpendicular to the three-fold axis.[19] Conduction in the two bands will be assumed to be independent, as has been done by ABELES and MEIBOOM[4] in their analysis of magnetoresistance. Then, as shown in the Appendix,

$$S_i = \frac{\sigma_{ei}S_e+\sigma_{hi}S_h}{\sigma_{ei}+\sigma_{hi}} \qquad (6)$$

where i stands for $\parallel$ or $\perp$, σ = conductivity and the subscripts e and h refer to electrons and holes. S_e and S_h may be called the partial Seebeck coefficients of the electrons and the holes respectively, and are defined by equations (A.4) and (A.5) of the Appendix. It is shown there that S_e and S_h themselves do not depend on direction; the observed anisotropy of S arises from the different mobilities of the two types of carriers.

ABELES and MEIBOOM[4] have calculated the mobilities of the two types of carriers from their magnetoresistance data, and get

$$\left(\frac{\sigma_e}{\sigma_h}\right)_{\parallel} = 9{\cdot}19, \quad \left(\frac{\sigma_e}{\sigma_h}\right)_{\perp} = 2{\cdot}12 \text{ at } 300^\circ\text{K}. \qquad (7)$$

From equations (6) and (7), one gets

$$S_e = -125{\cdot}3\ \mu\text{V}/^\circ\text{K},$$
$$S_h = +105{\cdot}1\ \mu\text{V}/^\circ\text{K at } 300^\circ\text{K}. \qquad (8)$$

These values are inserted in equation (A.4) of the Appendix and ξ_e and ξ_h are obtained by graphical interpolation from tables of Fermi integrals.[20] One then gets

$$\xi_e = 1{\cdot}6, \qquad \xi_h = 2{\cdot}3. \qquad (9)$$

The number of electrons (or holes) per cm^3, N, as calculated by ABELES and MEIBOOM[4], is equal to $2{\cdot}2\times10^{18}$ at 300°K. Also n, the number per ellipsoid, is given by

$$n = \frac{4\pi}{h^3}(2m_0kT)^{3/2}\mu^{3/2}F_{\frac{1}{2}}(\xi) \qquad (10)$$

where μ is the density-of-states effective mass in units of m_0. From equations (9) and (10) one calculates the effective masses for the electrons and the holes, getting the values shown in Table 1.

The result for the electrons is in excellent agreement with both sets of cyclotron-resonance data, though it is not possible to choose between the

Table 1. *Effective masses of electrons and holes*

	Aubrey and Chambers[2]	Galt *et al.*[3]	Present work
Electrons	$3{\cdot}9\times10^{-2}$	$5{\cdot}2\times10^{-2}$	$5{\cdot}5\times10^{-2}$ (three ellipsoids) $3{\cdot}5\times10^{-2}$ (six ellipsoids)
Holes	2·2*	$16{\cdot}2\times10^{-2}$	$9{\cdot}0\times10^{-2}$

* Value based on Heine's[9] arguments.

three-ellipsoid and the six-ellipsoid schemes. The result for the holes clearly confirms the light holes found by Galt *et al.*[3] This makes it somewhat puzzling that the holes do not contribute to the de Haas–van Alphen effect. But the values of $\beta_1^{-1} = 0{\cdot}068$ and $\beta_3^{-1} = 0{\cdot}92$ found by Galt *et al.* suggest that the most favourable configuration for observing such a contribution would be with the magnetic field parallel to the three-fold axis. But this is precisely the direction in which the torque on the sample disappears, and so Shoenberg's method would not work. The elegant technique recently used by Kunzler and Boyle[21], of studying the temperature changes of single crystals of bismuth upon magnetizing or demagnetizing, offers some hope for measurements in this direction. The heat-capacity data,[22] which seem to require a carrier of mass ~ 1, are subject to two uncertainties: (1) the quoted values for the electronic contribution show that, even at 1°K, it is only a few per cent of the total heat capacity, and (2) there is a possibility of a contribution from the pure quadrupole splitting of nuclear spin levels to the measured heat capacity. No observations have been reported on pure quadrupole resonance in bismuth, and so it is not possible to estimate the nuclear contribution to the heat capacity. It is thus clear that accurate measurements of the heat capacity of bismuth in the region below 0·1°K are needed.

Acknowledgements—The author is grateful to several colleagues for helpful discussions, and to Dr. J. K. Galt *et al.* for sending him their data before publication.

APPENDIX

What Herring calls the Π-approach to calculate S is used here. The Peltier coefficient Π is defined so that $e\Pi$ is the energy absorbed per carrier entering the material, which we shall label B. Imagine the material to be in contact with the standard material M, which acts as a source of carriers. Let the direction of the current be denoted by the subscript i, where $i = 1$, 2 or 3. The Fermi energy ζ is the same in the two materials, and a carrier entering B from M and occupying a state of energy E causes an absorption of energy equal to $E-\zeta$. Thus the average energy absorbed per carrier is:

$$e\Pi_i = \int (E-\zeta)\,\Sigma_i(\boldsymbol{k})\,d^3\boldsymbol{k} \Big/ \int \Sigma_i(\boldsymbol{k})\,d^3\boldsymbol{k}, \quad \text{(A.1)}$$

where the denominator is related to the conductivity σ_i by

$$\sigma_i = -\frac{e^2}{4\pi^3\hbar^2}\int \Sigma_i(\boldsymbol{k})\,d^3\boldsymbol{k} = -\frac{e^2}{4\pi^3\hbar^2}\int \tau_i\left(\frac{\partial E}{\partial k_i}\right)^2\left(\frac{\partial f_0}{\partial E}\right)d^3\boldsymbol{k}. \quad \text{(A.2)}$$

Let the energy-dependence of τ_i be E^p ($p = -\frac{1}{2}$ for pure lattice scattering). Inserting equation (4) or (5) into (A.2), changing to spherical coördinates and partially integrating, one easily finds that the directional dependence disappears from equation (A.1), and

$$\Pi = \frac{kT}{e}\left\{\frac{(\frac{5}{2}+p)F_{\frac{3}{2}+p}(\xi)}{(\frac{3}{2}+p)F_{\frac{1}{2}+p}(\xi)} - \xi\right\} \quad \text{(A.3)}$$

and therefore $S = \Pi/T$

$$= \frac{k}{e}\left\{\frac{(\frac{5}{2}+p)F_{\frac{3}{2}+p}(\xi)}{(\frac{3}{2}+p)F_{\frac{1}{2}+p}(\xi)} - \xi\right\} \quad \text{(A.4)}$$

where

$$F_n(\xi) = \int_0^\infty \frac{x^n\,dx}{e^{x-\xi}+1} \quad \text{(A.5)}$$

and

$$\xi = \frac{\zeta}{kT} \text{ for electrons,}$$

$$= \frac{E_0-\zeta}{kT} \text{ for holes.}$$

It also follows from equations (A.1) and (A.4), that, where both electrons and holes carry the current,

$$S_i = \frac{\sigma_{ei}S_e + \sigma_{hi}S_h}{\sigma_{ei} + \sigma_{hi}} \qquad \text{(A.6)}$$

The subscripts e and h refer to electrons and holes respectively, and $S_1 = S_2 = S_\perp$, and $S_3 = S_\parallel$.

REFERENCES

1. SHOENBERG D., *Progress in Low Temperature Physics* Vol. 2. p. 226. North-Holland Publishing Co., Amsterdam (1957).
2. AUBREY J. E. and CHAMBERS R. G., *J. Phys. Chem. Solids* **3,** 128 (1957).
3. GALT J. K., YAGER W. A., MERRITT F. R., CETLIN B. B. and BRAILSFORD A. D. To be published. Their results were briefly reported at the International Conference on the Electronic Properties of Metals at Low Temperatures, 25–29 August, 1958, held in Geneva, New York.
4. ABELES B. and MEIBOOM S., *Phys. Rev.* **101,** 544 (1956).
5. BOYDSTON R. W., *Phys. Rev.* **30,** 911 (1927).
6. BRIDGMAN P. W., *Proc. Amer. Acad. Arts Sci.* **63,** 351 (1929); *Proc. Nat. Acad. Sci.* **13,** 46 (1927).
7. SATO T., *J. Phys. Soc. Japan* **6,** 125 (1951).
8. SAVORNIN J. and POGGI A., *C. R. Acad. Sci. (Paris)* **238,** 656 (1954).
9. HEINE V., *Proc. Phys. Soc.* A**69,** 513 (1956).
10. WHITE G. K. and WOODS S. B., *Phil. Mag.* **3,** 342 (1958).
11. SALKOVITZ E. I., *Trans. Amer. Inst. Min. (Metall.) Engrs.* **206,** 176 (1956).
12. VICKERS W., *Trans. Amer. Inst. Min. (Metall.) Engrs.* **209,** 827 (1957).
13. NYSTROM J., *Ark. Mat. Astr. Fys.* **34A,** No. 27 (1947).
14. MEISSNER W., *Handbuch der Experimentalphysik* (Ed. W. WIEN and F. HARMS) Band XI, p. 401 Akademische Verlagsgesellschaft, Leipzig (1935).
    BORELIUS G., *Handbuch der Metallphysik* (Ed. G. MASING) Band I, Teil 1, p. 392 Akademische Verlagsgesellschaft, Leipzig (1935).
15. KOHLER M., *Ann. Phys., Leipzig* **40,** 196 (1941).
16. KAYE G. W. C. and ROBERTS J. K., *Proc. Roy. Soc.* A**104,** 98 (1923).
    KAYE G. W. C. and HIGGINS W. F., *Phil. Mag.* **8,** 1056 (1929).
17. NISHIOKA S., *Mem. Coll. Sci. Kyoto Univ.* A**25,** 147 (1949).
18. AIRAPETYANTS S. V. and BRESLER M. S., *Zh. Tekh. Fiz.* **28,** 1935 (1958).
19. HERRING C. and VOGT E., *Phys. Rev.* **101,** 944 (1956).
20. MADELUNG O., *Handbuch der Physik.* (Ed. S. FLUGGE) Band 20, p. 58 Springer, Berlin (1957).
21. KUNZLER J. E. and BOYLE W. S., *Bull. Amer. Phys. Soc.* **4,** 168 (1959).
22. KEESOM P. H. and PEARLMAN N., *Phys. Rev.* **96,** 897 (1954).
    RAMANATHAN K. G. and SRINIVASAN T. M., *Phys. Rev.* **99,** 442 (1955).
    KALINKINA I. N. and STREKOV P. G., *Sov. Phys. (JETP)* **34,** 426 (1958).

J. Phys. Chem. Solids Pergamon Press 1959. Vol. 11. pp. 274–277. Printed in Great Britain.

DIELECTRIC PROPERTIES OF SINGLE CRYSTALS OF $SrTiO_3$ AT LOW TEMPERATURES*

H. E. WEAVER†

Instrument Division, Varian Associates, Palo Alto, California

(*Received* 27 *February* 1959; *revised* 4 *June* 1959)

Abstract—The behavior with temperature variation of the "small-signal" dielectric constant of single crystals of $SrTiO_3$ has been measured from 296 down to 1·4°K, with a maximum value of 18,000 at 1·4°K. The temperature-dependence of the dielectric constant was observed to deviate from the classical Curie–Weiss law at ~ 50°K. The *D–E* curves ("large-signal") show a remnant or "spontaneous" polarization, and hence hysteresis, beginning at 45°K. A maximum value of the saturation polarization of 1·5 $\mu C/cm^2$ was observed at 1·4°K. These data are taken as evidence of ferroelectricity in $SrTiO_3$ below 45°K.

VOL
11
195

OVER the past few years various groups have reported on their investigations into the existence of a ferroelectric transition in $SrTiO_3$ at low temperatures. These results have varied from no evidence,[1,2] through the existence of the ferroelectric state under the prolonged application of a bias field,[3–5] to the predicted spontaneous occurrence of this state from the dielectric behavior at the transition temperature of barium–strontium mixed crystals when extrapolated[6,7] to pure $SrTiO_3$. It is the purpose of the present paper to report the existence of fairly well-defined hysteresis loops at 4·2°K and above. Typical hysteresis loops over the interesting temperature range are shown in Fig. 1. The circuit employed for the display of dielectric hysteresis is patterned after that used by SAWYER and TOWER.[8]

Evidence for the existence of hysteresis in $SrTiO_3$ may be clearly seen at 50°K and below. Above 40°K, but below 50°K, the *D–E* curves show only slight saturation effects, indicating a non-linear behavior with applied field. Above 50°K, the *D–E* curves are linear with applied field. A series of determinations of the saturation polarization from the dielectric hysteresis curves is plotted in Fig. 2. Within experimental error there appears to be no discontinuity in the temperature-dependent values of the saturation polarization. The maximum value of the saturation polarization was found to be $\sim 1{\cdot}5\ \mu C/cm^2$ at 1·4°K. The coercive field was estimated to be ~ 670 V/cm.‡

Measurements of the dielectric constant at a frequency of 1 kc/s and with applied fields < 1 V/cm (General Radio CRL bridge) over a temperature range from 296 down to 1·4°K, show a variation in value from 370 at room temperature to a maximum of ~ 18,000 at 1·4°K. Saturation of the dielectric constant with temperature variation was observed to begin at ~ 10°K. The low-temperature value is in agreement with that found by YOUNGBLOOD[1] and GRÄNICHER[3].

The temperature-dependence of the dielectric constant above liquid-nitrogen temperatures follows quite well that of the Curie–Weiss law for dielectrics, with $8{\cdot}64 \times 10^4$ for the constant of proportionality and 35°K for an extrapolated value of the Curie temperature (Fig. 3). At temperatures below 77°K, and particularly at 50°K, the dielectric

* Supported in part by the Signal Corps Research and Development Branch, Fort Monmouth, New Jersey. Contract No. DA-36-039 sc-73266.

† Present address: Physikalisches Institut der Universität, Zürich, Switzerland.

‡ All these measurements were made on plates cut from boules obtained from The National Lead Company. However, measurements performed by T. G. DUNNE (private communication) at I.B.M., Poughkeepsie, New York, on crystal plates grown from a saturated solution show similar behavior with temperature of the dielectric properties.

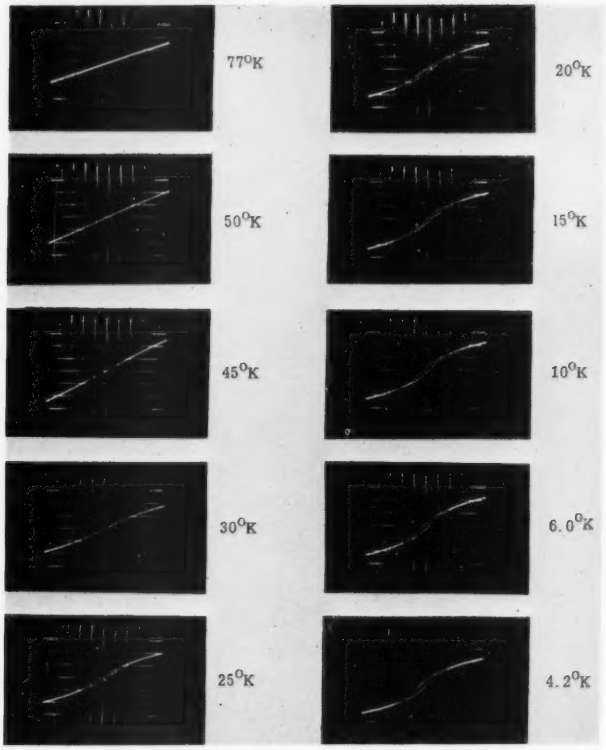

FIG. 1. Hysteresis loops in $SrTiO_3$ from 77 to 4·2°K. The crystal was cut parallel to one of the cube faces (in evidence on the original boule) and was approximately 0·03 cm thick, with an electroded area of ~ 0·15 cm^2. The sweep frequency was 200 c/s and sine wave. Vertical and horizontal scope calibrations are 10 and 20 V/cm respectively. The reference linear condenser had a value 0·02 μF.

[*facing page* 274

VOL
11
195

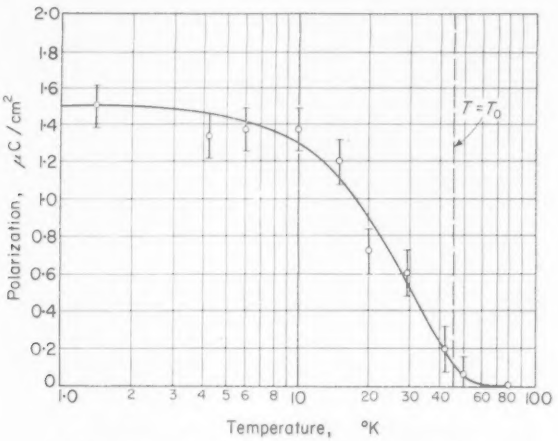

FIG. 2. Temperature-dependence of saturation polarization. The saturation polarization is not zero at $T = T_0$, though no hysteresis, and hence no spontaneous polarization, was detected above this temperature, because of the non-linear character of the D–E curves.

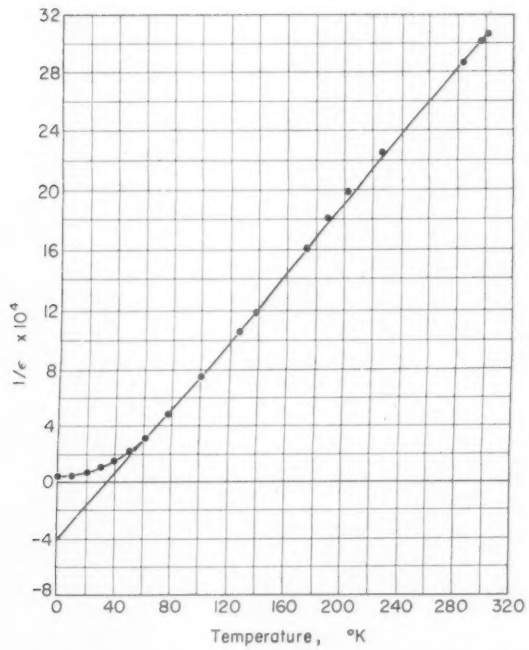

FIG. 3. Reciprocal of the dielectric constant of $SrTiO_3$ versus temperature.

constant deviates appreciably from the Curie law and in fact exhibits saturation at a temperature near 10°K.

The behavior with temperature of the small-signal dielectric constant does not appear to exhibit a maximum at the transition temperature, as might be expected for a material exhibiting a classical second-order transition. The extrapolated value of 35°K for a Curie temperature is thus thought to be questionable. However, the behavior of the dielectric constant over the entire temperature range may be described by a relation published by BARRETT[9]. His calculation is an extension of Slater's theory to include quantum effects, which may become important in those cases when the transitions occur at relatively low temperatures. The essential feature of BARRETT's calculation is the introduction of a characteristic temperature $T_1 = \hbar\omega/k$, where ω is the fundamental angular frequency of a harmonic oscillator in a potential well and may be thought of as that temperature below which quantum effects become important. His equation relating dielectric constant with temperature has the form:

$$\epsilon = \frac{M}{\frac{T_1}{2}\coth\frac{T_1}{2T} - T_0}$$

where in the two limiting cases of $T < T_1$:

$$\epsilon = \frac{M}{1/2T_1 - T_0}$$

and $T > T_1$:

$$\epsilon = \frac{M}{T - T_0}.$$

The equation as plotted in Fig. 4 has been written in terms of dimensionless parameters and has the form:

$$y = \frac{1}{\coth x - 1/x_0}$$

where:

$$y = \frac{\epsilon T_1}{2M}$$

$$x = \frac{T_1}{2T}$$

$$x_0 = \frac{T_1}{2T_0}.$$

Of the three possible choices of x_0, a rather good fit with the experimental points over the entire temperature range was obtained for $T_0 = +0{\cdot}453\,T_1$, or for $T_0 = +45°\text{K}$ and $T_1 \simeq 100°\text{K}$.[9] (This

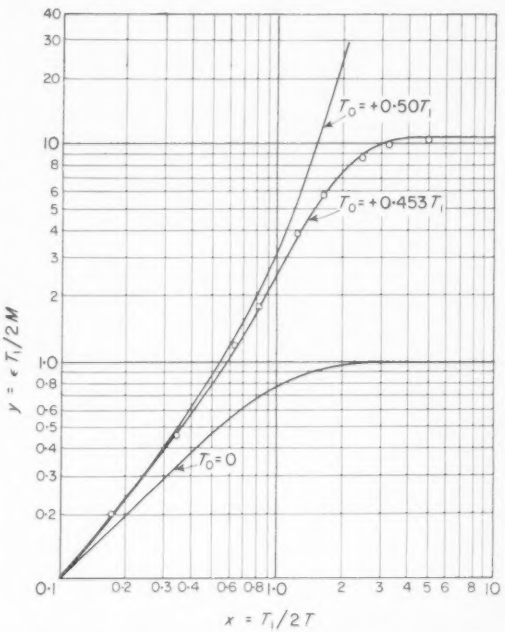

FIG. 4. Comparison of theoretical and experimental variation of the dielectric constant with temperature. The three smooth curves represent possible choices of the parameter $x_0 = T_1/2T_0$. The experimental points are circled.

temperature would correspond to an oscillator frequency of $2{\cdot}1 \times 10^{12}$ c/s or, in terms of wave numbers, 70 cm^{-1}, which very likely lies beyond the practical far-infrared region.) This value of 45°K for the transition temperature as a parameter in BARRETT's theory is in substantial agreement with the hysteresis data of 40–50°K, but higher than the value of 35°K predicted from extrapolation of the Curie–Weiss high-temperature data of Fig. 1. The transition appears to be of the second kind, as is evidenced from the plot of polarization versus temperature and from the fact that the hysteresis loops observed near the transitions were

always single and not double as is observed in $BaTiO_3$.*

The crystals were cut in thin plates parallel to one of the cube faces. Electrical contact was established by electroding the crystals with sputtered gold and mounting them between spring-loaded gold-plated contacts. All temperatures from 4·2 to 77·3°K were measured by a resistance thermometer, and all temperatures from 77 to 296°K were measured by a copper/Constantan thermocouple. Temperatures below 4·2°K were determined from measurements of helium vapor pressure as well as from the resistance thermometer.

Acknowledgements—The author would like to express his appreciation to Dr. R. C. REMPEL, of Varian Associates, for his contributions during the course of this work and to Prof. E. T. JAYNES for his continued interest in the program. The author is also indebted to Dr. G. BURNS and Dr. T. G. DUNNE of the Ferroelectric Group at I.B.M., Poughkeepsie, New York, for very profitable discussions and to Dr. BRICKENKAMP, of The National Lead Company, who was instrumental in supplying the single-crystal boules of $SrTiO_3$.

* In particular, it may be noted that the slope of the *D–E* curves at the Curie point always *decrease* with increasing applied field. This is a characteristic of second-order transitions as distinguished from first-order transitions.[10]

REFERENCES

1. YOUNGBLOOD J. F., *Phys. Rev.* **98,** 1201A (1955).
2. HULM J. K., *Proc. Phys. Soc.* A**63,** 1184 (1950).
3. GRÄNICHER H., *Helv. Phys. Acta* **29,** 210 (1956).
4. KÄNZIG W., *Ferroelectrics and Antiferroelectrics* Vol. 4, pp. 23, 66. Academic Press, New York (1957).
5. MÜLLER K. A., *Helv. Phys. Acta* **31,** 173 (1958).
6. RUSHMAN D. F. and STRIVENS M. A., *Trans. Faraday Soc.* **42A,** 231 (1946).
7. SMOLENSKII G. A., *Translations Bull. Acad. Sci. U.S.S.R.* 21, No. 2 (1954).
8. SAWYER C. B. and TOWER C. H., *Phys. Rev.* **35,** 269 (1930).
9. BARRETT J. H., *Phys. Rev.* **86,** 118 (1952).
10. JAYNES E. T., *Ferroelectricity* p. 77. Princeton University Press (1953).

J. Phys. Chem. Solids Pergamon Press 1959. Vol. 11. pp. 278–283. Printed in Great Britain.

SOME PHYSICAL PROPERTIES OF NEPTUNIUM METAL

III. THE ELECTRICAL RESISTIVITY AND THERMOELECTRIC POWER OF NEPTUNIUM METAL IN THE RANGE 300–900°K

J. A. LEE, J. P. EVANS, R. O. A. HALL and E. KING

Atomic Energy Research Establishment, Harwell

(*Received* 28 *May* 1959)

Abstract—The electrical resistance of a sample of neptunium metal has been measured between 300 and 900°K, and the resistivity of neptunium in its three allotropic modifications calculated. A measurement of the thermal e.m.f. of a neptunium/platinum thermocouple has been made within the temperature-stable range of each allotrope, and the corresponding absolute thermoelectric powers calculated. The results are discussed briefly.

VOL
11
195

1. INTRODUCTION

THE paper describes part of the work on the physical properties of neptunium metal that was undertaken when neptunium 237 became available in the United Kingdom in gram quantities.[1] The initial part of the programme, which confirmed the existence of three allotropic modifications, designated α, β and γ,[2,3] between 300°K and the melting point at 910°K, has been described previously.[4–6]

2. RESISTIVITY MEASUREMENTS

The handling of neptunium is complicated by its radioactivity. Ordinarily the problem is a consequence of its α-emission only, as the major isotopic constituent, neptunium 237, is neither β- nor strongly γ-active. The health hazard is directly comparable to that involved in handling uranium 233 or plutonium; work on quantities greater than a few milligrams must be carried out in glove boxes. The general techniques for this type of work are now firmly established;[7] all the handling of the neptunium metal was carried out in free-standing glove boxes, the box atmosphere being high-purity argon.

(a) *Specimen purity*

Analysis of the reduction billet[8] showed impurities to be present in the following weight percentages: calcium 0·34, uranium 0·22, nickel 0·06, magnesium 0·03, chromium 0·03, plutonium 0·03, aluminium 0·02, vanadium $< 0{\cdot}06$ and molybdenum $\leqslant 0{\cdot}05$. It is possible that the calcium and magnesium are largely removed by subsequent argon-arc melting. The measured density of an arc-melted sample was $20{\cdot}25 \pm 0{\cdot}02$ g/cm^3, as compared with the theoretical X-ray value 20·45 g/cm^3.

(b) *Experimental methods*

The resistivity was measured by standard potentiometric techniques, using a cylindrical rod of neptunium 4 cm long by 0·2 cm diameter, prepared from an arc-melted slug by casting under vacuum into a precision-bore silica tube. Measurements were made under vacuum in a resistance furnace, the specimen being held in a jig formed from a massive copper block, to reduce thermal gradients along the specimen length (Fig. 1). The specimen temperature was measured by a calibrated Chromel/Alumel thermocouple with its hot junction in touch contact with the specimen at the centre of its length. Potential and current contacts were made by spot welding four 0·010-in.-diameter copper leads to the rod, to reduce contact resistance; the potential leads were continuous from the specimen to the potentiometer.

Measurement of the resistance of the neptunium was made under equilibrium conditions; the temperature of the copper jig was held at a series

VOL.
11
1959

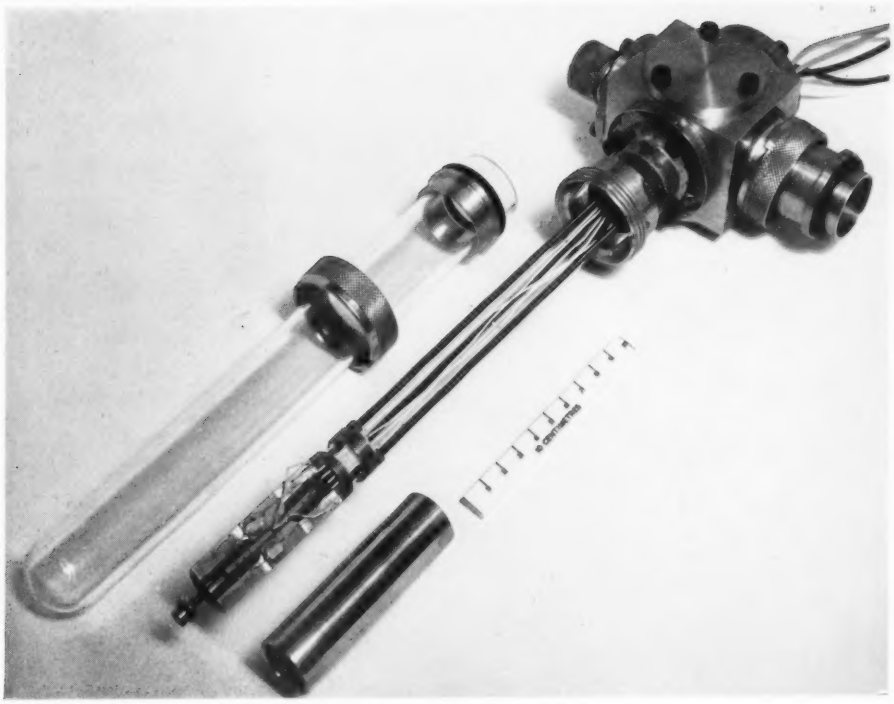

FIG. 1. Resistivity jig.

[facing page 278

VOL.
11
195

Table 1. *Resistivity of neptunium*

Phase	Run number	Temperature (°K)	Resistivity ($\mu\Omega$cm)
α	Heating 1	310	116·4
	Heating 3	314	116·1
	Heating 1	334	117·7
	Heating 1	347	117·8
	Heating 3	370	119·1
	Heating 1	373	119·3
	Cooling 1	425	120·5
	Heating 1	433	120·7
	Cooling 1	472	120·9
	Heating 1	512	120·8
	Heating 2	538	121·3
$\alpha \rightarrow \beta$ transformation	Heating	558±5	
β	Heating 2	586	105·3
	Heating 3	600	105·3
	Heating 2	612	106·2
	Heating 2	641	107·1
	Heating 2	669	107·9
	Heating 2	705	108·9
	Heating 2	740	109·5
	Heating 2	771	109·9
	Heating 3	773	109·7
	Cooling 3	828	109·8
$\beta \rightarrow \frac{1}{2}$	Heating	847±5	
	Cooling	847±5	
γ	Heating 3	873	109·8
	Heating 3	879	109·7
	Heating 3	896	109·4
	Heating 3	902	109·6

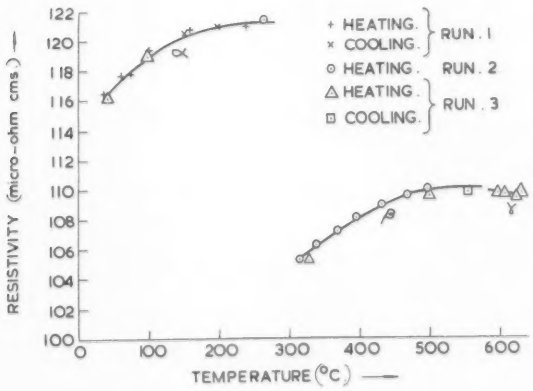

FIG. 2. Resistivity/temperature graph.

of fixed temperatures, and the variation in resistance with the electrical energy dissipated in the specimen was measured, the resistance of the specimen at zero power being determined by extrapolation.

(c) *Results*

The results given in Table 1 and shown graphically in Fig. 2 have been corrected for thermal expansion in the α and β phases and for change in volume at the $\alpha \rightarrow \beta$ and $\beta \rightarrow \gamma$ transformations, using the expansion coefficients and densities determined by X-ray parameter measurements, which are in good agreement with the values determined by dilatometric techniques.[5] No correction has been applied for thermal expansion within the γ phase, where a reliable value is not available.

For any one sample the maximum error in measurement arises from inaccuracy in determining the distance between the potential contacts and in measuring the rod diameter. These lead to an estimated accuracy of $\pm 0{\cdot}1$ per cent.

The rod showed no distortion after cycling through the phase changes, the length between the potential contacts and the specimen diameter being constant to within the accuracy of measurement. Surface oxidation was very slight. Measurements of the resistivity of the α-phase before and after cycling were in good agreement.

3. THERMAL E.M.F. MEASUREMENTS

The thermal e.m.f. measurements were made on the same neptunium rod as that used for the resistivity determinations.

(a) *Experimental methods*

A neptunium/platinum thermocouple was made by spot welding an equal length of 0·010-in.-diameter platinum lead to one end of the rod to form the hot junction and forming the cold junctions by spot welding copper leads to the other ends of the neptunium rod and the platinum wire. The welding operations were carried out in an argon-filled glove box, and good clean junctions were obtained.

The specimen jig is shown diagramatically in Fig. 3. The hot junction was enclosed in a copper cylinder, 1 cm long by 1 cm diameter, held in a close-fitting alumina crucible which was the former of a small resistance furnace. The cold junction was enclosed in a massive copper block.

The thermal e.m.f. of the couple was determined within the temperature-stable range of the three allotropic modifications, using standard potentiometric techniques. Measurements were made in a vacuum furnace, the cold junction being controlled at a fixed temperature at the lower end of the temperature-stable range of the phase, using the main furnace, whilst the hot-junction temperature was raised by means of the small subsidiary furnace. The temperatures of the two junctions were measured by calibrated Chromel/Alumel thermocouples in touch contact with the

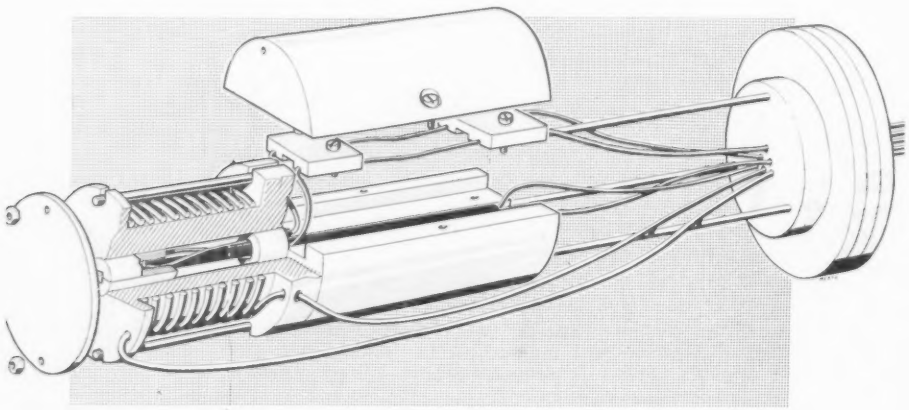

FIG. 3. Thermal e.m.f. jig.

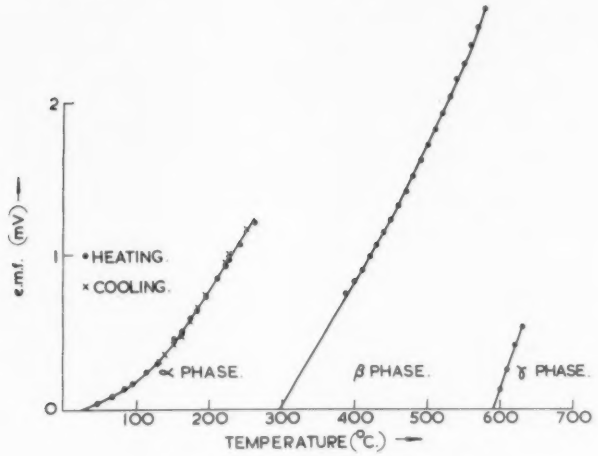

FIG. 4. E.m.f./temperature graph.

Phase	αU 300°K	βU 975°K	γU[11] 1100°K	αPu 300°K	βPu 400°K	γPu 500°K	δPu 600°K	δ′Pu 725°K	εPu[12] 800°K	αTh[10] 700°K	αNp 400°K	βNp 700°K	γNp 875°K
$10^3 \frac{\sigma\theta}{T}, \frac{\mu V}{(Deg)^2}$	26	21	20	51·7	25·0	18·4	6·2	3·2	5·3	-4	-7·2	-6	-3·2

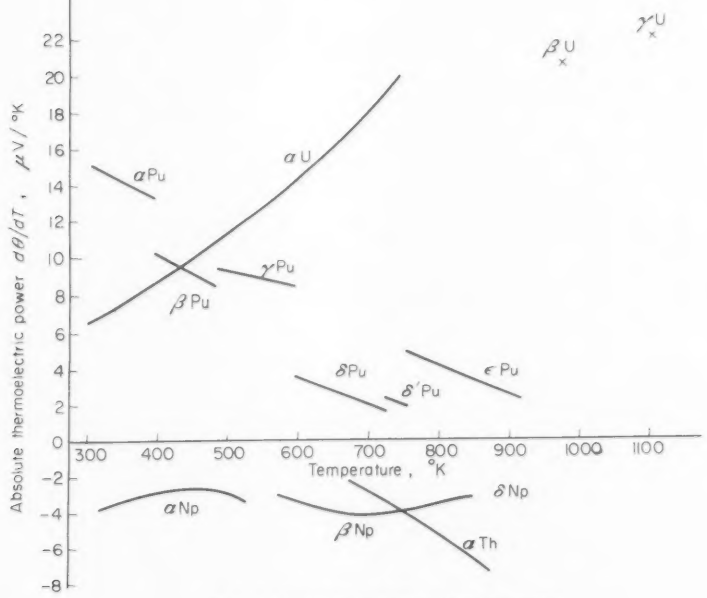

FIG. 5. Absolute thermoelectric power.

junctions. The measurements were made dynamically at a slow heating rate of 0·5°C/min.

(b) *Results*

The results are shown graphically in Fig. 4, where the values of the e.m.f. are plotted against the hot-junction temperature; the cold-junction temperature is given by the intersection of the plot with the abscissa. Fig. 5 shows the absolute thermoelectric power calculated from the slope of the e.m.f. temperature curve and the absolute thermoelectric power for platinum.[9] Values for thorium,[10] uranium[11] and plutonium[12] are included for comparison. The absolute thermoelectric power has a small negative value in all three of the neptunium phases.

4. DISCUSSION

RIDLEY's calculation of a Wigner–Seitz approximation to the outer electron wave function for metallic uranium,[13] and similar work by LEHMAN on thorium and uranium[14] have indicated that in metallic uranium the 7*s*, 7*p* atomic levels are raised in energy on forming the solid and are most unlikely to be occupied in the metal. The band formed from the 6*d* atomic levels is broad, ~ 6 eV wide, and the wave function very uniform over most of the atomic cell. The 5*f* states form a narrow band, $\sim 0{\cdot}5$–1 eV wide, and about the same energy. Both bands are partially occupied.

This picture is qualitatively similar to that deduced by FRIEDEL,[15] although his broad conduction band is based on 7*s*, 7*p* rather than 6*d* electrons, and his narrow, high density-of-states band on 6*d*–5*f* hybrids than almost entirely 5*f*. It resembles the band structure for the transition metals.

It seems likely that a similar picture holds for neptunium and plutonium. Experimentally the high specific heat for α-neptunium[4] and its large paramagnetic susceptibility[16] indicate a high density of states at the Fermi surface. The high absolute value of the resistivity could be attributed to the scattering of the conduction electrons into a narrow high-density band; a comparison of the function $\sigma/M\theta_D^2$, where σ is the specific conductivity, M the atomic weight and θ_D the Debye temperature, shows that the elements thorium, uranium, neptunium and plutonium fall into a well-defined series with $\sigma/M\theta_D^2 = 1{\cdot}17\times10^{-2}$, $0{\cdot}68\times10^{-2}$, $0{\cdot}27\times10^{-2}$ and $0{\cdot}17\times10^{-2}$ at room temperature for thorium, uranium, neptunium and plutonium respectively, a value of θ_D for neptunium = 117°K being deduced from its melting point by using the Lindemann expression.

Table 2 shows the variation of the temperature coefficient of resistivity with temperature in the three allotropes. For α-neptunium the coefficient falls from a positive value of 46×10^{-5} at 300°K to a value approaching zero at the top of its stable temperature range. A similar form is shown for the β phase, whilst the temperature coefficient of the γ phase is negative. Curves of this form, associated with anomolies in magnetic susceptibility, have been observed with the rare-earth metals; alternatively the decrease in the temperature coefficient of resistivity could be attributed to an increase in the number of carriers, though experimental data are too limited for any serious discussion.

Table 2. Temperature coefficients of resistivity

Phase	Temperature (°K)	Coefficient of resistivity × 10^5
α	300	46
	350	28
	400	18
	450	12
	500	6
	550	1
β	600	31
	840	0
γ	875	−6

The thermoelectric power is very sensitive to the form of the Fermi surface. It depends on the way in which the mean free path and the effective mass of the electrons, which determine electrical conductivities, vary with energy. Conventional theory leads to the expression for the thermoelectric power, $d\theta/dT$[17,18]

$$\frac{d\theta}{dT} = \frac{\pi^2k^2}{3e}\left\{\frac{1}{\sigma}\cdot\frac{d\sigma}{dE}\right\}_\zeta \cdot T \qquad (1)$$

where

$$\sigma(E) = \frac{e^2}{4\pi^3\hbar^2}\int \tau(K)\left(\frac{dE}{dK}\right)^2\frac{dS}{(\nabla E)} \qquad (2)$$

The subscript ζ in equation (1) means that the derivative is evaluated at the Fermi surface $\tau(K)$ is the relaxation constant and K is the wave vector defined so that $\hbar K$ is the momentum. The other symbols have their usual significance; e is negative. For pure metals this expression is valid whatever the relation between E and K at temperatures greater than the Debye temperature, i.e. it should hold for neptunium in the range in which the thermoelectric power has been measured.

To a first approximation we may discuss neptunium on a two-band picture. Bearing in mind the experimental data, the position is analogous to the case for uranium, which FRIEDEL has discussed in some detail.[15] We have two possibilities: either the Fermi surface is overlapped by a single inverted narrow band, with a high density of states, or it is overlapped by both a narrow band and a broad conduction band. In the former case a high positive value for the absolute thermoelectric power would correspond to a large negative slope for the density-of-states curve. In the latter case the conductivity would be to a large extent inversely proportional to the probability of transition from the conduction band to the narrow band,[19] and a high positive thermoelectric power would correspond to a narrow band with a high positive slope $d(NE)/d(E)$ and vice versa.

The absolute value of the thermoelectric power in all three phases of neptunium is small and negative, indicating that the slope of the density-of-states curve must be small.

Acknowledgements—The authors wish to thank Dr. M. B. WALDRON for his interest and encouragement in this work.

REFERENCES

1. NAIRN J. S., COLLINS D. A., MCKAY H. A. C. and MADDOCK A. G., *Conf. Peaceful Uses of Atomic Energy (Geneva)*, Paper No. 15/P/1458 (1958).
2. ZACHARIASEN W. H., *Acta Cryst., Camb.* **5,** 660 (1952).
3. ZACHARIASEN W. H., *Acta Cryst., Camb.* **5,** 664 (1952).
4. EVANS J. P. and MARDON P. G., *J. Phys. Chem. Solids* **10,** 311 (1959).
5. LEE J. A., MARDON P. G., PEARCE J. H. and HALL R. O. A., *J. Phys. Chem. Solids* **11,** 177 (1959).
6. MCKAY H. A. C., NAIRN J. S. and WALDRON M. B., *Conf. Peaceful Uses of Atomic Energy (Geneva)* Paper No. 15/P/304 (1958).
7. *Glove Boxes and Shielded Cells for Handling Radioactive Materials* (Ed. G. N. WALTON). Butterworths, London (1958).
8. ELDRED V. W. and CURTIS G. C., *Nature, Lond.* **179,** 910 (1957).
9. *Handbuch der Metallphysik* (Ed. G. MASING) Band 1, Teil 1, 398. Akad. Verlagsges., Leipzig (1935).
10. BODINE J. H. Jr., *Phys. Rev.* **102,** 1459 (1956).
11. DAHL A. and VAN DUSEN M. S., *J. Res. Nat. Bur. Stand.* **39,** 53 (1957).
12. LEE J. A. and HALL R. O. A., *Atomic Energy Research Estab. Rep.* M/R 2800 (1959).
13. RIDLEY E. C., *Proc. Roy. Soc.* A**243** 422 (1958); A**247,** 199 (1958).
14. LEHMAN GUY W., *U.S. Atomic Energy Commission Publ.*, NAA–SR–1839 (1957).
15. FRIEDEL J., *J. Phys. Chem. Solids* **1,** 175 (1956).
16. GARDNER W. E., private communication.
17. WILSON A. H., *Theory of Metals and Alloys*, Cambridge University Press (1953).
18. JONES H., *Proc. Phys. Soc.* **68,** 1191 (1955).
19. MOTT N. F. and JONES H., *Theory of the Properties of Metals and Alloys*, Oxford University Press (1936).

J. Phys. Chem. Solids Pergamon Press 1959. Vol. 11. pp. 284–287. Printed in Great Britain.

MEASUREMENT OF THE HALL EFFECT AND CONDUCTIVITY OF SUPER-PURE SILICON

A. HOFFMANN, K. REUSCHEL and H. RUPPRECHT

ZW-Laboratory, Pretzfeld, and Research Laboratory, Erlangen, Siemens-Schuckertwerke AG, Germany

(*Received* 3 *June* 1959)

Abstract—With the floating-zone technique we have obtained super-pure, uncompensated silicon of *p*-type with a resistivity above 100 000 Ωcm. The intrinsic conductivity of these samples reaches near to 40°C. The intrinsic density n_i obtained over a range from 50° to 100°C agrees quite closely with the n_i-values determined by other investigators. The distribution coefficient k of boron is slightly below 0·9.

VOL
11
195

If silicon is subjected to a sufficient number of zone passes in a floating zone-refining apparatus[1] under vacuum, the material obtained is uncompensated and its conductivity (in the extrinsic range) is determined by the boron content. The resistivity measured on such rods is a measure of the degree to which the boron concentration has been reduced in the preceding chemical process,* since boron can hardly be removed by zone refining as a result of its near-unity distribution coefficient.† After such a sample rod had been subjected to 71 zone passes (specimen 6), the variation of resistivity with temperature shown in Fig. 1 was obtained‡ and values of 150,000 Ω cm (300°K) were obtained at its pure end where the boron impurity level had been reduced to 10^{11} cm^{-3}. It therefore appeared reasonable to extend measurements on the intrinsic conductivity contained in the references (4–7) to lower temperatures. At first the measurements of the Hall effect and the conductivity were made above room temperature and evaluated. The single-crystal specimens, which were of the *p*-type at room temperature, were cut into plates 3×4×25 mm. To avoid adverse effects due to surface conductance, the surface was lightly ground (see Putley and Mitchell[7]). Pointed spring contacts of brass were used as probes. The equipment for low-temperature measurements was similar to that described by Weiss[8] and Rupprecht[9], except that a water bath was employed instead of liquid nitrogen. The electric field strength remained below 1 Vcm^{-1}. The Hall voltage was measured by a vibrating condenser electrometer.§ To obtain high sensitivity it proved necessary to compensate the zero voltage of the probes; likewise, compensation for false thermal effects was provided by reversing both the sign of the current and the direction of the magnetic field.

As is conventional, the electrical conductivity was logarithmically plotted against $1/T$ (Fig. 2). The intrinsic conductivity range was entered at as low a temperature as 40°C (specimen 6) and 50°C (specimen 5). At higher temperatures the curves are in good agreement with the intrinsic conductivity values found by Putley and Mitchell[7]. A corresponding plot of the Hall coefficient is shown in Fig. 3. The change in sign of the Hall

* For the hydrogen reduction of silicon halides see, for example, Hölbling and Theuerer.[2]

† With a great number of zone passes made at a slow moving rate, light evaporation still appears, which makes it possible to reduce the boron level by a factor between 2 and 5.

‡ The high number of zone passes was easily obtained with a fully automatic floating zone-refining apparatus, which R. Emeis had designed for our purposes. The principles of operation were discovered by R. Emeis, W. Keller, H. Quast and Th. Rummel; these differ essentially from those of Buehler's arrangement.[3]

§ Frieseke und Höpfner, Erlangen, Germany, Type No. 408.

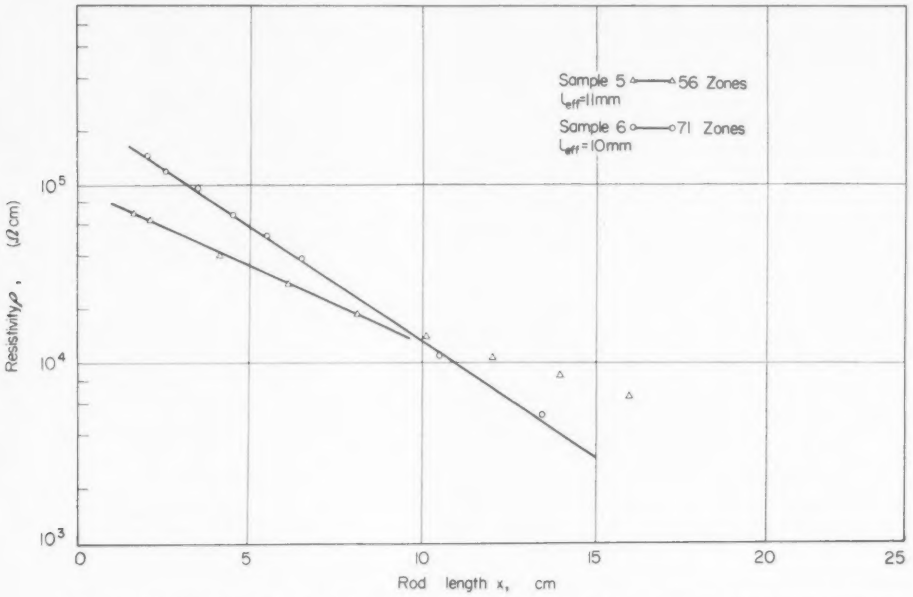

FIG. 1. Electrical resistivity as function of the rod length x of two zone-refined single crystals of silicon.

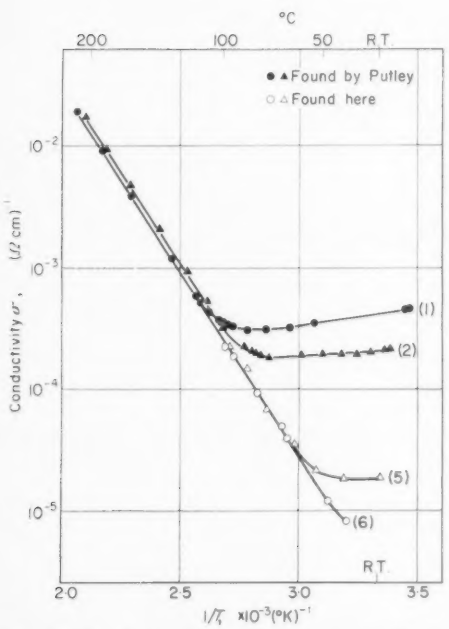

FIG. 2. Electrical conductivity of p-type silicon single crystals as a function of the temperature. The curves (1) and (2) are taken from a paper by PUTLEY and MITCHELL[7].

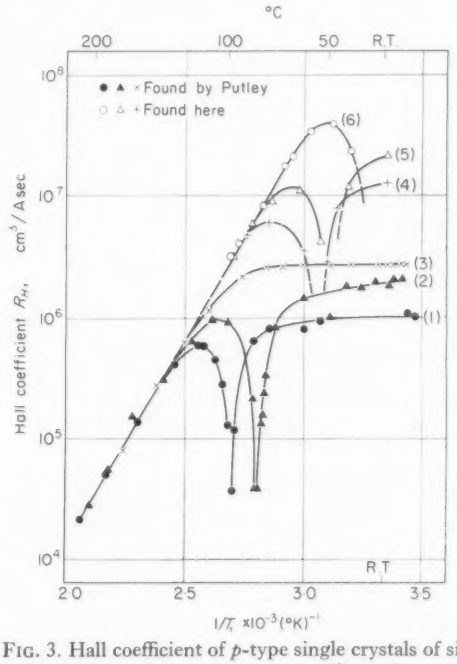

FIG. 3. Hall coefficient of p-type single crystals of silicon as a function of the temperature. The values marked correspond to those of Fig. 1. For comparison values for an n-type specimen according to PUTLEY and MITCHELL[7] are plotted (curve 3).

coefficient as indicated to the right of the intrinsic conductivity branch accounts for the concentration of holes at low temperatures. In the intrinsic range there is a satisfactory agreement with the electrical values given by PUTLEY and MITCHELL (curves 1–3). The measured values of the electrical conductivity σ and the Hall coefficient R_H can be expressed independently as a function of the intrinsic density n_i, assuming physically plausible mobilities. On the one hand, the electrical conductivity in the intrinsic range can be written

$$\sigma = en_i(\mu_n+\mu_p). \tag{1}$$

Assuming for the conductivity mobilities the values found by LUDWIG and WATTERS[10] or ZERBST and HEYWANG[11] in drift measurements, this equation can be solved for n_i. On the other hand, in the intrinsic conductivity range the Hall coefficient can be represented by the formula:

$$R_H = \frac{3\pi}{8}\cdot\frac{1}{en_i}\cdot\frac{b-1}{b+1}, \text{ where } b=\frac{\mu_n}{\mu_p}. \tag{2}$$

If the drift mobilities given by LUDWIG and WATTERS are introduced into this formula, values are obtained for the intrinsic density n_i which agree with those determined from the intrinsic conductivity to within a few per cent.

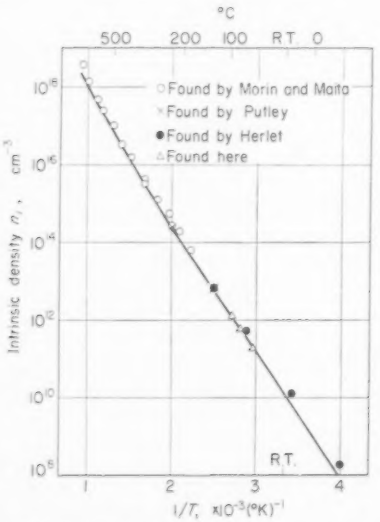

FIG. 4. Intrinsic density of silicon as a function of $1/T$. The line drawn represents the equation (3) given by PUTLEY and MITCHELL[7].

Fig. 4 shows the results for the variation of the intrinsic density with temperature obtained by a number of other workers.[5–7] It proves that the values obtained here fit very well with the formula given by PUTLEY and MITCHELL[7] (line drawn in Fig. 4):

$$\frac{n_i}{\text{cm}^{-3}} = 1{\cdot}61\times10^{20}\left(\frac{T}{300°\text{K}}\right)^{3/2}\exp\left(\frac{1{\cdot}206\text{ eV}}{2kT}\right). \tag{3}$$

However, the values of MORIN and MAITA[5] and those of HERLET[6] are about 10–20 per cent higher. Considering the other inaccuracies (especially as regards the mobility values assumed), very good agreement is obtained.*

Finally, the resistivity curves of Fig. 1, the values of which have been measured by the conventional two-probes method, can be used to calculate the distribution coefficient of the boron which accounts for the p-type of the specimen. On the assumption that the slope obtained after an adequate number of passes remains constant, PFANN[12] gives for the distribution coefficient k the relation

$$k = -\frac{l\dfrac{d\ln\rho}{dx}}{\exp\left(-l\dfrac{d\ln\rho}{dx}\right)-1}. \tag{4}$$

The gradient $d\ln\rho/dx$ can be taken from Fig. 1, some degree of uncertainty resulting only from the length l of the liquid zone. The effective length l_{eff} is generally somewhat smaller than the visible overall length, as the boundary between the solid and liquid zones is not a completely plane surface. The evaluation of the curves results in a value $k = 0{\cdot}87$ for specimen 6 and $k = 0{\cdot}89$ for specimen 5. These values are in very good agreement with those given by HALL[13], who calculated the distribution coefficient for boron as 0·9.

Acknowledgements—We are grateful to Dr. E. SPENKE and Prof. H. WELKER for the encouragement given in this work; special thanks are due to Mr. R. EMEIS for his aid in construction of equipment.

* Special mention should be made of the work of A. HERLET, who found the values for n_i by a completely different method, namely by the analysis of the forward characteristic of silicon rectifiers.[6]

REFERENCES

1. KECK P. H. and GOLAY M. J. E., *Phys. Rev.* **89,** 1297 (1953).
   EMEIS R., *Z. Naturf.* **9a,** 67 (1954).
   MÜLLER S., *Z. Naturf.* **9b,** 504 (1954).
2. HÖLBLING R., *Z. angew. Chem.* **40,** 655 (1927).
   THEUERER H. C., *Bell Lab. Record* **33,** 327 (1955).
3. BUEHLER E., *Rev. Sci. Instrum.* **28,** 453 (1957).
4. HEYWANG W., ZERBST M. and BISCHOFF F., *Naturwissenschaften,* **41,** 301 (1954).
   HEYWANG W. and ZERBST M., *Siemens-Z.* **31,** 85 (1957).
5. MORIN F. J. and MAITA J. F., *Phys. Rev.* **96,** 28 (1954).
6. HERLET A., *Z. angew. Phys.* **9,** 155 (1957).
7. PUTLEY E. H. and MITCHELL W. H., *Proc. Phys. Soc.* **72,** 193 (1958).
8. WEISS H., *Z. Naturf.* **8a,** 463 (1953).
9. RUPPRECHT H., *J. Phys. Chem. Solids* **6,** 144 (1958).
10. LUDWIG G. W. and WATTERS R. L., *Phys. Rev.* **101,** 1699 (1956).
11. ZERBST M. and HEYWANG W., *Z. Naturf.* **11a,** 608 (1956).
12. PFANN W. G., *Trans. Amer. Inst. Min.* (*Metall.*) *Engrs.* **194,** 747 (1952).
13. HALL R. N., *J. Phys. Chem.* **57,** 836 (1953).

VOL.
11
1959

J. Phys. Chem. Solids Pergamon Press 1959. Vol. 11. pp. 288–298. Printed in Great Britain.

DIFFUSION OF PHOSPHORUS IN SILICON OXIDE FILM

C. T. SAH*, H. SELLO* and D. A. TREMERE*

Fairchild Semiconductor Corporation, Palo Alto, California

(*Received* 17 *June* 1959)

Abstract—The system P_2O_5 (vapor), SiO_2 (thin film) and single-crystal silicon has been investigated by solid-state-diffusion techniques. The p-type silicon underneath the silicon oxide film was used as a "phosphorus detector". A rapid and complete chemical reaction apparently takes place between the SiO_2 and the diffusant, phosphorus or phosphorus oxide, forming a glass (or compound) of unknown composition $P_xSi_yO_z$ at the glass/silicon interface. A sharp boundary is found between the glass and unreacted SiO_2. The results indicate that the growth of the glass is limited by the diffusion of the phosphorus species in the glass with very little or no diffusant left to diffuse in the unreacted silicon dioxide after the complete reaction at the glass/silicon dioxide interface. The growth of this compound or glass follows the parabolic law and is experimentally given by $x_m^2/t_m = 1{\cdot}7 \times 10^{-7} \exp(-1{\cdot}46/kT_m)$ cm^2/sec or $x_m/\sqrt{(t_m)} = 250 \exp(-1{\cdot}46/2kT_m)\ \mu/\sqrt{(\text{hr})}$ over the temperature range 900–1250°C. Here x_m is the thickness of the glass, t_m the diffusion time and T_m the diffusion temperature (°K). The subscript m denotes the condition of complete masking of the silicon oxide against phosphorus, i.e. no n–p junction is formed.

Diffusion experiments in which the silicon oxide film failed to mask or only partially masked against P_2O_5, i.e. x_0^2/t_d was smaller than the value given for x_m^2/t_m, where x_0 is the original oxide thickness and t_d is the diffusion time, were also performed and could be interpreted by using a two-boundary diffusion model. In this case, a species of phosphorus or phosphorus oxide apparently diffuses through the glass with a diffusion coefficient, D_1, followed by the diffusion of phosphorus in the p-type silicon with a higher diffusion coefficient, D_2, to form a n–p junction underneath the glass. The segregation coefficient of phosphorus at the boundary between the glass and the silicon is apparently small. The transition region between complete masking and partial masking is well defined and occurs at a silicon oxide layer thickness < 500 Å. Such a rapid change represents the transition between the models discussed above: the model for the growth law of the glass in silicon oxide and the two-boundary diffusion model for partial masking.

1. INTRODUCTION

SILICON oxide films have been used for selective masking against impurity vapors during diffusion in silicon for semiconductor-device fabrication.[1] The completeness of masking of phosphorus, in general, can be controlled through several parameters: oxide thickness, diffusion temperature, diffusion time, impurity vapor pressure and impurity concentration (p-type) originally present in the silicon. Partial masking for the control of the total amount of impurity diffused into the silicon is also possible by adjusting the above parameters. A series of experiments were performed in which several of the above parameters were varied and in which phosphorus was used as the impurity atom. The results are discussed in terms of two approximate diffusion models.

2. EXPERIMENTAL APPARATUS AND TECHNIQUES

The oxide film was grown on silicon slices in a high-temperature, open-tube furnace containing a Mullite furnace tube of 45 mm inside diameter. The oxidizing atmosphere consisted of tank oxygen saturated with water at room temperature (around 25°C). The oxygen was allowed to flow over the silicon surface at a rate of 500 cc/min.

The silicon slices were p-type, 0·30 Ω-cm, $\sim 200\ \mu$ thick, cut from a single crystal of (100) orientation. One of the surfaces of the silicon slices was mechanically polished to a mirror finish with Linde A aluminum oxide powder. The other surface was lapped with carborundum powder of 1950 grit. All experimental data were obtained on the polished surface.

* Formerly of Shockley Transistor Corporation, where the experimental work was done.

The diffusion experiments were performed in a two-zone, open-tube furnace system similar to that described by FROSCH and DERICK[1]. The system is shown in Fig. 1. The carrier gas, N_2, was dried through a silica gel drier and a cold trap of dry ice and acetone mixture at −78·6°C. Traces of water in the carrier gas would cause

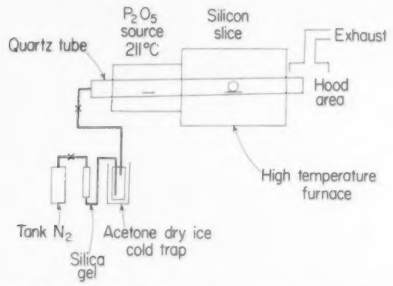

FIG. 1. Schematic of the two-zone phosphorus-diffusion furnace.

the life or the constancy of the vapor pressure of the P_2O_5 source to deteriorate rapidly and tend also to build up oxide on the silicon surface during diffusion. The carrier gas flow-rate was maintained at 200 cm³/min through a quartz furnace tube of 34 mm inside diameter. The furnace tube was thoroughly rinsed in tap and de-ionized water after each experiment and dried before being used again. Fresh and dry P_2O_5 powder was loaded in a cleaned and dried quartz boat and pushed into the low-temperature (source) zone of the furnace. The P_2O_5 was usually aged for 1 hr before the start of the experimental run. For all the experimental data presented, the source was held at 211°C. Fresh P_2O_5 was used every 4 or 5 hr.

The oxidation and the diffusion-furnace temperatures were controlled to within ±1°C over the entire duration of the experimental run by a thermocouple-controlled automatic system. The silicon samples and the P_2O_5 source were placed in the flat temperature zones where temperature variation over the zone was less than 1°C.

3. EXPLORATORY EXPERIMENT

In order to design a complete set of experiments to determine the diffusion characteristics of phosphorus in silicon oxide films, exploratory experiments were performed to ascertain that the reaction of phosphorus and silicon oxide would be accounted for by a diffusion model. The solution of the diffusion equation requires that the diffusion depth, x, be proportional to the square root of the diffusion time—the parabolic law. In the exploratory experiment, this relation was verified for the condition of complete masking at a diffusion temperature $T_d = 1100$°C. Oxides of various thicknesses, x_0 were grown, and the diffusion time, t_m, required for each oxide mask to fail, i.e. just before a n-skin is formed, was determined. The experimental results, shown in Fig. 2, indicated that a parabolic law was satisfied.

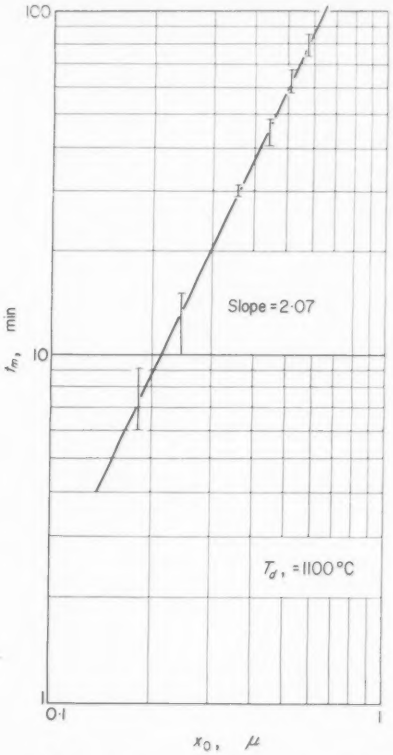

FIG. 2. Exploratory experimental results of the diffusion time, t_m, at which a silicon oxide film of a given thickness x_0 fails to mask against P_2O_5 vapor at a diffusion temperature $T_d = 1100$°C and a P_2O_5 temperature $T_s = 211$°C. The original resistivity is 0·3-Ω-cm p-type.

4. EXPERIMENTAL RESULTS

In view of the confirmation of the diffusion model from the preliminary experimental data, extensive experiments were designed to determine the mask-failure condition at various temperatures. Some partial-masking experiments were also performed and are discussed below.

(a) *Oxide films on silicon*

The oxide films were grown at two temperatures: 1200 and 1300°C. Accurate oxide-thickness measurements were obtained with a Beckman DK-2 spectrophotometer modified for reflectance

measurements. These reflectance measurements were accurate to better than 1 per cent and lie on a straight line. Thus, only solid lines are drawn in Fig. 3 rather than showing individual experimental points from the reflectance measurements.

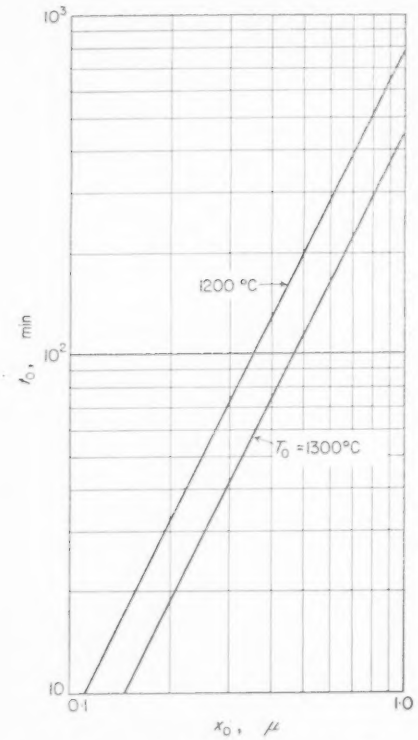

FIG. 3. The growth of the silicon oxide film on single-crystal silicon. Oxidation time, t_m, vs. oxide thickness, x_0, at oxidation temperatures $T_0 = 1200$ and 1300°C.

In addition, a uniform spacing was observed in the wavelengths of reflectance maxima and minima which follows the relationship $2nx_0 = m\lambda$, where $n = 1{\cdot}5$ is the index of refraction of silicon oxide, x_0 is the oxide thickness, m is the order of the reflectance maxima or minima and λ is the wavelength of light at the extremes. This suggests that the silicon oxide film had a rather uniform composition throughout the entire film.

The experimental data shown in Fig. 3 indicate a parabolic growth law for the oxide film. The activation energy of this process, estimated from the data at the two temperatures, is roughly 1·5 eV (35 kcal/g-mol). The results obtained by LIGENZA[2] and by LAW[3] on single-crystal silicon surfaces show an activation energy of 1·7 eV (40 kcal/g-mol) in the range 750–950°C. The activation energy compares favorably with that of BARRER[4], who obtained a value of 31·2 kcal/g-mol (1·36 eV) from permeability experiments on oxygen in fused silica.

Some published oxidation data for silicon are compared in Fig. 4. The data obtained by EVANS

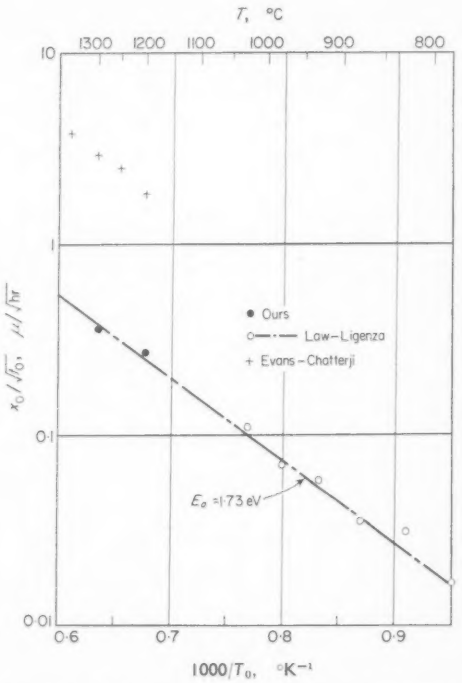

FIG. 4. The growth of the silicon oxide film on a silicon surface, $x_0/\sqrt{(t_0)}$ vs. $1/T_0$(°K), the reciprocal of the oxidation temperature.

and CHATTERJI[5] on polycrystalline silicon disagree in that they obtain films about ten times thicker at the same temperatures.

(b) *Silicon oxide mask-failure condition*

One series of experimental results is presented in Fig. 5. In this series the diffusion time, t_m, was fixed at 30 min (the subscript m denotes the masking condition). Silicon oxide layers of various thicknesses were prepared and exposed to P_2O_5.

Diffusion was performed at several closely spaced temperatures to determine T_m, the temperature at which the oxide fails to mask against P_2O_5. Mask failure was ascertained by the presence of an

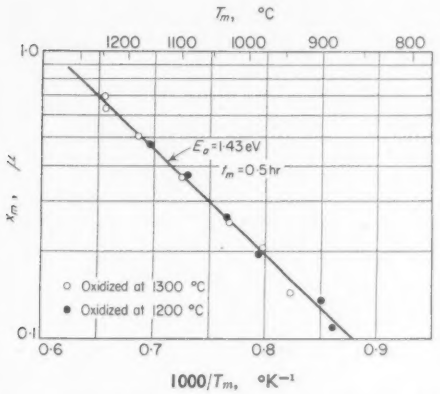

FIG. 5. The thickness at which the silicon oxide film fails completely to mask against P_2O_5 vapor at a diffusion time t_m = 30 min vs. the reciprocal of the diffusion temperature, $1/T_m$(°K).

n-skin underneath the glass. The *n*-skin was detected by a hot probe after the glass had been dissolved in hydrofluoric acid. Each point in Fig. 5 corresponds to about three to five trial $\frac{1}{2}$-hr diffusion runs.

From these data, the activation energy (E_a) of the diffusion process of phosphorus oxide in the silicon oxide film is found to be 1·43 eV.

The increase of the oxide thickness during diffusion has been neglected in the data of Fig. 5. This approximation is justified from two observations:

(1) The original oxide thickness, x_0, required for masking is considerably thicker than the additional increase during diffusion, as estimated from Fig. 4.

(2) There is no oxygen present other than that chemically combined in the P_2O_5 vapor during diffusion and that distributed and unreacted in the SiO_2 during the oxide-film growth.

Hence, it is probable that the additional oxide-film growth would be even less than anticipated from the data given in Fig. 4, since the latter correspond to a constant-surface-concentration oxygen source.

Another series of experiments was performed with a fixed oxide layer thickness $x_0 = 0{\cdot}36\ \mu$ obtained by oxidation at 1300°C for 1 hr. With several trial experiments at a given diffusion temperature, T_m, the diffusion time, t_m, at which the oxide layer failed to mask against P_2O_5, was obtained. The experimental data are presented in Fig. 6. These results indicate an activation energy of 1·47 eV, in agreement with the experiments of Fig. 5. Because of the thermal mass of the silicon

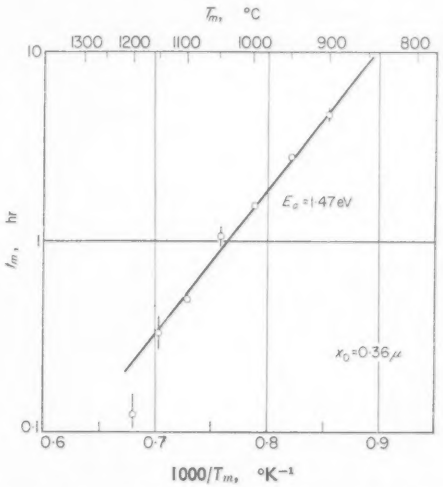

FIG. 6. The diffusion time, t_m, at which a silicon oxide film of thickness $x_0 = 0{\cdot}36\ \mu$ fails to mask against P_2O_5 vapor vs. the reciprocal diffusion temperature, $1/T_m$(°K).

slice and the sample boat, the high-temperature data at relatively short times t_m may not be accurate.

The experimental results of mask failure are analyzed by using a diffusion model. Thus, it may be assumed that

$$\frac{x_m}{2\sqrt{(D_1 t_m)}} = L \tag{4.1}$$

Here L is a constant and is a function of the boundary condition at the vapor/silicon oxide interface for the limiting case of complete reaction at the glass/silicon oxide interface; $D_1 = D_0 \exp(-E_a/kT_m)$ is the diffusion coefficient of phosphorus or an oxide of phosphorus in the phosphorus silicate glass produced by this diffusion;

x_m is the silicon oxide thickness and t_m is the diffusion time. The experimental data from Figs. (2), (5) and (6) are reduced by means of equation (4.1) and presented in Fig. 7. It is seen that the results from the three sets of experiments lie on one curve and are thus consistent with equation (4.1). The data can be fitted by the relation $x_m/\sqrt{(t_m)} = 250 \exp(-1{\cdot}46/2kT)\ \mu/\sqrt{(\text{hr})}$, or $x_m^2/t_m = 1{\cdot}7 \times 10^{-7} \exp(-1{\cdot}46/kT)\ \text{cm}^2/\text{sec}$.

In Fig. 7 the calculated square root of the diffusion coefficients is also plotted from data of partial-masking experiments discussed in the following section. The diffusion coefficient D_1 is the same as

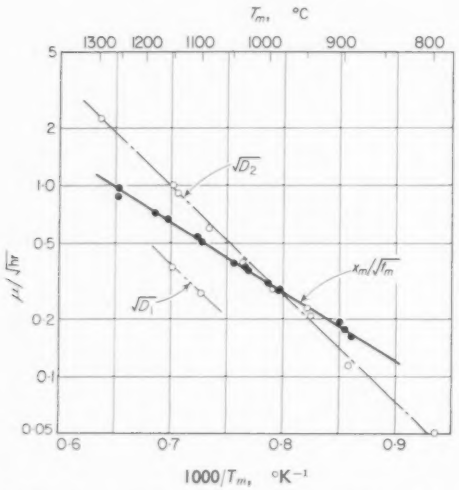

FIG. 7. The growth of the phosphorus silicate glass in a silicon oxide film on single-crystal silicon, $x_m/\sqrt{(t_m)}$ vs. the reciprocal temperature, $1/T_m$(°K).

that in equation (4.1), while D_2 is the diffusion coefficient of phosphorus in silicon, neglecting any concentration-dependence. The detailed calculations are discussed in a later section.*

(c) *Partial masking by silicon oxide*

The mask-failure conditions determined in the previous section, if exceeded, would result in an n–p junction in the silicon at a distance x_j beneath the silicon oxide. Several series of experiments were performed by fixing the diffusion temperature T_d and the diffusion time t_d while varying the oxide thickness. Thus, increasing amounts of phosphorus pass through the silicon oxide/silicon interface as the oxide layer gets thinner. The result of a typical experimental series is shown in Fig. 8.

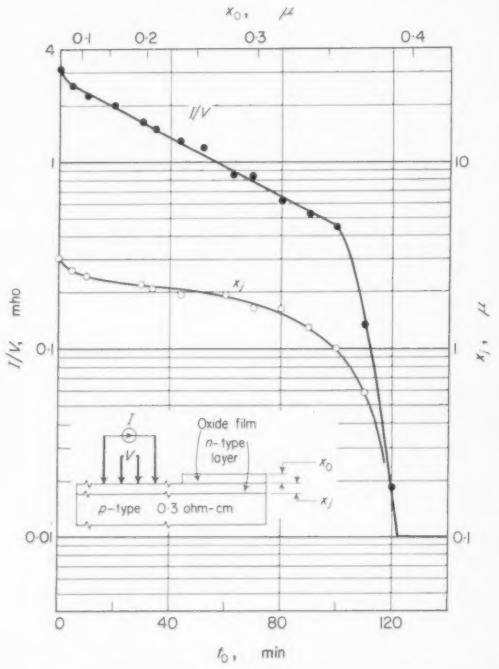

FIG. 8. The four-point probe resistance and the n–p junction depth of a n-type (phosphorus) layer formed by diffusion of phosphorus oxide through a silicon oxide film vs. the silicon oxide film thickness.

The sheet conductance (I/V) was obtained by the four-point probe technique,[6] while the n–p junction depth, x_j, was obtained by cylindrical grooving and subsequent staining with a solution of concentrated hydrofluoric acid containing 0·25 per cent nitric acid. Experimental results of junction depth in silicon vs. original oxide thickness are shown in Fig. 9. A linear region was observed for each case. However, an extremely rapid drop of junction depth occurs near the masking condition. This indicates the existence of a well-defined moving boundary or interface.

The sheet conductance measurement can be taken as an indication of the concentration of

* Data plotted for $\sqrt{(D_2)}$ in Fig. 7 in addition to the two values shown in Table 1 were obtained under the experimental conditions described in the text but with zero initial oxide thickness.

phosphorus at the silicon oxide/silicon interface. The sheet conductance can be calculated from:[7]

$$\frac{I}{V} = 4{\cdot}53 \int_0^{x_j} q\mu(C)[C_2(x) - C_3]\, dx \qquad (4.2)$$

Here q is the electronic charge, $\mu(C)$ is the majority carrier mobility, $C_2(x)$ is the concentration of phosphorus and C_3 is the impurity concentration originally present in the bulk silicon. The experimental I/Vx_j and the $C_2(0)$ calculated from I/Vx_j are plotted in Fig. 10. The theoretical calculations of $C_2(0)$ are discussed in detail in a later section. A

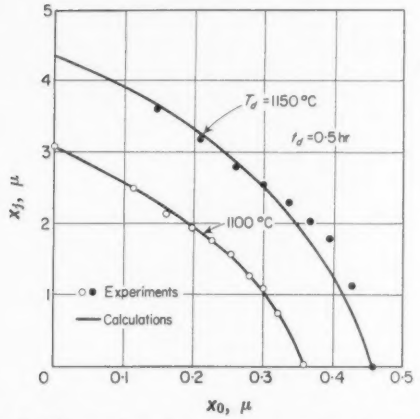

FIG. 9. The n–p junction depth, x_j, versus the oxide film thickness x_0 for a diffusion time $t_d = 0{\cdot}5$ hr and diffusion temperatures 1100 and 1150°C.

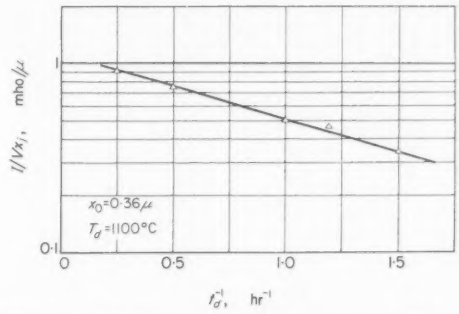

FIG. 11. The four-point probe resistance and junction depth of the n-type layer vs. the reciprocal diffusion time $1/t_d$. The n–p junction is formed by diffusion of phosphorus oxide through a silicon oxide layer of thickness $x_0 = 0{\cdot}36\,\mu$ at a diffusion temperature $T_d = 1100$°C.

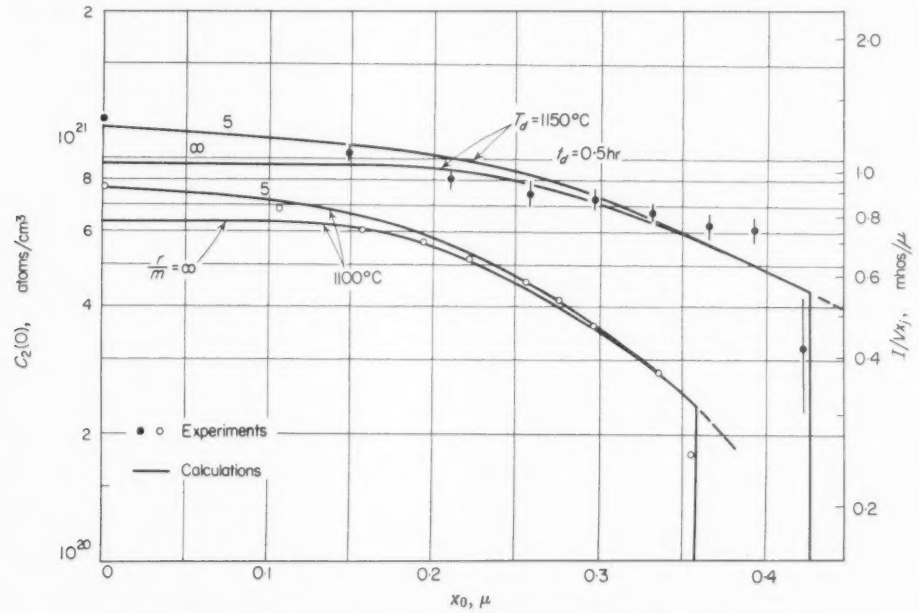

FIG. 10. $C(0)$ and I/Vx_j as a function of x_0^2. $C(0)$ is the phosphorus surface concentration or the phosphorus concentration at the interface of phosphorus silicate glass and silicon. The term x_0 is the silicon oxide thickness or phosphorus silicate glass thickness. Diffusion temperatures are 1100 and 1150°C.

rapid decrease of I/Vx_j near the mask-failure oxide thickness is again observed, giving further evidence of a well-defined moving boundary or interface.

An additional set of experiments was performed with a constant oxide-film thickness of 0·36 μ at a diffusion temperature $T_d = 1100°C$. The diffusion time, t_d, was varied. The experimental results shown in Fig. 11 indicate that the surface concentration of phosphorus is proportional to the quantity exp(—constant/t_d). This result is consistent with a diffusion model.

5. INTERPRETATION OF THE EXPERIMENTAL RESULTS

The experimental data have indicated a parabolic law in the temperature regions examined in these studies for the growth both of the oxide film on silicon and of a phosphorus silicate compound (or glass) in silicon oxide. These films are characterized by a rather homogeneous concentration and a very sharp and advancing boundary. The parabolic growth law suggests that diffusion is the limiting process.

The sharp and advancing boundary suggests that the concentration of the diffusing species decreases rapidly from the boundary. This in turn may correspond to a very rapid chemical reaction between the diffusant and the unreacted substrate at the boundary. Thus, one interpretation of the oxide film growth may be as follows: the oxygen diffuses in the silicon oxide film previously formed; as the diffusing oxygen reaches the boundary between the silicon oxide and the silicon, it rapidly oxidizes the unreacted silicon and forms a new layer of silicon oxide. The oxidation reaction is almost instantaneous compared with the diffusion rate of oxygen in the silicon oxide film, so that the process is diffusion-limited with a sharp and advancing boundary. A second possible mechanism is the diffusion of silicon atoms in the oxide. Upon reaching the surface, the silicon atoms react rapidly with the oxygen in the ambient and form an additional layer of oxide. At present, it is not possible to distinguish these two mechanisms from our data.

The binary system involving P_2O_5 and SiO_2 can be accounted for similarly. In this case, the diffusing species is probably an oxide of phosphorus diffusing in a phosphorus silicate glassy layer of an unknown composition ($P_xSi_yO_z$) referred to as the "glass". The reaction of the oxide of phosphorus and the unreacted silicon oxide at the interface between the glass and the silicon oxide is again very rapid, so that phosphorus concentration in the unreacted silicon oxide film decreases to zero in a very short distance from the interface.

The ternary system involving phosphorus oxide, silicon oxide and silicon can be analyzed following the same line as that discussed above. For such a system, two approximate models may be considered for physical simplicity: one model for the complete-masking experiments and the other for the partial-masking experiments. The model for the binary systems discussed above, i.e. O_2–Si or P_2O_5–SiO_2, may be used to account for the results of complete masking. For partial masking, namely, phosphorus diffusion in silicon through an oxide film, a two-boundary diffusion model is useful. In this case, it is assumed that the pregrown silicon oxide has completely reacted with the phosphorus species to form a phosphorus silicate glass. Thus, no further reaction takes place, and we need consider only the diffusion of phosphorus or an oxide of phosphorus in the glass with diffusion coefficient D_1 and the diffusion of the phosphorus in silicon with a diffusion coefficient D_2. The phosphorus surface concentration may be assumed to be proportional to the concentration of the oxide of phosphorus at the glass/silicon interface. The solution of this two-boundary diffusion problem has been worked out.[8]

There may exist a second, very thin, glassy layer formed between the diffusing phosphorus oxide and the unoxidized silicon, with a composition of ($P_uSi_vO_w$) Additional experiments must be performed to investigate this point. In this discussion, this second glassy layer, if it exists, is not considered.

(a) *Mathematics*

The mathematics of the two approximate physical models discussed can be formulated and the exact solutions obtained from Fick's diffusion equation with chemical reaction for the first case and without chemical reaction for the second case. The results obtained by using standard techniques[8] are listed below.

(i) *Growth of phosphorus silicate glass or silicon oxide film (Fig. 12)*

The boundary and the initial conditions and the diffusion equations are:

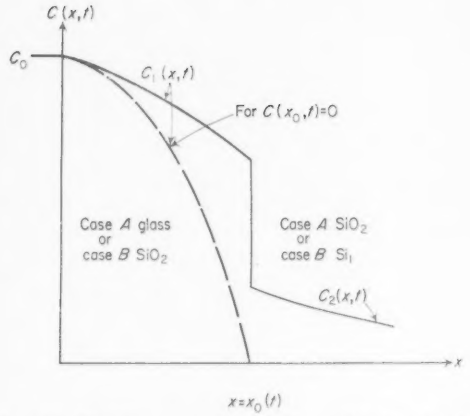

FIG. 12. The concentration profile of the film or glass-forming diffusant in the film or glass and in the unreacted silicon or silicon oxide.

$$D_1\frac{\partial^2 C_1}{\partial x^2}=\frac{\partial C_1}{\partial t} \qquad 0<x<x_0(t) \tag{5.1}$$

$$D_2'\frac{\partial^2 C_2}{\partial x^2}=\frac{\partial C_2}{\partial t}+\frac{\partial S_2}{\partial t}=(1+R)\frac{\partial C_2}{\partial t} \qquad x_0(t)<x<\infty \tag{5.2}$$

or $$D_2\frac{\partial^2 C_2}{\partial x^2}=\frac{\partial C_2}{\partial t} \qquad x_0(t)<x<\infty \tag{5.2a}$$

where $$D_2=D_2'/(1+R)$$

$$C_2=mC_1 \qquad x=x_0(t),\quad t>0 \tag{5.3}$$

$$D_1\frac{\partial C_1}{\partial x}+C_1\frac{dx_0}{dt}=D_2\frac{\partial C_2}{\partial x}+C_2\frac{dx_0}{dt} \qquad x=x_0(t),\quad t>0 \tag{5.4}$$

$$N\frac{dx_0}{dt}=-D_1\frac{\partial C_1}{\partial x}-C_1\frac{dx_0}{dt} \qquad x=x_0(t),\quad t>0 \tag{5.5}$$

$$C_1=C_0 \qquad x=0,\quad t>0 \tag{5.6}$$

$$C_2=0 \qquad x=\infty,\quad \text{all } t \tag{5.7}$$

$$C_1=C_2=0 \qquad x>0,\quad t<0 \tag{5.8}$$

The subscript 1 denotes the region of the glass or the oxide film bounded by $0<x<x_0(t)$, where $x_0(t)$ is the moving boundary. The subscript 2 denotes the region of the unreacted oxide film or the unreacted silicon. The D's are the corresponding diffusion coefficients and the C's are the concentration of the diffusants, i.e. phosphorus oxide or oxygen.

In equation (5.2) the reaction of the phosphorus oxide with silicon oxide or of oxygen with silicon is assumed to be in local equilibrium, so that the concentration of the reacted substance S_2 is directly proportional to the concentration C_2 of the substance free to diffuse. Thus, $S_2=RC_2$.

The rate of increase of the phosphorus silicate glass or the silicon oxide layer thickness is assumed to be proportional to the net rate of the number of diffusing atoms crossing the interface $x_0(t)$. Thus, (5.5) results where N is the concentration of the *reacted* oxygen in the silicon oxide or of the *reacted* phosphorus or phosphorus oxide in the glass, assuming that the amount of the diffusant crossing the interface is completely reacted.

At the interface between the silicon oxide and the silicon, it is assumed that the unreacted oxygen concentration in the unreacted silicon is proportional to that in the silicon oxide. This boundary condition is given by (5.3), where the factor m is the segregation coefficient at the corresponding interface. A similar boundary condition may be assumed for the case of phosphorus silicate glass formation.

The solution of equation (5.1) and (5.2) satisfying the boundary and initial conditions of (5.3)–(5.8) are:

$$\frac{x_0}{2\sqrt{(D_1t)}}=L=\text{constant} \tag{5.9}$$

where L is obtained from

$$\mathrm{m}\frac{(\sqrt{(\pi)}L\exp L^2\operatorname{erf}L)N-C_0}{\sqrt{(\pi)}L\exp L^2\operatorname{erf}L-1}=\frac{(\sqrt{(\pi)}rL\exp r^2L^2\operatorname{erfc}rL)N}{\sqrt{(\pi)}rL\exp r^2L^2\operatorname{erfc}rL+1} \tag{5.10}$$

$$C_1(x,t)=C_0-\frac{\sqrt{(\pi)}L\exp L^2}{\sqrt{(\pi)}L\exp L^2\operatorname{erf}L-1}(C_0-N)\times \operatorname{erf}\frac{x}{2\sqrt{(D_1t)}} \tag{5.11}$$

$$C_2(x,t)=\frac{\sqrt{(\pi)}rL\exp r^2L^2}{\sqrt{(\pi)}rL\exp r^2L^2\operatorname{erfc}rL+1}\times \operatorname{erfc}\frac{x}{2\sqrt{(D_2t)}} \tag{5.12}$$

Here $r=\sqrt{(D_1/D_2)}$. Thus, if the diffusant crossing the interface is completely reacted, it may be assumed that $C_2(x_0)=0$ and a simpler solution is obtained:

$$C_1(x,t)=C_0\left(1-\frac{\operatorname{erf}x/2\sqrt{(D_1t)}}{\operatorname{erf}L}\right) \tag{5.13}$$

$$C_0/N=\sqrt{(\pi)}L\exp L^2\operatorname{erf}L \tag{5.14}$$

The parabolic law of film growth is predicted by (5.9), while (5.14) can be used to obtain the diffusion constant D_1 if C_0 and N are known.

(ii) *Diffusion through a layer into a semi-infinite region—partial masking* (*Fig.* 13)

The boundary and the initial conditions are:

$$C_1(-x_0, t) = C_0 = \text{constant} \quad t > 0 \tag{5.15}$$

$$mC_1 = C_2 \qquad x = 0, \quad t > 0 \tag{5.16}$$

$$D_1\frac{\partial C_1}{\partial x} = D_2\frac{\partial C_2}{\partial x} \qquad x = 0, \quad t > 0 \tag{5.17}$$

$$C_1 = C_2 = 0 \qquad x > -x_0, \quad t < 0 \tag{5.18}$$

$$C_2 = 0 \qquad x = \infty, \quad \text{all } t \tag{5.19}$$

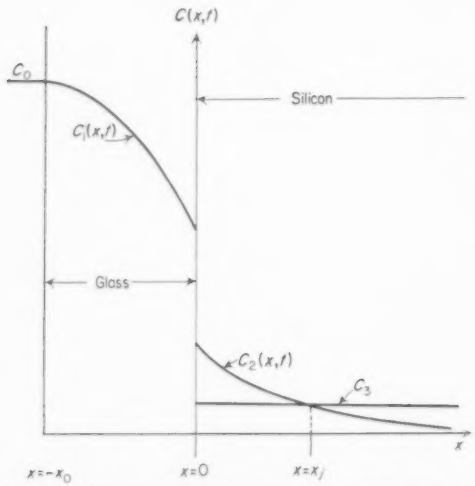

FIG. 13. The concentration profile of diffusing phosphorus oxide in phosphorus silicate glass and the concentration profile of phosphorus in silicon.

The subscript 1 denotes the region of the glass bounded by $-x_0 < x < 0$, where x_0 is the original oxide thickness and is a constant. The subscript 2 denotes the semi-infinite region of silicon. The D's and C's are the diffusion coefficients and the concentrations of the diffusant, respectively. The proportionality constant m is the "segregation coefficient" of phosphorus at the interface of silicon and phosphorus glass and has in general a different value from that given in case (i). The initial distribution of the diffusant in the glass is neglected in order to simplify the problem. Thus, (5.18) is assumed. The more exact initial condition for C_1 in place of (5.18) is given by (5.11) or (5.13), where t is replaced by $x_0^2/4D_1L^2$ given by (5.9).

The solutions of the diffusion equation satisfying equations (5.15)–(5.19) are:

$$C_1(x, t) = C_0 \sum_{n=0}^{\infty} \alpha^n \left\{ \operatorname{erfc}\frac{(2n+1)x_0+x}{2\sqrt{(D_1t)}} - \right.$$

$$\left. -\alpha \operatorname{erfc}\frac{(2n+1)x_0-x}{2\sqrt{(D_1t)}} \right\} \tag{5.20}$$

and

$$C_2(x, t) = m(1-\alpha)C_0 \sum_{n=0}^{\infty} \alpha^n \operatorname{erfc}\frac{(2n+1)x_0+rx}{2\sqrt{(D_1t)}} \tag{5.21}$$

Here $\alpha = (m-r)/(m+r)$ and $r = \sqrt{(D_1/D_2)}$.

(b) *Analysis of experimental data at diffusion temperatures of* 1100 *and* 1150°C

The data from partial-masking experiments may be correlated with the theoretical calculations of the preceding section through equation (5.21).

The surface concentration of phosphorus on silicon at the glass/silicon interface may be obtained from (5.21) by setting $x = 0$;

$$C(0) = C_2(0, t)$$

$$= m(1-\alpha)C_0 \sum_{n=0}^{\infty} \alpha^n \operatorname{erfc}\frac{(2n+1)x_0}{2\sqrt{(D_1t)}} \tag{5.22}$$

This is plotted in Fig. 14. For $x_0/2\sqrt{(D_1t)} > 0{\cdot}7$, only the first term of the series in (5.22) is significant, and the concentration profiles follow the complementary error function. The match between the theory and the experimental data shown in Fig. 10 gives $\sqrt{(D_1)} = 0{\cdot}27\ \mu/\sqrt{(\text{hr})}$ at 1100°C and $\sqrt{(D_1)} = 0{\cdot}37\ \mu/\sqrt{(\text{hr})}$ at 1150°C. It is seen from Fig. 10 that the lower limit for the factor r/m seems to be approximately 5.

The condition at the n–p junction can be obtained from (5.21) by setting $x = x_j$ and $c_2(x_j, t) = C_3$:

$$C_3 = m(1-\alpha)C_0 \sum_{n=0}^{\infty} \alpha^n \operatorname{erfc}\frac{(2n+1)x_0+rx_j}{2\sqrt{(D_1t)}} \tag{5.23}$$

If $x_0/2\sqrt{(D_1t)}$ is greater than $\sim 0{\cdot}7$, the series in

(5.23) can be approximated by the first term when x_0 and rx_j are comparable. Thus, the region of approximate proportionality between x_0 and x_j shown in Fig. 9 is expected. As x_0 becomes

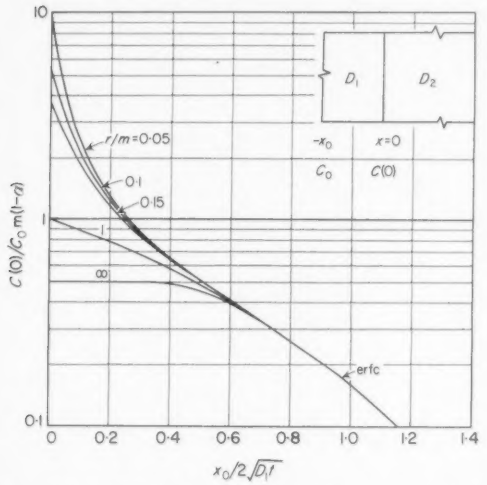

FIG. 14. The calculated phosphorus concentration at the glass/silicon interface as a function of the glass thickness (or oxide thickness) $x_0/2\sqrt{(D_1 t)}$.

smaller, the first several terms in (5.23) are comparable, and the junction depth x_j would increase less rapidly. Such a trend is also observed in the experimental results in Fig. 9. The behavior near the point of complete masking is not predicted by (5.23), even if one considers that C_3 outdiffuses into the glass and D_2 is concentration-dependent. In this region, the initial distribution of the diffusant in the glass becomes important, and the more accurate initial condition discussed previously for $C_1(x, 0)$ must be used in place of (5.18).

An approximate approach will be used in applying (5.23) to the experimental data given in Fig. 9. The result of the two-boundary diffusion model is derived on the assumption that the initial phosphorus or phosphorus oxide concentration in the glass is zero. However, it is actually not zero, being given by (5.18), with the time t replaced by $x_0^2/4D_1L^2$ as discussed before. Thus, we may make an approximation to include the initial distribution by taking the result given by (5.21) or (5.23) restricting their applicability to times greater than t_m, the time required for the diffusant to penetrate through the oxide of thickness x_0. Thus, we may replace the time t in (5.21) or (5.23) by $t_d - t_m = t_d - Ax_0^2$. We assume that $t_m = Ax_0^2$, where A depends on temperature only, since the masking condition follows the parabolic relation. Here t_d is the diffusion time. For a given diffusion condition, the argument of the complementary function in (5.23) must be a constant, so that we may write:

$$x_0 + rx_j = B\sqrt{(t_d - Ax_0^2)} \qquad (5.24)$$

by taking only the term $n = 0$. The constants A and B are empirically obtained by matching (5.24) to the experimental data and cannot be explicitly related to any of the physical quantities. However, approximate values of $r = \sqrt{(D_1/D_2)}$ may be obtained. From these values of r and the values of D_1 from (5.22), the values of D_2 may then be determined.

An independent check on D_2 may be made from the data at $x_0 = 0$ by using (5.22) and (5.23). Thus,

$$C_3/C(0) = \text{erfc}\, x_j/2\sqrt{(D_2 t)} \qquad (5.25)$$

in which $C(0)$, the phosphorus surface concentration on silicon at the silicon/glass interface, is obtained from (4.2) by using BACKENSTOSS's curves.[7] The self-consistent results obtained by matching the experimental data with (5.22), (5.24) and (5.25) are tabulated in Table 1. The calculated experimental value of L and C_0/N using (5.14) are also given.

Table 1

T_d (°C)	$C(0)$ $x_0 = 0$ (atoms/cm³)	$\sqrt{(D_1)}$ ($\mu/\sqrt{(\text{hr})}$)	$\sqrt{(D_2)}$ ($\mu/\sqrt{(\text{hr})}$)	$r = \sqrt{(D_1/D_2)}$	A	$B/2\sqrt{(D_1)}$	L	C_0/N
1100	$7{\cdot}9 \times 10^{20}$	0·27	0·80	0·34	3·46	2·69	0·927	3·17
1150	$1{\cdot}1 \times 10^{21}$	0·38	1·12	0·34	2·17	2·74	0·856	2·45

VOL. 11 1959

It is interesting to note that the ratio of the diffusion coefficients in the glass and in the silicon is relatively insensitive to temperature. From this ratio, we may make an estimate of the upper limit of the segregation coefficient, m, by using the estimated lower limit of 5 for r/m from Fig. 10. Thus, m is probably less than $r/5 = 0{\cdot}34/5 = 0{\cdot}07$.

6. SUMMARY

Experimental investigation of the diffusion of phosphorus oxide through a silicon oxide film on silicon indicates that the diffusion process can be described by two approximate models, while the transition region between the two models occurs at an oxide thickness of less than $\sim 0{\cdot}05\ \mu$. During the first step, the oxide layer is completely effective in masking against P_2O_5, so that there is no phosphorus-rich layer in the silicon beneath the silicon oxide film. In this case an oxide of phosphorus diffuses through an apparently glassy layer of a composition ($P_xSi_yO_z$) and upon reaching the interface between the glass and the silicon oxide it reacts very rapidly with the silicon oxide to form a new layer of the glass. (Another possibility is the diffusion of a silicon oxide in the glass toward the surface; upon reaching the surface it reacts with P_2O_5 in the vapor phase to form the glass.) Thus, the glass/silicon oxide interface is well defined and advances with a velocity which is limited by the diffusion rate of an oxide of phosphorus in the glass. The growth of the glass follows a parabolic law. Experimentally, it is determined that

$$x_m^2/t_m = 6{\cdot}25 \times 10^4 \exp(-1{\cdot}46/kT)\ \mu^2/\text{hr}$$
$$= 1{\cdot}7 \times 10^{-7} \exp(-1{\cdot}46/kT)\ \text{cm}^2/\text{sec}$$

for the growth of the phosphorus silicate glass in silicon oxide.

During the second step, at a later time, the silicon oxide film is completely penetrated by the glass, and an n–p junction is formed beneath the glass in the silicon from the n-type phosphorus impurity. This situation can be approximated by assuming that the glass reaches a final thickness equal to the thickness of the original silicon oxide and no reaction takes place between silicon and the diffusing phosphorus oxide species. Then, the model becomes that of diffusion of an oxide of phosphorus in the glass. As the oxide of the phosphorus reaches the glass/silicon interface, phosphorus atoms enter the silicon and diffuse away. The structural detail of the glass/silicon interface is not known, but it is approximately described by a small "segregation coefficient" for phosphorus between the glass and the silicon.

REFERENCES

1. Frosch C. J. and Derick L., *J. Electrochem. Soc.* **104,** 547 (1957).
2. Ligenza J. R., Unpublished work at Bell Telephone Laboratories.
3. Law J. T., *J. Phys. Chem.* **61,** 1200 (1957).
4. Barrer R. M., *Diffusion in and through Solids* p. 126. Cambridge University Press (1951).
5. Evans J. W. and Chatterji S. K., *J. Phys. Chem.* **62,** 1064 (1958).
6. Valdes L. B., *Proc. Inst. Radio Engrs.* **42,** 420 (1954).
7. Backenstoss G., *Bell Syst. Tech. J.* **37,** 699 (1958).
8. Crank J., *The Mathematics of Diffusion.* Clarendon Press, Oxford. (1956).

J. Phys. Chem. Solids Pergamon Press 1959. Vol. 11. pp. 299–302. Printed in Great Britain.

LOW-TEMPERATURE LATTICE HEAT CONDUCTION IN HIGH-RESISTIVITY ALLOYS

J. E. ZIMMERMAN

Scientific Laboratory, Ford Motor Company, Dearborn, Michigan

(*Received* 18 *June* 1959)

Abstract—It is shown theoretically that for high-resistivity alloys the lattice thermal conductivity K_l is proportional to T, the absolute temperature, and to ρ_0, the residual electrical resistivity. At higher temperatures (but $<\theta/20$) or lower resistivities, K_l becomes proportional to T^2 and independent of ρ_0; this is the behavior generally observed in alloys for which ρ_0 is less than $\sim 10\ \mu\Omega$ cm. The theory is verified by measurements on a series of silver–antimony alloys, in which ρ_0 varies between 12 and 40 $\mu\Omega$ cm.

1. INTRODUCTION

MOST measurements have shown that the lattice component of thermal conductivity in well-annealed metals and alloys is proportional to T^2, the square of the absolute temperature. This T^2 behavior has been shown theoretically to arise when the lattice waves are scattered predominantly by the conduction electrons,[1,2] and a number of experimental researches[3,4] have been interpreted successfully on this basis. Generally what is done is to write the thermal conductivity K as the sum of an electronic K_e and a lattice K_l term:

$$K = K_e + K_l = \frac{L_0 T}{\rho_0} + BT^2,$$

this equation being valid at temperatures where the lattice specific heat is proportional to T^3 and where the electrical resistivity has the residual value ρ_0. The constant L_0 is the Weidemann–Franz ratio $2{\cdot}45 \times 10^{-8}$ WΩ/deg.^{2}

In the course of measurements on some copper–nickel alloys (unpublished), we found that for high-resistivity specimens, containing of the order of 40 per cent nickel, the thermal conductivity could not be expressed by the above equation, but that an additional term, proportional to T and of the same order of magnitude as $L_0 T/\rho_0$, was required to fit the data. The same sort of behavior has been observed in the analogous silver–palladium alloy system by KEMP *et al.*[5] The question of whether this anomalous term is part of the electronic or of the lattice component has been answered by PIPPARD, who developed a theory of ultrasonic attenuation in metals and suggested that its application to the theory of lattice heat conduction would lead to a linear term in the lattice conductivity of the right order of magnitude to explain the experimental results.

2. THEORY

PIPPARD[6] has derived expressions for the attenuation of longitudinal and of transverse waves by the free electrons which, though of different analytic form, are nearly the same numerically, and practically identical in their dependence on ω, the frequency of the lattice wave, at least for low frequencies. For high frequencies, and this includes thermal frequencies for temperatures above 0·01°K, it is shown that the transverse wave attenuation levels off and becomes frequency-independent, in contrast to the longitudinal wave attenuation, which in the high-frequency limit is proportional to ω.

It has been recognized for a long time that in order to account for the observed magnitude of the lattice thermal conductivity as well as the ideal part of the electrical resistivity, it is necessary to postulate approximately equal transverse and longitudinal attenuations at thermal frequencies.[1,2] If we accept this postulate and apply PIPPARD's

equation for longitudinal attenuation to waves of all polarizations, then

$$\alpha = \frac{Nm}{\rho v_s \tau}\left(\frac{\frac{1}{3}\kappa^2 l^2 \tan^{-1}\kappa l}{\kappa l - \tan^{-1}\kappa l} - 1\right). \qquad (1)$$

The notation is the same as PIPPARD's, that is N is the number of electrons per unit volume, m is the electronic mass, ρ is the density of the solid, v_s is the velocity of sound, τ is the relaxation time of the electrons, κ is the phonon wave number and l is the electron mean free path. This may be substituted in the well-known equation for thermal conductivity of a gas of particles of heat capacity C_v and mean free path l_s;

$$K = \tfrac{1}{3} l_s v_s C_v. \qquad (2)$$

We identify l_s with $1/\alpha$, and, using the Debye specific-heat formula, we get for the lattice conductivity:

$$K_l = 3nkv_s(T/\theta)^3 \int_0^{T/\theta} \frac{z^4 e^z\, dz}{\alpha(az, z)(e^z - 1)^2}; \quad z = \frac{\hbar\omega}{kT} \qquad (3)$$

where n is the number of atoms per unit volume and the other symbols are conventional. As in specific-heat theory, we replace the upper limit of integration by infinity, with negligible error for temperatures less than $\theta/20$. Finally, for purposes of numerical calculation, we may substitute for τ and for l the appropriate functions of the residual electrical resistivity ρ_0, and for v_s the expression in the Debye temperature θ, namely,

$$\tau = \frac{m}{Ne^2\rho_0}, \quad l = v_0\tau, \quad v_s = \frac{k\theta}{\hbar}(6\pi^2 n)^{-\frac{1}{3}},$$

so that equation (3) may be reduced to:

$$\frac{K_l}{\rho_0 T} = \frac{3e^2k^3\rho\theta}{(6\pi^2)^{4/3}\hbar^2 m^2 v_0^2 n^{\frac{1}{3}}}\left[a^2 \int_0^\infty f(az, z)\, dz\right] \qquad (4)$$

where

$$a = \frac{mv_0(6\pi^2 n)^{\frac{1}{3}}}{Ne^2\theta}\frac{T}{\rho_0},$$

v_0 being the Fermi velocity. The dimensionless term in brackets in equation (4) has been integrated numerically and is plotted in Fig. 1 as a function of a, which is also a dimensionless quantity. For $a \gg 1$ there is an asymptotic approach to the straight dashed line, whose equation is $6{\cdot}131 + +13{\cdot}774\ a$. Thus at "high" temperatures and/or in metals of low resistivity, K_l becomes quadratic in T, in accordance with most experimental

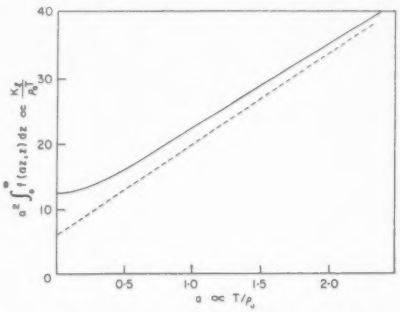

FIG. 1. A dimensionless plot showing K_l/T as a function of temperature.

observations. At the other extreme, however, K_l becomes linear in T, so that temperature-dependence alone does not distinguish between K_l and K_e, the electronic component of the conductivity.

Now the quantity a may be written also as $a = \kappa_m l$, where $\kappa_m = (kT/\hbar v_s)$ is roughly the predominant phonon wave number. Hence the preceding paragraph may be stated more explicitly by saying that a quadratic dependence of K_l upon T is expected if the predominant phonon wavelength is short compared to the electron mean free path, but K_l becomes linear in T in the opposite case.

As PIPPARD has pointed out,[7] at helium temperatures it should be necessary to look at alloys for which $\rho_0 > 10^{-5}$ Ωcm in order to see evidence of a linear dependence of K_l upon T. In principle it would also be possible to see this dependence in metals of lower resistivity at lower temperatures; in this case however the electronic conductivity usually swamps the lattice conductivity.

3. CHOICE AND PREPARATION OF SPECIMENS

The measurements on copper–nickel and on silver–palladium alloys alluded to in the Introduction indicate that a linear term in the lattice conductivity becomes appreciable at helium

temperatures when the electrical resistivity exceeds 10 $\mu\Omega$cm, in qualitative agreement with the curve of Fig. 1.

In view of the complicated band structure of these alloys, it appeared that a more rigorous test of the theory would be afforded by measurements on alloys of copper or of silver with a few per cent of arsenic or antimony, in which quite high resistivities can be attained[8] without perhaps changing the properties of the conduction electrons very much. Of the possible combinations, the silver–antimony system was chosen on the basis of ease of preparation.

The proper amounts of silver and antimony were melted together in a plumbago crucible, using boric acid flux. Mixing was promoted by shaking the crucible, after which the molten alloy was poured into a graphite mold preheated to 300 or 400°C, producing ingots of $\frac{1}{2}$ in. diameter 3 in. long. Specimens of rectangular cross-section $0{\cdot}100\times0{\cdot}150\times3$ in. were machined from the ingots. These were sealed individually into evacuated Vicor tubes and annealed for 20 hr. at 50–100° below the liquidus. Subsequent microscopic examination showed the grain size to be a few tenths of a millimeter. Care was taken not to deform the specimens in any way after annealing.

All specimens were analyzed chemically, the results being given in the next section. No specific tests for impurities were undertaken. The accuracy of the chemical analyses was such that we can say that the total impurity content was not more than $\sim 0{\cdot}1$ per cent.

4. EXPERIMENTAL METHOD AND RESULTS

The apparatus used for this work was conventional and will be described only briefly. A 500-Ω wire-wound $\frac{1}{2}$-W radio resistor in a copper foil sheath was clamped to one end of the specimen to serve as a heat source; the other end of the specimen was clamped to the wall of the evacuated calorimeter can; and two 0·1-W, 47-Ω Allen Bradley Resistors clamped at two intermediate points were used as thermometers. The thermometers were calibrated using the pressure over the helium bath and the Leiden 1955 vapor-pressure scale, a procedure which may give rise to errors of the order of a few tenths per cent.[9] The resistance temperature data were fitted by a "Clement equation".

$$\frac{\log R}{T} = A + B\log R + C\log^2 R.$$

Heat flow was adjusted to give one or two tenths of a degree temperature gradient along the specimen. Thermal- and electrical-conductivity measurements were made consecutively on one filling of liquid helium, the same clamps serving for electrical as well as for thermal contacts, so that the geometries for the two measurements were identical.

Residual-resistivity and composition data on the seven specimens are given in Table 1, and the measured thermal conductivities are shown in Fig. 2, where we have plotted $K\rho_0/T$ vs. T. On this system of co-ordinates the electronic thermal conductivity K_e appears as the horizontal dashed

Table 1

Specimen	Antimony (At. per cent)	ρ_0($\times10^{-6}\Omega$-cm)
1	1·83	12·4
2	2·72	17·1
3	3·62	24·7
4	3·98	28·3
5	4·71	33·2
6	5·68	39·5
7	—	30·6

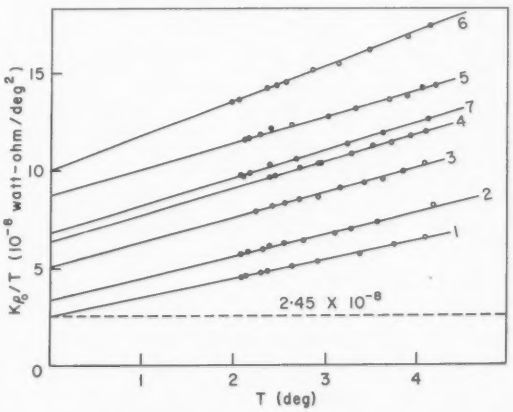

FIG. 2. Thermal conductivity of the alloys listed in Table 1 as a function of temperature. In the units used here, the electronic component of K for all specimens is represented by the horizontal dashed line at $2{\cdot}45\times10^{-8}$.

line at $2{\cdot}45\times10^{-8}$ WΩ/deg^2, the Wiedemann–Franz ratio.

It will be observed that the data for specimen 5 lie somewhat askew of the general trend. On the belief that this was somehow the result of composition inhomogeniety within the melt, specimen 7 was prepared from a melt in which special attention was given to mixing the ingredients. Specifically, the melt for 7 was made from mill cuttings from 4 and 6, and the cuttings were thoroughly mixed before melting. It is apparent that the data for specimen 7 are in good accord qualitatively with the rest of the data except those for specimen 5.

Specific-heat measurements were made on some of the alloys. These indicated that both the electronic and the lattice heat capacities increase by a few per cent with the addition of antimony. The measurements were not particularly accurate, owing to the thermometer calibration errors referred to above, and publication is withheld pending more reliable results. In any case, the changes in electronic and lattice capacities affect K_l oppositely, and for present purposes will be ignored.

5. DISCUSSION

Qualitatively, the picture which emerges is that the lattice conductivity between 2° and 4° can be fitted by an equation of the form

$$K_l = AT + BT^2,$$

where the coefficient A is about proportional to the electrical resistivity ρ_0, and B decreases slightly with increasing ρ_0. (Note that the slopes and intercepts in Fig. 2 must be multiplied by T/ρ_0 to give these coefficients.)

The most direct comparison with the theory is obtained by plotting K_l on the co-ordinates of Fig. 1, viz. $K_l/\rho_0 T$ vs. T/ρ_0. This has been done in Fig. 3, where we have shown that data of Fig. 2 as straight-line segments corresponding to the temperature range of $\sim$2–4°K. Two theoretical curves are shown. The solid curve was obtained from Fig. 1 and equation (4), using $\theta = 225°$, $V_0 = 1{\cdot}4\times10^8$ cm/sec, $N = n = 0{\cdot}59\times10^{23}$ cm^{-3} and $\rho = 10{\cdot}5$ g/cm^3. The dashed curve is simply the theoretical curve with arbitrary scale factors chosen to give a rough fit to the experimental data.

We feel that for this first attempt, the agreement between theory and experiment is fairly good. We do not observe the slight curvature exhibited by the theoretical curve of Fig. 3; however, the departure

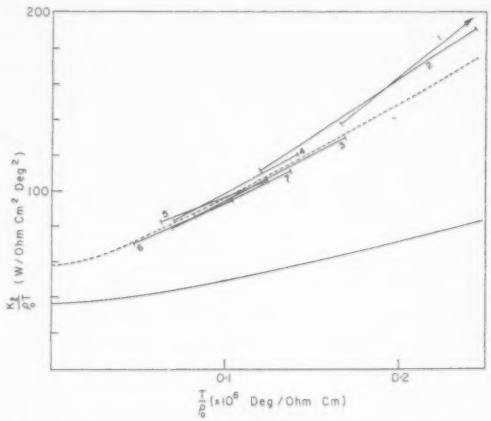

FIG. 3. Comparison between theory and experiment. (See text for explanation.)

of K_l from quadratic dependence on T for $\rho_0 > > 10\mu\Omega$ cm, and the general dependence of K_l on ρ_0, are in very good accord with the theory, considering the many simplifying assumptions involved in the derivation of the theoretical curve.

Acknowledgements—The author is particularly indebted to Professor A. J. PIPPARD for the discussion which led to this research, and to Dr. P. G. KLEMENS for several helpful discussions.

REFERENCES

1. MAKINSON R. E. B., *Proc. Camb. Phil. Soc.* **34,** 474 (1938).
2. KLEMENS P. G., *Handbuch der Physik*, Band 14, s. 253. Springer, Berlin (1956).
3. HULM J. K., *Proc. Phys. Soc.* B**64,** 207 (1951).
4. KEMP W. R. G., KLEMENS P. G. and TAINSH R. J., *Aust. J. Phys.* **10,** 454 (1957). Reference (6) contains a more comprehensive list of references pertinent to this point.
5. KEMP W. R. G., KLEMENS P. G., SREEDHAR A. K. and WHITE G. K., *Proc. Roy. Soc.* A**233,** 480 (1956).
6. PIPPARD A. B., *Phil. Mag.* **46,** 1104 (1955).
7. PIPPARD A. B., *J. Phys. Chem. Solids* **3,** 175 (1957).
8. MOTT N. F. and JONES H., *Properties of Metals and Alloys*. Oxford University Press (1936).
9. HOARE F. E. and ZIMMERMAN J. E., *Rev. Sci. Instrum.* **39,** 184 (1959).

J. Phys. Chem. Solids Pergamon Press 1959. Vol. 11. pp. 303–309. Printed in Great Britain.

LA STRUCTURE DES SUBSTANCES MAGNETIQUES

J. VILLAIN

Centre d'Etudes Nucléaires de Saclay, Gif s/Yvette (S. et O.), France

(*Received* 16 *June* 1959)

Résumé—Ce travail a pour objet la prévision systématique de la structure des substances magnétiques au-dessous du point de transition et l'étude des différents cas qui peuvent se présenter lorsque les ions magnétiques forment un réseau de Bravais. On se place dans une approximation de champ moléculaire, mais on ne fait aucune restriction concernant la portée des interactions d'échange. Après avoir déterminé (Section 1) la température critique et la structure magnétique à cette température sans supposer *a priori* l'existence d'une décomposition en sous-réseaux, on montre (Section 2) que cette structure reste stable en dessous de la température critique, et on étudie les divers cas possibles.

Il peut arriver en particulier que la structure magnétique ait une période incommensurable avec celle du réseau cristallin. L'example du réseau quadratique centré avec couplage entre premiers, seconds et troisièmes voisins (Section 3) fournit une bonne illustration de cette étude.

Abstract—The paper deals with the prediction of the structure of magnetic materials below the critical point. The molecular field approximation is used; exchange interactions with unlimited range are assumed; the magnetic ions are supposed to form a Bravais lattice. The critical temperature T_c is first calculated (Section 1) without assuming any decomposition of the crystal into sublattices, and the magnetic structure at T_c is given. It is next shown (Section 2) that the essential features of this structure persist below T_c, and the various possible cases are considered. It is possible that no decomposition into sublattices takes place, i.e. the magnetic structure and the nuclear structure have incommensurable periods. A detailed treatment is then given for the body-centered quadratic lattice (Section 3) with interaction between first, second and third neighbours.

1. L'APPROXIMATION DU CHAMP MOLÉCULAIRE

Nous considérerons un cristal comportant N ions magnétiques répartis aux noeuds R d'un réseau de Bravais. Le moment orbital étant supposé bloqué, nous appellerons S_R la valeur moyenne du spin porté par le noeud R, et nous supposerons que les spins ne sont couplés que par des interactions d'échange (ou de superéchange).

L'approximation du champ moléculaire, sous sa forme locale[1] consiste à supposer que l'action des autres spins sur le spin situé en R équivant à celle d'un champ magnétique fictif, dont on néglige les fluctuations, et qui est donné par:

$$H_R = \frac{2}{g\mu_B} \sum_{R'} J_{RR'} S_{R'}$$

où g est les rapport gyromagnétique (ici égal à 2), μ_B le magnéton de Bohr, et $J_{RR'}$ est une intégrale d'échange.

Nous ne ferons pas d'hypothèses sur la portée des interactions.

La fonction $\boldsymbol{S}_R$ de $\boldsymbol{R}$ est solution de l'équation

$$\boldsymbol{S}_R = U_R S \mathscr{B}\left(\frac{2S}{K_B T}\left|\sum_{R'} J_{RR'} \boldsymbol{S}_{R'}\right|\right) \qquad (1)$$

où

$$U_R = \frac{\sum_{R'} J_{RR'} \boldsymbol{S}_{R'}}{\left|\sum_{R'} J_{RR'} \boldsymbol{S}_{R'}\right|}$$

$\mathscr{B}$ est la fonction de Brillouin pour le spin S.

Il est fréquent que le système (1) admette une solution constante $\boldsymbol{S}_R = \boldsymbol{S}$. Les spins ont alors une configuration ferromagnétique. Nous nous intéresserons surtout ici au cas de l'antiferromagnétisme. Le système (1) admet alors une

solution stable non nulle telle que

$$\sum_R \boldsymbol{S}_R = 0.$$

La théorie d'un grand nombre de corps antiferromagnétiques a pu être faite en supposant, à la suite de NÉEL[2], que le réseau cristallin se décomposait, en dessous du point de Néel, en un certain nombre de sous-réseaux, tous les ions d'un même sous-réseau portant le même spin. Nous montrerons ici que l'on peut, connaissant la valeur des intégrales d'échange, trouver la structure magnétique sans faire une telle hypothèse *a priori*. La méthode présente les avantages suivants:

(1) elle évite des tâtonnements dans la recherche de la décomposition en sous-réseaux;

(2) elle permet de donner une liste des structures magnétiques compatibles avec un réseau cristallin donné et des valeurs raisonnables des interactions d'échange;

(3) elle est la seule méthode utilisable dans le cas où aucune décomposition en sous-réseaux n'est pas possible. Nous verrons que ce phénomène peut se produire quand les interactions ont une grande portée.

Quand

$$|\boldsymbol{S}_R| \ll S$$

l'équation (1) prend la forme linéaire suivante :

$$\boldsymbol{S}_R = \frac{2S(S+1)}{3K_BT} \sum_{R'} J_{RR'} \boldsymbol{S}_{R'} \qquad (2)$$

à laquelle une transformation de Fourier donne la forme simple :

$$T(\boldsymbol{k}) = \frac{2S(S+1)}{3K_BT} \zeta(\boldsymbol{k}) T(\boldsymbol{k}) \qquad (3)$$

où on a posé :

$$T(\boldsymbol{k}) = \sum_R \boldsymbol{S}_R \exp(i\boldsymbol{k} \cdot \boldsymbol{R})$$

$$\zeta(\boldsymbol{k}) = \sum_{R'} J_{RR'} \exp(i\boldsymbol{k} \cdot (\boldsymbol{R'} - \boldsymbol{R})).$$

Le système (2), et par suite le système (3), n'aura que la solution zéro pour des températures T supérieures à une température critique T_c. T_c est donc la température la plus élevée pour laquelle les systèmes (2) et (3) ont une solution non nulle. Par suite, on a :

$$K_BT_c = \frac{2S(S+1)}{3} \zeta(\boldsymbol{k}_0) \qquad (4)$$

où $\zeta(\boldsymbol{k}_0)$ est le maximum de $\zeta(\boldsymbol{k})$. Les points $\boldsymbol{k}_0$ forment dans l'espace réciproque un ensemble invariant par les translations du réseau réciproque, par symétrie par rapport à l'origine, et par les opérations de symétrie qui conservent le réseau réciproque.

Pour simplifier nous supposerons par la suite qu'il n'existe dans chaque maille du réseau réciproque que deux vecteurs $\boldsymbol{k}_0$ dont les extrémités sont symétriques par rapport au centre de la maille.

Pour $T = T_c$ le système (2) admet des solutions de la forme :

$$S_{R^\alpha} = \lambda_\alpha \cos(\boldsymbol{k}_0 \cdot \boldsymbol{R} - \phi_\alpha) \qquad (5)$$

où

$$\alpha = x, y, z.$$

2. LA STRUCTURE MAGNÉTIQUE AU-DESSOUS DE LA TEMPÉRATURE CRITIQUE

(a) Nous montrerons d'abord que, si les forces magnétocristallines sont négligeables, le système (1) admet des solutions de la forme (5) à toute température. Pour cela il faut d'abord s'assurer que si $\boldsymbol{S}_R$ est donné par (5) le champ moléculaire $\boldsymbol{H}_R$ en $\boldsymbol{R}$ est parallèle à $\boldsymbol{S}_R$. Il en est bien ainsi car :

$$H_{R^\alpha} = \frac{2\lambda_\alpha}{g\mu_B} \sum_{R'} J_{RR'} \cos(\boldsymbol{k}_0 \cdot \boldsymbol{R'} - \phi_\alpha)$$

$$= \frac{2\lambda_\alpha}{g\mu_B} \cos(\boldsymbol{k}_0 \cdot \boldsymbol{R} - \phi_\alpha) \sum_{R'} J_{RR'} \cos \boldsymbol{k}_0(\boldsymbol{R'} - \boldsymbol{R})$$

$$= \frac{2}{g\mu_B} \zeta(\boldsymbol{k}_0) S_{R^\alpha}.$$

L'expression (5) sera donc solution de (1), à condition que tous les spins aient le même module $|\boldsymbol{S}_R| = s$, où

$$s = S\mathscr{B}\left[\frac{S\zeta(\boldsymbol{k}_0)}{K_BT} s\right]$$

(b) *Stabilité de la solution trouvée*

La valeur de $\boldsymbol{k}_0$ n'intervient pas dans la démonstration précédente. Montrons que si $\boldsymbol{k}_0$ est défini

par la condition que $\zeta(\boldsymbol{k}_0)$ est le maximum de $\zeta(\boldsymbol{k})$, la structure trouvée est stable, c'est à dire que la variation d'énergie libre pour de petites variations $\delta\boldsymbol{S}_R$ des spins est positive, sauf pour une rotation d'ensemble du système de spins.

L'énergie libre est

$$F = K_B T \sum_{\boldsymbol{R}} \int_0^{S_{\boldsymbol{R}}/S} \mathscr{B}^{-1}(x)\, dx - \\ - \sum_{\boldsymbol{R}\boldsymbol{R}'\alpha} J_{\boldsymbol{R}\boldsymbol{R}'} S_{\boldsymbol{R}}{}^{\alpha} S'_{\boldsymbol{R}'}{}^{\alpha} + C. \tag{6}$$

En effet la condition d'équilibre

$$\frac{\partial F}{\partial S_{\boldsymbol{R}}{}^{\alpha}} = 0$$

donne bien l'équation (1). $\mathscr{B}^{-1}$ est la fonction inverse de la fonction de Brillouin.

En dérivant (6) deux fois on trouve :

$$\frac{1}{2}\frac{\partial^2 F}{\partial S_{\boldsymbol{R}}{}^{\alpha}\partial S_{\boldsymbol{R}'}{}^{\beta}} = -\delta_{\alpha\beta} J_{\boldsymbol{R}\boldsymbol{R}'} + \delta_{\alpha\beta}\delta_{\boldsymbol{R}\boldsymbol{R}'} \frac{\sum_{\boldsymbol{R}''} J_{\boldsymbol{R}\boldsymbol{R}''} S_{\boldsymbol{R}''}{}^{\alpha}}{S_{\boldsymbol{R}}{}^{\alpha}} + \\ + \delta_{\boldsymbol{R}\boldsymbol{R}'} \frac{K_B T}{2S^2 S_{\boldsymbol{R}}{}^2} \frac{S_{\boldsymbol{R}}{}^{\alpha} S_{\boldsymbol{R}}{}^{\beta}}{\mathscr{B}'\left(\dfrac{2S}{K_B T}\left|\sum_{\boldsymbol{R}''} J_{\boldsymbol{R}\boldsymbol{R}''}\boldsymbol{S}_{\boldsymbol{R}''}\right|\right)} - \delta_{\boldsymbol{R}\boldsymbol{R}'} \frac{S_{\boldsymbol{R}}{}^{\alpha}}{S_{\boldsymbol{R}}{}^2} \sum_{\boldsymbol{R}''} J_{\boldsymbol{R}\boldsymbol{R}''} S_{\boldsymbol{R}''}{}^{\beta}$$

où on a posé

$$\mathscr{B}'(x) = \frac{d}{dx}\mathscr{B}(x).$$

D'où

$$\delta F = \frac{1}{2} \sum_{\substack{\boldsymbol{R}\boldsymbol{R}' \\ \alpha\beta}} \frac{\partial^2 F}{\partial S_{\boldsymbol{R}}{}^{\alpha}\partial S_{\boldsymbol{R}'}{}^{\beta}} \delta S_{\boldsymbol{R}}{}^{\alpha}\delta S_{\boldsymbol{R}'}{}^{\beta} = \sum_{\boldsymbol{R}\boldsymbol{R}'} [\zeta(\boldsymbol{k}_0)\delta_{\boldsymbol{R}\boldsymbol{R}'} - J_{\boldsymbol{R}\boldsymbol{R}'}]\delta\boldsymbol{S}_{\boldsymbol{R}} \cdot \delta\boldsymbol{S}_{\boldsymbol{R}'} + \\ + \frac{1}{s^2}\left[\frac{K_B T}{2S^2\mathscr{B}'\left[\dfrac{2S}{K_B T}\zeta(\boldsymbol{k}_0)s\right]} - \zeta(\boldsymbol{k}_0)\right] \sum_{\boldsymbol{R}} (\boldsymbol{S}_{\boldsymbol{R}} \cdot \delta\boldsymbol{S}_{\boldsymbol{R}})^2.$$

On a utilisé l'équation (5).

Le deuxième terme du second membre est positif sauf si $\boldsymbol{S}_R$. $\delta\boldsymbol{S}_R = 0$ quelque soit $\boldsymbol{R}$, à condition que $T < T_c$.

Le premier terme est positif sauf si :

$$\delta S_{\boldsymbol{R}}{}^{\alpha} = \epsilon^{\alpha} \cos(\boldsymbol{k}_0 \cdot \boldsymbol{R} - \phi_{\alpha})$$

δF est donc positif ou nul et ne s'annule que pour des rotations d'ensemble de système de spins. La structure (5) est donc stable quèlque soit $T < T_c$.

(c) *Divers cas possibles*

Remarquons d'abord que, d'après l'équation (5), tous les spins sont perpendiculaires à la direction définie par les paramètres directeurs :

$$\frac{\sin(\phi_y - \phi_z)}{\lambda_x}, \quad \frac{\sin(\phi_z - \phi_x)}{\lambda_y}, \quad \frac{\sin(\phi_x - \phi_y)}{\lambda_z}.$$

On peut donc écrire, en choisissant convenablement les axes :

$$S_{\boldsymbol{R}}{}^{x} = \lambda_x \cos(\boldsymbol{k}_0\boldsymbol{R} - \phi), \qquad S_{\boldsymbol{R}}{}^{y} = \lambda_y \sin \boldsymbol{k}_0\boldsymbol{R},$$
$$S_{\boldsymbol{R}}{}^{z} = 0.$$

Ecrivons que

$$S_{\boldsymbol{R}}{}^2 = S - {}_{\boldsymbol{R}}{}^2 = S_0{}^2$$

$$\lambda_x^2 \cos^2(\boldsymbol{k}_0\boldsymbol{R}-\phi)+\lambda_y^2 \sin^2\boldsymbol{k}_0\cdot\boldsymbol{R}$$
$$=\lambda_x^2\cos^2(\boldsymbol{k}_0\cdot\boldsymbol{R}+\phi)+\lambda_y^2\sin^2\boldsymbol{k}_0\cdot\boldsymbol{R}$$
$$=\lambda_x^2\cos^2\phi.$$

On en déduit

$$\cos(\boldsymbol{k}_0\cdot\boldsymbol{R}-\phi)=\pm\cos(\boldsymbol{k}_0\cdot\boldsymbol{R}+\phi)$$

soit

$$\sin 2\boldsymbol{k}_0\cdot\boldsymbol{R}\sin 2\phi=0.$$

On est alors amené à distinguer trois cas :

(i) si $\boldsymbol{k}_0\cdot\boldsymbol{R}$ peut prendre des valeurs quelconques, on a $\sin 2\phi=0$ d'où $\lambda_x^2=\lambda_y^2$.

On a alors

$$S_R{}^x=s\cos\boldsymbol{k}_0\cdot\boldsymbol{R},\qquad S_R{}^y=s\sin\boldsymbol{k}_0\cdot\boldsymbol{R},$$
$$S_R{}^z=0. \tag{5a}$$

Cette structure est antiferromagnétique. Mais on ne peut en général trouver aucune décomposition en sous-réseaux.

Il convient de noter que les équations (5a) deviennent fausses si l'énergie magnéto-cristalline est appréciable.

(ii) Si $\boldsymbol{k}_0\cdot\boldsymbol{R}$ ne peut prendre que des valeurs multiples de π, tous les spins sont parallèles à une même direction. On a

$$S_R{}^x=s\cos\boldsymbol{k}_0\cdot\boldsymbol{R},\qquad S_R{}^y=S_R{}^z=0. \tag{5b}$$

Ce cas correspond à une structure soit ferromagnétique (alors $\boldsymbol{k}_0=0$) soit antiferromagnétique.

(iii) Si $\boldsymbol{k}_0\cdot\boldsymbol{R}$ ne peut prendre que des valeurs multiples de $\pi/2$, la solution (5) a la forme particulière suivante :

$$S_R{}^x=\lambda\cos(\boldsymbol{k}_0\cdot\boldsymbol{R}-\phi),$$
$$S_R{}^y=\lambda\sqrt{(\cos 2\phi)}\sin\boldsymbol{k}_0\cdot\boldsymbol{R},\qquad S_R{}^z=0.$$

Ou encore en faisant un changement d'axes

$$S_R{}^x=\lambda_x\cos\left(\boldsymbol{k}_0\boldsymbol{R}-\frac{\pi}{4}\right);$$

$$S_R{}^y=\lambda_y\sin\left(\boldsymbol{k}_0\cdot\boldsymbol{R}-\frac{\pi}{4}\right),\qquad S_R{}^z=0. \tag{5c}$$

Les spins prennent alternativement les valeurs $\boldsymbol{S},-\boldsymbol{S},\boldsymbol{S}'$ et $-\boldsymbol{S}'$. On a $|\boldsymbol{S}|=|\boldsymbol{S}'|$ mais la connaissance des interactions d'échange ne suffit pas à déterminer les directions $\boldsymbol{S}$ et $\boldsymbol{S}'$.

Compte tenu de l'énergie magnétocristalline deux cas sont possibles :

— ou bien $\boldsymbol{S}$ et $\boldsymbol{S}'$ sont dirigés suivant deux directions de facile aimantation,

— ou bien $\boldsymbol{S}$ et $\boldsymbol{S}'$ sont dirigés suivant une même direction de facile aimantation.

La présente théorie ne permet pas de choisir entre ces deux structures. Il se pourrait qu'on passe de la première à la seconde par l'action d'un champ magnétique relativement faible.

3. QUELQUES EXEMPLES

(a) *Chaine linéaire avec interaction entre premiers et seconds voisins*

Nous donnons cet exemple parce qu'il est le plus simple qui puisse présenter une structure du type (i).

En appelant J et J' les intégrales d'échange on peut écrire :

$$\zeta(k)=2(J\cos ka+J'\cos 2ka)$$

où a est la distance interatomique.

Les extrêma de ζ sont donnés par

$$\frac{d}{dk}\zeta(k)=0 \text{ soit}\qquad \sin ka(J+4J'\cos ka)=0.$$

Les solutions sont :

(1) $\sin ka=0$, d'où $\zeta(k)=2(J'\pm J)$

(2) $\cos ka=-\dfrac{J}{4J'}$, d'où $\zeta(k)=-2\left(J'+\dfrac{J^2}{8J'}\right)$.

Si $J'<-|J/4|$, c'est la seconde solution qui donne le maximum de $\zeta(k)$. La structure magnétique a bien la forme que nous avons désignée par (i) dans notre classification de la Section 2(c).

(b) *Réseau cubique à faces centrées avec interactions entre premiers et seconds voisins*

Ce problème a déjà été traité par ANDERSON[3] par une méthode différente; nous donnerons seulement les résultats. Ceux-ci sont résumés par le graphique de la Fig. 1. Suivant les valeurs des intégrales d'échange J et J' on trouve les quatre possibilités suivantes (on s'est conformé à la numérotation d'ANDERSON)

VOL 11 195

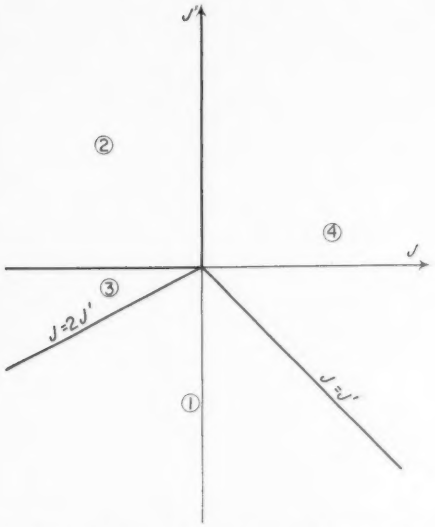

FIG. 1. Structures magnétiques possibles pour un corps cubique à faces centrées; interactions J et J' entre premiers et seconds voisins.

(1) Si $\begin{cases} J' < J/2 \\ J' < -J, \end{cases}$

$\boldsymbol{k}_0 = \pi/a(111)$, a étant le paramètre de la maille. On a une structure du type MnO.

(2) Si $J < 0 < J'$, $\quad \boldsymbol{k}_0 = \dfrac{2\pi}{a}(001).$

Les spins situés dans les plans $z = n$ (n entier) sont dirigés dans la même direction, mais en sens contraire, que les spins situés dans les plans $z = n + 1/2$.

(3) Si $J/2 < J' < 0$, $\quad \boldsymbol{k}_0 = \dfrac{\pi}{a}(111).$

La maille magnétique est quadratique, de côtés $2a$, $2a$, a; elle est représentée sur la Fig. 2. Les sites désignés respectivement par les signes ○, ⊙, ⊘ et ⊕ portent respectivement les spins $\boldsymbol{S}$, $-\boldsymbol{S}$, $\boldsymbol{S}'$ et $-\boldsymbol{S}'$. On a $\boldsymbol{S} = \boldsymbol{S}'$, mais la présente théorie ne permet pas de prévoir l'orientation relative de $\boldsymbol{S}$ et $\boldsymbol{S}'$.

(4) Si $\begin{cases} J > 0 \\ J > -J', \end{cases}$ $\quad \boldsymbol{k}_0 = 0.$

La substance est alors ferromagnétique.

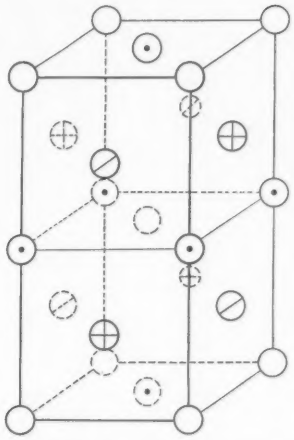

FIG. 2. Surstructure quadratique correspondant à la zone (3) de la Fig. 1.

Les sites ○ portent le spin $\boldsymbol{S}$
Les sites ⊙ portent le spin $-\boldsymbol{S}$
Les sites ⊘ portent le spin $\boldsymbol{S}'$
Les sites ⊕ portent le spin $-\boldsymbol{S}'$

Notre méthode nous a donc permis de retrouver les résultats d'ANDERSON, et de montrer qu'il n'y avait pas d'autres arrangements possibles que ceux qu'il avait prévus. Nous avons en outre précisé la structure (iii).

(c) *Réseau quadratique centré avec interactions entre premiers, seconds et troisièmes voisins*

C'est là un cas très fréquent (MnF_2, MnO_2, $MnAu_2$ etc.) qui nous intéresse en outre par le fait qu'il peut présenter les trois types (i), (ii), (iii) de structures rencontrés au Section 2(c); suivant les valeurs des intégrales d'échange.

En appelant J, J', J'' les intégrales d'échange, a et c, les côtés de la maille, $2\pi h/a$, $2\pi k/a$, $2\pi l/c$ les composantes du vecteur $\boldsymbol{k}$, on trouve :

$$\zeta(\boldsymbol{k}) = 8J \cos\pi h \cos\pi k \cos\pi l + \\ + 2J'(\cos 2\pi h + \cos 2\pi k) + 2J'' \cos 2\pi l.$$

Les extrema de cette expression sont donnés par le système:

$$\sin\pi h(J \cos\pi k \cos\pi l + J' \cos\pi h) = 0$$
$$\sin\pi k(J \cos\pi l \cos\pi h + J' \cos\pi h) = 0$$
$$\sin\pi l(J \cos\pi h \cos\pi k + J' \cos\pi h) = 0$$

Les solutions sont données par le Tableau 1.

Tableau 1

No.	$h\,k\,l$		$\zeta(\boldsymbol{k})$	Conditions d'existence
1	0 0 0 et 1 0 0	—	$4J'+2J''\pm 8J$	—
2	$\frac{1}{2}\,\frac{1}{2}\,0$	—	$2J''-4J'$	—
3	$\frac{1}{2}\,\frac{1}{2}\,\frac{1}{2}$	—	$-2J''-4J'$	—
4	$0\,0\,l$	$\cos \pi l = -\dfrac{J}{J''}$	$4J'-2J''-4\dfrac{J^2}{J''}$	$\lvert J''\rvert > \lvert J\rvert$
5	$h\,0\,0$	$\cos \pi h = -\dfrac{J}{J'}$	$2J''-4\dfrac{J^2}{J'}$	$\lvert J'\rvert > \lvert J\rvert$
6	$\frac{1}{2}\,0\,\frac{1}{2}$	—	$-2J''$	—
7	$h\,h\,l$	$\cos \pi h = -\dfrac{\sqrt{(J'J'')}}{\lvert J\rvert}$	$4\dfrac{J'^2J''}{J^2}-4J'$	$0 < J'J'' < J^2$
		$\cos \pi l = -\left\lvert\dfrac{J'}{J}\right\rvert$	$-2J''$	$\lvert J'\rvert < \lvert J\rvert$

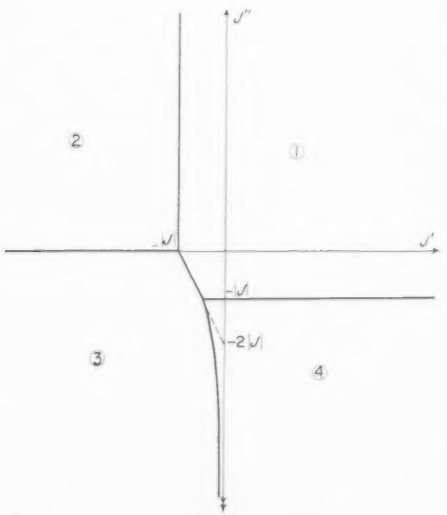

FIG. 3. Structures magnétiques possibles pour un corps quadratique centré, dans le plan J', J''. L'interaction J entre les sommets et les centres des mailles est considérée comme un paramétre constant.

On peut résumer la discussion par un graphique dans le plan $J'J''$ (Fig. 3). Seules les solutions 1, 2, 3, 4 peuvent correspondre à un maximum absolue de $\zeta(\boldsymbol{k})$ et le domaine de validité de ces solutions est limité par les droites :

$$J''=0, \qquad J'=-|J|, \qquad J''=-|J|,$$
$$2J'+J''+2|J|=0$$

et par l'hyperbole : $J'J''=J^2$.

Dans la classification du Section 2(c), les structures 1 et 2 se rattachent au type (ii), la structure 3 au type (iii) et la structure 4 au type (i),

La structure 1 est ferromagnétique ($J>0$) ou antiferromagnétique ($J<0$) du type MnF_2.

La structure 2, antiferromagnétique, correspond à une maille magnétique quadruple de la maille nucléaire (Fig. 4).

La structure 3 est aussi antiferromagnétique, mais la maille magnétique est huit fois plus grande que la maille nucléaire (Fig. 5). Il semble que le bioxyde de manganèse MnO_2 présente effectivement

cette structure,[4] les spins étant parallèles à deux directions perpendiculaires. Les conditions imposées à J, J' et J'' par la Fig. 3 semblent compatibles avec les positions des ions dans la maille de MnO_2.

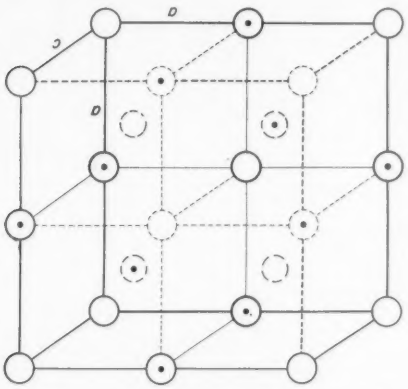

FIG. 4. Structure correspondant à la zone (2) de la FIG. 3. Mêmes notations que pour la Fig. 2.

Enfin la structure 4 correspond à une répartition hélicoïdale des moments magnétiques. Elle pourrait se présenter dans des corps où les ions magnétiques de la base de la maille seraient liés par

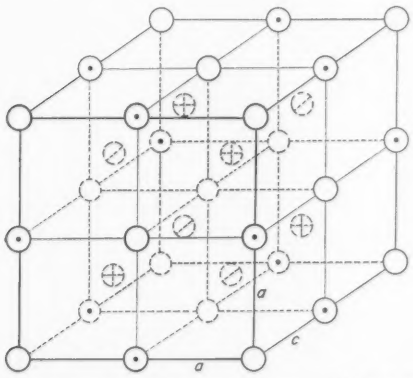

FIG. 5. Structure correspondant à la zone (3) de la Fig. 3. Mêmes notations que pour la Fig. 2.

échange direct, donc ferromagnétique, les spins situés sur l'axe c étant au contraire fortement couplés antiferromagnétiquement.

4. CONCLUSIONS

L'étude précédente montre que dans certaines substances magnétiques les moments peuvent présenter une répartition "hélicoïdale" définie par la formule (15a), avec une période qui peut n'être pas commensurable avec celle du réseau cristallin. Bien que cette dernière particularité ne semble pas avoir été indiquée antérieurement,* on sait qu'il existe des corps où les aimantations des divers sous-réseaux ne sont pas parallèles. Cette propriété peut se rencontrer dans le réseau de Bravais hexagonal[5] et aussi dans des réseaux à plusieurs atomes par maille, le mécanisme étant alors un peu différent de celui qui a été étudié ici.

Note ajoutée en épreuve: Une étude très semblable à la nôtre,[6] mais limitée au cas du réseau quadratique centré avec trois intégrales d'échange, a été publiée au moment où cet article était envoyé pour publication. Il y est fait état notamment de récents travaux de ERICKSON attribuant à MnO_2, une structure du type (i).

Remerciments—J'ai bénéficié pour ce travail de l'aide et des conseils de M. A. HERPIN et de M. P. G. DE GENNES; je les en remercie vivement.

BIBLIOGRAPHIE

1. NÉEL L., *le champ moléculaire de Weiss et le champ moléculaire local. Colloque national de magnétisme de Strasbourg 1957*. Editions du CNRS (1958).
2. NÉEL L., *Ann. Phys.*, Paris **5**, 232 (1936).
3. ANDERSON P. W., *Phys. Rev.* **79**, 350, 705 (1950).
4. ERICKSON R. A., Thèse, Agricultural and Mechanical College of Texas. (1952).
5. HIRONE T. et ADACHI K., *J. Phys. Soc. Japan* **12**, 156 (1957).
6. YOSHIMORI A., *J. Phys. Soc. Japan* **14**, 307 (1959).

* Toutefois des expèriences récentes de diffraction de neutrons permettent d'attribuer une telle structure à l'alliage $MnAu_2$ (A. HERPIN et P. MÉRIEL, communication privée).

J. Phys. Chem. Solids Pergamon Press 1959. Vol. 11. pp. 310–314. Printed in Great Britain.

DETERMINATION DE LA COMPOSITION A FUSION CONGRUENTE DE SEMICONDUCTEURS BINAIRES PAR ANALYSE THERMIQUE DIFFERENTIELLE

APPLICATION A Bi_2Te_3, Sb_2Te_3 et Bi_2Se_3

G. OFFERGELD et J. VAN CAKENBERGHE

European Research Associates, 95 rue Gatti de Gamond, Bruxelles

(*Received* 22 *April* 1959; *revised* 9 *July* 1959)

Abstract—The phase diagram of binary compounds is generally characterized by the existence of a maximum in the liquidus curve for a composition near the stoichiometric composition and by isothermal transitions corresponding to the melting of eutectic phases or to peritectic reactions. The amount of heat involved in these transitions is a linear function of the difference between the actual composition and the composition having a congruent melting point. By differential thermal analysis it is possible to determine the composition for which these thermal effects disappear and thus to measure the difference between the congruent and stoichiometric compositions.

1. INTRODUCTION

L'ÉTUDE des semiconducteurs a mis en évidence le fait que la plupart des composés minéraux présentent des écarts à la stoechiométrie. Ces écarts se traduisent par l'existence d'une concentration de porteurs de charges ne correspondant pas à celle que l'on peut calculer à partir de la connaissance de la largeur de la bande interdite. Lorsque la substance fond sans se décomposer, cet écart correspond dans le diagramme de phase à un déplacement du maximum de la courbe de liquidus.

La connaissance exacte de la composition correspondant au maximum du point de fusion est essentielle pour l'interprétation des propriétés électriques des monocristaux obtenus par fusion de zone ou par la méthode de Czochralski. Ces méthodes conduisent en effet à des substances dont la composition est identique ou très voisine de celle correspondant au maximum du point de fusion.

Par la mesure des propriétés électriques SATTERTHWAITE et URE[1] ont montré que le solide en équilibre avec un liquide de composition stoechiométrique Bi_2Te_3 n'avait pas le caractère intrinséque et que l'on s'approchait de l'état intrinsèque en solidifiant, dans des conditions d'équilibre thermodynamique, une très petite fraction d'un liquide de composition excédentaire en tellure (63 pour cent atomique). Les mesures électriques ne permettent cependant pas de distinguer l'origine des porteurs de charge, parce qu'elles confondent leurs variations de concentration dues à des défauts de réseau avec celles dues à des variations de composition chimique.[2] Il est donc nécessaire de disposer d'une méthode indépendante.

2. PRINCIPE DE LA MÉTHODE

Le principe de la méthode est illustré à l'aide de la Fig. 1, qui représente une partie d'un diagramme d'état idéal s'étendant de part et d'autre de la substance à fusion congruente C jusqu'aux températures de transition T_I et T_{II} (isothermes d'équilibre à trois phases à pression constante).

Au cours de l'analyse thermique différentielle de mélanges de compositions voisines mais différentes de C, il apparaitra un signal à T_I ou T_{II} suivant que le mélange contienne un excès de A ou de B par rapport à C.

Pour une vitesse de chauffe (ou de refroidissement) constante et une masse totale de substance donnée, la grandeur du signal de transition est

directement proportionnelle à l'excès du constituant A ou B. D'autre part, pour la composition congruente C aucun signal ne doit, en principe, s'observer.

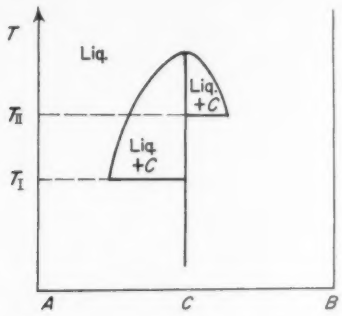

FIG. 1.

En pratique, deux types de difficultés peuvent se présenter dans l'application de cette méthode:

(1) Il existe une zone de solubilité solide autour du composé congruent C. Il faut alors opérer sur un échantillon trempé rapidement à partir du point de fusion, afin de réduire au minimum la formation d'une solution solide.

(2) La transition à observer s'effectue incomplètement (Ex. transition péritectique). Dans ce cas, pour obtenir le signal le plus grand lors du chauffage, il est nécessaire d'effectuer préalablement un recuit prolongé à une température légèrement inférieure à la température de transition, ce recuit étant suivi d'une trempe brusque afin de conserver le système dans un état correspondant à l'équilibre thermodynamique à cette température.

S'il existe des zones de solubilité solide, le système évoluera au cours de la mesure. Il est donc important de choisir judicieusement la vitesse de chauffe et de la maintenir constante afin de réaliser des expériences comparables.

3. TECHNIQUE EXPÉRIMENTALE

Chaque composé binaire examiné est préparé par pesée directe des constituants dans une ampoule en quartz. Après remplissage, l'ampoule est scellée sous vide et ensuite chauffée afin d'amener le mélange à l'état liquide. Le bismuth de départ a été préalablement traité par la méthode de la zone fondue jusqu'à atteindre un degré de pureté de 99·999 pour cent. L'antimoine utilisé provient de l' Associated "Lead Manufacturers" et possède également un degré de pureté de 99·999 pour cent. Le tellure et le sélénium ont été purifiés par triple distillation sous vide.

Dans l'appareil d'analyse thermique différentielle, l'ampoule contenant la substance à examiner repose directement sur le thermocouple de mesure.

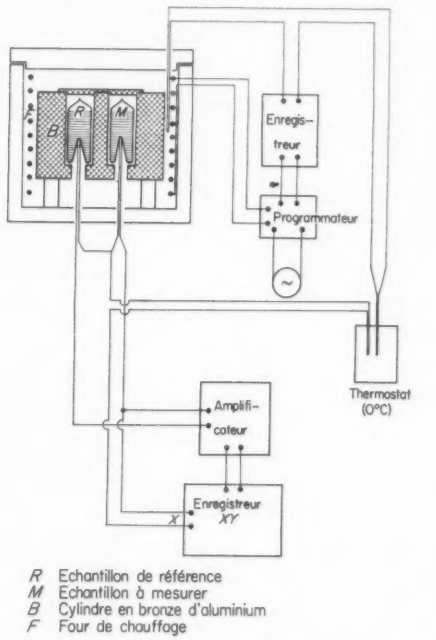

R Echantillon de référence
M Echantillon à mesurer
B Cylindre en bronze d'aluminium
F Four de chauffage

FIG. 2. Schéma du dispositif de mesure.

Sa température est comparée à celle d'une ampoule semblable contenant une quantité d'alumine ayant à peu près la même masse thermique que l'échantillon à mesurer. Les deux ampoules sont placées dans un bloc de bronze d'aluminium qui assure une bonne homogénéité thermique et amortit les oscillations de température dues au fonctionnement du régulateur.

Le bloc de bronze est chauffé dans un four dont la température varie linéairement en fonction du temps, grâce à un dispositif électronique à programme et réglage proportionnel.

Les phénomènes sont suivis au moyen d'un enregistreur XY. Le déplacement suivant l'axe des X est proportionnel à la tempèrature de l'échantillon. La différence de température entre

VOL. 11 1959

l'échantillon et le témoin est amplifiée par un amplificateur à vibreur et enregistrée suivant l'axe des *Y*. On obtient une déviation d'environ 28 mm par degré.

La Fig. 2 donne le schéma du dispositif.

4. RESULTATS

(a) *Système* Bi–Te

Le diagramme d'état indique l'existence d'une réaction péritectique à 540°C pour des compositions contenant un excès de bismuth (57 pour cent de Bi en poids).[3] D'autre part, dans le domaine de concentrations riches en tellure, il apparaît une transition eutectique à 413°C.[4] ABRIKOSOW *et al.*[3] ont montré que, contrairement aux données de HANSEN,[4] il n'y a pas de large région de solubilité solide autour du composé à point de fusion maximum.

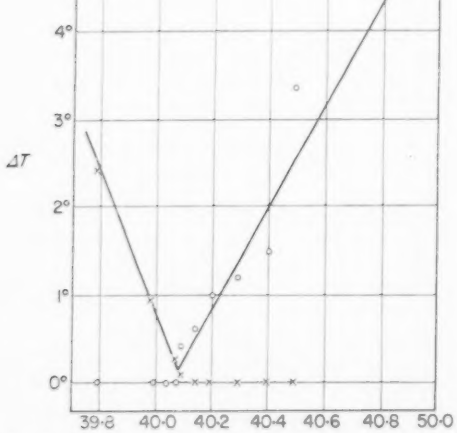

FIG. 3. Systeme Bi–Te. Amplitude des signaux de transition en fonction de la composition. Echantillons trempés.
× Transition eutectique à 413°C
O Transition péritectique à 540°C

Les Figs. 3 et 4 représentent les amplitudes des signaux en fonction de la composition, respectivement pour les échantillons trempés et recuits. On constate que le recuit prolongé n'a pas fait disparaître les signaux de transition péritectique observés sur les échantillons trempés, mais qu'au contraire dans l'ensemble la quantité de la phase péritectique a augmentée. La pente de la droite exprimant l'amplitude du signal pe'ritectique en fonction de la concentration est plus grande pour les échantillons recuits.

Pour la composition Bi 40,08 Te 59,92 on observe encore après recuit un signal de transition péritectique qui n'apparaît plus pour Bi 40,07

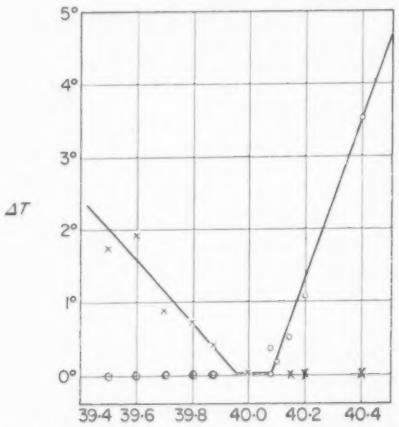

FIG. 4. Système Bi–Te. Amplitude des signaux de transition en fonction de la composition. Echantillons recuits.
× Transition eutectique à 413°C
O Transition péritectique à 540°C

Te 59,93. Ce résultat indique que la composition à point de fusion congruent correspond à des teneurs en bismuth inférieures à 40,08 pour cent. Remarquons que pour Bi 40,08 Te 59,92 trempé on observe un faible signal eutectique. La raison de cet effet n'est pas claire, mais on peut probablement l'attribuer à un défaut d'homogénéité résultant de la trempe. Ce défaut d'homogénéité introduit une imprécision dans la détermination de la composition congruente qui peut être estimée à partir des Figs. 3 et 4 comme étant Bi 40,065±0,015 Te 59,935±0,015.

La limite du domaine de solubilité solide du tellure dans le tellurure de bismuth à 500–525°C correspond à la composition la plus riche en tellure pour laquelle le signal de transition eutectique s'annule. L'extrapolation de la droite représentant l'amplitude du signal eutectique en fonction du titre des échantillons recuits fournit la valeur Bi 39,95±0,05 Te 60,05±0,05 (Fig. 4).

(b) *Système* Sb–Te

Le diagramme d'état[4] présente un eutectique

Sb_2Te_3–Te à 400°C et un eutectique Sb_2Te_3–Sb à 545°C. La Fig. 5 montre que les droites représentant l'amplitude des signaux de transition eutectique en fonction de la concentration s'extrapolent à la composition à fusion congruente Sb 40,4±0,05 Te 59,6±0,05.

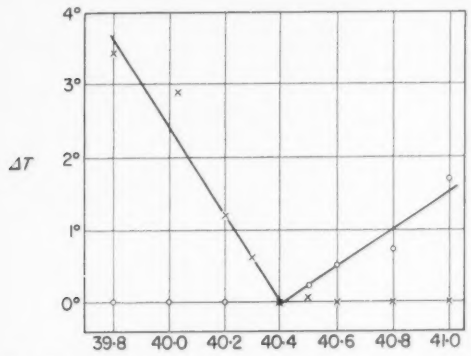

FIG. 5. Système Sb–Te. Amplitude des signaux de transition en fonction de la composition. Echantillons trempés.

× Transition eutectique à 400°C.
O Transition eutectique à 545°C

Ce résultat est confirmé par le fait que le palier de fusion devient de plus en plus net au fur et à mesure que l'on se rapproche de la composition congruente pour finalement être isotherme pour Sb 40,4 Te 59,6.

(c) *Système* Bi–Se

L'examen du diagramme de phase[4] montre :

(a) Pour des compositions excédentaires en bismuth la formation à 605°C de la phase péritectique BiSe.

(b) Dans le domaine de concentrations riches en sélénium la présence d'un isotherme de transition monotectique (situé également à 605°C), qui est suivi à 217° d'un palier eutectique.

L'extrapolation des droites exprimant l'amplitude des signaux de transition en fonction de la concentration montre que la composition à fusion congruente correspond à Bi 40,02±0,01 Se 59,98±0,01 (Fig. 6).

5. DISCUSSION

Pour les trois systèmes étudiés, la substance à fusion congruente contient toujours un excès de l'élément le plus électropositif (bismuth ou antimoine) par rapport à la composition stoechiométrique. Les mesures électriques montrent cependant que le signe des porteurs de charge est négatif dans Bi_2Se_3 et positif dans Bi_2Te_3 et Sb_2Te_3.

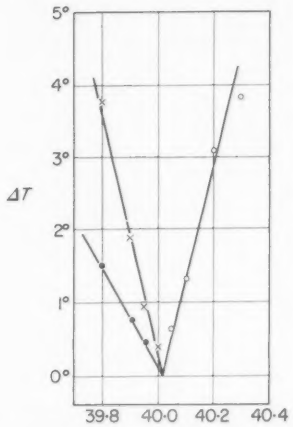

FIG. 6. Système Bi–Se. Amplitude des signaux de transition en fonction de la composition. Echantillons trempés.

× Transition monotectique à 605°C
• Transition eutectique à 217°C
O Transition péritectique à 605°C

Pour Bi_2Te_3 et Sb_2Te_3, ce résultat s'explique si l'on admet que les atomes de bismuth ou d'antimoine en excès se placent en position réticulaire de tellure (mécanisme d'anti-structure). Dans ces conditions, on obtient 3/5 de porteurs p par atome de bismuth excédentaire,[2] cette fraction 3/5 étant due au fait que les atomes excédentaires sont fixés partiellement dans des sites de tellure et partiellement dans des sites "normaux".

Dans le cas du séléniure de bismuth, la forte

Tableau 1

Composé	Sb ou Bi en excès (atomes/cm³ ×10¹⁹)	Densité des porteurs calculée (n/cm³ ×10¹⁹)	Densité des porteurs mesurée (n/cm³ ×10¹⁹)
Sb_2Te_3	21	12,5	7 à 10
Bi_2Te_3	3,1	1,9	0,8 à 3,4
Bi_2Se_3	1,05	3	2 à 4

différence de rayons atomiques et d'électronégativités des atomes de bismuth et de sélénium rendent probablement la substitution d'anti-structure beaucoup plus difficile. Il est possible qu'en ce cas le bismuth excédentaire se place en position interstitielle et cède trois électrons par atome.

Dans le Tableau 1, nous avons comparé la densité des porteurs de charges calculée suivant ces hypothèses avec les données de la littérature compilées par MOOSER et PEARSON[5].

On voit que l'accord entre les valeurs calculées et les valeurs mesurées est assez satisfaisant.

Remerciements—Ce travail a bénéficié de l'appui financier de la Société Union Carbide Corporation, New York, N.Y.

BIBLIOGRAPHIE

1. SATTERTHWAITE C. B. et URE R. W. Jr., *Phys. Rev.* **108,** 1164 (1957).
2. KRÖGER F. A., *J. Phys. Chem. Solids* **7,** 277 (1958).
3. ABRIKOSOW N. B., BANKINA V. F. et FEDOROVA G. A., *Questions de métallurgie et de la physique des semiconducteurs* pp. 91–96. Moscou (1957).
4. HANSEN M., *Constitution of Binary Alloys*. McGraw Hill, New York (1958).
5. MOOSER E. et PEARSON W. B., *J. Phys. Chem. Solids* **7,** 65 (1958).

VOL.
11
195

J. Phys. Chem. Solids Pergamon Press 1959. Vol. 11. pp. 315–333. Printed in Great Britain.

SPIN-WAVE RESONANCE IN A FERROMAGNETIC METAL

G. T. RADO and J. R. WEERTMAN

U.S. Naval Research Laboratory, Washington 25, D.C.

(*Received* 12 *March* 1959)

Abstract—The spin-wave resonance studied in this paper is a modified ferromagnetic resonance which is strongly influenced by the exchange interactions existing in the skin depth. Experimental observations of this resonance are reported, the underlying physical conditions are explained and a general "exchange boundary condition" is formulated and derived. A description is given of an experimental method for measuring both components of the complex equivalent permeability. Static measurements as well as resonance curves at 3000 and 4000 Mc/s are presented for monocrystalline and polycrystalline samples of a nickel–iron alloy having extremely low magnetocrystalline anisotropy. At room temperature the complete experimental resonance curves can be interpreted on the basis of the theory of AMENT and RADO by using an effective exchange stiffness constant, A, of $(3{\cdot}3 \pm 0{\cdot}5) \times 10^{-6}$ erg/cm and a spectroscopic splitting factor, g, of $2{\cdot}06 \pm 0{\cdot}01$. The agreement between theory and experiment would be destroyed if a LANDAU–LIFSHITZ or BLOCH damping term were included. Possible processes influencing the value of A are discussed. Experimental data taken at liquid-nitrogen temperature show an increase in the resonance line width and a decrease in the resonance field. Both effects are in qualitative but not quantitative agreement with the theory. A part of the discrepancy can be attributed to anomalous effects caused by the electronic mean free path.

1. INTRODUCTION

THE central problem in the ferromagnetic resonance of metals is the obscure physical origin of the observed line widths and shapes. Although some of the experimental resonance lines have been described formally by using phenomenological relaxation terms in the equation of motion, the magnitudes of the relaxation parameters required for this purpose have not been explained satisfactorily. Thus it is of considerable interest that in one particular kind of ferromagnetic resonance the role of the relaxation term is relatively unimportant. We refer to this particular resonance as "spin-wave resonance"[1–4] in order to contrast it with "ordinary ferromagnetic resonance".

The essential difference between these two phenomena is that in spin-wave resonance the effects of exchange are appreciable, so that the entire resonance curve can be interpreted fairly completely on the basis of an actual physical mechanism, namely the interplay between exchange effects and the skin effect in a ferromagnetic metal. In ordinary ferromagnetic resonance, on the other hand, exchange effects are negligible, and the interpretation of the resonance curve requires the use of poorly understood relaxation parameters.

The term spin-wave resonance was used recently to describe a different kind of resonance.[5,6] In the theory of KITTEL[5] and in the experiments of SEAVEY and TANNENWALD[6] the excitation of the spin waves is a dimensional effect and depends primarily on the specimen thickness. In our work, on the other hand, this excitation requires a nonuniform microwave field and thus depends on the skin effect. It is the latter kind of excitation which will be referred to as spin-wave resonance throughout the present paper.

The first experimental observation of spin-wave resonance was accomplished at room temperature and reported by us very briefly several years ago.[1] More accurate data and an extension of the experiments to liquid-nitrogen temperature have also been published in abbreviated form.[2] The present paper includes some theoretical considerations as well as a comprehensive account of our experimental method and results.

Section 2 contains a detailed explanation of the

special physical conditions which led to the feasibility of the spin-wave-resonance experiment and to the simplifying approximations of the associated theory.[3] In Section 3 we briefly recapitulate some results of the electromagnetic theory[3] which was worked out concurrently with the first experiments. We include a numerical justification of the approximations, as well as some comments on various relaxation terms and on a recent calculation[4] of the anomalous effects of the electronic mean free path on spin-wave resonance. This section also contains a formulation and derivation of a general "exchange boundary condition" and a brief consideration of the NÉEL surface anisotropy. Then we describe, in Section 4, the preparation of the polycrystalline and monocrystalline samples used in our measurements. These samples consist of a certain nickel–iron alloy which was heat treated to have a magnetocrystalline anisotropy of nearly zero at 77° K as well as at 300° K. The experimental method which we used for measuring the resonance curves is discussed in Section 5 and extended in the Appendix. This method involves a sufficiently accurate determination of both components of the complex equivalent permeability to permit a clear distinction between relaxation and exchange effects.

Except for certain static measurements, all the experimental data were taken at 3000 and 4000 Mc/s. In Section 6 we present and discuss the experimental results obtained at these two frequencies at both room temperature and liquid-nitrogen temperature.

2. PHYSICAL CONSIDERATIONS

The motion of the magnetization vector, $\boldsymbol{M}$, in a ferromagnetic material may often be described by the LANDAU–LIFSHITZ dynamical equation:

$$(1/\gamma)\partial\boldsymbol{M}/\partial t = \boldsymbol{M}\times\boldsymbol{H}+(2A/M_s^2)\boldsymbol{M}\times \times\nabla^2\boldsymbol{M}-(\lambda/\gamma M_s^2)\boldsymbol{M}\times(\boldsymbol{M}\times\boldsymbol{H}), \quad (1)$$

where $\gamma = ge/2mc$ is the magnetomechanical ratio and $M_s = |\boldsymbol{M}|$ is the saturation magnetization. The magnetic field, $\mathbf{H}$, includes the applied field as well as the demagnetizing field. The term containing the exchange stiffness constant, A, measures the exchange torque density due to any nonuniformity in the orientation of $\boldsymbol{M}$. In its present form, this term is valid only if the crystal structure of the material is cubic. The term containing the relaxation frequency, λ, provides a slightly simplified[3] phenomenological description of damping due to relaxation effects. A more general version of equation (1) would contain torque density terms due to magnetocrystalline anisotropy and stress. Such terms may be neglected under the experimental conditions encountered in the present work. In the ordinary ferromagnetic resonance of metals, the exchange term is always neglected as long as linear conditions prevail. In spin-wave resonance, on the other hand, the exchange term is necessarily retained, and in the particular case of the present experiments the relaxation term is negligible. Thus it is the dissipation of "special" eddy currents caused by the exchange effect which gives rise to the energy dissipation in this case.

In the interpretation of ordinary ferromagnetic resonance[7] there are two difficulties which do not occur in spin-wave resonance. Firstly, the spectroscopic splitting factor g ought to obey the KITTEL–VAN VLECK relation[8]:

$$g-2 = 2-g', \quad (2)$$

where g' is the magnetomechanical factor. Apart from some exceptions,[9] however, the experiments show that $g-2$ exceeds $2-g'$. Secondly, the more serious difficulty exists that the physical basis of the measured relaxation frequencies is not understood. While the experimental values of λ in metals are usually of the order of 10^8 or 10^9 sec^{-1}, the theoretical values are considerably smaller. When the present experiments were begun the discrepancy between theory and experiment amounted to several orders of magnitude. More recently, theoretical estimates by MITCHELL[10] have reduced it to around one order of magnitude. The discrepancy remains essentially unchanged if the λ-term of equation (1) is replaced by the BLOCH relaxation term.

Even before our first experiments, MACDONALD[11,12] and KITTEL and HERRING[13] independently suggested that exchange effects arising from the $\nabla^2\boldsymbol{M}$-term of equation (1) might play a role in ferromagnetic resonance. These authors concluded theoretically that at microwave frequencies the exchange effects are not likely to be of importance in pure metals at room temperature, or in alloys at any temperature. This conclusion

was shown to be invalid by electromagnetic calculations.[3] We now describe the physical considerations underlying our observation of exchange effects[1] in an alloy at room temperature.

In order to observe exchange effects, we must make the $\nabla^2\boldsymbol{M}$-term of equation (1) as large as possible. Thus $\boldsymbol{M}$ must be made to vary rapidly with position, a condition which requires that the skin depth be made small. For this purpose we achieved a situation in which the microwave permeability is unusually large. This was done by reducing the "stiffness" of the oscillating spin system through the use of a small "effective field". Thus we selected a material having a very small (essentially zero) anisotropy and employed unusually small static fields (around 50–100 Oe). In all previous resonance experiments the anisotropy was appreciable and the static field was around a few thousand oersteds. The smallness of the anisotropy in our experiments has the additional advantage of permitting us to use polycrystals as well as single crystals without causing complications due to lack of saturation.

It should be noted that a large value of the $\nabla^2\boldsymbol{M}$-term is a necessary but not a sufficient condition for observing exchange effects. The reason is the existence of the second independent condition that the competing term due to the effective field be relatively small. In other words, the resulting requirement is that the exchange stiffness energy be as large as possible in comparison to the effective Zeeman energy. It is seen that our choice of a small effective field does satisfy this resulting requirement.

It should be pointed out that the skin depth could be made very small even if the permeability were not very large. One way of doing this would be to use a relatively high frequency. However, the static field at resonance would then be large, so that there would be a contradiction (except in the case of an oriented monocrystal discussed in the next paragraph) with our independent condition that the effective field be small. This may be one of the reasons why appreciable exchange effects were not observed in any of the experiments performed at relatively high microwave frequencies (say 24,000 Mc/s) on metals in which λ has the usual large values. Another way of achieving a small skin depth consists in using a low temperature and hence a high conductivity. However, a decrease in temperature introduces two difficulties. In most metals it causes the anisotropy to be large and the anomalous effects due to the electronic mean free path to be appreciable.

It should be mentioned that spin-wave resonance in metals of relatively high anisotropy (e.g. nickel at room temperature) could perhaps be observed. Such an experiment, which we have not yet performed, would require the use of a large single crystal which is accurately oriented. An appropriately applied static magnetic field would effectively "flatten" the anisotropy energy surface and thus produce an effective field whose magnitude is sufficiently small to give rise to a large permeability.

A related experiment was recently carried out successfully by RODBELL[14] who measured resonances in an oriented iron whisker. In this material the value of λ seems to be unusually small. On the basis of the AMENT–RADO[3] formulas, RODBELL ascribed a large part of the observed line width to exchange effects.

3. THEORETICAL REMARKS

(a) Equivalent permeability

The equivalent permeability,[1,3] μ_{equ}, was defined as that complex permeability which is deduced from the (measured or calculated) surface impedance by using the classical skin-effect theory. Under certain assumptions, which are valid in our experiments, the combined solution of equation (1) and MAXWELL'S equations yields the AMENT–RADO[3] result:

$$\mu_{\text{equ}} = \mu_1 - i\mu_2 = \frac{\eta - \Omega^2 + i\Omega L + 2\epsilon(1+i)}{[\eta - \Omega^2 + i\Omega L + \epsilon(1+i)]^2} \quad (3)$$

where the dimensionless parameters are defined by:

$$\eta = H_z/(4\pi M_s), \quad (4a)$$

$$\Omega = \omega/(4\pi M_s\gamma), \quad (4b)$$

$$L = \lambda/(M_s\gamma), \quad (4c)$$

$$\epsilon^2 = A/(2\pi M_s{}^2\delta^2). \quad (4d)$$

Here ω is the circular frequency and H_z is the static field (including the demagnetizing field) parallel to the sample surface. The quantity

$$\delta = (c^2/2\pi\omega\sigma)^{\frac{1}{2}} \quad (5)$$

is the classical skin depth for permeability unity and σ is the conductivity. Gaussian units are used throughout.

The derivation of equation (3) involves, among other things, the approximation that each of the quantities η, Ω^2, ϵ, L^2 and ΩL be negligible compared to unity. To verify that this approximation is fulfilled, consider the following data (see Sections 4 and 6) pertaining to room temperature (29° C): $\omega/2\pi = 3\times10^9$ sec^{-1}, $4\pi M_s = 1{\cdot}345\times$ $\times10^4$ emu, $1/\sigma = 18{\cdot}25\times10^{-6}$ Ω cm $= 2{\cdot}03\times$ $\times10^{-17}$ sec, $A = 2{\cdot}88\times10^{-6}$ erg/cm, $g = 2{\cdot}07$ and $\lambda = 0$. These values lead to $\delta = 3{\cdot}93\times10^{-4}$ cm, $\Omega^2 = 5{\cdot}91\times10^{-3}$, $\epsilon = 1{\cdot}61\times10^{-3}$, $L = \Omega L$ $= 0$ and (with the representative value H_z $= 60$ Oe) $\eta = 4{\cdot}46\times10^{-3}$, so that the approximation in question is well fulfilled. It should be noted that λ is, of course, not really zero. However, if we use for λ the upper limit, $\lambda = 5{\cdot}01\times10^8$ sec^{-1}, obtained by (incorrectly) interpreting our experimental results on the basis of a relaxation (rather than exchange) theory, we find that the approximation is still adequately satisfied. Similar conclusions apply to the data taken at liquid-nitrogen temperature and/or 4000 Mc/s.

Equation (3), with $L = 0$, was verified by MacDonald[15] after applying the approximations of reference (3) to his earlier work.[12] This agreement supersedes his prediction[11,12] that there is no appreciable resonance shift due to exchange effects in metals at room temperature.

Next we make two remarks concerning the damping term in equation (1). In the first place, it was stated in reference (3) that a replacement of the Landau–Lifshitz damping by the Bloch damping in equation (1) is equivalent, in the approximation used, to replacing L by zero in the final result, equation (3). This statement is only valid, however, if the numerical value of the fictitious relaxation frequency

$$\lambda_f = M_s/(H_z T_2) \tag{6}$$

is of the same order of magnitude as that of the actual relaxation frequency, λ. Since the experimental values[16] of the Bloch relaxation frequency, $1/T_2$, are of the order of 10^9 sec^{-1}, and since in our experiment $M_s \approx 10^3$ emu and $H_z \approx 10^2$ Oe, it follows that λ_f is about 10^{10} sec^{-1}, which is at least an order of magnitude larger than the usual values (10^8–10^9 sec^{-1}) of λ. Additional calculation shows that a replacement of the Landau–Lifshitz damping by the Bloch damping in equation (1) is equivalent, in a more accurate approximation, to replacing L by $2\eta\lambda_f/(M_s\gamma)$ in the final result, equation (3). It is seen from equations (4) and (6) that this is equivalent to replacing λ by $1/(2\pi T_2)$, which is a plausible result. Thus the use of the Bloch damping does not lead to any essential modification of equation (3).

The second remark concerning the damping term in equation (1) deals with the possibility that λ may be field-dependent. This possibility is of some interest because we found (see Section 6) that the agreement between equation (3) and the experimental line shapes is worse if λ is assumed to be finite and field-independent than if it is assumed to be zero. Thus the question arises whether a field-dependent λ would improve the agreement between equation (3) and experiment. In an attempt to answer this question, line-shape computations were made on the basis of equation (3) and each of the following two assumptions: (*a*) the function $\lambda(H_z)$ is linear and (*b*) the function $\lambda(H_z)$ increases monotonically with H_z at small values of H_z and becomes independent of H_z at large values of H_z. Although these two assumptions were suggested by the experimental line shapes, it was found that neither (*a*) nor (*b*) is as successful as the assumption $\lambda = 0$ in producing agreement between equation (3) and experiment.

Finally, we mention a possible modification of equation (3) at low temperatures. It was pointed out by Rado[4] that in a ferromagnetic metal Ohm's law may not be valid at very low and even at moderately low temperatures. The reason is that the equivalent permeability may be so large that the electronic mean free path may not be negligible in comparison to an appropriately defined effective skin depth. Under certain assumptions the calculation leads to the result[4]

$$\mu_{\text{equ}}^{\text{corr}} = \mu_{\text{equ}}[1+(3l/8\delta)(2i\mu_{\text{equ}})^{\frac{1}{2}}], \tag{7}$$

where the square root is to be taken such that its real part is positive. Here μ_{equ} is the equivalent permeability calculated from equation (3) (which presumes the validity of Ohm's law), and $\mu_{\text{equ}}^{\text{corr}}$ is the value of μ_{equ} obtained as a result of a first-order correction arising from the anomalous effect

of the electronic mean free path, l. In the derivation of equation (7) it is assumed that the approximation

$$l \ll \delta/|2\mu_{\text{equ}}|^{\frac{1}{3}} \tag{8}$$

is fulfilled. It is further assumed, among other things, that the scattering of the conduction electrons at the metal surface is diffuse. If the scattering is specular, then the first-order correction vanishes so that $\mu_{\text{equ}}^{\text{corr}} = \mu_{\text{equ}}$ is obtained. Since equation (7) was derived without considering effects caused by H_z, it is worth noting that in our samples the fractional change of resistivity arising from an H_z contained within the resonance region is fairly small. When measured with a current parallel to the z-direction, the numerical value of this change is about 1·6 per cent at room temperature and 5·3 per cent at liquid-nitrogen temperature. As to a comparison of equation (7) with our experiments, it was shown[4] that there is qualitative but not quantitative agreement. The residual discrepancy may be caused by the inadequacy of the quasi-free electron model of conduction. This model forms the basis of the REUTER-SONDHEIMER[17] relation which was used in the derivation of equation (7).

The necessity for considering anomalous effects of the electronic mean free path in ferromagnetic metals was suggested independently by GUREVICH[18] in work submitted at about the same time as reference (4). The essential difference between the two calculations is that they envisage different physical situations. In the work of RADO[4] the static field is assumed to be parallel to the metal surface and the anomalous effects of l are treated, within the approximations of reference (3), to first order in the quantity $|2\mu_{\text{equ}}|^{1/2}l/\delta$; this situation corresponds to the experiments reported in the present paper. In the work of GUREVICH[18], on the other hand, the static field is assumed to be perpendicular to the metal surface and the anomalous effects of l are treated in certain limiting cases only; this situation does not correspond to experiments performed so far.

(*b*) *General exchange boundary condition*

An electromagnetic field in a ferromagnetic material must satisfy not only the usual boundary conditions of the Maxwell theory, but also the "exchange boundary condition" which arises from the $\nabla^2\boldsymbol{M}$-term of equation (1). Special forms of the latter condition are given in the literature and will be mentioned later on. A general form of the exchange boundary condition, on the other hand, is formulated and derived below. It was developed in a simple form* for another problem.[19]

The LANDAU–LIFSHITZ equation may be written in the form

$$(1/\gamma)\partial\boldsymbol{M}/\partial t = \boldsymbol{T}_{\text{vol}} + (2A/M_s^2)\boldsymbol{M}\times\nabla^2\boldsymbol{M}, \tag{9}$$

where $\boldsymbol{T}_{\text{vol}}$ is the sum of all the volume torque densities which arise from forces other than exchange. Thus $\boldsymbol{T}_{\text{vol}}$ may include anisotropy effects as well as the first and third terms appearing on the right-hand side of equation (1). Now introduce an arbitrary set of three mutually orthogonal unit vectors $\boldsymbol{i}_1$, $\boldsymbol{i}_2$, $\boldsymbol{i}_3$, and define M_1, M_2, M_3 by the equation

$$\boldsymbol{M} = M_1\boldsymbol{i}_1 + M_2\boldsymbol{i}_2 + M_3\boldsymbol{i}_3. \tag{10}$$

Insertion of equation (10) into equation (9) leads to:

$$\int_V [(1/\gamma)(\partial\boldsymbol{M}/\partial t) - \boldsymbol{T}_{\text{vol}}]\, dV = (2A/M_s^2)(\boldsymbol{i}_1 I_1 + \boldsymbol{i}_2 I_2 + \boldsymbol{i}_3 I_3), \tag{11}$$

where the integral extends over the volume V contained within a closed surface S. Here I_1, I_2, I_3 are given by:

$$I_1 = \int_V (M_2\nabla^2 M_3 - M_3\nabla^2 M_2)\, dV \tag{12}$$

plus two similar equations obtained by cyclic permutation of all the subscripts. Use of Green's theorem yields:

$$I_1 = \int_S [M_2(\partial M_3/\partial n) - M_3(\partial M_2/\partial n)]\, dS, \tag{13}$$

where $\partial/\partial n$ denotes the partial derivative in the direction of a unit vector, $\boldsymbol{n}$, which is normal to the surface. Equation (13) and two similar equations

* In the correction to the BLOCH $T^{\frac{3}{2}}$ law attempted in reference (19), all dipolar forces are neglected and it is assumed that the $\boldsymbol{T}_{\text{surf}}$ of the present paper is zero. Inclusion of dipolar forces would change the details of the predicted dependence of the saturation magnetization on the distance from the sample surface, but it would not alter the order of magnitude of the characteristic length Λ.

VOL. 11 1959

for I_2 and I_3 may now be inserted into equation (11) to give:

$$\int_V [(1/\gamma)(\partial \boldsymbol{M}/\partial t) - \boldsymbol{T}_{\text{vol}}]\, dV = (2A/M_s^2) \int_S \boldsymbol{M} \times (\partial \boldsymbol{M}/\partial n)\, dS. \quad (14)$$

Now let the volume V have the shape of a small, thin, pill box which is situated in such a way that one face is just inside the ferromagnet and the opposite face is just outside; this is the kind of volume used in the derivation of the boundary condition for the normal component of $\boldsymbol{D}$ or $\boldsymbol{B}$. In the limit of an infinitely thin pill box the left-hand side of equation (14) vanishes and the right-hand side must be augmented by any torque which acts specifically across the surface of the ferromagnet. Thus equation (14) results in the general exchange boundary condition:

$$(2A/M_s^2)\boldsymbol{M} \times (\partial \boldsymbol{M}/\partial n) + \boldsymbol{T}_{\text{surf}} = 0, \quad (15)$$

where $\boldsymbol{T}_{\text{surf}}$ is the sum of all the surface torque densities which arise from forces other than ferromagnetic exchange. Contributions to $\boldsymbol{T}_{\text{surf}}$ may arise, for example, from the NÉEL[20] surface anisotropy or from the presence of an antiferromagnetic layer on the surface of the ferromagnet. It should be noted that equations (15) and (9) are both based on a continuum model of the magnetization. Thus the validity of these equations is restricted to those situations in which the distances (e.g. spin wavelengths) characterizing appreciable changes in $\boldsymbol{M}$ are long compared to the lattice spacing of the ferromagnet.

If the deviations of the magnetization from saturation are small (as they are, for example, in microwave problems involving small signal powers) then it is convenient to write:

$$\boldsymbol{M} = M_s \boldsymbol{i}_z + \boldsymbol{m}, \quad (16)$$

where $\boldsymbol{m}$ satisfies the relations $|\boldsymbol{m}| \ll M_s$ and $\boldsymbol{m} \cdot \boldsymbol{i}_z = 0$. Thus the boundary condition (15) becomes:

$$(2A/M_s)\boldsymbol{i}_z \times (\partial \boldsymbol{m}/\partial n) + \boldsymbol{T}_{\text{surf}} = 0. \quad (17)$$

Three special cases of this equation will now be considered.

Case I

If $\boldsymbol{T}_{\text{surf}}$ is zero, then equation (17) yields the boundary condition

$$\partial \boldsymbol{m}/\partial n = 0 \quad (18)$$

at the surface of the ferromagnet. The special result (18) was derived independently and by different methods in three places[21,12,3] and implied[13] in a fourth. However, none of these derivations is entirely satisfactory. BROWN's[21] derivation is restricted to the static case, MACDONALD's[12] is essentially a plausibility argument and AMENT and RADO's[3] is restricted to conductors. The derivation leading to equation (18) is thus more general than those mentioned.

Case II

If $\boldsymbol{T}_{\text{surf}}$ is caused by the existence of a surface anisotropy energy density K_{surf}, then the first task is to find the form of $\boldsymbol{T}_{\text{surf}}$. The simplest case occurs when the anisotropy axis is parallel to $\boldsymbol{i}_z$. Although this case is unlikely to occur in practice, it leads in a particularly simple way to a boundary condition whose consequences can be readily compared with the experimental results. Almost all other cases involve a lack of static saturation near the surface of a ferromagnet used in a resonance experiment. In the present case it is reasonable to assume that:

$$\boldsymbol{T}_{\text{surf}} = \boldsymbol{m} \times \boldsymbol{i}_z K_{\text{surf}}/M_s \quad (19)$$

represents the effect of K_{surf} on the magnetization. Substitution of equation (19) into equation (17) gives

$$2A\partial \boldsymbol{m}/\partial n - K_{\text{surf}}\boldsymbol{m} = 0 \quad (20)$$

as the boundary condition at the surface of the ferromagnet. Equation (20) contains the limiting cases

$$\boldsymbol{m} = 0, \text{ provided } 2A\partial \boldsymbol{m}/\partial n \ll K_{\text{surf}}\boldsymbol{m}, \quad (21a)$$

and

$$\partial \boldsymbol{m}/\partial n = 0, \text{ provided } 2A\partial \boldsymbol{m}/\partial n \gg K_{\text{surf}}\boldsymbol{m}. \quad (21b)$$

If the spatial variation of $\boldsymbol{m}$ is exponential, as it usually is in a resonance experiment, then equations (21) are essentially equivalent to

$$\boldsymbol{m} = 0, \text{ provided } 2Ak \ll K_{\text{surf}}, \quad (22a)$$

and

$$\partial \boldsymbol{m}/\partial n = 0, \text{ provided } 2Ak \gg K_{\text{surf}}, \quad (22b)$$

where k is an "appropriate" propagation constant. In the AMENT–RADO[3] calculation, for example, a different k belongs to each of the three waves (so that $\partial \boldsymbol{m}/\partial n$ is not proportional to $k\boldsymbol{m}$), and it turns out that either of the two smaller k values are appropriate for use in equations (22). Since the anomalous skin effect causes the spatial variation of $\boldsymbol{m}$ to be non-exponential,[4] it follows that equations (21) rather than (22) must be used whenever this effect is appreciable.

Equation (22a) was obtained independently by KITTEL[5], who considered the same physical mechanism of surface anisotropy but used an atomic rather than a continuum method in his derivation.* It seems possible that materials exist in which K_{surf} is sufficiently large to make (22a) the correct boundary condition.

Equation (22b), on the other hand, is simply a qualified restatement of equation (18), the exchange boundary condition underlying the theory[3] which we use for quantitatively interpreting the experimental results of the present paper. Although the two arguments given below do indicate that under our particular experimental conditions equation (22b) is a better approximation than equation (22a), it must be remembered that the case under discussion (anisotropy axis parallel to $\boldsymbol{i}_z$) is probably unrealistic.

The first argument is that the use of appropriate numerical values ($A = 3{\cdot}3 \times 10^{-6}$ erg/cm, $k \sim 10^5$ cm^{-1}, and $K_{\text{surf}} \sim 0{\cdot}03$ erg/cm^2) shows the strong inequality contained in (22b) to be reasonably well satisfied. However, this value of K_{surf} represents only a rough estimate for our alloy, and it is not impossible that the inequality in question is in fact violated. Our estimate of K_{surf} was obtained by inserting the values of certain magnetostriction constants measured by BOZORTH and WALKER[22] into equation (17) of NÉEL'S[20] paper. This process involves the subtraction of two terms which are three to four times larger than their difference. An actual measurement of K_{surf} does not seem to have been made so far.

The second argument in favor of equation (22b) is much stronger: this equation leads to a resonance line shape which is given by equation (3) and agrees well with experiment (see Section 6). On the other hand, equation (22a) leads to a line shape which is given by

$$\mu_{\text{equ}} = 1/[\eta - \Omega^2 + i\Omega L + 2(1+i)\epsilon] \quad (23)$$

and definitely disagrees with experiment.

Equation (23) was derived by a simple calculation based on the methods and approximations of Appendix A of reference (3). It is interesting to note that as a result of these approximations there is no dependence of μ_{equ} on the boundary condition used for m_y. In fact, we obtain equation (3) or equation (23) depending on whether we take the boundary condition at $y = 0$ to be $\partial m_x/\partial y = 0$ or $m_x = 0$. (The co-ordinates x and y are respectively parallel and perpendicular to the sample surface.) The main point of interest, however, is the fact that in equation (23) the role of exchange (contained in ϵ) is the same as if the values of g (contained in Ω) and λ (contained in L) were slightly modified. Thus the line shape perdicted by equation (23) is the same kind of circle, on a μ_2 vs. μ_1 diagram, as that predicted by the relaxation formula, i.e. the formula obtained by putting $\epsilon = 0$ in equation (3) or equation (23). It will be seen in Section 6 that a plot of the experimental μ_2 vs. μ_1 definitely deviates from a circle.

Case III

In this case we again assume that $\boldsymbol{T}_{\text{surf}}$ is caused by the existence of a surface anisotropy, as in Case II, but now we take the anisotropy axis to be perpendicular to the sample surface. The anisotropy energy per unit area may then be written in the form $K_{\text{surf}} \cos^2\psi$, where K_{surf} can have either sign and ψ denotes the angle between the magnetization and the normal to the surface. (Although the surface anisotropy depends, in addition, on the orientation of the surface with respect to the crystalline axes,[20] the expression $K_{\text{surf}} \cos^2\psi$ occurs in many situations and thus constitutes a reasonable model.) Calculation then shows that the following two conditions are sufficient to assure that the magnetization near the sample surface will still be saturated along the z-direction. The first

* The inequality (15) of KITTEL'S[5] paper is easily shown to be equivalent to the condition $2A \ll K_{\text{surf}}$ contained in equation (22a) of the present paper. However, it should be noted that KITTEL chose both the static field and the anisotropy axis to be perpendicular to the sample surface.

is that 2η be negligible compared to unity, a requirement which is essentially fulfilled because it was shown in Section 3(a) that η itself is negligible compared to unity. The second condition for saturation to be maintained is that the ratio $\beta = K_{\text{surf}}/(2\pi M_s^2 A)^{1/2}$ does not exceed unity. This requirement is also fulfilled because β is $6{\cdot}15 \times 10^{-3}$ if K_{surf}, M_s and A have the numerical values cited above. Thus it is permissable to use equation (17) rather than the more general equation (15) as the basic boundary condition. Specifically, we obtain

$$\partial m_x/\partial y = 0$$

and

$$A\partial m_y/\partial y - K_{\text{surf}} m_y = 0$$

as the boundary condition for the present case. Since it was stated under Case II that the validity of equation (3) depends on the boundary condition used for m_x but does not depend on that used for m_y, it follows that the present situation leads to the same final result, namely equation (3), as the use of the orginal boundary condition (18).

Although we find the boundary condition $\partial m_x/\partial y = 0$ to be superior to $m_x = 0$ in our experimental situation, it is worth noting that the role of $\boldsymbol{T}_{\text{surf}}$ is not settled definitely because its direction may not correspond to Cases II or III and because the magnitude of K_{surf} can only be estimated. Additional comments on this problem are given in Section 6(a).

4. SAMPLE PREPARATION AND STATIC MEASUREMENTS

The samples were made from a piece of permalloy obtained from Dr. E. A. GAUGLER while he was at the Naval Ordnance Laboratory. This permalloy was analyzed to have the following composition: 66 atomic per cent nickel, a few tenths per cent each of cobalt and manganese and the balance iron. Two rods were fabricated by melting some of the material under a helium atmosphere in high-purity alumina crucibles.

The (polycrystalline) rods were then swaged from a diameter of 0·160 to 0·125 in.; the final length of each was 8·25 in. A single crystal of this permalloy was grown from the melt by V. J. FOLEN of this Laboratory. This rod, 4·25 in. in length, was centerless ground to a diameter of 0·125 in. and then etched deeply. Mechanical polishing of the specimens was done on a lathe. Paper buffed down with stearic acid was used in diminishing degrees of coarseness, the last being type 3/0. Final mechanical polishing was carried out with "Linde A" abrasive powder, followed by "Linde B", used in a paste of water and aerosol. To produce strain-free, unscratched surfaces, the samples were electropolished. A bath of 90 per cent orthophosphoric acid, 10 per cent chromic acid was used at room temperature. The specimen, held in a vertical position, was placed along the central axis of a 1·5-in.-diameter cylindrical nickel cathode. The polishing was done at a current density of about 15 A/in^2, usually for a period of 30–60 sec. Although scratch-free polished surfaces do result from this treatment, it was observed that the surfaces so obtained are wavy in texture. the waves having amplitudes and spacings about 0·001 cm in magnitude. The permeabilities measured after such treatment changed somewhat after each polishing. It was found that if a specimen were rotated at a high speed (about 1800 rev/min) during electropolishing, extremely smooth surfaces were obtained, and the permeabilities measured were reproducible from one polishing to the next. An electron-diffraction analysis of the surface of a permalloy test specimen was carried out by Dr. J. KARLE of this Laboratory. The surface of this test specimen had been prepared in the same manner as those of the other samples. The analysis indicated that the metal surface is covered by a layer of undetermined composition whose thickness is < 20Å.

The samples were annealed at 1200° C to relieve strains induced during cold working and then given an ordering anneal to produce an extremely small magnetocrystalline anisotropy. This latter anneal consists of cooling the samples at the rate of 60° C/hr from 600 to 300° C. Both heat treatments were carried out in a pure dry hydrogen atmosphere. (The purification of the hydrogen was accomplished by means of an activated charcoal trap to remove organic vapors, a palladium catalyst to promote the combination of any oxygen present with hydrogen to form water vapor and a drying agent to remove this water vapor.) Subsequent to the heat treatments the samples were again electropolished by means of the "rotation method" described above.

The results of certain static measurements performed on the samples are listed in Table 1.

Table 1. *Results of static measurements*

Temperature (°K)	$4\pi M_s$ $\times 10^{-4}$ (emu)	$\lvert K_1 \rvert$ $\times 10^{-3}$ (erg/cm^3)	Sign of K_1	$1/\sigma$ $\times 10^6$ (Ω cm)
302	1·345	$< 0{\cdot}6$	negative	18·25
77	1·406	< 1	unknown	6·47

The saturation magnetization, M_s, was measured ballistically by means of a pick-up coil which was wound directly on one of the sample rods and later removed for the microwave experiments. It was found that at room temperature the value of the magnetization, M, is within 1 per cent of M_s at an internal field of 10 Oe. At liquid-nitrogen temperature the values of M were found to be within 1 per cent of M_s at all fields used in the resonance experiments. The demagnetizing field was calculated from equation (2, 23) of STÄBLEIN and SCHLECHTWEG[23]. Its value is about 5 Oe for the static field at which the 3000 Mc/s resonance occurs in the polycrystalline (8·25 in.) rods. The corresponding value for the shorter (4·25 in.) single-crystal rod is roughly 26 Oe; this latter value is inaccurate and was not used for g-factor calculations.

Limiting values of the first-order magnetocrystalline anisotropy constant, K_1, were measured by V. J. FOLEN of this Laboratory by means of a torque method on single-crystal disks having the same composition and heat treatment as the samples used in the resonance experiments. The results (Table 1) are consistent with those of BOZORTH and WALKER[22]. From Table 1 it is found that the anisotropy field, which is $4\lvert K_1 \rvert/3M_s$ when K_1 is negative, definitely does not exceed 0·75 Oe at 302° K. This value is negligible in comparison to the line width and the resonance field of the microwave experiment. Although neither the second-order anisotropy constant nor the magnetostriction has been measured on our samples, published data[22] indicate that these additional contributions to the effective field are also negligible.

The static resistivity was measured on the actual rod samples employed in the microwave experiments. Currents of 3–5 A parallel to the rod axis (i.e parallel to the static field) were used, and effects arising from contact potential were eliminated by reversing the current. Since the measured resistivities varied over a range of about 3 per cent, only average values (referring to sample b) are listed in Table 1. Some values of magnetoresistance have already been mentioned (Section 3(a)).

5. MICROWAVE MEASUREMENT METHOD

(a) *Principles*

The two components of the complex equivalent permeability, $\mu_{equ} = \mu_1 - i\mu_2$, were measured by an improved and modified version of the method of JOHNSON and RADO[24]. This method had been used for the first simultaneous measurement of μ_1 and μ_2 in a ferromagnetic metal.[25] In the present work, the ferromagnetic speciment is again a cylindrical rod which constitutes the inner conductor of a half-wave coaxial cavity resonator operating in a slightly perturbed TEM mode. The cavity is shown in Fig. 1. To prevent the high microwave permeability of the specimen from causing an inconveniently large decrease in the quality factor, Q, of the resonator, all but a short section of the specimen is covered by a thin gold foil. The thickness of this foil ($\approx 10^{-3}$ in.) is large compared to the skin depth, but it is

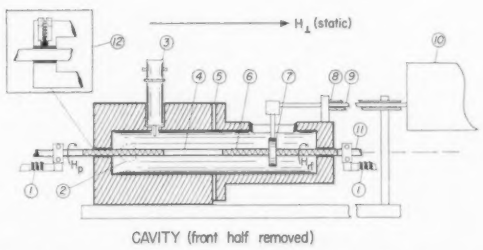

FIG. 1. Resonant cavity, drawn approximately to scale. (1) Gold foil pulse leads; (2), (3) microwave probes; (4) exposed section of permalloy rod; (5) mica insulator; (6) gold foil overlay; (7) polystyrene tuning bead; (8) fixed glass tube; (9) movable glass rod; (10) travelling microscope drive; (11) permalloy rod (electropolished); (12) detail of permalloy rod-to-cavity contact (same at each end of the cavity). The symbols $H_\perp$ (static), H_p and H_{rf} denote, respectively, the static solenoid field, the pulsed field and the microwave magnetic field. The inside length of the cavity is about half the free-space wavelength and its inside diameter is 0·500 in. The permalloy rod, whose diameter is within a few percent of 0·117 in., is covered by a gold foil of $(1{\cdot}1 \pm 0{\cdot}1) \times 10^{-3}$ in. thickness.

sufficiently small to cause only a negligible step-discontinuity in the cross-section of the inner conductor. As in the earlier work, a transmission cavity is used, the tuning is accomplished by means of a movable dielectric bead, and a pulsed field parallel to the microwave field is provided for reducing μ_{equ} to unity in the course of the experiment. The basic modification of the earlier apparatus is the addition of a solenoid to produce a static magnetic field which is parallel to the rod axis and thus perpendicular to the microwave field. When corrected for demagnetization, this static field furnishes the H_z for the resonance experiment. Additional modifications of the apparatus and some experimental details will be mentioned later on.

The directly measured quantities are certain frequency shifts and Q-values corresponding to a given H_z. From these quantities we compute μ_1 and μ_2 by using the appropriate formulas derived in reference (24). These formulas are rederived below. The present derivation is not only briefer than the earlier one, but it is also capable of being extended to the case of a cavity which has a discontinuity in its cross-section. This extension is outlined in the Appendix.

We start with SLATER's[26] general treatment of cavity resonators by the method of orthogonal functions. Simple modifications of his equation (III. 57) lead to:

$$\frac{1}{2Q}-i\frac{\Delta\omega}{\omega}=(1+i)\frac{\int_S(\mu_{\text{equ}}^{\frac{1}{2}}\delta/4)\boldsymbol{h}\cdot\boldsymbol{h}_0\,dS}{\int_V \boldsymbol{h}\cdot\boldsymbol{h}_0\,dV} \tag{24}$$

for an unloaded cavity oscillating at a circular frequency, ω, which is near to the resonance frequency of a particular normal mode. Here $\boldsymbol{h}_0$ is the microwave field of this normal mode, $\boldsymbol{h}$ is the total microwave field, and V and S are the volume and interior surface of the cavity, respectively. The quantity $\Delta\omega$ is the amount by which the circular frequency of the actual cavity exceeds that of a similar cavity having ideal walls. The parameters μ_{equ} and δ, which refer to the cavity walls, have already been defined.

We now apply equation (24) to a hypothetical cavity whose walls consist partly of perfect conductors and partly of a ferromagnetic metal, F, which is exposed to a static field H_z perpendicular to the microwave field. Denoting H_z by H, we obtain

$$(1/2Q)_{F,H}-i(\Delta\omega/\omega)_{F,H}=(1+i)\mu_{\text{equ}}^{1/2}R, \tag{25}$$

where R is an abbreviation for the dimensionless ratio

$$R=(\delta/4)\int_F \boldsymbol{h}\cdot\boldsymbol{h}_0\,dS\Big/\int_V \boldsymbol{h}\cdot\boldsymbol{h}_0\,dV. \tag{26}$$

The quantities δ and μ_{equ} occurring in equations (25) and (26) refer to the properties of F. Simple manipulation of equation (25) yields

$$\mu_1=-\frac{(1/2Q)_{F,H}(\Delta\omega/\omega)_{F,H}}{R^2}, \tag{27a}$$

$$\mu_2=\frac{(1/2Q)^2_{F,H}-(\Delta\omega/\omega)^2_{F,H}}{2R^2}. \tag{27b}$$

The next step consists in expressing $(1/2Q)_{F,H}$ and $(\Delta\omega/\omega)_{F,H}$ in terms of measurable quantities. For an actual cavity, denoted by C, we have the relation

$$(1/2Q)_C=(1/2Q)_F+(1/2Q)_N, \tag{28}$$

where N denotes the nonferromagnetic (but imperfectly conducting) part of the cavity walls. Equation (28) applies when the cavity is exposed to H_z and also when it is exposed to a saturating (pulsed) field P which is parallel to the microwave field. Subtraction of the resulting equations gives:

$$(1/2Q)_{F,H}-R=(1/2Q)_{C,H}-(1/2Q)_{C,P}, \tag{29a}$$

where the obvious condition $(1/2Q)_{N,H}=(1/2Q)_{N,P}$ was used, and the quantity $(1/2Q)_{F,P}$ (which corresponds to F being characterized by $\mu_{\text{equ}}=1$) was replaced by R, as required by an application of equation (24). In an analogous manner we obtain:

$$(\Delta\omega/\omega)_{F,H}+R=(\Delta\omega/\omega)_{C,H}-(\Delta\omega/\omega)_{C,P}, \tag{29b}$$

where $(-\Delta\omega/\omega)_{F,P}$ was replaced by R. The quantities appearing on the right-hand sides of equations (29) have been measured directly by methods to be discussed below. Since R can be calculated, the use of equations (29) in equations

(27) furnishes the experimental values of μ_1 and μ_2.

In calculating R by means of equation (26), we must remember that the perturbation method underlying equation (24) permits us to proceed as if the fields $\boldsymbol{h}$ and $\boldsymbol{h}_0$ referred to a cavity with ideal walls. Furthermore, we ignore the existence of the discontinuity caused by the gold foil. Experimental checks as well as the calculation outlined in the Appendix show that this approximation is justified in our cavity. Thus the effect of higher modes is negligible and $\boldsymbol{h}$ may be replaced by $\boldsymbol{h}_0$. The cavity operates in the TEM mode and its length is $\lambda_0/2$, half of the free-space wavelength. Using cylindrical coördinates r, θ, z, and omitting a constant factor, we have:

$$h_0 = h_\theta = (1/r)\cos k_0 z, \tag{30}$$

so that after some elementary integrations equation (26) yields

$$R = \left(\frac{k_0 L_s + \cos 2k_0 L_e \sin k_0 L_s}{\pi}\right)\left(\frac{\delta}{4a \ln b/a}\right), \tag{31}$$

where the first factor on the right-hand side will be denoted by f. Here k_0 is $2\pi/\lambda_0$, and a and b are the radii of the inner and outer conductor, respectively. The length of that section of the ferromagnetic sample which is not covered by the gold is denoted by L_s and the distance from the center of this section to either end of the cavity by L_e. Equation (31) involves the static conductivity through the quantity δ, the skin depth for permeability unity. Thus the eddy-current losses existing in the absence of microwave magnetization are essentially calculated rather than measured. Equations (27), (29) and (31) are in full agreement with the corresponding results of reference (24), even though in the earlier work μ_1 and μ_2 were derived via the attenuation and phase velocity of TEM waves perturbed by the cavity walls. This agreement is due to the equivalence of the basic approximations used in the two treatments, and it is a reflection of the fact that basically μ_1 and μ_2 are determined by the two components of the complex surface impedance. We note that the quantities $(1/2Q)_{F,H}$, $(-\Delta\omega/\omega)_{F,H}$, and R of the present paper correspond, respectively, to $\gamma\alpha_H$, $\gamma\beta_H$ and $\gamma\alpha_\infty(=\gamma\beta_\infty)$ of reference (24).

(b) *Procedures*

The input to the cavity is coupled to a stable microwave source and the output to a superheterodyne receiver. Both of these couplings are so loose (the cavity corresponds to an insertion loss of about 55 db) that the measured Q's may be regarded as unloaded Q's. The microwave source consists of a crystal-controlled oscillator, tunable over a small frequency range, whose output is fed to a system of overdriven tuned amplifiers which act as frequency multipliers. Crystals oscillating at 99·6, 99·8, 100·0, 100·2 and 100·4 kc/s are used. The oscillator frequency is continuously monitored by comparing it on an oscilloscope with the frequency of a standard signal broadcast by Station WWV. During the course of a Q-measurement, the frequency varies by less than one part in 10^6. The power output of the microwave source, in the 3000 as well as in the 4000 Mc/s region, is roughly 50 mW at each of five frequencies separated by 0·2 per cent. The frequency stability of this source is the same as that of the crystal oscillator, and its voltage stability is about 0·2 per cent for a period of several minutes.

All permeability determinations are carried out at a constant frequency of either 3000·00 or 4000·00 Mc/s. The measurements of changes in frequency required throughout the experiment are replaced by measurements of changes in resonant wavelength. The latter involve a movable dielectric bead, made of polystyrene, which is connected by means of a glass rod to a Gaertner travelling microscope drive. Use of the five stable frequencies permits us to obtain a calibration curve of dielectric bead position vs. cavity resonance frequency. The thickness and mean position of the bead are chosen in such a way that the calibration curve is practically linear over a limited but adequate range. A typical value of the calibration constant in the 3000 Mc/s experiment is about 0·022 dial divisions (on the indicator of the microscope drive) per kilocycle of frequency change. One dial division corresponds to a bead displacement of 10^{-3} cm. The motion of the bead is sufficiently smooth to allow a precision of 0·5 dial division in the measurement of the center of a cavity resonance curve. In contrast, the largest unidirectional frequency shift which occurs in the magnetic resonance (corresponding to a change in μ_1 from zero to its most negative value) amounts

to about 60 dial divisions if a representative f-valve is used.

The rectified output of the superheterodyne receiver can be connnected either to a d.c. microammeter or to a single-pulse voltmeter[27] specially developed for such experiments. In the former case, we measure the cavity transmission vs. bead position and obtain $(1/2Q)_{C,H}$ in a straightforward way. In the latter case, we measure the dependence on bead position of another quantity, namely, the ratio of the cavity transmission in the state P to the cavity transmission in a state H. By using the "straight-line method" described earlier,[24] we then deduce from these measurements the ratio $Q_{C,H}/Q_{C,P}$ and the difference $(\Delta\omega)_{C,H}-(\Delta\omega)_{C,P}$. Since the right-hand sides of equations (29) are now determined, the experimental values of μ_1 and μ_2 can be evaluated. In practice, however, another complication exists. Unless H_z is zero or very small, the pulsed field (which is around 500 or 1000 Oe) is insufficient to reduce μ_{equ} to unity. Furthermore, the single-pulse measurements are inherently slow and it is difficult to perform them accurately. Both of these objections are overcome by using the pulse method solely for measuring $(1/2Q)_{F,0}$ and $(\Delta\omega/\omega)_{F,0}$ via equations (29). These two quantities are then used in equations (27) to derive the μ_1 and μ_2 corresponding to the state $H_z=0$. To obtain the μ_1 and μ_2 corresponding to some other value of H_z, we substitute $(1/2Q)_{F,0}$ and $(\Delta\omega/\omega)_{F,0}$ into the simple difference equations:

$$(1/2Q)_{F,H}-(1/2Q)_{F,0}=(1/2Q)_{C,H}-(1/2Q)_{C,0}, \tag{32a}$$

$$(\Delta\omega/\omega)_{F,H}-(\Delta\omega/\omega)_{F,0}=(\Delta\omega/\omega)_{C,H}-(\Delta\omega/\omega)_{C,0}, \tag{32b}$$

whose right-hand sides can be measured without pulsing. The values of $(1/2Q)_{F,H}$ and $(\Delta\omega/\omega)_{F,H}$ furnished by equations (32) are then used in equations (27).

We now turn to a discussion of the f-factor defined in connection with equation (31). It is important that the values of L_s and L_e be chosen properly. L_s must be sufficiently large to minimize end effects due to the gold foil and sufficiently small to keep the cavity Q reasonably high. L_e, on the other hand, must be sufficiently large to fulfill the latter requirement, and it must be sufficiently small to prevent interactions between the perturbations caused by the gold foil and the dielectric bead. Both L_s and L_e were determined by means of a travelling microscope. In the 3000 Mc/s experiment, where the length of the cavity is ~ 5 cm, complete curves of μ_1 and μ_2 vs. H_z were measured with f-values ranging from $f=0{\cdot}0633$ corresponding to $L_s=1{\cdot}339$ cm and $L_e=2{\cdot}077$ cm, to $f=0{\cdot}1009$, corresponding to $L_s=1{\cdot}302$ cm and $L_e=1{\cdot}851$ cm. The fact that all the curves agreed within experimental error constitutes a verification of the expression for f contained in equation (31). At 3000 Mc/s and room temperature, and with a representative value of $f=0{\cdot}0749$, $Q_{C,0}$ is 513 and $Q_{C,H}$ at the magnetic resonance is $\sim 2{\cdot}6$ times smaller.

A few experimental details will now be mentioned. The gold foil used to cover part of the sample had previously been annealed at 800° C because it was found necessary that the gold be very soft and adhere closely to the sample rod. The uncovered section of the rod was located in its center in order that the demagnetizing field contributing to H_z be as uniform as possible. Duco cement thinned in acetone was used to secure the overlap of the gold foil. The quality of the contact between the gold and the uncovered permalloy section was improved by means of a ring-shaped layer of silver paint. It was found that the existence of gaps at this joint causes large changes in the measured frequency shifts. Although a few experiments indicated that even a gold thickness of 0·003 in. allows us to neglect the effects of the step in the inner conductor, all the final data were taken with a 0·001-in. gold covering.

At 3000 Mc/s the experimental results were reproduced in two different brass cavities and in one gold-plated cavity. Several methods were used for making a good but strain-free contact between the inner conductor and the end plates of the cavity. One method employed soft gold shims. Another method, which proved invaluable in the liquid-nitrogen-temperature experiments, involved the use of appropriate spring contacts to allow for a longitudinal and radial differential thermal expansion between the cavity and the permalloy rod (see Fig. 1). It was found that good electrical contact is maintained when the force necessary to slide the rod with respect to the cavity

is considerably less than 2 lb. This upper limit represents a pressure of 0·2 kg/mm², from which we obtain (by using the known magnetostriction constant) an equivalent field of ~ 1 Oe. The pulsing leads as well as the potential leads for the resistivity measurements are attached to the sample (outside the cavity) with spring mechanisms to prevent straining. A similar cavity was used at 4000 Mc/s.

By changing the signal power over a range of 12 db, it was found at both 300 and 77° K that the cavity resonance frequencies (and hence the values of μ_{equ}) are independent of the microwave amplitude. When a brass rod was inserted into the cavity, neither a solenoid field (up to ~ 150 Oe) nor a pulsed field caused observable effects.

The following modifications were made to adapt the apparatus to liquid-nitrogen-temperature experiments. Soldered underneath the base plate of the cavity was a continuous circuit of wave-guide through which liquid nitrogen flowed constantly during the measurements. The cavity, the rod and the base plate (but not the microscope drive) were covered by a double-walled shield which was filled with liquid nitrogen. A foam polystyrene shield was used to enclose the whole ensemble, and all holes were plugged up with fibreglass. The air space thus enclosed was filled with helium gas which was kept at liquid-nitrogen temperature and at a constant flow rate. The helium gas helped to establish and maintain good thermal equilibrium, prevented freeze-up and offered the additional advantage of having a dielectric constant which does not vary as rapidly with temperature as that of air. Frequent measurements of the static resistivity indicated an essentially constant temperature. This was verified by the extreme constancy of the microwave results throughout a run. The tuning arrangement worked as well at 77 as at 300° K, and the closeness of the thermal expansion coefficients of gold and permalloy in this range insured that the gold foil was neither detached from the sample nor strained. At both frequencies the 300° K curves were remeasured after the sample had been exposed to 77° K. No evidence of thermal hysteresis was found.

6. EXPERIMENTAL RESULTS AND DISCUSSION

(a) *Room temperature*

Fig. 2 shows the measured values of μ_1 and μ_2 as a function of H_z at 3000 Mc/s. Theoretical curves, based on equation (3), are also shown. The parameters $A = 2{\cdot}88 \times 10^{-6}$ erg/cm, $g = 2{\cdot}07$, $\lambda = 0$ and the static room-temperature resistivity were used in fitting the theoretical curves to the experimental data by means of the method described in reference (3). Only two unknown parameters (A and g) are involved, because the static resistivity is directly measured. It is seen that at resonance μ_2 is large and H_z relatively small, in agreement with the qualitative requirements (see Section 2) for observations of exchange effects. In addition, the quantitative agreement between experiment and theory is seen to be good. This includes the characteristic asymmetries of the "exchange only" curves, as well as the observation and prediction of negative values of μ_2. It should be emphasized that in the presence of exchange effects a negative μ_2 does not violate the second law of thermodynamics. The reason[28] is that in this case μ_{equ} does not describe a point relation (such as a tensor) connecting the microwave flux density with the microwave field. In fact, μ_{equ} is merely a measure of the complex surface impedance, and μ_2 can have either sign.

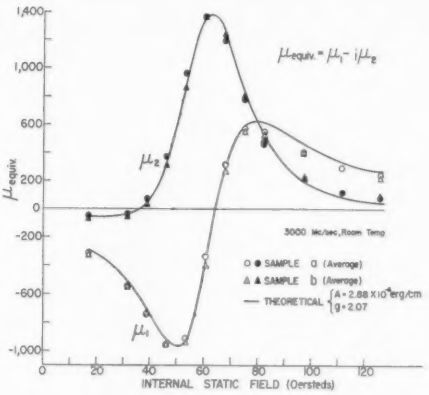

FIG. 2. Measured and calculated values of $\mu_{\text{equ}} = \mu_1 - i\mu_2$ at room temperature, 3000 Mc/s. Data for samples *a* and *b* are shown. The theoretical curves are calculated from equation (3) by using $A = 2{\cdot}88 \times 10^{-6}$ erg/cm, $g = 2{\cdot}07$, $\lambda = 0$ and the static room-temperature resistivity.

In Fig. 3 we show curves of μ_2 vs. μ_1 with H_z as a parameter. The value of H_z increases from zero to infinity in a clockwise direction along each

of the curves. Experimental data taken on a single crystal are compared with the data used in Fig. 2, which pertain to two polycrystalline samples. The agreement is seen to be very good. Although this was expected in view of the very low magnetocrystalline anisotropy of our alloy, it is interesting

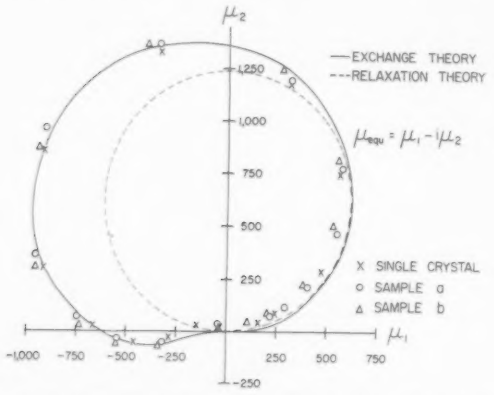

FIG. 3. Measured and calculated values of $\mu_{equ} = \mu_1 - i\mu_2$ at room temperature, 3000 Mc/s. Data for samples *a* and *b* for the single crystal are shown. The solid curve (exchange only) is calculated on the basis of equation (3) by using $A = 2{\cdot}88 \times 10^{-6}$ erg/cm, $\lambda = 0$, and the static room-temperature resistivity; the value of g is 2·07. The dashed curve (relaxation only) is calculated on the basis of equation (3) by using $\lambda = 5{\cdot}01 \times 10^8$ sec^{-1}, $g = 2{\cdot}30$ and $A = 0$.

to find that grain boundary effects can definitely be excluded. The "egg-shaped" curve (solid line) is an "exchange only" theoretical curve based on the same parameters as the theoretical curve of Fig. 2. The dashed curve, on the other hand, is a "relaxation only" theoretical curve based on equation (3) and the parameters $\lambda = 5{\cdot}01 \times 10^8$ sec^{-1}, $g = 2{\cdot}30$ and $A = 0$. It is seen that the exchange curve agrees with the experimental results, whereas the relaxation curve does not agree. Other relaxation curves, based on different values of λ and g, are equally unsatisfactory. This follows from the easily demonstrated fact that the relaxation curve is necessarily a circle which has its center on the μ_2 axis and which is tangent to the μ_1 axis at the origin. Furthermore, an interpretation based on "relaxation only" yields the unreasonably large g-value of 2·30. This value disagrees not only with the prediction of equation (2) but also with the direct measurement of $g = 2{\cdot}12$ which we performed on a thin disk of our alloy at about 24000 Mc/s, a frequency where the exchange effects in this material are small. The measured value[29] of g' for an alloy having a composition similar to that of our samples is around 1·90, so that the value of $g = 2{\cdot}07$ obtained on the basis of the exchange interpretation is consistent with equation (2). It should also be noted that an interpretation based on "exchange plus relaxation" would be less satisfactory than the "exchange only" interpretation. The reason is that a situation in which neither A nor λ vanishes gives rise to some curve intermediate between the solid curve and the dashed curve of Fig. 3. Finally, we recall that the arguments given in Section 3(a) eliminate some other kinds of relaxation effects also.

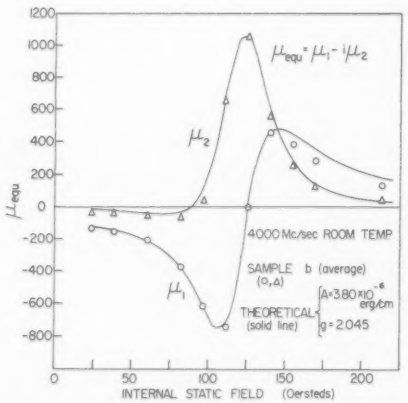

FIG. 4. Measured and calculated values of $\mu_{equ} = \mu_1 - i\mu_2$ at room temperature, 4000 Mc/s. Data for sample *b* are shown. The theoretical curves are calculated from equation (3) by using $A = 3{\cdot}80 \times 10^{-6}$ erg/cm, $g = 2{\cdot}045$, $\lambda = 0$ and the static room-temperature resistivity.

We now turn to the 4000 Mc/s results. Experimental data and a theoretical curve analogous to those of Fig. 2 are shown in Fig. 4. Again there is good quantitative agreement between experiment and the "exchange only" theory. However, the parameters $A = 3{\cdot}80 \times 10^{-6}$ erg/cm and $g = 2{\cdot}045$ required to fit the 4000 Mc/s curves are somewhat different from the corresponding values obtained at 3000 Mc/s. In the case of A, at least, the difference (amounting to roughly 30 per cent) might well be significant. An explanation of this difference is not yet available. On the other hand, the

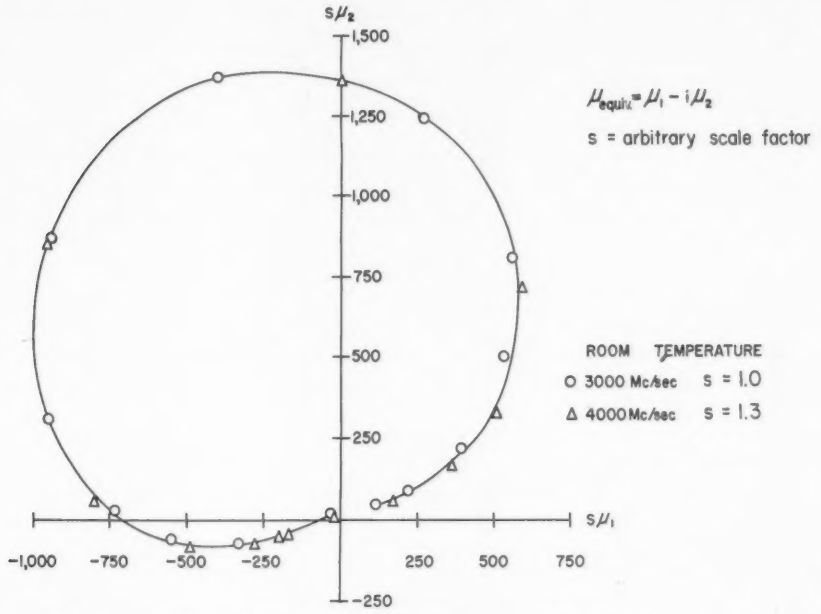

FIG. 5. Measured values of $\mu_{equ} = \mu_1 - i\mu_2$ at room temperature, 3000 and 4000 Mc/s for sample *b*.

line shapes observed at the two frequencies are in good agreement, as shown in Fig. 5, so that an important prediction of the exchange theory[3] is verified. The value of the arbitrary scale factor, *s*, appearing in Fig. 5 was chosen to be unity at 3000 Mc/s. If the values of A measured at the two frequencies were the same, then the value of *s* at 4000 Mc/s would be $(4/3)^{\frac{1}{2}} = 1{\cdot}15$ rather than 1·3. This means that the theory needs to be refined unless an unsuspected systematic error of 15 per cent can be uncovered in the permeability measurements.

By averaging the values of A and g deduced from the experimental data at the two frequencies, we obtain the "measured" results:

$$A = (3{\cdot}3 \pm 0{\cdot}5) \times 10^{-6} \text{ erg/cm}, \qquad (33a)$$

$$g = 2{\cdot}06 \pm 0{\cdot}01, \qquad (33b)$$

at room temperature. The g-value was discussed above, and the A-value will now be compared with values obtained by other methods.

KONDORSKIY and FEDOTOV[30] made measurements of the approach to absolute saturation at low temperatures in an alloy of composition similar to that used in our experiments. On the basis of the BLOCH $T^{\frac{3}{2}}$-law, one may deduce from their data values for A of $1{\cdot}0 \times 10^{-6}$ and $0{\cdot}81 \times 10^{-6}$ erg/cm, depending on the thermal history of their samples.

Soon after our first experiments, BEAN[31] derived an A-value for 65 Permalloy from his measurements of the surface energy of a collapsing domain wall. His result is $A = (1{\cdot}0 \pm 0{\cdot}2) \times 10^{-6}$ erg/cm at room temperature.

We now consider six possible explanations for the factor-of-three "discrepancy" between our A-value and the A-values obtained by the two other methods.

(1) The interaction of spin waves and elastic waves, a mechanism discussed by SIMON[32] and by KITTEL[33] in related problems, might conceivably play a role in spin-wave resonance. Preliminary calculations based on the simplifying assumption of elastic isotropy show, however, that the effects of this interaction are negligible under the conditions of our experiment.

(2) Contributions to the line width arising from two mechanisms of the "non-exchange" type can probably be ruled out. One such mechanism is pure relaxation broadening, including broadening

due to processes whose mathematical form differs from the LANDAU–LIFSHITZ or BLOCH expression, and the other is broadening due to lack of technical saturation. Neither of these mechanisms can produce the observed negative values of μ_2, and static measurements (see Section 4) have shown that our samples are technically saturated in the resonance fields used. Moreover, the existence of appreciable local fields is improbable because there is agreement between the line shapes at 3000 and 4000 Mc/s (Fig. 5) where the resonance fields differ by a factor of two.

(3) It is well known that a calculation of A from first principles is not available for any material, and that the basic theory of spin waves[34] is subject to numerous limitations. However, A can be defined operationally in terms of the coefficient of $\boldsymbol{M}\times\nabla^2\boldsymbol{M}$ in equation (1), and this definition does not require a detailed knowledge of the exchange effect. The results of RODBELL[14] show, moreover, that the value of A derived from resonance measurements on selected iron whiskers bounded by (100) crystallographic planes (where, according to NÉEL[20], the surface anisotropy vanishes) is consistent with that derived from previous $T^{\frac{1}{2}}$-law measurements on polycrystalline bulk iron. Thus it is unlikely that these two methods should yield different A-values as long as complicating effects of the kind discussed under (4), (5) and (6) are negligible.

(4) It is not inconceivable that in some materials there are additional exchange-dependent energy losses whose effect on the resonance curve could be described by assigning a larger (and possibly frequency-dependent) value to the "effective A". One possible source of such losses might be the incompleteness of the atomic order in our alloy. However, this particular possibility is not very promising, because it seems to require that the atomic distribution possesses Fourier components whose wavelengths are not negligible compared to the skin depth.

(5) Another source of exchange-dependent energy loss may arise as follows. Let us suppose that the actual value of the surface anisotropy is very much (at least 163 times) larger than the estimated value obtained in Section 3(b) on the basis of the phenomenological NÉEL theory. In that case β will exceed unity and the magnetization near the sample surface will not be saturated. Specifically, a calculation of the type mentioned under Section 3(b), Case III, shows that a static magnetic structure similar to that in a domain wall should exist near the surface. It is planned to extend this calculation to the dynamic case in order to determine whether the non-alignment of the magnetization is capable of producing additional eddy-current losses which may be described, at least for a limited range of the relevant parameters, by choosing a larger value for the effective A. Similar remarks apply to situations in which the direction of $\boldsymbol{T}_{\text{surf}}$ does not correspond to Cases II and III of Section (3b). Such situations may also give rise to a lack of magnetic saturation near the sample surface, even if K_{surf} is not unexpectedly large.

(6) Finally, we recall that the surface of the metal samples is covered by a layer of undetermined composition whose thickness is < 20 Å (see Section 4). Future experiments may make it possible to eliminate this layer or to determine whether it is caused primarily by the action of the atmosphere or of the electropolishing. Although it is not feasible, at present, to decide whether this layer can give rise to an increased effective A, it seems reasonable to simulate the role of this layer theoretically by using a larger value for the surface anisotropy. In this case the extended calculation mentioned under item (5) may clarify the nature of the effects caused by the surface layer. Additional experiments, involving single crystals with specific exposed faces, are also being considered.

We summarize this discussion by noting that the factor-of-three discrepancy between the A-values is probably not caused by the effects described under (1), (2) and (3). As to possibility (4), it appears to be unlikely but has not been eliminated. The most promising explanations seem to be (5) and (6), and these are now being investigated.

(b) *Liquid-nitrogen temperature*

In Fig. 6 we compare the 77° K results with those obtained at 300° K. Experimental data taken at 3000 Mc/s are shown along with appropriate theoretical predictions. Curves 1 and 1′, which are included for comparison, present the measured and calculated room-temperature permeabilities previously given in Fig. 2. The liquid-nitrogen-temperature results are shown in the experimental curves 2 and 2′ and in the theoretical curves 3 and

3′. Since the temperature-dependence of g and A is not known theoretically, curves 3 and 3′ are based on the reasonable assumption that g as well as the ratio A/M_s^2 has the same value at 77 as at 300° K. As for the static resistivity, the value measured at 77° K was used for calculating curves 3 and 3′ of Fig. 6. The ratio of the scale factors assigned to the calculated curve at 3000 and 4000 Mc/s is 1·33 rather than the theoretically predicted $(4/3)^{\frac{1}{2}} = 1{\cdot}15$. This deviation is due to the apparent frequency-dependence of A at 300° K. It is seen from Fig. 7 that the discrepancy

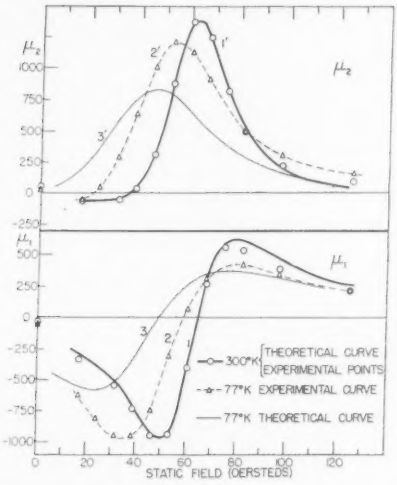

FIG. 6. Measured and calculated values of $\mu_{equ} = \mu_1 - i\mu_2$ at 3000 Mc/s for sample *b*. Curves 1 and 1′ are theoretical curves calculated from equation (3) by using $A = 2{\cdot}88 \times 10^{-6}$ erg/cm, $g = 2{\cdot}07$, $\lambda = 0$ and the static room temperature resistivity; the experimental points at room temperature are also shown. Curves 2 and 2′ are the observed resonance curves at liquid-nitrogen temperature, and 3 and 3′ the theoretical curves expected at this temperature on the basis of the static liquid-nitrogen-temperature resistivity and the same A/M_s^2 and g as those used for curves 1 and 1′.

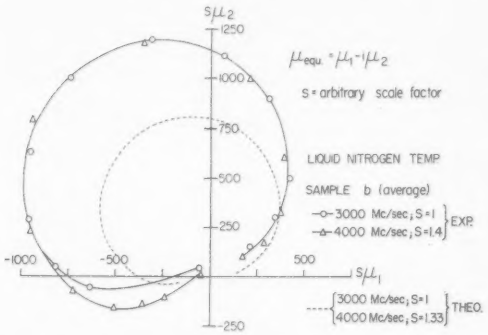

FIG. 7. Measured and calculated values of $\mu_{equ} = \mu_1 - i\mu_2$ at liquid-nitrogen temperature, 3000 and 4000 Mc/s for sample *b*. The dashed curve is calculated on the basis of equation (3) by using $\lambda = 0$, the liquid-nitrogen-temperature resistivity, and an A/M_s^2 corresponding to the room temperature value of M_s and to $A = 2{\cdot}88 \times 10^{-6}$ erg/cm for 3000 Mc/s and $A = 3{\cdot}80 \times 10^{-6}$ erg/cm for 4000 Mc/s. Because of the apparent variation of A with frequency, the ratio of the scale factor, s, at the two frequencies had to be chosen as 1·33 in order to make the two theoretical curves coincide; theory predicts that this ratio be $(4/3)^{1/2} = 1{\cdot}15$.

3 and 3′ by means of equation (3). The theory predicts that as the temperature is lowered the exchange broadening of the resonance line increases and the resonance field decreases. Both effects have been observed qualitatively (Fig. 6), but neither is as large as would be expected theoretically. It should also be noted that the negative values of μ_2 predicted by the exchange theory have been observed at 77 as well as at 300° K.

The frequency-dependence of the 77° K resonance line shapes is shown by the solid curves of Fig. 7. As explained in the caption, the dashed curve is calculated on the basis of equation (3) by using assumptions analogous to those involved in between theory and experiment at 77° K is about the same at 4000 as at 3000 Mc/s. Since the experimental line shape (at both frequencies) is even more asymmetric than the theoretical "exchange only" line shape, the explanation of this discrepancy cannot be based on the usual relaxation effects which yield a symmetrical resonance line. The discussion given in Section 3(a) indicates, on the other hand, that a part of this discrepancy can be attributed to certain anomalous effects[4] caused by the electronic mean free path at low temperatures. However, a quantitative determination of A is not yet feasible at 77° K.

Acknowledgements—We wish to thank W. S. AMENT for many useful discussions, V. J. FOLEN for growing the single crystal and measuring its anisotropy, and M. MALOOF for invaluable assistance with the electronic instrumentation.

APPENDIX

We outline a method of calculation which permits the derivation of μ_1 and μ_2 from measurements of Q's and frequency shifts performed with a cavity whose cross-section contains geometrical discontinuities. Although we are concerned with the special problem of a gold foil which partially covers the ferromagnetic inner conductor of a coaxial cavity, the general method is applicable to other problems and other geometries. No calculations of this kind appear to have been published, and it seems likely that other experimental situations will arise (especially in connection with single crystals) where geometrical discontinuities are difficult to avoid.

The basic point is the known fact that the conductivity and permeability of the metallic walls of a microwave cavity can almost always be regarded as producing merely a perturbation of the fields which would exist if the walls were perfect conductors. Thus equations (24), (25) and (26) are usually applicable, and the effect of a geometrical discontinuity in the cross-section of the cavity appears solely in the value of R. In our particular problem the discontinuity caused by the gold foil is small so that it is useful to write

$$R = R_0(1+\Delta), \tag{A.1}$$

where R_0 is the value of R given by equation (31) and Δ is assumed to be a real number small compared to unity. Within this approximation, which is verified by the result of the calculation, equations (27) remain valid provided R^2 is replaced by $R_0^2(1+2\Delta)$. By using methods similar to those leading to equations (29), we then obtain:

$$\mu_1(1+2\Delta) = \mu_1^{(0)}+[(\mu_R^{(0)})^2+(\mu_L^{(0)})^2]\Delta+\Delta^2, \tag{A.2a}$$

$$\mu_2(1+2\Delta) = \mu_2^{(0)}+[(\mu_R^{(0)})^2-(\mu_L^{(0)})^2]\Delta, \tag{A.2b}$$

where $\mu_1^{(0)}$ and $\mu_2^{(0)}$ denote, respectively, the values of μ_1 and μ_2 which would be deduced from the experimental data if the existence of the geometrical discontinuity were ignored, so that equations (27), (29) and (31) could be applied. The symbols $\mu_R^{(0)}$ and $\mu_L^{(0)}$ are abbreviations for $|\mu_{\text{equ}}^{(0)}|+\mu_2^{(0)}$ and $|\mu_{\text{equ}}^{(0)}|-\mu_2^{(0)}$, respectively. Equations (A.2) make it possible to calculate μ_{equ} from $\mu_{\text{equ}}^{(0)}$ (and hence from experimental data) once Δ is known. In our experiment $|\mu_1^{(0)}|$ and $|\mu_2^{(0)}|$ are sufficiently large to permit us to rewrite equations (A.2) in the simplified form:

$$\mu_{\text{equ}} = \mu_{\text{equ}}^{(0)}(1-2\Delta), \tag{A.3}$$

which is valid throughout the resonance curve except in the immediate vicinity of the points corresponding to $\mu_1^{(0)} = 0$ and $\mu_2^{(0)} = 0$. Equation (A.3) shows that the correction due to the geometrical discontinuity amounts to a scale factor only. In view of the previously described method[3] for extracting the value of A from the measured μ_{equ} by means of equation (3), it is seen without further calculation that in the case $\lambda = 0$, which obtains in our experiments, the factor $(1-2\Delta)$ has no effect other than to cause an increase of A by the factor $(1+4\Delta)$.

The final step is the calculation of Δ. Since this is rather involved and leads to lengthy final formulas, we merely describe some of the procedures and give a numerical result. The first task is to determine the $\boldsymbol{h}$ appearing in equation (26). This $\boldsymbol{h}$ can no longer be replaced by $\boldsymbol{h}_0$, but it can be calculated by assuming that the cavity walls are perfect conductors. The cavity consists of three regions, the radius of the center conductor having the value a in the middle region and $a+\Delta a$ (where Δa is the gold foil thickness) in the two end regions; the radius of the outer conductor has the value b throughout. In each region we set up principal mode (TEM) waves propagating in both directions along the cavity axis. To satisfy the boundary conditions, it is necessary to assume higher-order (TM) waves also. Each of the two discontinuities gives rise to an infinite number of such waves decaying exponentially in both directions away from the discontinuity. We assume that the discontinuities are sufficiently far from each other and from the end plates of the cavity to permit us to calculate the effect of each discontinuity separately. The results of the calculation show that these assumptions are justified in our experimental situation. The solution of the boundary problem at an isolated discontinuity is given in a general form in Section 5(a) of the paper by WHINNERY *et al.*[35] and this solution has been adapted to the present situation. We achieve a number of simplifications by a consistent use of the approximation $\Delta a/a \ll 1$. In calculating the various wave amplitudes numerically, we find that for our values of the parameters the functions L_p and M_p appearing in Reference (35) can be approximated by the Hahn functions S_p and U_p, respectively. The available table [35] of values for $S_p(x)$ had to be extended for our purposes by computing this function for values of x close to unity. These computations were performed by Dr. B. LEPSON on the NAREC computer at this Laboratory. The values of U_p were obtained by interpolation from the tables of STRACHEY and WALLIS[36].

Having calculated $\boldsymbol{h}$ and $\boldsymbol{h}_0$, we next perform the integrations in equation (26) to obtain R. Equation (A.1) is then used to find Δ. Both $\boldsymbol{h}$ and $\boldsymbol{h}_0$ have θ-components only. The field h is given by h_0 plus a series of first-order Bessel functions, the latter consisting of linear combinations of Bessel functions of the first and second kinds. Since the boundary conditions on the inner and outer conductor cause h_0 to be orthogonal to each term in this series, h can be replaced by h_0 in the volume integral (but not in the surface integral) appearing in equation (26). A further simplification results from the fact that in each region of the cavity h_0 is given by equation (30) plus a small perturbation which is proportional to $\Delta a/[ar \ln (b/a)]$. In the volume integral the range of z-values extends over the resonant length of the cavity. This length was calculated by using the boundary conditions at the end plates and the known field h. Since h is not symmetrical with respect to the center of the

VOL 11 195

cavity if the location of the discontinuities (and hence the f-factor) is arbitrary, proper normalization of h is important. In the surface integral the range of z-values extends, of course, only over the region between the two discontinuities. Considerable simplification results from the fact that under our experimental conditions the higher-order waves, which cannot be neglected completely, are nevertheless far below cut-off.

For numerical calculations we used the following representative values of the parameters: $a = 0{\cdot}0585$ in., $b = 0{\cdot}250$ in., $\Delta a = 0{\cdot}001$ in., $\lambda_0 = 10$ cm, $L_s = 1{\cdot}285$ cm and $L_e = 1{\cdot}917$ cm. Our result is

$$2\Delta = 2{\cdot}59 \text{ per cent} \qquad \text{(A.4)}$$

which represents the algebraic sum of $+2{\cdot}64$ per cent arising from the perturbation of the principal mode and $-0{\cdot}05$ per cent arising from the higher-order modes. The latter contribution is seen to be relatively small, primarily because the higher-order waves are far below cut-off. Thus a quasi-static calculation, based on continuity of principal wave voltage and current at the discontinuities, would have been adequate in this particular case. Equations (A.4) and (A.3) show that the values of $\mu_{\text{equ}}{}^{(0)}$ deduced from experiment should be reduced by $2{\cdot}59$ per cent to obtain μ_{equ}. This correction is within the experimental error and was neglected. It should be noted, however, that in other experimental situations the largest contribution to Δ will also be due to the perturbation of the principal mode. Since this contribution is exactly proportional to $\Delta a/a$, or to some analogous fractional change in dimensions, it is seen that the discontinuity effects can easily become appreciable.

REFERENCES

1. Rado G. T. and Weertman J. R., *Phys. Rev.* **94,** 1386 (1954).
2. Weertman J. R. and Rado G. T., *J. Appl. Phys.* **29,** 328 (1958).
3. Ament W. S. and Rado G. T., *Phys. Rev.* **97,** 1558 (1955).
4. Rado G. T., *J. Appl. Phys.* **29,** 330 (1958).
5. Kittel C., *Phys. Rev.* **110,** 1295 (1958).
6. Seavey M. H., Jr. and Tannenwald P. E., *Phys. Rev. Letters* **1,** 168 (1958); *J. Appl. Phys.* **30,** 227*s* (1959).
7. Kittel C., *J. Phys. Radium* **12,** 291 (1951).
   Van Vleck J. H., *Physica, 's Grav.* **17,** 234 (1951).
   Bloembergen N., *Proc. Inst. Radio Engrs.* **44,** 1259 (1956).
8. Kittel C., *Phys. Rev.* **76,** 743 (1949).
   Van Vleck J. H., *Phys. Rev.* **78,** 266 (1950).
9. Barlow G. S. and Standley K. J., *Proc. Phys. Soc. Lond.* B**69,** 1052 (1956).
10. Mitchell A. H., *Phys. Rev.* **105,** 1439 (1957).
    Kittel C. and Mitchell A. H., *Phys. Rev.* **101,** 1611 (1956).
11. MacDonald J. R., *Proc. Phys. Soc. Lond.* A**64,** 968 (1951).
12. MacDonald J. R., Ph.D. Thesis, Oxford (1950) (unpublished).
13. Kittel C. and Herring C., *Phys. Rev.* **77,** 725 (1950).
14. Rodbell D. S., *Bull. Amer. Phys. Soc.* **2,** 128 (1957); *J. Appl. Phys.* **30,** 187S (1959).
15. MacDonald J. R., *Phys. Rev.* **103,** 280 (1956).
16. Young J. A. Jr. and Uehling E. A., *Phys. Rev.* **94,** 544 (1954).
    Bloembergen N., *Phys. Rev.* **78,** 572 (1950).
17. Reuter G. E. H. and Sondheimer E. H., *Proc. Roy. Soc. Lond.* A**195,** 336 (1948).
18. Gurevich V. L., *J. Exp. Theor. Phys.* (*U.S.S.R.*) **33,** 1497 (1957); *Soviet Phys. JETP* **6** 1155 (1958).
19. Rado G. T., *Bull. Amer. Phys. Soc.* **2,** 128 (1957).
20. Néel L., *J. Phys. Radium* **15,** 225 (1954).
21. Brown W. F. Jr., *Phys. Rev.* **58,** 736 (1940).
22. Bozorth R. M. and Walker J. G., *Phys. Rev.* **89,** 624 (1953).
23. Stäblein F. and Schlechtweg H., *Z. Phys.* **95,** 630 (1935).
24. Johnson M. H. and Rado G. T., *Phys. Rev.* **75,** 841 (1949).
25. Johnson M. H., Rado G. T. and Maloof M., *Phys. Rev.* **71,** 322 (1947).
26. Slater J. C., *Rev. Mod. Phys.* **18,** 441 (1946).
27. Rado G. T., Johnson M. H. and Maloof M., *Rev. Sci. Instrum.* **20,** 927 (1949).
28. Rado G. T., *Trans. Inst. Radio Engrs.* (PGAP) **AP-4,** 512 (1956).
29. Scott G. G., *Phys. Rev.* **103,** 561 (1956).
    Meyer A. J. P. and Brown S., *J. Phys. Radium* **18,** 161 (1957).
30. Kondorskiy E. and Fedotov L. N., *Bull. Acad. Sci. U.S.S.R. Ser. Phys.* **16,** 432 (1952).
31. Bean C. P., *Proceedings of the Pittsburgh Conference on Magnetism and Magnetic Materials* p. 365 (1955); *Bull. Acad. Sci. U.S.S.R. Ser. Phys.* **21,** 1183 (1957).
32. Simon G., *Z. Naturforsch.* **13a,** 84 (1958).
33. Kittel C., *Phys. Rev.* **110,** 836 (1958).
34. Van Kranendonk J. and Van Vleck J. H., *Rev. Mod. Phys.* **30,** 1 (1958).
35. Whinnery J. R., Jamieson H. W. and Robbins T. E., *Proc. Inst. Radio Engrs.* **32,** 695 (1944).
36. Strachey C. and Wallis P. J., *Phil. Mag.* **37,** 87 (1946).

On the stability of non-stoichiometric compounds

(*Received* 21 *April* 1959)

In a recent letter to this journal, F. A. Kröger pointed out some of the electrical effects of non-stoichiometry.[1] In considering crystalline compounds where one of the components is present in excess of the concentration required by the simple stoichiometric ratio, several mechanisms for accomodating the excess atoms were described. The electrical consequences of these mechanisms were discussed, with the tacit assumption that the compounds, when stoichiometric, are ideal semiconductors with the exact electron-to-atom ratio required to fill their valence bands. This assumption is undoubtedly correct for the majority of semiconductors that have been investigated, and is easily seen in the *AB* compounds with the ZnS structure and with an electron-to-atom ratio of 4:1.

Attention should be called to compounds that, if stoichiometric, have electrons slightly in excess of the capacity of the valence band. These excess electrons must be accommodated in the conduction band. At temperatures below the intrinsic range, a plot of resistivity versus $1/T$ would be expected to be similar to that of a normal metal or an extrinsic semiconductor with activated donor electrons. When the intrinsic range is reached, the slope of the curve will reverse because of the increase in the number of carriers, and the material then behaves like a typical intrinsic semiconductor.

If, however, the energy gap between the valence band and the conduction band is greater than the energy involved in forming a vacancy (Schottky defect), the stoichiometric compound may not be stable; for more energy will be involved in lifting the electron over the energy gap than in creating a vacancy. The latter can be looked upon as substituting an atom that does not contribute any electrons in a site normally occupied by one that does, thereby lowering the electron-to-atom ratio of the compound. If a sufficient number of vacancies is formed, the e/a ratio may be lowered to exactly the capacity of the valence band, and it will no longer be necessary to accommodate any electrons at a higher energy level.

It is also possible that these sites are occupied by an impurity atom that may be either foreign to the compound or else a constituent atom that would not normally occupy that position. The electrons of this impurity atom will probably lie in an impurity level somewhere between the top of the valence band and the bottom of the conduction band. The presence of the foreign atom in the site may relieve, to some degree, the local strain in the structure caused by the vacancy, and thus make this impure compound the one of lower energy.

An example of a non-stoichiometric compound whose stability can be explained by the above reasoning is the mineral stromeyerite, AgCuS. If stoichiometric, stromeyerite would have eight valence electrons for every three atoms, or an e/a ratio of 2·66. Its principal Brillouin zone, determined from three strong X-ray reflections—(112), (130) and (004)—has an e/a capacity of only 2·63.[2] The next larger zone, with a capacity of 2·69, is determined from the (112) and (130) reflections alone. As the (004) is the most intense X-ray reflection, it seems likely that there is an effective energy gap between the two zones, and that the principal zone, which determines the valence band, will be filled to capacity and the excess electrons of the stoichiometric compound must be accommodated in the conduction band at a higher level.

Experimental evidence indicates that AgCuS does not exist as a stable stoichiometric compound. Schwartz[3] and Suhr[4] found from polished sections and from X-ray diffraction data that either metallic silver or Ag_3CuS_2 appeared with stromeyerite when equal atomic proportions of the elements or the sulfides were sintered together. Suhr concluded that stromeyerite is either silver-deficient or else has a structure in which some copper atoms occupy silver positions.

More recently, Djurle determined that the stable compound has atomic proportions $Ag_{0.93}Cu_{1.07}S$.[5] From the structure[2] it is evident that the copper positions are quite distinct from the silver positions, both in co-ordination number and in bond lengths. Therefore, the copper can definitely be considered as an impurity when it proxies for silver in the structure. It is therefore proposed that this non-stoichiometric composition is the stable one; because when the impurity

copper atoms, whose electrons lie in an impurity level below the conduction band, are substituted for the silver atoms, less energy is involved than the energy necessary to lift the electrons of the silver atoms from the valence band to the conduction band.

With the purpose of confirming the above proposals, the band gap energy and electrical properties of stromeyerite are being investigated. This work is supported in part by the United States Air Force on Contract A.F. 61(052)–178.

Geological Museum A. J. FRUEH, Jr.*
University of Oslo, Norway

VOL. 11 1959

References

1. KRÖGER F. A., *J. Phys. Chem. Solids* **7,** 277 (1958).
2. FRUEH A. J., *Z. Krist.* **106,** 299 (1955).
3. SCHWARTZ G. M., *Econ. Geol.* **30,** 128 (1935).
4. SUHR N., *Econ. Geol.* **50,** 347 (1955).
5. DJURLE S., *Acta Chem. Scand.* **12,** 1427 (1958).

Magnetic-dipole-induced normal mode in gadolinium iron garnet

(*Received* 30 *March* 1959)

THE magnetic properties of garnets can be calculated by the Néel model in terms of inter-sublattice and intra-sublattice exchange fields.(1) Because of the vector relation $\boldsymbol{M}\times\boldsymbol{M}=0$, the resonant frequency solutions of the dynamic equations of motion between the sub-lattices depend only on the inter-sublattice exchange fields. To obtain by resonance methods any information about the intra-sublattice exchange fields, one must be able in some way to subdivide a sublattice into distinguishable parts. It is the purpose of this note to point out that the magnetic-dipole anisotropy allows such a distinguishable decomposition.

Fig. 1 represents 1/8 of the garnet unit cube with all the oxygen removed. A particular c_i (or d_i) sublattice is defined as all the c (or d) sites contained in parallel planes one-half a unit cell spacing apart and perpendicular to one of the three crystal axes. Two of the parallel planes will contain one pair of opposite faces of the cube shown in Fig. 1. The calculation of the dipole anisotropy for these sublattices was facilitated by a table for the dipole fields at the 1/8 grid points of a simple cubic

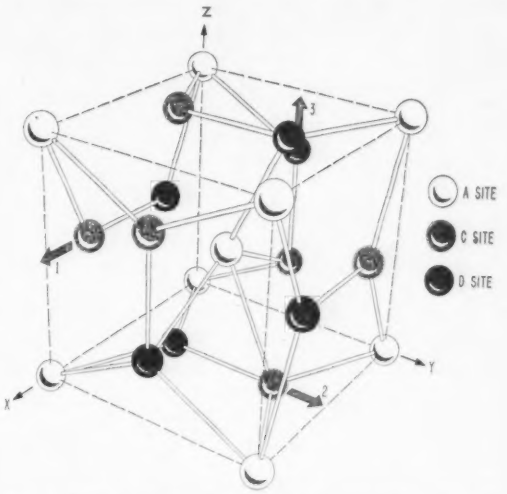

FIG. 1. The figure shown is 1/8 of a garnet unit cube with the oxygen missing.

lattice, kindly furnished to the author by L. R. WALKER, of the Bell Telephone Laboratories. The condition under which it might be possible to excite this dipole-induced mode is obviously one in which the exchange forces which act on the sublattice are not overwhelmingly larger than the dipole anisotropy fields. A favorable material for the observation of this resonance mode, then, is gadolinium iron garnet, where the c sites are relatively weakly coupled to the $a+d$ sites and the c_i and c_j coupling is even weaker.(1) The resonant frequency for the c sub-lattice mode is

$$(\omega/\gamma) = H^{E}_{c_i(a\bar{d})} - 3H^{E}_{c_ic_j},$$

where $H^{E}_{c_i(a\bar{d})}$ means the exchange field seen at the c_i sites arising from all the $a+d$ sites and similarly for $H_{c_ic_j}$. The values for these fields as a function of temperature are given graphically in reference (1). Over most of the temperature range $\omega/\gamma \simeq 4\times10^5$ G. The value of the susceptibility (χ) at this frequency is found to be given roughly by the relation

$$\chi \approx \frac{(H_{\mathrm{dip}})^2 M_{a+d}}{H_E{}^2 \Delta H} \simeq 10^{-3}$$

* Present address: Department of Geological Sciences, McGill University, Montreal, P.Q., Canada.

where (H_{dip}) is an average dipole anisotropy field arising from the c_i sub-lattices, H_E the exchange fields acting on the c_i sites, ΔH the resonant line width and M_{a+d} the magnetization of the $a+d$ sub-lattices. Methods of observing such a resonance have been previously discussed.[2]

The details of the calculations will be published as a Naval Research Laboratory Report.

U.S. Naval Research Laboratory J. I. KAPLAN
Washington 25, *D.C.*

References

1. PAUTHENET R., Thesis, Grenoble (1958).
2. KAPLAN J. and KITTEL C., *J. Chem. Phys.* **21**, 760 (1953).
SCHLÖMANN F. S., *J. Phys. Chem. Solids* **2**, 214 (1957).

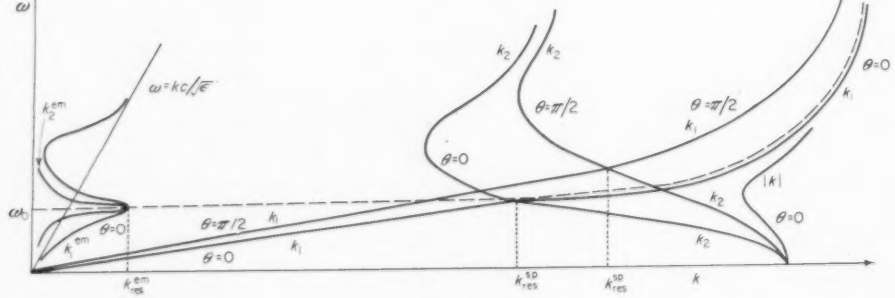

FIG. 1.

The theory of spin waves*

(*Received* 19 *February* 1959)

1. IN a previous paper[1] a single law of dispersion has been found for both spin waves and electromagnetic waves. For an extraordinary wave propagated in the direction of a static magnetic field H, it is

$$k^2 = \frac{\omega-\omega_0-j\alpha\omega+\omega^2\epsilon\beta/c^2}{2\beta}[1\pm\sqrt{(1+\chi)}], \quad (1)$$

where

$$\chi = \frac{4(\omega^2/c^2)\epsilon\beta(\gamma B+j\alpha\omega-\omega)}{(\omega-\omega_0-j\alpha\omega+\omega^2\epsilon\beta/c^2)^2}, \qquad \omega_0 = \gamma H,$$

$k = 2\pi/\lambda$ is the wave number in a ferromagnetic, $\beta = \gamma H_{ex}a^2$, H_{ex} is the effective field of the exchange forces, a the distance between neighbouring spins, $\gamma = 2{\cdot}8$ Mc/s per Oe is the magnetomechanical ratio, M_S is the saturation magnetization, $\alpha = \Delta H/H$, where ΔH is the half-width of the ferromagnetic resonance curve, and $B = H+4\pi M_S$.

When the phase velocity $v_\phi = \omega/k$ of the wave is of the order of the velocity of light $c/\sqrt{\epsilon}$, relativistic effects (displacement currents) are of importance, and equation (1) becomes the dispersion relation for electromagnetic waves found in Ref. (2):

$$k^2 = \frac{\omega^2}{c^2}\epsilon\frac{\omega-\gamma B}{\omega-\gamma H}. \quad (2)$$

For $v_\phi \ll c/\sqrt{\epsilon}$ (the static approximation), on the other hand, the exchange interaction is dominant, and equation (1) becomes, for $\alpha = 0$, the dispersion relation for spin waves

$$\omega = \omega_0+\beta k^2 \quad (3)$$

shown by the dashed line in Fig. 1.

It follows from this new approach that, for $k \to 0$, the dispersion relation (3) ceases to be valid, and is replaced by (2), so that the use in Ref. (3–7) of the relation (3) for *plane* waves with

* Reprints of this Letter are available from the translator, Dr. J. B. SYKES, 46 North Court Road, Abingdon, Berkshire, England.

VOL. 11 1959

$k \to 0$, neglecting absorption and the effects of propagation, is, strictly speaking, no more than an approximation.

2. The question arises of the exact manner in which electromagnetic waves pass into spin waves as the wavelength decreases. At first sight it might seem that, as $\lambda \to 0$, k increases, $v_\phi = \omega/k$ decreases, and the electromagnetic waves change continuously into spin waves. This conception is valid, however, only if no losses occur. In the ferromagnetics at present known, however, the losses are considerable, and in equation (1) we have $\chi \ll 1$.* As when $\alpha = 0$, the relativistic effects cease to be predominant as k increases, but their place is taken at resonance first of all by dissipation processes rather than exchange forces; the electromagnetic waves are damped, i.e. the wave amplitude falls by a factor of e over a distance less than the wavelength (k is complex; $k = k_1 - jk_2$, with $k_2 > k_1$). Only when k increases past $k_{\text{res}}^{\text{sp}}$ (Fig. 1) do dissipation processes give way to exchange interaction as the dominant effect (the spin-wave region).

3. The corresponding calculations are as follows. Expanding equation (1) as a power series in χ, we find that the double sign in front of the root gives two branches of the dispersion curve:

$$k^2 = (\omega - \omega_0 - j\alpha\omega)/\beta \quad \text{(spin branch)}, \tag{4}$$

$$k^2 = \frac{\omega^2}{c^2}\epsilon(\omega - \gamma B - j\alpha\omega)/(\omega - \omega_0 - j\alpha\omega) \tag{5}$$

(electromagnetic branch).

Fig. 1 shows the curves $k_1(\omega)$ and $k_2(\omega)$ for the two branches (4) and (5). On the left is the electromagnetic branch k^{em}, and on the right the spin branch k^{sp}. For clarity, the figure is not to scale. In the region below resonance ($\omega_0 - \omega \gg \alpha\omega$), we expand equation (5) as a power series in $\xi = \alpha\omega/(\omega_0 - \omega)$:

$$k_1 = \alpha\omega/\sqrt{[4\beta(\omega_0 - \omega)]},\ k_2 = \sqrt{\left(\frac{\omega_0 - \omega}{\beta}\right)},$$
$$\tan\delta = k_2/k_1 \gg 1. \tag{6}$$

The spin waves are damped ($k_2 > k_1$), but the damping is due to the phase relations between the field components rather than to absorption ($\tan\delta \sim 1/\alpha$).

In the resonance region ($|\omega - \omega_0| \ll \alpha\omega$), equation (4) becomes

$$k_{1,2} = \frac{1}{\sqrt{2}}\sqrt{\frac{\alpha\omega}{\beta}}\left(1 \mp \frac{\omega_0 - \omega}{2\alpha\omega}\right). \tag{7}$$

The physical cause of the damping is now absorption ($k_2 \sim \sqrt{\alpha}$) and not phase relations.

For $\omega - \omega_0 \gg \alpha\omega$ we have

$$k_1 = \sqrt{\left(\frac{\omega - \omega_0}{\beta}\right)},\ k_2 = \alpha\omega/\sqrt{[4\beta(\omega - \omega_0)]}. \tag{8}$$

The depth of penetration $\Lambda = 1/k_2$ reaches a maximum at $\omega \approx 2\omega_0$, and decreases as $\omega \to \infty$, whereas for the electromagnetic branch the maximum occurs for $\omega = 0$ or ∞.

As we see from Fig. 1, absorption separates the region of propagation of spin and electromagnetic waves by a wide interval of wave numbers $k_{\text{res}}^{\text{em}} < k < k_{\text{res}}^{\text{sp}}$ in which electromagnetic waves do not exist and spin waves are damped. In our examples we have for $Y_3Fe_2(FeO_4)_3$ $k_{\text{res}}^{\text{em}} = 480$ cm^{-1}, $k_{\text{res}}^{\text{sp}} = 4000$ cm^{-1}; for $MgO \cdot MnO \cdot Fe_2O_3$ $k_{\text{res}}^{\text{em}} \approx 10$ cm^{-1}, $k_{\text{res}}^{\text{sp}} \approx 10^5$ cm^{-1}.

The skin effect in spin waves is pronounced, and even for $Y_3Fe_2(FeO_4)_3$ the penetration depth Λ does not exceed 10^{-2} cm. In particular, for this reason spin waves are mainly generated not by the penetration of the field from the surface but by excitation throughout the volume (because of the presence of inhomogeneities of dimension $d \leqslant 1/k_{\text{res}}^{\text{sp}}$ and the non-linear relation between the spin and electromagnetic branches.[5])

4. When the wave is propagated at an arbitrary angle θ to the magnetic field H, ω and ω_0 in formulae (4)–(8) must be replaced by $\bar{\omega}$ and $\bar{\omega}_0$, where $\bar{\omega} = \sqrt{(\omega^2 + \frac{1}{4}\omega_M^2)}$, $\bar{\omega}_0 = \omega_0 + \frac{1}{2}\omega_M$, and $\omega_M = 4\pi M_S\gamma \sin^2\theta$ (except in the term $\alpha\omega$, where ω may remain). The physical picture of the transition from electromagnetic waves to spin waves is the same as for $\theta = 0$.

5. The extraordinary waves have been considered so far. The ordinary wave also has a spin branch ($k^2 = -(\bar{\omega}_0 + \bar{\omega} + j\alpha\omega)/\beta$), and the gap in wave numbers between the electromagnetic and spin branches is greater by two or three orders of

* The smallest losses occur in garnets: for a single crystal of yttrium garnet $Y_3Fe_2(FeO_4)_3$ and $f = 10^{10}$ c/s, $\Delta H \approx 0{\cdot}3$ Oe[8], but even in this case $\alpha = 10^{-4}$, $\chi < 10^{-3}$. For a polycrystalline specimen of $MgO \cdot MnO \cdot Fe_2O_3$, ΔH reaches 300 Oe[9] and $\alpha = 0{\cdot}1$, $\chi < 10^{-7}$. Thus absorption is more important than propagation effects.

magnitude than for extraordinary waves. Waves of this type are always damped ($k_2 = \sqrt{[(\tilde{\omega}_0 + \tilde{\omega})/\beta]} > k_1$).

M. A. GINTSBURG

References

1. GINTSBURG M. A., *J. exp. theor. Phys.* (*USSR*) **35,** 1047 (1958); *J. exp. theor. Phys.* (*USSR*) **35,** 730 (1959).
2. POLDER D., *Phil. Mag.* **40,** 99 (1949).
3. HERRING C. and KITTEL C., *Phys. Rev.* **81,** 869 (1951).
4. CLOGSTON A. M., SUHL H., WALKER L. R. and ANDERSON P. W., *J. Phys. Chem. Solids* **1,** 129 (1956).
5. SUHL H., *J. Phys. Chem. Solids* **1,** 209 (1957).
6. SUHL H., *Proc. Inst. Radio Engrs.* **44,** 1270 (1956).
7. WALKER L. R., *J. Appl. Phys.* **29,** 318 (1958).
8. LECRAW R. C., SPENCER E. G. and PORTER C. S., *J. Appl. Phys.* **29,** 326 (1958).
9. SENSIPER S., *Proc. Inst. Radio Engrs.* **44,** 1323 (1956).

Comments on the above letter by Dr. M. A. Gintsburg

(*Received* 1 *June* 1959)

WE have read Dr. GINTSBURG's letter with interest and welcome the opportunity to comment on it. It is our feeling that, while the usual dispersion law for plane waves should be modified for the effects of loss and propagation in the way he has indicated, such changes do not affect the situations dealt with in his References (4–7).

To clarify this opinion we consider first the relation between ω and k for propagation along the applied magnetic field, in the form

$$k^2 = \left[\frac{\omega(1-j\alpha)-\omega_0}{\beta}\right] + \left[\frac{4\pi\gamma M_0}{\beta}\,\frac{1}{\dfrac{c^2k^2}{\epsilon\omega^2}-1}\right]$$

(equivalent to GINTSBURG's solution (1)).* The first term on the right is the familiar spin-wave expression modified by loss. We ask when the second term is comparable with the first. This may happen when $|k|$ is sufficiently small provided that

$$\left|1-\frac{\omega_0}{\omega}-j\alpha\right| \sim \frac{\dfrac{4\pi\gamma M_0}{\omega}}{\left|\dfrac{c^2}{\beta\epsilon\omega}\left(1-\dfrac{\omega_0}{\omega}-j\alpha\right)-1\right|}$$

or

$$\left|1-\frac{\omega_0}{\omega}-j\alpha\right| \sim \left\{\frac{(4\pi\gamma M_0)(\gamma H_e)a^2\epsilon}{c^2}\right\}^{\frac{1}{2}}$$

since

$$\frac{c^2}{\beta\epsilon\omega} \gg 1.$$

For $Y_3Fe_2(FeO_4)_3$ the right-hand side is about $5\text{–}10\times10^{-7}$ and even for the least lossy material at present available ($\alpha \sim 10^{-5}$) the equality is never satisfied. The spin-wave formula is thus modified by loss but not by propagation. In a material with a much lower value of the product, M_0H_e, and comparable loss, propagative corrections might enter.

Suppose, however, that loss is ignored; then the spin-wave formula requires correction in a frequency range given by

$$\left|1-\frac{\omega_0}{\omega}\right| < \left\{\frac{(4\pi\gamma M_0)(\gamma H_e)a^2\epsilon}{c^2}\right\}^{\frac{1}{2}}$$

and a range of k satisfying

$$0 < |k| < \left(\sqrt{(\epsilon)}\frac{\omega}{c}\cdot\frac{1}{a}\right)^{\frac{1}{2}}\left(\frac{4\pi\gamma M_0}{\gamma H_e}\right)^{\frac{1}{2}}$$

which for $Y_3Fe_2(FeO_4)_3$ at 5 kMc corresponds to a wavelength of about 4×10^{-3} cm. Similar results follow if we examine propagation at an angle to the applied magnetic field. They may be summarized by saying that, for a given applied frequency and magnetic field, either there are no long-wavelength spin waves allowed at all or there will be a small spread of angles,

$$\delta\theta \sim \left\{\frac{(4\pi\gamma M_0)(\gamma H_e)a^2\epsilon}{c^2}\right\}^{\frac{1}{2}},$$

about some angle $\theta(\omega, \omega_0)$, in which the spin-wave spectrum from $|k| = 0$ to

$$|k| = \left(\sqrt{(\epsilon)}\frac{\omega}{c}\cdot\frac{1}{a}\right)^{\frac{1}{2}}\left(\frac{4\pi\gamma M_0}{\gamma H_e}\right)^{\frac{1}{2}}$$

will need correction for propagation.

In the cases considered in References (4–7) of

* It should be recalled that for a finite sample, $\omega_0 = \gamma H_i$, where H_i is the demagnetized d.c. field inside the sample.

VOL. 11 1959

GINTSBURG's letter it is assumed, and usually stated explicitly, that one is dealing with finite samples. These are supposed to be "electromagnetically small" in the sense that the ratio of sample dimension to electromagnetic wavelength in the sample (with the permeability taken equal to unity) is small. Under such circumstances we feel that by working directly from Maxwell's equations and the equation of motion of the magnetization, it may be shown that electromagnetic corrections are of order (sample dimensions/electromagnetic wavelength)^2, see References 1 and 2. The spectrum of disturbances in such a sample consists of plane waves, whose wavelength is so short that the shape of the boundaries affects only the over-all demagnetizing factors, and long-wavelength modes for which the boundary shape is critical. The plane waves will, unless the sample is too small, be describable by the usual spin-wave expression. The long-wavelength disturbances can be calculated magnetostatically if the sample is electromagnetically small and yet so large that exchange torques are small for wavelengths of the order of the sample size. Such disturbances may be resolved into plane waves, although this is a somewhat unnatural expansion. The distribution of such plane wave amplitudes as a function of $|k|$ will have a maximum in the neighborhood of 2π/sample dimensions. The only members of this collection of plane waves which are affected by propagation are those which lie in the very narrow angular region mentioned earlier and have a sufficiently short wavelength. We believe that the propagation correction term of order (dimension/electromagnetic wavelengths)^2 comes from integrating over this perturbed part of the spectrum.

Thus, for finite samples of the size considered in References (4–7) it appears to us that the breakdown of the usual spin-wave dispersion formula for certain critical combinations of field, frequency and direction of propagation has little over-all effect.

Bell Telephone Laboratories
Murray Hill, New Jersey

A. M. CLOGSTON
H. SUHL
L. R. WALKER

References

1. HURD R. A., *Canad. J. Phys.* **36,** 1072 (1958).
2. MERSEREAU J. E., *J. Appl. Phys.* **30,** 184*s* (1959).

Y*

Optical absorption in *n*-type gallium phosphide

(*Received* 2 *June* 1959)

INFRARED transmission measurements at room-temperature have been made between 1 and 10 μ for a number of polycrystalline *n*-type gallium phosphide specimens. The specimens were taken from solid bars which were prepared by reacting gallium with phosphorus at a pressure of 20 atm. All of the samples show a broad absorption band in the 1–4 μ region. The absorption at wavelengths $> 4\,\mu$ increases with wavelength and with the free-carrier concentration. The absorption at the longer wavelengths is typical of normal free-carrier absorption observed in many semiconductors.[1] The 1–4 μ absorption band also increases with the electron concentration and does not occur in *p*-type material. The solid curve in Fig. 1 gives the wavelength-dependence of the room-temperature absorption coefficient for a

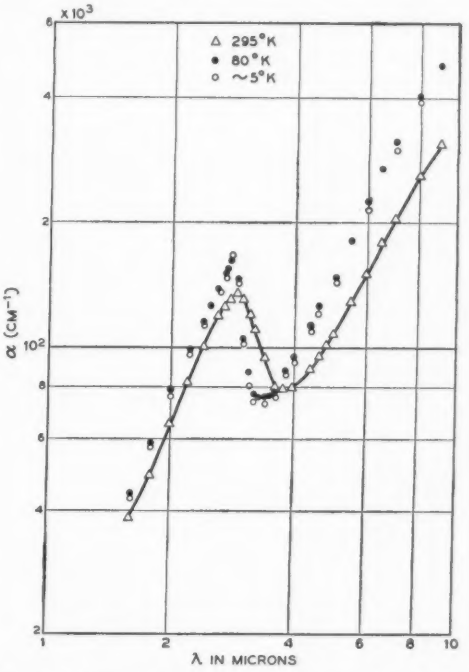

FIG. 1. Absorption coefficient versus wavelength for an *n*-type specimen of 1×10^{18} cm^{-3} carrier concentration. The data are given for three temperatures.

sample of 1×10^{18} carrier concentration. The low-energy threshold for the absorption band is $\sim 0{\cdot}31$ eV ($4{\cdot}0\,\mu$). The absorption could therefore arise from transitions between two sets of conduction-band minima with $\sim 0{\cdot}3$ eV separation. This explanation for the presence of an electronic absorption band has previously been proposed for *n*-type silicon[2] and gallium arsenide.[3]

In order to determine whether any of the different conduction-band minima are separated by

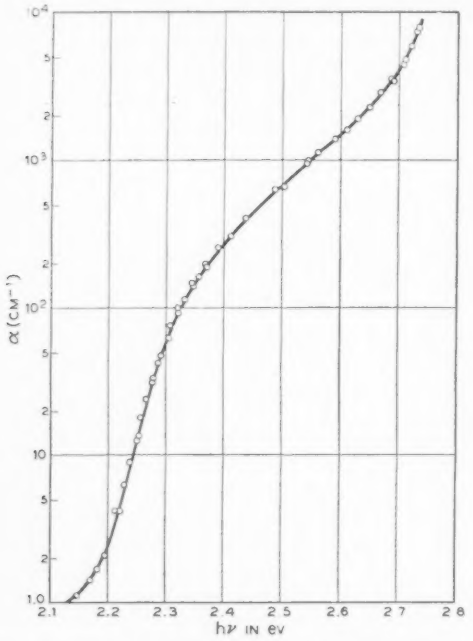

FIG. 2. Absorption coefficient as a function of photon energy for the fundamental absorption edge.

$\sim 0{\cdot}3$ eV, measurements of the fundamental absorption edge have been made. Fig. 2 shows the absorption coefficient as a function of photon energy. If the tail on the absorption edge, at the lowest values of α, is disregarded and a threshold energy ($h\nu_t$) of 2·20 eV is used, a $\log\alpha$ versus $\log(h\nu-h\nu_t)$ plot yields the curve in Fig. 3. For $10 \lesssim \alpha \lesssim 1000\ \text{cm}^{-1}$, the data satisfy a relationship of the type $\alpha \propto (h\nu-h\nu_t)^n$, where $n = 2{\cdot}2$. The value of n is close to the theoretically predicted value of 2·0 for indirect transitions.[1] This observation is consistent with the measurements reported for the effect of pressure on the absorption edge.[4] From those pressure measurements it was concluded that the deepest minima in the conduction band are in the [100] directions. If the rapid rise in absorption for $\alpha \gtrsim 10^3\ \text{cm}^{-1}$ (see Fig. 3) is interpreted as the onset of direct transitions, then the energy of separation between the [100] minima and the minimum at $k = 0$ is $\sim 0{\cdot}35$ eV.

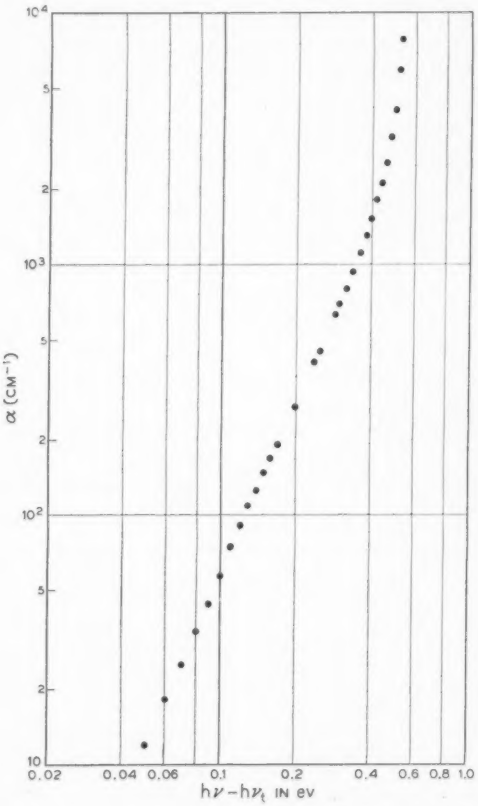

FIG. 3. Absorption coefficient of Fig. 2 at photon energy $h\nu$ as a function of $h\nu-h\nu_t$, where $h\nu_t = 2{\cdot}20$ eV. The linear portion of the curve has a slope of 2·2.

This energy is close to the threshold energy of $\sim 0{\cdot}31$ eV for the absorption band. It should be pointed out that we have neglected the effect of the distribution of carriers in the [100] minima, as well as the energy of the phonons which must accompany the electron transitions between the two portions of the conduction band. However, these energies are of the order of only a few hundredths of 1 eV.

VOL. 11 1959

Hall-coefficient and resistivity measurements as a function of temperature were made for the same material as that used in obtaining the optical data given in Fig. 1. An impurity activation energy of $\sim 0{\cdot}05$ eV was estimated from a log carrier concentration versus $1/T°K^{-1}$ plot. The carrier concentration decreased by a factor of ~ 100 between room temperature and liquid-nitrogen temperature. Therefore, at low temperature, the absorption band should be due to the excitation of the electrons from the chemical levels to the $k = 0$ minimum. In Fig. 1 a shift of the threshold to higher energy by $\sim 0{\cdot}05$ eV is observed when the specimen is cooled to low temperatures. This agreement, however, may be largely accidental, since we have neglected the possibility of a relative shift with temperature of the two minima.

An alternative, but less likely, explanation for the absorption band is that it arises from levels $\sim 0{\cdot}31$ eV below the bottom of the conduction band. These deep levels cannot be the ordinary chemical donor states responsible for the room-temperature concentration of free carriers. Since the absorption band is dependent on the carrier concentration, the $\sim 0{\cdot}31$ eV levels would have to be due to the same chemical impurity as that which is responsible for the free carriers or to some additional impurity whose density varies with carrier concentration.

Bell Telephone Laboratories
Murray Hill, New Jersey

W. G. SPITZER
M. GERSHENZON
C. J. FROSCH
D. F. GIBBS

References

1. FAN H. Y., *Rep. Progr. Phys.* **19,** 107 (1956).
2. SPITZER W. G. and FAN H. Y., *Phys. Rev.* **108,** 268 (1957).
3. SPITZER W. G. and WHELAN J. M., *Phys. Rev.* (to be published).
4. EDWARDS A. L., SLYKHOUSE T. E. and DRICKAMER H. G. (to be published).

Conductivity and structure of Bi_2Te_3*

(*Received* 8 *May* 1959; *revised* 8 *June* 1959)

IT seems worth pointing out the consistency of the model for chemical bonding of Bi_2Te_3 proposed by DRABBLE and GOODMAN[1] with the electrical-conductivity mechanism proposed by various other investigators.[2]

Roughly speaking, this mechanism is as follows: Bismuth occupies sites on the $Te^{(1)}$ or $Te^{(2)}$ sublattice acting as an acceptor, while tellurium occupies sites on the Bi sublattice acting as a donor. Thus, an excess of bismuth leads to *p*-type conductivity while an excess of tellurium leads to *n*-type conductivity. Let us now examine this mechanism in the light of Reference (1).

Consider first tellurium replacing bismuth: we note that if the former donates its $5s^25p^4$ electrons to the bonds with its three $Te^{(1)}$ and three $Te^{(2)}$ nearest neighbors, after the respective *p*- and sp^3 d^2-orbitals have been filled, there remains an unbound electron; this is equivalent to a localized energy level near the continuum of conductivity states formed from the corresponding orbitals (donor-type level).

If a Bi atom replaces a $Te^{(1)}$ atom and if the former contributes its $6p^3$ electrons to the bond with the three nearest Bi neighbors, we find one unfilled *p*-orbital; this too is equivalent to a localized energy level near the continuum of conductivity states formed from the corresponding orbitals (acceptor-type level). Again, if a Bi atom replaces a $Te^{(2)}$ atom and if the former contributes its $6s^26p^3$ electrons, we find an unfilled sp^3d^2 orbital, giving rise to an energy level of the same type as in the preceding case. At present it is still unclear which of these two levels participates more readily in *p*-type conduction phenomena.

If it is assumed that the difference in the effective electronegativities of $Te^{(1)}$ and Bi substituting for $Te^{(1)}$ is negligible, then an alternative scheme which results in only one possible acceptor-type level is as follows. Since the *p*-orbital bonds between $Te^{(1)}$ and Bi are stronger than the sp^3d^2 bonds (see reference (1)), from the energetics of the situation one may expect that when Bi replaces $Te^{(1)}$ the *p*-bonds with the neighboring Bi sites remain undisturbed at the expense of one of the sp^3d^2 orbitals. Thus the same localized level results as in the case of Bi replacing $Te^{(2)}$.

Energy Conversion Group,
Department of Electrical Engineering,
Massachusetts Institute of Technology,
Cambridge, Mass.

O. P. MANLEY

* This work has been carried out on Contract AF33(616)–3984.

References

1. DRABBLE J. R. and GOODMAN C. H. L., *J. Phys. Chem. Solids* **5**, 142 (1958).
2. KRÖGER F. A. and VINK H. J., *Solid State Physics* (Ed. F. SEITZ and D. TURNBULL) Vol. 3. Academic Press, New York (1953).

The structure of ZnSb–CdSb alloys

(*Received* 15 *June* 1959)

SEMICONDUCTING compounds ZnSb and CdSb and their alloys have received much attention recently,[1–3] so that a better knowledge of their crystal structure is desirable.

The crystal structure of pure ZnSb and CdSb is well known. According to ALMIN[4] both compounds have the same structure, viz. an orthorhombically deformed tetrahedral arrangement. Little has been published about the structure of their alloys. PILAT *et al.*[3], on the basis of measurements of the electric properties of ZnSb–CdSb alloys, postulate the existence of a ternary compound $CdZnSb_2$.

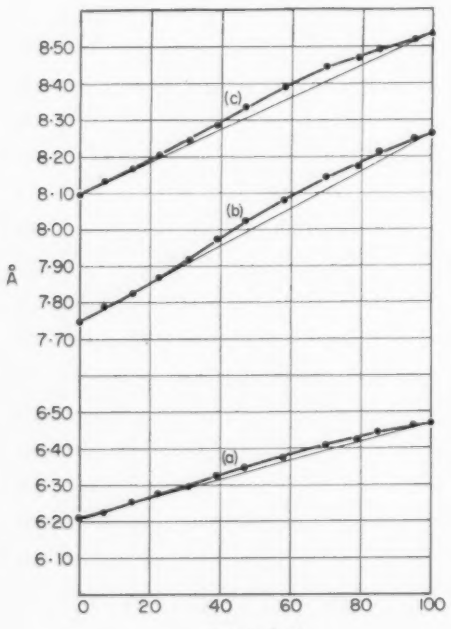

FIG. 1.

The object of the present work was to ascertain whether, and if so to what extent, there is solid solubility of each antimonide in the other and also whether there are any ternary compounds.

Alloys for X-ray analysis were prepared from pure components in evacuated and sealed silica tubes. Rapidly air-cooled alloys were reheated to 400°C and then slowly cooled to 250°C in one week. Alloys prepared in this way were pulverized and the powder was heat treated in evacuated and sealed silica tubes at 250°C for 24 hr. The composition of the homogeneous alloys was determined by chemical analysis.

X-ray analysis was done by the powder method, using Fe*K* and Cu*K* radiation. Lattice parameters were calculated by the least-squares procedure from 10–14 reflections at Bragg angles of about 45°. A continuous dependence of the lattice parameters on composition over the whole range from pure ZnSb to pure CdSb was found (Fig. 1), indicating complete solid solubility. No structural change at 50 mol. per cent CdSb, as predicted by PILAT *et al.*[3], was observed. As can be seen from Fig. 1, ZnSb–CdSb solid solutions show rather large positive deviations from Vegard's law.

The possible occurrence of ordering in alloys of intermediate compositions will be examined further.

Institute of Technical Physics K. TOMAN
Czechoslovak Academy of Sciences
Prague, Czechoslovakia

References

1. ŠMIROUS K., *Comm. Congr. Internat. Physique Etat Solide* (*Bruxelles*, 1958). Academic Press, New York (in the press).
2. JUSTI E. and NEUMANN G. Private communication.
3. PILAT I. M., CHIZH L. D. and VOYTYSHEN S., *Zh. Tekh. Fiz.* **28**, 786 (1958).
4. ALMIN K. E., *Acta Chem. Scand.* **2**, 400 (1948).

The temperature-dependence of the refractive index of silicon

(*Received* 4 *May* 1959; *revised* 6 *June* 1959)

RECENTLY a paper concerning the temperature-dependence of the refractive index of silicon appeared in this journal,[1] in which a measurement

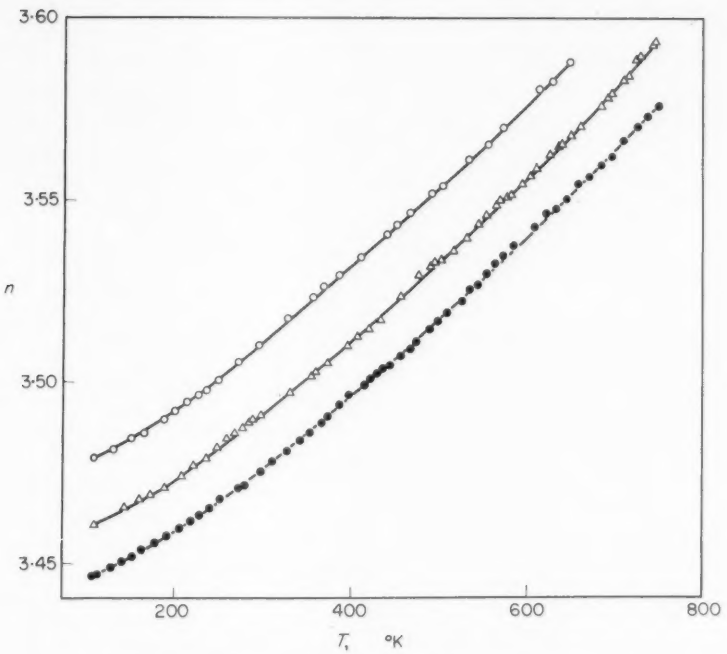

FIG. 1. Variation of the refractive index (n) for silicon with temperature (T) at three wavelengths (λ):
○——○——○ $\lambda = 1{\cdot}259\ \mu$,
△——△——△ $\lambda = 1{\cdot}407\ \mu$,
●——●——● $\lambda = 1{\cdot}564\ \mu$.

of the dependence was reported in the wavelength range 1–5μ and the temperature range 77–400°K.

We have measured the temperature-dependence of the refractive index of silicon in the wavelength range 1·1–1·8μ and the temperature range 109–750°K by the method of minimum deviation, as described earlier.[2,3] A silicon prism was prepared from a p-type single crystal with a resistivity of $\sim 380\ \Omega$ cm. The prism angle was 17° 51·4′. The error in the measurement of the deviation was about 0·3′. The corresponding error in the refractive index (n) was $\sim 0{\cdot}0004$. The temperature was determined by means of a copper Constantan thermocouple with an error of ~ 1°K in the middle of the range and ~ 2°K at the ends of the temperature range. The refractive index at room temperature agrees well with the results of SALZBERG and VILLA[4]. (Our value of n is systematically 0·0015 lower than theirs in the same wavelength range at the same temperature.) The temperature-dependence $n = f(T)$ for three wavelengths (λ) is given in Fig. 1. We can show that at temperatures $T \lesssim 170$°K the relationship $n \sim T^2$ is valid. The dependence $dn/dT = f(T)$ is shown in Fig. 2. It can be seen that the extrapolation of this curve (or rather of its straight part) to low temperatures passes through the origin at absolute zero temperature.

These results are in good agreement with ANTONČÍK's theory of the temperature-dependence of the refractive index of homopolar crystals.[5] In Fig. 3 the relationship $dn/dT = f(\lambda)$ at $T = 300$°K is compared with the theoretical curve

$$\frac{dn}{dT} = -\frac{n^2-1}{2n}\beta - \frac{1}{n}\cdot\frac{Ne^2}{\pi m}\cdot\frac{\nu_0}{(\nu_0^2-\nu^2)^2}\cdot\frac{d\nu_0}{dT}. \qquad (1)$$

This expression is applicable beyond the fundamental absorption edge of the semiconductors or

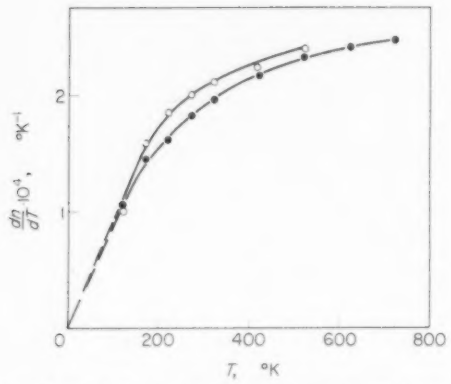

FIG. 2. Variation of the temperature coefficient of the refractive index (dn/dT) for silicon with temperature at two wavelengths:
○——○——○ $\lambda = 1{\cdot}259\ \mu$,
●——●——● $\lambda = 1{\cdot}564\ \mu$.

insulators when some assumptions made in Ref. (3) are valid.

In our case we substitute in equation (1) the values: $\nu_0 = 8{\cdot}1 \times 10^{14}\ \text{sec}^{-1}$ from Ref. (6), $d\nu_0/dT = -6{\cdot}36 \times 10^{10}\ \text{sec}^{-1}\ (°\text{C})^{-1}$ (from Ref. (7) assuming that

$$d\nu_0/dT = \frac{1}{h} \cdot \frac{dE_g}{dT},$$

at $T = 300°\text{K}$), the volume expansion coefficient $\beta = 7 \times 10^{-6}\ (°\text{C})^{-1}$ from Ref. (8) at $\sim T = 300°\text{K}$,

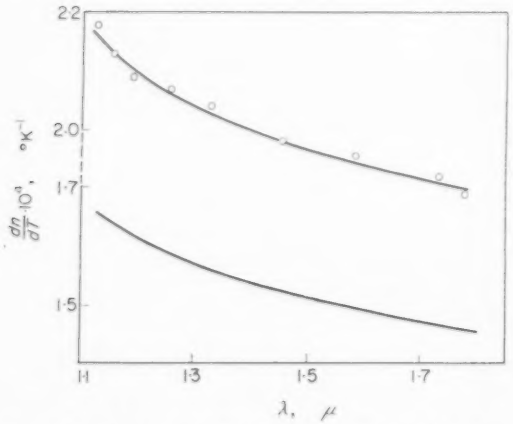

FIG. 3. Variation of dn/dT for silicon with wavelength at room temperature: ○——○——○ experimental, ——— theoretical curve calculated from equation (1).

$Ne^2/\pi m = 4{\cdot}05 \times 10^{30}\ \text{sec}^{-2}$ (N being the number of silicon atoms in 1 cm^3).

When we take into account the simplified assumptions made in Refs. (3) and (5), we can say that the agreement between the experimental and theoretical results is satisfactory—at least qualitatively.

The quantitative agreement between the results of CARDONA *et al.*[1] and our own is not very satisfactory. When we extrapolate our $1/n \cdot dn/dT$ to long wavelengths (zero frequency), we get $(4{\cdot}8 \pm 0{\cdot}2) \times 10^{-5}(°\text{C})^{-1}$ at $T = 300°\text{K}$, which is about 25 per cent higher than the average value of CARDONA *et al.* It is true that the latter value is determined as an average of the dependence $n = f(T)$ in the temperature range 77–400°K, which is certainly lower than the temperature coefficient at 300°K because of the nonlinear dependence of the refractive index on temperature. But it is unlikely that the discrepancy between these two values can be accounted for by this effect or by the errors in the results. It is to be noted that the same holds also for germanium,[2,3] the difference in this case being even greater—about 40 per cent. For the latter case the results of RANK *et al.*[9], which are ~ 10 per cent higher than ours, are also available. These discrepancies have not yet been accounted for. It is possible that free carriers affect the refractive index.

Details of this work will be published in the *Czechoslovak Journal of Physics.*

Department of Physics F. LUKEŠ
Natural Science Faculty
University of Brno
Czechoslovakia

References

1. CARDONA M., PAUL W. and BROOKS H., *J. Phys. Chem. Solids* **8,** 204 (1959).
2. LUKEŠ F., *Czech. J. Phys.* **8,** 253 (1958).
3. LUKEŠ F., *Czech. J. Phys.* **8,** 423 (1958).
4. SALZBERG C. D. and VILLA J. J., *J. Opt. Soc. Amer.* **47,** 244 (1957).
5. ANTONČÍK E., *Czech. J. Phys.* **6,** 209 (1956).
6. MOSS T. S., *Proc. Phys. Soc. Lond.* B**66,** 141 (1953).
7. MACFARLANE G. C., MCLEAN T. P., QUARRINGTON J. E. and ROBERTS V., *Phys. Rev.* **111,** 1245 (1958).
8. GIBBONS D. F., *Phys. Rev.* **112,** 136 (1958).
9. RANK D. H., BENNETT H. E. and CRONEMEYER D. C., *J. Opt. Soc. Amer.* **44,** 13 (1954).

The high-voltage photoeffect in ZnS single crystals

(*Received* 21 *June* 1959)

A NEW photovoltaic effect in ZnS single crystals has recently been observed,[1–4] which differs from the usual types in two principal ways: the photovoltage is much higher than the voltage corresponding to the energy gap and changes its sign with the wavelength of the light. In non-activated crystals, to which the present communication refers, the photovoltage has a sharp peak at a wavelength near 3400 Å. If its sign here is regarded as positive, there are on both sides of this peak regions of negative photovoltage (which we will refer to as long- and short-wavelength negative regions). Except in Reference (2), it is stressed in all the papers mentioned above that this effect is connected with the presence of stacking faults within the crystal.

There are two basic possibilities to explain this effect. We can imagine that inside the crystal an internal field is present which is additive along the crystal; this may be due either to the one-directional symmetry of the crystal (in the way suggested by CHEROFF and KELLER[2]) or to the forces acting on current carriers in the stacking faults which, according to MERZ[3], may all be additive. There are important objections to this possibility however. In fact, in this case a high voltage must exist in the dark inside the crystal that is of the same value as the observed photovoltage at high illumination (cf. Reference (5)). This voltage must be somehow compensated so that the resulting voltage observed at the ends of an unilluminated crystal is zero. This cannot be done at the contacts, where voltages only of the order of the gap can be realized.

The other possibility is a model consisting of a series of potential barriers of alternating sign inside the crystal. The observed temperature-dependence of the photovoltage and its dependence on the intensity of illumination could be explained by a model of this kind. The question is how the barriers are constructed so that the photovoltages on them do not cancel out along the crystal. The model suggested by MERZ[3] would in fact give zero photovoltage on high illumination (cf. Reference (5) for a general discussion).

The model we propose is based on the experimental facts that the effect exists only when stacking faults are present and that the gaps of the cubic $E_{G(\text{cub})}$ and hexagonal structures $E_{G(\text{hex})}$ differ by about 0·1 eV (cf. References (6), (7)). Then two further assumptions are made, the correctness of which remains to be confirmed experimentally:

(*a*) The photoeffect in the barriers between the cubic and hexagonal structures decreases sharply on the short-wavelength side.

(*b*) Inside each structure a concentration gradient of donors is present which leads to the generation of potential barriers inside the structures. These barriers are more or less similar along the crystal.

By combining the barriers at the stacking faults (corresponding to the difference in the gaps of the two structures) and the barriers due to a concentration gradient of donors, a unit can be constructed as shown in Fig. 1. In this very simple case, the

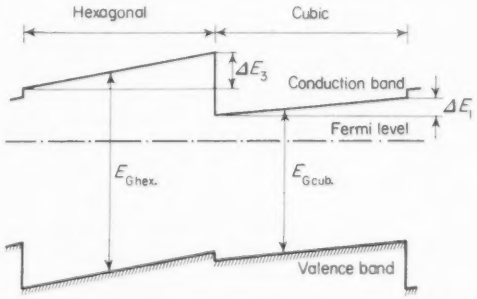

FIG. 1. An example of the band structure to explain the high-voltage photoeffect. The difference between $E_{G(\text{cub})}$ and $E_{G(\text{hex})}$ is exaggerated. The donor concentration decreases from left to right. The sign of the photovoltage is positive when the left-hand side is positive.

energy levels at the beginning of the unit are exactly the same as at the end of the unit; we can build up a series of such units and all photovoltages in them are additive.

Irradiating such a unit with photons of energy $E_{G(\text{cub})}$, we obtain a negative photovoltage which at a high illumination level has the value $-\Delta E_1/e$ (negative long-wavelength region). If we increase the energy of the photons, a photovoltage in the barriers in the stacking faults appears which is positive and attains the value $\Delta E_2/e = (E_{G(\text{hex})} - -E_{G(\text{cub})})/e > \Delta E_1/e$ (cf. References (5), (8))

(positive peak). If the photon energy is increased still further, a negative photovoltage in the barrier in the hexagonal structure appears which attains the value $-\Delta E_3/e$. At this point, the resulting photovoltage is zero: $-\Delta E_1/e+\Delta E_2/e-\Delta E_3/e=0$ (see Fig. 1). At still shorter wavelengths, $\Delta E_2/e$ decreases according to assumption (*a*) and a negative photovoltage appears again (negative short-wavelength region). It is easily seen that provided that the chief concepts are retained, one can obtain qualitatively similar results with less symmetrical structures of barriers.

The sharp decrease of the photovoltaic effect on the short-wavelength side (assumption (*a*)) has been observed in several semiconductors (e.g. PbS[9] and CdS[10]), but not yet satisfactorily explained. We suggest that with the barriers in the stacking faults this may due to their thinness. Electrons and holes with large velocities created by the absorption of high-energy photons pass through the thin barrier without any effect on its height and therefore set up no photovoltage.

It is difficult to demonstrate the plausibility of assumption (*b*). A distribution of the kind required would be realized, for example, by the following mechanism. Let us suppose that the change from the cubic to the hexagonal structure during the growth of the crystal is caused by an increase in donor concentration (or alternatively by a decrease in acceptor concentration in compensated samples). When it decreases below a certain limit, the cubic structure appears again. In such a case, the gradients in the units would be as shown in Fig. 1, supposing the crystal started to grow on the left. This example is intended to show clearly what the distribution of donors should be like rather than to suggest that such a mechanism really operates.*

The fundamental idea in the proposed model is a system of competing barriers of two types; in this way it tries to relate the high-voltage photoeffect to the conventional theory of photovoltaic effects. It accounts well for the qualitative features of the observed phenomena and gives the right order of magnitude for the photovoltage per barrier ($\sim 0{\cdot}1$ eV). It offers a plausible explanation of the pyroelectric effect observed by LEMPICKY[4]; if, when the crystal is heated, the barriers in the stacking faults tend to disappear more quickly than the concentration barriers, then a positive voltage would appear, as observed. It is hoped that the model may prove useful as a working hypothesis for further experiments aiming at elucidating the nature of the high-voltage photoeffect in ZnS.

Acknowledgements.—I wish to express my sincere thanks to Dr. S. P. KELLER, Dr. F. HERMAN, Dr. W. J. MERZ, Dr. D. NORTH, Dr. A. ROSE and Dr. H. K. HENISCH for valuable discussions, to Dr. A. LEMPICKY for making available his excellent experimental work prior to publication and to many of my colleagues in the Institute of Technical Physics for helpful suggestions.

Institute of Technical Physics J. TAUC
Czechoslovak Academy of Sciences
Prague, Czechoslovakia

References

1. ELLIS S. G., HERMAN F., LOEBNER F. E., MERZ W. J., STRUCK C. W. and WHITE J. G., *Phys. Rev.* **109,** 1860 (1958).
2. CHEROFF G. and KELLER S. P., *Phys. Rev.* **111,** 98 (1958).
3. MERZ W. J., *Helv. Phys. Acta* **31,** 625 (1958).
4. LEMPICKY A., *Bull. Amer. Phys. Soc.* **4,** No. 1, 36 (1959); *Phys. Rev.* **113,** 1204 (1959).
5. TAUC J., *Rev. Mod. Phys.* **29,** 308 (1957).
6. KRÖGER E. A., *Physica* **7,** 1 (1940).
7. BIRMAN J. L., *J. Phys. Chem. Solids* **8,** 35 (1959).
8. TAUC J. and ZÁVĚTOVÁ M., *Czech. J. Phys.* **9,** 572 (1959).
9. MITCHELL G. R. and GOLDBERG A. E., *Phys. Rev.* **93,** 1421 (1954).
10. REYNOLDS D. C., LEIES G., ANTES L. L. and MARBURGER R. E., *Phys. Rev.* **96,** 533 (1954).

* *Note added in proof:* In a recent discussion with the author, Dr. MERZ has proposed that the barriers inside the cubic and hexagonal structures may be due to intrinsic forces acting on the carriers owing to the unidirectivity of the crystal axis, as suggested by CHEROFF and KELLER[2], instead of by concentrationg radients of donors. The proposed model applies also for this case; the sign of the photovoltage is now connected with the direction of the growth of the crystal.

Some further results on ferromagnetism in relation to superconductivity

(*Received* 27 *March* 1959; *revised* 12 *May* 1959)

IN this note we report some extensions of our recent work[1] on ferromagnetism and superconductivity. Some time ago, one of the authors[2] pointed out that the superconducting transition temperature appeared to vary almost periodically with the nominal valence of the constituent atoms, attaining maxima near 3, 5 and 7 electrons per atom. No satisfactory explanation of this regularity has yet been found.

VOL. 11 1959

It occurred to us to look for a similar regularity in the variation of ferromagnetic Curie points. Unfortunately we have so far been able to try this only in the vicinity of seven valence electrons. Fig. 1 shows our results.

We made up specimens of AB_2 Laves phases in which B ranged from rhenium to platinum (where

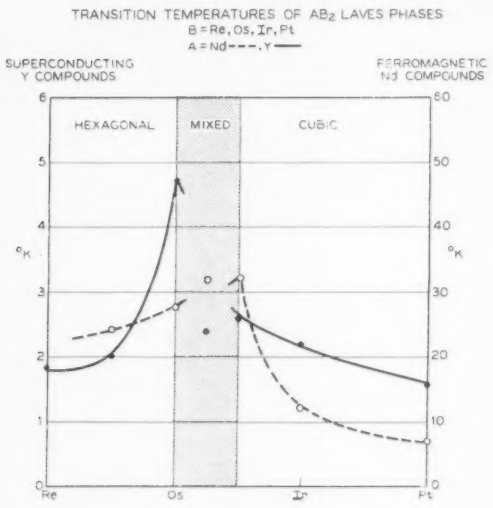

FIG. 1

necessary, via mixtures of adjacent elements), corresponding to a nominal valence variation from ~ 6 to ~ 8 valence electrons. When the A constituent was yttrium, the compounds were superconducting with a variation of transition temperature following the previously established rules. When the A constituent was neodymium, they were ferromagnetic, with Curie points varying in a similar fashion. This seems to indicate that near an average valence seven, at any rate, the valence plays a critical part, not only in superconductivity, but also in ferromagnetism, when (as is likely here) the magnetism is due to indirect exchange between magnetic ions via conduction electrons.

One point on the transition-temperature curve (just above osmium) was out of line. However, we found that in the range just above osmium, our crystals were mixed hexagonal and cubic, and a degradation of transition temperature due to structural mixture is quite common.

In regard to materials exhibiting what appears to be simultaneous ferromagnetism and superconductivity, we were able to improve on our previous results,[1] which related to the solutions $Ce_{1-x}Gd_xRu_2$, by studying the system $Y_{1-x}Gd_xOs_2$. The new results, shown in Fig. 2, represent a distinct improvement. In the first place, the

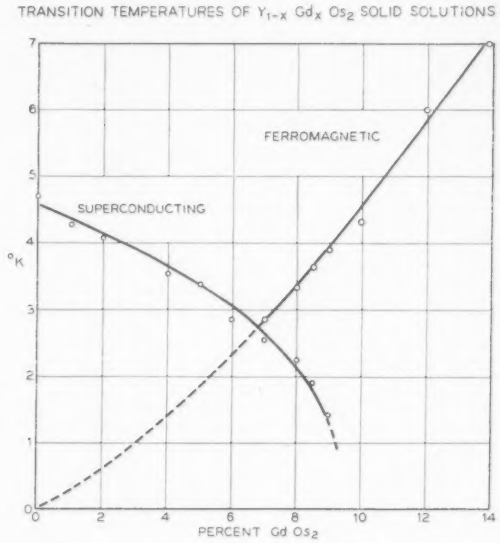

FIG. 2

effective number of valence electrons of yttrium is much less in doubt than that of cerium. Hence we obtain much better agreement of the superconducting branch with the qualitative predictions of theory,[3] in which the valence was assumed fixed. Secondly, the two branches (superconducting and ferromagnetic) overlap in a more clear-cut fashion.

The tests for superconductivity and ferromagnetism were both carried out in the same apparatus, which has been described by HULM and others.[4,5] They consist of measuring ballistically the mutual conductance of a concentric coil system, the core of which is the metal sample. In the superconducting range the mutual inductance is greatly reduced and calibration permits the superconducting volume to be evaluated. In the ferromagnetic state the opposite behavior occurs.

The ferromagnetic Curie points were determined in two ways: (1) the small field susceptibility was measured and showed a maximum in the close

vicinity of the Curie point; (2) the sample was polarized below the Curie point, which was then defined as the temperature at which the remanence disappeared. This was determined by flipping the sample in and out of the mutual inductance system with no magnetic field present, and observing the induced voltage. The two temperatures usually agreed within 1°.

In those samples that became first superconducting, the possible occurrence of ferromagnetism at a lower temperature could not be checked in the described manner. Those whose Curie points exceeded the superconducting transition temperature, however, were readily seen to become superconducting by the above method, and furthermore appeared to retain their full remanence in zero field after cooling into and reheating out of the superconducting state.

At this point we still do not know if the two phenomena coexist in the same volume element, or merely exist side by side in some kind of alternating domain pattern, involving the disappearance of ferromagnetism in part at the superconducting transition temperature.

Note added 16 *June* 1959: The magnetic saturation moment in (Y,Gd)Os_2 indicates 7 Bohr magnetons per gadolinium atom. The remanence corresponds to between 3 and 4 Bohr magnetons per gadolinium atom, varying somewhat from one sample to the next. This ferromagnetism in dilute solutions is not to be confused with the antiferromagnetism of dilute solutions of the transition elements, such as manganese in copper.[6]

Bell Telephone Laboratories
Murray Hill, N.J.

H. SUHL
B. T. MATTHIAS
E. CORENZWIT

References

1. MATTHIAS B. T., SUHL H. and CORENZWIT E., *Phys. Rev. Lett.* **1,** 449 (1958).
2. MATTHIAS B. T., *Progress in Low Temperature Physics* Vol. 2 (1957).
3. SUHL H. and MATTHIAS B. T., submitted to *Phys. Rev.*
4. HULM J. K. and MATTHIAS B. T., *Phys. Rev.* **82,** 273 (1951).
5. MATTHIAS B. T. and HULM J. K., *Phys. Rev.* **87,** 799 (1952).
6. OWEN J., BROWNE M. E., ARP V. and KIP A. F., *J. Phys. Chem. Solids* **2,** 85 (1957).
   SCHMITT R. W. and JACOBS I. S., *J. Phys. Chem. Solids* **3,** 324 (1957).

VOL
11
195

VOL.
11
1959